Related titles

Physical Properties and Applications of Polymer Nanocomposites
(ISBN: 978-0-8493-9297-9)

Nanofibers and Nanotechnology in Textiles
(ISBN: 978-1-84569-105-9)

Nanotechnology in Eco-Efficient Construction: Materials, Processes and Applications
(ISBN: 978-0-85709-544-2)

Woodhead Publishing Series in Civil and Structural Engineering: Number 62

Innovative Developments of Advanced Multifunctional Nanocomposites in Civil and Structural Engineering

Edited by

Kenneth J. Loh and Satish Nagarajaiah

Notices
Knowledge and best practice in this field are constantly changing. As new research and experience broaden our understanding, changes in research methods, professional practices, or medical treatment may become necessary.

Practitioners and researchers must always rely on their own experience and knowledge in evaluating and using any information, methods, compounds, or experiments described herein. In using such information or methods they should be mindful of their own safety and the safety of others, including parties for whom they have a professional responsibility.

To the fullest extent of the law, neither the Publisher nor the authors, contributors, or editors, assume any liability for any injury and/or damage to persons or property as a matter of products liability, negligence or otherwise, or from any use or operation of any methods, products, instructions, or ideas contained in the material herein.

For information on all Woodhead Publishing publications
visit our website at http://store.elsevier.com/

Working together
to grow libraries in
developing countries

www.elsevier.com • www.bookaid.org

List of contributors

Sergei M. Bachilo   Rice University, Houston, TX, USA

Ellie Brown   University of Texas at Arlington, Arlington, Texas, USA

Antonella D'Alessandro   University of Perugia, Perugia, Italy

Siqi Ding   School of Civil Engineering, Dalian University of Technology, Dalian, China

Sufen Dong   School of Civil Engineering, Dalian University of Technology, Dalian, China; School of Architecture and Civil Engineering, Inner Mongolia University of Science and Technology, Baotou, China

Branko Glisic   Princeton University, Princeton, NJ, USA

Sumit Gupta   University of California-San Diego, La Jolla, CA, USA

Baoguo Han   School of Civil Engineering, Dalian University of Technology, Dalian, China

Tsung-Chin Hou   National Cheng Kung University, Tainan, Taiwan

Simon Laflamme   Iowa State University, Ames, IA, USA

Bo Mi Lee   University of California-Davis, Davis, CA, USA

Hui Li   Key Lab of Structures Dynamic Behavior and Control (Harbin Institute of Technology), Ministry of Education, Harbin, China; School of Civil Engineering, Harbin Institute of Technology, Harbin, China

Kenneth J. Loh   University of California-Davis, Davis, CA, USA; University of California-San Diego, La Jolla, CA, USA

Bryan R. Loyola   Sandia National Laboratories, Livermore, CA, USA

Yi-Lung Mo   University of Houston, Houston, TX, USA

Satish Nagarajaiah   Rice University, Houston, TX, USA

Jinping Ou   Key Lab of Structures Dynamic Behavior and Control (Harbin Institute of Technology), Ministry of Education, Harbin, China; School of Civil Engineering, Harbin Institute of Technology, Harbin, China; School of Civil and Hydraulic Engineering, Dalian University of Technology, Dalian, China

Rachel Howser Roberts Energo Engineering, KBR Company, Houston, TX, USA

Navid Sakhavand Rice University, Houston, TX, USA

Rouzbeh Shahsavari Rice University, Houston, TX, USA; Smalley Institute for Nanoscale Science and Technology, Houston, TX, USA

Shengwei Sun School of Civil Engineering, Harbin Institute of Technology, Harbin, China

Peng Sun Rice University, Houston, TX, USA

Filippo Ubertini University of Perugia, Perugia, Italy

Naveen Verma Princeton University, Princeton, NJ, USA

R. Bruce Weisman Rice University, Houston, TX, USA

Huigang Xiao Key Lab of Structures Dynamic Behavior and Control (Harbin Institute of Technology), Ministry of Education, Harbin, China; School of Civil Engineering, Harbin Institute of Technology, Harbin, China

Ning Xie School of Materials Science and Engineering and Shandong Provincial Key Laboratory of Preparation and Measurement of Building Materials, University of Jinan, Jinan, Shandong, China; School of Civil Engineering, Harbin Institute of Technology, Harbin, China

Yongchao Yang Rice University, Houston, TX, USA

Hui Yao Michigan Technological University, Houghton, MI, USA; School of Traffic and Transportation Engineering, Changsha University of Science and Technology, China

Nur Yazdani University of Texas at Arlington, Arlington, Texas, USA

Zhanping You Michigan Technological University, Houghton, MI, USA

Xun Yu Department of Mechanical Engineering, New York Institute of Technology, New York, USA

Qiangqiang Zhang Key Lab of Structures Dynamic Behavior and Control (Harbin Institute of Technology), Ministry of Education, Harbin, China; School of Civil Engineering, Harbin Institute of Technology, Harbin, China

Liqing Zhang School of Civil Engineering, Dalian University of Technology, Dalian, China

Woodhead Publishing Series in Civil and Structural Engineering

Introduction to advanced nanocomposites in civil, structural, and construction engineering

Kenneth J. Loh [1,2], Satish Nagarajaiah [3]
[1]University of California-Davis, Davis, CA, USA; [2]University of California-San Diego, La Jolla, CA, USA; [3]Rice University, Houston, TX, USA

1.1 Historical perspectives

Advances in civil, structural, and construction engineering materials are one of the crucial prerequisites for the growth and expansion of human civilizations. Ancient civilizations transformed their knowledge of materials and engineering principles to build some of the greatest civil engineering marvels. The Egyptian Pyramids, Greek Temple of Artemis, Roman aqueducts, and Great Wall of China are just a few among a long list of impressive structures that mark the state of advancement and prosperity of their times. It should be recognized that the discovery and development of appropriate building materials (e.g., mortar, mud mixed with straw, and volcanic sand, among others) made these structures possible. In addition, technological and material advancements were associated with every period of human history, such as during the Middle Ages, Renaissance, and First and Second Industrial Revolutions, among others.

From the perspectives of civil, structural, and construction engineering, it can be argued that one of the key historical turning points of modern history dates back to 1824 with the invention of Portland cement by Joseph Aspdin (Hewlett, 1998). It was found that this material hardens and crystallizes to give it impressive strength. The incorporation of aggregates thereafter to create concrete, which is characterized by greater compression strengths, served as the foundation for building large-scale structures. However, it was not until the mid-nineteenth century when reinforced concrete (RC) was invented; this composite material incorporated steel reinforcement bars that provided tensile load-carrying capacity to complement the surrounding concrete's high compressive strength (Slaton, 2001). The invention of RC and other related civil, structural, and construction engineering advancements paved the way for the construction of various modern civil engineering marvels, such as the Hoover Dam and Panama Canal, to name just a few.

1.2 Multifunctional and multiscale cementitious composites

As societal needs in the late twentieth century drove the demand for higher-performance, sustainable, and resilient infrastructure systems, engineers utilized multiscale design principles for developing innovative cementitious composites. Some notable examples include the development of ultra-high-performance concrete (Wang et al., 2015), fiber-reinforced cementitious composites (FRCCs) (Brandt, 2008), and engineering cementitious composites (ECCs) (Li, 2012), to name a few. These advances embodied multiscale composite material design principles so as to achieve enhanced material performance. In the case of FRCCs and ECCs, greater ductility and strain-hardening behavior were achieved by an improved understanding of micromechanics and the incorporation of microscale fibers in the cement matrix. Not only were mechanical properties enhanced by controlling fiber−matrix interactions, fiber geometries, and fiber materials, but some studies also showed that FRCCs exhibited self-sensing and self-healing properties (Li, 2012).

The advent of new materials and characterization tools in the nanotechnology domain paved the way for the design of next-generation cementitious composites that not only were multiscale but also possessed multiple intrinsic engineering functionalities (i.e., they were multifunctional). Nanotechnology, by definition, entails the incorporation, manipulation, and control of materials with at least one dimension that is less than 100 nm (Poole and Owens, 2003). In particular, since Iijima (Iijima, 1991) discovered carbon nanotubes (CNTs) in 1991 and subsequent characterization studies revealed their impressive multifunctional properties (Baughman et al., 2002), it was only natural that the field shifted toward deriving innovative techniques for creating CNT-enhanced cementitious composites for civil, structural, and construction engineering (Parveen et al., 2013; Sobolev et al., 2006; Konsta-Gdoutos et al., 2010a,b). Like FRCCs and ECCs, these CNT-based cementitious composites sought to leverage the superior intrinsic material properties of CNTs (e.g., their Young's modulus, tensile strength, electrical conductivity, and thermal properties). Although early investigations focused on improving the bulk material's mechanical and fracture properties (Konsta-Gdoutos et al., 2010a,b), other studies explored the possibilities of creating multifunctional load-bearing cementitious composites that are also capable of self-sensing and other relevant properties (Chung, 2012).

1.3 Book outline

This book is structured into three parts that coincide with how nanotechnology has affected three main application areas in civil and construction engineering since the dawn of the twenty-first century.

The first part presents the direct incorporation of carbon-based nanomaterials in cementitious composites to obtain multifunctional construction materials that could not only resist but also self-sense the loads or deformations incurred by the structure.

Pioneering work by Sobolev et al. (2006) and Konsta-Gdoutos et al. (2010a,b) demonstrated the possibility of enhancing the properties of cementitious composites, such as concrete, with nanomaterials. This research motivated many researchers to explore other nanomaterials, such as nano-silica and nano-titanium dioxide, as additives for nanomodified concrete to improve the compressive strength and ductility of concrete. CNTs or carbon nanofibers were also used to improve the strength, modulus, and ductility of concrete by modifying the cement properties through nanomodification. CNTs were also used to make the concrete multifunctional, namely, by nanoengineering them with self-sensing, deicing, sound absorption, or damping properties, in addition to their fundamental mechanical or load-bearing property. The chapters presented in the first part of the book present recent developments in this field.

The second part is centered on pavements, which comprise one of the most frequently used civil constructions that is also often overlooked due to its pervasiveness, as well as how they can be nanoengineered for improved performance, damage sensing, self-heating, and durability. Pioneering work by Li et al. (2006, 2007) demonstrated the possibility of using nanoparticles for enhancing the fatigue performance and abrasion resistance of concrete pavement. This research motivated the development of novel cementitious materials with nanoparticles, as well as the use of other nanomaterials, for self-heating and enhanced fatigue properties of pavements. The chapters presented in the second part of the book present recent developments in this field.

The third part of this book examines recent, cutting-edge, technological advancements in nanocomposites and coatings that can be applied onto existing in-service systems or embedded within new civil infrastructure systems for sensing and structural health monitoring (SHM). Pioneering work by Li et al. (2004) and Dharap et al. (2004) demonstrated that nanofilm strain sensors designed using CNTs could sense structural strain response at the macroscale for SHM applications. This research motivated the development of strain-sensitive CNT−polymer nanofilms and nanocomposites that could be rapidly coated onto large structural surfaces or efficiently embedded in infrastructure materials, such as in cement-based materials and fiber-reinforced polymer composite structures. Hou et al. (2007) and Loh (2008) showed that techniques such as electrical impedance tomography, when coupled with multifunctional nanofilms, allowed for sensing strain at every location of the film and enabled damage detection and localization. These CNT-based nanofilms were also utilized to efficiently and effectively modify the cement−aggregate interface of mortar and concrete while achieving spatial structural sensing (Gupta et al., 2015). Most recently, promising noncontact strain-sensing technology has been developed using CNTs (less than 1% by weight), urethane coating (similar to most commercial paints), and portable laser-based near-infrared spectroscopy (Withey et al., 2012 Sun et al., 2005), which provides surface strain maps−based, randomly positioned strain measurements for detecting and locating regions of localized damage with a novel data analysis approach (Yang et al., 2015). The chapters presented in the third part of the book present recent developments in this field.

The book concludes with a brief summary of future research challenges that need to be addressed before nanotechnology and nanocomposites can be widely implemented in civil, structural, and construction engineering.

References

Baughman, R.H., Zakhidov, A.A., de Heer, W.A., 2002. Carbon nanotubes-the route towards applications. Science 297, 787−792.

Brandt, A.M., 2008. Fibre reinforced cement-based composites after over 40 years of development in building and civil engineering. Composites Structures 86 (1−3), 3−9.

Chung, D.D.L., 2012. Carbon materials for structural self-sensing, electromagnetic shielding, and thermal interfacing. Carbon 50 (9), 3342−3353.

Dharap, P., Li, Z., Nagarajaiah, S., 2004. Nanotube film based on single-wall carbon nanotubes for strain sensing. Nanotechnology 15, 378−382.

Gupta, S., Gonzalez, J., Loh, K.J., 2015. Damage detection using smart concrete engineered with nanocomposite cement-aggregate interfaces. In: Proceedings of the 10th International Workshop on Structural Health Monitoring, Stanford, CA.

Hewlett, P.C. (Ed.), 1998. Lea's Chemistry of Cement, fourth ed. Elsevier, Oxford, London.

Hou, T.-C., Loh, K.J., Lynch, J.P., 2007. Electrical impedance tomography of carbon nanotube composite materials. In: Proceedings of SPIE − Sensors and Smart Structures Technologies for Civil, Mechanical, and Aerospace Systems, San Diego, CA.

Iijima, S., 1991. Helical microtubules of graphitic carbon. Nature 354, 56−58.

Konsta-Gdoutos, M.S., Metaxa, Z.S., Shah, S.P., 2010a. Highly dispersed carbon nanotube reinforced cement based materials. Cement and Concrete Research 40 (7), 1052−1059.

Konsta-Gdoutos, M.S., Metaxa, Z.S., Shah, S.P., 2010b. Multi-scale mechanical and fracture characteristics and early-age strain capacity of high performance carbon nanotube/cement nanocomposites. Cement and Concrete Composites 32 (2), 110−115.

Li, Z., Dharap, P., Nagarajaiah, S., 2004. Carbon nanotube film sensors. Advanced Materials 16, 640−643.

Li, H., Zhang, M.-H., Ou, J.-P., 2006. Abrasion resistance of concrete containing nano-particles for pavement. Wear 260 (1−2), 1262−1266.

Li, H., Zhang, M.-H., Ou, J.-P., 2007. Flexural fatigue performance of concrete containing nano-particles for pavement. International Journal of Fatigue 29 (7), 1292−1301.

Li, V.C., 2012. Tailoring ECC for special attributes: a review. International Journal of Concrete Structures and Materials 6 (3), 135−144.

Loh, K.J., 2008. Development of Multifunctional Carbon Nanotube Nanocomposite Sensors for Structural Health Monitoring (PhD thesis). Department of Civil & Environmental Engineering, University of Michigan, Ann Arbor, MI.

Parveen, S., Rana, S., Fangueiro, R., 2013. A review on nanomaterial dispersion, microstructure, and mechanical properties of carbon nanotube and nanofiber reinforced cementitious composites. Journal of Nanomaterials 2013, 1−19, 710175.

Poole Jr., C.P., Owens, F.J., 2003. Introduction to Nanotechnology. John Wiley & Sons, Hoboken, NJ.

Slaton, A.E., 2001. Reinforced Concrete and the Modernization of American Building, 1900−1930. The Johns Hopkins University Press, Baltimore, MD.

Sobolev, K., Flores, I., Hermosillo, R., Torres-Martinez, L.M., 2006. Nanomaterials and nanotechnology for high-performance cement composites. In: Proceedings of ACI Session, Denver, CO.

Sun, Peng, Bachilo, Sergei M., Bruce Weisman, R., Nagarajaiah, Satish, 2015. Carbon Nanotubes as Non-Contact Optical Strain Sensors in Smart Skins. J. Strain Analysis for Engineering Design. http://dx.doi.org/10.1177/0309324715597414 (web-published 8/10/2015).

Wang, D., Shi, C., Wu, Z., Xiao, J., Huang, Z., Fang, Z., 2015. A review on ultra high performance concrete: Part II. hydration, microstructure and properties. Construction and Building Materials 96, 368−377.

Withey, P.A., Vemuru, V.A.M., Bachilo, S.M., Nagarajaiah, S., Weisman, R.B., 2012. Strain paint: noncontact strain measurement using single-walled carbon nanotube composite coatings. Nano Letters 12, 3497−3500.

Yang, Y., Sun, P., Nagarajaiah, S., Bachilo, S.M., Weisman, R.B., 2015. High-resolution detection of local structural damage from low-resolution random strain field measurements. (Journal paper in review).

Development of carbon nanofiber aggregate for concrete strain monitoring

2

Rachel Howser Roberts [1], Yi-Lung Mo [2]
[1]Energo Engineering, KBR Company, Houston, TX, USA; [2]University of Houston, Houston, TX, USA

2.1   Introduction

The concept of using fibers to reinforce brittle materials is not novel. In fact, it can be traced back to ancient times when straw was added to mud bricks (ACI Committee 544, 1996). The modern development of the use of fibers in the construction industry began in the 1960s with the addition of steel fibers to reinforced concrete structures. This was closely followed by the addition of polymeric fibers, glass fibers, and carbon fibers in the 1970s, 1980s, and 1990s, respectively (Li, 2002). Fibers improve brittle materials such as concrete by enhancing conductivity, tensile strength, ductility, and toughness (Chen and Chung, 1993a; Gao et al., 2009; Li et al., 2007b, 2004; Shah and Naaman, 1976).

Short-fiber composites are a type of strain sensor based on the concept of short electrically conducting fiber pull-out that accompanies slight and reversible crack opening. The electrical conductivity of the fibers enables the direct current (DC) electrical resistivity of the composites to change in response to strain damage or temperature, allowing sensing (Bontea et al., 2000; Chen and Chung, 1996; Chung, 1995; Gao et al., 2009; Li et al., 2004).

Fiber research in concrete construction is an ongoing field, and the self-sensing capabilities of carbon nanofibers (CNFs) embedded within concrete is examined in this chapter. Because of past success at the University of Houston (UH) demonstrating that self-consolidating CNF concrete (SCCNFC) can be used as a strain sensor (Gao et al., 2009; Howser et al., 2011), a CNF aggregate (CNFA) was developed that can be used to determine localized damage in concrete structures. The CNFA is $2.54 \times 2.54 \times 2.54$ cm so that it is roughly the same size as a normal aggregate found in the concrete matrix. The development of a CNFA is significant in that it is possible to use the strain-sensing capabilities of SCCNFC with a greatly reduced cost because only the CNFAs placed in the structure would contain CNFs. The CNFA is self-sensing and can be used to monitor early strength, determine the localized damage, and measure the temperature of the structure in which it is embedded. The CNFAs can be embedded in reinforced or prestressed concrete structures. This chapter will include test results in which CNFAs were embedded in concrete cylinders and tested monotonically and cyclically in axial compression.

The section will also include test results in which a system of aggregates were embedded in small-scale reinforced concrete beams.

2.2   Nanotechnology in concrete

Despite the fact that nanotechnology is a relatively recent development in scientific research, the concept was introduced in 1959 by Nobel Prize winner Richard Feynman's lecture, "There's Plenty of Room at the Bottom" (Feynman, 1960). Feynman spoke of the possibility of direct manipulation of individual atoms as a powerful form of synthetic chemistry, and decades later, the concept morphed into the field of nanotechnology. According to the National Science Foundation and National Nanotechnology Initiative, the definition of nanotechnology includes the following (Roco, 2007):

*   The size range of the material structures should be approximately 100 nm;
*   The nanotechnology should have the ability to measure or transform at the nanoscale; and
*   There should be properties that are specific to the nanoscale as compared to the macro- or micro scale.

Following this definition, in the past 25 years nanotechnology has expanded from Feynman's idea and now finds applications in fields ranging from medical devices to nano-reinforced concrete.

While nanotechnology awareness is increasing in the construction industry, practical widespread application is lacking. Bartos (2006) presents three reasons for this phenomenon:

*   The nature of the construction industry differs greatly from other industries researching nanotechnology. Final construction industry products are typically not mass-produced and require relatively long service lives, differentiating them from the products from the micro-electronics, information technology, and automotive industries.
*   Historically, there is a very low level of investment in construction research and development.
*   Research in nano-related research and development requires very high initial capital investment.

Despite these difficulties, there have been significant advances in the nanoscience of cementitious materials due to an increase in the understanding of basic phenomena in cement at the nanoscale, including structural and mechanical properties of the hydrate phases, origins of cement cohesion, cement hydration, interfaces in concrete, and mechanisms of degradation (Mondal et al., 2007; Sanchez and Sobolev, 2010). A major nanotechnology application, which is the focus of this chapter, is the inclusion of nanosized reinforcement in cement-based materials such as carbon nanotubes (CNTs) or CNFs.

2.2.1   Fiber-reinforced concrete

Concrete, composed of fine and coarse aggregates held together by a hydrated cement binder, is one of the most important construction materials because of its diverse

application in project areas, including foundations, high-rise tower components, highways, and dams. Due to hydrated cement's brittle nature and low tensile strength, reinforcement consisting typically of rebar or fibers is added to the concrete. Fibers are typically used in two forms: short randomly dispersed fibers in a cementitious matrix or a continuous mesh of fibers used in thin sheets.

Randomly dispersed fibers enhance material properties by bridging cracks. The cracking process within concrete begins with the onset of isolated nanocracks. These nanocracks grow together to form localized microcracks, which lead to macrocracks. These macrocracks widen to form cracks visible with the naked eye. Fibers arrest these cracks by forming bridges across them. With increasing tensile stress, a bond failure eventually occurs, and the fiber will pull out of the concrete, allowing the crack to widen.

2.2.2 Nano-reinforcement in cement-based materials

Since the discovery of CNTs in the 1990s (Iijima, 1991), implementation of the unique mechanical, thermal, and electronic properties of carbon-based nano-reinforcement in cement-based composites has been desirable. Single-wall CNTs (SWCNTs), multiwall CNTs (MWCNTs), and CNFs are graphene ring-based materials with aspect ratios greater than 1000 and large surface areas (Li et al., 2007a, 2005; Sanchez and Sobolev, 2010). CNTs and CNFs are extremely stiff and strong with moduli of elasticity in the range of terapascals and tensile strength on the order of gigapascals (Makar and Beaudoin, 2004; Salvetat et al., 1999; Sanchez and Sobolev, 2010). SWCNTs consist of a single graphene sheet wrapped into a seamless cylinder, whereas, as the name suggests, MWCNTs are multiple concentric sheets of graphene wrapped around a hollow core. CNFs are cylindrical nanostructures with graphene layers arranged as stacked cones, cups, or plates. CNFs are advantageous because their stacked structure presents exposed edge planes not present in CNTs that introduce increased surface area and better bond characteristics. Because of their structure, CNFs are easier to produce and cost 100 times less than SWCNTs (Kang et al., 2006). Due to the increased bond surface and lower cost, CNFs are more attractive than CNTs for application in cement-based composites.

2.2.3 CNT and CNF dispersion

The majority of nano-reinforced composite research consists of polymers containing CNTs or CNFs (Coleman et al., 2006; Makar et al., 2005; Sanchez and Sobolev, 2010). One key reason for this is because uniform dispersion is difficult in cement-based materials. Well-dispersed CNFs result in a uniform calcium–silicate–hydrate (CSH) gel formation, which improves the structural and electrical properties of the concrete (Chung, 2005). CNTs and CNFs are inherently hydrophobic and attracted to one another due to van der Waals forces, causing the fibers to agglomerate and hindering their dispersion in solvents (Baughman et al., 2002, 1999; Hilding et al., 2003; Makar and Beaudoin, 2004; Tzeng et al., 2004).

Several solutions have been proposed, including dispersing the fibers through milling, ultrasonification, high shear flow, elongational flow, functionalization, and

surfactant and chemical dispersement systems (Hilding et al., 2003; Konsta-Gdoutos et al., 2010; Woo et al., 2005; Yu and Kwon, 2012). These methods primarily fall into two categories: mechanical and chemical dispersion. The mechanical dispersion methods, such as ultrasonification, although effective in separating the fibers, can fracture them, decreasing their aspect ratio. Chemical methods use surfactants or functionalization to make the fibers less hydrophobic, reducing their tendency to agglomerate. However, many of the chemicals used can digest the fibers, reducing their effectiveness. The surfactants also often cause bubbles to form in the composite, negatively affecting the strength of the material.

Chen and his colleagues (Chen and Chung, 1993b; Chen et al., 1997) studied dispersion of carbon microfibers in cement paste. It was argued that the use of microscopy to assess the degree of fiber dispersion is tedious, difficult, and ineffective. Instead, Chen and his colleagues proposed studying the mechanical and electrical properties because both properties are negatively affected by poor dispersion. They studied the mechanical and electrical properties of cement containing carbon microfibers when methylcellulose, methylcellulose plus silica fume, and latex were each in turn added to the paste. Chen and his colleagues discovered that the addition of methylcellulose and silica fume enhanced both the electrical and mechanical properties of the material, thus aiding in the dispersion of the carbon microfibers.

Gao et al. (2009) proposed a dispersion method specifically for CNF/CNT dispersion in cement-based materials that eliminates the drawbacks mentioned here. In this method, a high-range water reducer (HRWR) is used to create a self-consolidating concrete (SCC). The American Concrete Institute (ACI) Committee 237 Self-Consolidating Concrete offers the following definition for SCC (ACI Committee 318, 2011): "Self-consolidating concrete (SCC) is highly flowable, non-segregating concrete that can spread into place, fill the formwork, and encapsulate the reinforcement without any mechanical consolidation."

SCC is a product of technological advancements in the field of underwater concrete technology, where the mixtures must ensure high fluidity and high resistance to washout and segregation. Okamura originally advocated SCC in 1986, and the first success with SCC occurred in 1988 (PCI TR-6-03, 2003). The use of SCC gained wide acceptance for savings in labor costs, shortened construction time, a better finish, and an improved work environment (Gaimster and Foord, 2000; Khayat et al., 1999; Okamura and Ozawa, 1995; Tanaka et al., 1993).

Advancement in SCC technology was due to the introduction of new chemical admixtures that improved and controlled the SCC rheological properties such as melamine, naphthalene, polycarboxylate, and acrylic-based HRWR superplasticizers and viscosity-modifying agents (VMAs).

Gao et al. (2009) proposed adding CNF to SCC because acceptable SCC is not only highly flowable, but also highly stable and homogeneous on a macro scale. The Precast/Prestressed Concrete Institute (PCI) stipulates the following criteria for SCC (PCI TR-6-03, 2003):

- Filling ability: The property that determines how fast SCC flows under its own weight and completely fills intricate spaces with obstacles, such as reinforcement, without losing its stability.

- Passing ability: The ability of SCC to pass through congested reinforcement and adhere to it without application of external energy.
- Stability: the ability of SCC to remain homogeneous by resisting segregation, bleeding, and air popping during transport and placing as well as after placement.

Gao et al. (2009) studied SCC containing CNFs to see if it was also homogeneous on the nanoscale. In Gao et al.'s mixing procedure, HRWR, water, and CNFs are mixed in a laboratory-grade blender while simultaneously fine aggregate, coarse aggregate, and cement are combined in a centrifugal mixer. The CNF mixture is then slowly added to the mixer to gain a homogeneous mix. The fresh concrete was used to create cylinders that were tested in compression. After the test, pieces of the cylinders were observed under a scanning electron microscope (SEM). The SEM showed significant CNF clumping in specimens made of normal CNF concrete and uniform distribution in SCC containing CNFs.

2.2.4 Strain-sensing ability of CNT/CNF cement-based materials

Smart materials are materials that sense their environment and respond to changes in strain, temperature, moisture, pH, and/or electric or magnetic fields. CNT/CNF composites qualify as smart materials because they can measure strain and temperature (Chung, 2000, 1995; Gao et al., 2009; Howser et al., 2011; Li et al., 2007a, 2004; Yang and Chung, 1992). There are two types of strain sensing, reversible and irreversible. The measurement of irreversible strain allows static structural health monitoring, whereas the sensing of reversible strain permits dynamic load monitoring. Structural health monitoring is the process of implementing a damage detection and characterization strategy for engineering structures. Dynamic load monitoring can detect load application and removal in real time. These are important technologies because they gauge the ability of a structure to perform its intended function despite aging, degradation, or disasters. Typically, monitoring reversible strain is more difficult because of the requirement of monitoring in real time. Additionally, reversible strain tends to be smaller than irreversible strain (Chen and Chung, 1996).

Strain sensing refers to the ability to measure an electrical or optical response corresponding to a strain. Chen and Chung (1996) give the following requirements for a structural sensor:

1. Wide strain and stress range of detection (from small strains up to failure)
2. Response is reversible upon stimulus removal (necessary for repeated use of the sensor)
3. Ease of measuring the response (without the need of expensive peripheral equipment)
4. Presence of the sensor has no negative effect on the structural properties of the structure
5. Chemical stability and durability
6. Low cost

Current commonly used strain sensors include strain gauges, fiber-optic sensors, and piezoelectric sensors; all suffer from high cost, poor durability, and the need for expensive peripheral equipment, including electronics and lasers. Due to these drawbacks, the use of sensors in civil structures is uncommon (Chen and Chung, 1996). CNT/CNF composites could become a better option as a reliable strain sensor because

the list points (1) through (5) are applicable. CNTs and CNFs are currently somewhat expensive, CNTs more so than CNFs; however, technology may provide a way to make them cheaper in the future.

Short-fiber composites were found to be a class of strain sensor based on the concept of short electrically conducting fiber pull-out that accompanies slight and reversible crack opening. For a CNT/CNF composite to have strain-sensing ability, the fibers must be more conductive than their embedded matrix, of diameter smaller than the crack length, and well dispersed. Their orientations can be random, and they do not have to touch one another (Chung, 2000, 1998, 1995). The electrical conductivity of the fibers enables the direct current (DC) electrical resistivity of the composites to change in response to strain damage or temperature, allowing sensing (Chung, 2000, 1998, 1995; Gao et al., 2009; Howser et al., 2011; Li et al., 2004; Yang and Chung, 1992).

2.2.5   Carbon fiber cement and mortar self-sensing applications

Near the time that CNTs were discovered, researchers were adding carbon microfibers to cement-based materials and studying their mechanical properties. In 1992 while studying the mechanical properties of carbon microfibers dispersed in mortar, Yang and Chung (1992) noted that the electrical resistivity of mortar containing these fibers dramatically decreased by up to several orders of magnitude.

This idea of electrically conducting concrete led Chen and Chung (1993a) to propose an intrinsically smart concrete containing carbon microfibers. Chen and Chung prepared mortar cubes containing carbon microfibers. While testing them cyclically, they discovered that the electrical resistivity of the concrete increased irreversibly upon compressive loading up to approximately one-third the compressive strength of the mortar. After this point, the resistance reversibly increased and decreased upon loading and unloading of the specimens. Chen and Chung concluded that carbon fiber−reinforced concrete serves as a smart structural material. Chen and Chung (1996) followed this experiment with a more detailed cyclic experiment on carbon microfiber mortar under cyclic loads. After this test, they concluded that the initial irreversible behavior is due to permanent damage associated with the fiber−matrix interface weakening. They attributed the reversible behavior to crack opening with fiber pull-out and crack closing with fibers pushing back in.

CNTs are the most conductive fibers presently known and are, therefore, more ideal for electrical applications than their microscale counterparts (Thess et al., 1996; Wei et al., 2001). CNTs and CNFs are also attractive for use in cement-based composites because of strength and high aspect ratios (Makar and Beaudoin, 2004; Salvetat et al., 1999; Sanchez and Sobolev, 2010). Li et al. (2007a) proposed adding MWCNTs to mortar for improved mechanical properties and confirmed that the flexural and compressive strength of the concrete was enhanced. The same group later studied the electrical volume resistivity of cement paste containing CNTs measured using the four-probe method (Narayan et al., 2004). They applied a cyclic compressive load to a $40.0 \times 40.0 \times 160.0$ mm rectangular prism made of the material. The

fractional change in the volume resistivity oscillated up to approximately 10% with the oscillation of the compressive load.

Gao et al. (2009) expanded the work on self-sensing cement-based materials by studying 152.4×305 mm cylinders made of concrete, rather than cement or mortar, containing CNFs. Gao et al. crushed the cylinders monotonically and studied the electrical resistance variation. They observed electrical resistance variations up to 80% and concluded that concrete-containing CNFs can be used for self-structural health monitoring.

Howser et al. (2011) continued Gao et al.'s work and extended it to a full-scale reinforced concrete column containing CNFs. A SCCNFC column was built and tested under a reversed cyclic load. Howser et al. examined the structural behavior and the self-sensing ability of the material. The results were compared to the structural behavior and self-sensing ability of a traditional self-consolidating reinforced concrete (SCRC) and a self-consolidating steel fiber concrete (SCSFC) specimen. In Howser et al.'s test, the peaks and valleys in the electrical resistance readings of the SCCNFC match the peaks and valleys of the applied force and the strain in the concrete. Although the peaks and valleys in the electrical resistance readings of the SCRC and SCSFC specimens occasionally matched, there was not enough correspondence to safely assume that these concretes could be used as a reversible strain sensor. It was concluded that when an appropriate dosage of CNFs is used, SCCNFC can be used for self-structural health monitoring.

From the tests performed by Gao et al. (2009) and Howser et al. (2011), it was determined that SCCNFC follows the definition for nanotechnology set forth by the National Science Foundation and National Nanotechnology Initiative (Roco, 2007). The size range of the CNFs is approximately 100 nm, the SCCNFC is able to measure damage in the composite, and the CNFs have properties that are specific to the nanoscale.

2.3   Development of the carbon nanofiber aggregate

Despite past success at the UH demonstrating that SCCNFC can be used as a strain sensor (Gao et al., 2009; Howser et al., 2011), the use of the material for full-scale infrastructure is impractical due to the high cost of CNFs. SCCNFC costs nearly 20 times as much as normal concrete. In response, a CNFA was developed to determine localized strain in concrete structures. The development of a CNFA is significant because it is possible to use the strain-sensing capabilities of SCCNFC with a greatly reduced cost because only the CNFAs placed in the structure would contain CNFs.

2.3.1   Electrical resistance measurement technique

The four-probe method was chosen to measure the electrical resistance in the CNFA specimens. In this method, current is supplied to a pair of current leads (1 and 4) and the voltage drop can be measured across the inner connections (2 and 3), as shown
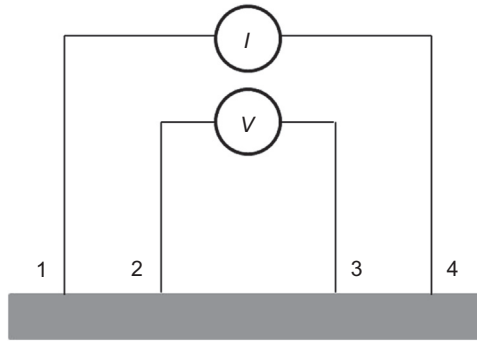
Figure 2.1 Four-probe method for determining electrical resistance.

in Figure 2.1. Since the resistance of CNFAs is much higher than the resistance of the wires, this method is quite accurate for determining the electrical resistance variation of the CNFAs.

The calculations required for this method are quite simple. One can determine the resistance using Ohm's law,

$$V = RI, \tag{2.1}$$

where:

    V: voltage (V),
    R: resistance (Ω), and
    I: current (A).

The electrical resistance variation (ERV) can be determined as

$$\text{ERV} = \frac{R_i - R_0}{R_0}, \tag{2.2}$$

where:

    ERV: electrical resistance variation,
    R_i: resistance at Step I, and
    R_0: initial resistance.

The four-probe method was accomplished by creating four steel meshes and embedding them inside of the CNFAs. Figure 2.2 shows a schematic of the CNFA with the four embedded meshes.

2.3.2 CNFA size

For size optimization, the CNFA needed to be large enough to accommodate the meshes required for the four-probe method; however, it had to be appropriately sized so that it did not cause casting problems when it was embedded in a larger structure.
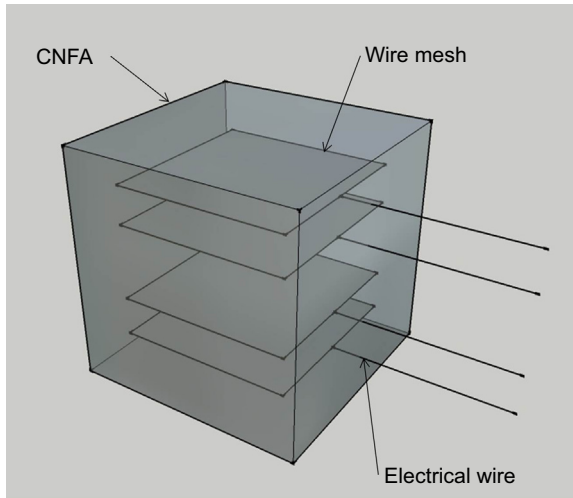
Figure 2.2 CNFA schematic.

According to the American Concrete Institute (ACI) (ACI Committee 318, 2011), the nominal maximum size of coarse aggregates shall not be larger than:

1. One-fifth the narrowest dimension between sides of forms, nor
2. One-third the depth of slabs, nor
3. Three-fourths the minimum clear spacing between individual reinforcing bars or wires, bundles of bars, individual tendons, bundled tendons, or ducts.

However, these limitations on maximum size of the aggregate may be waived if, in the judgment of the licensed design professional, the workability and methods of consolidation of the concrete are such that the concrete can be placed without honeycombs or voids. The optimal CNFA size chosen was $2.54 \times 2.54 \times 2.54$ cm. This allowed for both reasonable construction limitations as outlined by points (1) through (3) above and manageable space in which to place the four wire meshes needed for the four-probe method.

2.3.3 Mortar mix design

The CNFA is made of a CNF mortar consisting of the typical mortar ingredients of cement and fine aggregate as well as admixtures. A study was carried out to determine the optimal mix design. The first admixture was an HRWR. It was proven by Gao et al. (2009) that an HRWR capable of creating SCC also aids in the dispersion of fibers. The mortar needed to be self-consolidating so that it would flow under its own weight, flowing around the meshes without creating voids with no mechanical vibration. The second admixture was silica fume. Chen and his colleagues (Chen and Chung, 1993b; Chen et al., 1997) proved that silica fume also increases the dispersion of fibers in cement-based materials. The third admixture was the CNFs, which allow the mortar

mixture to become self-sensing. The properties of the materials used in the mix are as follows:

1. Cement: The cement used was ASTM Type III Portland cement. Type III was chosen for its decreased curing time for quicker CNFA manufacturing.
2. Fine aggregate: The fine aggregate used was Quikrete® Premium Play Sand, which is a washed, dried, and screened fine sand.
3. High-range water reducer (HRWR): Glenium® 3400 HES is a polycarboxylate admixture from BASF Chemical Co.
4. Silica fume: Rheomac® SF100 is a dry, densified silica fume admixture from BASF Chemical Co.
5. Carbon nanofibers: Pyrograf Products, Inc., PR-19-XT-LHT-OX fibers were used in this study. The specific gravity of the fibers is 0.0742. The diameter of the fibers is 149 nm and the length is 19 μm, resulting in an aspect ratio of 128. Gao et al. (2009) completed an extensive study on various CNFs and found PR-19-XT-LHT-OX fibers to have the best self-sensing behavior in concrete.

Several researchers have studied CNF concentrations in cement-based mixtures. Chen and Chung (1993a) studied the electrical and mechanical properties of carbon microfibers in concentrations of 0.5% by weight of cement. They saw a decrease in electrical resistivity of up to 83% when compared to normal concrete. Chen and Chung (1996) later studied carbon microfibers in concentrations of 0−4% by weight of cement in mortar and 0.5−3% by weight of cement in concrete. Their results showed that carbon microfibers in concrete and mortar created a reversible damage sensor by measuring the ERV. They found that increasing the fiber content in the mortar did not have appreciable effects on the change in ERV. In concrete, they found that increasing the fiber content increased the ERV. Gao et al. (2009) found that increasing the fiber content in CNF concrete by more than 0.7% by weight of cement caused fiber clumping. They found 0.7% by weight of cement was the optimal concentration. Howser et al. (2011) successfully used 0.7% CNFs by weight of cement in a reinforced concrete column test.

A study on the fiber concentration in mortar was carried out to discover the optimal concentration for the CNFAs (Howser and Mo, 2013). Over 100 CNFAs with varying percentages of CNFs were tested in compression, and the ERV was measured to find the optimal percentage. Before the test began, the CNF dispersion, or lack thereof, could be observed at some concentrations with the naked eye. Figure 2.3 shows a series of CNFAs with different CNF concentrations (i.e., 0.00%, 0.25%, 0.50%, 0.75%, 1.00%, 1.25%, 1.50%, and 1.75% by weight of cement). It can easily be seen that the color of the mortar becomes darker with each increase of CNF concentration up to 1.75%. This was caused by severe clumping of CNFs in the mortar mixture at 1.75%. At this concentration, extreme fiber clumping was observed during the casting procedure, and the CNFAs containing 1.75% by weight of cement were damaged before testing due to the clumping. Visible clumps were observed in tested CNFAs containing 1.00% CNFs by weight of cement. From this visual inspection, it was clear that the optimal concentration was likely less than 1.00% CNFs by weight of cement.

Over the course of a year, over 100 CNFAs were tested in monotonic compression. The manufacturing techniques used evolved over time, so the results from the tests are
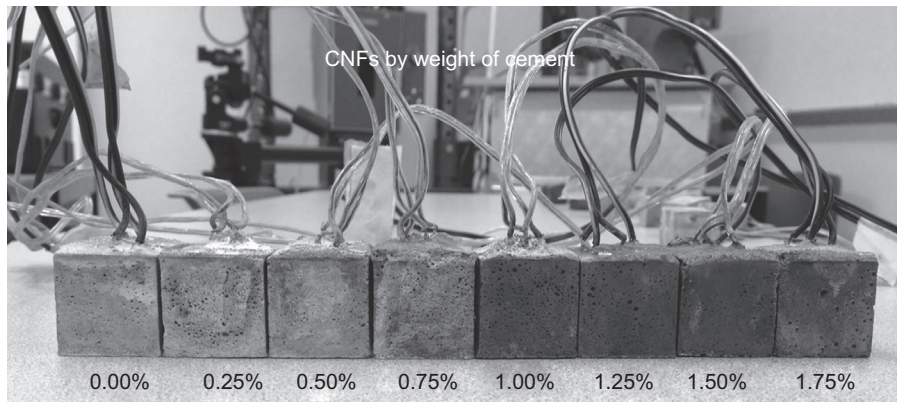
Figure 2.3 Color gradation of CNF mortar mixes.

not completely comparable; however, there is a clear trend between the concentration of CNFs per weight of cement and the maximum ERV recorded, as show in Figure 2.4. The maximum ERVs recorded for each CNF concentration were averaged, and the standard deviations were calculated. Figure 2.4 shows the average ERV plus and minus one standard deviation. Some of the variance in the results is due to the change in manufacturing practices. A CNF concentration with respect to the weight of cement of 0.70% exhibited the largest change in ERV, which matched the results found by Gao et al. (2009).

Based on results from the tests completed to determine the optimal CNF dosage, a mix design was developed to optimize the material and electrical properties. See Table 2.1 for the final CNFA mix design proportioned by the total weight of the mortar.
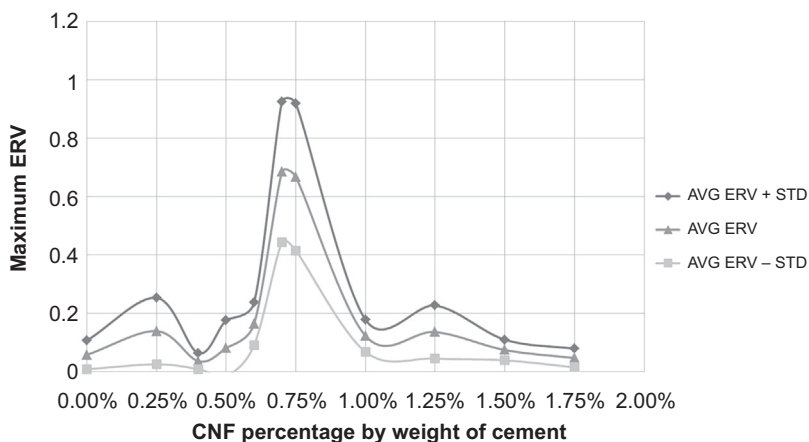
Figure 2.4 Relationship between CNF percentage and ERV.

Table 2.1 **CNFA mix design**

Material	Total mortar weight (%)
Fine aggregate	52.9
Cement	28.6
Water	12.14
Silica fume	4.29
HRWR	1.957
CNFs	0.200

2.4 Damage detection of CNFAs embedded in concrete specimens

The primary purpose for developing CNFAs is for strain monitoring. The CNF mortar is self-sensing and can be used to determine the damage in the CNFAs. The CNFAs can be embedded in reinforced or prestressed concrete structures and used to determine the localized damage in a structure. For the purpose of compressive strain monitoring, the CNFAs were embedded in concrete cylinders and tested in compression to determine a relationship between compressive strain and electrical resistance. A system of embedded CNFAs was also used for the structural health monitoring of a small-scale beam tested monotonically.

2.4.1 CNFA embedded in concrete cylinders tested in compression

2.4.1.1 Specimen construction

The goal of the experiment was to measure how the electrical resistance of an embedded CNFA varies with strain. The CNFAs were embedded in 7.62×15.24 cm cylinders. Because the electrical resistance in the CNFAs is affected by both temperature and strain, type K thermocouples were also embedded in the cylinders. A hole was drilled in the center of the cylinder molds to allow the CNFA and thermocouple wires to exit the concrete. Each mold was filled halfway with SCC, the CNFA was placed in the fresh SCC, and more SCC was placed on top. A thermocouple was epoxied to the top of the CNFAs. SCC was used because it required no mechanical vibrations. Vibrations may cause the orientation of the CNFA to change. Figure 2.5 shows a CNFA and thermocouple placed in fresh SCC.

2.4.1.2 Experimental setup

To measure the electrical resistance, the outer wires of the CNFA were connected in series with a 5.6 kΩ resistor and a 10 V power supply. The voltage drops across the
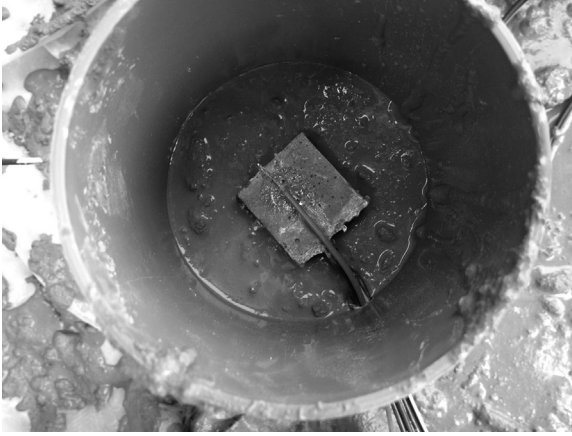
Figure 2.5 CNFA and thermocouple in fresh SCC.

inner wires of the CNFA and resistor were measured using the data acquisition system dSpace. There was an impedance problem within the data acquisition system, so differential amplifiers were placed between each component of the circuit and the data acquisition system. Figure 2.6 shows the electrical resistance measurement setup.
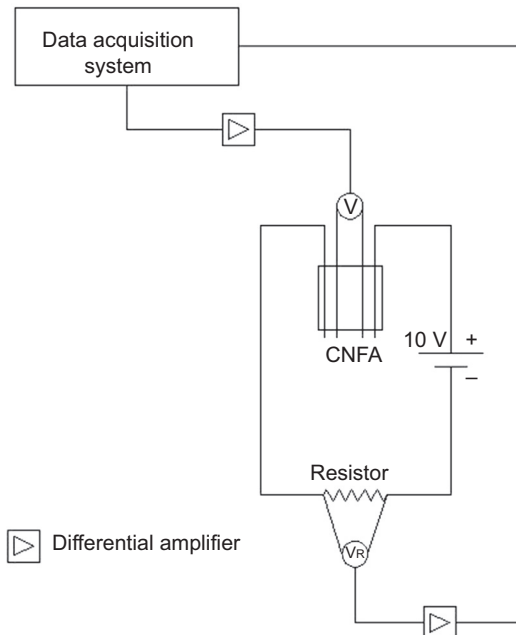
Figure 2.6 Electrical circuit and connection to data acquisition system for cylinder compression experiments.

The cylinders were tested in a Tinius Olsen Hydraulic Tester. The force was measured directly from the hydraulic tester. The strain was monitored using an extensometer, shown in Figure 2.7. The extensometer measured the smeared strain across the center 50.8 mm of the cylinder. To ensure the failure occurred in this region, steel pipe clamps were used to confine each cylinder 25.4 mm from the top and bottom, as shown in Figure 2.7.

2.4.1.3   Group 1 experimental results

Three different experimental groups with varying temperatures and load types were tested in this experiment, as shown in Table 2.2. Group 1 consisted of 12 cylinders tested in monotonic compression at room temperature. The ERV showed several definite trends across all of the cylinders. Typical stress versus time, strain versus time, ERV, and voltage variation (VV) versus time relationships for three cylinders are shown in Figure 2.8. VV is defined as the change in voltage divided by the original voltage. From the ERV curves, it is apparent when each cylinder began loading as the ERV increases from 0 simultaneously with the stress and strain. The maximum ERV occurs near a strain of 0.001 for each case. From the VV curves, failure is clearly shown by a sudden drastic change in the negative direction.

Although the trends are similar, there is considerable variation in the ERV values. Figure 2.9 shows the mean ERV versus strain relationship for the 12 tested cylinders. The standard deviation of the raw data is so large that a model would be impractical for use. A model and calibration factor were developed based on the limited data to show promise in the future use of CNFAs with acceptable variation in the results.

Figure 2.7 Cylinder compression experimental setup.

Table 2.2 Cylinder compression experimental groups

Group	Temperature range	Load type
Group 1	Room temperature	Monotonic compression
Group 2	Frozen	Monotonic compression
Group 3	Room temperature	Cyclic compression
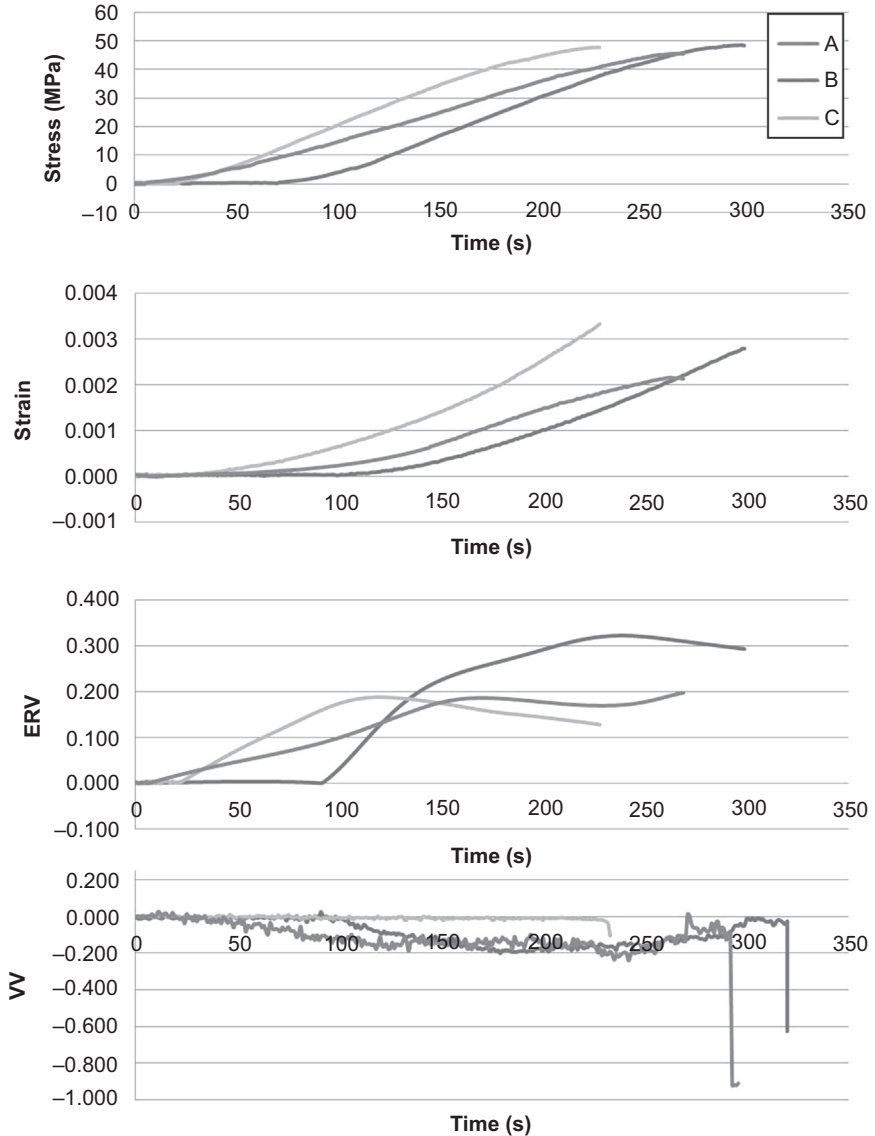
Figure 2.8 Typical stress, strain, and voltage variation (VV) ERV results for cylinders tested in compression at room temperature.
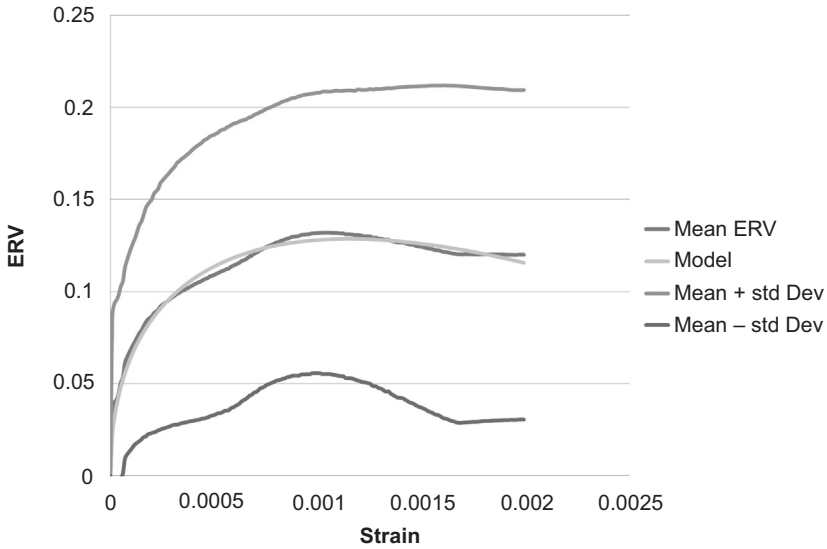
Figure 2.9 Strain versus ERV for Group 1.

Cornell's Creative Machines Lab developed a free mathematical software, Eureqa, that determines mathematical equations that describe sets of data in their simplest form (Schmidt and Lipson, 2009). The mean ERV and strain data were entered into Eureqa, and an equation was developed with a coefficient of determination of 0.985:

$$\text{ERV} = 7.59\sqrt{\varepsilon} - 112\varepsilon, \tag{2.3}$$

where:

   ERV: electrical resistance variation, and
   ε: strain.

The mathematical model is graphed in Figure 2.9.

After testing, a calibration factor was developed to reduce the variation in the tested results. The calibration factor is based from the initial slope of the ERV-versus-strain relationship. For each tested cylinder, the strain and ERV were recorded at a stress of 6.89 MPa. The calibration factor was determined as:

$$C = \frac{\text{ERV}_{c1}}{\varepsilon_{c1}}, \tag{2.4}$$

where:

   C: calibration factor;
   ERV_{c1}: calibration ERV, the ERV at a stress of 6.89 MPa; and
   ε_{c1}: calibration strain, the strain at a stress of 6.89 MPa.

Equation (2.4) was used to find the mean calibration factor for the data, which was 393. The calibration factor was added to Eqn (2.3),

$$ERV_c = \frac{C}{393}\left(7.59\sqrt{\varepsilon} - 112\varepsilon\right). \qquad (2.5)$$

The raw data can be calibrated for comparison as:

$$ERV_c = \frac{393}{C}ERV, \qquad (2.6)$$

where ERV_c is calibrated ERV.

The calibrated ERV standard deviation for each CNFA was calculated for the modeled behavior. Figure 2.10 shows the modeled behavior plus and minus one standard deviation for the calibrated CNFAs. The average coefficient of variation reduced from 77.6% for the uncalibrated CNFAs to 9.8% for the calibrated CNFAs. This shows that, in the future, CNFAs may be individually calibrated prior to embedment in concrete to achieve more consistent ERV results.

2.4.1.4 Group 2 experimental results

Because it was found that ERV can be greatly affected by cold temperatures, a series of cold to frozen cylinders was tested monotonically in compression. The mean temperature of each cylinder during testing is shown in Table 2.3. Please note that Cylinder F, although cold, was not frozen during testing. Cylinder C's
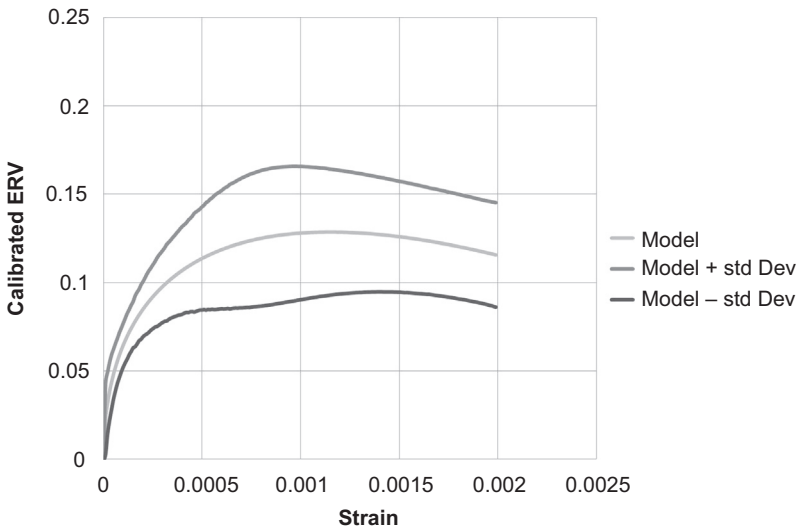
Figure 2.10 Strain versus calibrated ERV for Group 1.

Table 2.3 **Group 2 cylinder temperatures**

Cylinder	Mean temperature during testing (°C)
A	−8.24
B	−8.64
C	0.978
D	−7.41
E	−5.44
F	6.55

temperature was nearly at the freezing point and was considered frozen for the purposes of this experiment. The temperatures of the cylinders in Group 1 were also recorded for comparison purposes. The cylinders in Group 1 were all tested at approximately 22 °C.

Research in the 1960s proved that concrete is brittle at low temperatures (Lentz and Monfore, 1966; Monfore and Lentz, 1962), and this phenomenon was observed during the cylinder tests. The stress-versus-strain relationships for Group 1 exhibited an initial elastic modulus, strain softening, and failure between a strain of 0.002 and 0.003. The cylinders in Group 2 exhibited no strain softening and failed at similar stresses between a strain of 0.0015 and 0.002.

A similar phenomenon was observed in the ERV-versus-strain relationship for Group 2. The ERVs were calibrated using the same method developed for Group 1. Figure 2.11 shows the ERV-versus-strain relationships for the modeled behavior from Group 1 and the six CNFAs tested in Group 2. The relationships in Group 1 exhibited early softening behavior at a strain of about 0.0002. The five frozen cylinders maintained their original slopes until softening behavior began near a strain of 0.001. Cylinder F, which was cold but not frozen, behaved more like the modeled behavior from Group 1. Additional testing is required to extend the model to include strain and temperature effects.

2.4.1.5   *Group 3 experimental results*

Group 3 consisted of three cylinders tested cyclically. Previous work has qualitatively shown that carbon fiber cement−based composites have the potential for structural health monitoring because when the strain versus time and electrical properties for a cyclic test were plotted together, the peaks and valleys in the data sets occurred simultaneously (Chung, 2000, 1995; Howser et al., 2011). Chung (2000) measured the change in fractional resistivity, stress, and strain in a small-scale carbon fiber latex cement paste specimen. The specimen was tested cyclically in compression. Chung showed that although the electrical properties were able to detect the peaks and valleys
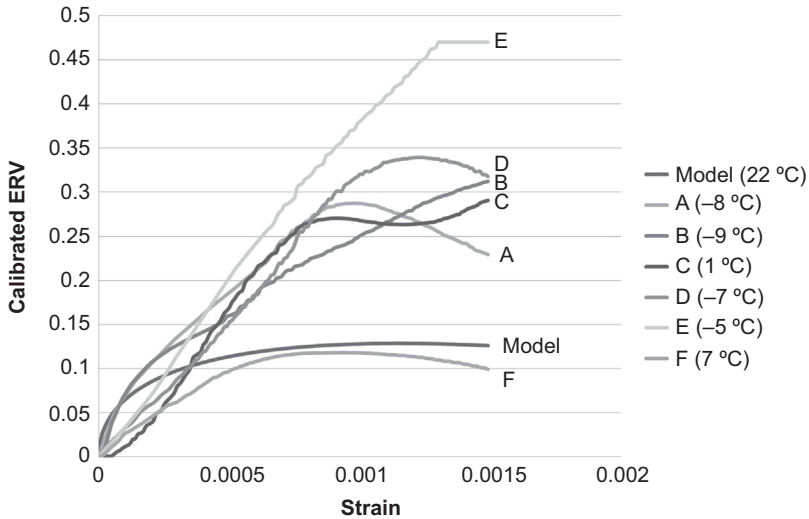
Figure 2.11 Strain versus calibrated ERV for Group 2.

in the strain, the electrical properties drifted during the experiment. Ideally, the embedded CNFAs will behave equally as well as the specimens made entirely of a carbon fiber cement composite material.

Displacement control was used to test the cylinders in Group 3. A base displacement of 0.0381 mm was chosen. Two cycles were applied at n times the base displacement, where $n = 1, 2, 3$, and so on until failure. One cycle consists of loading the cylinder in compression to the desired displacement and returning the actuator to the zero displacement position.

The results for the stresses, strains, and ERVs for Cylinders A, B, and C are shown in Figures 2.12–2.14, respectively. Qualitatively, the experiment was successful. The peaks and valleys of the stress, strain, and ERV coincide for all three cylinders. The CNFAs had a difficult time detecting the first two cycles in each test, but the strain was quite small for these cycles. The same drift behavior that was observed in Chung's experiment (2000) occurred in the present experiment.

Although three specimens were not enough to create a comprehensive model, some simple modifications were made to the model found for Group 1 in an attempt to predict the cyclic behavior of embedded CNFAs. The model is shown graphically in Figure 2.15.

Following Figure 2.15, if the embedded CNFA is loaded monotonically in compression from Points A to B, it will follow the virgin curve, which corresponds to Eqn (2.5). If the CNFA is loaded and then unloaded, following Points A, C, and D, Section AC is modeled using Eqn (2.5), and Section CD is modeled as:

$$R_u = ERV_t - \frac{2}{3} \frac{C}{393} (7.59\sqrt{\varepsilon_t} - 112\varepsilon_t), \tag{2.7}$$
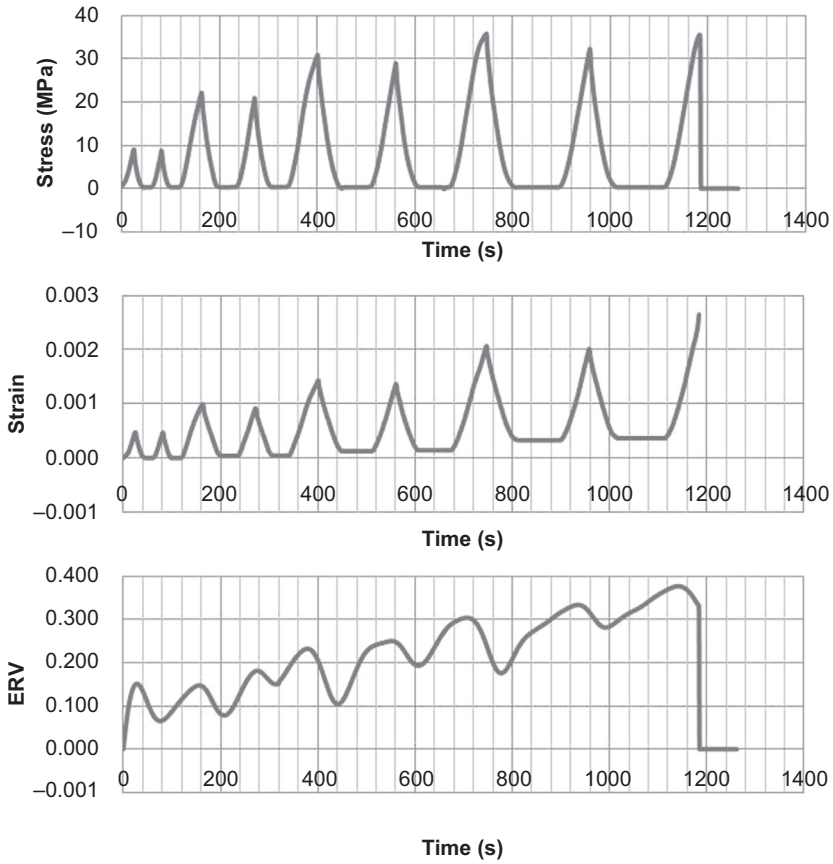
Figure 2.12 Group 3 Cylinder A stress, strain, and ERV versus time.

where:

R_u: unloading turning point factor,
ERV_t: calibrated ERV at the turning point,
C: calibration factor calculated from Eqn (2.4), and
ε_t: strain at turning point,

$$ERV_u = \frac{2}{3} \frac{C}{393} \left(7.59\sqrt{\varepsilon} - 112\varepsilon\right) + R_u, \tag{2.8}$$

where:

ERV_u: calibrated unloading ERV, and
ε: strain.
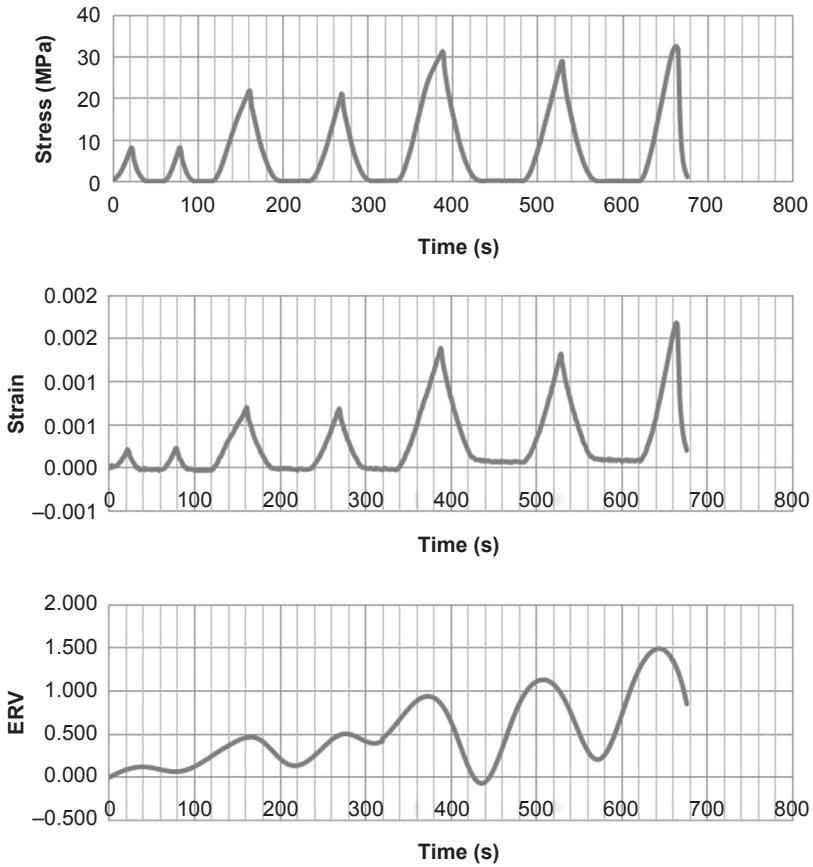
Figure 2.13 Group 3 Cylinder B stress, strain, and ERV versus time.

If the CNFA is reloaded after being unloaded, such as from Point D to E, the section is modeled as:

$$R_r = ERV_t - \frac{C}{393}\left(7.59\sqrt{\varepsilon_t} - 112\varepsilon_t\right), \tag{2.9}$$

where:

R_r: reloading turning point factor

$$ERV_r = \frac{C}{393}\left(7.59\sqrt{\varepsilon} - 112\varepsilon\right) + R_r, \tag{2.10}$$

where ERV_r is calibrated reloading ERV.
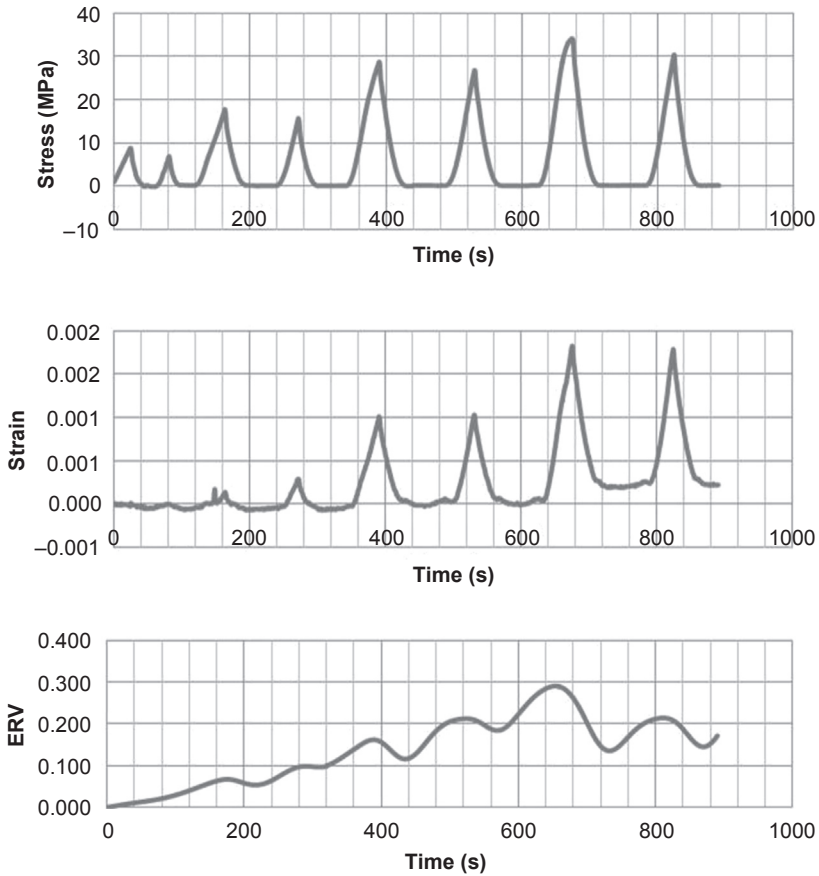
Figure 2.14 Group 3 Cylinder C stress, strain, and ERV versus time.
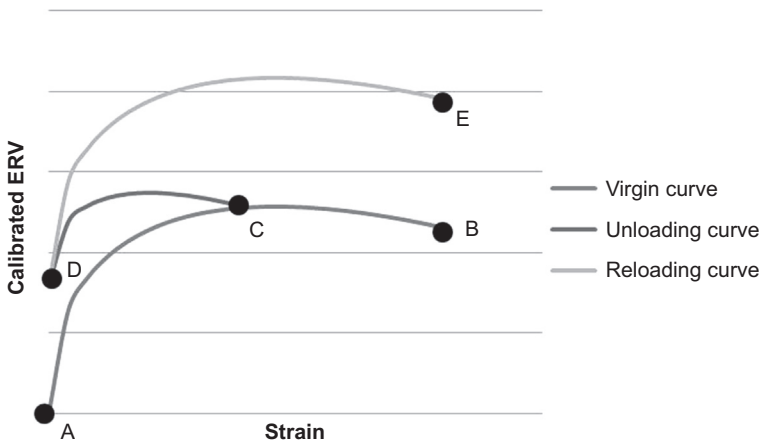
Figure 2.15 Cyclic compressive strain versus calibrated ERV model.
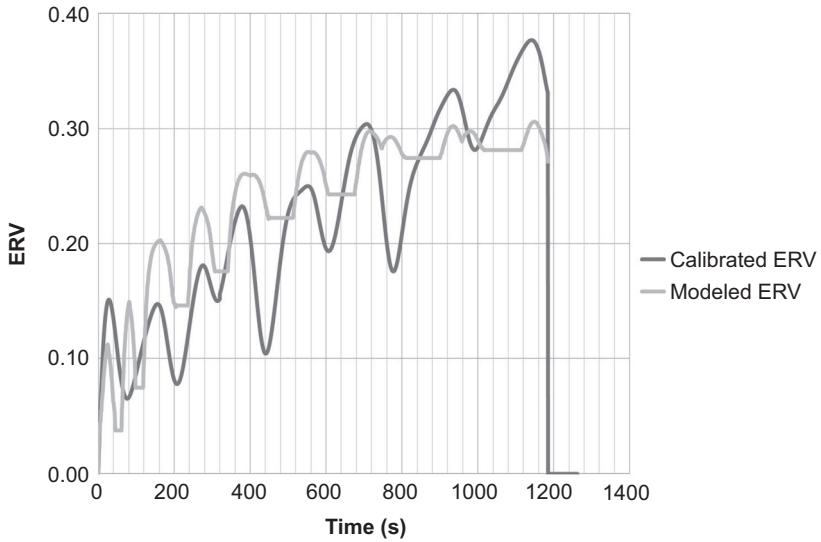
Figure 2.16 Group 3 Cylinder A calibrated and modeled ERV versus time.

All subsequent loading and reloading are modeled using Eqns (2.7)−(2.10).

The three cyclically tested CNFAs were modeled using the cyclic model with satisfactory results. Figures 2.16 and 2.17 show the calibrated and modeled ERV for Cylinder A versus time and strain, respectively. Figures 2.18−2.21 show the same relationships for Cylinders B and C, respectively.
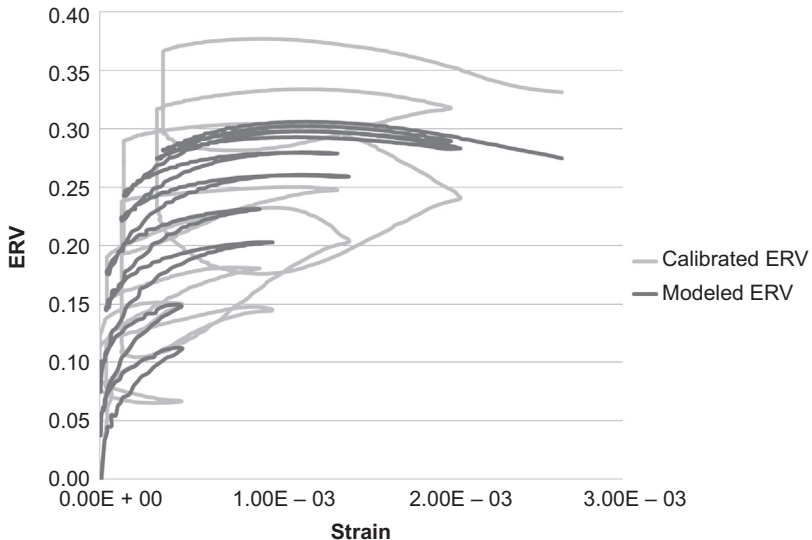
Figure 2.17 Group 3 Cylinder A calibrated and modeled ERV versus strain.
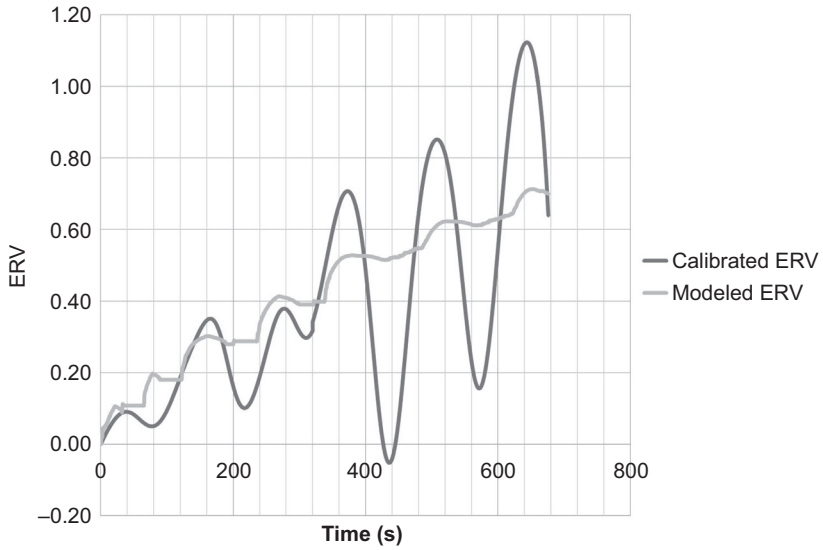
Figure 2.18 Group 3 Cylinder B calibrated and modeled ERV versus time.
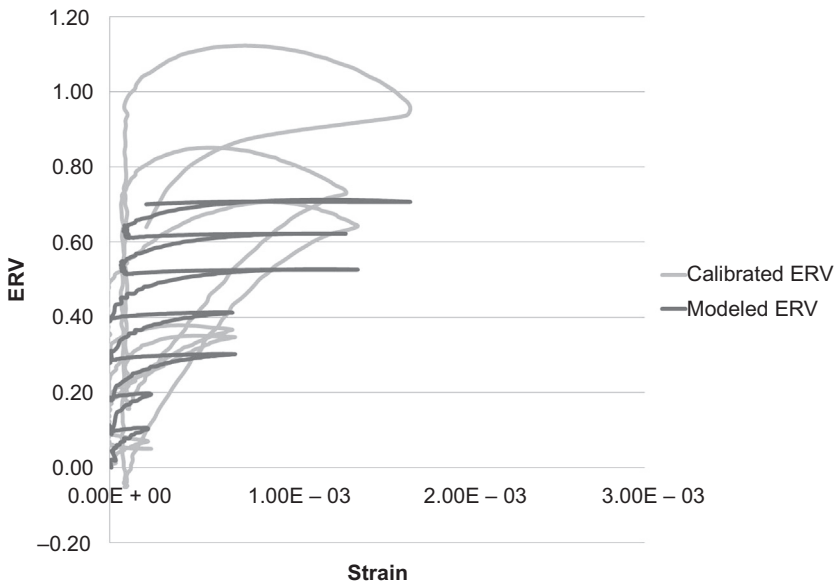
Figure 2.19 Group 3 Cylinder B calibrated and modeled ERV versus strain.
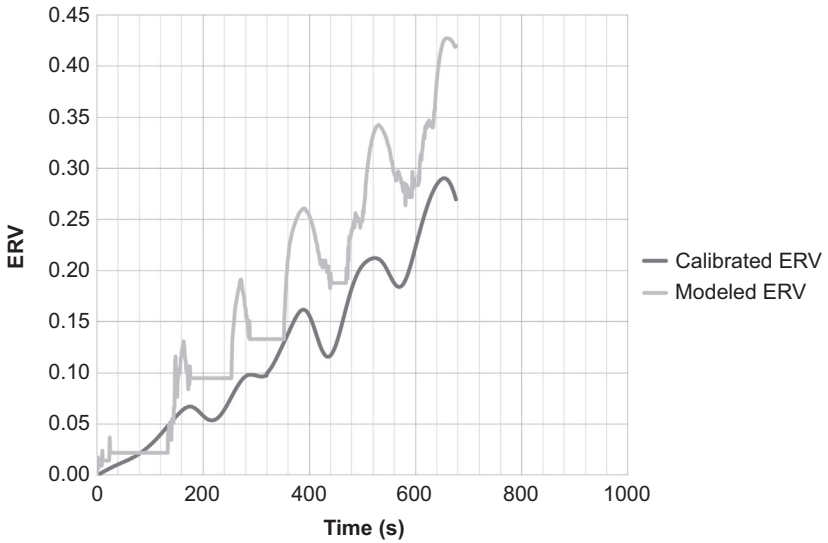
Figure 2.20 Group 3 Cylinder C calibrated and modeled ERV versus time.
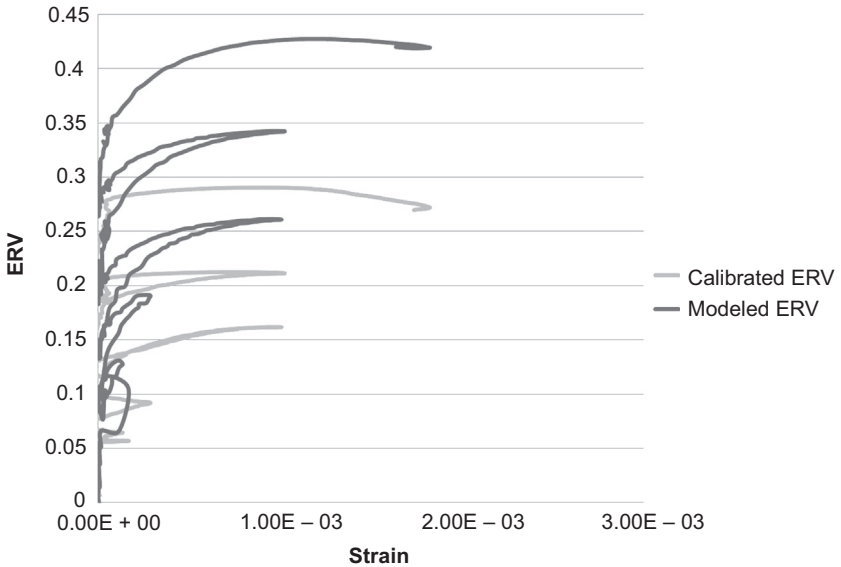
Figure 2.21 Group 3 Cylinder C calibrated and modeled ERV versus strain.

2.4.2 System of CNFAs embedded in reinforced concrete beam tested in flexure

2.4.2.1 Specimen construction

A small-scale beam was designed for the purpose of testing the application of CNFAs in a reinforced concrete structure. The cross-section of the beam was 152.4 mm square and contained three United States (US) #3 longitudinal rebar in the tension region and 2 US #2 rebar in the compression region. The beam also contained US #2 stirrups with a typical spacing of 63.5 mm. The stirrups in the central portion of the beam, where there was no shear, were placed to hold the CNFAs in place. The beam was 533 mm long. The beam cross-section and elevation view are shown in Figures 2.22 and 2.23, respectively. The beam was instrumented with six CNFAs as shown in Figures 2.22 and 2.23.

Because of the small rebar size, the stirrups were bent by hand and welded to the longitudinal reinforcement. The rebar adjacent to the CNFA locations was coated with epoxy so that the electrical properties of the rebar did not affect the electrical properties of the CNFAs. After the rebar cage was constructed, CNFAs were tied into place using zip ties. Figure 2.24 shows the installed CNFAs and the rebar cage within the formwork. SCC was used for the beam because of close rebar spacing. SCC is not as prone to honeycombing as normal concrete.

2.4.2.2 Experimental setup

To measure the electrical resistance, the outer wires of the six CNFAs were connected in series with a 5.6 kΩ resistor and a 10 V power supply, as shown in Figure 2.25. The voltage drops across the inner wires of the CNFAs and resistor were measured using the data acquisition system dSpace, also shown in Figure 2.25. There was an impedance problem within the data acquisition system, so differential amplifiers were placed between each component of the circuit and the data acquisition system, as shown in Figure 2.25.

The beam was tested in a Tinius Olsen Hydraulic Tester using the four-point bending method depicted in Figure 2.26. The four-point bending method was chosen because the moment is constant between the two loading points, where three CNFAs
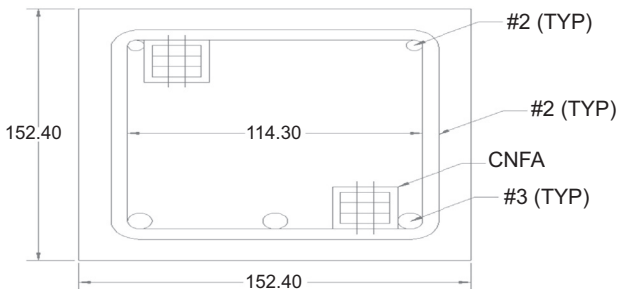
Figure 2.22 Beam cross-section (units in millimeters).
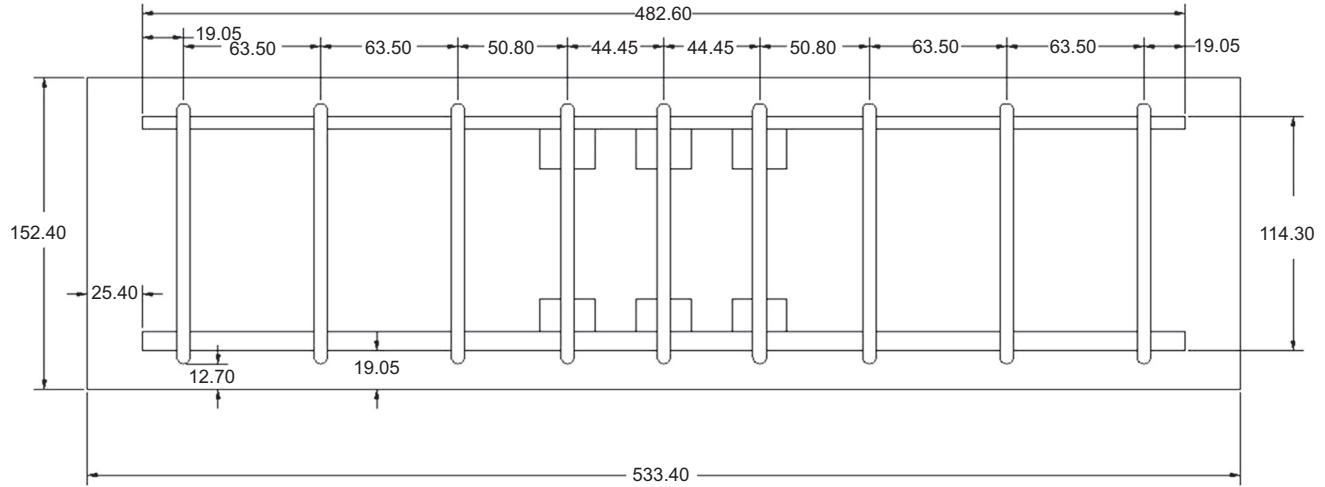
Figure 2.23 Beam elevation view (units in millimeters).
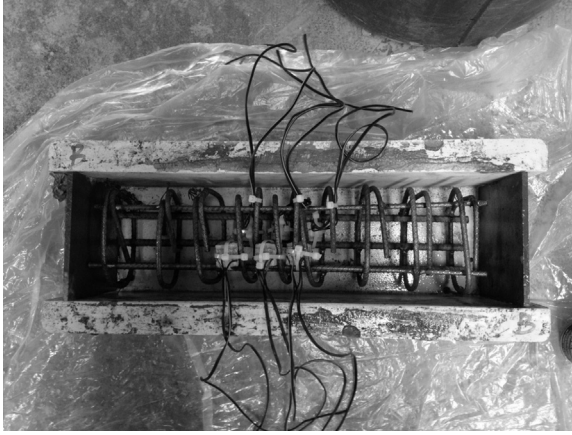
Figure 2.24 Installed CNFAs and rebar cage in formwork.
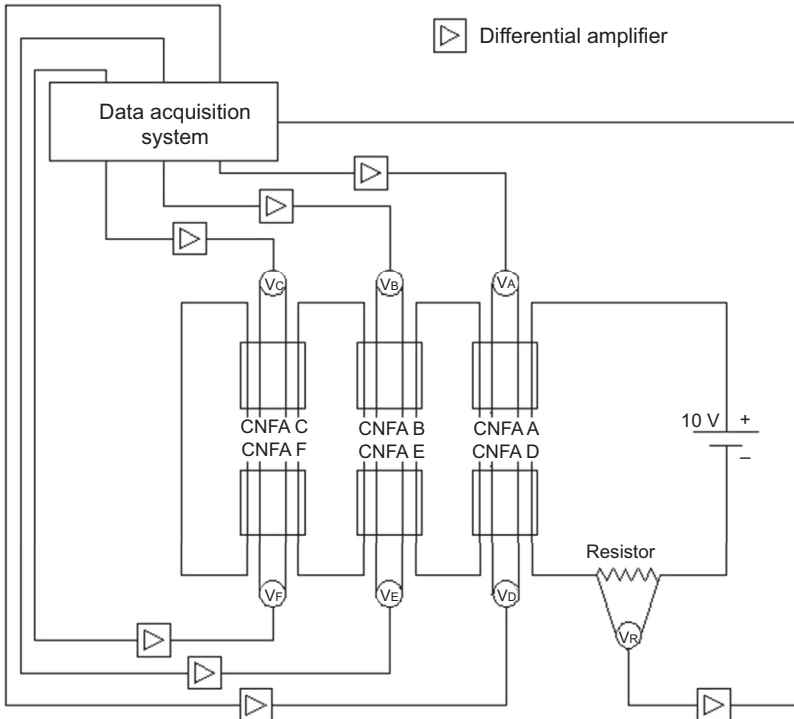
Figure 2.25 Electrical circuit and connection to data acquisition system for beam experiment.
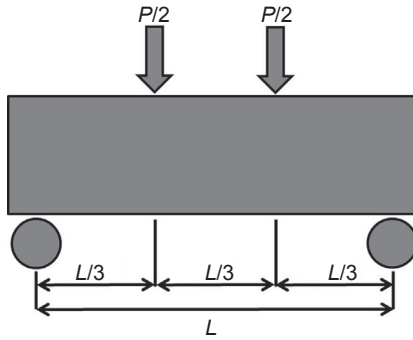
Figure 2.26 Four-point bending method.
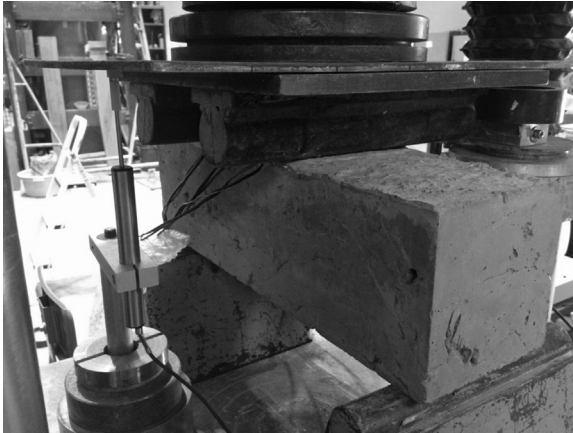
Figure 2.27 Beam experimental setup.

were placed in both the compression and tension regions. In Figure 2.26, the span L is 457 mm and P is the total force. The force was measured directly from the Tinius Olsen Hydraulic Tester. The displacement was monitored using two linear variable differential transformers (LVDTs). The experimental setup is shown in Figure 2.27.

2.4.2.3 Experimental results

The beam was expected to fail in flexure and crushing similarly to the previously tested small-scale reinforced concrete beam shown in Figure 2.28; however, the concrete strength was 70% higher than expected and the beam failed in shear, as shown in Figure 2.29. Figure 2.30 shows the force-versus-displacement relationship of the beam.

The sensors were embedded in the flexure critical region rather than the shear critical region, so the collected data were not ideal. For simplicity, the strains were

Figure 2.28 Previously tested reinforced concrete beam with flexural and crushing failure modes.
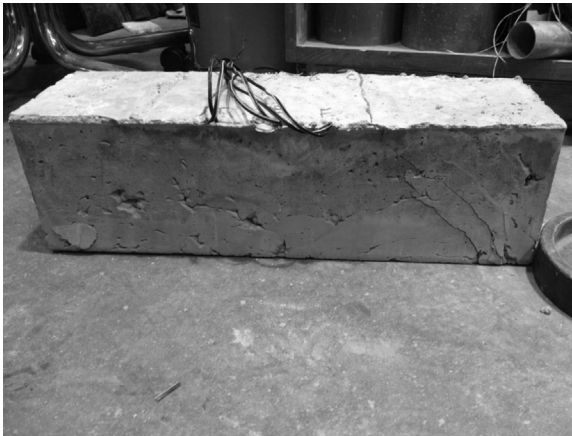
Figure 2.29 Tested reinforced concrete beam with shear failure mode.

calculated using Euler−Bernoulli beam theory (Timoshenko, 1953). The flexural strains were very low at failure, and the CNFAs are less stable at low strains. The ERVs were calibrated based on their initial ERV-versus-strain relationship. Figure 2.31 shows the calibrated ERV-versus-strain relationship. The calibration factor specifies that the calibration factor should be calculated at a stress of 6.89 MPa; however, the three CNFA in the compression region, CNFAs A, B, and C, did not reach a stress of 6.89 MPa during the test. Their maximum stress was 3.29 MPa. They were cali-brated at a stress of 2.07 MPa. The strain in the compression region was so small that no conclusions could be determined on the appropriateness of the compression model. The three CNFAs in the tension region, CNFAs D, E, and F, were calibrated
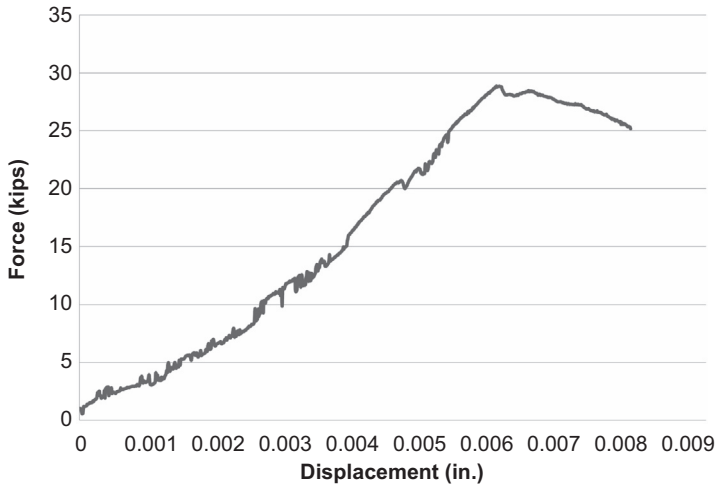
Figure 2.30 Beam force versus displacement.
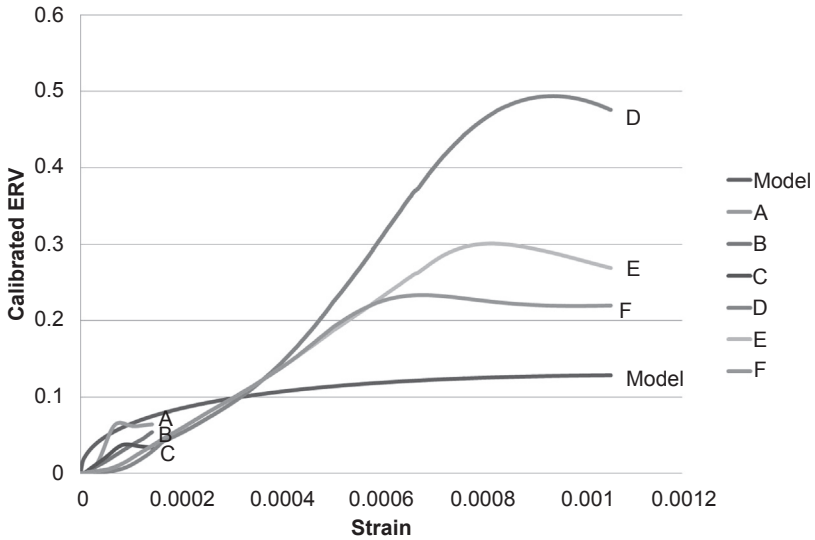
Figure 2.31 Beam calibrated ERV versus strain.

at 6.89 MPa. They did not match the compression model well, which implies that the tension and compression behavior of the CNFAs is different. This was expected because concrete is not isotropic. There were not enough data from the test to create a tension model.

Figure 2.32 Crack at loading point with loading equipment in place.

The load-carrying capacity of the beam began to decrease after a sudden large crack formed at one of the loading points, near CNFA A. Figure 2.32 shows the crack with all of the loading equipment in place. Figure 2.33 shows the crack and its proximity to CNFA A (the wires closest to the crack), which was embedded 12.7 mm below the surface of the concrete. At the exact time that the crack suddenly opened, the ERV in CNFA A suddenly dropped. This occurred simultaneously with the peak recorded load, as shown in Figure 2.34. This proves that CNFAs are capable of detecting localized, catastrophic damage.
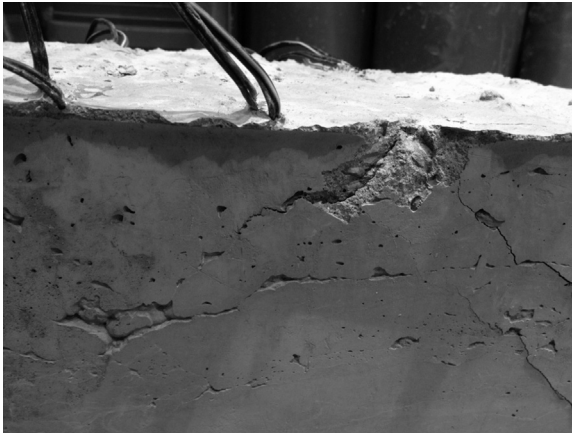
Figure 2.33 Crack at loading point.
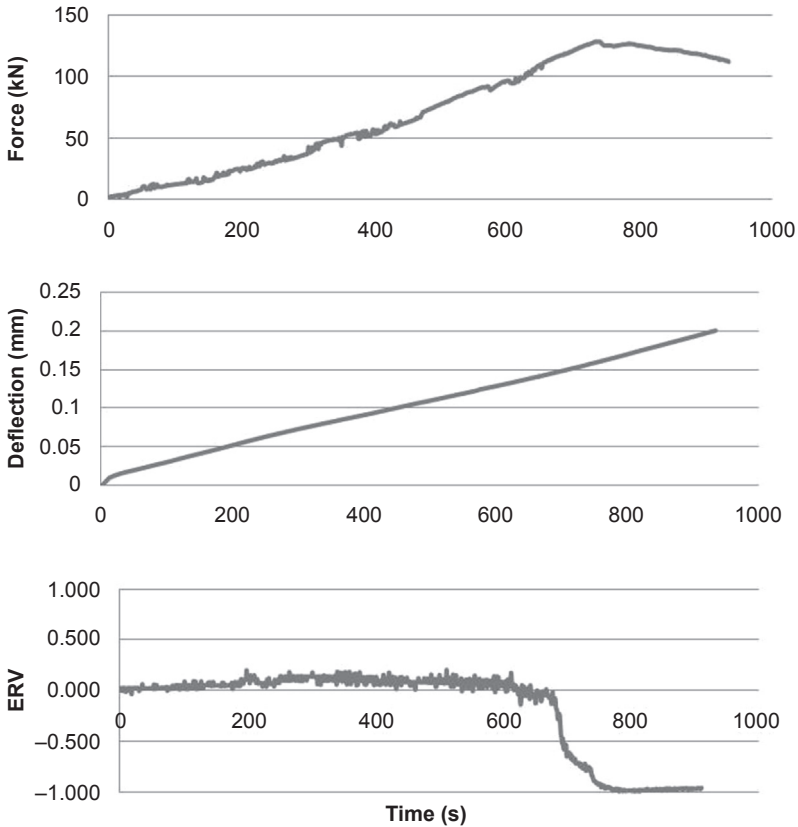
Figure 2.34 Beam force, displacement, and ERV of CNFA A versus time.

2.5   Conclusions and future trends

A carbon nanofiber aggregate (CNFA) was developed with self-sensing capabilities. The CNFA is a $2.54 \times 2.54 \times 2.54$ cm cube of mortar containing 0.70% carbon nanofibers (CNFs) by weight of cement. The electrical resistance is measured in the CNFAs through the embedding of four steel meshes and the use of the four-probe method. Preliminary testing was completed to prove that CNFAs are multifunctional sensors capable of monitoring strain in concrete structures.

Three groups of cylinders with embedded CNFAs were tested in compression. The first group was tested in monotonic compression at room temperature. The second group was frozen, then tested monotonically. The third group was tested cyclically at room temperature. The following conclusions were made from the study:

- A qualitative assessment of the electrical data from a CNFA embedded in a cylinder can show when loading began on the cylinder, a strain of approximately 0.001, and failure.

- Although the raw ERV values have a large coefficient of variation from the mean ERV values, a calibration factor can be applied to the ERV value to obtain a reasonable coefficient of variation. A model was developed to estimate the ERV-versus-strain relationship.
- Frozen cylinders are brittle. The ERV-versus-strain behavior is similar to the stress-versus-strain behavior in the lack of strain softening for frozen cylinders.
- Qualitatively, cyclic stress and strain can be assessed from the ERV-versus-time relationship. The peaks and valleys of all three relationships coincide during cyclic loading. A model was developed to estimate the cyclic ERV-versus-strain relationship.

A small-scale reinforced concrete beam with six embedded CNFAs was tested monotonically using the four-point bending method. The following conclusions were made from the study:

- CNFAs behave differently if they are tested in tension rather than compression. This was expected because concrete is not isotropic.
- CNFAs are capable of detecting localized catastrophic damage in reinforced concrete structures.

Many past researchers have shown that cement-based materials containing CNF are capable of qualitative strain and damage monitoring. These test results show that CNFAs are not only capable of qualitative monitoring but also on the brink of quantitative monitoring. Factors such as improved CNFA construction techniques, implementing a correlation factor based on more test results, and determining the relationship between ERV and temperature should reduce the ERV variation to a reasonable level for CNFA monitoring applications in industrial projects.

Acknowledgments

References

ACI Committee 318, 2011. Building Code Requirements for Structural Concrete. American Concrete Institute, Farmington Hills, Michigan.

ACI Committee 544, 1996. State-of-the-Art Report on Fiber Reinforced Concrete Reported by ACI Committee 544. American Concrete Institute, Farmington Hills, Michigan.

Bartos, P., 2006. Nanotechnology in construction: a roadmap for development. In: Nanotechnology of Concrete: Recent Developments and Future Perspective. American Concrete Institute, Denver, CO, pp. 1−14.

Baughman, R.H., Cui, C.X., Zakhidov, A.A., Iqbal, Z., Barisci, J.N., Spinks, G.M., Wallace, G.G., Mazzoldi, A., de Rossi, D., Rinzler, A.G., Jaschinski, O., Roth, S., Kertesz, M., 1999. Carbon nanotube actuators. Science 284, 1340−1344.

Baughman, R.H., Zakhidov, A.A., de Heer, W.A., 2002. Carbon nanotubes−the route toward applications. Science 297, 787−792.

Bontea, D.-M., Chung, D.D.L., Lee, G.C., 2000. Damage in carbon fiber-reinforced concrete, monitored by electrical resistance measurement. Cem. Concr. Res. 30, 651−659.

Chen, P.-W., Chung, D.D.L., 1993a. Concrete reinforced with up to 0.2 vol% of short carbon fibres. Composites 24, 33−52.

Chen, P.-W., Chung, D.D.L., 1993b. Carbon fiber reinforced concrete for smart structures capable of non-destructive flaw detection. Smart Mater. Struct. 2, 22−30.

Chen, P.-W., Chung, D.D.L., 1996. Concrete as a new strain/stress sensor. Compos. Part B Eng. 27, 11−23.

Chen, P.-W., Fu, X., Chung, D.D.L., 1997. Microstructural and mechanical effects of latex, methylcellulose, and silica fume on carbon fiber reinforced cement. ACI Mater. J. 94, 147−155.

Chung, D.D.L., 1995. Strain sensors based on the electrical resistance change accompanying the reversible pull-out of conducting short fibers in a less conducting matrix. Smart Mater. Struct. 4, 59−61.

Chung, D.D.L., 1998. Composite Material Strain/Stress Sensor. US Pat. 5817944.

Chung, D.D.L., 2000. Cement reinforced with short carbon fibers: a multifunctional material. Compos. Part B Eng. 31, 511−526.

Chung, D.D.L., 2005. Dispersion of short fibers in cement. J. Mater. Civ. Eng. 17, 379−383.

Coleman, J.N., Khan, U., Blau, W.J., Gun'ko, Y.K., 2006. Small but strong: a review of the mechanical properties of carbon nanotube−polymer composites. Carbon N.Y. 44, 1624−1652.

Feynman, R., 1960. There's plenty of room at the bottom. Eng. Sci. 23, 22−36.

Gaimster, R., Foord, C., 2000. Self-compacting concrete. Concrete 34, 23−25.

Gao, D., Sturm, M., Mo, Y.L., 2009. Electrical resistance of carbon-nanofiber concrete. Smart Mater. Struct. 18.

Hilding, J., Grulke, E.a., George Zhang, Z., Lockwood, F., 2003. Dispersion of carbon nanotubes in liquids. J. Disper. Sci. Technol. 24, 1−41.

Howser, R.N., Dhonde, H.B., Mo, Y.L., 2011. Self-sensing of carbon nanofiber concrete columns subjected to reversed cyclic loading. Smart Mater. Struct. 20, 085031.

Howser, R.N., Mo, Y.L., 2013. Development of carbon nanofiber aggregate. In: Structures Congress 2013. American Society of Civil Engineers, Pittsburgh, PA, p. 12.

Iijima, S., 1991. Helical microtubules of graphitic carbon. Nature 354, 11−14.

Kang, I., Heung, Y.Y., Kim, J.H., Lee, J.W., Gollapudi, R., Subramaniam, S., Narasimhadevara, S., Hurd, D., Kirikera, G.R., Shanov, V., Schulz, M.J., Shi, D., Boerio, J., Mall, S., Ruggles-Wren, M., 2006. Introduction to carbon nanotube and nanofiber smart materials. Compos. Part B Eng. 37, 382−394.

Khayat, K.H., Hu, C., Monty, H., 1999. Stability of self-consolidating concrete, advantages, and potential applications. In: First International RILEM Symposium on Self-Compacting Concrete. Stockholm, Sweden, pp. 143−152.

Konsta-Gdoutos, M.S., Metaxa, Z.S., Shah, S.P., 2010. Multi-scale mechanical and fracture characteristics and early-age strain capacity of high performance carbon nanotube/cement nanocomposites. Cem. Concr. Compos. 32, 110−115.

Lentz, A.E., Monfore, G.E., 1966. Thermal of Portland aggregate conductivities cement paste, and concrete down to very low temperatures. J. PCA Res. Dev. Lab. 8, 27−33.

Li, G.Y., Wang, P.M., Zhao, X., 2005. Mechanical behavior and microstructure of cement composites incorporating surface-treated multi-walled carbon nanotubes. Carbon N.Y. 43, 1239−1245.

Li, G.Y., Wang, P.M., Zhao, X., 2007a. Pressure-sensitive properties and microstructure of carbon nanotube reinforced cement composites. Cem. Concr. Compos. 29, 377−382.

Li, H., Xiao, H., Yuan, J., Ou, J., 2004. Microstructure of cement mortar with nano-particles. Compos. Part B Eng. 35, 185−189.

Li, H., Zhang, M., Ou, J., 2007b. Flexural fatigue performance of concrete containing nano-particles for pavement. Int. J. Fatigue 29, 1292−1301.

Li, V.C., 2002. Large volume, high performance applications of fibers in civil engineering. J. Appl. Polym. Sci. 83, 660−686.

Makar, J., Beaudoin, J., 2004. Carbon nanotubes and their application in the construction industry. In: 1st International Symposium on Nanotechnology in Construction. National Research Council Canada, Paisley, Scotland, pp. 331−341.

Makar, J., Margeson, J., Luh, J., 2005. Carbon nanotube/cement composites−early results and potential applications. In: 3rd International Conference on Construction Materials: Performance, Innovations and Structural Implications. National Research Council Canada, Vancouver, British Columbia, Canada, pp. 1−10.

Mondal, P., Shah, S.P., Marks, L., 2007. A reliable technique to determine the local mechanical properties at the nanoscale for cementitious materials. Cem. Concr. Res. 37, 1440−1444.

Monfore, G.E., Lentz, A.E., 1962. Physical properties of concrete at very low temperatures. J. PCA Res. Dev. Lab. 4, 33−39.

Narayan, R.J., Kumta, P.N., Sfeir, C., Lee, D.-H., Choi, D., Olton, D., 2004. Nanostructured ceramics in medical devices: applications and prospects. J. Miner. Met. Mater. Soc. 56, 38−43.

Okamura, H., Ozawa, K., 1995. Mix-design for self-compacting concrete. Concr. Libr. Jpn. Soc. Civil Eng. 25, 107−120.

PCI TR-6-03, 2003. Interim Guidelines for the Use of Self-Consolidating Concrete in Precast/ Prestressed Concrete Institute Member Plants. Precast/Prestressed Concrete Institute, Chicago.

Roco, M., 2007. National nanotechnology initiative-past, present, future. In: Handbook on Nanoscience, Engineering and Technology. CRC Press, Boco Raton, FL, pp. 3.1−3.26.

Salvetat, J.-P., Bonard, J.-M., Thomson, N.H., Kulik, A.J., Forró, L., Benoit, W., Zuppiroli, L., 1999. Mechanical properties of carbon nanotubes. Appl. Phys. A Mater. Sci. Process. 69, 255−260.

Sanchez, F., Sobolev, K., 2010. Nanotechnology in concrete − a review. Constr. Build. Mater. 24, 2060−2071.

Schmidt, M., Lipson, H., 2009. Distilling free-form natural laws. Science 324, 81−85.

Shah, S.P., Naaman, A.E., 1976. Mechanical properties of glass and steel fiber reinforced mortar. ACI J. Proc. 73, 50−53.

Tanaka, K., Sato, K., Watanabe, S., Arima, I., Suenaga, K., 1993. Development and utilization of high-performance concrete for the construction of the Akashi Kaikyo bridge. ACI Spec. Publ. 140 (140), 25−52.

Thess, A., Lee, R., Nikolaev, P., Dai, H., Petit, P., Robert, J., Xu, C., Lee, Y.H., Kim, S.G., Rinzler, A.G., Colbert, D.T., Scuseria, G.E., Tomanek, D., Fischer, J.E., Smalley, R.E., 1996. Crystalline ropes of metallic carbon nanotubes. Science 273, 483−487.

Timoshenko, S., 1953. History of Strength of Materials. McGraw-Hill, New York.

Tzeng, Y., Huang, T., Chen, Y., Liu, C., Liu, Y., 2004. Hydration properties of carbon nano-tubes and their effects on electrical and biosensor applications. New Diam. Front. Carbon Technol. 14, 193−201.

Wei, B.Q., Vajtai, R., Ajayan, P.M., 2001. Reliability and current carrying capacity of carbon nanotubes. Appl. Phys. Lett. 79, 1172.

Woo, L.Y., Wansom, S., Ozyurt, N., Mu, B., Shah, S.P., Mason, T.O., 2005. Characterizing fiber dispersion in cement composites using AC-Impedance Spectroscopy. Cem. Concr. Compos. 27, 627−636.

Yang, X., Chung, D.D.L., 1992. Latex-modified cement mortar reinforced by short carbon fibres. Composites 23, 453−460.

Yu, X., Kwon, E., 2012. Carbon Nanotube Based Self-sensing Concrete for Pavement Structural Health Monitoring. Washington, DC. http://ntl.bts.gov/lib/45000/45000/45066/3789.pdf.

Carbon nanofibers in cement composites: mechanical reinforcement

Nur Yazdani, Ellie Brown
University of Texas at Arlington, Arlington, Texas, USA

3.1 Introduction

Carbon nanofibers (CNFs) are defined as cylindrical nanostructures with graphene layers constructed in the shape of cups, cones, or plates, with an average diameter of 70−200 nm and an average length of 50−200 μm (Yazdani and Mohanam, 2014). Even though CNFs got their start within the field of physical chemistry, they now have a wide range of applications and have received increased attention in recent years in multiple disciplines within engineering and materials science (Hammel et al., 2004), medicine (Tran et al., 2009), geochemistry (Moura and Lago, 2009), energy research, electronics, and others. Currently, CNF is used in various applications within these disciplines. They can be constructed by various methods, such as the vapor-grown carbon nanofiber (VGCF) or the floating-catalyst process, and most often come in a powdered form (Figures 3.1 and 3.2).

The history of CNF can be traced back to over a century ago. CNF was first patented in 1889 as carbon filaments grown from gases containing carbon, and then for the next half century, their existence was considered a detriment to chemical research because of their capability to block reactors and deactivate catalysts in Fisher−Tropsch synthesis and steam reforming processes, among others (Zhu et al., 2005). This negative
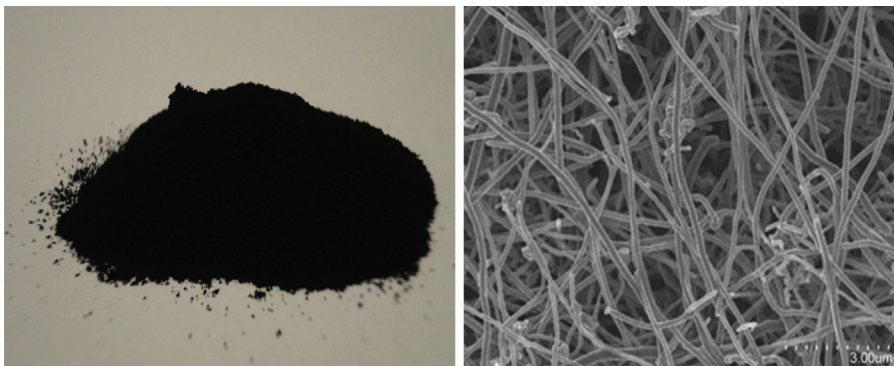
Figure 3.1 CNF in powdered form and a scanning electron microscopy image of CNF at 3 μm. Pyrograf.
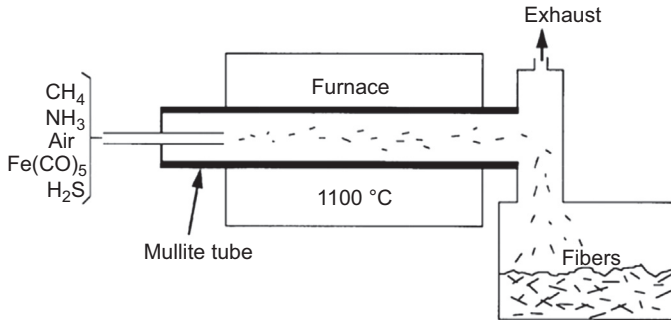
Figure 3.2 Method for synthesizing VCGFs.
Tibbetts et al. (2007).

association tied to these carbon filaments was what ultimately led to their characterization, for researchers wanted to find ways to inhibit their formation (De Jong and Geus, 2000). This characterization has proved useful, because modern studies of CNF have been based on this early research.

CNF research came into the limelight in 1950 when the electron microscope became popular in analyzing specimens at the nanoscale level (Hughes and Chambers, 1889). In 1970, Japanese researchers manufactured VGCFs with a diameter of 1 μm and a length greater than 1 mm (Koyama and Endo, 1973).

3.2 General properties

CNFs have high electrical conductivity, high thermal conductivity, and favorable chemical properties. CNFs possess exceptional mechanical properties, such as the elastic modulus, which can be as high as 600 GPa, and the tensile strength, which can be as high as 8.7 GPa. Basic physical properties of CNFs are presented in Table 3.1. Figure 3.3 shows the basic physical structure of CNFs. The core of the

Table 3.1 Properties of CNF-PR-24-XT-LHT

Fiber diameter, nm (average)	100
Fiber length, μm (average)	50−200
CVD carbon overcoat present on fiber	No
Surface area, m^2/g	43
Dispersive surface energy, mJ/m^2	155
Moisture, wt%	<5
Iron, ppm	<14,000
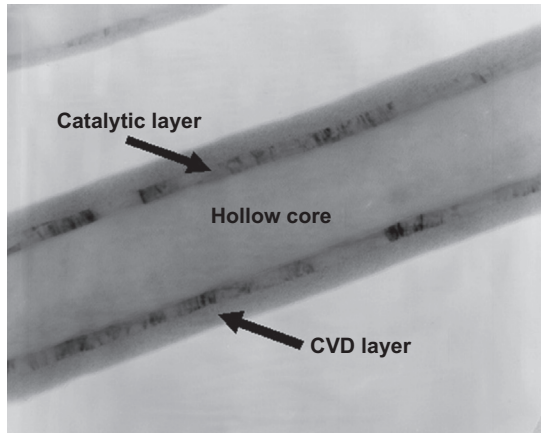
Pyrograf.

Figure 3.3 Vapor-grown CNF.
Pyrograf III.

nanofiber is hollow and is surrounded by a cylindrical fiber grown from a catalyst particle. The fiber is composed of graphite basal planes stacked 25° from the longitudinal axis of the fiber (Tibbetts et al., 2007).

CNFs are also highly adsorptive for organic materials (Morgan, 2005) and can withstand temperatures up to 3000 °C due to their superior electrical properties. This makes them excellent conductors of electricity as well as shielders of sources of electromagnetism. The conductivity values for VGCF composites are high, so they provide significant protection from electromagnetic interference. Reported values are a 45 db shielding effectiveness at 200 MHz for 15 wt% heat-treated VGCFs in a vinyl ester matrix, with large differences found with varying composite preparation techniques (Figure 3.4) (Tibbetts et al., 2007). Approximate resistivity values required for static discharge, electrostatic painting, and radiofrequency interference shielding are indicated in Figure 3.4. Data from three different types of fibers are plotted and compared to a superposition model for graphitized and as-grown fibers.

CNFs also have good dampening abilities. Composites with CNFs show an increase in dynamic modulus along with a decrease in damping losses associated with a 1—5% by weight inclusion of CNFs. As the material softens at around 100 °C, the damping increases with temperature, which is attributed to the enhanced thermal conductivity of the composites (Tibbetts et al., 2007).

3.3 Application in cement composites

The utilization of CNF in cement composites began in the 1990s, when carbon fibers were first introduced in cement mortar (Chen and Chung, 1993). The amount of carbon fiber used for the study was 0.2% by weight of cement. This research produced a composite with increases of 85% in flexural strength, 205% in flexural toughness, and 22% in compressive strength, respectively.
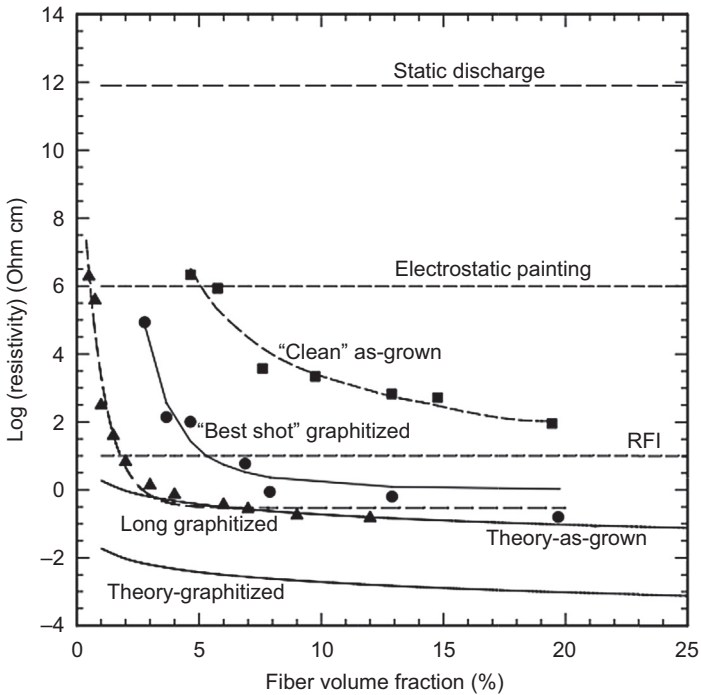
Figure 3.4 Resistivity of VGCF composites.
Tibbetts et al. (2007).

Chung (2000) presented research on cement—matrix structural composites for smart structures. The functions that were addressed were strain sensing, damage sensing, temperature sensing, vibration reduction, and electromagnetic radiation reflection, among others. The study revealed increased flexural strength and flexural toughness, improved impact resistance, reduced drying shrinkage, and enhanced freeze—thaw durability, as compared to composites without these structures. Four years later, Li et al. (2004) presented work on the microstructure of cement mortar with nanoparticles. The compressive strength and flexural strength of the cement mortar with nanoparticles were higher than in plain cement paste. The scanning electron microscopy images from this work suggested that the nanoparticles were not simply acting as filler, but also as an activator to promote hydration (Figure 3.5).

Chung (2005) investigated the dispersion of CNFs in cement, which led to a major breakthrough in the usage of carbon fibers in cement paste. The dispersion of fibers was determined by measuring the electrical resistivity of the cement, which is inversely proportional to the dispersion of fibers. This research concluded that the usage of silica fume (15% by weight of cement) and methyl cellulose (4% by weight of cement) caused lesser electrical resistivity and a higher tensile strength than in plain mortar.

A few years later, Li et al. (2006) studied the abrasive resistance of concrete containing nanoparticles. They found that the abrasive resistance of concrete was improved significantly by the addition of nanoparticles. The compressive strength

Figure 3.5 Mixture with the highest flexural strength.
Li et al. (2004).

and flexural strength were also improved when the nanoparticles and the fiber content were 1% of the cement weight. These properties had a linear relationship, as depicted in Figure 3.6. This relationship was expressed by:

$$I_a = \frac{f_{cu}}{\theta_1 f_{cu} + \theta_2}$$

where:

I_a is the index of abrasion resistance of concrete,
f_{cu} is the compressive strength, and
θ_1 and θ_2 are constants that can be obtained by curve-fitting techniques.

In 2007, another study on the flexural fatigue performance of concrete with nanoparticles indicated that concrete containing 1% of nanoTiO$_2$ by the mass of cement had the best flexural fatigue strength (Li et al., 2007). Gao et al. (2009) performed testing on the mechanical and electrical properties of self-consolidating concrete with CNFs. The concrete containing 1% CNFs produced the best performance in terms of compressive strength as well as electrical resistivity.

Concrete and cement composite materials normally have to be reinforced with bars, rods, or steel−plastic fibers in order to compensate for their relative lack of tensile strength. The introduction of CNFs in these materials has gained popularity in recent
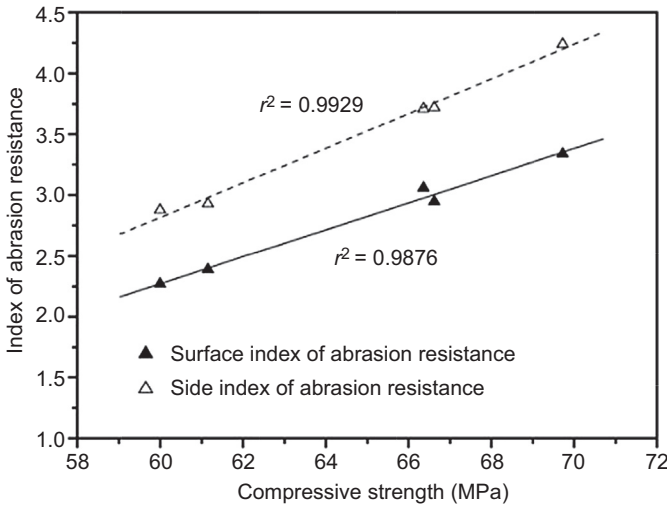
Figure 3.6 Abrasion resistance index of concrete with nanoparticles as a function of compressive strength.
Li et al. (2006).

years due to their excellent mechanical properties. The strength of concrete is based on certain factors, such as water−cement (w/c) ratio, size of pores in the cement, binding between the aggregate and the cement, and micro cracking in the cement, among others. Introduction of CNFs in the cementitious materials provides extraordinary strength increase, and controls cracks and forms bridge mechanisms within the cement matrix at the nanoscale level (Mohanam, 2012).

CNFs are now cheaper and more easily available as compared to the early 2000s. Short fibers were used earlier as an admixture for reducing drying shrinkage, to increase flexural toughness, and also to increase flexural strength. Introduction of CNFs in cement-based materials was not initially successful because of the high aspect ratio, which ranges from 250 to 2000. If the aspect ratio is high, the dispersion of CNFs is difficult due to van der Waals interactions, which tend to agglomerate them in bundles (Mohanam, 2012).

A research study in 2012 was conducted on the compressive strength of CNF cement composites at different w/c ratios and at 0.1% and 0.2% CNF ratios with super plasticizer (SP). The parameters were based on findings from a previous study (Manzur and Yazdani, 2010). A surfactant (plasticizer) was used at a 0.008 ratio to cement to get a homogeneous dispersion of CNFs in water. The CNFs were sonicated for 15 min using a tip horn type sonicator with 12 mm size and an amplitude of 120 μm. The sonication was done in 30 s cycle intervals to prevent overheating of the suspensions. The ASTM C109 test procedure was used to determine the compressive strength using 50 mm cubes (ASTM, 2013a). The mortar consisted of 1 part of cement and 2.75 parts of graded sand. After sonication, the nanoparticles were mixed with cement and sand for 4 min. After mixing, the mortar was placed in molds, demolded after 24 h, and

stored in a lime-saturated water tank. The samples were loaded to failure in a universal testing machine at 7, 14, and 28 days of age. The loading rate was 890−1800 N/sec. The ASTM C348 test procedure was used to evaluate the flexural strength of the mortar using a sample size of 40 × 40 × 160 mm (ASTM, 2014) and the same mixing technique. A three-point loading setup was used with a loading rate of 2640 + 110 N.

The dosage rate of 0.1% CNF composites showed very high strength after 7 days because CNF accelerates the hydration process (Figure 3.7). The w/c ratio of 0.4 displayed maximum strength of 40 MPa and the w/c ratio of 0.50 yielded minimum strength of 25 MPa at 7 days. Even at 28 days, the w/c ratio of 0.4 produced superior strength of 52 MPa. A w/c ratio of 0.4 achieved significant strength gain at all tested ages compared to the other CNF composites. This mix proportion was found to be the optimal combination for 0.1% CNF composites.

CNF cement composites of 0.2% ratio gave high early strength at 7 days compared to 0.1% composites. The w/c ratio of 0.35 produced superior strength at 7, 14 and 28 days. Maximum compressive strength of 54 MPa was observed for 0.2% CNF composites with a w/c ratio of 0.35 at 28 days, which was the maximum of all the CNF composites. When the dosage rate is high, CNF composites perform better with lower w/c ratios. However, the difficulty in having lower w/c ratios is the workability issue. At a lower w/c ratio, the agglomeration of the CNF was significant and the mixing process more difficult. The workability was only qualitatively ascertained in this study. Therefore, the optimum w/c ratio that gives maximum strength with good workability is the key for producing superior CNF cement composites. CNF composites with a w/c ratio of 0.45 also achieved the highest strength gain as well as superior workability (Mohanam, 2012).
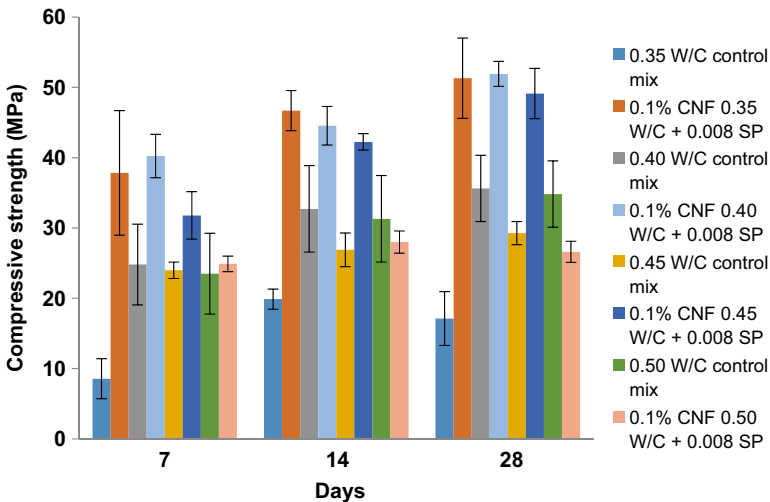
Figure 3.7 Compressive strength of 0.1% CNF composites versus control samples. Mohanam (2012).
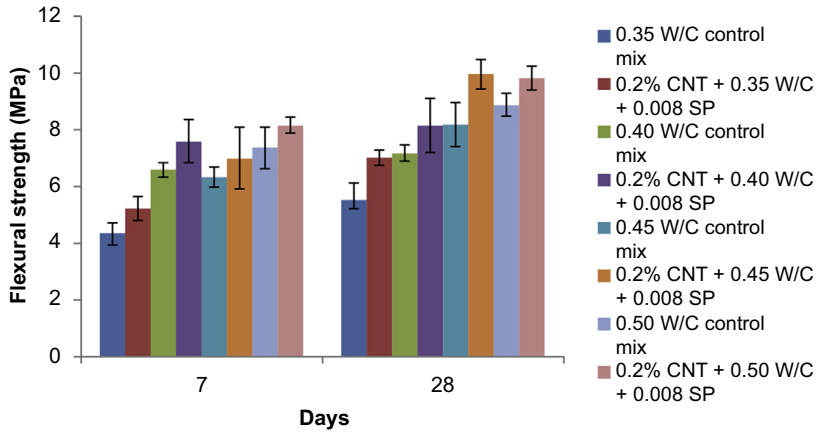
Figure 3.8 Flexural strength of 0.2% CNT cement composites versus control samples. Mohanam (2012).

The addition of CNF also caused an increase in flexural strength. The w/c ratio of 0.45 yielded the maximum flexural strength for 0.1% CNF composites at both 7 and 28 days. Again, the CNF composite exhibited high early strength due to an early hydration process. The flexural strength of 0.2% CNF composites at a w/c ratio of 0.35 produced maximum strength at 7 days, whereas a w/c ratio of 0.45 gave highest strength at 28 days (Figure 3.8). A maximum flexural strength of 9.7 MPa was obtained for 0.2% CNF composites, the highest of both dosage rates of CNF composites.

In the same study (Mohanam, 2012), the ASTM C1437 test procedure was used to calculate the flow of the mortar (ASTM, 2013b). The flow value is an indicator of the workability and ease of placement of cement mortars. The compressive strength of CNF composites decreased in general with increasing flow values for both 0.1% and 0.2% mixing ratios. This pattern indicated that the CNF mortar with higher compressive strengths would be relatively more difficult to work with in the field. The bleeding tendency was evaluated using the ASTM C940 test procedure (ASTM, 2010), and the ASTM C807 test procedure was used to determine the setting time of CNF composites using the vicat apparatus (ASTM, 2013c). None of the tested samples exhibited any bleeding. The CNF composites set about 25 min faster on average than the plain-mortar control samples. CNF accelerates the mortar hydration process, resulting in faster setting times.

3.4   Challenges

One of the major difficulties in the application of CNFs both within concrete composites and in other materials is the tendency of CNFs and other nanomaterials to group and entangle, attracting each other to form either bundles or ropes due to van der Waals
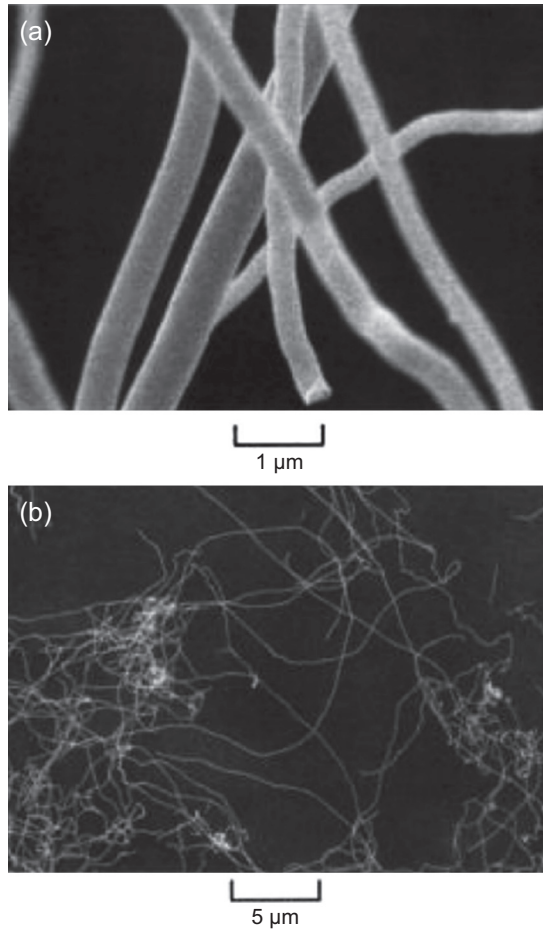
Figure 3.9 The clumping tendency of CNFs.
Tibbetts et al. (2007)

force (Figure 3.9). Ultrasonication, a method used to disperse the nanoparticles, is a good potential solution for this, but it needs further research (Mohanam, 2012). High-energy mixing machines have also been used in an attempt to further disperse nanoparticles of all kinds (Vera-Agullo et al., 2009).

Another research emphasis should be on the grain size of cement used in mixtures with CNFs. CNFs do uniformly disperse in water with the help of a sonicator, but they re-agglomerate when they are mixed with cement. To eradicate this difficulty, micro cement could be used in place of ordinary cement (Mohanam, 2012).

CNFs also have a tendency to adsorb large amounts of water due to their high surface area. Since a major goal of applying CNFs in concrete materials is to reduce the cost and environmental impact of construction materials, this is an issue that will need to be addressed (Vera-Agullo et al., 2009).

3.5   The future of CNFs

CNFs have a broad range of potential uses. They have great potential in aviation as ablation-resistant rocket motor insulation. Testing has determined that CNFs improve the ablation resistance of multiple types of polymers due to their resistance to erosion and charring (Tibbetts et al., 2007). In order for this to be broadly applicable, the problem of CNFs amalgamating must first be solved, as this will lower polymers' mechanical properties, thermal resistivity, and retardation to fire. Aviation also has a need for conductive adhesives for the purpose of controlling and dissipating the buildup of electrostatic charges at key joints. Traditional electrically conductive composite adhesives generally include silver or nickel, or other forms of carbon, but the issue with these materials is that these additives weaken the mechanical properties and bonding capability of the adhesives. Because some CNFs have high electrical conductivity, recent efforts have been made to investigate how they could be incorporated into aeronautical adhesives. CNFs also show promise in this field as good electromagnetic shields. When the CNFs were coated in nickel, they not only increased adhesion but also created a highly effective electromagnetic interference shield over a large bandwidth (Figure 3.10) (Baur and Silverman, 2007).

   The future of CNFs is bright for other industries as well. One of the most exciting advances in medicine is the application of CNFs in supporting neural regeneration by designing an electrically conductive "scaffold" that would be able to hold bioactive materials in order to support growth of neurons. Research has shown that neurons grown on CNFs coated in bioactive molecules have increased length and increased number of neurite branches when compared to nanostructures that do not have the bioactive coating. This would be beneficial for patients with diseases such as Parkinson's, epilepsy, or mental illness (Tran et al., 2009). In geochemistry, CNFs have potential as absorbents that have shown to be able to remove oil slicks on water (Figure 3.11) (Moura and Lago, 2009). Recent research in this field has also discovered that lava
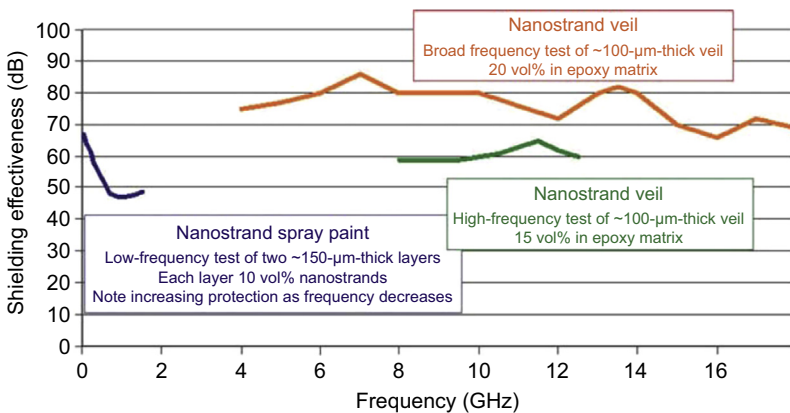
Figure 3.10 Summary of shielding effectiveness for composites with nickel coating and an epoxy-infused nickel nanostrand veil of two different thicknesses.
Baur and Silverman (2007).
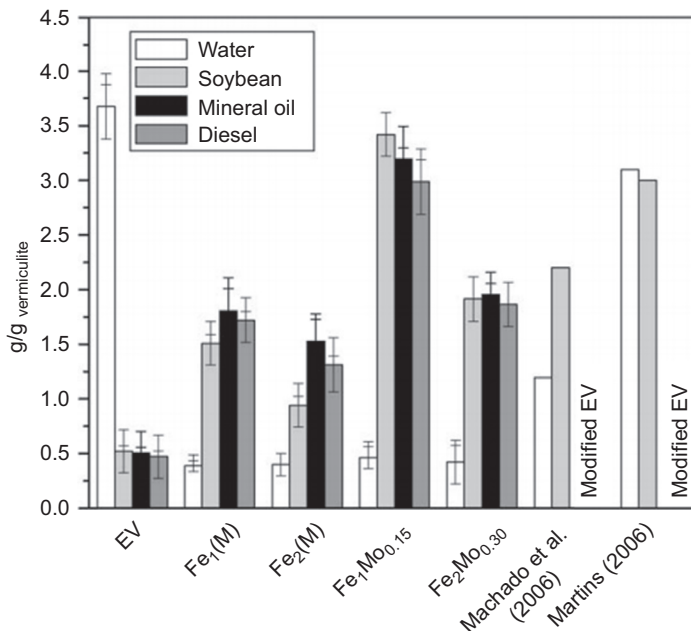
Figure 3.11 Absorption of water and spilled oils by the hydrophobic vermiculite-nanostructured carbon composites and two other modified expanded vermiculite absorbents. Moura and Lago (2009).

has the ability to be a catalyst in the production of CNFs and carbon nanotubes, and suggests that they may be a naturally occurring allotrope of carbon (Mracek et al., 2011). Further understanding of this phenomenon could lead to a greater understanding of these structures, their role in the genesis of geomaterials, and their potential uses in cement composites.

References

American Society for Standard Testing and Materials (ASTM), 2010. Standard Test Method for Expansion and Bleeding of Freshly Mixed Grouts for Preplaced-aggregate Concrete in the Laboratory. ASTM C 940-10.

American Society for Testing and Materials (ASTM), 2013a. Standard Test Method for Compressive Strength of Hydraulic-Cement Mortars. ASTM C 109-13.

American Society for Standard Testing and Materials (ASTM), 2013b. Standard Test Method for Flow of Hydraulic Cement Mortar. ASTM C 1437-13.

American Society for Standard Testing and Materials (ASTM), 2013c. Standard Test Method for Time of Setting of Hydraulic Cement Mortar by Modified Vicat Needle. ASTM C 807-13.

American Society for Standard Testing and Materials (ASTM), 2014. Standard Test Method for Flexural Strength of Hydraulic-cement Mortars. ASTM C 348-14.

Baur, J., Silverman, E., 2007. Challenges and opportunities in multifunctional nanocomposite structures for aerospace applications. MRS Bulletin 32, 328−334.

Chen, P.W., Chung, D.D.D.L., 1993. Concrete reinforced with up to 0.2 vol% of short carbon fibers. Composites 24 (1), 33−52.

Chung, D.D.L., 2000. Cement-matrix composites for smart structures. Smart Materials and Structures 9, 389−401.

Chung, D.D., 2005. Dispersion of short fibers in cement. Journal of Materials in Civil Engineering 17 (4), 379−383.

De Jong, K.P., Geus, J.W., 2000. Carbon nanofibers: catalytic synthesis and applications. Catalysis Reviews Science and Engineering 42 (4), 481−510.

Gao, D., Sturm, M., Mo, Y.L., 2009. Electrical resistance of carbon nanofiber concrete. Smart Materials and Structures 18 (9), 095039.

Hammel, E., Tang, X., Trampert, M., Schmitt, T.T., Mauthner, K., Eder, A., Potschke, P., 2004. Carbon nanofibers for composite applications. Carbon 42 (5−6), 1153−1158.

Hughes, T.V., Chambers, C.R., 1889. Manufacture of Carbon Filaments. US Patent No. 405, 480.

Koyama, T., Endo, M., 1973. Structure and growth process of vapor-grown carbon fibers. Oyo Butsuri (Japan) 42, 690−696.

Li, H., Xiao, H.G., Yuan, J., Ou, J., 2004. Microstructure of cement mortar with nano-particles. Composites Part B: Engineering 35 (2), 185−189.

Li, H., Zhang, M.H., Ou, J.P., 2006. Abrasion resistance of concrete containing nano-particles for pavement. Wear 260 (11−12), 1262−1266.

Li, H., Zhang, M.H., Ou, J.P., 2007. Flexural fatigue performance of concrete containing nano-particles for pavement. International Journal of Fatigue 29 (7), 1292−1301.

Machado, L.C.R., Lima, F.W.J., Paniago, R., 2006. Polymer coated vermiculite-iron composites: novel floatable magnetic adsorbents for water spilled contaminants. Applied Clay Science 31, 207−215.

Manzur, T., Yazdani, N., 2010. Strength enhancement of cement mortar with carbon nanotubes: early results and potential. Journal of Transportation Research Records 2 (2142), 102−108.

Martins, J., 2006. Upgraded Process for the Production of Hydrophobized Expanded Vermiculite Application thereof, Patent WO. 2006017919.

Mohanam, V., 2012. Comparative Application of Two Nanoparticles in Cement Mortar. University of Texas at Arlington (Thesis).

Morgan, P., 2005. Carbon fibers and their composites. CRC, 27(2005).

Moura, F.C.C., Lago, R.M., 2009. Catalytic growth of carbon nanotubes and nanofibers on vermiculite to produce floatable hydrophobic "nanosponges" for oil spill remediation. Applied Catalysis B-Environmental 90 (3−4), 436−440.

Mracek, J., Randall, D.F., Stengelin, R.M., Hesjedal, T., 2011. Are carbon nanotubes a naturally occurring material? hints from methane CVD using lava as a catalyst. Current Nanoscience 7 (3), 294−296.

Tibbetts, G.G., Lake, M.L., Strong, K.L., Rice, B.P., 2007. A review of the fabrication and properties of vapor-grown carbon nanofiber/polymer composites. Composites Science and Technology 67 (7−8), 1709−1718.

Tran, P.A., Zhang, L., Webster, T.J., 2009. Carbon nanofibers and carbon nanotubes in regenerative medicine. Advanced Drug Delivery Reviews 61 (12), 1097−1114.

Vera-Agullo, J., Chozas-Ligero, V., Portillo-Rico, D., García-Casas, M.J.J., Gutiérrez-Martínez, A., Mieres-Royo, J.M., Grávalos-Moreno, J., 2009. Mortar and concrete reinforced with nano-materials. Book Nanotechnology in Construction 3, 383−388.

Yazdani, N., Mohanam, V., 2014. Carbon nano-tube and nano-fiber in cement mortar: effect of age and dosage rate. International Journal of Material Science 4 (2), 45−52.

Zhu, Y.A., Sui, Z.J., Zhao, T.J., Dai, Y.C., Cheng, Z.M., Yuan, W.K., 2005. Modeling of fishbone-type carbon nanofibers: a theoretical study. Carbon 43 (8), 1694−1699.

Self-sensing of nano-carbon black concrete

4

Huigang Xiao [1,2], *Hui Li* [1,2], *Jinping Ou* [1,2,3]
[1]Key Lab of Structures Dynamic Behavior and Control (Harbin Institute of Technology), Ministry of Education, Harbin, China; [2]School of Civil Engineering, Harbin Institute of Technology, Harbin, China; [3]School of Civil and Hydraulic Engineering, Dalian University of Technology, Dalian, China

4.1 Introduction

Civil infrastructures usually suffer from fatigue load, environmental corrosion, and/or natural disasters. To improve the safety of infrastructures, structural health monitoring (SHM) is becoming more and more important. SHM is normally performed by measuring the strain/stress of a structure's critical zone with sensors; the health of the structure can be evaluated based on the measured information, which can be used when deciding whether or not to repair the structure (Scott et al., 1996). Traditional strain sensors (such as optical fiber sensors, electrical resistance strain gauges, and piezoelectric ceramics) have been widely used in SHM (Chen, 1995; Li et al., 2006; Austin et al., 1999; Claus et al., 1988). However, the cost and durability of traditional sensors, and the comparability between traditional sensors and concrete, are limited, motivating us to develop a new generation of sensors that is more preferable for concrete structures.

The recently developed, multifunctional, nanomaterials-enabled concrete provides an efficient way to improve the safety of concrete structures. By incorporating some conductive nanomaterials (such as carbon nanofiber or carbon black) with concrete, the concrete can be conductive and piezoresistive (Li et al., 2006; Xiao et al., 2011a), which is so-called smart concrete. Smart concrete is a new generation of structure materials that developed from carbon fiber reinforced concrete (CFRC) in the 2000s and 2010s by utilizing the piezoresistivity for sensing strain (Wen and Chung, 2001; Reza et al., 2003; Song et al., 2006; Han and Ou, 2007; Ou and Han, 2009; Yu and Kwon, 2009) or by utilizing the relation between damage and resistance for sensing damage (Chen and Liu, 2008; Wang et al., 1998). To improve the application of smart concrete in health monitoring, some approaches such as using smart concrete as surface coating (Wen and Chung, 2001) or as structural materials (Song et al., 2006; Chen and Liu, 2008) have been proposed. Recently, an advanced application approach that uses smart concrete as an embedded strain sensor was proposed. In this approach, a standard cubic strain sensor was fabricated with smart concrete (Han and Ou, 2007; Ou and Han, 2009). The CBCC-based strain sensor is just this kind of embedded cement-based sensor (Xiao and Li, 2006). The strain-sensing property, humidity insulation method, and piezoresistive model of CBCC-based strain sensor have been

studied to promote the application of CBCC-based strain sensors (Xiao et al., 2011b, 2010; Li et al., 2008).

4.2 Piezoresistivity of nano-carbon black concrete

4.2.1 Materials and test methods

Carbon black (CB) of 120 nm came from Liaoning Tianbao Energy Co., Ltd (Liaoning, China). The specific gravity of CB was 1.98 g/cm^3. CB in the amount of 5%, 10%, 12%, 15%, 20%, and 25% by weight of cement (i.e., 3.11%, 6.04%, 7.22%, 8.79%, 11.39%, and 13.85% by volume of composite, respectively) was used, and the corresponding mixture types were called A-5, A-10, A-12, A-15, A-20, and A-25, respectively. The cement used was Portland cement (P.O42.5) from Harbin Cement Company (Harbin, China). The water−cement ratio was 0.4 for all specimens. A water-reducing agent, UNF (one kind of naphthalene sulfonic acid and formaldehyde condensates), was used in the amount of 1.5% by weight of cement. The water-reducing agent could increase the dispersion of CB particles and facilitate the workability of the mixture. The defoamer, tributyl phosphate (made in China), was used in the amount of 0.13 vol% to decrease the number of air bubbles.

Defoamer and UNF water-reducing agent were dissolved in water, then CB was added and stirred at high speed in a mortar mixer for 3 min. This mixture and the cement were mixed at high speed for 2 min. After this, the mix was poured into oiled molds to form prisms of 30 × 40 × 50 mm for compressive testing. After pouring, an external vibrator was used to facilitate compaction and decrease the number of air bubbles. The samples were demolded after 24 h and then cured in a moist room (relative humidity 100%) for 28 days. Afterward, the specimens were dried in an oven at 60 °C for 2 days to extract redundant water to eliminate the polarization effect on resistance measurement. The dried specimens were then tested at ambient temperature.

DC electrical resistance measurement was made in the longitudinal axis, using the four-probe method, in which copper nets served as electrical contacts. The copper nets were placed into the specimen when pouring the mix into molds. Four contacts were placed across the whole cross-section of 30 × 40 mm of the specimen; these were all perpendicular to the longitudinal axis and symmetrically positioned with respect to the midpoint along the height of the specimen (i.e., two contacts were in planes above the midpoint, and two contacts were in planes below the midpoint). The outer two contacts (36 mm apart) were for passing current. The inner two contacts (20 mm apart) were for measuring the voltage (see Figure 4.1).

A DC circuit developed by Han (Han et al., 2007) was used to measure the resistance of the specimen as follows:

$$R_i = U_i \cdot R_r / U_r, \tag{4.1}$$

where: R_r is the standard reference resistor, U_r is the voltage applied on the reference resistor, and U_i and R_i are the voltage and resistance between the two inner contacts of the specimen, respectively; U_i and U_r were collected using the data acquisition board.
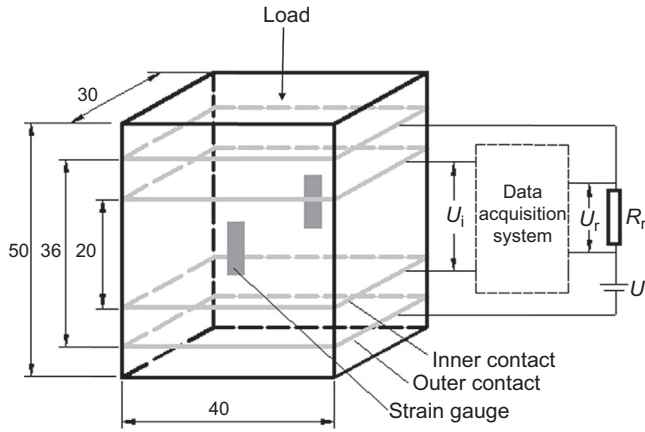
Figure 4.1 Schematic of the experimental setup (mm).

Compressive testing was performed on a 30×40 mm side of each specimen. The strain was measured by using strain gauges attached to the middle of the opposite sides of a specimen and parallel to the stress axis. Compressive testing under force control was conducted using a hydraulic mechanical testing system with 120 kN maximum loading capacity. The scheme of monotonically static loading up to specimen failure was arranged. During the loading process, DC electrical resistance measurement was simultaneously made in the stress axis, using the four-probe method as described in this chapter. Three specimens of each type of mixture were tested.

4.2.2 Piezoresistivity of CBCC under monotonic and cycle loading

Figure 4.2 shows the resistivity (ρ) as a function of CB volume content (V) of CB-filled composites. It can be observed from Figure 4.2 that the resistivity of the composites
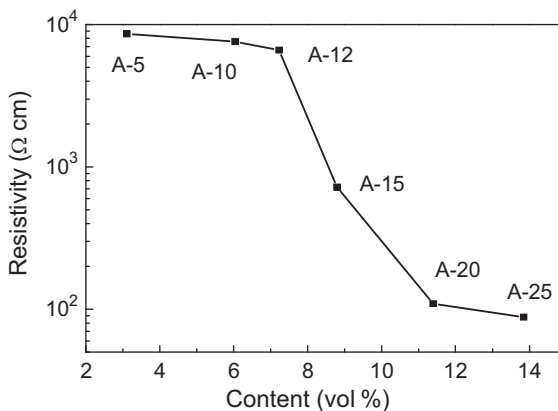
Figure 4.2 Logarithm of resistivity as a function of volume content of CB.
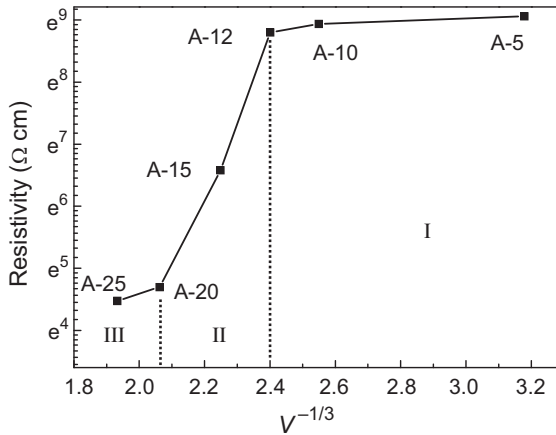
Figure 4.3 Natural logarithm of resistivity as a function of $V^{-1/3}$.

decreased dramatically with increasing CB content from 7.22 to 11.39 vol% (i.e., from A-12 to A-20). The resistivity of the composites varied slightly outside the above range. The content range over which the resistivity varied precipitously was called the percolation threshold. Therefore, in this study, the percolation threshold zone of the composites was CB in the amount of $7.22 \sim 11.39$ vol%.

According to the tunneling effect theory, the natural logarithm of resistivity of composites $\ln(\rho)$ is a linear function of potential barrier width (s) (i.e., the distance between CB particles). Furthermore, it is well accepted that distribution of CB particles is random and the average distance between particles is proportional to $V^{-1/3}$. Thus, $\ln(\rho)$ is a linear function of $V^{-1/3}$. For clear observation, the $V^{-1/3}$ and natural logarithm of resistivity were, respectively, nominated as abscissa and ordinate, and the curve in Figure 4.2 was redrawn in Figure 4.3. The curve can be divided into three stages according to the variation of slope. The curve from 7.22 to 11.39 vol% in Figure 4.3 was just linear, so the tunneling effect dominated the conductivity and electromechanical properties of the composites in stage II.

Tunneling current is an exponential function of barrier width, implying a precipitous change of resistivity upon distance between CB particles. The distance between CB particles is shortened with increasing compressive strain on specimens. As a consequence, the resistivity of composites decreases with increasing compressive strain.

4.2.3 Resistivity of CBCC with various contents of CB

Figure 4.4 shows the fractional change in resistivity versus the compressive strain curves of A-15. Additionally, the distance between probes was shortened during loading, which induced change in electrical resistance. However, it could be observed from Figure 4.4 that the change in resistance induced by this factor was very small and negligible. The resistance was essentially proportional to the volume resistivity that was selected as a measurement in this study. For A-15, the resistivity
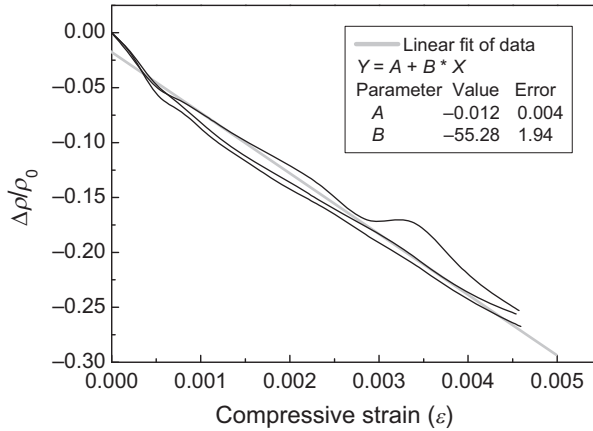
Figure 4.4 Fractional change in resistivity of A-15 as a function of compressive strain.

decreased linearly with increasing compressive strain up to failure of the specimens except for a small perturbation over the strain range of [0.003−0.004], which indicated the occurrence of micro cracks. The three curves for the three specimens of this mixture were almost the same, indicating that the results were repeatable. Linear fit of the experimental data showed that the relationship between the fractional change in resistivity and compressive strain was nearly linear. The fractional change in resistivity per unit strain (i.e., the strain gauge factor) was 55.28, as shown in Figure 4.4.

Figure 4.5 presents the strain−stress curves of A-15. It can be seen from Figure 4.4 that the strength of the CB-filled composite could reach more than 40 MPa. Therefore,
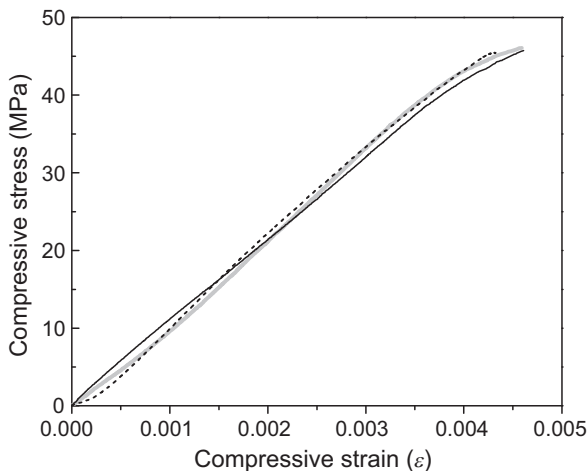
Figure 4.5 Stress−strain curves of A-15.
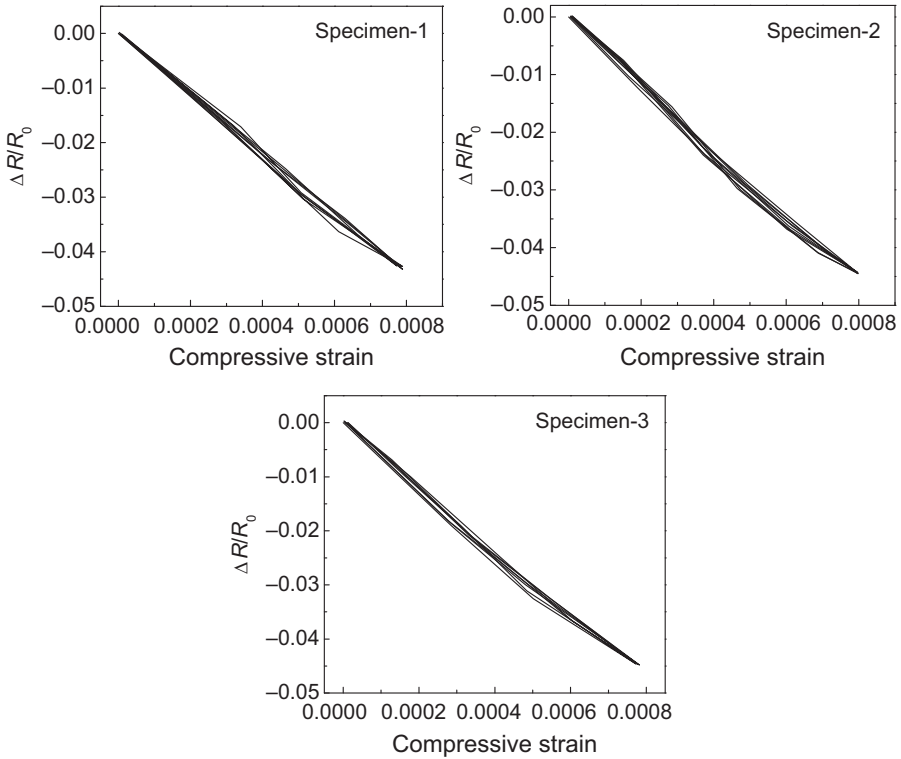
Figure 4.6 Piezoresistivity of CBCC sensor under cyclic loading with an amplitude of 10 kN.

it can be used as a structural material like common concrete. Similar results have been obtained for other mixtures. In the following text, CBCC denotes the cement-based composites filled with 15% carbon black.

Figure 4.6 shows the piezoresistive behavior of three CBCC sensors under cyclic loading with an amplitude of 10 kN (i.e., the stress ratio, amplitude with respect to the ultimate strength, is about 0.2). At this cyclic loading, the strain amplitudes were about 800 με. CBCC sensors exhibited stable and repeatable strain-sensing ability during the whole cyclic loading process that the gauge factor did not change upon cycle number, and the initial resistances remained constant after each cycle, indicating that nearly no damage occurred in this cyclic loading. Figure 4.7 shows the piezoresistive behavior of three CBCC sensors under cyclic loading with an amplitude of 35 kN (i.e., the stress ratio, amplitude with respect to the ultimate strength, is about 0.7). At this cyclic loading, the strain amplitudes were about 2700 με. The piezoresistivity curves of each cycle were similar. However, the initial resistances of CBCC sensors increased after each cycle, expressing as the curves shifted upward upon cycle number. The results indicated that damage occurred and gradually accumulated with cyclic loading, because no remarkable time drift of the resistance occurred for the CBCC sensors (Li et al., 2008).
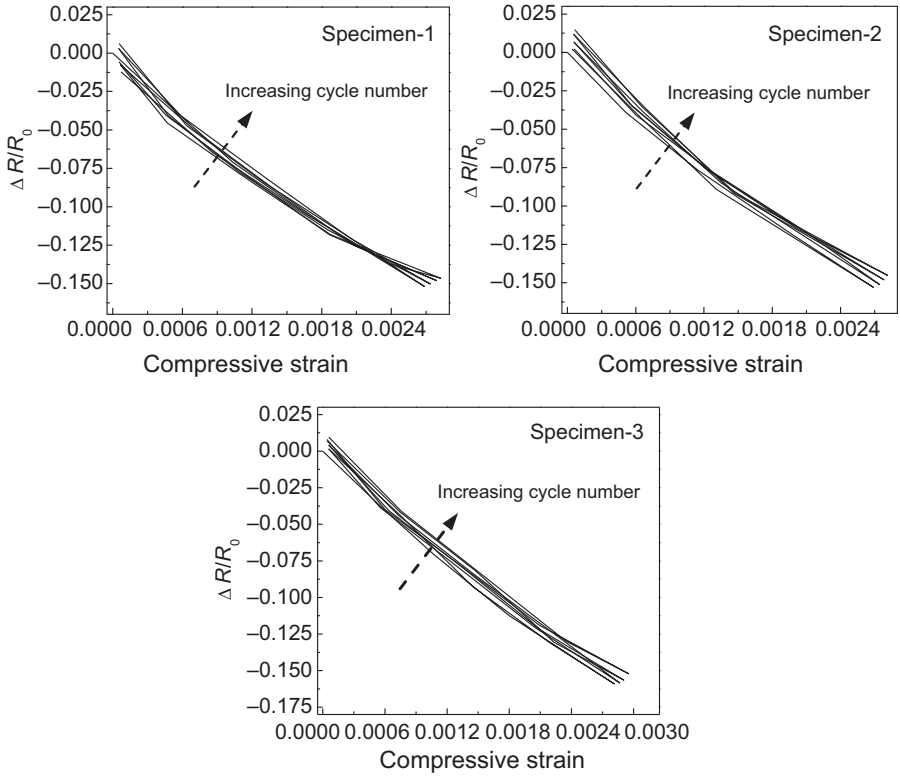
Figure 4.7 Piezoresistivity of CBCC sensor under cyclic loading with an amplitude of 35 kN.

4.3 Modeling of piezoresistivity of cement-based composite

According to tunneling effect theory (Simmons, 1963), current density in a tunneling resistor formed by two adjacent CB particles at a low-voltage region can be depicted by the following equation:

$$J = \left[3(2m\varphi)^{1/2}/2S_0\right](e/h)^2 U \cdot \exp\left[-(4\pi S_0/h)(2m\varphi)^{1/2}\right], \qquad (4.2)$$

where: J is current density; m, e, and h are the electron mass, charge on an electron, and Planck's constant, respectively; and φ, S_0, and U are the height of tunneling potential barrier, tunneling width, and voltage applied across the tunneling resistor, respectively. R_{t0} denotes the tunneling resistor, and A and S_0 denote the section area and length of the resistor, respectively. Then, the resistance of the resistor can be obtained as

$$R_{t0} = k_1 S_0 \exp(k_2 S_0), \qquad (4.3)$$

where: $k_1 = (2/3)(2m\varphi)^{-1/2}(e/h)^{-2}A^{-1}$ and $k_2 = (4\pi/h)(2m\varphi)^{1/2}$.

For a given composite, k_1 and k_2 are constants. S_0 can be obtained as follows:

$$S_0 = D\left[(\pi/6)^{1/3}V_c^{-1/3} - 1\right], \tag{4.4}$$

where: V_c and D are the volume concentration and diameter of CB particles, respectively. Equation (4.2) indicates that even a slight change of S_0 may cause a large change of resistance. Conductive networks in CBCC are composed of a large number of R_0, and the change in resistance of CBCC is the integrated result of the change of each R_{t0}. Therefore, the piezoresistivity model of CBCC will be established based on the resistance behavior of each R_{t0}. The resistance of each R_{t0} under strain can be quantified with Eqn (4.3); hence, the key task of the modeling is to obtain the deformation of each R_{t0} under external strain.

The microstructure of CBCC was observed with scanning electron microscopy to study the characteristics of the conductive network of CBCC. Figure 4.8(a) shows the microstructure of CBCC, in which the bright spherical objects and rounded hollowness denote CB particles. To see the pattern of conductive networks clearly, CB particles are emphasized in a white background, as shown in Figure 4.8(b). The conductive path is formed by adjacent CB particles and is presented in Figure 4.8(b) by joining the CB particles. Based on the schematic characteristics of a conductive network, a conductive model is proposed, as shown in Figure 4.8(c). First, R_{t0} is connected in series to form a resistor element R_0. Then, R_0 forms the conductive network by connections in parallel and then series. It can be easily derived that the fractional change of resistance of CBCC is equal to that of R_0. Therefore, piezoresistivity modeling of CBCC is focused on the behavior of R_0 under external loading.

The resistance value of each R_{t0} can be calculated based on Eqns (4.2) and (4.3). The orientation direction of each R_{t0} is assumed to be uniformly distributed by considering the infinite and randomly distributed CB particles in CBCC. Figure 4.9(a) and (b) show the schematics of orientation and distribution of a tunnel resistor, respectively. Assume

(a) (b) (c)
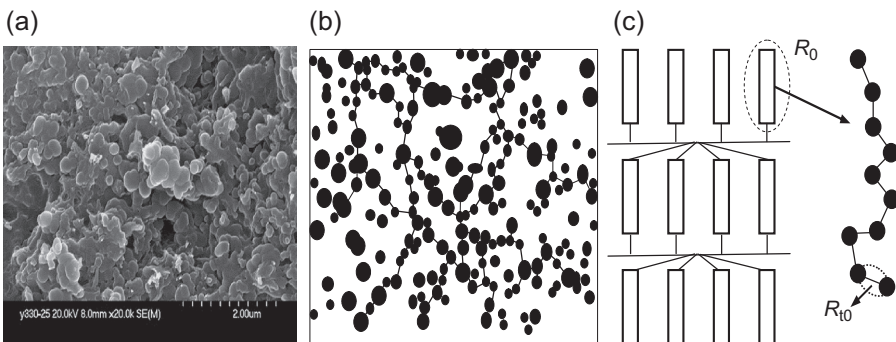
Figure 4.8 Schematic of conductive network in CBCC. (a) SEM picture, (b) schematic picture, and (c) conductive network model.
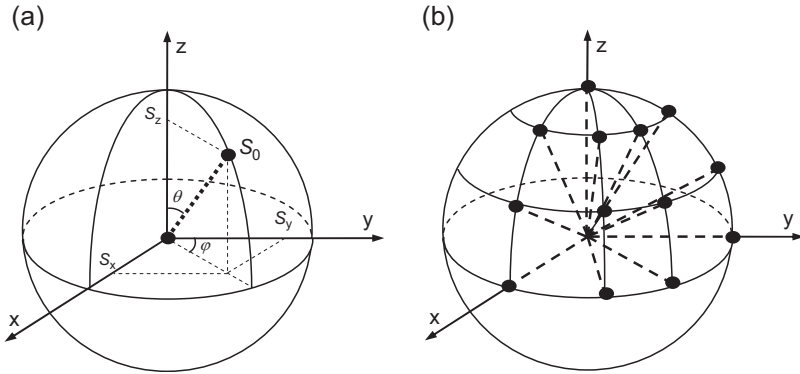
Figure 4.9 Schematic of (a) orientation and (b) distribution of R_{t0}.

that there are a total of $4 \times 3(M + 1)^2$ of R_{t0} in the space and each $4(M + 1)^2$ of R_{t0} surrounds a coordinator. For example, $4(M + 1)^2$ of R_{t0} is first defined by θ_z and φ_z, as shown in Figure 4.9(a). Both θ_z and φ_z should be over the range of $(0, 2\pi)$; however, considering the symmetrical characteristic of R_{t0} in each quadrant, $\theta_z, \varphi_z \in [0, \pi/2]$ is sufficient to represent the orientation character of R_{t0} and is adopted in this chapter. Therefore, θ_z and φ_z are in

$$\theta_z, \varphi_z = [0, \pi/2M, \pi/M, 3\pi/2M, \cdots, \pi/2(M - 1), \pi/2], \tag{4.5}$$

where: θ_x, φ_x, and θ_y, φ_y are defined in the same way as θ_z, φ_z. Hence, the resistance behavior of CBCC can be described by the $3(M + 1)^2$ of R_{t0}. As shown in Figure 4.9(b), the distribution of CB particles defined by the above method is not uniform in space so that the distribution density is higher near each coordinate, but it is uniform in calculating the effect of multiaxial strain on resistance.

When CBCC is load free, the original length of R_{t0} is S_0, and R_0 is the sum of $3(M + 1)^2$ of R_{t0} as

$$R_0 = 3(M + 1)^2 k_1 S_0 \exp(k_2 S_0). \tag{4.6}$$

Then, assuming that CBCC is subjected to multiaxial strain of ε_{mx}, ε_{my}, and ε_{mz} in each axis, the corresponding strain of R_{t0} in each axis direction can be calculated as

$$\varepsilon_{x,y,z} = \frac{\varepsilon_{mx,my,mz}}{V_c(E_m/E_c) + V_m}, \tag{4.7}$$

where: V_c and V_m are the ratio of volume occupied by CB and matrix to the whole volume of composite, respectively; and E_c and E_m are the modulus of CB and matrix,

respectively. The length of R_{t0} under multiaxial strain changes from S_0 to $S_{\varepsilon x}$, $S_{\varepsilon y}$, or $S_{\varepsilon z}$ as

$$S_{\varepsilon x} = S_0 \sqrt{\cos^2\theta_x(1+\varepsilon_x)^2 + \sin^2\theta_x \sin^2\varphi_x(1+\varepsilon_y)^2 + \sin^2\theta_x \cos^2\varphi_x(1+\varepsilon_z)^2},$$

$$S_{\varepsilon y} = S_0 \sqrt{\cos^2\theta_y(1+\varepsilon_y)^2 + \sin^2\theta_y \sin^2\varphi_y(1+\varepsilon_x)^2 + \sin^2\theta_y \cos^2\varphi_y(1+\varepsilon_z)^2},$$

$$S_{\varepsilon z} = S_0 \sqrt{\cos^2\theta_z(1+\varepsilon_z)^2 + \sin^2\theta_z \sin^2\varphi_z(1+\varepsilon_x)^2 + \sin^2\theta_z \cos^2\varphi_z(1+\varepsilon_y)^2}.$$

$$(4.8)$$

Equation (4.8) indicates that even under the same external strain status, the strain of each R_{t0} with a different orientation angle is different. Therefore, based on Eqns (4.6) and (4.8), the resistance of CBCC under multiaxial strain changes from R_0 to R as

$$R = \sum_{i=1}^{M+1} \sum_{j=1}^{M+1} k_1 S_0 [F_x \exp(k_2 S_0 F_x) + F_y \exp(k_2 S_0 F_y) + F_z \exp(k_2 S_0 F_z)],$$

$$(4.9)$$

where:

$$F_x = \sqrt{\begin{array}{l} \cos^2\left(\dfrac{(i-1)\pi}{2M}\right)(1+\varepsilon_x)^2 + \sin^2\left(\dfrac{(i-1)\pi}{2M}\right)\sin^2\left(\dfrac{(j-1)\pi}{2M}\right)(1+\varepsilon_y)^2 \\[3mm] + \sin^2\left(\dfrac{(i-1)\pi}{2M}\right)\cos^2\left(\dfrac{(j-1)\pi}{2M}\right)(1+\varepsilon_z)^2, \end{array}}$$

$$F_y = \sqrt{\begin{array}{l} \cos^2\left(\dfrac{(i-1)\pi}{2M}\right)(1+\varepsilon_y)^2 + \sin^2\left(\dfrac{(i-1)\pi}{2M}\right)\sin^2\left(\dfrac{(j-1)\pi}{2M}\right)(1+\varepsilon_x)^2 \\[3mm] + \sin^2\left(\dfrac{(i-1)\pi}{2M}\right)\cos^2\left(\dfrac{(j-1)\pi}{2M}\right)(1+\varepsilon_z)^2, \end{array}}$$

$$F_z = \sqrt{\begin{array}{l} \cos^2\left(\dfrac{(i-1)\pi}{2M}\right)(1+\varepsilon_z)^2 + \sin^2\left(\dfrac{(i-1)\pi}{2M}\right)\sin^2\left(\dfrac{(j-1)\pi}{2M}\right)(1+\varepsilon_x)^2 \\[3mm] + \sin^2\left(\dfrac{(i-1)\pi}{2M}\right)\cos^2\left(\dfrac{(j-1)\pi}{2M}\right)(1+\varepsilon_y)^2. \end{array}}$$

Hence, the change in resistance of CBCC can be calculated as

$$\frac{R}{R_0} = \frac{1}{3(M+1)^2} \sum_{i=1}^{M+1} \sum_{j=1}^{M+1} \{F_x \exp[k_2 S_0(F_x - 1)] + F_y \exp[k_2 S_0(F_y - 1)]$$
$$+ F_z \exp[k_2 S_0(F_z - 1)]\}.$$

$$(4.10)$$

Conducting series expansion on the exponent function in Eqn (4.10), the following equation can be obtained:

$$\frac{R}{R_0} = \frac{1}{3(M+1)^2} \sum_{i=1}^{M+1} \sum_{j=1}^{M+1} (F_x + F_y + F_z)$$

$$+ \frac{k_2 S_0}{3(M+1)^2} \sum_{i=1}^{M+1} \sum_{j=1}^{M+1} \left(F_x^2 - F_x + F_y^2 - F_y + F_z^2 - F_z \right)$$

$$+ \frac{(k_2 S_0)^2}{6(M+1)^2} \sum_{i=1}^{M+1} \sum_{j=1}^{M+1} \left[F_x (F_x - 1)^2 + F_y (F_y - 1)^2 + F_z (F_z - 1)^2 \right] + \cdots$$

$$(4.11)$$

The first item of the right-hand side in Eqn (4.11) is the inherent behavior of the integrated change in length of each R_{t0} under external strain and is denoted as $\overline{S}/S_0$, which represents the resistance change trend of CBCC under multiaxial strain. $k_2 S_0$ is denoted as β, which represents the sensitivity factor of CBCC and is dependent on the intrinsic property of CBCC. Therefore, $\overline{S}/S_0$ and β represent the piezoresistivity characteristics (trend and sensitivity factor) of a composite. Considering the uncertainty in CBCC synthesis, β is best obtained from a simple uniaxial compressive test and can then be utilized to predict the resistance behavior of CBCC under complex loading and environmental conditions. The applicability of obtaining β from a simple compressive test will be validated by utilizing it in predicting resistance behavior under other effects (CB concentration and temperature). Orientation uniformity of R_{t0} is dependent on the value of M. $M \geq 30$ can meet the precision requirement of calculation.

For CBCC, considering the strain gauge factor of 55.5 (Li et al., 2006), coefficient β can be calculated as 337, and k_2 is then obtained as 3.45 nm^{-1}. Utilizing these parameters, the model can predict the strain gauge factors of a composite under various complex strain statuses. Besides predicting the resistance behavior of CBCC under various strain states, the model can be used to predict the resistance behavior of CBCC under various ambient conditions by transforming such conditions into strain.

Thermal expansion will lead to a change in S_0 that may cause a change in strain gauge factor. By substituting thermal expansion strain into the proposed model, the strain gauge factors under various temperatures can be predicted. Experiments were conducted for CBCC. The thermal expansion coefficient (TEC) of CBCC in the longitudinal direction and transverse direction was measured as 16.5 and 13.9, respectively. The slight discrepancy of TECs in different directions was caused by the embedded electrical probes. Taking the distance S_0 under 20 °C as the baseline, the original distances between each two adjacent CB particles under various temperatures can be calculated based on the measured TEC. Then, based on the proposed model, strain gauge factors of CBCC under various temperatures were obtained, as shown in Figure 4.10. The theoretical strain gauge factors change slightly from 55.197
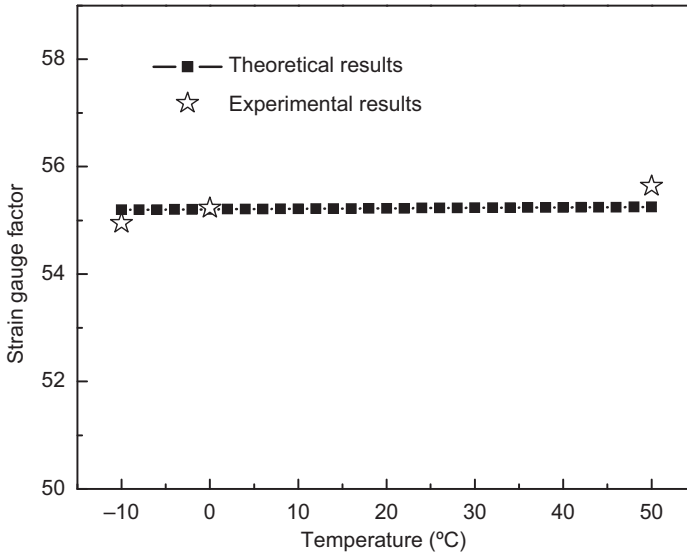
Figure 4.10 Effect of temperature on the strain gauge factors.

($-10\,°C$) to 55.249 (50 °C), indicating that the effect of temperature on strain gauge factor is slight. The experimental measured strain gauge factors — 54.95 ($-10\,°C$), 55.23(20 °C), and 55.64 (50 °C), respectively, as shown in Figure 4.10 — also show a small dependence on temperature.

The strain gauge factor is dependent on the original distance S_0 between each two adjacent CB particles. Simultaneously, S_0 is a function of CB concentration. Therefore, the strain gauge factor is dependent on CB concentration. By transforming the change in CB concentration into the change in original distance, S_0, the effect of CB concentration on the strain gauge factor can be predicted with the proposed model. In addition, the applicability of defining β from a simple piezoresistivity test can be validated in this section by comparative study between theoretical and experimental results.

The strain gauge factors of CBCC with various concentrations of CB are obtained as shown in Figure 4.11. Because the model is proposed based on tunnel effect theory, the CB concentration range is limited to a near-percolation threshold that varies from 8.79 to 11.39 vol% (Scott et al., 1996), and the experimental data of such CB concentrations (i.e., 8.79 vol% and 11.39 vol%) are compared with the theoretical results. As shown in Figure 4.11, the strain gauge factor decreases with CB concentration, which can be attributed to the decrease of the original S_0 due to CB concentration. The theoretical strain gauge factor of CBCC with CB particles in the amount of 11.39 vol% is 38.4, close to the experimental result of 37.71. The comparison between modeling and experimental results indicates that the model and the defined β are applicable.
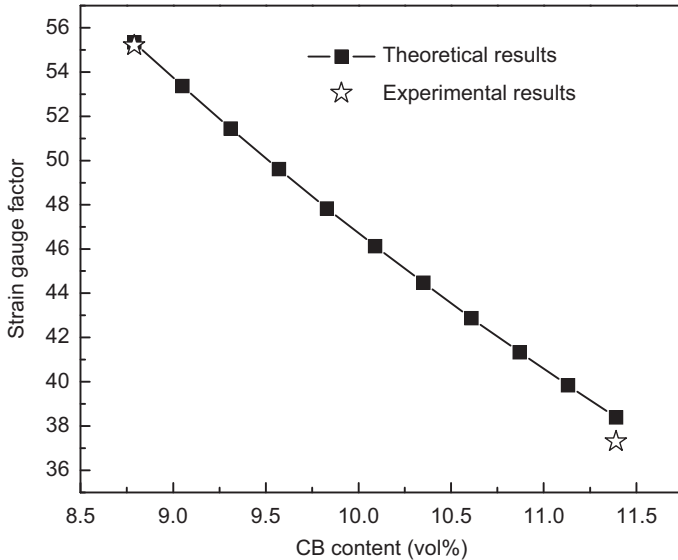
Figure 4.11 Model and experimental results of the effect of CB concentration on strain gauge factors.

4.4 Self-sensing concrete structures

4.4.1 Materials and experimental methods

CBCC sensors were made with carbon black−filled cement-based composite, which is a material with piezoresistivity that described in Section 4.2. The resistance of CBCC sensors was measured using the four-probe method in which copper nets served as electrical contacts. The copper nets were placed into the specimen when pouring the mix into molds. Four contacts were placed across the whole cross-section of 30×40 mm. The two outer contacts (36 mm apart) were for passing the current. The inner two contacts (20 mm apart) measured the voltage. The parameters of free CBCC sensors are shown in Table 4.1.

Concrete beams were made with C40 concrete. The cement used was Portland cement P.O32.5. The fine aggregate was natural river sand with a fineness modulus

Table 4.1 Properties of CBCC sensors

Strain-sensing properties		Mechanical properties			
Resistivity (Ω cm)	Gauge factor	Strength (MPa)	Peak strain ($\mu\varepsilon$)	Modulus ($\times 10^4$ MPa)	Poisson ratio
719.4 ± 53.7	55.5 ± 2.87	44.7 ± 0.32	4400 ± 136	1.44 ± 0.06	-0.17 ± 0.015

Table 4.2 Mix proportions of concrete columns (kg/m³)

Strength grade	Cement	Water	Sand	Coarse aggregate
C40	435	190	535	1240
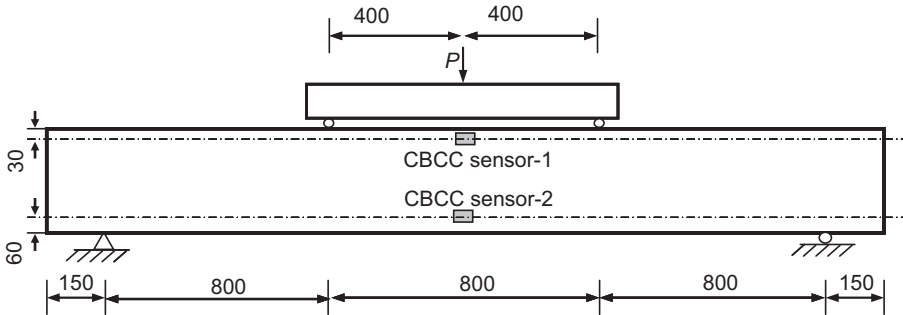
Figure 4.12 Schematic of the loading arrangement and CBCC sensor locations (mm).

of 2.94. The coarse aggregate was crushed diabase with a maximum radius of 20 mm. A water-reducing agent (FDN) and silica fume (average radius is 100 nm) were used. The mix proportions are shown in Table 4.2. The configuration of concrete beam is shown in Figure 4.12. The width was 150 mm, depth was 300 mm, and clear span of concrete beam was 240 mm (overall span was 270 mm). The upper constructional bar was plain steel bar with yield stress of 235 MPa. The hooping bar was plain steel bar with yield strength of 235 MPa, spacing 100 mm at the two side one-third spans. The under-reinforcing bar was HRB335 (hot rolled ribbon steel bars) with yield strength of 345 MPa and Young's modulus of 200 GPa.

As shown in Figure 4.12, a point load P was distributed into two equal point loads before applying on the simple beam, dividing the clean span of beam into three equal spans. Based on the normal material mechanics, the resulted loading on the middle span was pure flexion and on the two side spans was combined flexion and shear. Hence, three different stress states were generated in the beam (i.e., uniaxial compression and uniaxial tension in the top and bottom of the middle span, respectively, and combined compression and shear in the top of the side span). CBCC sensors were located at those three different stress zones and were named CBCC sensor-1 and CBCC sensor-2, respectively, as shown in Figure 4.12. The sides of CBCC sensors coincided with those of concrete beams for a 30 mm side parallel to beam depth, 40 mm side parallel to beam width, and 50 mm side parallel to beam span. Also, the CBCC sensor center was coincident with the beam width center. The distance of CBCC sensor-1 center from the beam top was 30 mm, and that of CBCC sensor-2 center from the beam bottom was 60 mm. Because the resistance measurement of CBCC

Figure 4.13 Experimental setup.

sensors was made along the 50 mm side, compressive or tensile strain along the span would be measured by CBCC sensors. Strain gauges, servicing as a reference, were attached on the side surfaces of beams corresponding to the locations of CBCC sensors for evaluating the performance of CBCC sensors.

Three beams with embedded CBCC sensors were prepared. Load was applied with a jacking apparatus at step of 10 kN measured by a load cell as shown in Figure 4.13. First, cyclic load with amplitude of 20 kN was applied on the beams for three cycles, and then amplitude was increased to 30 kN for another three cycles. After that, monotonic load was applied until the reinforcing bar yield (marked by the phenomenon of strain continuous to increase under an approximately constant load) and then unload. During the loading and unloading procedure, strain was measured by embedded CBCC sensors and strain gauges.

Three concrete cylinders were made with the same concrete when pouring concrete beams. After 28 days of curing at the same condition with concrete beams, a uniaxial compressive test was conducted on these cylinders with a Materials Testing System (MTS) to get the basic mechanical properties of concrete.

4.4.2 Mechanical behavior of concrete beams

Because the main purpose of this article is to demonstrate the strain-sensing property of embedded CBCC sensors under different stress states, only a brief description of the beams' mechanical behavior is given here.

The compressive strength, modulus, and peak strain of C40 concrete obtained from the compressive test on cylinders are 35.3 MPa, 2.56 MPa, and 2016 $\mu\varepsilon$, respectively. For the concrete beams, no cracks appeared during 20 kN amplitude of cyclic loading. In the procedure of 40 kN amplitude of cyclic loading, small upward-developing cracks were observed on the beam's bottom. In the procedure of monotonic loading,

cracks progressively extended after 40 kN and speeded up after 90 kN. When the load reached about 140 kN, cracks propagated sharply into the top portion of beams and the beams entering the yielding region.

4.4.3   Compressive strain-sensing properties of CBCC sensor-1

Based on the performance of CBCC sensor-1, the compressive strain-sensing property of an embedded CBCC sensor under a uniaxial compression state was established, together with the previous studies on a free CBCC sensor to provide a comprehensive understanding of this property. Strain measured by embedded CBCC sensors was calculated based on the fractional change in resistance with a strain gauge factor of 55.5 as shown in Table 4.1.

Figure 4.14 shows the compressive strain measured by CBCC sensor-1 and strain gauge upon the load applied on a concrete beam by a jacking apparatus. As shown in Figure 4.14(a), under cyclic load with an amplitude of 20 kN, the measured strain of CBCC sensor-1 agrees well with that of the strain gauge. The strain amplitude is about 90 με. Nearly no residual strain occurs after each loading−unloading cycle,

Figure 4.14 Strain-sensing property of CBCC sensor-1: (a) under cyclic loading with an amplitude of 20 kN, (b) under cyclic loading with an amplitude of 40 kN, and (c) under monotonic loading until reinforcing bar yield followed by unloading.

indicating that no damage occurs in the top of pure flexion span. Figure 4.14(b) shows a good agreement between the measured strain of CBCC sensor-1 and that of strain gauge under 40 kN amplitude of cyclic load. The strain amplitude is about 240 με. The measured strain amplitudes for 20 and 40 kN both agree well with the theoretical values, indicating that embedded CBCC sensors have a repeatable and precise compressive strain-sensing ability. Figure 4.14(c) shows the measured strain under monotonic loading. Reinforcing bar enters the yield region after the load reaches about 130 kN (corresponding to 1000 με, marked as the "shift" in the strain−load curve), which means the concrete beam cannot bear further increasing load. Unload was then conducted after reinforcing bar yield. Before reinforcing bar yields, the measured strain of CBCC sensor agrees well with that of strain gauge. In reinforcing bar yield region, the strain measured by CBCC sensor becomes smaller than that measured by strain gauge. During the unloading procedure, strain measured by CBCC sensor-1 approaches that measured by strain gauge quickly and then keeps agreement. A residual strain of about 400 με was measured by both CBCC sensor-1 and strain gauge at the end of unloading. The reasonable measured strain of CBCC sensor-1 in whole testing procedures indicates that embedded CBCC sensors under uniaxial compression are competent for measuring compressive strain of a reinforced concrete member.

The slight inaccuracy of CBCC sensors at the reinforcing bar yield region is attributed to the Poisson ratio enhancement of concrete at that region. As measured by strain gauge, the compressive strain of concrete reaches 1000 με when the reinforcing bar yields, meaning the concrete enters the plastic deformation stage that results in an increase in Poisson ratio based on the normal knowledge of concrete. However, the piezoresistivity of CBCC material is multiaxial strain dependent, and the strain gauge factor will decrease upon Poisson ratio (Xiao et al., 2010). Therefore, the increasing Poisson ratio of concrete at the stage of reinforcing bar yield generates a bigger transverse deformation condition for the embedded CBCC sensors relative to a free CBCC sensor, resulting in the discrepancy between the real and being-used gauge factors. However, the gauge factor used here to calculate strain is still the calibrated gauge factor, 55.5. Hence, the strain measured by CBCC sensors becomes lower than that measured by the strain gauge. The experimental results indicate that a gauge factor modification method for CBCC sensors should be developed to get a precise sensing result under all loading stages. Regardless, an embedded CBCC sensor under uniaxial compression state appears to be competent for measuring the repeatable compressive strain of concrete within a normal load level.

4.4.4 Compressive strain-sensing properties of CBCC sensor-2

Based on the performance of CBCC sensor-2, the tensile strain-sensing property of an embedded CBCC sensor under uniaxial tension was established. As shown in Figure 4.15(a), under 20 kN amplitude of cyclic load, the tensile strain amplitude is about 140 με. A residual strain of about 45 με remains after the first cycle, indicating that micro cracks occur under this tensile strain level. As shown in Figure 4.15(b), under 40 kN amplitude of cyclic load, the strain increases sharply upon load after exceeding 180 με and a residual strain of 400 με occurs after the first cycle, indicating
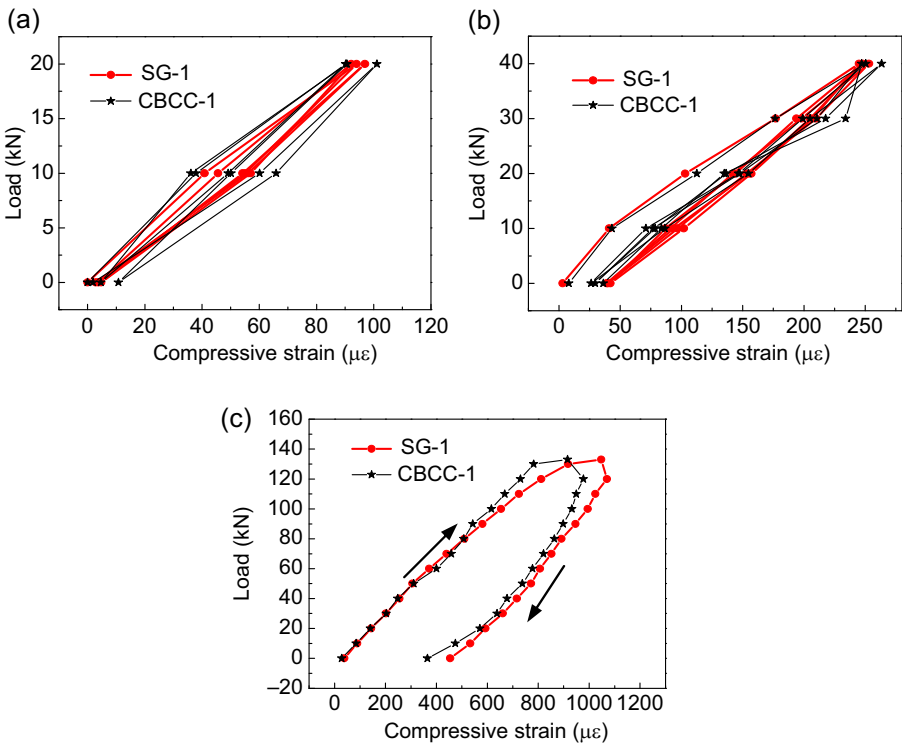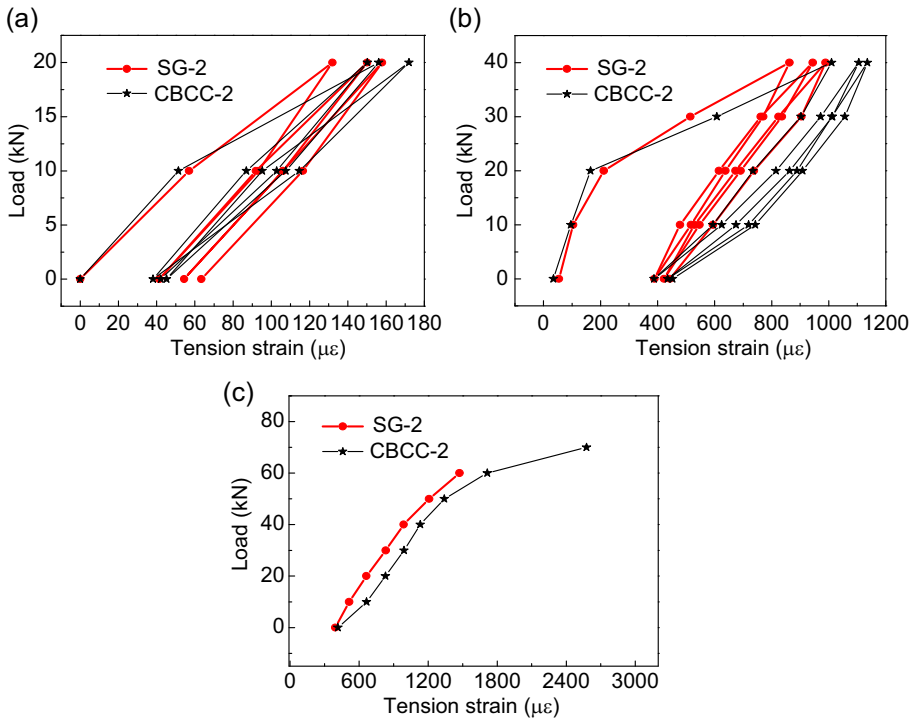
Figure 4.15 Strain-sensing property of CBCC sensor-2: (a) under cyclic loading with amplitude of 20 kN, (b) under cyclic loading with amplitude of 40 kN, and (c) under monotonic loading.

the continuous opening and accumulation of micro cracks in this region. Although the strain amplitude measured by CBCC sensor-2 is a little higher than that measured by strain gauge, the reasonable and approximately agreeing results indicate that CBCC sensors can be used to measure small tensile strain. Figure 4.15(c) shows that, after about 1400 με, strain gauge outs work and CBCC sensor-2 outs work soon, meaning that macro-cracks form in concrete beams and propagate through CBCC sensors. The experimental results indicate that CBCC sensors are competent for measuring a small level of tensile strain.

4.5 Future of multifunctional nano-concrete

Concrete structures constitute a large portion of civil infrastructures, but their reliability is relatively low because of wide material discreteness and a complex service environment. Consequently, the safety of concrete structures is an important problem that receives attention at all times in civil engineering. Therefore, it is necessary to take reasonable measures to monitor the state of concrete structures. In order to monitor the performance and state of concrete structures during their service periods, information on the structural state needs to be obtained by appropriate monitoring technologies.

Now, local monitoring for concrete structures is usually achieved by embedding such sensors as electric-resistant strain gauges, optic sensors, piezoelectric ceramic, shape memory alloys, and fiber-reinforced polymer bars in key structural positions. However, these sensors have such drawbacks as poor durability, low sensitivity, high cost, and unfavorable compatibility with concrete structures. Smart concrete has favorable piezoresistivity, great durability, and good compatibility with concrete structures and so on, and it can therefore be used to develop retrofit or new installations, including traffic monitoring, weighing in motion, corrosion monitoring of rebar, and strain-sensing coating.

Acknowledgments

References

Austin, T., Singh, M., Gregson, P.J., Dakin, J.P., Powell, P.M., 1999. Damage assessment in hybrid laminates using an array of embedded fiber optic sensors. In: Proc. The SPIE Conference on Smart Systems for Bridges, Structures and Highways, Newport Beach, California, March SPIE. 3671, pp. 281−287.

Chen, B., Liu, J.Y., 2008. Damage in carbon fiber-reinforced concrete, monitored by both electrical resistance measurement and acoustic emission analysis. Construction and Building Materials 22, 2196−2201.

Chen, J.C., 1995. Intelligent monitoring system for suspension bridge damage detection. In: Proc. of Bridge into the 21st Century Conference, Hongkong, October, 25.

Claus, R.O., Mckeenman, J.C., May, R.G., et al., 1988. Opitical fiber sensors and signal processing for smart materials and structures ARO smart Materials. In: Structures and Mathematical Issues Workshop Proceeding. Virginia Polytechnic Institute and state University Blacksburg, VA, pp. 15−16.

Han, B.G., Ou, J.P., 2007. Embedded piezoresistive cement-based stress/strain sensor. Sensors and Actuators A 138, 294−298.

Han, B.G., Guan, X.C., Ou, J.P., 2007. Electrode design, measuring method and data acquisition system of carbon fiber cement paste piezoresistive sensors. Sensors and Actuators A: Physical 135, 360−369.

Li, H., Ou, J.P., Zhao, X.F., 2006. Structural health monitoring system for the Shandong Binzhou Yellow river highway bridge. Computer-Aided Civil and Infrastructure Engineering 21 (4), 306−317.

Li, H., Xiao, H.G., Ou, J.P., 2006. Effect of compressive strain on electrical resistivity of carbon black-filled cement-based composites. Cement and Concrete Composites 28, 824−828.

Li, H., Xiao, H.G., Ou, J.P., 2008. Electrical property of cement-based composites filled with carbon black under long-term wet and loading condition. Composites Science and Technology 68, 2114−2119.

Ou, J.P., Han, B.G., 2009. Piezoresistivie cement-based strain sensors and self-sensing concrete components. Journal of Intelligent Material Systems and Structures 20, 329−336.

Reza, F., Batson, G.B., Yamamuro, J.A., Lee, J.S., 2003. Resistance changes during compression of carbon fiber cement composites. Journal of Materials in Civil 15, 476−483.

Scott, W.D., Charles, R.F., Michael, B.P., Daniel, W.S., 1996. Damage Identification and Health Monitoring of Structural and Mechanical Systems from Changes in Their Vibration Characteristics: A Literature Review (Report of Los Almos Lab).

Simmons, J.G., 1963. Generalized formula for the electric tunnel effect between similar electrodes separated by a thin insulating film. Journal Applied Physics 34, 1793−1803.

Song, X.H., Zheng, L.X., Li, Z.Q., 2006. Temperature compensation in deformation testing for smart concrete structures. Key Engineering Materials 326−328, 1503−1506.

Wang, S., Shui, X., Fu, X., Chung, D.D.L., 1998. Early fatigue damage in carbon-fibre composites observed by electrical resistance measurement. Journal of Materials Science 33, 3875−3884.

Wen, S.H., Chung, D.D.L., 2001. Carbon fiber-reinforced cement as a strain-sensing coating. Cement and Concrete Research 31, 665−667.

Xiao, H.G., Li, H., March, 2006. A study on the application of CB-filled cement-based composites as a strain sensor for concrete structures. In: (SPIE)Nondestructive Evaluation and Health Monitoring of Aerospace Materials, Composites, and Civil Infrastructure. San Diego, CA, USA.

Xiao, H.G., Li, H., Ou, J.P., 2010. Modeling of piezoresistivity of carbon black filled cement-based composites under multi-axial strain. Sensors and Actuators A: Physical 160, 87−93.

Xiao, H.G., Li, H., Ou, J.P., 2011a. Self-monitoring properties of concrete columns with embedded cement-based strain sensors. Journal of Intelligent Material Systems and Structures 22, 191−200.

Xiao, H.G., Li, H., Ou, J.P., 2011b. Strain sensing properties of cement-based sensors embedded at various stress zones in a bending concrete beam. Sensors and Actuators A: Physical 167, 581−587.

Yu, X., Kwon, E., 2009. A carbon nanotube/cement composite with piezoresistive properties. Smart Materials and Structures 18, 1−5.

Hybrid cementitious materials: nanoscale modeling and characterization

5

Rouzbeh Shahsavari [1,2], Navid Sakhavand [1]
[1]Rice University, Houston, TX, USA; [2]Smalley Institute for Nanoscale Science and Technology, Houston, TX, USA

5.1   Introduction

Cement paste owes its remarkable cohesive strength primarily to the calcium−silicate−hydrate (C-S-H) gel, an amorphous-like gel with a clay-like backbone (Allen et al., 2007; Taylor, 1986). With the presence of zeolitic-type pores and water in interlaminar distances (Pellenq et al., 2008), C-S-H has a very complex structure that makes it nontrivial to come up with unified strategies to improve and control the mechanical properties and performance of cementitious materials at larger scales (Pellenq et al., 2008; Alizadeh et al., 2011). Here, we review some of the efforts in nanoengineering cement paste to enhance its mechanical properties. There are two venues leading toward material property improvement, and the first is engineering the nanoparticle forces within C-S-H. The less ordered layers in C-S-H are shown to be akin to tobermorite and jennite lamellae (Figure 5.1) (Muller et al., 2012; Richardson, 1999). The stacking defects in C-S-H are filled with highly mobile hydrated calcium ions
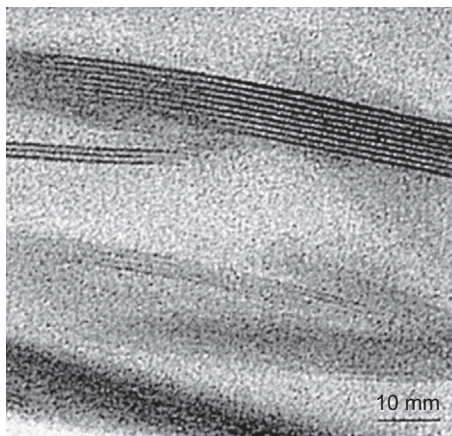
Figure 5.1 Transmission electron microscopy (TEM) of C-S-H shows a tobermorite-like layered structure (Merlin et al., 2002).

(Pellenq et al., 2008). The discontinuous lamellae of C-S-H provide an opportunity to increase the individual lamellae bonding forces. This method will affect the strength and stiffness of C-S-H but not its brittleness (Pellenq et al., 2008).

The second strategy is to improve the interparticle forces through incorporation of a low-concentration softer matrix. Many natural biocomposites that have adapted this method demonstrate an excellent balance of mechanical properties. For instance, despite being made of 95% brittle aragonite, nacre in abalone shell is ∼3000 times tougher than aragonite (Espinosa et al., 2009; Lin et al., 2006). Reinforcing the cement paste with admixtures seems to be a more realistic method than increasing intrinsic cohesive forces. Therefore, understanding the complex mechanisms of biological structures paves the road to mimic the structure of natural materials and synthesize cementitious composites with analogous or perhaps better mechanical properties.

5.1.1 Biomimetic hybrid materials design

Comparison of the synergy of mechanical properties in natural and synthetic composites reveals important features. As shown in Figure 5.2, ceramics are highly stiff but are very brittle. On the other hand, polymers are very ductile and flaw-tolerant but deform easily with small forces (low stiffness and strength). Generally speaking, polymers and other softer fibers or particles are typically added to stiff materials to enhance their ductility (Corni et al., 2012). Composites are usually made combining two or more materials with contrasting properties to achieve the desired level of synergistic properties. Although this strategy is executed poorly with synthetic materials, natural materials
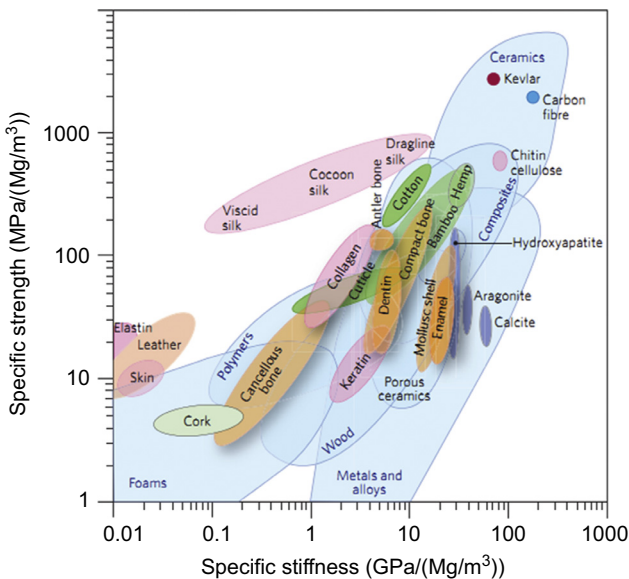
Figure 5.2 Material−property relationship for natural and synthetic materials (Wegst et al., 2015). Unlike synthetic materials, natural materials reach their mechanical properties under ambient conditions with a limited number of constituents.

have mastered this strategy over the course of thousands of millions of years of evolution. For instance, the addition of a few percent of a soft biopolymer to a stiff calcite yields a stiff and tough nacre, better known as the inner layer of abalone seashell (Sakhavand and Shahsavari, 2015).

The success of natural materials in their superior mechanical properties is attributed to a number of different traits, including the presence of multiple contrasting materials; the particular architecture of the composite to channel, control, and arrest the cracks; and in some cases their hierarchical structure at the nano, micro, and macro levels. Over the years, different methods have been utilized to replicate the structure of natural materials, such as nacre and nacre-like (platelet−matrix) composites, in the lab environment. Launey et al. (2009) used freeze casting—entrapment of solutes between ice crystals—to synthesize an alumina (Al_2O_3)−polymer composite and reported simultaneous high strength and toughness (Figure 5.3). Chemical grafting of the interface strengthened the bonding at the interface of polymer and platelets, hence further increasing both strength and toughness. Alumina−polymer was also produced by gel casting and hot pressing, a simple and fast method with promising results in high-scale production of nacre-like composites (Bonderer et al., 2008). Ekiz et al. (2009) utilized hot-press-assisted slip casting (HASC) to produce an alumina−epoxy composite. The failure mechanism of their composite was mostly governed by debonding of the epoxy−alumina interface rather than sliding of the alumina platelets on the epoxy matrix. Although similar strength values as those of nacre were reported for this composite, the debonding behavior reveals inefficiency in the composite structure that reduces its possible maximum properties.

Biomineralization is another technique in which hard platelet crystals are mineralized in a solution of soft biomolecules. Various platelet−matrix composites such as potassium sulfate−polymer (Oaki et al., 2006) and ZnO−polymer (Tseng et al., 2009) are synthesized with this method. The slow procedure and lower than expected mechanical properties are the key drawbacks of this method. Other methods include
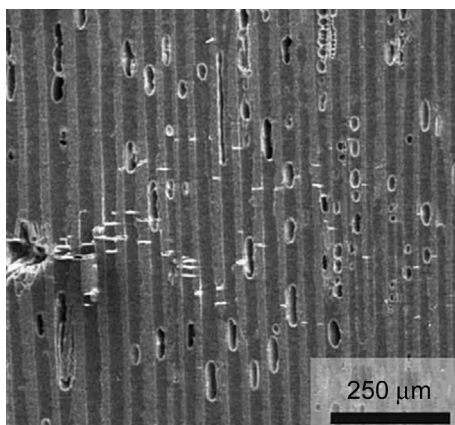
Figure 5.3 Scanning electron micrography (SEM) image of (Al_2O_3)−polymer shows the layered nacre-like structure. Al_2O_3 is the ceramic platelets, and the polymer is the matrix (Launey et al., 2009).

extrusion and roll compaction (Wang et al., 2000), layer-by-layer self-assembly (Tang et al., 2003a), centrifugation (Chen et al., 2008), evaporation (Bennadji-Gridi et al., 2006), and electrophoretic deposition (Lin et al., 2009). In brief, after using different techniques and various constituents, researchers have reported successful synthesis of nacre-like composites that combines hard and soft materials for a tough and strong composite. In the next two sections, we focus on similar efforts to incorporate soft materials into the cement paste to achieve material property enhancement.

5.2 Hybrid polymer−cement composites

By combining platelet-like ceramic building blocks and organic polymer matrices, nature creates hybrid materials such as bone, teeth, and mollusk shells that have an outstanding balance of stiffness, strength, and flaw tolerance (Espinosa et al., 2009; Fratzl et al., 2004; Gao, 2006). This has inspired fabrication of several advanced human-made polymer matrix composites with inorganic reinforcing materials such as cement, clays, glass, graphite, SiC, and mica (Bonderer et al., 2008; Beaudoin et al., 2009a; Rexer and Anderson, 1979; Tang et al., 2003b). Polymer-incorporated cement is one type of hybrid cement nanocomposite that has received extensive attention since the release of a commercial polymer−clay nanocomposite at Toyota Labs (Kojima et al., 1993). Experiments using X-ray diffraction (XRD), nuclear magnetic resonance (NMR), and Fourier transform infrared spectroscopy (FTIR) techniques on cement−polymer nanocomposites have revealed successful incorporation of polymer chains into the nanopores of C-S-H (Merlin et al., 2002; Okamoto, 2003; Mojumdar and Raki, 2005). Three possible thermodynamic forms for polymer− layered silicate composites have been proposed (Okamoto, 2003) (Figure 5.4): a) conventional microcomposites in which the polymer chains encompass layered clay-like stacks in two separate phases; b) intercalated nanocomposites in which the polymer penetrates the interlayer of the silicate chains without destroying the layered structure

(a)   (b)   (c)
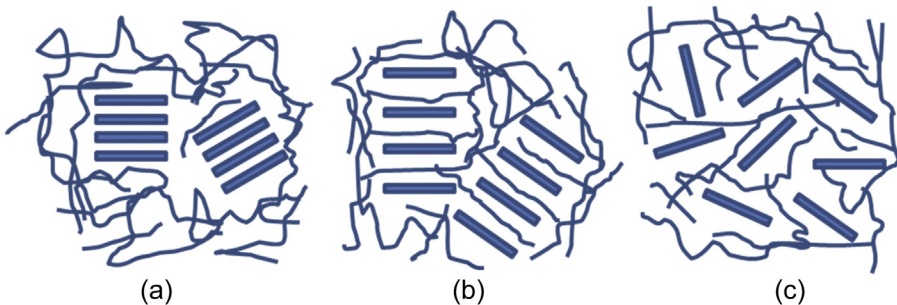
Figure 5.4 Possible composite materials through the interaction of polymer and layered silicate: (a) conventional composite, (b) intercalated nanocomposite, and (c) exfoliated nanocomposite. This chapter on the small interfacial region where polymer interacts with the surface of the calcium−silicate−hydrate system.

of the system; and c) exfoliated nanocomposites in which the silicate layers are destroyed and separated in the polymer matrix.

In all such hybrid polymer−cement composites, the interface is oftentimes the bottleneck to understand and improve the properties of the hybrid systems, as the behavior of the bulk components of the composite is relatively more simple and predictable. Given the complexity of the cement molecular structure and variety of the phenomena that govern mechanical properties of hybrid cementitious composites, understanding the interfacial interactions in hybrid cementitious materials is a key challenge. In this regard, computational modeling at small scales is necessary to reveal the physics and chemistry of the interactions of the cement paste with other constituents. This will be discussed in detail in the next section.

5.2.1 Nanoscale modeling

Advancements in computational technology and access to low-cost computational facilities have turned computational experiments into applicable means of studying materials at submicro levels. The molecular dynamics method is a widely used computational tool in this area. Unlike experiments, computational methods are able to rapidly screen the various phenomena, model many systems, and replicate laboratory tests. Therefore, simulations can be utilized to predict interactions and properties of materials, thus guiding experiments in a more cost-effective and timely manner. The recent decoding of the molecular structure of cement hydrate (i.e., various combinatorial C-S-H phases with a full spectrum of industrial stoichiometries) (Pellenq et al., 2009; Abdolhosseini Qomi et al., 2014) has elevated the field of computational cement science at a completely different level, compared to years ago. In this context, the development of reliable potentials, so-called force field functions (Shahsavari et al., 2011) that describes complex interactions of the atoms in C-S-H, is a key toward any modeling and property evaluation in cement-based materials. Although many modeling reports including molecular dynamics and first-principles quantum calculations are available on the structure and mechanics of cementitious materials (Jalilvand and Shahsavari, 2014; Shahsavari et al., 2009; Shahsavari and Chen, 2015; Wu et al., 2011; Kalinichev et al., 2007), the simulation of hybrid cementitious materials such as polymer−cement composites is relatively rare.

Sakhavand et al. (2013) utilized molecular dynamics simulations to confirm a strong hydrogen bond (H-bond) network at the interface of a crystalline cement, known as tobermorite, and poly(vinyl alcohol) (PVA). They successfully identified and ranked the strength of various hydrogen bonds using potential of mean force and time correlation functions (Figure 5.5). The same group concluded that interfacial hydrogen bonding between oxygens of PVA (Op) and nonbridging oxygens (Onb) of silicate chains in tobermorite is critical to adhesion of the polymer to cement.

Using more accurate modeling via first-principles quantum calculations, Sakhavand et al. (2013) also reported that intramolecular H-bonding in PVA increases the intermolecular adhesion of PVA to tobermorite, a result that is not intuitive without advanced modeling capabilities. By quantifying the strength of the interface by pulling the polymer strand on the tobermorite, a slip-stick motion in PVA−cement composites
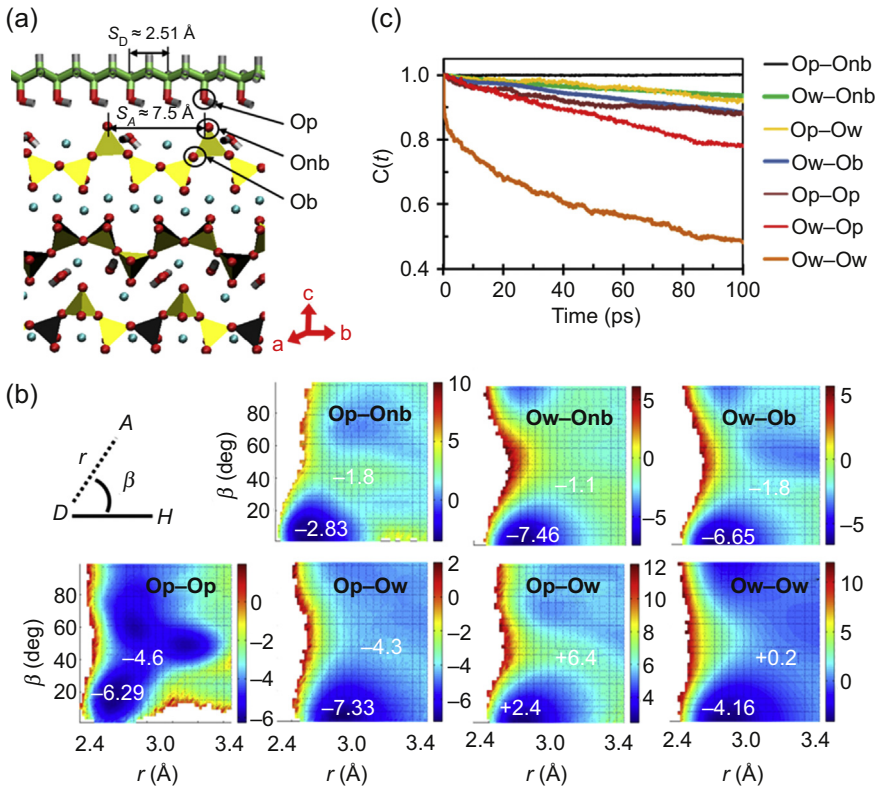
Figure 5.5 (a) Close-up atomistic snapshot of the PVA−tobermorite interface. Op refers to oxygen of PVA; and Ob and Onb denote, respectively, bridging and nonbridging oxygen atoms of silicates. (b) Potential of mean force plots for possible H-bonds in the PVA−tobermorite system calculated from MD simulations. In all cases, the magnitude of the global minima and the saddle points are shown with a white color. The inset on the top left shows a schematic picture of an H-bond denoted by an acceptor (A), a donor (D), and the hydrogen atom (H). (c) H-bond time correlation functions for different types of H-bonds. In the legend, the first and second atoms separated by the dash line indicate the donor and acceptor sites, respectively (Sakhavand et al., 2013).

was observed, suggesting that polymer strands provide extra toughness for the hybrid composite while bridging the particles under large deformations (Sakhavand et al., 2013). This interesting phenomenon was later verified via a systematic size−effect study, indicating that in contrast to the common intuition, a finite optimum length of polymer strands provides the most efficient composite to exhibit maximum mechanical properties (Sakhavand and Shahsavari, 2015; Sakhavand et al., 2013).

As an effort to simulate the failure of fiber-reinforced polymer concretes, Büyüköztürk et al. (2011) studied debonding of the epoxy polymers from the silica surface in wet and dry environments. They were able to quantify the weakening processes of the interfacial interactions. However, the effects on mechanical properties of
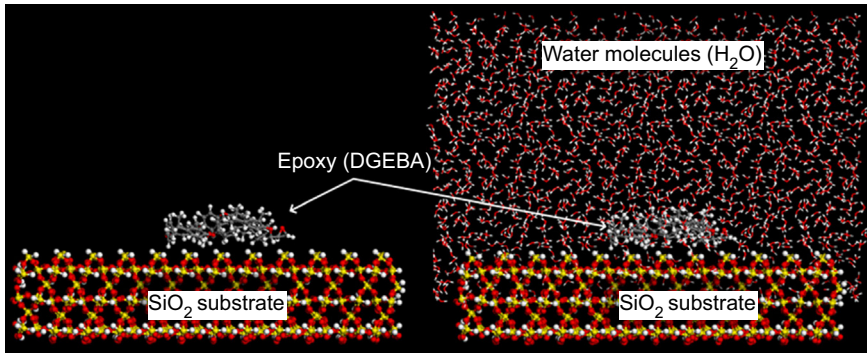
Figure 5.6 Schematic of molecular dynamics simulation of epoxy—silica in dry (left) and wet (right) environments (Büyüköztürk et al., 2011).

the system are yet to be explored. In another study, Dai et al. (2011) also used molecular dynamics to confirm agglomeration of organic monomers in the C-S-H matrix (Figure 5.6).

In general, the ultimate goal of these simulations at the nanoscale is predicting the interaction of polymer and cement and quantifying the hybrid properties of the systems, such as mechanical, thermal, and durability characteristics. Although in their infancy, these findings can provide guiding hypotheses for experiments to better synthesize, control, and characterize the properties of hybrid cementitious composites. The next section provides some of the high-level characterization attempts in polymer—cement composites.

5.2.2 Characterization

Polymer-incorporated concrete is one common type of hybrid cementitious material that has received extensive attention. Matsuyama and Young (1998, 1999a,b) used a wide range of anionic, cationic, and neutral polymers such as poly(methacrylic acid) (PMA), poly(4-vinyl benzyl trimethylammonium chloride), and PVA to examine intercalation of the polymer chains in the C-S-H interlayer. They achieved up to a 1.5 nm ($\sim$100%) increase in the interlayer spacing of C-S-H. This is a significant observation, because C-S-H is a low-swelling-capacity material.

In 2002, Van Damme and his colleagues (Merlin et al., 2002) attempted to synthesize C-S-H—polymer nanocomposites with water-soluble polymers. By using PVA and a variety of other polymers, they reported that, unlike smectite clays, intercalation of neutral or cationic polymers is a hard process. However, they did not study the mechanical properties of their nanocomposite specimens. In another work, the same group prepared their mixture by adding trialkoxysilane and tetraethoxysilane to C-S-H. They proved the incorporation of organic groups in C-S-H without disrupting the inorganic framework. Minet et al. (2006) proposed an alternative method to directly link small-sized organic groups in the interlayer space of C-S-H (Figure 5.7). Their NMR plots of the C-S-H nanocomposite depict intense Q1 and Q2 peaks that are
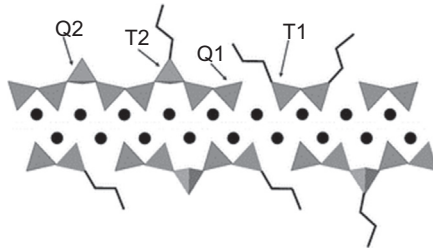
Figure 5.7 Schematic of organic groups linked to the interlayer spacing of hybrid calcium silicate materials. Q1 and Q2 correspond silicate tetrahedral species of C-S-H, bonded to either ethyl or aminopropyl silanes. By incorporating trialkoxysilane species, T1 and T2, some of the Q species are replaced (Minet et al., 2006).

not present in pure inorganic C-S-H. These peaks are a result of the Q species proximity to trialkoxysilanes. Their experimental results proved ethyl groups are close to the silica tetrahedra.

Silva and Monteiro (2006) showed the effect of polymers on the hydration of cement. In another study, they modified cement paste with 20% weight of poly(ethylene-co-vinyl acetate) (EVA) (Silva and Monteiro, 2005). However, they did not report possible material properties enhancement in their work. Mojumdar and Raki (2005) reported hydrogen bonding in composites of C-S-H with varying concentrations of PVA, a high-molecular-weight nonionic polymer (Figure 5.8). Their scanning electron microscopy (SEM) images of the C-S-H polymer nanocomposite showed initiation of PVA crystallites on the inorganic surface. Using FITR spectra, they depicted the shift of the (−OH) bond in PVA from $3421 \, \text{cm}^{-1}$ (Yu et al., 2003) to high frequencies of $3431-3411 \, \text{cm}^{-1}$ in the C-S-H−PVA compound. It was later confirmed that hydrogen bonding occurred between the inorganic and organic material nucleate PVA crystalline sites (Sakhavand et al., 2013). Because PVA is a water-soluble polymer, its incorporation into C-S-H will remarkably increase the water retention of C-S-H. This effect can potentially improve the cement workability, prevents dry-out, and can increase PVA's adhesion to porous materials such as concrete and ceramic (Ohama, 1995).

In another study, the same group incorporated poly(acrylic acid) (PAA) into C-S-H (Mojumdar and Raki, 2006) and reported intercalation of PAA as well as exfoliation of C-S-H. Their differential scanning calorimetry (DSC) traces of C-S-H−polymer nanocomposite and individual PAA and C-S-H showed a higher glass transition temperature compared to that of the bulk PAA. They claimed that these types of materials are useful in corrosive and high-temperature environments.

Beaudoin et al. (2009b) performed a ^{29}Si MAS NMR spectroscopy for different C-S-H−polymer nanocomposites to provide useful information on polymer interactions in C-S-H. They studied the incorporation of various entities such as polyethylene glycol (PEG) (Beaudoin et al., 2009a), 18hexadecyltrimethylammonium (HDTMA) (Beaudoin et al., 2008), dimethyl sulfoxide (DMSO), and methylene blue (MB). They showed that the interaction of the organic entities with C-S-H increases the degree of polymerization of the silicate chains. Their observation of the increase in the Q2−Q1
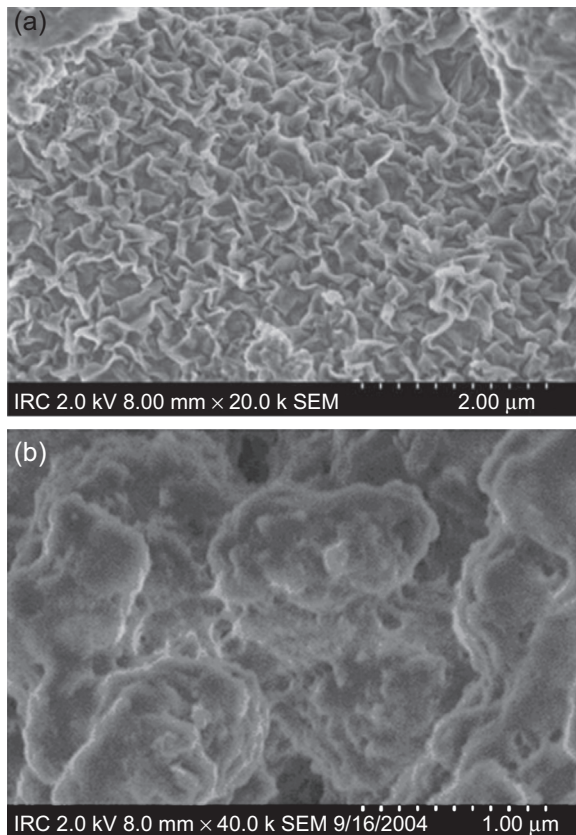
Figure 5.8 SEM micrographs of (a) synthetic C-S-H (Mojumdar and Raki, 2006) and (b) pure PVA (Mojumdar and Raki, 2005).

ratio of the C-S-H—polymer nanocomposites indicated the chemical shift of the silicon near the organic molecules. This proved the existence of some types of binding between the polymer and C-S-H. Based on their observations, they suggested that, besides inter-calations, the polymer chains are mainly absorbed in the missing silica tetrahedral in silica chains, and thus bridge the gaps between them. However, they did not provide supporting results or insights regarding the types of interactions between C-S-H and organic molecules. In a recent study, ^{29}Si MAS NMR spectroscopy was again used by Alizadeh et al. (2011) to show incorporation of polyaniline in C-S-H (Figure 5.9).

Considering the rheological behavior, polymeric dispersants are typically used to enhance the rheology of concentrate particle suspensions such as concrete. Popova et al. (2000) were able to show adsorption of large amounts of superplasticizers on C-S-H. Because the ionic strength is high in concrete, comb copolymers with an adsorbing backbone and nonadsorbing side chains will be very effective for concrete. As another example, adsorption of copolymers onto C-S-H show that the superplasti-cizer adsorption cancels the strong ion correlation forces that exist between surfaces at
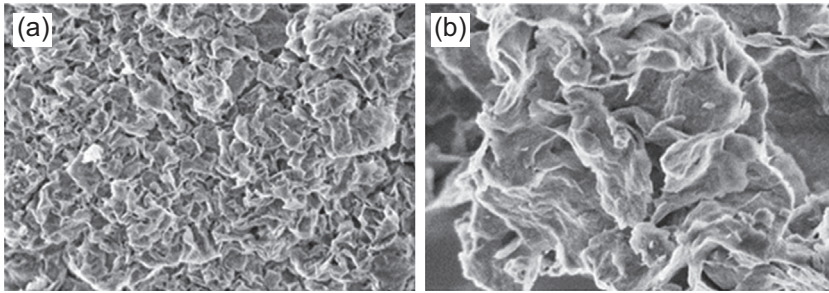
Figure 5.9 SEM images depicting the morphological differences between (a) C-S-H (C/S = 0.8) and (b) C-S-H−polyaniline (C/S = 0.8). Each image is approximately 3 micrometers across.

close separation (Flatt et al., 2008). A model is proposed that can describe the adsorption conformation of the utilized polymers (Flatt et al., 2008). Aside from polymers and soft materials, which have been studies for years, there is another emerging class of fillers known as low-dimensional materials that hold great promise for creating a step-change in various prosperities of hybrid cementitious materials. This area will be the subject of our next discussion.

5.3　Cementitious composites reinforced with low-dimensional materials and nanoparticles

Concrete is a quasi-material with a strong compression strength (>200 MPa), but relatively weak tension, flexural, and fracture toughness. Although reinforcing steel bars can partially overcome these issues, they are not able to prevent local cracking and allow the structure to resist high flexural loads. Low-dimensional materials such as one-dimensional (1D) carbon nanotubes (CNTs), 2D graphene, and hexagonal boron nitride (hBN) sheets have been (Figure 5.10) recently the subject of increasing interest as multifunctional additives to reinforce concrete at the nanolevel. These additives
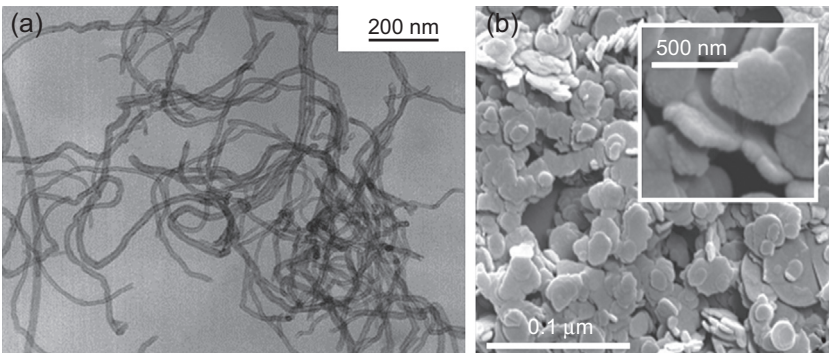
Figure 5.10 SEM images of multiwall carbon nanotubes (Li et al., 2005) (left) and boron nitride sheets (right) (Rafiee et al., 2013).

concurrently exhibit various superb properties such as ultrahigh strength, ultrahigh thermal conductivity, and super hydrophobicity, which are highly desired for modern engineering of cementitious materials that can function in multiple ways. From a mechanical standpoint, which is a key feature of structural cementitious materials, these nanofillers with their huge surface areas can inhibit crack growth and increase toughness by a number of mechanisms, including crack bridging, crack bifurcations, and pulling out of matrix mechanisms (Rafiee et al., 2013) Various improvements in terms of strength, elastic behavior, and thermal and electrical advantages of such hybrid composites have been reported, which are presented as follows.

5.3.1 Nanoscale modeling

Similar to polymer−cement nanocomposites, nanoscale simulations of cementitious materials modified by low-dimensional 1D and 2D fillers are relatively rare. In this context, perhaps more efforts have been devoted to modeling CNTs and cement-based materials. For instance, simulations are used to investigate the effect of CNT weight percentage, chirality, and diameter on the Young's modulus of the cement−CNT composite (Sindu et al., 2012). It was shown that there is an optimum percentage of CNTs for incorporation in the cement. However, given that the molecular phases of C-S-H were only recently discovered (Pellenq et al., 2009; Abdolhosseini Qomi et al., 2014), the reliability of previous modeling efforts in inferring nanoscale phenomena suitable for hybrid C-S-H−based materials is at stake. More recently, Rafiee et al. (2013) utilized molecular dynamics to confirm the experimental results on the effect of 2D superhydrophobic hBN sheets to enhance the absorption capacity of cement paste for hydrocarbons (vs water). In this study, they used tobermorite as a crystalline analog of cement hydrate (C-S-H), which is true for C-S-H phases with calcium-to-silicon (C/S) ratios ~ 1. However, such studies must be extended to more realistic C-S-H phases with various C/S ratios spanning ~ 0.7 to ~ 2.3, which is the typically observed stoichiometry of C-S-H in cement-based materials. Compared to computational nanoscale modeling, there is generally more research on synthesis and characterization of low-dimensional materials in cement, which will be discussed next.

5.3.2 Characterization

Since the discovery of graphene (a single layer of carbon atoms in graphite) less than a decade ago, low-dimensional materials have gained extensive attention for their remarkable mechanical, thermal, and electrical properties. Recently, several attempts have been made to incorporate them in cementitious materials, with some success in achieving high-performance composites.

The highest compressive strength of a CNT−cement nanocomposite was reported in 2008 (Cwirzen et al., 2008). Cwirzen et al. achieved a 50% increase in the compressive strength using a multiwall carbon nanotube (MWCNT) sample. For the same sample, Sáez De Ibarra et al. (2006) achieved a 227% improvement in the Young's modulus. In another study, over 600% improvement in Vicker's hardness at early
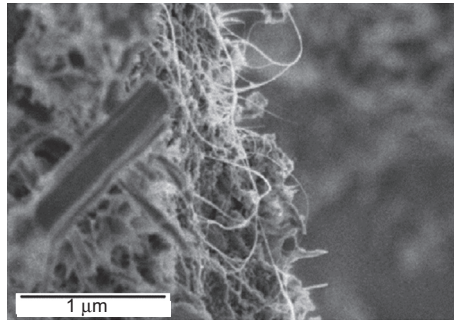
Figure 5.11 Single-wall carbon nanotubes (SWCNTs) pulling out of the hydrated SWCNT−C-S-H composite when cracked (Makar and Chan, 2009).

ages of hydration for a 2% single-wall carbon nanotube (SWCNT) with a low water-to-cement (w/c) ratio was reported (Makar et al., 2005). In contrast, samples with a 0.8 w/c ratio showed reduction in strength in all the time periods. Makar and Chan (2009) suggested that the observed behavior improvement depended on both sample composition and hydration time. They showed that C-S-H nucleates on the entire surface of SWCNTs (Figure 5.11). Formation of such a dense C-S-H that is tightly bonded to SWCNTs provides reinforcing behavior for C-S-H.

Electrical properties of MWCNT−cement nanocomposites have also been investigated. Significant improvement in DC electrical conductivity (on the order of 130−170 Ω-cm) as compared to control samples have been reported (Li et al., 2005). Formation of C-S-H along MWCNTs was previously reported (Li et al., 2005). Makar and Chan (2009) claimed that the same phenomenon is dominant in SWCNT−cement as well. Tyson et al. (2011) examined properties of CNTs and carbon nanofibers (CNFs) incorporated in the cement paste. They reported a 150% increase in the ultimate displacement compared to pure cement paste, which provides higher ductility for structures. Young's modulus, fracture toughness, and flexural strength have been lower compared to pure cement paste at early stages. However, at 28 days, most of their composite samples had better properties than pure cement paste. A recent atomic force microscopy (AFM) observation (Alkhateb and Cheng, 2012) of graphene−cement nanocomposite has indicated promising results in improving the elastic behavior and strength of cementitious nanocomposites. They also carried out molecular dynamics simulations that revealed the interfacial bridging role of functionalizing graphene with improved overall strength of the nanocomposite. CNFs have been used to increase tension strength of the cement paste. However, they typically reduce the compressive strength and ductility.

A recent study (Rafiee et al., 2013) reported successful incorporation of graphene oxide (GO) and boron nitride (BN) sheets in the cement paste, thus improving both mechanical properties and the ability to absorb hydrocarbons. They concluded that BN sheets yield better results than GO and the combination of GO and BN (Figure 5.12). However, further studies are needed to confirm such effects in more controlled conditions and environments, for instance a direct impact on C-S-H.
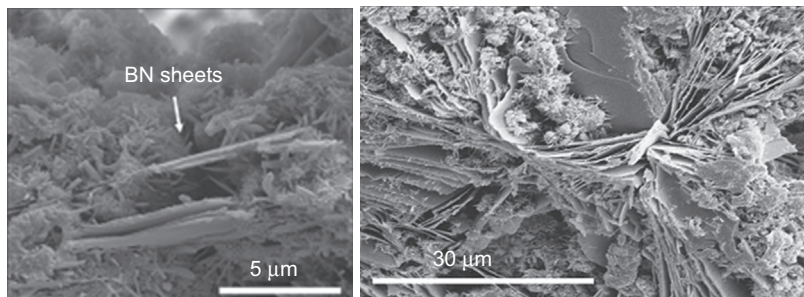
Figure 5.12 SEM images of the fractured surface of BN−cement (left) and a BN−GO−cement composite (right) (Rafiee et al., 2013).

5.4 Discussion and summary

This chapter provided an overview of modeling, synthesis, and characterization of various hybrid cementitious materials. Following the traces of natural and biological materials in combining multiple constituents to produce high-performance composites, several research groups have attempted to synthesize hybrid cementitious materials with controlled structure and enhanced properties such as concurrent ductility, strength, and/or thermal conductivities. Irrespective of the final property and/or application, the "interface" in all hybrid materials is typically the bottleneck in understanding, controlling, and improving various hybrid properties of the cementitious composites. In this context, nanoscale modeling, although in its infancy, provides a key tool as an atomistic "lens" to fully understand and predict the behavior of hybrid cement-based materials.

Polymer−cementitious composites are a key class of hybrid cementitious materials with reported mechanical property enhancement. Most of the studies are focused on incorporation of polymer in C-S-H as the primary source of mechanical properties in cement-based materials. Via nanoscale modeling, it was shown that hydrogen bonding between polymer matrices and the C-S-H phase forms a strong interfacial network that bridges hybrid polymer−cement layers. More importantly, it was shown that an existence of a finite polymer length is the key to creating high-strength, high-toughness cement−polymer composites (Sakhavand et al., 2013; Sakhavand and Shahsavari, 2015). Such computational modeling can provide significant information to guide synthesis and characterization experiments, which were extensively discussed for hybrid polymer−cement composites.

Low-dimensional materials such as CNTs, graphene, and hBN are another class of nanomaterials that more recently have been considered as multifunctional filers for hybrid cementitious composites. With huge surface areas and a tendency toward agglomeration, the major challenge in this category of fillers seems to be their homogeneous dispersion in the cement paste. Although some researchers reported increased property enhancement, the underlying interfacial physics and chemistry are yet to be fully explored. More precisely, understanding how a small percentage of such nanomaterials yields considerable increase in hybrid properties of the composite can help synthesis of efficient composites with desired material properties.
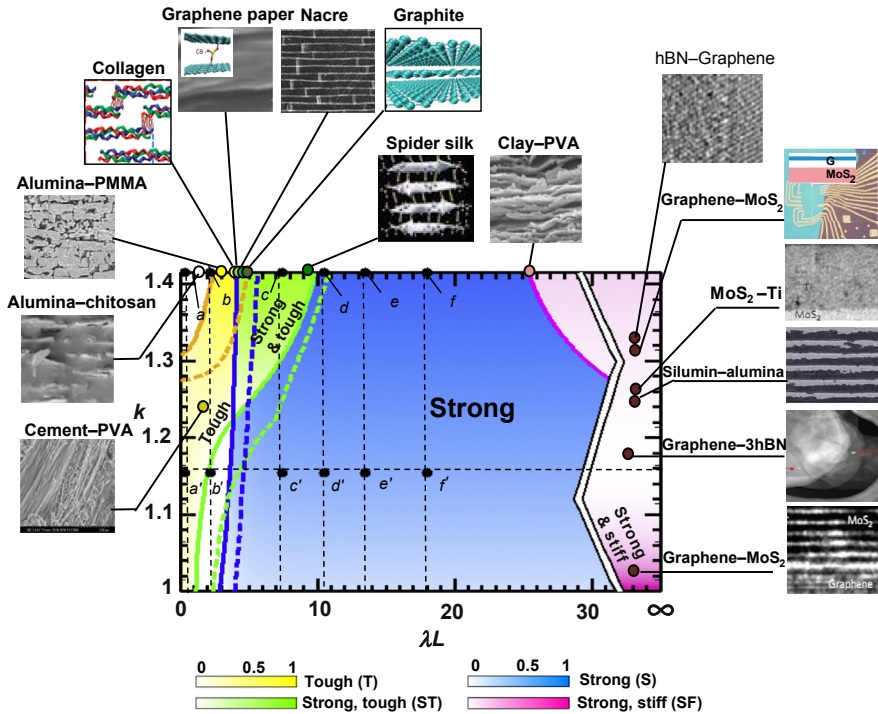
Figure 5.13 Composition—structure—property diagram shows an interplay of mechanical properties (strength toughness, stiffness) with the microstructure of platelet—matrix composites for natural and biomimetic composites. λL and k are dimensionless universal parameters applicable to various constituents (Sakhavand and Shahsavari, 2015).

Nanoscale modeling is an underutilized method for investigating the structures and properties of hybrid cementitious materials. Modeling on this scale provides a new method for developing physical insights and identifying design variables. Furthermore, investigations via nanoscale modeling will inform processes and algorithms for synthesizing and characterizing hybrid cement-based materials in the future. Such studies can greatly benefit and contribute to emerging composition—structure— property relationships recently being advanced for complex natural and biomimetic materials. As an example, Figure 5.13 shows a universal design map (Sakhavand and Shahsavari, 2015) that can be used for design and optimization of mechanical properties of various natural and synthetic platelet—matrix composites, including hybrid layered cementitious materials. Similar knowledge-based design approaches may be applied to cementitious nanocomposites and can control their interfacial properties and architectures through using particular constituents (polymer, low-dimensional materials, etc.), geometrical attributes (length scales, volume fraction, layer thickness, etc.), new synthesis methods (e.g., intercalation and exfoliation), and so on to expedite and advance the discovery of novel hybrid cementitious materials. This research vision will place hybrid cementitious materials on equal footing

with crystalline systems and alloys in the current applications of structure−property relationships in design, thereby providing an enormous impact in modern engineering and applications of multifunctional infrastructure materials.

Acknowledgment

References

Abdolhosseini Qomi, M.J., et al., 2014. Combinatorial molecular optimization of cement hydrates. Nature Communication 5, 1−10.

Alizadeh, R., Beaudoin, J., Raki, L., Terskikh, V., 2011. C−S−H/polyaniline nanocomposites prepared by in situ polymerization. Journal of Material Science 46, 460−467.

Alkhateb, H., Al-Ostaz, A., Cheng, A., 2013. Material genome for graphene-cement nanocomposites for infrastructure applications. ASCE Journal of Nanomechanics and Micromechanics 3 (3), 67−77.

Allen, A.J., Thomas, J.J., Jennings, H.M., 2007. Composition and density of nanoscale calcium−silicate−hydrate in cement. Nature Materials 6, 311−316.

Beaudoin, J.J., Dramé, H., Raki, L., Alizadeh, R., 2008. Formation and characterization of calcium silicate hydrate−hexadecyltrimethylammonium nanostructure. Journal of Materials Research 23, 2804−2815.

Beaudoin, J., Dramé, H., Raki, L., Alizadeh, R., 2009a. Formation and properties of C-S-H−PEG nano-structures. Materials and Structures 42, 1003−1014.

Beaudoin, J.J., Raki, L., Alizadeh, R., 2009b. A ^{29}Si MAS NMR study of modified C−S−H nanostructures. Cement and Concrete Composites 31, 585−590.

Bennadji-Gridi, F., Smith, A., Bonnet, J.-P., 2006. Montmorillonite based artificial nacre prepared via a drying process. Materials Science and Engineering: B 130, 132−136.

Bonderer, L.J., Studart, A.R., Gauckler, L.J., 2008. Bioinspired design and assembly of platelet reinforced polymer films. Science 319, 1069−1073.

Büyüköztürk, O., Buehler, M.J., Lau, D., Tuakta, C., 2011. Structural solution using molecular dynamics: fundamentals and a case study of epoxy-silica interface. International Journal of Solids and Structures 48, 2131−2140.

Chen, R., Wang, C-A., Huang, Y., Le, H., 2008. An efficient biomimetic process for fabrication of artificial nacre with ordered-nanostructure. Material Science Engineering, C 28, 218−222.

Corni, I., et al., 2012. A review of experimental techniques to produce a nacre-like structure. Bioinspiration and Biomimetics 7 (031001).

Cwirzen, A., Habermehl-Cwirzen, K., Penttala, V., 2008. Surface decoration of carbon nanotubes and mechanical properties of cement/carbon nanotube composites. Advances in Cement Research 20, 65−73.

Dai, W., Shui, Z., Duan, P., 2011. Molecular dynamics simulation on calcium silicate hydrate doped organic molecules. In: Chen, R. (Ed.), Intelligent Computing and Information Science, vol. 134. Springer, Berlin Heidelberg, pp. 155−160.

Ekiz, O., Dericioglu, A.F., Kakisawa, H., 2009. An efficient hybrid conventional method to fabricate nacre-like bulk nano-laminar composites. Material Science Engineering, C 29, 2050−2054.

Espinosa, H.D., Rim, J.E., Barthelat, F., Buehler, M.J., 2009. Merger of structure and material in nacre and bone: perspectives on de novo biomimetic materials. Progress in Material Science 54, 1059−1100.

Flatt, R.J., Schober, I., Raphael, E., Plassard, C.d., Lesniewska, E., 2008. Conformation of adsorbed comb copolymer dispersants. Langmuir 25, 845−855.

Fratzl, P., Burgert, I., Gupta, H.S., 2004. On the role of interface polymers for the mechanics of natural polymeric composites. Physical Chemistry Chemical Physics 6, 5575−5579.

Gao, H., 2006. Application of fracture mechanics concepts to hierarchical biomechanics of bone and bone-like materials. International Journal of Fracture 138, 101−137.

Jalilvand, S., Shahsavari, R., 2014. Molecular mechanistic origin of nanoscale contact, friction and scratch in complex particulate systems. ACS Applied Materials and Interfaces.

Kalinichev, A.G., Wang, J., Kirkpatrick, R.J., 2007. Molecular dynamics modeling of the structure, dynamics and energetics of mineral−water interfaces: application to cement materials. Cement and Concrete Research 37, 337−347.

Kojima, Y., Usuki, A., Kawasumi, M., Okada, A., Fukushima, Y., Kurauchi, T., Kamigaito, O., 1993. Mechanical properties of nylon 6-clay hybrid. Journal of Materials Research 8, 1185−1189.

Launey, M.E., et al., 2009. Designing highly toughened hybrid composites through nature-inspired hierarchical complexity. Acta Materialia 57, 2919−2932.

Li, G.Y., Wang, P.M., Zhao, X., 2005. Mechanical behavior and microstructure of cement composites incorporating surface-treated multi-walled carbon nanotubes. Carbon 43, 1239−1245.

Lin, A.Y.M., Meyers, M.A., Vecchio, K.S., 2006. Mechanical properties and structure of *Strombus gigas*, *Tridacna gigas*, and *Haliotis rufescens* sea shells: a comparative study. Materials Science and Engineering: C 26, 1380−1389.

Lin, T.-H., Huang, W.-H., Jun, I.-K., Jiang, P., 2009. Electrophoretic co-deposition of biomimetic nanoplatelet−polyelectrolyte composites. Electrochemistry Communications 11, 1635−1638.

Makar, J.M., Chan, G.W., 2009. Growth of cement hydration products on single walled carbon nanotubes. Journal of the American Ceramic Society 92, 1303−1310.

Makar, J.M., Margeson, J.C., Luh, J., 2005. Carbon Nanotube/cement Composites - Early Results and Potential Applications. 3rd International Conference on Construction Materials: Performance. Innovation and Structural Implications, Vancouver, B.C, pp. 1−10.

Matsuyama, H., Young, J.F., 1998. Intercalation of polymers in calcium silicate hydrate: a new synthetic approach to biocomposites? Chemistry of Materials 11, 16−19.

Matsuyama, H., Young, J.F., 1999a. Synthesis of calcium silicate hydrate/polymer complexes: Part I. Anionic and nonionic polymers. Journal of Materials Research 14 (10).

Matsuyama, H., Young, J.F., 1999b. Synthesis of calcium silicate hydrate/polymer complexes: Part II. Cationic polymers and complex formation with different polymers. Journal of Materials Research 14 (8).

Merlin, F., et al., 2002. Cement-polymer and clay-polymer nano- and meso-composites: spotting the difference. Journal of Materials Chemistry 12, 3308−3315.

Minet, J., et al., 2006. Organic calcium silicate hydrate hybrids: a new approach to cement based nanocomposites. Journal of Materials Chemistry 16, 1379−1383.

Mojumdar, S., Raki, L., 2006. Synthesis, thermal and structural characterization of nanocomposites for potential applications in construction. Journal of Thermal Analysis and Calorimetry 86, 651−657.

Mojumdar, S.C., Raki, L., 2005. Characterization and properties of calcium silicate hydrate polymer nanocomposites. In: Proceedings of the American Ceramic Society 107th Annual Meeting, pp. 1−10.

Muller, A.C.A., Scrivener, K.L., Gajewicz, A.M., McDonald, P.J., 2012. Densification of C−S−H measured by 1H NMR relaxometry. The Journal of Physical Chemistry C 117, 403−412.

Oaki, Y., Kotachi, A., Miura, T., Imai, H., 2006. Bridged nanocrystals in biominerals and their biomimetics: classical yet modern crystal growth on the nanoscale. Advanced Functional Materials 16, 1633−1639.

Ohama, Y., 1995. Handbook of Polymer-modified Concrete and Mortars Properties and Process Technology. NOYES publications, Park Ridge, New Jersey, USA.

Okamoto, M., 2003. Polymer/layered Silicate Nanocomposites. Rapra Technology Ltd.

Pellenq, R.J.M., et al., 2009. A realistic molecular model of cement hydrates. Proceedings of the National Academy of Sciences 106, 16102−16107.

Pellenq, R.J.-M., Lequeux, N., Van Damme, H., 2008. Engineering the bonding scheme in C-S-H: the iono-covalent framework. Cement and Concrete Research 38, 159−174.

Popova, A., Geoffroy, G., Renou-Gonnord, M.-F., Faucon, P., Gartner, E., 2000. Interactions between polymeric dispersants and calcium silicate hydrates. Journal of the American Ceramic Society 83, 2556−2560.

Rafiee, M.A., et al., 2013. Hexagonal boron nitride and graphite oxide reinforced multifunctional porous cement composites. Advanced Functional Materials 23, 5624−5630.

Rexer, J., Anderson, E., 1979. Composites with planar reinforcements (flakes, ribbons)—a review. Polymer Engineering and Science 19, 1−11.

Richardson, I.G., 1999. The nature of C-S-H in hardened cements. Cement and Concrete Research 29, 1131−1147.

Sáez De Ibarra, Y., Gaitero, J.J., Erkizia, E., Campillo, I., 2006. Atomic force microscopy and nanoindentation of cement pastes with nanotube dispersions. Physica Status Solidi A 203, 1076−1081.

Sakhavand, N., Shahsavari, R., 2015. Universal composition−structure−property maps for natural and biomimetic platelet−matrix composites and stacked heterostructures. Nature Communication 6.

Sakhavand, N., Muthuramalingam, P., Shahsavari, R., 2013. Toughness governs the rupture of the interfacial H-bond assemblies at a critical length scale in hybrid materials. Langmuir 29, 8154−8163.

Shahsavari, R., Chen, L., 2015. Screw dislocations in complex, low symmetry oxides: core structures, energetics and impact on crystal growth. ACS Applied Materials and Interfaces.

Shahsavari, R., Buehler, M.J., Pellenq, R.J.M., Ulm, F.-J., 2009. First-principles study of elastic constants and interlayer interactions of complex hydrated oxides: case study of tobermorite and jennite. Journal of Amecian Ceramic Society 92, 2323−2330.

Shahsavari, R., Pellenq, R.J.M., Ulm, F.-J., 2011. Empirical force fields for complex hydrated calcio-silicate layered materials. Physical Chemistry Chemical Physics 13, 1002−1011.

Silva, D.A., Monteiro, P.J.M., 2005. ESEM analysis of polymeric film in EVA-modified cement paste. Cement and Concrete Research 35, 2047−2050.

Silva, D.A., Monteiro, P.J.M., 2006. The influence of polymers on the hydration of portland cement phases analyzed by soft X-ray transmission microscopy. Cement and Concrete Research 36, 1501−1507.

Sindu, B.S., Sasmal, S., Gopinath, S., 2012. Numerical simulation of CNT incorporated cement. World Academy of Science, Engineering and Technology.

Tang, Z.-Y., Lu, Y., Hu, Q.-S., 2003a. Direct synthesis of ferrocenylmethylphosphines from ferrocenylmethyl alcohols and their application as ligands for room temperature Pd(0)-catalyzed Suzuki cross-couplings of aryl bromides. ChemInformatics 34, 297−300.

Tang, Z., Kotov, N.A., Magonov, S., Ozturk, B., 2003b. Nanostructured artificial nacre. Nature Materials 2, 413−418.

Taylor, H.F.W., 1986. Proposed structure for calcium silicate hydrate gel. Journal of the American Ceramic Society 69, 464−467.

Tseng, Y.-H., Lin, H.-Y., Liu, M.-H., Chen, Y.-F., Mou, C.-Y., 2009. Biomimetic synthesis of nacrelike faceted mesocrystals of ZnO−Gelatin composite. Journal of Physical Chemistry C 113, 18053−18061.

Tyson, B.M., Al-Rub, R.K.A., Yazdanbakhsh, A., Grasley, Z., 2011. Carbon nanotubes and carbon nanofibers for enhancing the mechanical properties of nanocomposite cementitious materials. Journal of Materials in Civil Engineering 23, 1028−1035.

Wang, C.-A., Huang, Y., Zan, Q., Guo, H., Cai, S., 2000. Biomimetic structure design—a possible approach to change the brittleness of ceramics in nature. Material Science Engineering, C 11, 9−12.

Wegst, U.G.K., Bai, H., Saiz, E., Tomsia, A.P., Ritchie, R.O., 2015. Bioinspired structural materials. Nature Materials 14, 23−36.

Wu, W., Al-Ostaz, A., Cheng, A., Song, C., 2011. Computation of elastic properties of Portland cement using molecular dynamics. Journal of Nanomechanics and Micromechanics 1, 84−90.

Yu, Y.H., Lin, C.Y., Yeh, J.M., Lin, W.H., 2003. Preparation and properties of poly(vinyl alcohol)-clay nanocomposite materials. Polymer 44, 3553−3560.

Smart cement paste with carbon nanotubes

6

Filippo Ubertini [1], Simon Laflamme [2], Antonella D'Alessandro [1]
[1]University of Perugia, Perugia, Italy; [2]Iowa State University, Ames, IA, USA

6.1 Introduction

We are living the beginning of a new industrial revolution based on the development of a new level of scientific and technological progress. The application of complex theories based on quantum physics has enabled researchers to achieve nanoscale developments in material science and electronics. Nanoscale modified materials possess mechanical, electrical, and thermal properties that are significantly improved compared to those at the micro and macro scales. This is due to the relatively larger surface area at the nano level, which can make materials more chemically active and can affect their strength and/or electrical properties. Quantum effects can dominate the behavior of matter at the nanoscale, affecting optical, electrical, and magnetic behavior of materials.

Similarly, many properties of cementitious materials, such as their electrical conductivity, are affected by their micro and nanobehavior (Mondal et al., 2008). The addition of micro- and nanofibers to cementitious matrices allows the modification of materials' properties (Li et al., 2007). In particular, carbon nanotubes (CNTs) are ideal candidates for casting smart cementitious composites, because of their piezoresistive characteristics that cause changes in electrical resistivity upon strain. When the amount of CNTs in the composite matrix reaches a critical fraction, percolation starts and the material becomes a conductor. In order to achieve a conductor, it is crucial to properly disperse the conductive particles within the matrix. This new class of modified strain-sensitive cementitious materials, termed *self-sensing*, transduces mechanical strain acting upon them into variations in their electrical properties, such as resistance and reactance. Thus, self-monitoring is achieved by correlating the variation of the applied stresses with the variation of appropriate parameters and properties of the material, in particular the electrical resistance. The variation in the resistivity (or in the electrical resistance) can be measured to assess mechanical deformation, and this information can be exploited for the purpose of structural diagnosis. For example, a smart cementitious material can be used to monitor the emergence and evolution of damage such as microfractures. Notable advantages of the sensing principle are that the electrical resistance requires a relatively simple instrumentation, provides directional information on strain, and enables detection of microstructural changes (Chung and Wang, 2003). Also, using a cementitious matrix allows easy embedment of the sensor within concrete elements and can then transform structures into distributed sensor network systems.

6.2   State of the art

Until 1992, studies on monitoring concrete structures with nondestructive methods centered on the embedment of various types of sensors (Measures, 1993). N. Muto (Muto et al., 1992) was the first to propose concrete with self-monitoring properties, using carbon fibers and glass. The advantage of the composite was a substantial gain in the bonding characteristics of the embedded agents. In related work to "smart" concrete, Chen and Chung researched in 1993 the addition of carbon fibers into concrete admixtures. Carbon fibers were recognized as particularly suited to be used in the case of cementitious materials as they could simply be added to the admixture as normal aggregates. In their earliest publication on the topic, Chen and Chung (1993) analyzed the electrical properties and self-sensitivity of cementitious materials fabricated with various types of additives. The effect of damage in the nanomodified cementitious materials was studied by measuring the electrical resistivity during compression cycles in elastic and plastic conditions. It was found that the cycles were dominated by the formation and opening of cracks during loading and the partial closure of cracks during unloading. They noted an opposite variation of the electrical resistance, and therefore of the resistivity, in elastic and plastic regimes and an increase of background electrical resistance due to irreversible damage. Dispersion of the nanoparticles was attained with methyl cellulose, latex, or silica fume. The addition of conductive additives to the matrix resulted in improved conductivity of the composite even when the fraction of the nanoparticles was below the percolation threshold, as discussed in the Introduction. When the volume fraction was below the percolation threshold, the electrical conductivity of the composite was found to be strongly dependent on the degree of dispersion of the fibers.

Correct and uniform dispersion of the nanotubes within the cement matrix is a primary concern for achieving composites with good electrical properties. CNTs have two main geometrical characteristics: the nanometric size and a high specific surface. These two factors are responsible for the poor solubility and difficult dispersion of nanotubes within the matrix. This difficulty is due to the fact that the increase of specific surface area also increases the van der Waals attraction forces between the aggregates (Lourie and Wagner, 1998). Also, the nanosized particles tend to spontaneously agglomerate due to their nanoscale dimension.

There are three main approaches to disperse the nanotubes in water (Han et al., 2011):

1. Mechanical methods, based on the use of mechanical mixers;
2. Physical methods, based on the use of dispersants that operate a non-covalent surface modification or on the use of ultrasounds;
3. Chemical methods, through a covalent surface modification.

The presence of dispersants in an aqueous solution containing nanotubes is sometimes crucial to avoid the presence of bundles (Konsta-Gdoutos et al., 2010). Ultrasonic treatments are often used to obtain good dispersion.

Cementitious materials are subjected to polarization (Sihai and Chung, 2001), a phenomenon that commonly occurs in dielectric materials exposed to an electric field. The induced polarization is a result of the electric field, which is generated in the

opposite direction to the applied electric field and creates a current. The polarization causes an apparent increase in electrical resistance during the measurement process. A higher conductivity of the material will cause a faster polarization effect (Cao and Chung, 2004).

The scientific literature in the last decade shows a growing interest for the use of nanomaterials in the construction industry, especially regarding the use of nanoparticles with smart properties.

The most frequently used fillers for the electrical characterization of cement matrices are nano-SiO_2 and nano-Fe_2O_3 particles (Li et al., 2003), carbon nanofibers (CNFs) (Xu and Liu, 2007), carbon black (CB), single-walled CNTs (SWCNTs), and multiwalled CNTs (MWCNTs) (Gao et al., 2009; Coppola et al., 2011). Hybrid mixes of different particles have also been studied, including CNTs and nickel powders (Han et al., 2012.), or carbon fibers and CNTs (Azhari and Banthia, 2012). Nanoparticles have been added to cement paste (Coppola et al., 2011; Han et al., 2007; Han and Ou, 2007; Banthia, 2009), mortar (Li et al., 2003), conventional concrete (Xu and Liu, 2007), and self-compacting concrete (Gao et al., 2009).

The exploitation of the piezoresistivity of the composite materials for strain sensing was addressed in Refs. (Han et al., 2007; Han and Ou, 2007; Banthia, 2009; Han et al., 2009; Yu and Kwon, 2009). In 2006, the first theoretical study on the self-sensitivity of fiber-reinforced cement-based materials with carbon particles was published (Wen and Chung, 2006). The model leveraged the concept that piezoresistivity was due to the pullout of the fibers that passed through the microcracks that formed during the opening of cracks. This provoked an increase in the electrical contact resistance of the fiber−matrix interface. Most of the studies available in literature have focused so far on the static response of nanotechnology-modified cement-based materials, whereas their dynamic response has been little investigated. The response of nanomodified strain-sensing composite materials to dynamic loads is almost unexplored (Dong et al., 2011; Loh and Chang, 2011), with only a few studies devoted to cementitious materials (Materazzi et al., 2013; Ubertini et al., 2014a,b; D'Alessandro et al., 2014).

6.3   Potential applications

Structural health monitoring systems provide information about the performance and status of the structures through the observation of their in-service behavior. By using appropriate algorithms, it is possible to establish an automatic link between the experimental observation and the conditions of the structure, promptly recognizing anomalies of behavior due to incipient damage. Traditional monitoring systems based on sensors wired to a central unit for collection and analog-to-digital conversion of the data are difficult to apply to large structures. In particular, management and the maintenance of these systems limit large-scale applications. Also, the utilization of off-the-shelf sensors provides discrete point measurements only, thus providing partial information and limiting structural diagnosis capabilities. Instead, the technology of self-sensing nanocomposite cement-based materials allows the integration of self-sensing properties from biological systems into cementitious structures by

transforming the surface of concrete structures into infinite sets of potential embedded sensors with enhanced durability and ease of utilization.

Examples of possible applications include monitoring of concrete and asphalt pavements. For instance, experimental results showed a great capability of the material to reveal the presence of compressive and impulsive loads, like those resulting from passage of vehicles. They also find great applicability to historic structures by supplementing mortar with sensing capabilities, enabling static and dynamic monitoring. Thus, an integrated system of nanocomposite cement-based sensors could be used to monitor changes in the vibration signature before and after a seismic event to quickly assess structural condition. This state of the art demonstrates the growing interest of the scientific community in understanding the behavior and potential applications of self-sensing cementitious materials. Many researchers worldwide are investigating the potential of nanostructured concrete and composite materials subjected to static, cyclic, and dynamic loads. Studies available in the literature indicate that the sensors made with nanomodified cementitious materials can be effectively used in structural health monitoring.

6.4 Fabrication process of carbon nanotube cement paste sensors

This section describes the fabrication process of a CNT cement-paste sensor (CNTCS) as used in Materazzi et al. (2013), Ubertini et al. (2014a,b), and D'Alessandro et al. (2014). The cementitious matrix of the sensors is a cement paste. Cement paste is more homogeneous and potentially more strain-sensitive than cement mortar or concrete, because there is no sand or coarse aggregates. The cement paste consists of a mixture of Portland cement type 42.5 with a water−cement ratio between 0.40 and 0.43. The nanotubes dispersed in the composite are Arkema Multi-Wall Carbon Nanotubes (MWCNTs), type Graphistrength C100. They are used in the amount of 2% by mass of cement. Sky 521 plasticizer, based on second-generation polycarboxylate ether polymers, is added to the mix in the amount of 1% by mass of cement to increase workability. Physical dispersants are used to improve the dispersion of nanotubes. For prisms of dimension $40 \times 40 \times 160 \text{ mm}^3$ (Figure 6.1(b−d)), the same Sky 521 is
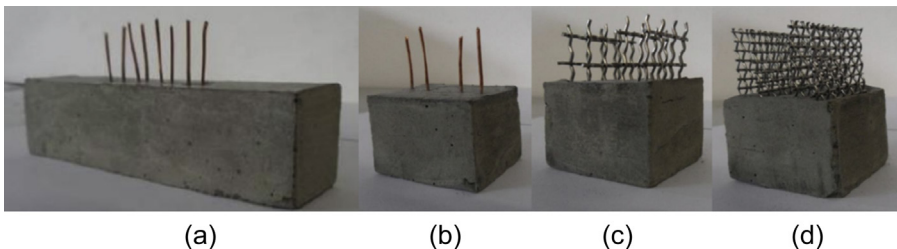

(a)   (b)   (c)   (d)

Figure 6.1 Different models of CNTCS: parallelepipeds (a), prisms with wire (b), and net electrodes (c−d).

also used as a dispersant. For parallelepipeds of dimension $40 \times 50 \times 40$ mm^3 (Figure 6.1(a)), an acrylate copolymer ammonium salt solution (ByK154) is used instead. The electrodes are made using nets of stainless steel or copper wires, embedded in the center of the samples and placed symmetrically along the central axis.

6.4.1 Physical properties of MWCNTs and mix design

Table 6.1 summarizes the relevant properties of the carbon nanotubes used in the fabrication process. MWCNT were selected with a carbon content greater than 90%. These MWCNTs have an outer mean diameter between 10 and 15 nm and a length between 0.1 and 10 μm. They are formed by multiple concentric cylindrical graphene sheets and characterized by an enhanced sensitivity to stress changes compared to SWCNTs due to the higher probability of forming contact points. The utilization of MWCNTs results in a significant decrease of electrical resistivity with strain.

Table 6.2 lists the mix design of the cement paste with CNTs and ammonium polyacrylate−based dispersant used in the fabrication of the CNTCSs. The third column (content/sample) shows the quantities used for a single sample.

6.4.2 Dispersion of MWCNTs and casting of CNTCSs

As mentioned in this chapter, the dispersion of MWCNTs in a cementitious matrix is rather delicate, because the nanoparticles tend to agglomerate in aqueous solutions. In order to create a bundle-free homogeneous three-dimensional net, MWCNTs are dispersed in the cement matrix in two stages. In stage 1, MWCNTs are spread in deionized water with a sequence of different types of subsequent mixing processes. In stage 2, cement powder is added to the water suspension along with the plasticizer.

Table 6.1 **Properties of MWCNTs used in the experimentation**

Components	MWCNTs
Appearance	Black powder
Apparent density	50−150 kg/m^3
Mean agglomerate size	200−500 μm
Weight loss at 105 °C	<1%
C content	>90 wt%
Free amorphous carbon	Not detectable (SEM/TEM)
Mean number of walls	5−15
Outer mean diameter	10−15 nm
Length	0.1−10 μm

Table 6.2 **Cement paste mix design**

Components	Content/m^3	Content/sample
MWCNTs	33.0 kg	3.9 g
Portland cement 42.5	1652.0 kg	195 g
Polycarboxylate ether-based plasticizer	16.5 kg	1.9 g
Ammonium polyacrylate-based dispersant	3.3 kg	0.4 g
Water	710.0 kg	84.0 g
W/c	0.43	0.43

Figure 6.2 illustrates the fabrication process of CNTCSs. First, an aqueous solution is obtained by mixing deionized water, the dispersant (Figure 6.2(a)), and the MWCNTs (Figure 6.2(b)). The mixing procedure consists of 10 min of magnetic stirring (Figure 6.2(c)), followed by 15 min of sonication (Figure 6.2(d)) and 15 min of mechanical mixing at 1500 rpm (Figure 6.2(e)). The ultrasound device used in the sonication process is a Vibra Cell Bioblock Scientific model 75,043 at 225 W. To avoid excessive evaporation during sonication, the solution is kept immersed in a bath of cooled water. After mixing nanotubes, cement is added to the aqueous solution to make the paste (Figure 6.2(f)). A plasticizer is added to enhance workability. Then, the composite is manually stirred and poured into the molds (Figure 6.2(g)), and electrodes are embedded (Figure 6.2(h)). After solidification, the samples are unmolded for curing (Figure 6.2(i)).

The control of the effective dispersion of CNTs is conducted using a scanning electron microscope (SEM). Figure 6.3 shows a few representative micrographs. There is
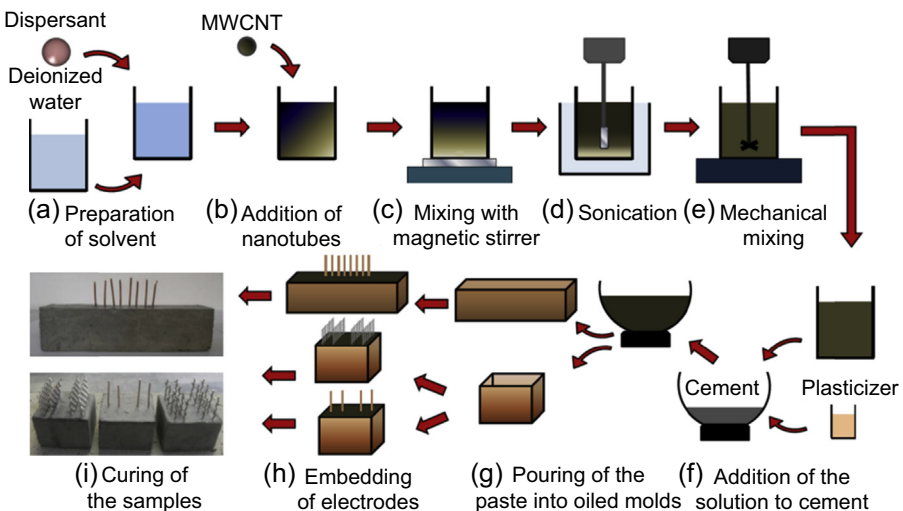
Figure 6.2 Fabricating process of CNTCSs.

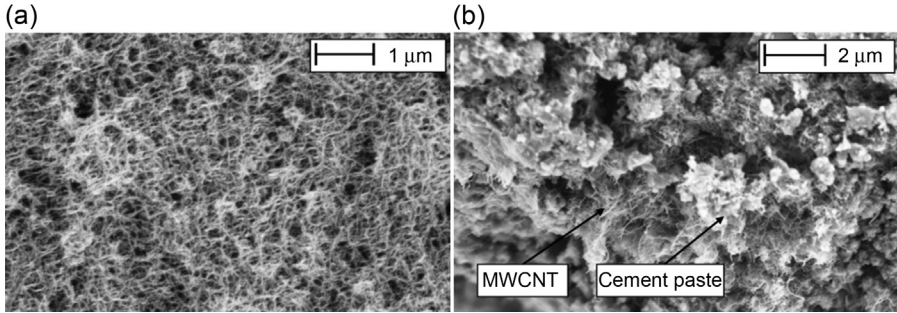**Figure 6.3** SEM images of dispersion of MWCNTs in water solution (a) and cement paste (b).

good dispersion in the aqueous solution (Figure 6.3(a)) and in the hardened cement paste (Figure 6.3(b)).

6.5 Electrical modeling of nanocomposite sensors

Cement paste has a dielectric behavior and consequently exhibits an electrical polarization effect. When a dielectric is subjected to an electrical field, the material polarizes by orienting the dipole moments of the molecules that have random orientations under normal conditions. The result of this phenomenon is an electrical field in the direction opposite to the applied electrical field. This is due to the formation of dipoles. It follows that the sensor cannot be modeled as a simple resistor, but as an interconnected system of capacitors and resistors.

6.5.1 Unstrained response and polarization

Some authors (Han et al., 2007, 2012) suggest to model the electrical behavior of cement-based composites doped with carbon fibers and CNTs by a capacitor and a resistor in parallel (Figure 6.4). Assuming a similar model for CNTCSs, the evolution of the electrical current, I, produced by a constant voltage difference, ΔV, is governed by the following differential equation:

$$\dot{I} + \frac{R_0 + R}{CR_0R}I = \frac{\Delta V}{CR_0R} \tag{6.1}$$

where R_0 is the contact resistance of the electrodes, and R and C are the internal resistance and capacitance of the sensor, respectively. In Eqn (6.1), the dot denotes time differentiation and $I(0) = \Delta V/(R + R_0)$. When the sensor is unstrained, all the electrical parameters in Eqn (6.1) are treated as constants and the current is given by

$$I = \frac{\Delta V}{R + R_0} \left(\frac{R}{R_0} \exp\left(-\frac{R + R_0}{CRR_0}t\right) + 1 \right) \tag{6.2}$$
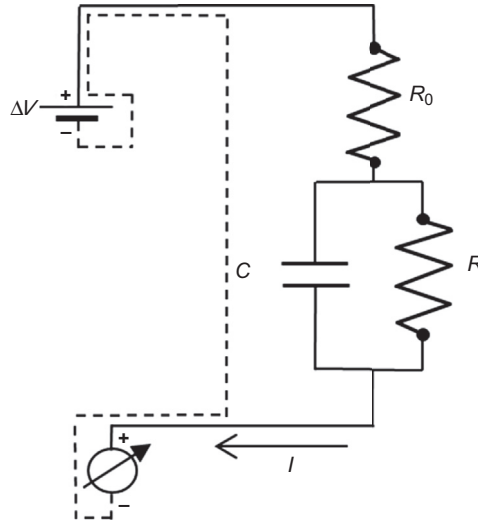
Figure 6.4 Depiction of the proposed electrical model of a CNTCS using a coaxial cable for data acquisition (the continuous line denotes the center core of the cable and the electrical path through the specimen, and the dashed line denotes the metallic shield of the cable).

6.5.2 Identification of sensors' electrical properties

The electrical behavior of the sensors under a step change in the input voltage is measured to validate the equivalent circuit model schematized in Figure 6.4. The experimental setup for this test is shown in Figure 6.5. A National Instruments NI PXIe-1073 chassis is used for data acquisition (Figure 6.5(a)). The system hosts a module, model NI PXI-4130, which provides the stabilized potential difference

(a)   (b)

Figure 6.5 Experimental setup: data acquisition system (a), and detailed view of coaxial cables attached to net electrodes of CNTCS (b).

applied to the electrodes of the specimens through coaxial cables (Figure 6.5(b)). A high-speed digital multimeter, model (NI) PXI-4071, is used to acquire current intensity outputted by the sensor.

Step response tests are conducted for both wire electrodes and net electrodes placed at distances of 1, 2, and 4 cm. Output data are optimally fitted using Eqn (6.2) to identify salient parameters (identification of R_0, R, and C; Figure 6.4). Results are shown in Figure 6.6 for the case of net electrodes, and the identified parameters are summarized in Table 6.3 for both specimens with wire electrodes and with net electrodes.

Figure 6.6 Comparison between experimental results and analytical predictions for the polarization tests on CNTCSs with net electrodes placed at distances of (a) 1 cm, (b) 2 cm, and (c) 4 cm, respectively.
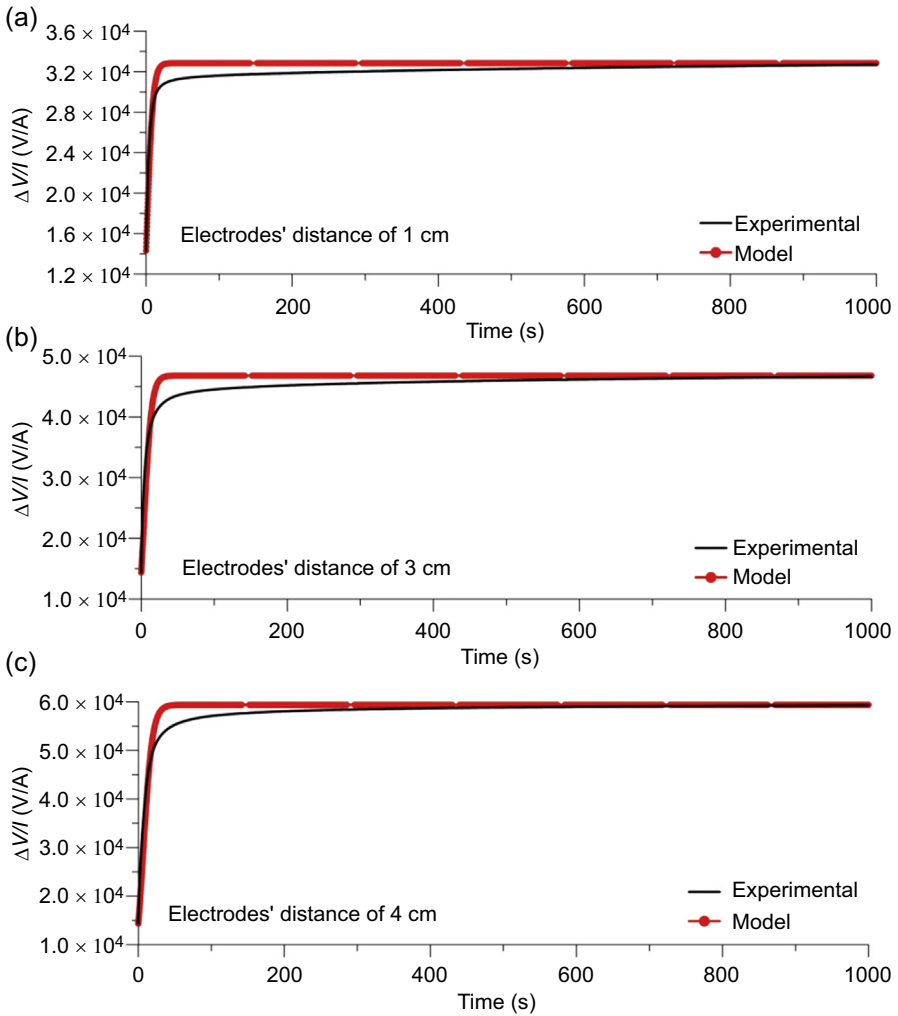
Table 6.3 **Model parameters from polarization tests for specimen with wire and net electrodes (D'Alessandro et al., 2014)**

	Wire electrodes			Net electrodes		
	1 cm	2 cm	4 cm	1 cm	2 cm	4 cm
R_0 (kΩ)	101.8	83.4	56.7	85.6	79.2	95.1
R (kΩ)	17.7	31.7	128.8	27.0	30.9	14.6
C (μF)	53,600	39,400	3900	19,755	11,260	7125
Correlation	0.9996	0.9989	0.9764	0.9998	0.9990	0.9717

Correlation coefficients between theoretical predictions and experimental results are also presented for completeness.

Results show a close match between model responses and experimental data. As hypothesized, the contact resistance does not vary with the distance between electrodes. Conversely, both the internal resistance and the capacitance show a high dependence on the distance between electrodes.

6.6 Vibration monitoring

In this section, the capability of CNTCSs to monitor vibration signatures is examined. First, experiments are conducted under quasi-static load cycles to obtain the stress–strain constitutive relation in the elastic conditions. Second, an in-depth dynamic characterization of the sensors is conducted using a uniaxial test machine to apply harmonic compression loads.

6.6.1 Quasi-static response

The test setup for the quasi-static load cycle test is shown in Figure 6.7. The instrumentation consists of the acquisition systems of the loads and the strain gauges attached onto the sensors, the electrometer, and the actuator. The application of the axial load to the cement paste samples is produced by a hydraulic press, type MTS Model 243.40T, operating under force control. Data of the applied load are acquired using a PC-controlled data acquisition system for the MTS Force Transducer Model 661.23F-01. A digital Keithley Electrometer, model 6517B, is used to induce voltage and conduct electrical measurements. A Spider8 device samples and records the axial deformation of the cement paste at midheight using off-the-shelf strain gauges positioned on the lateral surfaces and on opposite faces. Figure 6.7(b) shows a specimen under test. The two internal electrodes of the CNTCS, placed at a distance of 2 cm, are used in the experiment to provide the voltage to the sensor and to measure the variation of electric current. To limit the effects of polarization on the results, a constant potential difference of 30 V, without load, is applied to the sensors during 1000 s prior to testing.
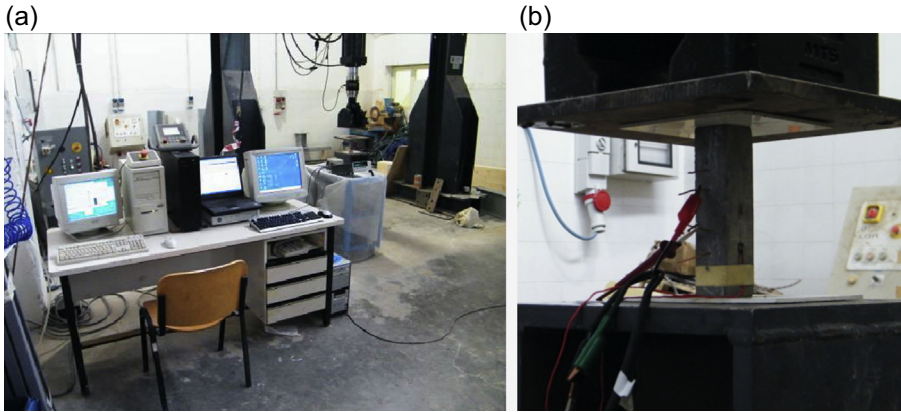
Figure 6.7 (a) Experimental setup; and (b) positioning of the sample.
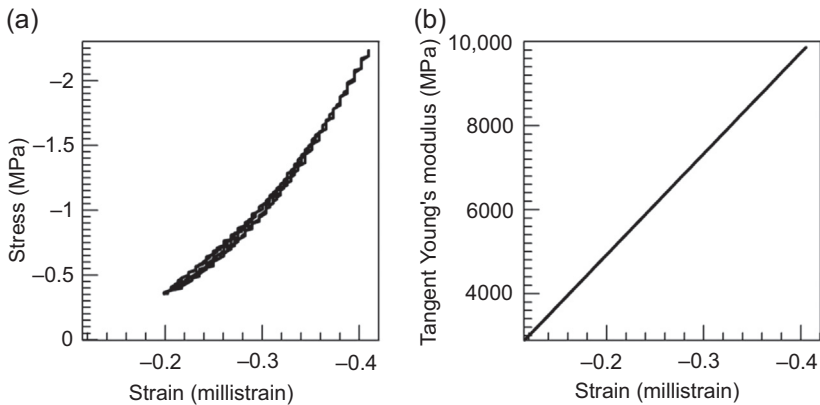
Figure 6.8 Measured stress–strain constitutive relationship of the sensors (a), and tangent Young's modulus versus strain (b).

Figure 6.8 shows the stress–strain relationship measured from the test. The strain (average between the two strain gauges) is expressed in millistrain units. The stress–strain relation appears to be nonlinear in the very low stress-amplitude range. The tangent Young's modulus of the cement paste is estimated from a quadratic interpolation of the measured stress–strain curve (Figure 6.8(b)).

6.6.2   Dynamic characterization

The study of the dynamic behavior of the CNTCS is initiated by evaluating its response to a cyclic load at (1) constant frequencies and (2) variable frequencies.

At constant frequencies, the individual responses in the range of 0.1–1.0 Hz with steps of 0.1 Hz, 1.5–3.0 Hz with steps of 0.5 Hz, and 3.0–5.0 Hz with steps of 1 Hz

are investigated. Each load test consists of applying a force of 2 kN for 240 s, followed by a harmonic load ranging from 2 to 4 kN, which corresponds to axial stress of 1.25 and 2.5 MPa, respectively. The load and the deformation are measured at a sampling frequency of 10 Hz for frequencies ≤ 1 Hz, and 25 Hz for larger frequencies. Output current intensity is sampled with a frequency of 13.5 Hz.

At variable frequencies, the response is investigated by conducting a frequency sweep in the range of $0.1-5.0$ Hz. The initial load of 2 kN is kept constant for 70 s. Ten load cycles with 14 different frequencies are performed: from 0.1 to 0.5 Hz with steps of 0.1 Hz, 0.75 Hz, from 1.0 to 4.0 Hz with steps of 0.5 Hz, and 5.0 Hz. Tests are conducted with increasing frequencies (forward sweep test) and decreasing frequencies (backward sweep test). Each test has an approximate duration of 340 s. The loads and the deformations are acquired at 25 Hz, and current intensity is sampled at 13.5 Hz. The electrical resistance is obtained by dividing the applied voltage of 30 V by the measured current.

Figure 6.9 shows time histories of the applied load and of the corresponding electrical resistance for a few selected typical values of the loading frequency, along with the corresponding normalized power spectral density (PSD) function. The application of a compressive load produces a decrease of the electrical resistance. Upon compression, the MWCNTs get closer, which increases conductivity (Chen and Chung, 1993; Azhari and Banthia, 2012). Another feature in the signal is the increase in electrical resistance during the initial application of the constant load, which is due to the polarization of the cement paste. There is an excellent correlation between the axial strain and the electric resistance during the application of the harmonic loads, even if the effect of sampling errors is greater for frequencies above 2.5 Hz. Figures 6.10 and 6.11 show the good fit between the waveforms of measured strain and electrical resistance.

Figure 6.12 shows the experimental setup of the tests for the dynamic validation. The actuator consists of a servo-controlled pneumatic universal testing machine (IPC Global UTM-14P) of 14 kN load capacity (Figure 6.12(a)). The sensing specimen (Figure 6.12(b)), precompressed at 1 kN, is subjected to harmonic loads with frequencies ranging from 0.25 to 15 Hz. The investigated frequency range covers the typical natural frequencies of civil structures. The CNTCS specimen remains in the linear elastic range of strain during the test. The tests are conducted by providing a stabilized voltage input of 2 V with a source unit NI PXI-4130. The output measurements are performed with a high-speed digital multimeter, model NI PXI-4071, installed in an NI PXIe-1073 (Figure 6.12(c)) at a sampling rate of 1000 Hz.

The electrical current of the CNTCS (and the measured electrical resistance) varies with strain and is affected by polarization. As discussed in Section 3.1, the electrical resistance asymptotically reaches the internal electrical resistance in unstrained conditions due to the polarization effect. Polarization can be eliminated using a high-pass filter. The relation between change in resistance and strain can be expressed in terms of a gauge factor:

$$\frac{\Delta R}{R_0} = \lambda_{\text{CNTCS}} \Delta \varepsilon \tag{6.3}$$
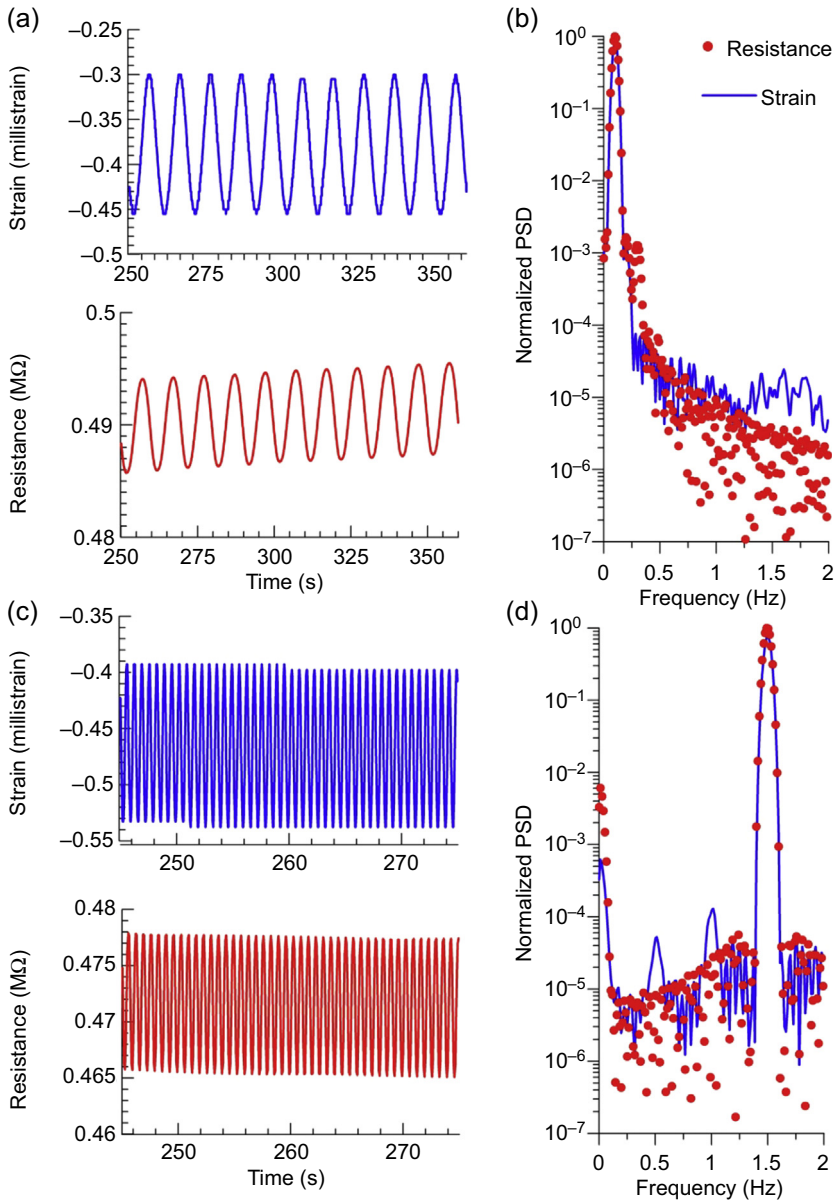
Figure 6.9 Time histories of strain and corresponding electrical resistance for frequencies of 0.1 and 1.0 Hz (a, c) and relative normalized power spectral density (b, d).

where λ_{CNTCS} is the CNTCS gauge factor and R_0 is the value of its unstrained internal electrical resistance. Because CNTCSs are strain rate dependent, their strain-to-signal relationship is nonlinear. It follows that λ_{CNTCS} is not constant over wide ranges of strain.
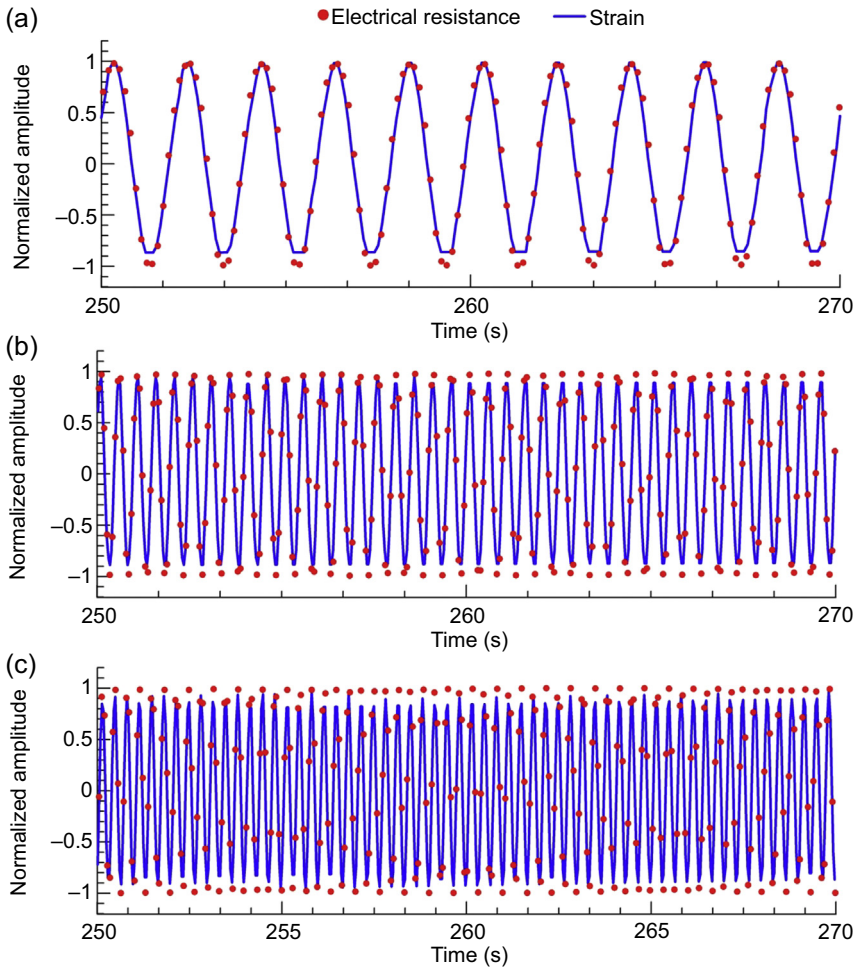
Figure 6.10 Normalized strain and electrical resistance versus time for 0.5 Hz (a), 2.0 Hz (b), and 3.0 Hz (c).

Figure 6.13 shows the responses over the range of 0.25−4 Hz. Figure 6.14 is a plot of the variation in the sensor's signal as a function of strain, where the resistance is normalized by its maximum value ΔR_{max} and strain is normalized by the maximum $\Delta \varepsilon_{max}$. Data in Figure 6.13 are taken from the range of 0.25−0.5 Hz with a load amplitude from 0.5 to 1.5 kN. Results confirm the nonlinearity of Eqn (6.3). The sensitivity of the sensor is higher during compression.

Figure 6.15 shows the frequency response function (FRF) of CNTCSs in the range of 0.25−15 Hz. The FRF is obtained by taking the ratio of the response over the excitation input in the frequency domain, normalized to the value obtained at 15 Hz. The frequency response of the CNTCS increases monotonically. The FRF exhibits a slightly nonlinear input−output relation of the sensor, in particular at low frequencies.
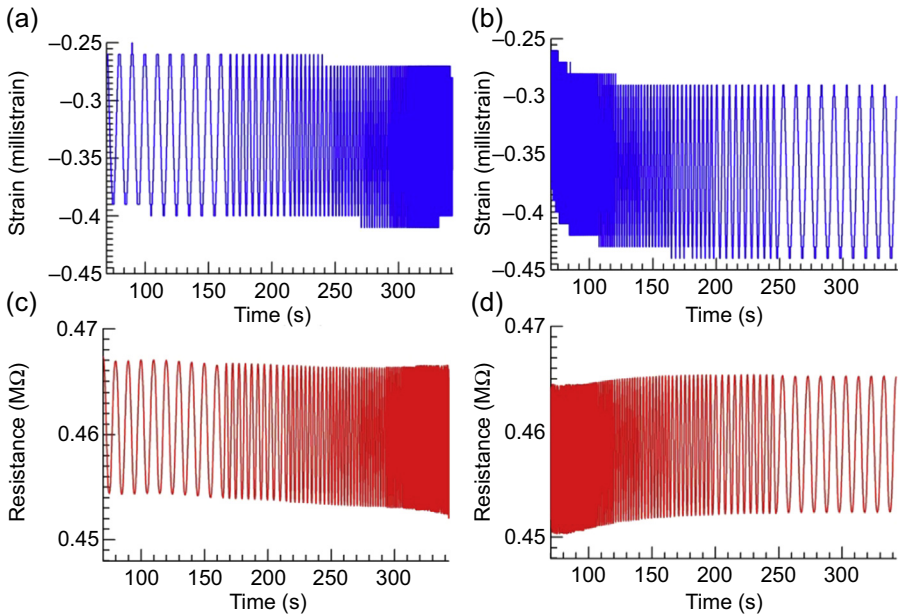
Figure 6.11 Measured strain and corresponding measured electric resistance versus time: test with forward sweep of the frequency from 0.1 to 5.0 Hz (a, c); and test with backward sweep of the frequency from 5.0 to 0.1 Hz (b, d).

At higher frequencies, the dynamic behavior is almost linear. This is due to the strain-rate dependency of the fractional change in resistance of the nanomodified composite (Azhari and Banthia, 2012). The frequency dependence of the sensors is currently a limitation in sensing applications. This issue can be resolved by implementing a strain-rate-dependent electromechanical model. However, this behavior is not significant in modal identification studies.

6.7   Full-scale validation

In this section, the performance of CNTCSs at dynamic monitoring of a full-scale concrete beam is investigated and benchmarked against off-the-shelf sensors. The laboratory test setup is presented first, followed by the presentation of results obtained on a full-scale concrete beam.

6.7.1   Laboratory test setup

The performance of CNTCs at dynamic sensing is verified on a reinforced concrete beam. The beam is simply supported, with a span of 400 cm and a rectangular cross-section of 20×30 cm^2. Supports consist of vertical steel plates partially embedded in the beam.
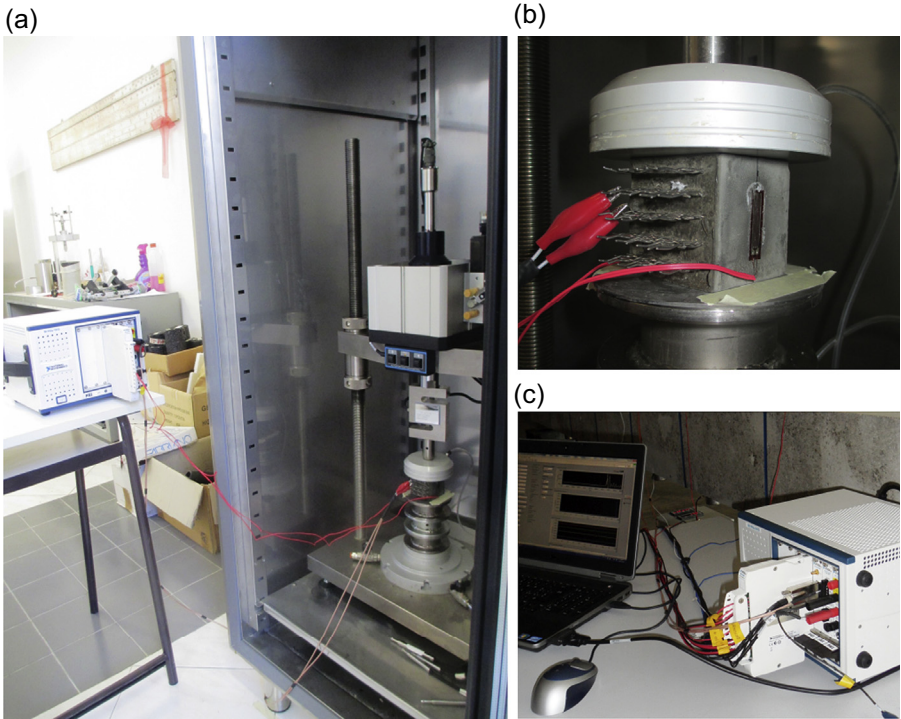
Figure 6.12 Test setup for the dynamic validation: (a) uniaxial test machine with the sensor; (b) view of the tested CNTCS; and (c) view of the DAQ system for the CNTCS.
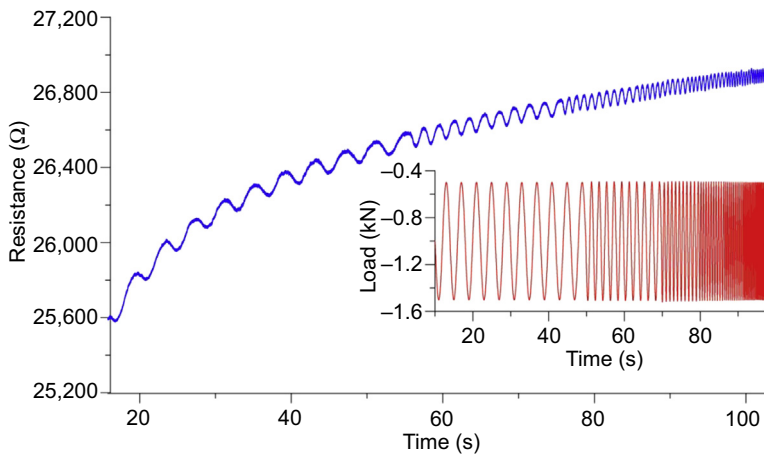
Figure 6.13 Sensor's response and applied load for the dynamic validation.
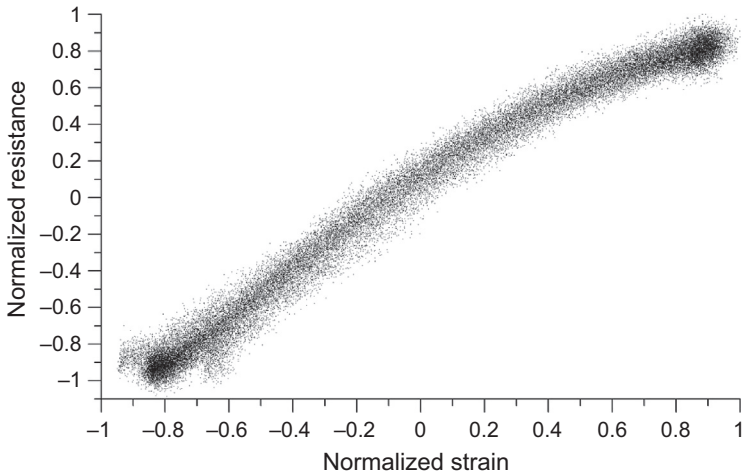
Figure 6.14 Normalized sensor's output variations versus normalized strain.
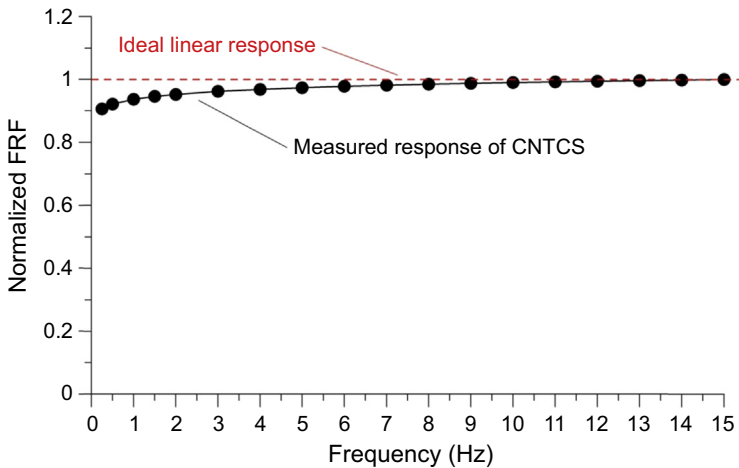
Figure 6.15 Normalized frequency response function of CNTCS.

Boundary conditions allow rotation in the vertical plane while restraining rotation in the horizontal—transverse plane. The beam is instrumented with seven accelerometers, model PCB 393C, equally spaced and deployed on the bottom surface of the beam. Seven electric strain gauges measure the strain on the top surface of the beam at the same locations of the accelerometers. Strain gauges are 6 cm long, and they have a nominal resistance of 120 Ω and a gauge factor of 2.1.

The beam is dynamically excited through random hits exerted by means of an instrumented hammer, model PCB 086D20C41. One CNTCS is applied to the top surface of the beam using a mechanical connection made of L-shaped steel elements connected to the beam with four bolts. The purpose of the mechanical connection is to simulate
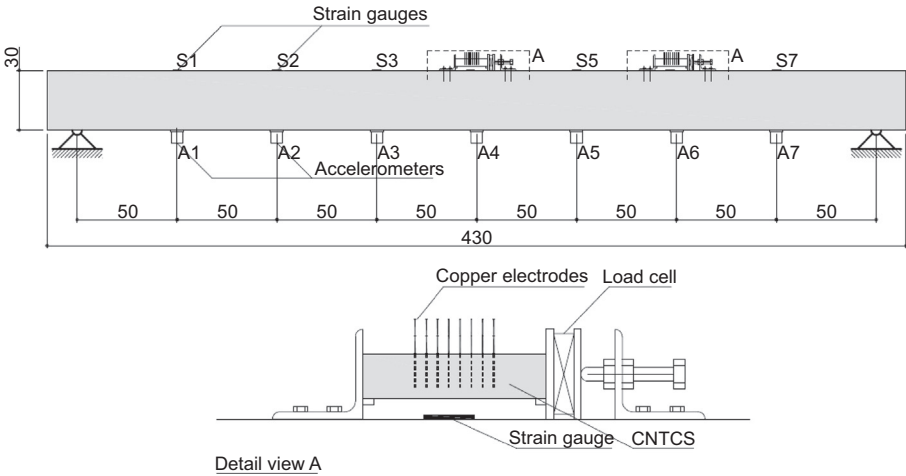
Figure 6.16 Layout of the experimental setup and plans of the investigated RC beam (dimensions in centimeters).

embedment of the sensor while enabling full access for experimental purposes. Two positions for the CNTCS are considered: at midspan and at quarter-span. The CNTCS is precompressed at 1.5 kN using a digital load cell to control the load.

Data from hammer, strain gauges, accelerometers, and CNTCS are simultaneously acquired through an NI PXIe-1073 containing specific modules. A power source with stabilized potential difference is applied through a module within the DAQ system. The output of the CNTCS is sampled at 1000 Hz. Prior to conducting the test, a constant potential difference of 15 V is applied to the sensor for a total duration of 30 min to reduce the polarization effect.

Figure 6.16 is a schematic representation of the test setup, and Figure 6.17 shows a photograph of the DAQ system, the hammer, and the test beam.

6.7.2 Results

Figure 6.18 shows the time history of the data acquired with the sensor placed at midspan. The signal in Figure 6.18(a) corresponds to the raw data. Figure 6.18(b) shows the result after using a high-pass filter above 10 Hz, which effectively eliminates the residual polarization effect.

Hammer hits are observable in the time−history plot of the CNTCS's output. A clean signal is observed in the detailed view of Figure 6.18(c). It is worth noting by comparing Figure 6.18(c) and (d) that the signal-to-noise ratio is high at small strain levels. Comparison of these waveforms in Figure 6.18(c) and (d) also outlines the nonlinearity of the relation between variation in electrical resistance of the CNTCS and strain measured through the strain gauge. Another observation is that the noise level observed in the signal of the CNTCS is much smaller compared to results reported in the literature for cement-based sensors. This is due to the shielding effect of the coaxial cable connecting the power source, sensor, and data acquisition system.
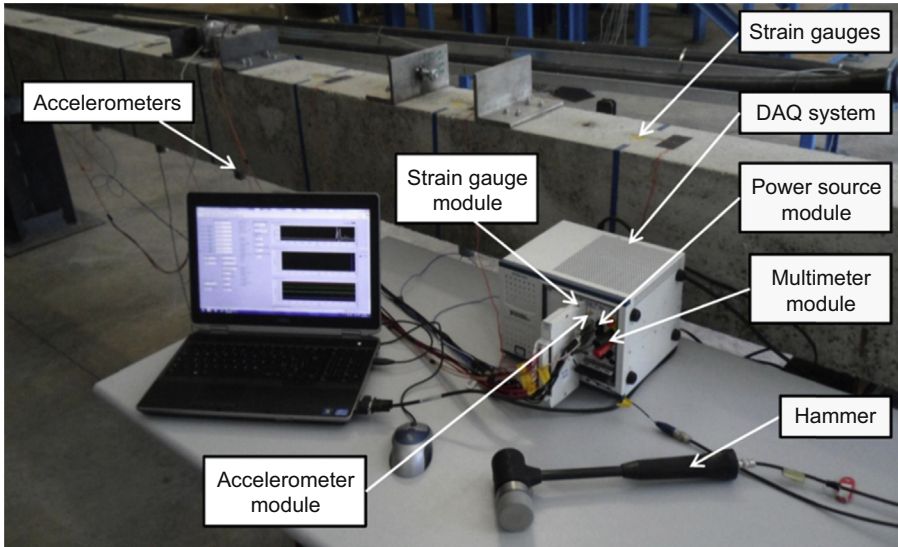
Figure 6.17 Experimental setup: photo image of test beam, instrumented hammer, and DAQ system.

Data acquired in the vibration tests are used for dynamic modal identification using the well-established technique of frequency domain decomposition (FDD). The results obtained using acceleration data allow one to clearly identify 12 modes of vibration in the interval between 0 and 500 Hz. Those are five vertical modes (V1, V2A, V2B, V3, and V4), five lateral modes (L1−L5), and two additional lateral modes named LS1 and LS2. Similar results are obtained using data recorded from the strain gauges.

Natural frequencies predicted by analytical Euler−Bernoulli beam theory (assuming a simply supported elastic beam in the vertical plane and a clamped−clamped one in the horizontal plane) and those identified using acceleration and strain data are summarized in Table 6.4. High-order modes are not successfully identified using data recorded by the strain gauges due to a higher measurement noise in comparison to data recorded by the accelerometers.

Mode shapes resemble those from beam theory. Modes V2A and V2B are similar anti-symmetric modes and conceivably represent a splitting of mode V2 due to cracking in the beam, as observed in other studies (Zonta and Modena, 2001). Modes LS1 and LS2 are associated with the lateral movement of the supports, slightly rolling over their bases.

Figure 6.19 shows a comparison between the normalized PSD of CNTCS's output and the first singular value of the PSD matrix of vertical acceleration data. These results show that all the peaks corresponding to vertical modes in acceleration data are visible in the PSD of CNTCS's output. Some peaks associated with lateral modes are also visible in such a PSD plot, such as the two peaks around the frequency of mode V1 and likely corresponding to modes LS2 and L1. The peak associated with mode LS1 is probably not visible because it is contained within the filtered region. Peaks associated with modes L2, L3, L4, and L5 are also visible.
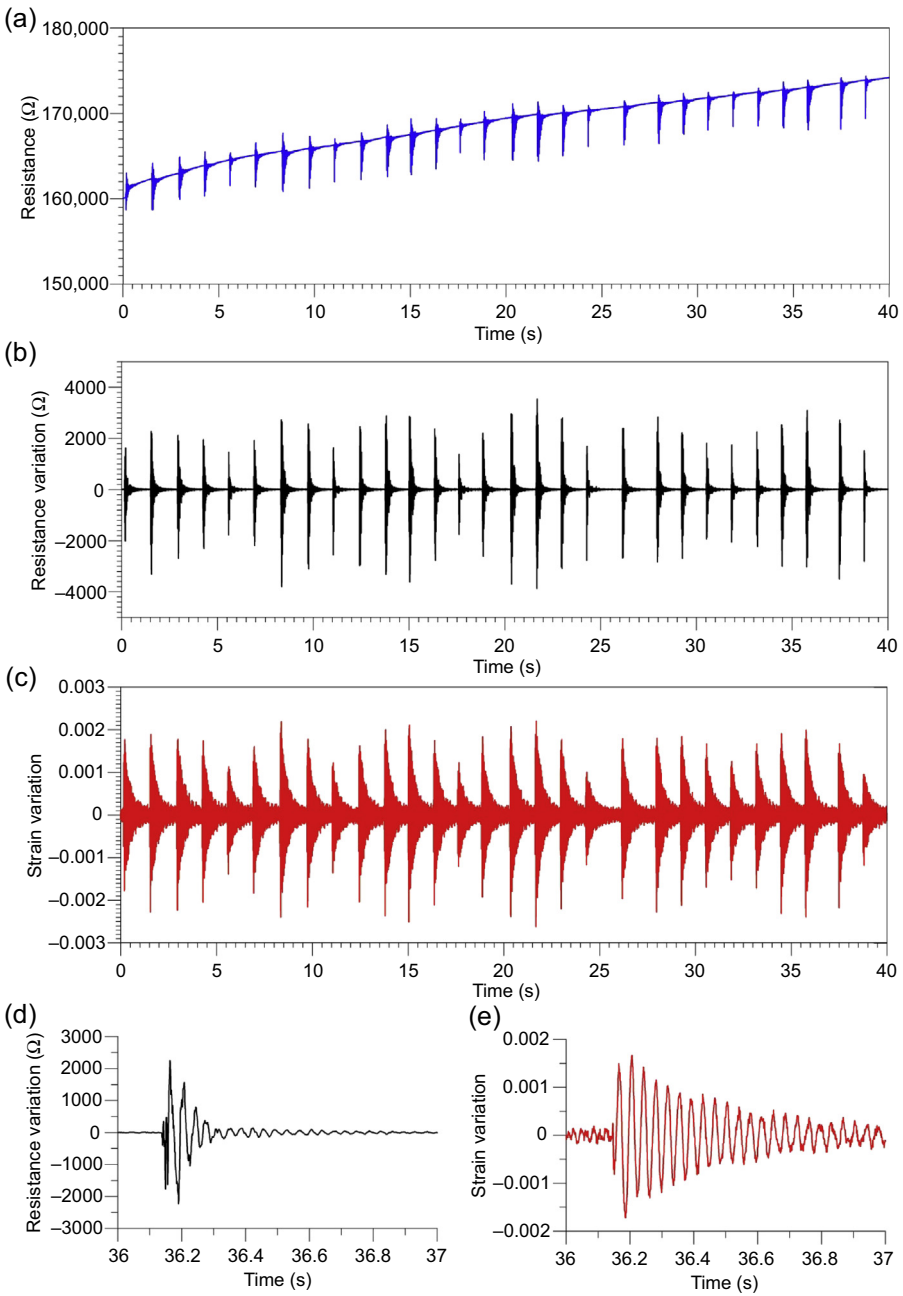
Figure 6.18 Vibration monitoring of the RC beam using CNTCS placed at midspan: sensor output before high-pass filtering (a); sensor output after high-pass filtering (b); output of the strain gauge placed at the location of the CNTCS (c); blowup on sensor output (d); and detailed window plot of the output of the strain gauge (e).

Table 6.4 Identified (ID) natural frequencies (Hz) of the reinforced concrete beam using off-the-shelf accelerometers and strain gauges by means of the FDD technique (Δ denotes the relative difference between analytical frequencies and frequencies identified from acceleration data) (Ubertini et al., 2014a)

Mode	Analytical	ID (accel.)	ID (strain)	Δ (%)
LS1	—	5.13	—	—
LS2	—	19.78	19.78	—
V1	25.22	27.10	27.10	7.4
L1	38.11	32.71	37.35	14.2
V2A	100.9	82.52	81.79	18.2
L2	105.1	93.75	93.75	10.8
V2B	100.9	113.5	113.5	12.5
V3	227.0	171.1	171.1	24.6
L3	206.0	192.1	192.6	6.7
L4	340.5	322.8	—	5.2
V4	403.5	431.4	—	6.9
L5	508.6	477.3	—	6.1
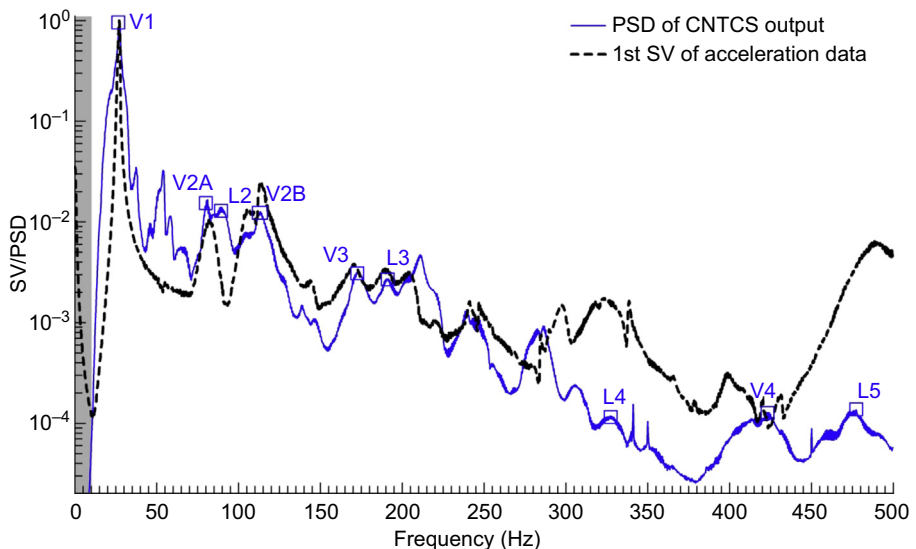
Figure 6.19 Identification of natural frequencies with CNTCS: first normalized singular value (SV) of vertical acceleration data (dashed line); and normalized PSD of the output of CNTCS (continuous line; the gray area denotes a filtered region).

Table 6.5 **Identified (ID) natural frequencies (Hz) using acceleration data and CNTCS's output (Δ denotes the relative difference between the two classes of values) (Ubertini et al., 2014a)**

Mode	V1	V2A	V2B	V3	V4
ID (accel.)	27.10	82.52	113.5	171.1	431.4
ID (CNTCS)	27.10	81.05	113.3	172.9	423.6
Δ (%)	0.0	1.8	0.2	1.0	1.8

Additional peaks are visible in the CNTCS output. They are likely attributed to super-harmonic components, whose presence is caused by the electromechanical behavior of the CNTCS.

A comparison between the frequencies of the vertical modes identified from acceleration data and from the CNTCS's output is listed in Table 6.5. The good agreement between the identified frequencies confirms the ability of the CNTCS to work as a dynamic sensor for output-only modal identification.

6.8   Concluding remarks

This chapter presented an overview of a cement-based nanocomposite for strain sensing. The sensor, termed CNTCS, was fabricated using a cement paste doped with CNTs.

Starting from the state of the art, summarizing the evolution of knowledge since the first invention of strain-sensing cement-based composites, this chapter has discussed the main difficulties in the material's preparation, and presented an effective procedure to achieve proper dispersion of the nanotubes in the composite material for the fabrication of prismatic sensors. Experimental results from laboratory validation have been presented. These results demonstrated that the electrical behavior can be characterized by using a lumped electrical circuit model containing resistors and capacitors. The model was effective at modeling the polarization effect of the cement paste. Tests under compressive loading have shown the ability of the material to work as a strain gauge, owing to the piezoresistive nature of the nanocomposite cement paste. The resulting gauge factor of the CNTCS was one order of magnitude greater than those of typical resistive-based strain gauges. More importantly, the novel sensor was capable of measuring strain at high sampling rates, which enables vibration-based monitoring. This significantly enlarges the potential applications of CNTCS in structural health monitoring.

This vibration-based monitoring capability has been investigated by conducting vibration tests on a full-scale reinforced concrete beam. Results from this test have demonstrated that the novel sensor compares well against mature technologies at vibration monitoring, such as accelerometers and strain gauges. In particular, the CNTCS is

suitable for output-only modal identification of vibrating structures. It thus represents a step toward the realization of self-monitoring concrete structures, a revolutionary yet realistic technology of the future.

References

Azhari, F., Banthia, N., 2012. Cement-based sensors with carbon fibers and carbon nanotubes for piezoresistive sensing. Cement and Concrete Composites 34, 866−873.

Banthia, N., 2009. Fiber reinforced concrete for sustainable and intelligent infrastructure. In: SBIDCO − 1st Int. Conf. Sustainable Built Environ. Infrastructures Developing Countries.

Cao, J., Chung, D.D.L., 2004. Electric polarization and depolarization in cement-based materials, studied by apparent electrical resistance measurement. Cement and Concrete Research 34, 481−485.

Chen, P.W., Chung, D.D.L., 1993. Carbon fiber reinforced concrete for smart structures capable of non-destructive flaw detection. Smart Materials and Structures 2, 22−30.

Chung, D.D.L., Wang, S., 2003. Self-sensing of damage and strain in carbon fiber polymer-matrix structural composites by electrical resistance measurement. Polymers and Polymer Composites 11 (7), 515−525.

Coppola, L., Buoso, A., Corazza, F., 2011. Electrical properties of carbon nanotube cement composites for monitoring stress conditions in concrete structures. Applied Mechanics Materials 82, 118−123.

D'Alessandro, A., Ubertini, F., Materazzi, A.L., Porfiri, M., 2014. Electrical modelling of carbon nanotube cement-based sensors for structural dynamic monitoring. Nanoforum 2014-AIP Conference Proceeding 1603, 23−30.

Dong, B., Xing, F., Li, Z., 2011. Electrical response of cement-based piezoelectric ceramic composites under mechanical loadings. Smart Materials Research. 2011 (2011), Article ID 236719, 7 pp. http://dx.doi.org/10.1155/2011/236719.

Gao, D., Sturm, M.S., Mo, Y.L., 2009. Development of carbon nanofiber self-consolidating concrete. In: Second Int. Symp. Des. Perform. Use Self-Consolidating Concrete, pp. 126−134.

Han, B., Ou, J., 2007. Embedded piezoresistive cement-based stress/strain sensors. Sensors and Actuators A 138, 294−298.

Han, B., Guan, H., Ou, J., 2007. Electrode design, measuring method and data acquisition system of carbon fiber cement paste piezoresistive sensors. Sensors and Actuators A 135, 360−369.

Han, B., Yu, X., Kwon, E., 2009. A self-sensing carbon nanotube/cement for traffic monitoring. Nanotechnology 20, 5 pp.

Han, B., Yu, X., Ou, J., 2011. Multifunctional and smart nanotube reinforced cement-based materials. In: Gopalakrishnan, K., Birgisson, B., Taylor, P., Attoh-Okine, N. (Eds.), Nanotechnology in Civil Infrastructure. A Paradigm Shift. Springer-Verlag, Berlin, Heidelberg, pp. 1−48.

Han, B., Zhang, K., Yu, X., Kwon, E., Ou, J., 2012. Electrical characteristics and pressure-sensitive response measurements of carboxyl MWCNY/cement composites. Cement and Concrete Composites 34, 794−800.

Han, B., Qiao, G., Jiang, H., 2012. Piezoresistive Response Extraction for Smart Cement-based Composites/Sensors. Journal of Wuhan University of Technology-Mater. Sci. Ed. 27 (4), 754−757.

Konsta-Gdoutos, M.S., Metexa, Z.S., Shah, S.P., 2010. Highly-dispersed carbon nanotube reinforced cement-based materials. Cement and Concrete Research 40 (7), 1052−1059.

Li, H., Xiao, H., Ou, J., 2003. A study on mechanical and pressure-sensitive properties of cement mortar with nanophase materials. Cement and Concrete Research 34, 435−438.

Li, G.Y., Wang, P.M., Zhao, X., 2007. Pressure-sensitive and microstructure of carbon nanotube reinforced cement composites. Cement and Concrete Composites 29, 377−382.

Loh, K.J., Chang, D., 2011. Zinc oxide nanoparticle-polymeric thin films for dynamic strain sensing. Journal of Material Sciences 46, 228−237.

Lourie, O., Wagner, D.E., 1998. Buckling and collapse of embedded carbon nanotube. Physical Review Letters 81 (8), 1638−1641.

Materazzi, A.L., Ubertini, F., D'Alessandro, A., 2013. Carbon nanotube cement-based transducers for dynamic sensing. Cement and Concrete Composites 37, 2−11.

Measures, R.M., 1993. Smart structure technology and its potential for civil engineering. Applications of Fiber Optic Sensors in Engineering Mechanics 17−38.

Mondal, P., Shah, S.P., Marks, L.D., 2008. Nanoscale characterization of cementitious materials. ACI Materials Journal 105, 174−179.

Muto, N., Yanagida, H., Nakatsuji, T., Sugita, M., Ohtsuka, Y., Arai, Y., 1992. Design of intelligent materials with self-diagnosing function for preventing fatal fracture. Smart Materials and Structures 1 (4), 324−329.

Sihai, W., Chung, D.D.L., 2001. Electric polarization in carbon fiber-reinforced cement. Cement and Concrete Research 31, 141−147.

Ubertini, F., Materazzi, A.L., D'Alessandro, A., 2014a. Natural frequencies identification of a reinforced concrete beam using carbon nano tube cement-based sensors. Engineering Structures 60, 265−275.

Ubertini, F., Laflamme, S., Ceylan, H., Materazzi, A.L., Cerni, G., Saleem, H., D'Alessandro, A., Corradini, A., 2014b. Novel nanocomposite technologies for dynamic monitoring of structures: a comparison between cement-based embeddable and soft elastomeric surface sensors. Smart Materials and Structures 23 (4), 12 pp.

Wen, S., Chung, D.D.L., 2006. Model of piezoresistivity in carbon fiber cement. Cement and Concrete Research 36, 1879−1885.

Xu, Z., Liu, Z., 2007. Fatigue damage in smart carbon fiber Concrete by electrical resistance measurement. Key Engineering Materials 348−349, 435−438.

Yu, X., Kwon, E., 2009. A carbon nanotube/cement composite with piezoresistive properties. Smart Materials and Structures 18, 5 pp.

Zonta, D., Modena, C., 2001. Observations on the appearance of dispersive phenomena in damaged structures. Journal of Sound and Vibration 241, 925−933.

Tomographic imaging of cementitious materials

<div style="text-align:right">**7**</div>

Tsung-Chin Hou
National Cheng Kung University, Tainan, Taiwan

7.1   Introduction

Cracking in cement-based structures, such as those constructed of reinforced concrete, can result from a variety of factors, including externally applied loads, shrinkage, and poor construction methods, among many others. When making an assessment of the general state of the health of such structures, cracks must be reliably quantified and their significance determined. For example, small cracks affecting only the external aesthetic of the structure should be differentiated from those that reduce its strength, stiffness, and long-term durability (ACI, 1998). Detailed visual inspection of the surface of the structure remains a common method for detecting cracks; systematic crack mapping allows inspectors to monitor the progression of cracks and to hypothesize the nature of their origins (Bungey et al., 2006). After suspicious cracks are encountered, nondestructive (e.g., ultrasonic inspection) and partially destructive (e.g., core holes) testing can be carried out by trained inspectors to determine crack features below the structural surface (ACI, 1998). However, all of these methods require the use of trained personnel to execute, rendering them as tedious and expensive. In contrast, automated sensor technologies are needed for permanent installation so that accurate assessments of crack damage could be made without requiring a trained professional to visually inspect the structure.

A variety of approaches have been proposed for automated structural health monitoring of concrete structures. Generally, many of these approaches call for the installation of external sensors to measure global and local structural responses to loading. Early work explored the use of vibration measurements (e.g., accelerations) to identify global modal properties that change when structural damage is present. Particularly for civil structures, environmental variability often hinders accurate correlation of modal property changes to damage (Doebling et al., 1998). Alternatively, local structural measurements including strain and deformation have also been proposed for crack detection. Based on the applied structural loading and the corresponding component response, various damage index methods have been proposed for the quantification (often on a scale from 0 to 1) of cracking degree (Park and Ang, 1985; Kratzig et al., 1989). Although damage index models perform well when predicting cracks in laboratory elements, the inability to precisely measure loads on full-scale concrete structures renders this approach difficult to apply in more practical settings.

Perhaps the best approach for automated structural health monitoring of concrete structures entails the adoption of the sensors available in the nondestructive

evaluation (NDE) field. In particular, passive and active stress wave approaches have been proposed for NDE evaluation of concrete structures. Acoustic emission (AE) sensing is foremost among the passive stress wave methods. AE employs piezoelectric elements to capture the stress waves generated by cracks (Ouyang et al., 1991; Shah and Choi, 1999); however, although AE has played a critical role in the laboratory, its success in the field has been limited to only a handful of applications (Mindess, 2004). In contrast, active stress wave methods have proven more accurate for crack detection. Active sensing entails the use of piezoelectric transducers to introduce short ultrasonic stress waves into a concrete element, and using the same transducer, or another, to measure the stress waves after they have propagated through the element. For example, pulse−echo (using one transducer) and pitch−catch (using two transducers) techniques are capable of characterizing cracks in actual concrete structures (Carino, 2004). In structural elements whose geometry guides the stress wave in a specific direction, the ultrasonic stress waves are termed guided waves (Raghavan and Cesnik, 2007); some examples of guided wave techniques to characterize damage in concrete include Na et al. (2002), Luangvilai et al. (2002), and Jung et al. (2000). A direct extension of the active stress wave approach is the electromechanical impedance spectra method in which the electromechanical impedance spectrum of a piezoelectric transducer is used to detect cracking in the vicinity of the transducer (Park et al., 2000, 2006). Some challenges associated with active sensing in cement-based materials include significant wave attenuation over long distances and internal heterogeneities causing wave scattering and complex ultrasonic speckle patterns.

Compared to other NDE methods, utilization of the electrical properties of cement-based materials for crack detection has garnered less attention from the civil engineering community. Historically, electrical properties have been investigated for tracking the formation of microstructural properties during hardening (Han et al., 2005) and to quantify the potential for corrosion of buried steel reinforcement (Lauer, 2004). In contrast, this study will utilize the electrical properties of cementitious materials as a novel approach to automated health monitoring of civil structures. First, the relationship between electrical conductivity and strain will be quantified so that it can be established that cement-based materials are self-sensing. Because in theory a measurement for strain can be made wherever the material is, a novel approach to measuring conductivity over spatial areas is introduced next. Termed electrical impedance tomography (EIT), this inverse tomographic approach offers 2D and 3D conductivity maps for structural elements instrumented with electrodes upon their surface. Conceptually, the EIT approach is similar to the ultrasonic tomographic methods (Rose and Ditri, 1990) used to map wave attenuation properties of structural elements using dense arrays of surface-mounted piezoelectric transducers. As a result of cement being piezoresistive, EIT conductivity maps offer a direct measurement of strain fields. Furthermore, cracks can be imaged as conductivity reductions because cracks are nonconducting across their widths. Although applicable to any cement-based composite, this chapter presents the experimental investigation of the application of EIT to image strain fields and cracks in fiber-reinforced cementitious composite (FRCC) structural elements.

7.1.1 Electrical conduction in cementitious materials

Conductivity (σ) is a fundamental material property that quantifies the ability of the material to carry a current when placed in an electrical field. Specifically, the current flow density, J, is linearly proportional to the electric field, E, through conductivity (Mayer and Lau, 1990): $J = \sigma E$. Resistivity (ρ), the inverse of conductivity, is the volumetric resistance, R, of a unit cube as measured across one dimension. Resistivity is reported in terms of Ω m, whereas conductivity is reported using the units S/m (Ω^{-1} m^{-1}). With conductivities ranging from 10^{-3} to 10^{-6} S/cm, cementitious materials are classified as semiconductors (Whiting and Nagi, 2003). In cement, the current generated by an electric field is based on ionic conduction. The high concentration of calcium, potassium, and sodium salts within the pore water and water$-$cement gel are mobilized by the electric field to create electrical current (Hansson and Hansson, 1983). Because the ions in water are the primary charge carrier, the conductivity of cementitious materials naturally exhibits strong dependency on moisture content.

Considerable attention has been paid in recent years to measuring and interpreting the electrical properties of cement composites, including reinforced concrete. Specifically, the electrical properties of cement can be used to assess the microstructural details of the material (Han et al., 2005). For example, very early work in the field explored correlations between direct current (DC) conductivity measurements and the setting times of Portland cement composites (Calleja, 1953; Hammond and Robson, 1955). More profound insight to the hydration process has been gained since the 1990s through the use of electrical impedance spectroscopy (EIS). EIS measures conductivity as a function of the angular frequency of an applied alternating current (AC) signal (McCarter and Brousseau, 1990). Impedance spectra obtained by EIS can be used to track hydration processes, identify the porosity of cured cement, and characterize interfacial properties (e.g., cement$-$steel or cement$-$aggregate interfaces). The electrical properties of cement also serve as a basis for assessing the corrosion potential of reinforced concrete (Lauer, 2004). When reinforcement steel corrodes, the cement conductivity is a measure of how easy it is for ions to flow between the anodic and cathodic sites on the buried reinforcement. It has not been until very recently that the electrical properties of cementitious materials have been explored for damage detection, including the identification of cracking (Peled et al., 2001; Chung, 2001; Hou and Lynch, 2005a).

7.1.2 Traditional electrical measurement techniques

Multiple measurement methods have been proposed for measuring the conductivity of cement-based materials. In general, the measurement methods proposed can be broadly classified as either two-point or four-point probe methods. In two-point probe methods (Figure 7.1(a)), two electrodes are used to apply an electrical current, I, and to also measure the corresponding drop in voltage, V, across the cement specimen. Electrodes must be in intimate contact with the cement-based specimen to induce an ionic current within the specimen. Metallic electrodes either can be surface mounted using conductive gels and pastes, or can be embedded directly into the wet concrete prior to
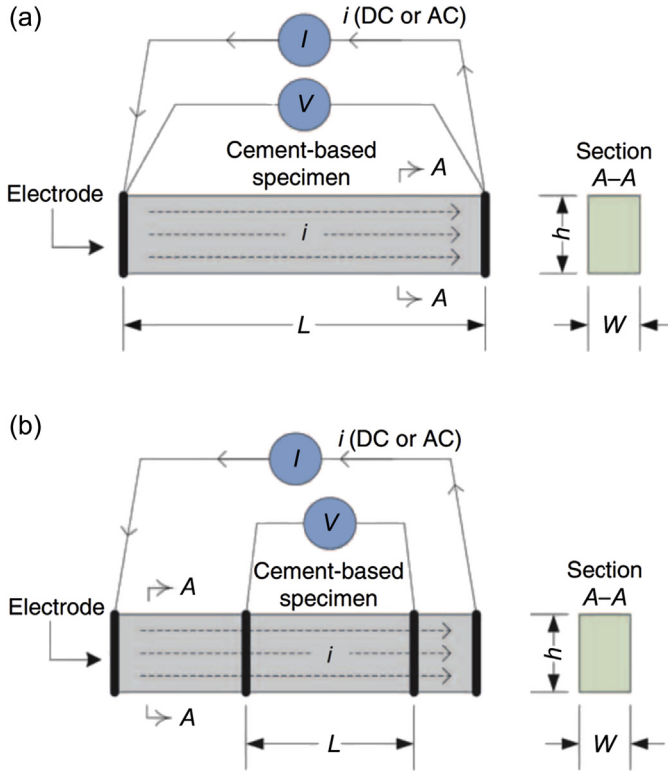
Figure 7.1 Conductivity measurement based upon the (a) 2-point and (b) 4-point probe techniques.

hardening (Whiting and Nagi, 2003). If a DC is applied across the specimen area, conductivity can be calculated:

$$\sigma = \frac{1}{V} \frac{L}{wh} \tag{7.1}$$

where L, w, and h correspond to the electrode spacing, specimen width, and specimen height, respectively. Although two-point DC probe measurements are easy to take, they do suffer from two major drawbacks. First, contact impedance at the electrode−cement interface in the two-point probe method introduces a time-dependent reduction in conductivity. Contact impedance originates from the electrochemical reactions that naturally occur in the test specimen in the vicinity of the electrode (Vilhunen et al., 2002). For example, electrons flowing into a specimen at the electrode induce pore water to decompose into hydrogen (H_2) and hydroxide ions (OH^-) (Hansson and Hansson, 1983). Similarly, free hydroxide ions can react at the other electrode to produce electrons (e^-) that then flow into the electrode as well as produce oxygen (O_2) and water (H_2O). These reaction

by-products accumulate at the electrode−specimen interface, resulting in a back electromagnetic field. The second drawback of DC two-point methods is the measurement error introduced by polarization of the specimen. Polarization is the separation of positive and negative ions trapped within the cement pores; as ions separate, less current is carried, resulting in a reduction in the conductivity measurement (Hansson and Hansson, 1983). As a result, AC is preferred because contact impedance and polarization effects do not have sufficient time to develop under an alternating field (Whiting and Nagi, 2003). When AC signals are used in the two-point probe method, Eqn (7.1) is still valid using the amplitude of the current and voltage.

The four-point probe method is the preferred approach for measuring the conductivity of cement-based materials (Millard, 1991). As the name suggests, the method employs four independent electrodes along the length of a specimen (Figure 7.1(b)). The two outermost electrodes are used to drive an electric current (DC or AC) into the medium, whereas the two inner electrodes are responsible for measuring the electrical potential developed over the length, L. Again, if it is assumed the cross-sectional area of the specimen is w by h, then Eqn (7.1) is still valid. In the four-point probe method, the effects of contact impedance are minimized because the measurement and excitation electrodes are separated. As a result, four-point probe methods provide a more consistent measurement of electrical conductivity when compared to two-point probe methods.

A specialized version of the four-point probe method is the Wenner technique (Gowers and Millard, 1999). Although this approach was originally developed for in situ measurement of soil conductivity, it has been widely applied to measurements in cementitious materials. In the Wenner technique, four electrodes equally spaced (by a) along a straight line are applied to the surface of a cementitious specimen, as shown in Figure 7.2. If the specimen is assumed to be an infinite half-space, then conductivity can be calculated:

$$\sigma = \frac{1}{V}\frac{1}{2\pi a} \tag{7.2}$$

Both DC and AC electrical excitations can be used, but generally AC excitations greater than 100 Hz are preferred (Han et al., 2005). Some care must be exercised when using the Wenner technique. For example, test specimens must be sufficiently thick (generally, thicknesses four times greater than the electrode spacing) to ensure that the assumption of an infinite half space is valid. Similarly, measurements must be made away from specimen edges and corners.

EIS is a more sophisticated electrical characterization technique based on AC signals. Similar to the aforementioned four-point probe measurement method, two probes are employed to apply an AC signal to the specimen, whereas two inner electrodes measure voltage (Figure 7.3(a)). In EIS, a frequency response analyzer (FRA) is adopted to measure both the amplitude and phase of the voltage measurement relative to the applied sinusoidal current (Barsoukov and Macdonald, 2005). Using amplitude and phase, θ, the complex-valued impedance of the material can be measured as a
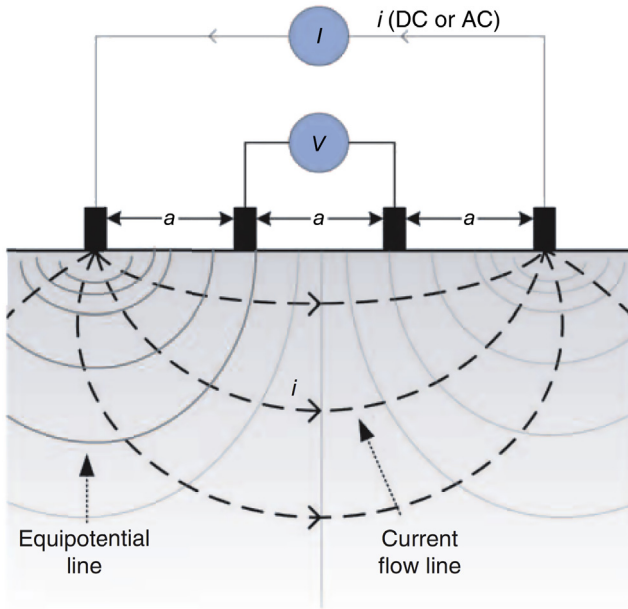
Figure 7.2 Wenner technique: a 4-point probe conductivity measurement based upon surface contact.
Adapted from Millard (1991).

function of applied AC frequency, ω. The frequency is varied from low to high frequencies with complex impedance,

$$Z = \frac{V_A \sin(\omega t + \theta)}{I_A \sin(\omega t)}, \tag{7.3}$$

plotted on the complex plane. The real and imaginary components are associated with the conductivity and capacitive properties of the specimen, respectively. For many cementitious materials, the impedance plot consists of two semicircular traces as shown in Figure 7.3(b). The low-frequency semicircular trace corresponds to the behavior of the electrode, whereas the high-frequency trace corresponds to that of the cementitious material (Han et al., 2005). Such distinctive impedance plots also permit the use of equivalent parallel resistor—capacitor (RC) circuits (Figure 7.3(c)) to model the electrical behavior of the material.

7.1.3 Engineered cementitious composites

Because concrete is brittle in nature and cracks when subjected to tensile strain, engineered cementitious composites (ECCs) emerged recently to address the shortcomings of concrete (as well as high-strength concrete). ECC is a family of engineered, high-performance, FRCCs. Featuring high tensile ductility, restrained crack width,
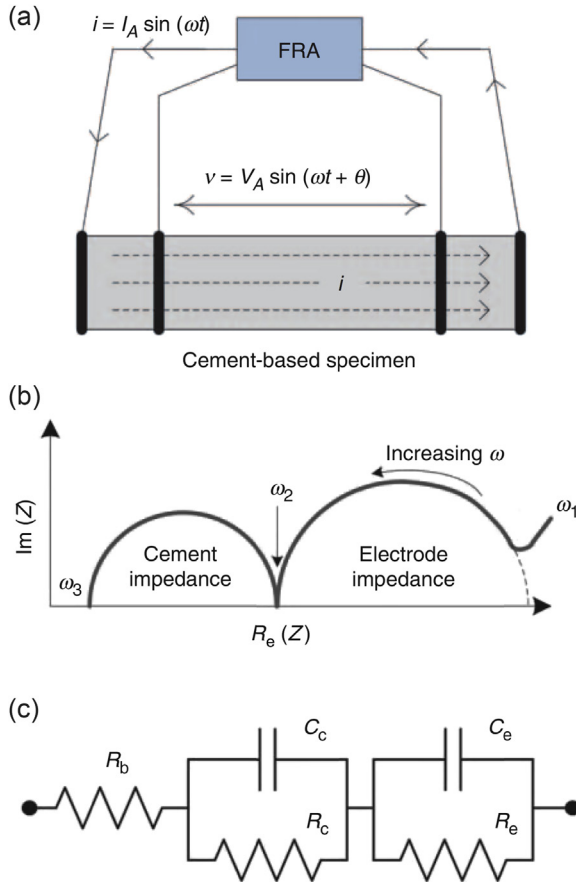
Figure 7.3 Electrical impedance spectroscopy: (a) experimental setup; (b) typical impedance plot on the complex plane *(Adapted from Han et al. (2005))*; and (c) equivalent circuit model.

and strain-hardening capabilities, ECC is typically designed with low volume fraction ($\leq 2\%$) of randomly distributed fibers of a specific type and property. Perhaps a commonly seen version, ECC M45, best demonstrates the stress−strain relationship of ECC (Wang, 2005). Specifically in that example, the tensile ductility of over 3% is achieved by developing multiple cracks, with the crack width limited to around 60 µm. The features of multiple cracking as well as restrained crack width serve as a potential remedy for overcoming the brittle nature of normal concrete, particularly when structural ductility and durability (e.g., most infrastructure) are primary concerns.

Apart from the fundamental characteristic—the high tensile ductility of ECC—many other material functions associated with specific structural applications of ECC have also been studied recently. Challenges of exploring the extra functionality of ECC are to incorporate the desired attributes into ECC such as light weight, high

early strength, self-healing, self-sensing, self-thermal control, impact and fire resistance, and so on without eliminating or even limiting its fundamental characteristic. Through the micromechanics-based analysis, systematic composition modification and readjustment are proposed to achieve specific functions for structural applications while preserving the ductile characteristic (Li, 2012). Wang and Li (2003) employed lightweight fillers to investigate lightweight ECC. The four types of fillers investigated were polymeric microform, hollow glass bubble, expanded perlite sand, and air bubbles generated by air entrainment admixture. For the case of hollow glass bubble inclusion, composites with a density of 1.45 g/cm^3, tensile ultimate tensile strength of 4.31 MPa, and tensile strain greater than 4% are achieved while restraining the crack width within 80 μm.

The repairing tasks of bridges and structures demand the use of high-early-strength cementitious materials. According to the recommendations and requirements of various Departments of Transportation and the US Federal Highway Administration for high-early-strength ECC (HES-ECC), the target minimum compressive strength was set at 17.2 MPa at 4 h and 48.3 MPa at 28 days (Li and Li, 2011). Several composition modifications have been investigated to attain the high early strength, including: replacing Type I Portland cement with Type III, the exclusion of fly ash, lowing the water-to-cement ratio to 0.36, the use of a polycarboxylate-based superplasticizer, and the use of a calcium nitrite−based accelerator. The HES-ECC studied by Wang (2005) has shown that over 25 MPa at 4 h was achieved while the tensile strain capacity was reduced to 1% due to reduced intrinsic natural flaws. By adding polystyrene beads as artificial flaws to trigger the initiation of multiple cracks, the reengineered HES-ECC showed a restoration of tensile strain capacity of around 3% after three days (Yang, 2007; Li, 2009). Another featured function of ECC for structural application is the self-healing capability attributed to controlled crack widths and the resulting higher degree of rehydration afterward. This function is achieved by using high volumes of fly ash (HFA-ECC) that would result in tighter crack widths between 16 and 55 μm, as compared to 27−95 μm with ECC M45 (Yang et al., 2007).

7.1.4 *Self-sensing fiber-reinforced cementitious composites*

Although concrete continues to be a dominant material used in the design of large civil structures, the material is inherently brittle and prone to cracking when loaded in tension. Short fibers have been proposed in lieu of coarse aggregates to enhance the mechanical properties of the cement matrix (Balaguru and Shah, 1992). A variety of fiber types have been proposed in the literature, including polymeric, metallic, and carbon fibers. FRCC can be designed to exhibit strength and ductility in tension, thereby rendering them attractive for use in tension and shear-dominated structural elements. Optimization of the fiber−matrix interface by mechanical (e.g., hooked fibers) or chemical means (e.g., fiber coatings) leads to energy dissipation by thin microcracks whose formation is arrested by the fibers. This microscale behavior leads to tensile strain-hardening and high damage tolerance in tension (Parra-Montesinos, 2005). In recent years, strain-hardening FRCC materials have found application in the design of coupling beams in shear walls (Wight et al., 2006), bridge decks (Kim et al.,
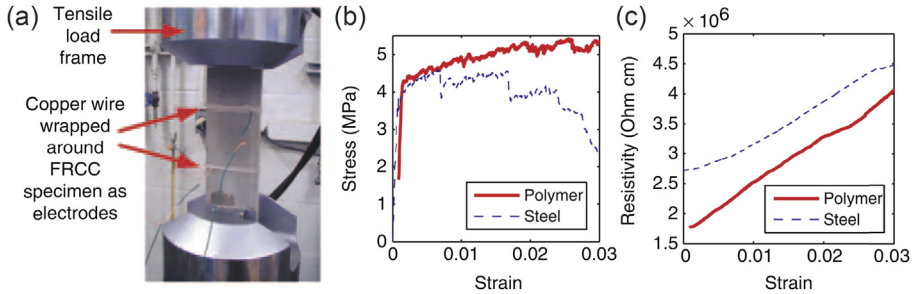
Figure 7.4 (a) FRCC plate element loaded in monotonic axial tension as resistivity is measured by 2-point probing; (b) stress and (c) resistivity versus strain plots for polymeric and steel fiber FRCC plates.

2004; Naaman and Chandrangsu, 2004), retaining walls (Kunieda and Rokugo, 2006), and extruded pipes (Stang and Pedersen, 1996).

Because of the growing importance of FRCC materials, this study will explore their electrical properties for sensing the mechanical behavior of FRCC structural elements. Other researchers have also begun to study the piezoresistivity (i.e., strain-induced resistivity changes) of FRCC materials with the aim of using them as their own sensors (Chung, 2001; Reza et al., 2003; Hou and Lynch, 2005b; Li et al., 2006). The addition of sensing functionality with mechanical functionality has led to FRCC being classified as a "multifunctional" material (Chung, 2003).

Prior to cracking, change in FRCC resistivity occurs linearly with strain in both tension and compression. For example, the piezoresistive properties of FRCC plate elements employing polymeric and steel fibers have been studied by Hou and Lynch (2005b). As shown in Figure 7.4(a), the two-point probe method assisted by a digital multimeter is used to measure the change in material conductivity as tensile strain is applied to each FRCC element. The stress−strain curves (Figure 7.4(b)) for the two plates reveal ductile strain-hardening behavior. Resistivity−strain curves (Figure 7.4(c)) also reveal fairly linear trends for each fiber type.

7.1.5 Electrical impedance tomography

Two- and four-point probe methods suffer from inherent limitations when used to characterize the electrical properties of cementitious materials. For example, they do not provide a measurement of material conductivity at a given point; rather, they measure the average conductivity between the electrodes. Therefore, if the electrodes are spaced too far apart, inhomogeneities that may exist between the electrodes are not directly observed because their influence on the conductivity measurement is averaged out. Should a mapping of conductivity over the area of a cement element be sought, the Wenner technique can be employed. Numerous vendors sell handheld equipment to make four-point probe conductivity measurements based on the Wenner technique (Bungey et al., 2006). However, repeated measurement across a structural element can be both labor-intensive and time-consuming.
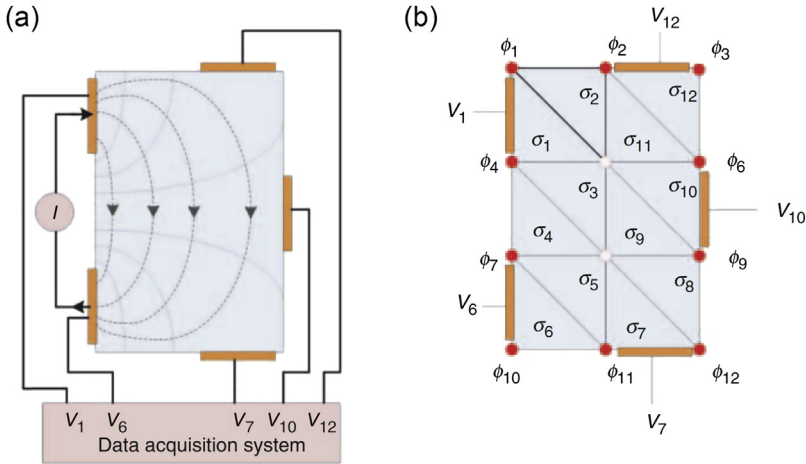
Figure 7.5 (a) Experimental approach to data collection for EIT conductivity mapping; (b) finite element formulation of the forward problem.

An autonomous means of measuring the spatial distribution of FRCC conductivity is sought. Because FRCC materials are piezoresistive, conductivity maps could be used to measure 2D strain fields within an FRCC structural element. Furthermore, cracks are physical inhomogeneities that block the flow of electricity; cracks would therefore appear as regions of near-zero conductivity within the conductivity maps. EIT is proposed herein for mapping the spatial distribution of conductivity over structural surfaces. EIT has been widely adopted for anomaly detection in geophysical exploration (Zhdanov and Keller, 1994) and biomedical imaging (Webster, 1990).

EIT is a more sophisticated approach to measuring material conductivity than the two- and four-probe methods. Unlike the probe methods, EIT is a combination of both electrical probing and the use of analytical models describing the flow of electricity in the test specimen. Therefore, conductivity mapping by EIT can be broken down into three major parts. First, the specimen under study is stimulated by a regulated current while electrical voltages are measured along the specimen boundary. Second, an analytical model that predicts the boundary voltages to the same AC stimulation is formulated; this model is often referred to as the forward problem because the distribution of conductivity is assumed known. However, the conductivity distribution is unknown; hence, the inverse problem is solved by varying the assumed conductivity distribution of the forward problem until convergence between experiment and model is achieved. Figure 7.5 summarizes the EIT approach to conductivity determination.

7.1.6 Electrical stimulation and data collection

EIT employs measurement of voltages along the boundary of a test specimen. First, electrodes are affixed to the surface of the specimen as shown in Figure 7.5(a); the electrodes are used to introduce electrical currents and to measure voltage. Typically, electrodes are installed equidistant from one another to simplify the forward-problem model. In this study, the adjacent electrode protocol to data

collection is adopted (Heikkinen et al., 2002). In this approach, a regulated current (DC or AC) is applied to a pair of adjacent electrodes. On the remaining electrodes, the resulting voltage is measured and recorded. The process is repeated using the same electrical excitation until every combination of adjacent electrode pairs has been employed.

7.1.7   Formulation of the forward problem

The flow of electrical current within a 2D body, Ω, can be modeled by the 2D Laplace equation:

$$\nabla \cdot [\sigma(x, y)\nabla\phi(x, y)] = I(x, y) \tag{7.4}$$

where σ, ϕ, and I are conductivity, electric potential, and current, respectively, at point (x, y). Assuming current is applied only on the boundary of the body, the right-hand side of Eqn (7.4) is then set equal to zero. For a known distribution of conductivity, the forward problem allows the electrical potential to be uniquely calculated at every point in the body based on the current applied at the body boundary, $\partial\Omega$, if Dirichlet (voltage is continuously measurable on the body boundary) and Neumann (the integral of current along the boundary is zero) boundary conditions are assumed. Regardless, analytical solutions to the Laplace equation are not tractable except in cases of specimens defined by simple geometries and minimal conductivity variations (Lionheart et al., 2005). Hence, numerical solutions are generally pursued with finite difference, boundary element, and finite element methods (FEMs) all previously proposed. The FEM, though, is the most common numerical approach for modeling Eqn (7.4).

   The FEM formulation adopted in this study is termed the complete electrode model (CEM). This approach begins by meshing the body into discrete triangular elements as shown in Figure 7.5(b). The conductivity of the jth element is assumed constant, σ_j. Variation of electric potential across the body is assumed to be a linear sum of electrical potential at element vertices, ϕ_i, multiplied by predefined shape functions, w_i (Lionheart et al., 2005):

$$\phi(x, y) = \sum_1^N \phi_i w_i(x, y) \tag{7.5}$$

where the shape function takes the unit value at the ith vertex and zero at all other vertices. N corresponds to the number of nodes in the mesh. Along the element boundaries, different shape functions can be employed, but second-order polynomials are adopted in this study. Assuming voltages are measured on electrodes two at a time with the first electrode held fixed as the reference electrode, then the vector of electrodes can be approximated as (Vauhkonen, 1997):

$$V = \sum_1^{L-1} V_j n_j \tag{7.6}$$

where $n_j = [1, 0, 0,..., -1,..., 0]^T$ (with -1 in the jth indexed term of the vector) and V_j is the voltage of the jth element. Due to the lack of differentiability of the shape functions, w and n, variational methods are employed to yield the weak form of the 2D Laplace equation. The solution for each element is assembled into a global linear equation for the specimen:

$$\mathbf{A}\,\mathbf{x} = \mathbf{b} \tag{7.7}$$

where $\mathbf{A} \in \Re^{(N+L-1)\times(N+L-1)}$ is the sparse system matrix calculated using the element conductivities, $\mathbf{x} = [\mathbf{\Phi V}]^T$, $\mathbf{b} = [\mathbf{0\ I}]^T$, $\mathbf{\Phi} = [\phi_1\ \phi_2\ ...\ \phi_N]^T$, $\mathbf{V} = [V_1\ V_2\ ...V_L]^T$, and $\mathbf{I} = [1\ 0\ 0\ ...\ -1\ ...\ 0]^T$. For the example presented in Figure 7.5(b), 12 triangular elements, 12 vertices ($N = 12$), and five electrodes ($L = 5$) are used. Therefore, $\mathbf{V} = [V_1\ V_6\ V_7\ V_{10}\ V_{12}]^T$, and $\mathbf{I} = [1\ -1\ 0\ 0\ 0]^T$. Although theoretically the forward problem can be solved for $\mathbf{x}$ by $\mathbf{x} = \mathbf{A}^{-1}\,\mathbf{b}$, the sparsity of $\mathbf{A}$ requires more robust approaches to inversion such as the use of LU decomposition, among others. Numerical procedures for LU decomposition can be found in Chapra and Canale (2009), and many commercially available softwares including MATLAB offer ready to use tools.

7.1.8   Solution to the inverse problem

The EIT problem is the inverse of the forward problem; in other words, EIT finds the optimal mapping of conductivity, $\sigma(x, y)$, based upon voltage measurements along the boundary. The solution of the inverse problem requires the forward problem to be run repeatedly as the assumed distribution of conductivity is varied ($\sigma' = \sigma + \Delta\sigma$), so as to minimize the mean square error between the measured voltages and the model predicted electric potentials:

$$f(\sigma') = \frac{1}{2}\|\phi(\sigma') - V\|^2 \tag{7.8}$$

The changes in conductivity, $\Delta\sigma$, between successive runs of the forward problem are based on the Newton−Raphson iterative method and are expressed as:

$$\Delta\sigma = -\left[\phi'(\sigma)^T\phi'(\sigma)\right]^{-1}\phi'(\sigma)[\phi(\sigma) - V] \tag{7.9}$$

where $\phi'(\sigma)$ is the Jacobian matrix of the FEM boundary potential.

The Jacobian matrix, $\phi'(\sigma)$, represents the voltage changes at the electrodes due to small perturbations in the assumed conductivity distribution. With boundary potentials depending on element conductivity nonlinearly, the ill-conditioned nature of the Jacobian typically requires regularization techniques (e.g., Tikhonov regularization) to provide stable iterative convergence to the final conductivity distribution (Barber, 1989; Lionheart et al., 2005).

Unfortunately, the ill-posed inverse problem is defined by an underdetermined set of equations. As a result, a single set of boundary voltages corresponding to an applied current is insufficient to accurately map the body conductivity. Therefore, boundary voltage

measurements corresponding to multiple applied current distributions are needed to yield a stable and accurate solution. For this reason, the adjacent electrode approach applies current to every combination of adjacent electrodes. Repeated boundary measurements provide sufficient data to render the EIT inverse problem overdetermined.

7.1.9 Experimental methods

ECCs, a unique strain-hardening FRCC designed using polymeric fibers (Li et al., 2002), are adopted to evaluate the application of EIT sensing for the measurement of strain and the identification of crack damage. ECCs are constructed using Type 1 Portland cement, silica sand as a fine aggregate, fly ash, and short polyvinyl alcohol (PVA) fibers for reinforcement. To control the growth of cracks and to attain strain-hardening behavior in tension, the surface of the PVA fiber is chemically treated to tailor the micromechanical properties of the fiber−matrix interface. Only a small amount of PVA fibers is necessary to attain optimal mechanical properties; in this study, a 2% volume fraction of PVA fibers is used. To build test specimens, a wet ECC mixture is poured into molds where they remain for seven days to harden. Once seven days have passed, the specimens are removed from the molds and cured until testing, which occurs no earlier than 28 days after casting. The first set of test specimens constructed are ECC plates that are 30.5 cm long and with cross-sectional areas of 7.6×1.3 cm^2 (Figure 7.6(a)). The second specimen employed is an ECC beam, which is more representative of a realistic structural element. The beam is 140 cm long, 15.2 cm deep, and 7.6 cm wide. For both sets of specimens, no steel reinforcement is employed.

7.1.10 Data acquisition

To conduct EIT sensing on the test specimens, each specimen is instrumented with copper electrodes. Adhesive copper tape (6.3 mm wide and 0.7 mm thick) is attached
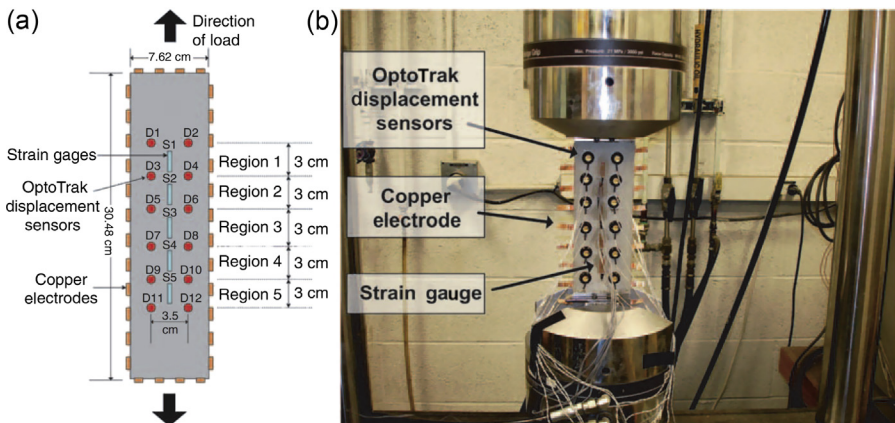

Figure 7.6 (a) ECC plate specimen under monotonic and cyclic axial loading; (b) ECC plate specimen loaded into the tensile load frame.

to the surface of the test specimens to serve as electrodes. To ensure the copper—cement contact is conductive, additional silver colloidal paste is used to attach the electrodes. AC electrical signals are applied to an adjacent set of electrodes using a high-precision current generator (Keithly 6221). As the AC current is applied to the element, electric potential (voltage) is measured at all of the other electrodes using a standard laboratory data acquisition system (National Instruments). Standard shielded coaxial wires, roughly 1 m in length, are used to attach the data acquisition system to the copper electrodes. MATLAB is used to execute the tomographic reconstruction algorithms. The FEM model of each test specimen is meshed with 384 triangular elements.

Strain is also measured by three traditional methods for many of the loaded specimens. First, metal foil strain gauges (Texas Measurements) with nominal resistance of 120 Ω and a gauge factor of 2.1 are installed on the surface of the ECC specimens using epoxy. An additional approach to measuring strain is by optical methods using the OptoTrak Certus motion capture system. The system consists of a 3020 OptoTrak camera position sensor (111 × 31.5 × 21.5 cm), markers, and a system control unit. The markers are reflective nodes (approximate diameter 1 cm) that are attached to the specimen surface using standard glue. 2D motion of the markers is accurately measured by the 3020 OptoTrak camera position sensor with a resolution of 50.01 mm. To achieve this resolution, the camera position sensor is placed 2 m from the instrumented test specimen. The last approach is to calculate strain using the actuator displacement as measured by the load frame's linear variable differential transformer (LVDT).

7.1.11 Monotonic tensile loading

Four rectangular ECC plate specimens are prepared for monotonic tensile loading. First, 32 copper electrodes are attached to the sides of the plate as shown in Figure 7.6(a). On the long sides of the specimen, 12 electrodes are attached to each side; the shorter sides each have four electrodes attached. The electrodes are installed to be equidistant from one another. The specimens are labeled as specimen MT1 through MT4. Twelve OptoTrak markers are glued to the front surface of specimen MT1; the markers are oriented in two vertical rows and separated by 3 cm from one another. The marker orientation divides the plate specimen into five regions labeled as regions 1 through 5. Along the vertical center line of the specimen, five metal foil strain gauges are attached; the gauges are separated such that each region has its own strain gauge. Strain gauges and OptoTrak markers are not installed on specimens MT2 through MT4.

Specimen MT1 is gripped by an MTS load frame and monotonically loaded in tension. Prior to the application of axial load, the copper electrodes are used to perform EIT sensing of the specimen. These data will be used to derive a baseline conductivity map of the unloaded plate specimen. The load frame is commanded to apply tension load to the plate with the actuator displacement controlled. Applied force and actuator displacement are recorded from which stress and strain of the specimen can be calculated. The actuator is paused at 0.05, 0.1, 0.2, 0.3, 0.4, 0.5, 0.75, 1, 1.25, and 1.5%

strain. When paused, EIT sensing is conducted to collect electrical data for reconstruction of conductivity maps of the instrumented specimen. In addition, strain and displacement of the OptoTrak markers are measured. After 1.5% strain has been achieved, the test is terminated.

Specimens MT2 through MT4 are loaded into the MTS load frame for monotonic tensile loading. Again, before axial load is applied to the specimens, EIT sensing is conducted to obtain baseline tomographic data. Next, each specimen is loaded with the actuator operated in displacement control mode to strain levels of 0.5, 1, and 2.4% strain. At each strain level, the load is paused and EIT sensing conducted. After 2.4% strain, each specimen is loaded until failure. At the point of failure, EIT sensing is again performed.

7.1.12 Cyclic axial loading

Again, 32 copper electrodes are attached to the boundary of plate specimen CT1 in the same configuration as specimens MT1 through MT4 (Figure 7.6(a)). Before the specimen is gripped in the MTS load frame, EIT sensing is performed to derive a baseline conductivity map of the unloaded specimen. The specimen is then gripped in the MTS load frame, and two tension−compression cycles are applied. The specimen is cyclically loaded with the following peak strains: first, 0.32% strain in tension; second, 0.5% strain in compression; third, 1.2% strain in tension; fourth, 1% strain in compression; and then, finally, 2% strain in tension. After 2% tensile strain is achieved, the specimen is monotonically loaded until failure. Along the two cycles of loading, the application and relaxation of axial load are paused and EIT conductivity maps are calculated.

7.1.13 Monotonic three-point bending

The ECC beam is instrumented with 32 copper electrodes mounted to the bottom face of the beam. A section roughly 38.1 cm long and 7.6 cm wide is delineated in the center of the beam by the electrodes (Figure 7.7). Twelve electrodes are attached along each of the long sides of this region, and four electrodes are attached on each of the
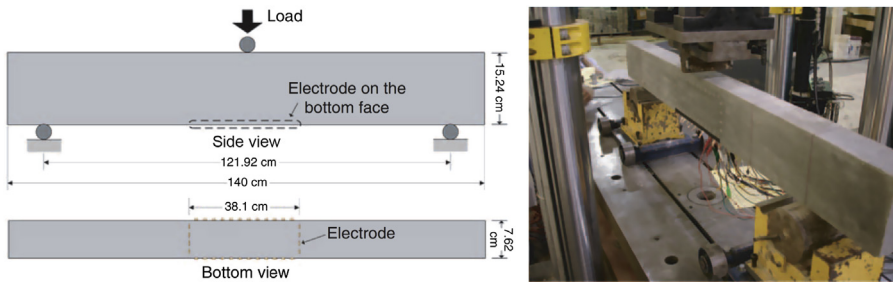

Figure 7.7 Unreinforced ECC beam loaded in 3-point bending with conductivity measured on the bottom beam face.

shorter sides. The beam is placed upon the bed of an Instron general purpose load frame; roller supports spaced 121.9 cm apart support the beam at two ends, and an actuator applies load at the center of the beam's top face. An EIT conductivity map is acquired prior to the application of load. Once load is applied, the test is paused at displacements of 0.2 and 0.6 cm so that EIT conductivity maps of the beam's lower face can be acquired. After a displacement of 0.6 cm is achieved, the beam is loaded till failure.

7.2 Results and discussion

7.2.1 Specimen MT1

Specimen MT1 is monotonically loaded in tension in order to estimate the sensitivity of the piezoresistive effect of ECC materials. The stress−strain curve of the monotonically loaded plate is presented in Figure 7.8(a). The plate initiates strain hardening at 0.2% strain (as calculated from the load frame displacement). The application of tension is paused three times while the plate is elastic (denoted as P1, P2, and P3). After strain hardening, the test is again paused as denoted by points P4 through P10. Each time the test is paused, an EIT conductivity map of the plate is obtained. The conductivity of the specimen is averaged across each of the specimen's five regions (as delineated in Figure 7.6(a)) and compared to the average conductivity prior to the application of load (effectively at P0). The percentage change in average conductivity versus the average strain (as calculated from the load frame displacement) is plotted in Figure 7.8(b) for each specimen region. As can be seen in the plot, each region exhibits a nearly linear change in conductivity as a function of strain.

The strain calculated using the load frame displacement represents an average strain for the entire specimen. In contrast, the OptoTrak sensor system can measure strain in localized regions of the specimen. Similarly, the EIT conductivity maps provide a measurement of the ECC conductivity over the complete instrumentation area. As a result, for each of the regions defined by the location of the OptoTrak markers (regions 1 through 5), the localized strains measured by the OptoTrak camera are compared to the average resistivity of the region. To calculate the average resistivity, the conductivities of the triangular elements of the EIT conductivity map are averaged and inverted to yield the average resistivity. For each region of specimen MT1, the averaged resistivity is plotted versus the local strain as measured by the OptoTrak system in Figure 7.9. The piezoresistive effect is evident with resistivity increasing in tandem with strain. Furthermore, the resistivity changes are fairly linear with gauge factors of 15.0, 14.3, 15.6, 15.4, and 15.4 for regions 1 through 5, respectively.

7.2.2 Specimens MT2, MT3, and MT4

Specimens MT2, MT3, and MT4 are loaded monotonically in uniaxial tension until failure (damage localization). During loading, stress−strain responses are recorded as shown in Figures 7.10(a), 7.11(a), and 7.12(a), respectively. All three specimens
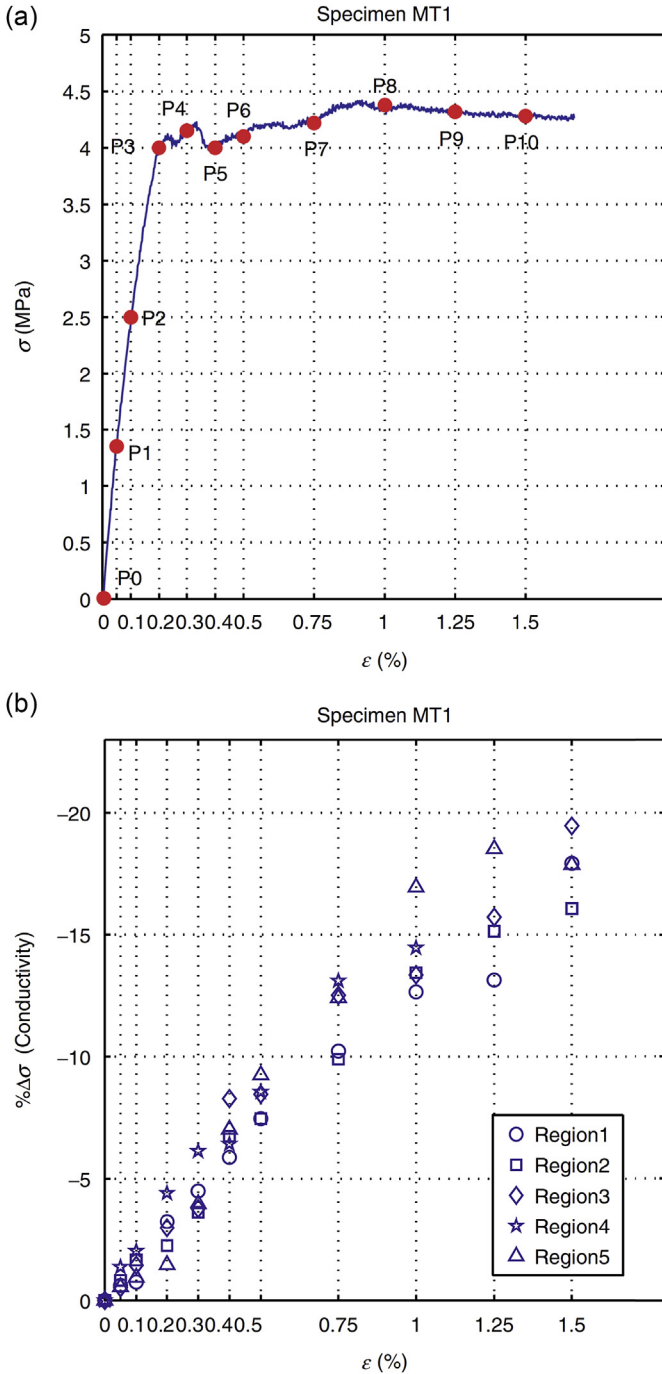
Figure 7.8 Monotonic tensile loading of specimen MT1: (a) stress–strain response; (b) percentage change of conductivity as a function of the average specimen strain.
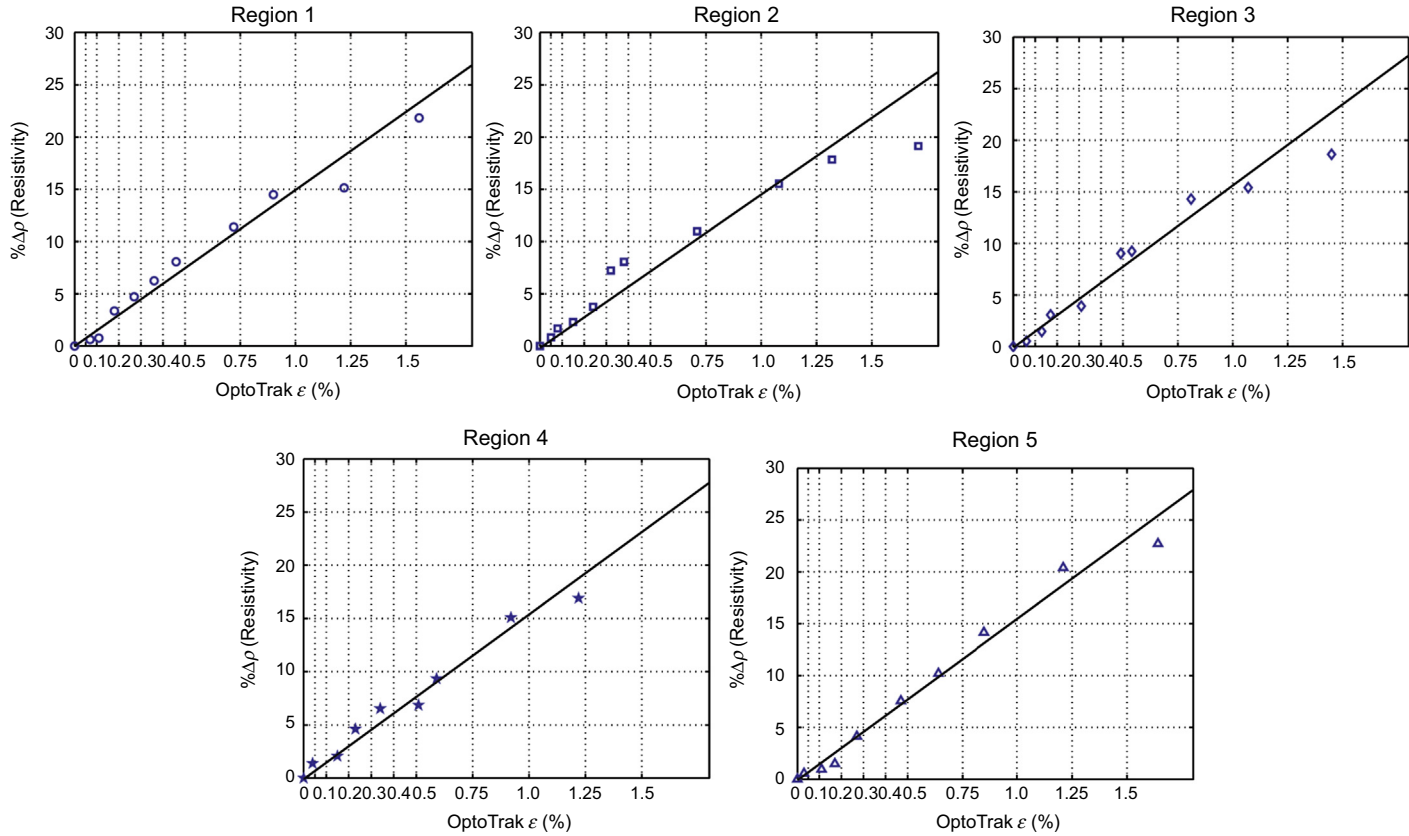
Figure 7.9 Change in average resistivity of region 1 through 5 versus strain as measured by the OptoTrak optical sensors installed in that region.
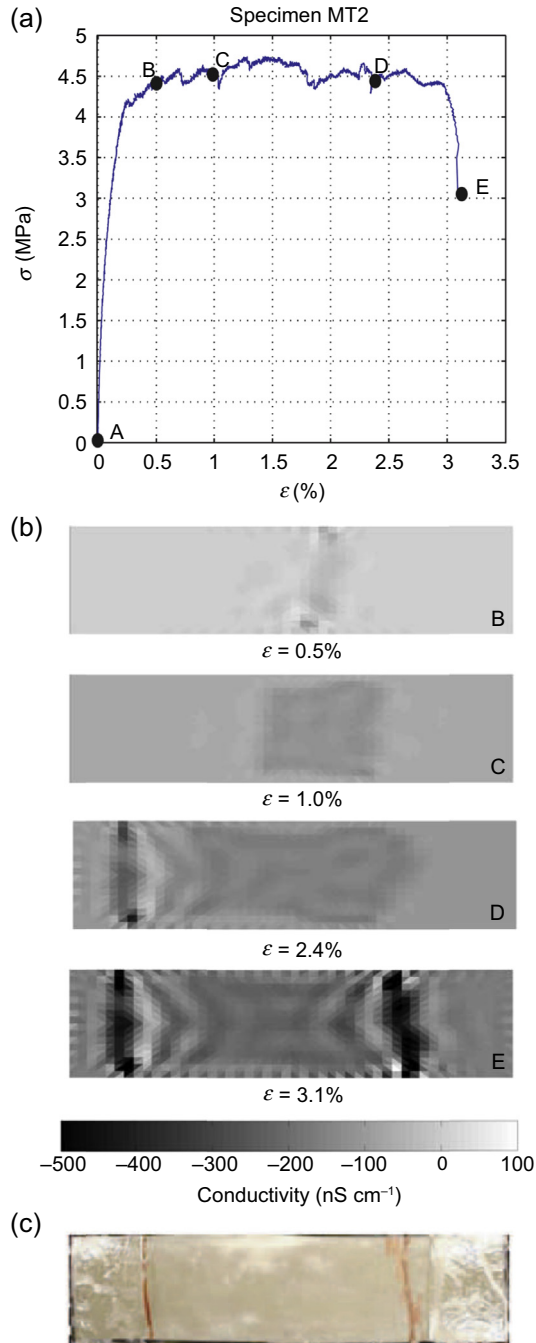
Figure 7.10 Monotonic tensile loading of specimen MT2: (a) stress–strain response; (b) change in conductivity from the baseline for four levels of strain; (c) final specimen with cracks highlighted.
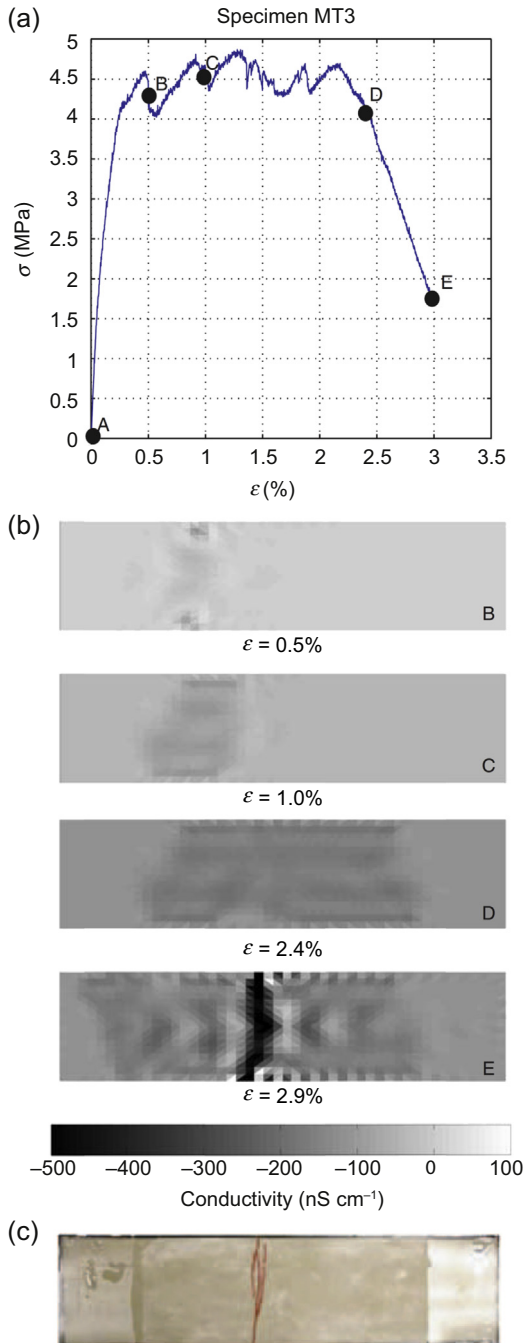
(a)

(b)

$\varepsilon = 0.5\%$

$\varepsilon = 1.0\%$

$\varepsilon = 2.4\%$

$\varepsilon = 2.9\%$

Conductivity (nS cm^{-1})

(c)

Figure 7.11 Monotonic tensile loading of specimen MT3: (a) stress−strain response; (b) change in conductivity from the baseline for four levels of strain; (c) final specimen with crack highlighted.
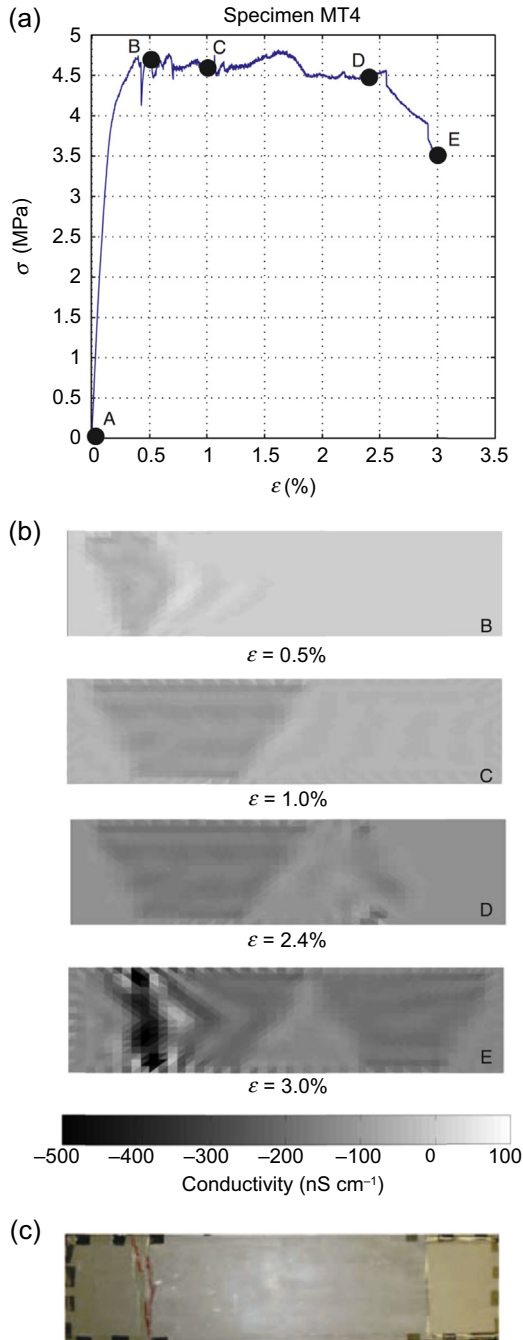
Figure 7.12 Monotonic tensile loading of specimen MT4: (a) stress–strain response; (b) change in conductivity from the baseline for four levels of strain; (c) final specimen with crack highlighted.

undergo strain hardening after reaching 0.25% strain. The ultra-ductility of the ECC material is evident by the ultimate strain levels reached by each of the three plates; specimens MT2, MT3, and MT4 all fail at strains in excess of 2.5%.

When the specimens achieve 0.5% strain, the application of load is paused and an EIT conductivity map is acquired. To observe a change in conductivity, the conductivity map acquired at point A (i.e., unloaded) will be subtracted from those acquired during loading. As can be seen in Figures 7.10(b), 7.11(b), and 7.12(b), the maps of the change in conductivity of the specimens at point B reveal reductions in conductivity consistent with strain (i.e., the piezoresistive effect). Furthermore, regions of microcracking that occur during strain hardening are evident in the conductivity maps. For example, in specimen MT2, a thin band of concentrated conductivity change in the center of the element reveals the strain-hardening microcracking. Specimens MT3 and MT4 also have regions of microcracking that are evident toward the left side of their EIT conductivity maps.

Monotonic tensile loading of the specimens continues until 1% strain is achieved. At point C, the average conductivity for each specimen reduces consistently with strain. However, regions of microcracking where conductivity reductions are greater have grown significantly. For example, for specimen MT4, the thin region of microcracking at 0.5% strain has grown to occupy nearly half of the specimen. Similarly, in specimen MT2, the region of microcracking is in the center of the specimen and occupies nearly a quarter of the specimen length.

The tests are continued until damage localizes into large cracks (i.e., failure). The large cracks can be seen in the EIT conductivity maps as major reductions in conductivity, some as large as 500 nS cm. For example, in Figure 7.10(b), two large cracks can be seen in the EIT conductivity map at the two ends of the specimen. The cracks imaged in the EIT maps precisely capture the location and geometric orientation of the true damage state of the specimen as pictured in Figure 7.10(c). The locations of the cracks in the actual test specimen are highlighted using a red felt tip marker to enhance the comparison. For specimen MT3, the macrocrack forms in the center of the specimen as can be seen in the final EIT conductivity map (Figure 7.11(b)) and the picture of the final specimen (Figure 7.11(c)). Again, in specimen MT4, the ECC plate develops a large crack toward the left side of the specimen (Figure 7.12(c)). This crack is successfully captured by the EIT conductivity map at 3.0% strain (Figure 7.12(b)).

7.2.3   Specimen CT1

Plate specimen CT1 is loaded cyclically in axial tension and compression. Again, the distribution of change in specimen conductivity (i.e., conductivity minus the baseline conductivity) is mapped at multiple points along the cyclic loading profile. As can be observed in Figure 7.13(a), the specimen is first loaded in tension until it reaches a tensile strain of 0.32% (point B). At this strain level, a narrow band of microcracking can be observed toward the left side of the specimen as shown in the EIT conductivity maps of Figure 7.13(b). As the specimen is unloaded back to 0% strain (point C), the change in conductivity in the region of microcracking recovers, suggesting the closure of the cracks. The plate is then loaded in compression to 0.5% strain (point D). When
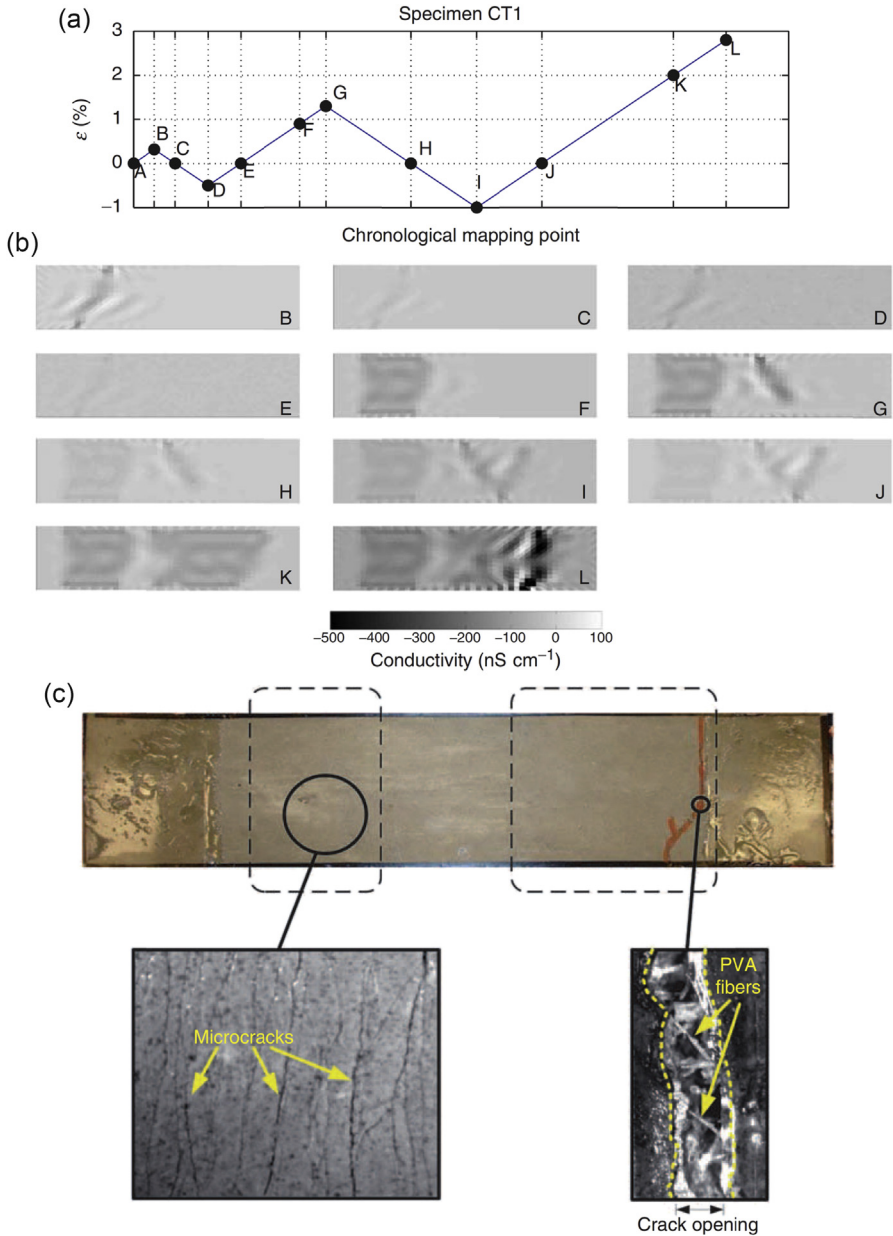
Figure 7.13 Cyclic axial loading of specimen CT1: (a) chronological application of tensile and compressive strain; (b) mapping of conductivity changes at points B through L; (c) picture of failed specimen (point L) with close-up views of cracking fields and fibers bridging a macro-scale crack.

loaded in compression, the narrow crack field once again becomes evident, although the conductivity reduction is less pronounced than when the element is loaded in tension. Even though the cracks introduced in tension have closed, because they do not close perfectly, some reduction in conductivity is expected. When the specimen is reloaded in tension to 1% strain (point F), the microcracks from point B reopen and additional microcracks form, yielding a larger field of microcracking at the left side of the specimen. As the ECC specimen is further loaded in tension to 1.3% strain (point G), a second field of microcracks emerges near the center of the specimen. Thereafter, the specimen is loaded to 1% strain in compression (point I). Again, the microcracks present in the specimen can still be observed in the EIT conductivity maps even though they have closed. This is likely due to their inexact closure and the occurrence of some crushing at the crack surface. After achieving a peak compressive strain of 1%, the specimen is loaded in tension until failure, which occurs at 2.8% strain (point L). When loaded in tension, the microcracking field in the center of the specimen continues to grow until a large millimeter-wide crack is introduced on the right side of the specimen at 2.8% tensile strain. The location and geometry of the crack are evident in the EIT conductivity map. The EIT conductivity map compares well with a photo of the failed specimen (Figure 7.13(c)).

At each point of cyclic loading, the percentage of change in conductivity is averaged over the entire specimen. This percentage change in conductivity is superimposed over the chronological plot of applied strain, as shown in Figure 7.14. The percentage change in conductivity varies in linear proportion with strain when loaded in tension. If the gauge factor of the specimen is calculated at the points of peak tension (points B, G, L), the gauge factor is found to be 8.5, 13.1, and 15.4, respectively. The increase in gauge factor is due to the accumulation of microcracking in the specimen. When the specimen is unloaded between successive tension−compression peaks, the
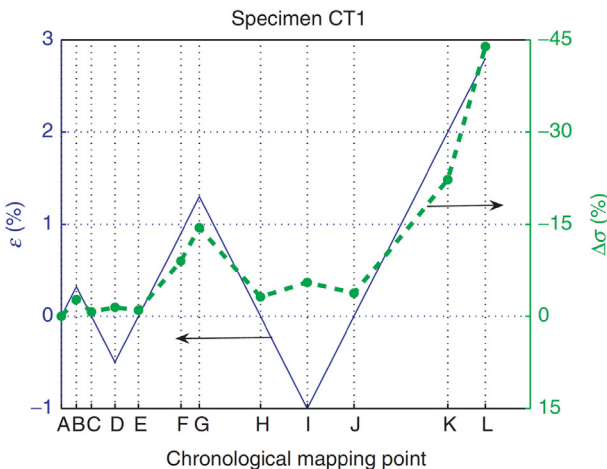

Figure 7.14 Average conductivity change for each load point superimposed with the applied strain pattern.

accumulation of microcracking prevents the specimen from fully recovering its initial conductivity. As can be seen, in Figure 7.14, the residual change in conductivity at points C, E, H, and J is 0.7, 1.0, 3.1, and 3.7%, respectively. When the element is placed in compression, the specimen conductivity still reduces but at a much smaller rate in compression than when in tension. The effective gauge factor for the element is calculated at points D and I as -3.0 and -5.2, respectively.

7.2.4 Beam specimen

In the last set of experiments, the ECC beam specimen is loaded in three-point bending while EIT conductivity maps of the lower face of the beam are taken at four points along the monotonically applied force–displacement curve (denoted as points A, B, C, and D in Figure 7.15(a)). The absolute EIT conductivity maps are presented in Figure 7.15(c). The formation of cracking initiates at point B with a field of microcracking observable in the center of the EIT conductivity map. The field of microcracking appears to resemble a "V" shape with one side of the beam experiencing more microcracking than the other. As the load is applied, the beam begins to soften
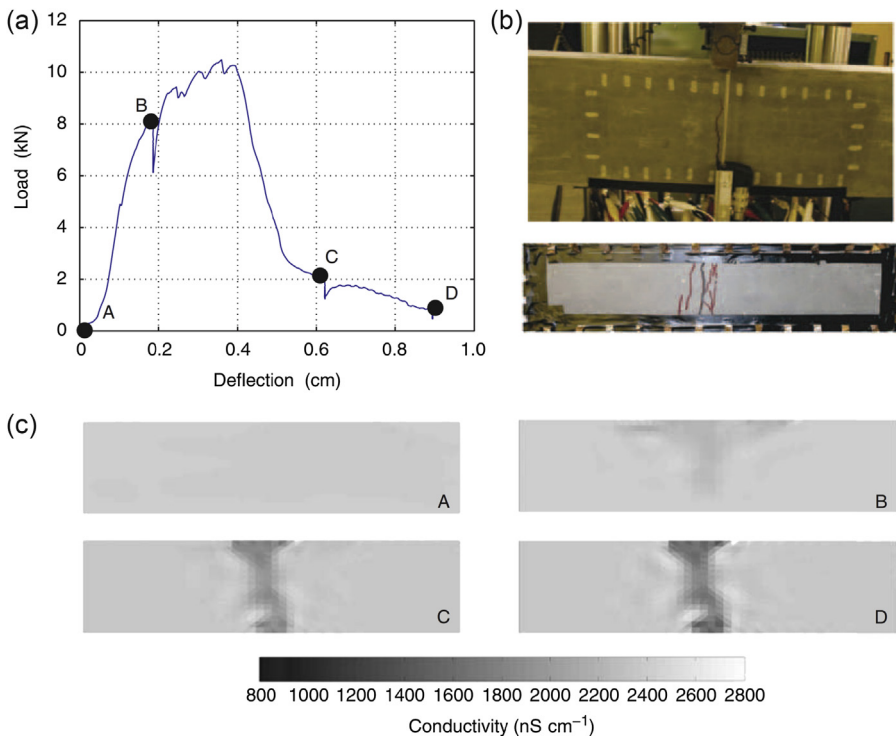

Figure 7.15 Beam specimen one under 3-point bending: (a) load-deflection curves; (b) side and bottom face damage with cracks highlighted; (c) absolute conductivity maps at points A through D.

at a deflection of 0.4 cm; softening is due to the formation of a macrocrack. At point C, the EIT conductivity map reveals the crack at the center of the beam; the crack width is measured using a crack gauge and is 3 mm wide. The crack is further widened by displacing the beam to 0.9 cm (point D). At this point, the change in absolute conductivity is significantly greater (a reduction of 1600 nS cm). With the load still applied, the crack opening is 5 mm. Pictures of the final cracked specimen are presented in Figure 7.15(b).

7.3 Conclusions

The lasting contribution of this work is the introduction of EIT as a powerful new NDE tool for health monitoring of cementitious structures. EIT offers true multidimensional sensing that can be automated for unattended long-term operation in actual concrete structures. In this study, EIT sensing is validated upon ECC specimens loaded in axial tension, axial compression, and bending. EIT conductivity maps reveal the piezoresistive nature of ECC structural elements loaded in tension. The tensile gauge factor of ECC, as determined by EIT conductivity mapping, is shown to be between 13 and 15. Although the piezoresistivity of cementitious materials has been proposed for self-sensing strain, we are of the opinion that this approach would be challenging to practically apply in actual field structures. As witnessed in this work, microcracking in the cementitious specimen alters the gauge factor; gauge factors are shown to increase with the accumulation of cracking. Other challenges also exist, including the sensitivity of the material's electrical properties with environmental influences like temperature and humidity.

The more likely use of EIT sensing is for damage characterization of cement-based structures. As one of the few truly distributed sensing approaches, EIT has the ability to accurately locate cracks as well as quantify their geometric features. As this work has shown, the geometric propagation of dense fields of microcracks, strain hardening, and crack localization in FRCC elements were all easily captured by the EIT conductivity maps. This work largely restricted its application to 2D surfaces of the ECC specimens. However, the EIT formulation is general and can be applied to 3D. For example, electrodes mounted to the outer surface of structural elements would be capable of imaging the element's internal structure. This could be powerful for identifying cracks below the surface that are impossible to detect during visual inspection.

Although this work lays a firm foundation for EIT sensing in civil structures, additional work is needed to further develop this novel technique. This study only considered the use of ECC materials for EIT sensing; other cementitious materials including concrete must be explored. The inclusion of conductive fibers in a cement matrix opens new and exciting avenues of exploration because fiber interfaces and volume fractions can be varied to adjust the nominal conductivity and piezoresistive gauge factor of the material. An additional advantage of conductive fibers is that conductive fiber FRCC materials experience an increase in conductivity when loaded in compression (Chung, 2003). This is in contrast to the polymeric fibers employed in

this study; polymeric fibers are nonconducting, resulting in decreases in conductivity when specimens are loaded in compression. Another challenge envisioned for EIT sensing is the inclusion of steel reinforcement in structural specimens. The presence of reinforcement steel in the structure could alter the EIT map. However, the location of reinforcement is generally known a priori and can therefore be included at the outset of the EIT inverse solution. This would preserve the accuracy of the EIT approach when mapping the conductivity of just the cementitious material.

Acknowledgments

References

ACI, 1998. Causes, Evaluation and Repair of Cracks in Concrete Structures. Report Number ACI224.1R-93. American Concrete Institute, Farmington Hills, MI.

Balaguru, P.N., Shah, S.P., 1992. Fiber-reinforced Cement Composites. McGraw-Hill, New York, NY.

Barber, D.C., 1989. A review of image reconstruction techniques for electrical impedance tomography. Medical Physics 16, 162−169.

Barsoukov, E., Macdonald, J.R., 2005. In: Impedance Spectroscopy Theory, Experiment, and Applications. Wiley, Hoboken, NJ.

Bungey, J.H., Millard, S.G., Grantham, M.G., 2006. Testing of Concrete in Structures. Taylor and Francis, London, UK.

Calleja, J., 1953. Determination of setting and hardening time of high-alumina cements by electrical resistance techniques. Journal of the American Concrete Institute 25, 249−256.

Carino, N.J., 2004. Stress wave propagation methods. In: Malhotra, V.M., Carino, N.J. (Eds.), Handbook on Nondestructive Testing of Concrete. CRC Press, Boca Raton, FL.

Chapra, S.C., Canale, R.P., 2009. Numerical Methods for Engineers (6e). McGraw-Hill, New York, NY.

Chung, D.D.L., 2001. Cement-based electronics. Journal of Electroceramics 6, 75−88.

Chung, D.D.L., 2003. Multifunctional Cement-Based Materials. Marcel-Dekker, New York, NY.

Doebling, S.W., Farrar, C.R., Prime, M.B., 1998. A summary review of vibration-based damage identification methods. Shock and Vibration Digest 30, 91−105.

Gowers, K.R., Millard, S.G., 1999. Measurement of concrete resistivity for assessment of corrosion severity of steel using Wenner technique. ACI Materials Journal 96, 536−541.

Hammond, E., Robson, T.D., 1955. Comparison of electrical properties of various cements and concretes. The Engineer 199, 114−115.

Han, N., van Beek, A., Koenders, E.A.B., 2005. Electrical methods. In: Reinhardt, H.W., Grosse, C.U. (Eds.), Advanced Testing of Cement Based Materials During Setting and Hardening − Final Report of RILEM TC 185-ATC. RILEM, Bagneux, France. Technical Report 31.

Hansson, I.L.H., Hansson, C.M., 1983. Electrical resistivity measurement of Portland cement based materials. Cement and Concrete Research 13, 675−683.

Heikkinen, L.M., Vilhunen, T., West, R.M., Vauhkonen, M., 2002. Simultaneous reconstruction of electrode contact impedances and internal electrical properties: II. Laboratory experiments. Measurement Science and Technology 13, 1855−1861.

Hou, T.C., Lynch, J.P., 2005a. Conductivity-based strain monitoring and damage characterization of fiber reinforced cementitious structural components. In: Proceedings of the SPIE − The International Society for Optical Engineering, vol. 5765, pp. 419−429.

Hou, T.C., Lynch, J.P., 2005b. Monitoring strain in engineered cementitious composites using wireless sensors. In: Proceedings of the 11th International Conference on Fracture, Turin, Italy.

Jung, Y.C., Na, W.B., Kundu, T., Ehsani, M., 2000. Damage detection in concrete using Lamb waves. In: Proceedings of SPIE − The International Society for Optical Engineering, vol. 3995, pp. 448−458.

Kim, Y.Y., Fischer, G., Li, V.C., 2004. Performance of bridge deck link slabs designed with ductile engineered cementitious composite. ACI Structural Journal 101, 792−801.

Kratzig, W.B., Meyer, I.F., Meskouris, K., 1989. Damage evolution in reinforced concrete members under cyclic loading. In: Proceedings of the 5th International Conference on Structural Safety and Reliability, San Francisco, CA, pp. 795−802.

Kunieda, M., Rokugo, K., 2006. Recent progress on HPFRCC in Japan required performance and applications. Journal of Advanced Concrete Technology 4, 19−33.

Lauer, K.R., 2004. Magnetic/Electrical methods. In: Malhotra, V.M., Carino, N.J. (Eds.), Handbook on Nondestructive Testing of Concrete. CRC Press, Boca Raton, FL.

Li, M., 2009. Durability of Concrete Repair through Ductility and Crack Width Control in ECC (PhD thesis). The University of Michigan.

Li, M., Li, V.C., 2011. High-early-strength ECC for rapid durable repair: material properties. ACI Materials Journal 108, 3−12.

Li, V.C., Wu, C., Wang, S., Ogawa, A., Saito, T., 2002. Interface tailoring for strain hardening PVA-ECC. ACI Materials Journal 99, 463−472.

Li, V.C., 2012. Tailoring ECC for specific attributes: a review. International Journal of Concrete Structures and Materials 6, 135−144.

Li, H., Xiao, H.G., Ou, J.P., 2006. Effect of compressive strain on electrical resistivity of carbon black-filled cement-based composites. Cement and Concrete Composites 28, 824−828.

Lionheart, W., Polydorides, N., Borsic, A., 2005. The reconstruction problem. In: Holder, D.S. (Ed.), Electrical Impedance Tomography: Methods, History, and Applications. IoP, London, UK.

Luangvilai, K., Punurai, W., Jacobs, L.J., 2002. Guided wave technique to characterize repaired Concrete. In: AIP Conference Proceedings, pp. 1220−1226.

Mayer, J.W., Lau, S.S., 1990. Electronic Materials Science: For Integrated Circuits in Si and GaAs. Macmillan, New York, NY.

McCarter, W.J., Brousseau, R., 1990. The A.C. responses of hardened cement paste. Cement and Concrete Research 20, 891−900.

Millard, S.G., 1991. Reinforced Concrete resistivity measurement techniques. In: Proceedings of the Institution of Civil Engineers, Part 2: Research and Theory, vol. 91, pp. 71−88.

Mindess, S., 2004. Acoustic emission methods. In: Malhotra, V.M., Carino, N.J. (Eds.), Handbook on Nondestructive Testing of Concrete. CRC Press, Boca Raton, FL.

Na, W.B., Kundu, T., Ehsani, M.R., 2002. Ultrasonic guided waves for steel bar concrete interface testing. Materials Evaluation 60, 437−444.

Naaman, A.E., Chandrangsu, K., 2004. Innovative bridge deck system using high-performance fiber-reinforced cement composites. ACI Structural Journal 101, 57−64.

Ouyang, C., Landis, E., Shah, S.P., 1991. Damage assessment in concrete using quantitative acoustic emission. Journal of Engineering Mechanics 117, 2681−2698.

Park, S., Ahmad, S., Yun, C.B., Roh, Y., 2006. Multiple crack detection of concrete structures using impedance-based structural health monitoring techniques. Experimental Mechanics 46, 609−618.

Park, Y.J., Ang, A.H.S., 1985. Mechanistic seismic damage model for reinforced concrete. Journal of Structural Engineering 111, 722−739.

Park, G., Cudney, H.H., Inman, D.J., 2000. Impedance-based health monitoring of civil structural components. Journal of Infrastructure Systems 6, 153−160.

Parra-Montesinos, G.J., 2005. High-performance fiber-reinforced cement composites: an alternative for seismic design of structures. ACI Structural Journal 102, 669−675.

Peled, A., Torrent, J.M., Mason, T.O., Shah, S.P., Garboczi, E.J., 2001. Electrical impedance spectra to monitor damage during tensile loading of cement composites. ACI Material Journal 98, 313−322.

Raghavan, A., Cesnik, C.E.S., 2007. Review of guided-wave structural health monitoring. Shock and Vibration Digest 39, 91−114.

Reza, F., Yamamuro, J.A., Batson, G.B., Lee, J.S., 2003. Smart behavior of carbon fiber cement composites in compact tension. In: Proceedings of the 16th ASCE Engineering Mechanics Conference, Seattle, WA.

Rose, J.L., Ditri, J.J., 1990. Ultrasonic computed tomography considerations in the NDE of solid materials. In: IEEE 1990 Ultrasonics Symposium Proceedings, pp. 991−995.

Shah, S.P., Choi, S., 1999. Nondestructive techniques for studying fracture processes in concrete. International Journal of Fracture 98, 351−359.

Stang, H., Pedersen, C., 1996. HPFRCC − extruded pipes. In: Proceedings of the 4th Materials Engineering Conference, Washington, DC, pp. 261−270.

Vauhkonen, M., 1997. Electrical Impedance Tomography and Prior Information (PhD thesis). Kuopio University, Kuopio, Finland.

Vilhunen, T., Kaipiom, J.P., Vauhkonen, P.J., Savolainen, T., Vauhkonen, M., 2002. Simultaneous reconstruction of electrode contact impedances and internal electrical properties: I. Theory. Measurement Science and Technology 13, 1848−1854.

Wang, S., 2005. Micromechanics Based ECC Matrix Design (PhD thesis). The University of Michigan.

Wang, S., Li, V.C., 2003. Material design of lightweight PVA-ECC. In: Naaman, A.E., Reinhardt, H.W. (Eds.), Proceedings of HPFRCC, pp. 379−390 (Ann Arbor).

Webster, J.G., 1990. Electrical Impedance Tomography. Hilger, Bristol, England.

Whiting, D.A., Nagi, M.A., 2003. Electrical Resistivity of Concrete − A Literature Review, PCA R&D Serial No. 2457. Portland Cement Association, Skokie, IL.

Wight, J., Parra-Montesinos, G., Canbolat, A., 2006. HPFRCC coupling beams for earthquake-resistant wall structures. In: Proceedings of the IABSE Symposium on Structures and Extreme Events, Lisbon, Portugal, pp. 114−115.

Yang, E.H., 2007. Designing Functionalities into ECC Materials via Micromechanics (PhD thesis). The University of Michigan.

Yang, E.H., Yang, Y., Li, V.C., 2007. Use of high volumes of fly ash to improve ECC mechanical properties and material greenness. ACI Materials Journal 104, 303−311.

Zhdanov, M.S., Keller, G.V., 1994. Geoelectrical Methods in Geophysical Exploration. Elsevier, Amsterdam.

Nano carbon material−filled cementitious composites: fabrication, properties, and application

8

Baoguo Han[1]*, Shengwei Sun*[2]*, Siqi Ding*[1]*, Liqing Zhang*[1]*,
Sufen Dong*[1,3]*, Xun Yu*[4]

[1]School of Civil Engineering, Dalian University of Technology, Dalian, China; [2]School of Civil
Engineering, Harbin Institute of Technology, Harbin, China; [3]School of Architecture and
Civil Engineering, Inner Mongolia University of Science and Technology, Baotou, China;
[4]Department of Mechanical Engineering, New York Institute of Technology, New York, USA

8.1   Introduction

Both nano-materials and carbon materials are attracting more and more attention in the field of materials science and technology. Carbon materials with nanoscale structures, also called nano carbon materials or nano-carbon materials (NCMs), not only show better properties than conventional or microscale carbon materials but also exhibit novel characteristics that conventional carbon materials do not have. They provide a new approach to develop composites with high-performance and multifunctional properties.

Cementitious materials are the second most used resource in the world after water. They have a direct and visible impact on the world's resources, energy consumption, and carbon dioxide emissions. The development of high-performance and multifunctional cementitious materials is a sustainable direction. The potential benefits of this technology include improved infrastructure reliability and longevity, enhanced structural performance and durability, improved safety against natural hazards and vibrations, and a reduction in life-cycle costs in operating and managing civil infrastructures.

Owing to their remarkable mechanical, chemical, electrical, and thermal properties; excellent nanoscale effects; low density; and excellent chemical and thermal stability, NCMs offer the possibility to develop a new generation of tailored, high-performance, and multifunctional cementitious composites. Extensive research endeavors demonstrated the potential of various NCMs, including carbon nanofibers (CNFs), carbon nanotubes (CNTs), and nano graphite platelets (NGPs), for enhancing cementitious materials (Chen et al., 2011; Pacheco-Torgal and Jalali, 2011; Chyad, 1989; Sanchez and Sobolev, 2010; Chen and Poon, 2009; Raki et al., 2010; Sobolev and Gutiérrez, 2005; Mukhopadhyay, 2011; Parveen et al., 2013; Li et al., 2005; Gao et al., 2009; Huang, 2012; Han et al., 2011a, 2013a).

The aim of this chapter is to provide a systematic review of the major progress and advances in the fabrication, properties, and applications of NCM-filled cementitious composites. The improvement mechanism of the NCMs to cementitious materials is also discussed.

## 8.2	Introduction of NCMs

### 8.2.1	Introduction of CNTs

CNTs are carbon materials with a hollow cylindrical nanostructure. They are generally a few nanometers in diameter and several microns in length (as shown in Figure 8.1(a)). CNTs are categorized as single-walled CNTs (SWCNTs) and multi-walled CNTs (MWCNTs). In recent years, CNTs have been widely applied in a variety of fields due to their excellent physical properties, such as high strength and Young's modulus (the tensile strength and Young's modulus of CNTs are, respectively, 20 times and 10 times those of carbon fibers (CFs)), high bonding force with matrix (the interlaminar shear strength of CNT-reinforced epoxy materials is 10 times that of CF-reinforced epoxy materials), large deformation and high ductility (the elongation at break of CNTs is 18%, which is 18 times that of CFs), high aspect ratio
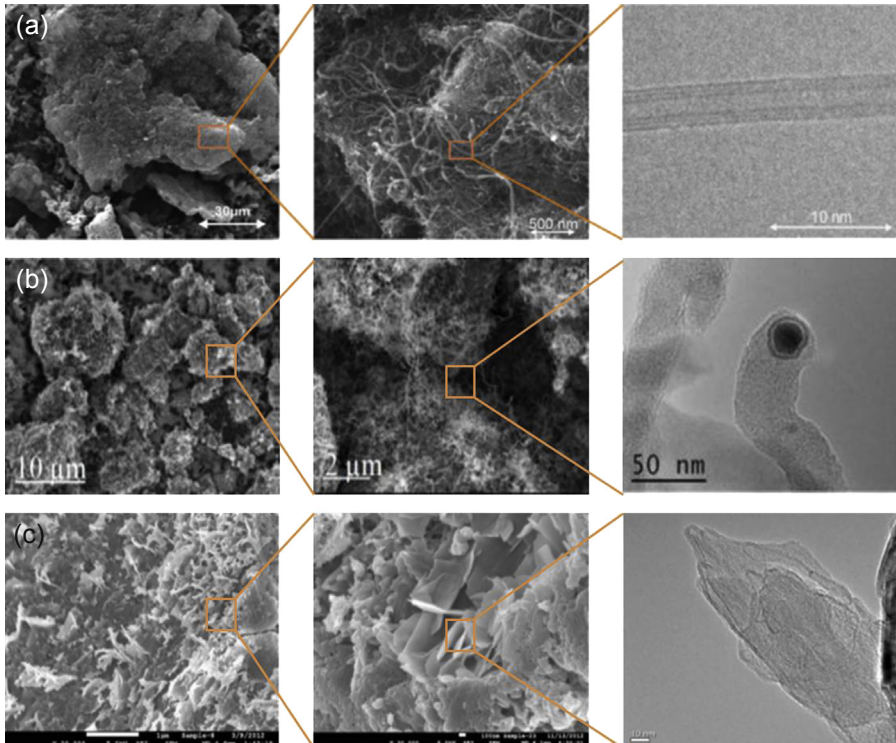

Figure 8.1 Photos of NCMs: (a) CNTs; (b) CNFs; and (c) NGPs.

(>500), and excellent electrical conductivity. The extremely high aspect ratio, hollow structure, and low density of CNTs make them ideal to form a conductive and mechanical reinforcement network inside a concrete matrix with a CNT concentration level as low as 0.05 wt%. CNTs also have interesting piezoresistive properties. When CNTs are subjected to stress or strain, their electrical properties will change with the level of stress or strain, expressing a linear and reversible piezoresistive response even for a large strain of 3.4%. In addition, the small diameter and high aspect ratio of CNTs are very favorable for motivating field emission conduction. Because CNTs are superior to CFs in many respects and can be used as reinforcements to transfer the reinforcement behavior from the macroscale to the nanoscale level, it is promising to develop high-performance and multifunctional cementitious materials without adding any additional weight and sacrificing other properties of cementitious materials.

8.2.2   Introduction of CNFs

Like CNTs, CNFs are also quasi-one-dimensional (1D) carbon materials, and their diameters are between those of CNTs and CFs (as shown in Figure 8.1 (b)). They can be categorized as hollow CNFs or solid CNFs according to their structural characteristics. Their diameters are generally in the range of 10 to 500 nm, and their lengths range from 0.5 to 200 μm. CNFs, having a higher degree of crystalline orientation, are preferred for electrical and thermal conductivity. They not only possess low density, high modulus, high strength, high conductivity, and thermal stability the same as the CFs fabricated with a chemical vapor deposition growth method, but also have advantages such as a small number of defects, large aspect ratio, large surface area, and compact structure (http://cnx.org/content/m22580/latest/?collection=col10700/latest).

8.2.3   Introduction of NGPs

NGPs are another type of carbon-based conductive nanoparticle that is produced from graphite (as shown in Figure 8.1 (c)). Graphene oxide (GO) is a single layer of NGPs that have been oxidized to intersperse the carbon layers with oxygen molecules. The structure of NGPs is 2D platelets consisting of a few to several graphene layers with an overall thickness in the nanometer scale and the particle diameter ranging from submicron size up to 100 μm (Huang, 2012; Geim and Novoselov, 2007; Nalla et al., 2010).

8.3   Dispersion of NCMs in cementitious composites

Because the strong van der Waals forces cause agglomeration of the nanoparticles, a major issue in fabricating high-quality NCM-filled cementitious composites is to homogeneously distribute NCMs in cementitious materials. Poor dispersion will lead to the formation of defects in the matrix and limit the nano-enhancement effect.

Research has been performed to improve the dispersion of NCMs in the cementitious composites. There are two common methods used to disperse NCMs. The first method is to mechanically separate the NCMs by ultrasonic ball milling or

high-shear mixing. The second method involves chemically altering the surface of the NCMs by the creation of either covalent or noncovalent bonds (Xie et al., 2005). Moreover, the mechanical method is often used in combination with the chemical method mentioned in this chapter (Parveen et al., 2013; Han et al., 2011c, Fu et al., 2001; Hamon et al., 2002; Wong et al., 1998; Bahr and Tour, 2002; Moore et al., 2003; Sanchez and Ince, 2009; Sanchez, 2009). The dispersion methods of NCMs in previous research are summarized in Tables 8.1, 8.2, and 8.3.

Recently, researchers have proposed novel approaches to solve the dispersion issue of CNTs. The primary approach is to adopt commonly used water-reducing admixtures (including plasticizers and superplasticizers) as surfactants. The National Research Council Canada (2009) has shown that a small amount of CNTs can be dispersed by ultrasonication in water containing 5% superplasticizer. Shah et al. (2009a) also achieved an effective dispersion of MWCNTs with different lengths and concentrations in cementitious materials by applying ultrasonic energy in combination with polycarboxylate-based superplasticizers. Yazdanbakhsh et al. (2012) performed a 3D simulation study, and stated that only when cement particles are also distributed homogeneously without any agglomeration, the degradation effect of cement particles on the homogeneous distribution of CNTs within cementitious materials is negligible (Yazdanbakhsh and Grasley, 2012). Meanwhile, Han et al. (2011c) pointed out that the effective dispersion of superplasticizers to CNTs and CNFs can contribute to their double-dispersion effect on CNTs, CNFs, and cement particles. Huang also employed a superplasticizer to obtain proper dispersion of NGPs in cementitious materials (Huang, 2012). Therefore, dispersing NCMs with water-reducing admixtures is an excellent method for fabricating NCM-filled cementitious composites.

In addition, Nasibulin et al., Cwirzen et al., Ludvig et al., and Dunens et al. proposed dispersing CNTs and CNFs in the cementitious composites by growing CNTs and CNFs directly on the surface of cement, fly ash (conventional admixtures for fabricating cementitious materials), or sand through in situ synthesis (as shown in Figure 8.2) (Han et al., 2011c, Nasibulin et al., 2013; Moisala et al., 2003; Nasibulin et al., 2007; Mudimela et al., 2009; Cwirzen et al., 2009a, Ludvig et al., 2011; Dunens et al., 2009).

8.4   Properties of NCM-filled cementitious composites

8.4.1   Properties of CNT-filled cementitious composites

8.4.1.1   Mechanical properties of CNT-filled cementitious composites

Since early investigations showed that CNTs have strong effects on the hydration process and hardness of cementitious composites, so far much research has been performed on the mechanical properties of CNT-filled cementitious composites. The different concentrations of CNTs show different effects on the mechanical properties of cementitious composites. The use of 0.05 wt% CNTs as the reinforcement for producing and forming non-autoclave concrete can increase its compressive strength by

Table 8.1 **Summary of dispersion methods of CNTs in cementitious materials**

| Researchers | Morphology of CNTs | Categories of dispersion methods | | Mechanical treatment |
| | | Chemical treatment | | |
		Covalent	Noncovalent	
Markar et al. (Markar et al., 2005)	MWCNTs (diameter: 10 nm, length: 10 μm)	—	Isopropanol	Ultrasonication (4 h) + mixing
Cwirzen et al. (Cwirzen et al., 2008)	MWCNTs	Polyacrylic acid polymers (2.1 wt% of water) and carboxylation	Arabic gum (AG) (2%)	Ultrasonication (2−15 min) + mixing
Shah et al. (Shah et al., 2011; Shah et al., 2009a; Konsta-Gdoutos et al., 2008)	SWCNTs (diameter < 2 nm, length < 20 μm)	—	—	Ultrasonication
Ibarra et al. (Saez De Ibarra et al., 2006)	Short MWCNTs (diameter: 9.5 nm, length: 1.5 μm); long MWCNTs (diameter < 8 nm, length: 10−30 μm)	—	AG (1.0 and 2.0 wt%)	Mixing
Tyson et al. (Tyson et al., 2011; Abu Al-Rub et al., 2011; Yazdanbakhsh et al., 2009; Abu Al-Rub et al., 2012)	MWCNTs (diameter: 10−30 nm, length: 0.5−500 μm)	—	Superplasticizer (1.25 wt%)	Ultrasonication (30 min) + mixing (7 min)
Li et al. (Li et al., 2005)	MWCNTs (diameter: 10−100 nm, length: 5−15 or 1−2 μm)	Sulfuric acid and nitric acid (3:1 by volume)	—	Mixing (15 min)

Table 8.1 **Continued**

Researchers	Morphology of CNTs	Categories of dispersion methods		
		Chemical treatment		Mechanical treatment
		Covalent	Noncovalent	
Collins et al. (Collins et al., 2012)	MWCNTs (diameter: 10−20 nm, length: 10−30 μm); SWCNTs (diameter: 1−2 nm, length: 5−30 μm)	—	Polycarbonate, lignosulfonate	Magnetic stirring + ultrasonication (12 min)
Azhari (Azhari, 2008; Azhari and Banthia, 2012)	MWCNTs (diameter: 15−20 nm, length: 0.1−10 μm)	—	Methylcellulose (0.4 wt%); superplasticizer	Ultrasonication (1 h) + mixing; high-speed hand mixer
Keriene et al. (Kerienė et al., 2013)	MWCNTs (diameter: 20−40 nm, length: 10−30 μm)	—	Carboxymethylcellulose	Ultrasonication (3 min)
Konsta-Gdoutos et al. (Konsta-Gdoutos et al., 2010a,b; Metaxa et al., 2009, 2012)	—	—	—	Ultrasonication + mixing; ultracentrifugation
Chaipanich et al. (Chaipanich et al., 2010)	MWCNTs	—	—	Ultrasonication (10 min) + mixing
Yu et al. (Yu et al., 2007)	MWCNTs (diameter: 10−30 nm, length: 10−30 μm)	—	Sodium dodecyl sulfate (SDS)	Ultrasonication
Mendoza et al. (Mendoza et al., 2013)	MWCNTs	—	Superplasticizer	Ultrasonication
Singh et al. (Singh et al., 2013)	MWCNTs (diameter: 8−25 nm, length: 120 nm)	—	—	Ball milling (6 h)

Bharj et al. (Bharj et al., 2014)	MWCNTs (diameter: 10−30 nm, length: 1−2 μm)	—	—	Stirring (15 min) + ultrasonication (90 min) + mixing (3 min)
Hunashyal et al. (Hunashyal et al., 2011a)	MWCNTs	—	Ethanol	Ultrasonication (90 min)
Yu et al. (Yu and Kwon, 2009)	MWCNTs (diameter: 10−80 nm, length: 0.1−1000 μm)	Mixed solution of H_2SO_4 and HNO_3	SDS (0.2 wt%)	Ultrasonication (1 h) + mixing
Musso et al. (Musso et al., 2009)	MWCNTs (diameter < 8 nm, length: 10−30 μm, −COOH content 3.86 wt%)	—	Acetone	Ultrasonication (4 h) + mixing
Han et al. (Han et al., 2009)	MWCNTs (diameter: 20−40 nm, length: 5−15 μm)	Carboxylation	Sodium dodecylbenzene sulfonate (SDBS) (1.4×10^{-2} mol/L)	Magnetically stirring (3 min) + ultrasonication (2 h) + mixing (3 min)
Luo et al. (Luo, 2009; Luo et al., 2009)	CNTs (diameter: 12−40 nm, length: 10 μm)	—	SDBS (0.15−0.2 g/mL), Triton X-100 (0.15 g/mL)	Magnetically stirring (10 min) + ultrasonication (2 h, Power: 40 W) + mixing (4 min)
Kim et al. (Kim et al., 2014)	CNTs	—	Silica fume (0−30 wt%)	Mixing (6 min)
Veedu (Veedu, 2011)	MWCNTs (diameter: 20−40 nm, length: 5−15 μm)	—	Acetone or ethanol + methylcellulose	Ultrasonication + mixing
Guo et al. (Guo, 2013)	MWCNTs (diameter: 10 nm, length: 10 μm)	—	AG (0.45 g/L)	Ultrasonication (30 min, frequency: 40 kHz, power: 180 W) + mixing (6 min)

Note: Some information that references do not provide is not listed in the table.

Table 8.2 Summary of dispersion methods of CNFs in cementitious materials

Researchers	Morphology of CNFs	Categories of dispersion methods	
		Chemical treatment	Mechanical treatment
Tyson et al. (Tyson, 2013; Tyson et al., 2011; Abu Al-Rub et al., 2011, Yazdanbakhsh et al., 2009)	Diameter: 60–150 nm, length: 30–100 μm	Superplasticizer (1.25 wt%)	Ultrasonication (15 min) + mixing (7 min)
Metaxa et al. (Metaxa et al., 2010, Metaxa et al., 2012)	Diameter: 100–150 nm, length: 30–100 μm	—	Ultrasonication + mixing
Yazdanbakhsh et al. (Yazdanbakhsh et al., 2010, Yazdanbakhsh et al., 2012; Shah et al., 2010)	Diameter: 60–150 nm, length: 30–100 μm	Superplasticizer treatment	Ultrasonication (15 min) + mixing (7 min); ball milling (15 h)
Sanchez et al. (Sanchez and Ince, 2009; Gay and Sanchez, 2010)	Diameter: 70–200 nm, length: 30–100 μm	Silica fume (10 wt%)	Mixing (15 min); ultrasonication (30 min)
Howser et al. (Howser et al., 2011)	—	Superplasticizer	Mixing (3 min)
Peyvandi et al. (Peyvandi et al., 2013a,b)	Diameter: 60–150 nm, length: 30–100 μm	Polyacrylic acid	Ultrasonication (30 min) + microwave radiation (10 min) + stirring (overnight)
Baeza et al. (Baeza et al., 2013)	Diameter: 20–80 nm, length: ≥30 μm	—	Ultrasonication + mixing
Zhao et al. (Zhao et al., 2009)	Diameter: 20–100 nm	AG	Magnetically stirring; ultrasonication
Nasibulina et al. (Nasibulina et al., 2012, Nasibulina et al., 2010)	—	Growing CNFs directly on cement (clinker) particles	—
Han et al. (Han et al., 2011c)	Diameter: 100–150 nm, length: 50–200 μm	Aqueous solution with superplasticizer (0.4–1 wt%)	Magnetically stirring (1 min) + ultrasonication (2 h) + mixing (5 min)
Gao et al. (Gao et al., 2009)	—	SDS	Mixing (3 min)

Note: Some information that references dose not provide is not listed in the table.

Table 8.3 **Summary of dispersion methods of NGPs in cementitious materials**

Researchers	Morphology of NGPs	Categories of dispersion methods	
		Chemical treatment	Mechanical treatment
Huang (Huang, 2012)	Size of 3—18 µm, thickness of 3—70 nm	Superplasticizer (Darex super 20, 0.4 wt%)	Ultrasonication (time: 2 h)
Singh et al. (Singh et al., 2011)	—	—	Mixing and ball milling (time: 5 h)

Note: Some information that references do not provide is not listed in the table.
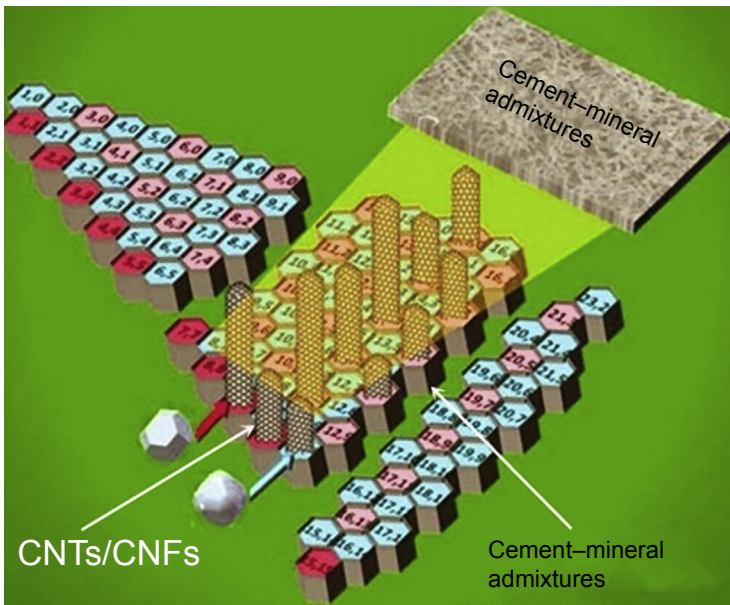
Figure 8.2 CNTs and CNFs synthesized on cement—mineral admixtures.

70% (Yakovlev et al., 2006). The cementitious composites filled with small amounts of MWCNTs (0.048 and 0.08 wt%) exhibit a 15—55% increase in the Young's modulus and an 8—40% increase in flexural strength. An over 45% increase in the 28-day flexural strength is realized with the addition of 0.08 wt% MWCNTs (Konsta-Gdoutos et al., 2010a; Shah et al., 2009b). The addition of 0.05% and 0.1% SWCNTs and 0.1% and 0.2% MWCNTs provides a 10—90% increase in the Young's modulus and hardness of cementitious composites (Saez De Ibarra et al., 2006). Low

water−cement ratio cementitious composites with 2% SWCNTs show 600% improvement in hardness at early ages, but essentially have no improvement after 14 days of hydration (Makar et al., 2005). The use of 0.5 and 1 wt% CNTs in fly ash (20% by weight of cement) cement paste results in higher compressive strength of the cementitious composites. The highest compressive strength of the cementitious composites at 28 days is 54.7 MPa, which is almost 2 times of that of plain Portland cement paste (Chaipanich et al., 2010). Matthew J. Bolton et al. found that the use of 0.1 wt% CNTs can increase the tensile strength and reduce the compressive strength of the CNT-filled cementitious composites. When more than 0.2 wt% of CNTs is added, there are small increases in both compressive and tensile strength of the CNT-filled cementitious composites (MacKenzie and Bolton, 2009). Veedu observed that the flexural strength and compressive strength of CNT-filled cementitious composites are 30% and 100% greater, respectively, than those of CF-filled cementitious composites (Veedu, 2011). Hunashyal et al. investigated the behavior of MWCNT-filled cementitous-composite round bars and found that the tensile strength of the cementitious composites with 0.5 wt% CNTs increases by 19%. Tensile modulus of the cementitious composites with 0.5 wt% MWCNTs is increased by 70.9% compared to that of plain ones (Hunashyal et al., 2011b). The flexural strength of the cementitious composite with 0.75 wt% MWCNTs is increased by 43.75% (Hunashyal et al., 2011a). Zuo et al. added 0.5 wt% CNTs to CFs and cementitious composites, resulting in the highest increases in the compressive and splitting tensile strengths (by 18.4% and 21.8%, respectively) (Zuo et al., 2014). Morsy et al. investigated the behavior of cementitious composites made from MWCNTs and nanoclay materials. The compressive strength of the control specimen with 0−0.1% CNTs increases with the increase of CNTs until it reaches an optimal amount of 0.02% and then starts to drop (Morsy et al., 2011; Siddique and Mehta, 2014).

The type and structure of CNTs were found to be very important with respect to the mechanical properties. Adding 0.5 wt% as-grown and annealed MWCNTs to plain cement paste can induce an improvement in the flexural and compressive properties of the cementitious composites (Musso et al., 2009). The cement paste incorporating hydroxyl-functionalized MWCNTs reveals an increase in the compressive strength of nearly 50% even with only 0.045−0.15 wt% MWCNTs (Cwirzen et al., 2008). Carboxyl-functionalized MWCNTs can increase the compressive strength up to 19%, and the flexural strength increases up to 25%. The use of CNTs can improve the deformation ability of cement mortar, and it leads to a significant increase of the failure strain (Li et al., 2005). The addition of 0.5% carboxyl-functionalized MWCNTs can obtain enhancements of 149.32% and 34.96% in fracture toughness and critical opening displacement, respectively, compared to those obtained with the plain cement paste (Luo et al., 2011). However, Musso et al. obtained a significant reduction in flexural and compressive strength of carboxyl-functionalized MWCNT-filled cementitious composites compared to those of pristine cement paste (Musso et al., 2009).

The length of CNTs also affects their dispersion behavior and is therefore a controlling factor for the mechanical properties of cementitious composites. In particular, higher concentrations of short MWCNTs (10−30 μm) are required to achieve effective reinforcement, whereas smaller amounts of longer MWCNTs (10−100 μm) are

needed to achieve the same level of mechanical properties (Konsta-Gdoutos et al., 2010a; Shah et al., 2009b).

Dispersion of CNTs has been identified as one of the principal factors that mostly affects the mechanical properties. The use of 0.2% MWCNTs with different surfactants can increase the flexural and compressive strength of the cementitious composites by 35.45% and 29.5%, respectively. The fracture toughness and critical opening displacement of the CNT-filled cementitious composites with 0.5% MWCNTs can be enhanced by 175.21% and 54.77%, respectively, compared to those with the plain cement paste (Luo, 2009). Nasibulin et al. (2009) found that the in situ—grown CNT-filled cementitious composites reveal as high as two times increases in the compressive strength compared with that of plain cement paste. Ludvig et al. (2009) achieved a 34.28% increase in the tensile strength by using an in situ—grown cement—CNT hybrid containing 0.3% CNTs. Sobolkina et al. investigated the dispersion of CNTs and its effect on the mechanical properties of the cement matrix. The application of sodium dodecyl sulfate (SDS) as a surfactant leads to a severe drop in the strength of the cementitious composites. No distinct increase in compressive strength is observed after modifying the cement paste with CNTs in a concentration of 0.05% by weight of cement in comparison with the reference composites (Sobolkina et al., 2012).

8.4.1.2 Electrical and sensing properties of CNT-filled cementitious composites

The CNT-filled cementitious composites can have good conductivity when the concentration of CNTs reaches the percolation threshold. The electrical resistivity of SPCNTs (cementitious composites with 0.5% carboxyl-functionalized CNTs) and PCNTs (cementitious composites with 0.5% unfunctionalized CNTs) is 149 and 130 Ω cm, respectively (Li et al., 2005). Saafi (2009) found that there is a sudden decrease in the electrical resistance as the concentration of SWCNTs increases from 0 to 0.5 vol%. The electrical resistance decreases when the concentration of SWCNTs increases from 0.5 to 1 vol%. Azhari (2008) found that the addition of SWCNTs at 1% and MWCNTs at 1% or 3% slightly decreases the electrical resistivity of the cementitious composites, whereas a hybrid containing 3% MWCNTs and 15% CFs yields a very low electrical resistivity. Nasibulin et al. (2009) and Cwirzen et al. (2008, 2009b) studied electrical resistivity of CNT-filled cementitious composites made of cement—CNT hybrid. They found that the cementitious composites reveal as high as 40 times increase in the electrical conductivity compared to plain cement paste.

Li et al. (2007) observed the pressure-sensitive responses of cement paste with MWCNTs. The compressive sensitivity of SPCNTs is higher than that of PCNTs. Mohamed Saafi (2009) successfully fabricated self-sensing concrete by using SWCNTs as functional filler. The CNT-filled cementitious composites with an SWCNT volume of 0.5% exhibited a low sensitivity to the applied stress compared to those with an SWCNT volume of 1%. Yu et al. (2007) found that the electrical resistance of the cementitious composites filled with 0.1% non-covalent surface modification MWCNTs by SDS changes synchronously with the compressive stress. The resistance changes of the cementitious composites filled with 0.1% carboxyl-functionalized MWCNTs also

correspond to the stress load levels. But the latter presents a stronger sensing response and higher signal-to-noise ratio than the former (Yu et al., 2007).

Han et al. (2010a) also compared the sensing behaviors of MWCNT-filled cementitious composites with different water contents under uniaxial compression. They found that the water content has a strong effect on the electrical and sensing properties of the cementitious composites. The electrical conductivity of the cementitious composites increases with water content, whereas the sensing sensitivities first increase and then decrease with the increase of water content. Han et al. (2010b, 2012b) studied the variation of the electrical resistance of cement paste and cement mortar reinforced with carboxyl-functionalized MWCNTs under repeated compressive loading and impulsive loading. They found that the change in electrical resistances of both cement paste with 0.1% MWCNTs and cement mortar with 0.4% MWCNTs is strongly related to the repeated compressive loading in every cycle. It is worth noting that the addition of fine aggregates (i.e., sand) decreases the sensitivity of the sensing response of the composites, albeit at a higher CNT concentration (Han et al., 2010a,b, 2012b). In addition, Han et al. (2009, 2010b, 2011b, 2012b) also studied the sensing properties of the CNT-filled cementitious composites with different concentration levels of CNTs, water−cement ratios, and types of dispersant under different stress amplitudes and loading rates (Han et al., 2012a,b, 2011b; Yu and Kwon, 2009).

8.4.1.3 Other properties of CNT-filled cementitious composites

Damping, thermal, electromagnetic interference (EMI), and other properties of CNT-filled cementitious composites were also explored. For example, Luo observed that the critical damping ratio of cementitious composites with 2% MWCNTs is 1.6 times that of plain ones (Luo, 2009; Luo et al., 2013). Han et al. (2013a) found that even a very small dosage of MWCNTs can help to decrease water absorptivity coefficient, water permeability coefficient, and gas permeability coefficient of cementitious composites. This indicates that CNTs can effectively improve the transport properties and durability of cementitious composites. Yakovlev et al. (2006) observed that the modification of foam concretes by the addition of CNTs allows lowering the heat conductivity by 20% (from 0.07 to 0.056 W/m K). Veedu (2011) stated that the thermal performance of CNT-filled cementitious composites is at least 35% and 85% greater than that of CF-filled and unmodified ones, respectively. Al-Rub et al. (2011) found that incorporation of CNTs treated by the functional groups (−COOH and −OH) produces an increase in workability of the cementitious composites. Shukla et al. (2012) studied the smoke detection property of cementitious composites with MWCNTs, and found that the DC transient studies depicted an increase in electrical conductivity when the composites are exposed to smoke. Kerienė et al. (2013) observed that the non-autoclaved aerated concrete and autoclaved aerated concrete with MWCNTs are more stable during exploitation than those cementitious composites without these additions. In addition, Singh et al. (2013) and Guo (2013) found that the high value of EMI shielding effectiveness (SE) of MWCNT-filled cementitious composites is dominated by absorption rather than reflection. Adding 0.6 wt% MWCNTs into cementitious materials can lead to a 27% decrease in electromagnetic wave reflectivity at a frequency of 2.9 GHz.

Gong et al. studied the effects of CNTs on the dielectric and piezoelectric properties of PZT cementitious composites. The dielectric constant and dielectric loss increase with increasing CNT content. The piezoelectric strain factors and the piezoelectric voltage factors are all increased with increasing CNT content up to 0.3 vol%. The highest piezoelectric strain factor and piezoelectric voltage factor values are 62 pC/N and 60×10^{-3} Vm/N, respectively, which are 41% and 28% higher than those of the composites without CNTs (Gong et al., 2011).

Zuo et al. (2014) employed 0.5 wt% CNTs to improve the positive thermoelectric power of the CF—cementitious composites, which leads to a 260% increase in the positive thermoelectric power (from 8.8 to 22.6 μV/°C).

8.4.2 Properties of CNF-filled cementitious composites

8.4.2.1 Mechanical properties of CNF-filled cementitious composites

The reinforcement effect of the CNFs on the cementitious composites had been studied, and sorts of properties of the cementitious composites had been improved. Gao et al. (2009) added 1% CNFs into concrete, which improves the compressive strength of the concrete by 42.7% compared to plain concrete when CNF concentration is 0.16%.

Tyson et al. observed that 0.2 wt% CNFs can result in a maximum increase of 150% in peak displacement of the cementitious composites. The largest increase in flexural strength and fracture toughness (which occurred at seven days) of the CNF-filled cementitious composites is 82% and 270%, respectively. This is most likely attributed to the higher aspect ratios of the CNFs (i.e., approximately 1000 for CNFs vs 150 for CNTs), which makes CNFs more effective as reinforcements because of their larger interaction with the cement matrix (Tyson et al., 2011).

Yazdanbakhsh (2013) obtained a more than 250% increase in flexural strength of the cementitious composites with the concentration of 1.0 wt% CNFs in cement. In addition, the increase in Young's modulus and resilience of the cementitious composites are 68% and 430%, respectively.

Shah et al. (2010) studied the flexural strength rate of the nanocomposites incorporating CNFs up to the 28th day of hydration. The composites filled with CNFs at all ages exhibited higher flexural strength than plain cement paste. The use of CNFs results in an up to 45% increase in the flexural strength.

Nasibulina et al. (2012) studied CNF-filled mortar with CNF—clinker hybrid material prepared by a direct synthesis of CNFs on the surface of clinker particles. The best results, which were an almost three times increase in compressive strength, were obtained for the composites with the CNF concentration of 0.4%. However, the increase in flexural strength is not so significant.

8.4.2.2 Electrical and sensing properties of CNF-filled cementitious composites

Researchers also investigated the electrical and sensing properties of CNF-filled cementitious composites. Gao et al. (2009) found that the electrical resistance of the

cementitious composites with 1% CNFs shows an 80% maximum reduction compared to the plain ones. The cementitious composites have stable sensing property as the CNF concentration is between 1% and 2%. Han et al. (2011b) observed that the cementitious composites with CNFs present stable and repeatable sensing properties under repeated compression. The sensing response sensitivity depends heavily on the types and concentrations of CNFs. Galao et al. (2013) studied the sensing properties on CNF-filled cementitious composites. They found that all composites with different CNF dosages show good strain-sensing capacities for curing periods of 28 days.

8.4.3   Properties of NGP-filled cementitious composites

Huang (2012) observed that the addition of NGPs increases the flexural strength of cementitious composites by 82% compared to the plain ones. The electrical property of the composites is significantly modified, and the composites become highly conductive. Pan et al. (2013) reported that only 0.05% GO can improve the flexural strength of cementitious composites from 41% to 59% and the compressive strength from 15% to 33%. Lv et al. (2013) found that GO nanosheets can remarkably increase the tensile/flexural strength of the corresponding cementitious composites. Especially, when the content of GO is 0.03%, the tensile, flexural, and compressive strength of cementitious composites increase by 78.6%, 60.7%, and 38.9%, respectively.

Du et al. (2013) studied the sensing behavior of NGP-filled cementitious composites with different contents of NGPs (0−4.8 wt%), and observed that NGP-filled cementitious composites exhibit a decrease in electrical resistivity and good sensing property when NGP contents are in the range from 2.4 to 3.6 vol%. Singh et al. (2011) found that the SE_T (total SE) of the GO−ferrofluid−cementitious composites is 46 dB, which is much higher than that of the pristine cementitious composites (4 dB). Peyvandi et al. (2013a,b) investigated the contributions of NGPs to the durability of cementitious composites, and observed that NGPs significantly improve the moisture transport performance and acid resistance of composites at a low dosage (0.05 vol% of cementitious composites).

8.5   Enhancement mechanisms of NCMs on properties of cementitious composites

8.5.1   Enhancement mechanisms of CNTs and CNFs on properties of cementitious composites

The enhancement of CNTs and CNFs on the properties of cementitious composites mainly results from the extensive distributing enhancement network of CNTs and CNFs in cementitious composites (as shown in Figure 8.3).

The following factors also contribute to the mechanical property: Simone Musso found that the high-temperature annealing treatments remove lattice defects from
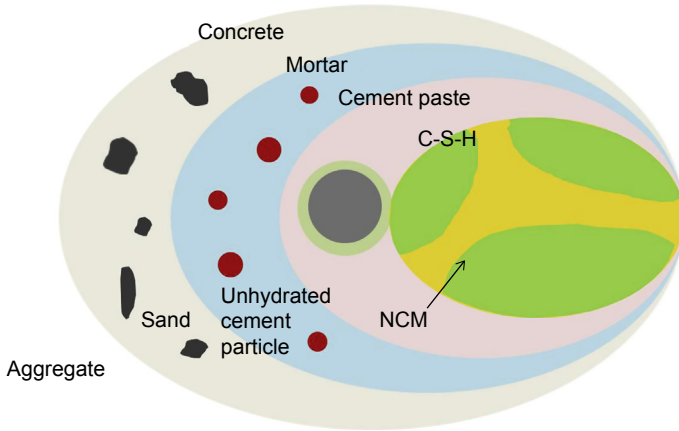
Figure 8.3 Structures of NCM-filled cementitious composites.

the walls of CNTs, hence obviously increasing CNTs' and the cementitious composites' mechanical strength (Musso et al., 2009). Makar and Chan (2009) observed that the CNTs appeared to act as nucleating sites for the C_3S hydration products, thus accelerating the hydration reaction of the C_3S and increasing the amount of high-stiffness C-S-H (as shown in Figure 8.4) (Konsta-Gdoutos et al., 2010b). Vera-Agullo concluded that either CNFs or CNTs accelerate the hydration process and the compressive strength at early ages, improving the flexural strength at 28 days (Vera-Agullo et al., 2009). Shah et al. found that the autogenous shrinkage in CNT-filled cementitious composites reduces at least 30% after 96 h compared to the same composites without CNTs. Li et al. (2005), Konsta-Gdoutos et al. (2010b) and Chaipanich et al. proposed that the addition of CNTs/CNFs fines pore size distribution and decreases
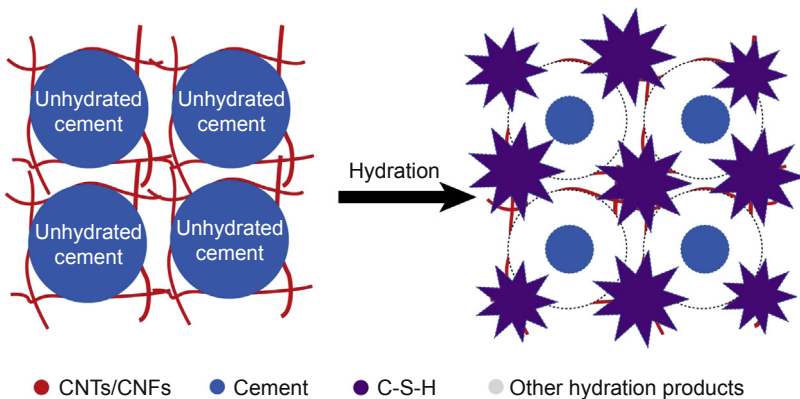
Figure 8.4 Schematic presentation of nucleating effect of CNTs and CNFs. Before hydration, CNTs and CNFs are bundled on the surface of unhydrated cement particles. After hydration, CNTs and CNFs are coated with high-density C-S-H gel and other hydration products.

the porosity (or nanoporosity) of cementitious composites by filling the gaps (or pores) between the hydration products, such as C-S-H and ettringite (Han et al., 2011a; Nochaiya and Chaipanich, 2011). Makar et al. (2005) found that a dense C-S-H formation that appears to be tightly bonded to CNTs produces reinforcing behavior (Makar and Beaudoin, 2004). Li et al. (2005) and Cwirzen et al. (2008) concluded that the interfacial interactions between the groups of functionalized CNTs' surfaces and hydrations (e.g., C-S-H and calcium hydroxide) of cement will produce a high bonding strength, and increase the load transfer efficiency from cement matrix to the reinforcement (as shown in Figure 8.5). Tyson et al. also proposed that the delayed enhancements in strength, ductility, and toughness, accompanied with a reduction in stiffness, are likely because of a change in the bonding between the CNTs and the cement matrix. At early ages, more CNTs are pulled out, allowing for higher strain capacities. At the 28-day test, the bonding between CNTs and cement matrix increases to the point at which the CNTs are more susceptible to breaking rather than gradually pulling out (Tyson et al., 2011). Makar et al. (2005) and Nasibulin et al. (2009) observed that CNTs are anchored well inside the hydration products and cross-crack. Makar et al. (2005) also proposed that the pinning effect and the efficient crack bridging can inhibit the crack growth at the very preliminary stage of crack propagation within composites, when the cracks in the matrix encounter distributed CNTs. Veedu (2011) observed that the CNTs form a stitching on fracture surfaces, diverting crack energy into a matrix and inhibiting crack propagation. Li et al. (2005) concluded that the bridge coupling effect of CNTs guarantees the load transfer across voids and cracks.

For the conductive property, Lu et al., Wang et al., Chen et al., Li et al., and Han et al. proposed that the electrical resistance of CNT-filled cementitious composites comes from two sources: the intrinsic resistances of nanotubes and matrix and the contact resistance (i.e., the resistance between connecting CNTs or the resistance of the matrix connecting the crossing nanotubes and through which electrical tunneling occurs) (as shown in Figure 8.6). The contact resistance at nanotube junctions is rather complicated and depends on the concentration and physical properties of nanotubes, tunneling gap at contact points, and conductive properties of matrix filling the tunneling gap (Li and Chou, 2008). Saafi (2009) and Azhari (2008) found that the
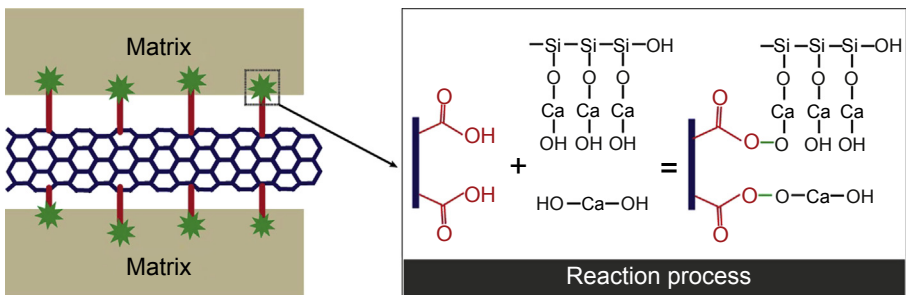
Figure 8.5 Schematic presentation of strength bonding between functionalized CNTs/CNFs and the matrix, and typical reaction process between functional groups (−COOH) and the hydration products.
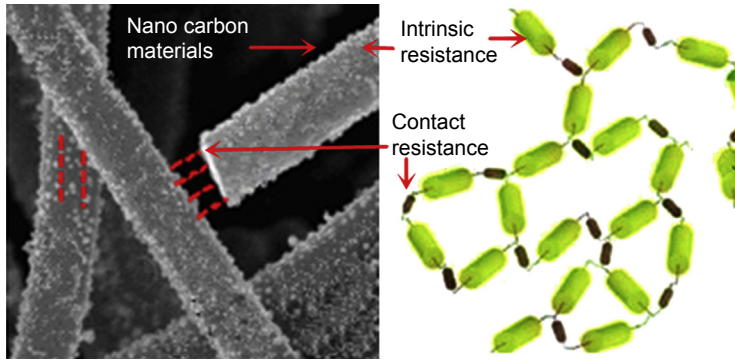
Figure 8.6 Schematic diagram of basic conductive element in a conductive network of NCM-filled cementitious composites.

more contact points between CNTs, the lower the electric resistivity will be. Sun et al. proposed the mechanism of sensing properties through conductive model analysis and experimental verification. They pointed out that both the change in intrinsic resistance of CNTs and the change in contact resistance between adjacent CNTs have contributed to the sensing property of the composite, but the latter is the leading contributing factor (Sun et al., 2014). There are three basic types of conduction mechanisms (i.e., contacting conduction, tunneling conduction, and field emission conduction) contributing to the contact resistance (Han et al., 2011a; Grujicic et al., 2003; Wang et al., 2009; Li and Chou, 2008). The above-mentioned conduction types coexist in composites and interrelate with each other. One or several factors among these aspects may be dominant for a specific CNT/CNF-filled cementitious composite. In general, the conductive characteristic of CNT/CNF-filled cementitious composites can be described by the percolation phenomenon.

In addition, the electrical resistivity of CNT/CNF-filled cementitious composites would change when the composites deform under loading. Several factors may contribute to the sensing property: Li et al. proposed that the nanotube length and diameter will alter, resulting in the change of nanotube intrinsic resistance, when the CNT-filled cementitious composites are deformed under external loading (Li et al., 2007). Li et al. (2007), Yu and Kwon (2009), Han et al. (2009), Saafi (2009), and Azhari (2008) concluded that the separation between CNTs will be reduced or increased (i.e., the tunneling conduction is enhanced or weakened) when the nanocomposites are deformed under compressive or tensile loading. This leads to the change of electrical resistivity of the nanocomposites under external load, expressing strong sensing responses (Azhari and Banthia, 2012). It should be noted that the above-mentioned factors work together to contribute to the sensing property of CNT/CNF-filled cementitious composites, but only one or several of them are leading at certain percolation zones. Therefore, the percolation threshold is an important parameter for designing and optimizing sensing property of CNT/CNF-filled cementitious composites. Generally, the CNT/CNF concentration above the percolation threshold is beneficial for the sensing sensitivity under tension, whereas that below

the percolation threshold is beneficial for the sensing sensitivity under compression (Han et al., 2011a).

Singh et al. and Guo et al. proposed that the presence of conducting CNTs/CNFs in the insulating cementitious matrix results in the formation of more interfaces and a heterogeneous system due to some space charge accumulating at the interface that contributes toward the higher microwave absorption in the composites (as shown in Figure 8.7). The dielectric constant increases with increase of MWCNT content, which improves the capability to shield electromagnetic waves. The increase in MWCNT leads to reduction of skin depth and increase in AC conductivity along with improvement of input impedance. This not only enhances the amount of electromagnetic radiation penetrating inside the shield but also increases the effective absorption capability. Therefore, the CNTs/CNFs embedded in concrete matrix increase the interfacial polarization and the effective anisotropy energy of composites, which lead to the high SE of CNT/CNF-filled cementitious composites (Singh et al., 2013; Guo, 2013). Gong et al. (2011) concluded that the CNTs act as conductive filler dispersed in the cement matrix, improving the poling efficiency of the PZT cementitious composites and enabling the poling process to be carried out at room temperature.

8.5.2 Enhancement mechanisms of NGPs on properties of cementitious composites

As a type of 2D nanoparticle, NGPs possess the "small size effect" that enables NGPs to serve as nuclei. For example, GO nanosheets can regulate formation of flower-like
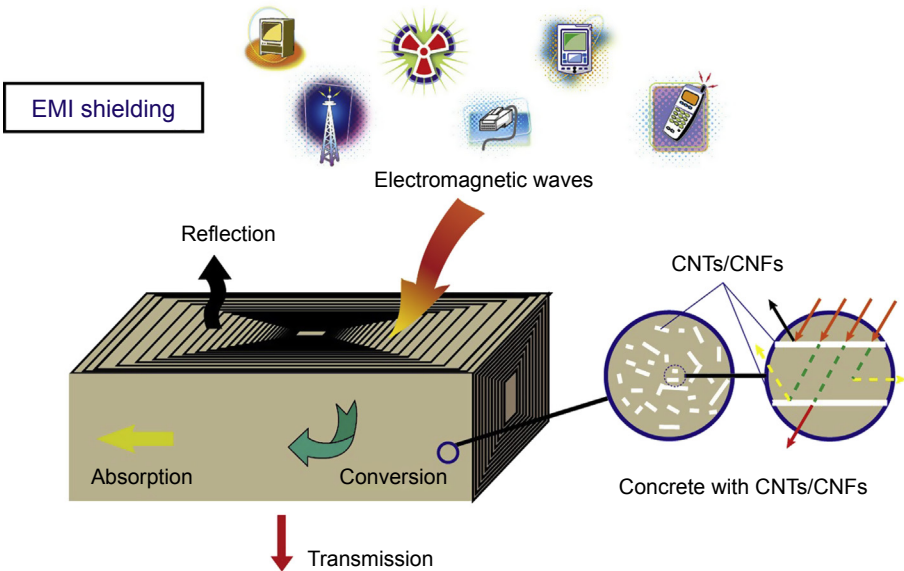
Figure 8.7 Schematic presentation of the EMI shielding of CNT/CNF-filled cementitious composites.

crystals. Huang et al. concluded that the formed network structure of cement hydration products around the NGPs can improve the homogeneity and compactness of the hardened cementitious composites. For example, the addition of 0.05% GO decreases the total porosity of cementitious composites from 32.6% to 28.2%. NGPs also have the "surface effect," which leads to enormous interface areas. At the interface, NGPs can show an intimate bonding with the cement matrix due to strong van der Waals forces. The large aspect ratio and plate shape of NGPs provide them with strong ability to block and divert the microcracks, which can slow down crack propagation and formation of the crack network. The bridge effect of NGPs can delay crack origination and prevent crack opening up. Besides, NGPs can enhance mechanical properties of these composites via a crack-arresting effect and improvement in the interfacial transition zone of NGP-filled cementitious composites (Huang, 2012).

For the electrical property of NGP-filled cementitious composites, Huang proposed several theories on the mechanism of the contributions of NGPs to cementitious materials based on the characteristics of NGPs. NGPs have pi electrons that participate in interlayer pi bonding, which make them good electrical-conducting materials. Besides, the carbonation process with temperatures of up to 1050 °C during fabrication of NGPs left a large excess of holes in the valence band. This characteristic of NGPs contributes to the electrical property of NGP-filled cementitious composites through the following paths: (1) electronic conduction and hole conduction through NGPs by tunneling effect; and (2) electronic conduction and hole conduction through contacting conduction of NGPs (as shown in Figure 8.8) (Huang, 2012). Both factors contribute to the electrical property of NGP-filled cementitious composites, and one of them may be dominant according to the content of NGPs.

The mechanism of action of NGPs on the EMI property of NGP-filled cementitious composites is similar to that of CNF/CNT-filled cementitious composites. Singh et al. (2011) concluded that the presence of conducting NGPs in the insulating matrix results in the formation of more interfaces and a heterogeneous system due to some space charge accumulating at the interface that contributes toward the higher microwave absorption in the composites.
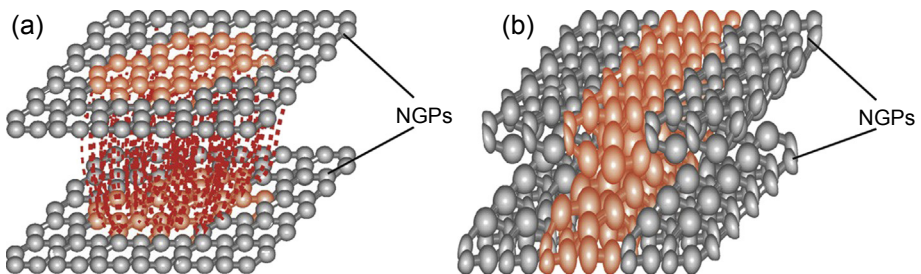
Figure 8.8 Schematic presentation of the electrical conduction mechanisms of NGPs. (a) Tunneling effect and (b) contacting effect.

8.6   Applications

The current applications of NCM-filled cementitious composites include two aspects. One is to enhance the mechanical performance and durability of structures or components. For example, Hunashyal et al. (2011a) investigated the behavior of beams fabricated with MWCNT-filled cementitious composites. The flexural strength of the beam was increased by 43.75% from MWCNT additions of 0.75 wt%. Gao et al. (2010) employed CNFs in cylinders to enhance the mechanical properties. The peak compressive strength of the cylinders increased 21.4% when the CNF concentration was 1%. And the stiffness of the cylinders containing CNFs is greater than that of the plain ones. Howser et al. (2011) observed that the addition of CNFs to concrete increases the strength and ductility of a column. The self-consolidating CNF concrete (SCCNFC) column has an ultimate normalized capacity that is 30.7% higher and a deflection that is 34.9% higher than the self-consolidating reinforced concrete (SCRC) column. The ductility of the SCCNFC column is 35.1% higher than the SCRC column's ductility. Peyvandi et al. (2013b) added modified NGPs into the dry-cast concrete pipes in an aggressive sanitary sewer environment to improve their durability characteristics, including the moisture absorptivity and acid resistance, thus increasing their service life in sanitary sewer applications.

Another application is to use the functional performances of NCM-filled cementitious composites for structural health monitoring (as shown in Figure 8.9) or traffic detection (as shown in Figure 8.10). For example, Howser et al. (2011) built shear-critical columns with cementitious composites containing CNFs. The columns are capable of strain self-sensing under a reversed cyclic load and damage
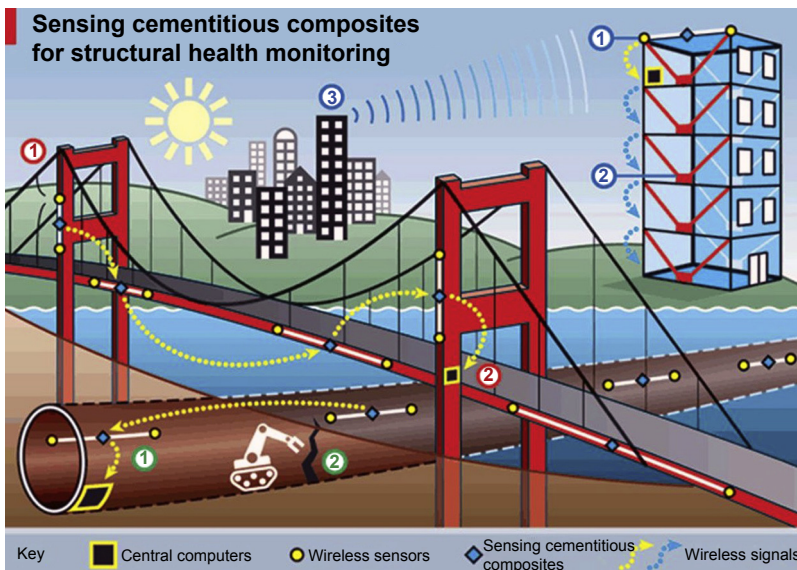
Figure 8.9 Sensing cementitious composites with NCMs for structural health monitoring.
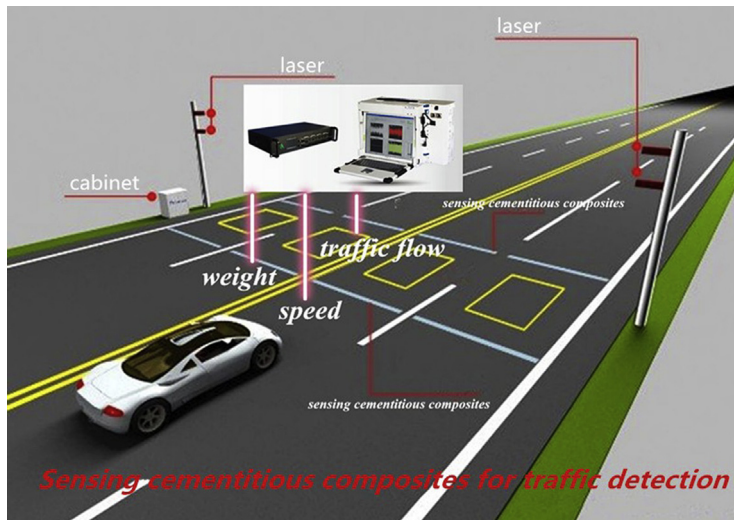
Figure 8.10 Sensing cementitious composites with NCMs for traffic detection.

self-assessment. Saafi (2009) embedded cementitious composites with SWCNTs into the tensile region of beams to set up the self-sensing structures subjected to monotonic and cyclic bending. The self-sensing structures can detect crack propagation and damage accumulation during loading. Baeza et al. (2013) embedded and bonded cementitious composites with CNFs into different service locations of reinforced beam. The cementitious composites with CNFs can achieve elastic strain sensing of the compression and tension regions of beams and are capable of measuring strains on the surface of a structural element (Han et al., 2011a; Howser et al., 2011; Saafi, 2009; Mo and Roberts, 2013). Han et al. developed self-sensing pavements with cementitious composites containing CNTs and investigated the feasibility of using the self-sensing pavements for traffic monitoring with vehicular loading experiments. The proposed self-sensing pavement system can accurately detect the passing of different vehicles under different vehicular speeds and test environments (Han et al., 2009, 2011a, 2012b, 2013b). Materazzi et al. aimed to develop CNT-filled cementitious sensors for possible application in dynamic response measurements and structural health monitoring of concrete structures. Based on the results, the investigated specimens can be considered available sensors that appear to be suitable for performing dynamic measurements in civil engineering concrete structures (Materazzi et al., 2013).

8.7 Conclusions

Ultra-miniature nano-materials are bringing tremendous change to the world, including the field of construction, expanding the horizon of research in multifunctional cementitious composites. Their extraordinary physical properties, size effect, and chemical and thermal stability are beneficial for enhancing the mechanical,

electrical, thermal, electromagnetic-shielding, and corrosion resistance properties of cementitious materials.

Although a number of research efforts have been conducted in this area in recent years, many challenges still need to be addressed. Future work on NCM-filled cementitious composites may include investigations regarding the enhancement effect of NCMs to concrete with coarse aggregate, other structural and functional properties of NCM-filled cementitious composites such as durability, thermoelectric and corrosion resistance properties, the precise explanation of the enhancement mechanism of NCMs to cementitious composites by numerical simulation or a new characterization method, and the performance of the structure made of NGP-filled cementitious composites.

NCM-filled cementitious composites can help us develop infrastructure with elegantly integrated excellent structural performance, high durability, and multifunctional capability, thus improving safety, serviceability, reliability, and durability of infrastructure. As a new generation of construction materials, they will promote sustainable development in the field of cementitious materials and structures.

Acknowledgments

References

Abu Al-Rub, R.K., Ashour, A.I., Tyson, B.M., 2012. On the aspect ratio effect of multi-walled carbon nanotube reinforcements on the mechanical properties of cementitious nanocomposites. Construction and Building Materials 35, 647−655.

Abu Al-Rub, R.K., Tyson, B.M., Yazdanbakhsh, A., Grasley, Z., 2011. Mechanical properties of nanocomposite cement incorporating surface-treated and untreated carbon nanotubes and carbon nanofibers. Journal of Nanomechanics and Micromechanics 2, 1−6.

Azhari, F., 2008. Cement-Based Sensors for Structural Health Monitoring. University of British Columbia, Canada (Dissertation for the Degree of Master of Applied Science).

Azhari, F., Banthia, N., 2012. Cement-based sensors with carbon fibers and carbon nanotubes for piezoresistive sensing. Cement and Concrete Composites 34, 866−873.

Baeza, F.J., Galao, O., Zornoza, E., Garcés, P., 2013. Multifunctional cement composites strain and damage sensors applied on reinforced concrete (RC) structural elements. Materials 6, 841−855.

Bahr, J.L., Tour, J.M., 2002. Covalent chemistry of single-wall carbon nanotubes. Journal of Materials Chemistry 12, 1952−1958.

Bharj, J., Singh, S., Chander, S., Singh, R., 2014. Experimental study on compressive strength of cement-CNT composite paste. Indian Journal of Pure & Applied Physics 52, 35−38.

Chaipanich, A., Nochaiya, T., Wongkeo, W., Torkittikul, P., 2010. Compressive strength and microstructure of carbon nanotubes-fly ash cement composites. Materials Science and Engineering: A 527, 1063−1067.

Chen, J., Poon, C., 2009. Photocatalytic construction and building materials: from fundamentals to applications. Building and Environment 44, 1899−1906.

Chen, S., Collins, F., Macleod, A., Pan, Z., Duan, W., Wang, C., 2011. Carbon nanotube-cement composites: a retrospect. The IES Journal Part A: Civil and Structural Engineering 4, 254−265.

Chyad, F.A., 1989. The Effects of Metastable Zirconia on the Properties of Ordinary Portland Cement. University of Bradford (Dissertation for the Degree of Doctor).

Collins, F., Lambert, J., Duan, W.H., 2012. The influences of admixtures on the dispersion, workability, and strength of carbon nanotube-OPC paste mixtures. Cement and Concrete Composites 34, 201−207.

Cwirzen, A., Habermehl-Cwirzen, K., Penttala, V., 2008. Surface decoration of carbon nanotubes and mechanical properties of cement/carbon nanotube composites. Advances in Cement Research 20, 65−73.

Cwirzen, A., Habermehl-Cwirzen, K., Nasibulina, L.I., Shandakov, S.D., Nasibulin, A.G., Kauppinen, E.I., Mudimela, P.R., Penttala, V., 2009a. CHH Cement Composite. Nanotechnology in Construction 3. Springer, 181−185.

Cwirzen, A., Habermehl-Cwirzen, K., Shandakov, D., Nasibulina, L.I., Nasibulin, A.G., Mudimela, P.R., Kauppinen, E.I., Penttala, V., 2009b. Properties of high yield synthesised carbon nano fibres/portland cement composite. Advances in Cement Research 21, 141−146.

Du, H., Quek, S.T., Dai Pang, S., 2013. Smart Multifunctional Cement Mortar Containing Graphite Nanoplatelet. SPIE Smart Structures and Materials+Nondestructive Evaluation and Health Monitoring. International Society for Optics and Photonics, 869238-869238-10.

Dunens, O.M., Mackenzie, K.J., Harris, A.T., 2009. Synthesis of multiwalled carbon nanotubes on fly ash derived catalysts. Environmental Science & Technology 43, 7889−7894.

Fu, K., Huang, W., Lin, Y., Riddle, L.A., Carroll, D.L., Sun, Y., 2001. Defunctionalization of functionalized carbon nanotubes. Nano Letters 1, 439−441.

Galao, O., Baeza, F.J., Zornoza, E., Garcés, P., 2013. Strain and damage sensing properties on multifunctional cement composites with CNF admixture. Cement and Concrete Composites 46, 90−98.

Gao, D., Sturm, M., Mo, Y.L., 2009. Electrical resistance of carbon-nanofiber concrete. Smart Materials and Structures 18, 095039.

Gao, D., Mo, Y.L., Peng, L.M., 2010. Mechanical and electrical properties of carbon-nanofiber self-consolidating concrete. In: Proceedings of the 12th International Conference on Engineering, Science, Construction, and Operation in Challenging Environments. USA: Honolulu, pp. 2577−2585.

Gay, C., Sanchez, F., 2010. Performance of carbon nanofiber-cement composites with a high-range water reducer. Transportation Research Record: Journal of the Transportation Research Board 2142, 109−113.

Geim, A.K., Novoselov, K.S., 2007. The rise of graphene. Nature Materials 6, 183−191.

Gong, H., Zhang, Y., Quan, J., Che, S., 2011. Preparation and properties of cement based piezoelectric composites modified by CNTs. Current Applied Physics 11, 653−656.

Grujicic, M., Cao, G., Gersten, B., 2003. Enhancement of field emission in carbon nanotubes through adsorption of polar molecules. Applied Surface Science 206, 167−177.

Guo, Z., 2013. Study on the Electromagnetic Wave Absorbing Properties of Multi-walled Carbon Nanotube/cement Composites. Dalian University of Technology, Dalian, China (Dissertation for the Master Degree in Engineering).

Hamon, M.A., Hui, H., Bhowmik, P., Itkis, H., Haddon, R.C., 2002. Ester-functionalized soluble single-walled carbon nanotubes. Applied Physics A 74, 333−338.

Han, B., Yu, X., Kwon, E., 2009. A self-sensing carbon nanotube/cement composite for traffic monitoring. Nanotechnology 20, 445501.

Han, B., Yu, X., Ou, J., 2010a. Effect of water content on the piezoresistivity of MWNT/cement composites. Journal of Materials Science 45, 3714−3719.

Han, B., Yu, X., Kwon, E., Ou, J., 2010b. Piezoresistive multi-walled carbon nanotubes filled cement-based composites. Sensor Letters 8, 344−348.

Han, B., Yu, X., Ou, J., 2011a. Multifunctional and Smart Carbon Nanotube Reinforced Cement-based Materials. Nanotechnology in Civil Infrastructure. Springer, 1−47.

Han, B., Yu, X., Zhang, K., Kwon, E., Ou, J., 2011b. Sensing properties of CNT-filled cement-based stress sensors. Journal of Civil Structural Health Monitoring 1, 17−24.

Han, B., Zhang, K., Yu, X., Kwon, E., Ou, J., 2011c. Fabrication of piezoresistive CNT/CNF cementitious composites with superplasticizer as dispersant. Journal of Materials in Civil Engineering 24, 658−665.

Han, B., Yu, X., Kwon, E., Ou, J., 2012a. Effects of CNT concentration level and water/cement ratio on the piezoresistivity of CNT/cement composites. Journal of Composite Materials 46, 19−25.

Han, B., Zhang, K., Yu, X., Kwon, E., Ou, J., 2012b. Electrical characteristics and pressure-sensitive response measurements of carboxyl MWNT/cement composites. Cement and Concrete Composites 34, 794−800.

Han, B., Yang, Z., Shi, X., Yu, X., 2013a. Transport properties of carbon-nanotube/cement composites. Journal of Materials Engineering and Performance 22, 184−189.

Han, B., Zhang, K., Burnham, T., Kwon, E., Yu, X., 2013b. Integration and road tests of a self-sensing CNT concrete pavement system for traffic detection. Smart Materials and Structures 22, 015020.

Howser, R.N., Dhonde, H.B., Mo, Y.L., 2011. Self-sensing of carbon nanofiber concrete columns subjected to reversed cyclic loading. Smart Materials and Structures 20, 085031.

Huang, S., 2012. Multifunctional Graphite Nanoplatelets (GNP) Reinforced Cementitious Composites. National University of Singapore, Singapore (Dissertation for the Degree of Master of Engineering).

Hunashyal, A.M., Sundeep, G.V., Quadri, S.S., Banapurmath, N.R., 2011a. Experimental investigations to study the effect of carbon nanotubes reinforced in cement-based matrix composite beams. Proceedings of the Institution of Mechanical Engineers, Part N: Journal of Nanoengineering and Nanosystems 225, 17−22.

Hunashyal, A.M., Tippa Sagar, V., Quadri, S.S., Banapurmath, N.R., 2011b. Experimental investigation on effect of carbon nanotubes and carbon fibres on the behavior of plain cement mortar composite round bars under direct tension. ISRN Nanotechnology, 1, 6 pp.

Kerienė, J., Kligys, M., Laukaitis, A., Yakovlev, G., Špokauskas, A., Aleknevičius, M., 2013. The influence of multi-walled carbon nanotubes additive on properties of non-autoclaved and autoclaved aerated concretes. Construction and Building Materials 49, 527−535.

Kim, H.K., Nam, I.W., Lee, H.K., 2014. Enhanced effect of carbon nanotube on mechanical and electrical properties of cement composites by incorporation of silica fume. Composite Structures 107, 60−69.

Konsta-Gdoutos, M.S., Metaxa, Z.S., Shah, S.P., Gettu, R., 2008. Nanoimaging of highly dispersed carbon nanotube reinforced cement based materials. In: Seventh Intl. RILEM Symp. On Fiber Reinforced Concrete: Design and Applications, Chennai, India, pp. 125−131.

Konsta-Gdoutos, M.S., Metaxa, Z.S., Shah, S.P., 2010a. Highly dispersed carbon nanotube reinforced cement based materials. Cement and Concrete Research 40, 1052−1059.

Konsta-Gdoutos, M.S., Metaxa, Z.S., Shah, S.P., 2010b. Multi-scale mechanical and fracture characteristics and early-age strain capacity of high performance carbon nanotube/cement nanocomposites. Cement and Concrete Composites 32, 110−115.

Li, C., Chou, T., 2008. Modeling of damage sensing in fiber composites using carbon nanotube networks. Composites Science and Technology 68, 3373−3379.

Li, G., Wang, P., Zhao, X., 2005. Mechanical behavior and microstructure of cement composites incorporating surface-treated multi-walled carbon nanotubes. Carbon 43, 1239−1245.

Li, G., Wang, P., Zhao, X., 2007. Pressure-sensitive properties and microstructure of carbon nanotube reinforced cement composites. Cement and Concrete Composites 29, 377−382.

Ludvig, P., Ladeira, L., Calixto, J., 2009. In-situ synthesis of multiwall carbon nanotubes on portland cement clinker. In: 11th International Conference on Advanced Materials. Rio de Janeiro, Brazil.

Ludvig, P., Calixto, J.M., Ladeira, L.O., Gaspar, I.C., 2011. Using converter dust to produce low cost cementitious composites by in situ carbon nanotube and nanofiber synthesis. Materials 4, 575−584.

Luo, J., Duan, Z., Li, H., 2009. The influence of surfactants on the processing of multi-walled carbon nanotubes in reinforced cement matrix composites. Physica Status Solidi (a) 206, 2783−2790.

Luo, J., Duan, Z., Xian, G., Li, Q., Zhao, T., 2011. Fabrication and fracture toughness properties of carbon nanotube-reinforced cement composite. The European Physical Journal Applied Physics 53, 30402.

Luo, J., Duan, Z., Xian, G., Li, Q., Zhao, T., 2013. Damping performances of carbon nanotube reinforced cement composite. Mechanics of Advanced Materials and Structures 46, 90−98.

Luo, J., 2009. Fabrication and functional properties of multi-walled carbon nanotube/cement composites. Harbin Institute of Technology, Harbin, China (Dissertation for the Doctoral Degree in Engineering).

Lv, S., Ma, Y., Qiu, C., Sun, T., Liu, J., Zhou, Q., 2013. Effect of graphene oxide nanosheets of microstructure and mechanical properties of cement composites. Construction and Building Materials 49, 121−127.

Mackenzie, K.J., Bolton, M.J., 2009. Electrical and mechanical properties of aluminosilicate inorganic polymer composites with carbon nanotubes. Journal of Materials Science 44, 2851−2857.

Makar, J.M., Beaudoin, J.J., 2004. Carbon nanotubes and their application in the construction industry. Special Publication-Royal Society of Chemistry 292, 331−342.

Makar, J.M., Chan, G.W., 2009. Growth of cement hydration products on single-walled carbon nanotubes. Journal of the American Ceramic Society 92, 1303−1310.

Makar, J.M., Margeson, J., Luh, J., 2005. Carbon nanotube/cement composites-early results and potential applications. In: Proceedings of the 3rd International Conference on Construction Materials: Performance, Innovations and Structural Implications, Vancouver, Canada, pp. 1−10.

Materazzi, A.L., Ubertini, F., Alessandro, A.D., 2013. Carbon nanotube cement-based transducers for dynamic sensing of strain. Cement and Concrete Composites 37, 2−11.

Mendoza, O., Sierra, G., Tobón, J.I., 2013. Influence of super plasticizer and $Ca(OH)_2$ on the stability of functionalized multi-walled carbon nanotubes dispersions for cement composites applications. Construction and Building Materials 47, 771−778.

Metaxa, Z.S., Konsta-Gdoutos, M.S., Shah, S.P., 2009. Carbon Nanotubes Reinforced Concrete. ACI Special Publication, 267.

Metaxa, Z.S., Konsta-Gdoutos, M.S., Shah, S.P., 2010. Carbon nanofiber-reinforced cement-based materials. Transportation Research Record: Journal of the Transportation Research Board 2142, 114−118.

Metaxa, Z.S., Konsta-Gdoutos, M.S., Shah, S.P., 2012a. Carbon nanofiber cementitious composites: effect of debulking procedure on dispersion and reinforcing efficiency. Cement and Concrete Composites 36, 25−32.

Metaxa, Z.S., Seo, J.T., Konsta-Gdoutos, M.S., Hersam, M.C., Shah, S.P., 2012b. Highly concentrated carbon nanotube admixture for nano-fiber reinforced cementitious materials. Cement and Concrete Composites 34, 612−617.

Mo, Y.L., Roberts, R.H., 2013. Carbon nanofiber concrete for damage detection of infrastructure. In: Nanotechnology and Nanomaterials: Advances in Nanofibers (Chapter 5), ISBN 978-953-51-1209-9, pp. 125−143. http://dx.doi.org/10.5772/57096.

Moisala, A., Nasibulin, A.G., Kauppinen, E.I., 2003. The role of metal nanoparticles in the catalytic production of single-walled carbon nanotubes-a review. Journal of Physics: Condensed Matter 15, S3011.

Moore, V.C., Strano, M.S., Haroz, E.H., Hauge, R.H., Smalley, R.E., Schmidt, J., Talmon, Y., 2003. Individually suspended single-walled carbon nanotubes in various surfactants. Nano Letters 3, 1379−1382.

Morsy, M.S., Alsayed, S.H., Aqel, M., 2011. Hybrid effect of carbon nanotube and nano-clay on physico-mechanical properties of cement mortar. Construction and Building Materials 25, 145−149.

Mudimela, P.R., Nasibulina, L.I., Nasibulin, A.G., Cwirzen, A., Valkeapää, M., Habermehl-Cwirzen, K., Malm, J.E., Karppinen, M.J., Penttala, V., Koltsova, T.S., 2009. Synthesis of carbon nanotubes and nanofibers on silica and cement matrix materials. Journal of Nanomaterials 2009 (29), 3pp.

Mukhopadhyay, A.K., 2011. Next-generation Nano-based Concrete Construction Products: A Review. Nanotechnology in Civil Infrastructur. Springer, pp. 207−223.

Musso, S., Tulliani, J., Ferro, G., Tagliaferro, A., 2009. Influence of carbon nanotubes structure on the mechanical behavior of cement composites. Composites Science and Technology 69, 1985−1990.

Nalla, V., Polavarapu, L., Manga, K.K., Goh, B.M., Loh, K.P., Xu, Q., Ji, W., 2010. Transient photoconductivity and femtosecond nonlinear optical properties of a conjugated polymer-graphene oxide composite. Nanotechnology 21, 415203.

Nasibulin, A.G., Pikhitsa, P.V., Jiang, H., Brown, D.P., Krasheninnikov, A.V., Anisimov, A.S., Queipo, P., Moisala, A., Gonzalez, D., Lientschnig, G., 2007. A novel hybrid carbon material. Nature Nanotechnology 2, 156−161.

Nasibulin, A.G., Shandakov, S.D., Nasibulina, L.I., Cwirzen, A., Mudimela, P.R., Habermehl-Cwirzen, K., Grishin, D.A., Gavrilov, Y.V., Malm, J.E., Tapper, U., 2009. A novel cement-based hybrid material. New Journal of Physics 11, 023013.

Nasibulin, A.G., Koltsova, T., Nasibulina, L.I., Anoshkin, I.V., Semencha, A., Tolochko, O.V., Kauppinen, E.I., 2013. A novel approach to composite preparation by direct synthesis of carbon nanomaterial on matrix or filler particles. Acta Materialia 61, 1862−1871.

Nasibulina, L.I., Anoshkin, I.V., Shandakov, S.D., Nasibulin, A.G., Cwirzen, A., Mudimela, P.R., Habermehl-Cwirzen, K., Malm, J.E., Koltsova, T.S., Tian, Y., 2010. Direct synthesis of carbon nanofibers on cement particles. Transportation Research Record: Journal of the Transportation Research Board 2142, 96−101.

Nasibulina, L.I., Anoshkin, I.V., Semencha, A.V., Tolochko, O.V., Malm, J.E., Karppinen, M.J., Nasibulin, A.G., Kauppinen, E.I., 2012. Carbon nanofiber/clinker hybrid material as a highly efficient modificator of mortar mechanical properties. Materials Physics and Mechanics 13, 77—84.

Nochaiya, T., Chaipanich, A., 2011. Behavior of multi-walled carbon nanotubes on the porosity and microstructure of cement-based materials. Applied Surface Science 257, 1941—1945.

Pacheco-Torgal, F., Jalali, S., 2011. Nanotechnology: advantages and drawbacks in the field of construction and building materials. Construction and Building Materials 25, 582—590.

Pan, Z., Duan, W., Li, D., Collins, F., 2013. Graphene Oxide Reinforced Cement and Concrete. Google Patents. WO2013096990 A1.

Parveen, S., Rana, S., Fangueiro, R., 2013. A review on nanomaterial dispersion, microstructure and mechanical properties of carbon nanotube and nanofiber reinforced cementitious composites. Journal of Nanomaterials 80, 19 pp.

Peyvandi, A., Sbia, L.A., Soroushian, P., Sobolev, K., 2013a. Effect of the cementitious paste density on the performance efficiency of carbon nanofiber in concrete nanocomposite. Construction and Building Materials 48, 265—269.

Peyvandi, A., Soroushian, P., Balachandra, A.M., Sobolev, K., 2013b. Enhancement of the durability characteristics of concrete nanocomposite pipes with modified graphite nano-platelets. Construction and Building Materials 47, 111—117.

Raki, L., Beaudoin, J., Alizadeh, R., Makar, J., Sato, T., 2010. Cement and concrete nanoscience and nanotechnology. Materials 3, 918—942.

Saafi, M., 2009. Wireless and embedded carbon nanotube networks for damage detection in concrete structures. Nanotechnology 20, 395502.

Saez De Ibarra, Y., Gaitero, J.J., Erkizia, E., Campillo, I., 2006. Atomic force microscopy and nanoindentation of cement pastes with nanotube dispersions. Physica Status Solidi (a) 203, 1076—1081.

Sanchez, F., 2009. Carbon nanofibre/cement composites: challenges and promises as structural materials. International Journal of Materials and Structural Integrity 3, 217—226.

Sanchez, F., Ince, C., 2009. Microstructure and macroscopic properties of hybrid carbon nanofiber/silica fume cement composites. Composites Science and Technology 69, 1310—1318.

Sanchez, F., Sobolev, K., 2010. Nanotechnology in concrete-a review. Construction and Building Materials 24, 2060—2071.

Shah, S.P., Konsta-Gdoutos, M.S., Metaxa, Z.S., 2009a. Highly-Dispersed Carbon Nanotube-Reinforced Cement-Based Materials. U.S. Patent Application 12/322,842.

Shah, S.P., Konsta-Gdoutos, M.S., Metaxa, Z.S., Mondal, P., 2009b. Nanoscale Modification of Cementitious Materials. Nanotechnology in Construction 3. Springer, pp. 125—130.

Shah, S.P., Konsta-Gdoutos, M.S., Metaxa, Z.S., 2010. Exploration of fracture characteristics, nanoscale properties and nanostructure of cementitious matrices with carbon nanotubes and carbon nanofibers. In: Proceedings of the 7th International Conference on Fracture Mechanics of Concrete and Concrete Structures.

Shah, S.P., Konsta-Gdoutos, M.S., Metaxa, Z.S., 2011. Advanced Cement Based Nano-composites. Recent Advances in Mechanics. Springer, pp. 313—327.

Shukla, P., Bhatia, V., Gaur, V., Basniwal, R.K., Singh, B.K., Jain, V.K., 2012. Multiwalled carbon nanotubes reinforced portland cement composites for smoke detection. Solid State Phenomena 185, 21—24.

Siddique, R., Mehta, A., 2014. Effect of carbon nanotubes on properties of cement mortars. Construction and Building Materials 50, 116—129.

Singh, A.P., Mishra, M., Chandra, A., Dhawan, S.K., 2011. Graphene oxide/ferrofluid/cement composites for electromagnetic interference shielding application. Nanotechnology 22, 465701.

Singh, A.P., Gupta, B.K., Mishra, M., Chandra, A., Mathur, R.B., Dhawan, S.K., 2013. Multiwalled carbon nanotube/cement composites with exceptional electromagnetic interference shielding properties. Carbon 56 (5), 86−96.

Sobolev, K., Gutiérrez, M.F., 2005. How nanotechnology can change the concrete world. American Ceramic Society Bulletin 84, 14−18.

Sobolkina, A., Mechtcherine, V., Khavrus, V., Maier, D., Mende, M., Ritschel, M., Leonhardt, A., 2012. Dispersion of carbon nanotubes and its influence on the mechanical properties of the cement matrix. Cement and Concrete Composites 34, 1104−1113.

Sun, S., Yu, X., Han, B., 2014. Sensing mechanism of self-monitoring CNT cementitious composite. Journal of Testing and Evaluation 1−42.

Tyson, B.M., 2013. Carbon Nanotube and Nanofiber Reinforcement for Improving the Flexural Strength and Fracture Toughness of Portland Cement Paste. Texas A&M University, Texas, America (Dissertation for the Degree of Master of Science).

Tyson, B.M., Al-Rub, R.K.A., Yazdanbakhsh, A., Grasley, Z., 2011. Carbon nanotubes and carbon nanofibers for enhancing the mechanical properties of nanocomposite cementitious materials. Journal of Materials in Civil Engineering 23, 1028−1035.

Veedu, V.P., 2011. Multifunctional Cementitious Nanocomposite Material and Methods of Making the Same. Google Patents. US7875211 B1.

Vera-Agullo, J., Chozas-Ligero, V., Portillo-Rico, D., García-Casas, M.J., Gutiérrez-Martínez, A., Mieres-Royo, J.M., Grávalos-Moreno, J., 2009. Mortar and Concrete Reinforced with Nanomaterials. Nanotechnology in Construction 3. Springer, pp. 383−388.

Wang, L., Ding, T., Wang, P., 2009. Influence of carbon black concentration on piezoresistivity for carbon-black-filled silicone rubber composite. Carbon 47, 3151−3157.

Wong, S.S., Joselevich, E., Woolley, A.T., Cheung, C.L., Lieber, C.M., 1998. Covalently functionalized nanotubes as nanometre-sized probes in chemistry and biology. Nature 394, 52−55.

Xie, X., Mai, Y., Zhou, X., 2005. Dispersion and alignment of carbon nanotubes in polymer matrix: a review. Materials Science and Engineering: R: Reports 49, 89−112.

Yakovlev, G., Kerienė, J., Gailius, A., Girnienė, I., 2006. Cement based foam concrete reinforced by carbon nanotubes. Materials Science 12, 147−151.

Yazdanbakhsh, A., 2013. Production, Characterization, and Mechanical Behavior of Cementitious Materials Incorporating Carbon Nanofibers. Texas A&M University, Texas, America.

Yazdanbakhsh, A., Grasley, Z., 2012. The theoretical maximum achievable dispersion of nanoinclusions in cement paste. Cement and Concrete Research 42, 798−804.

Yazdanbakhsh, A., Grasley, Z.C., Tyson, B., Al-Rub, R.A., 2009. Carbon Nano Filaments in Cementitious Materials: Some Issues on Dispersion and Interfacial Bond. ACI Special Publication, 267.

Yazdanbakhsh, A., Grasley, Z., Tyson, B., Abu Al-Rub, R.K., 2010. Distribution of carbon nanofibers and nanotubes in cementitious composites. Transportation Research Record: Journal of the Transportation Research Board 2142, 89−95.

Yazdanbakhsh, A., Grasley, Z., Tyson, B., Al-Rub, R.A., 2012. Challenges and benefits of utilizing carbon nanofilaments in cementitious materials. Journal of Nanomaterials 2012, 7 (3), 4661−4677.

Yu, X., Kwon, E., 2009. A carbon nanotube/cement composite with piezoresistive properties. Smart Materials and Structures 18, 055010.

Yu, J., Grossiord, N., Koning, C.E., Loos, J., 2007. Controlling the dispersion of multi-wall carbon nanotubes in aqueous surfactant solution. Carbon 45, 618−623.

Zhao, J., Shi, D., Lian, J., 2009. Small angle light scattering study of improved dispersion of carbon nanofibers in water by plasma treatment. Carbon 47, 2329−2336.

Zuo, J., Yao, W., Wu, K., 2014. Seebeck effect and mechanical properties of carbon nanotube-carbon fiber/cement nanocomposites. Fullerenes, Nanotubes and Carbon Nanostructures 23 (5), 383−391.

Nanoclay modified asphalt

9

Hui Yao [1,2], *Zhanping You* [1]

[1]Michigan Technological University, Houghton, MI, USA; [2]School of Traffic and Transportation Engineering, Changsha University of Science and Technology, China

9.1 Introduction

Nowadays, there are far more highways and expressways being constructed and maintained in the world. Due to climate change and global warming, engineers are now required to find a solution to the problem of how to modify and improve the quality and lifespan of pavements. Nanomaterials have been introduced and used for pavement engineering to improve pavement performance.

Currently, two major kinds of modifiers are used in asphalt modification for road construction. Fibers and polymers, such as styrene butadiene styrene (SBS), styrene butadiene rubber (SBR), ethylvinyl acetate (EVA), crumb rubber, and carbon fibers, are also used. The performance of SBS-modified binder in asphalt mixtures has been investigated by many researchers. The microstructure of SBS-modified asphalt binder has also been studied in previous research. The SBS modifier significantly improved the low-temperature performance of the modified asphalt binder, and slightly enhanced the high-temperature performance, as well as the resistance to permanent deformation (Ahmedzade et al., 2007; Al-Hadidy and Yi-qiu, 2010; Awanti et al., 2008; Cortizo et al., 2004; Fu et al., 2007; Iskender et al., 2012; Khodaii and Mehrara, 2009; Larsen et al., 2009; Liu and Bao, 2007; Liu et al., 2007, 2010a; Ouyang et al., 2006a; Shang et al., 2011; Wu et al., 2009; Yildirim, 2007). Compared to the base asphalt binder, the SBR-modified asphalt binder prevented the pavement from low-temperature cracking, and increased the low-temperature ductility. The viscosity and elastic recovery ability of SBR-modified asphalt binder also increased (Yildirim, 2007; Li et al., 2011; Zhang et al., 2005, 2008, 2009; Zhang and Yu, 2011). The addition of EVA into the base asphalt binder increased the high-temperature performance of modified asphalt mixture (Airey, 2002). Crumb rubber is widely used in road construction and research due to environmental protection and the use of waste products. When the crumb rubber was added into the base asphalt binder, the viscosity and rheological properties improved. The rutting resistance and thermal cracking of the modified asphalt mixtures significantly enhanced the base asphalt mixture. The research results also show that the rubber type, content, binder type, and mixing condition affect the performance of modified asphalt binders and mixtures (Abdelrahman and Carpenter, 1999; Bertollo et al., 2003; Huang and Mohammad, 2002; Kim et al., 2001; Wang et al., 2013, 2012; Xiang et al., 2009; Xiao et al., 2009). The addition of carbon fibers into the base asphalt also showed improvement of the adhesion characteristics and cracking resistance at low

temperatures. The enhanced network and high connectivity of fiber-modified asphalt binder were shown in the microstructure at high magnifications (Jamal Khattak et al., 2013; Khattak et al., 2013, 2012; Yang et al., 2011; Yao et al., 2013).

Nanomaterials, are widely used and applied in the industry and research field as they bring innovations. Nanomaterials are defined as materials with at least one dimension that falls in the length scale of 1−100 nm. Nanomaterials are used in pavement engineering for their small size and large surface area. Recent research showed that the rutting and fatigue-cracking resistance of asphalt binders and mixtures improved with the addition of nanomaterials. Nanoclay and carbon nanofiber were used as additives to modify the asphalt binder. The complex shear modulus of nanomodified asphalt binders increased relative to the control asphalt binder, as well as the failure temperature and high-temperature performance grade. The rutting resistance performance of nanoclay and the carbon fiber modified asphalt mixtures was also enhanced (Goh et al., 2011; Ghile, 2006; Jahromi and Khodaii, 2009; You et al., 2011; Khattak et al., 2011; Xiao et al., 2011). Nanosized hydrated lime was selected as the additive to blend with a warm-mix-asphalt (WMA) mixture. The moisture susceptibility of the WMA mixture was investigated in the study (Cheng et al., 2011). In addition, the combination of nano-SiO_2 and SBS was used to mix with the stone matrix asphalt, and the physical and mechanical properties of asphalt binders and mixtures were show to improve (Mojtaba et al., 2012). In this study, two kinds of nanoclay were used to modify the asphalt, and the performance was evaluated.

9.2　Key problem and motivation

Pavement distresses are one of the main problems in maintaining the pavement lifecycle. To prevent the pavement from permanent deformation and low-temperature cracking, modifications to the asphalt mixtures are needed. Nanomaterials have some incredible features that can fundamentally change the properties of asphalt binders and mixtures. The chemical reactions or physical dispersions between asphalt and nanomaterials can alter the microstructures and compositions of asphalt binders, and strengthen the elastic performance of an asphalt binder at high temperatures, as well as the viscous property at low temperatures. Based on the literature review (You et al., 2011; Drozd et al., 2011; He and Shi, 2008; Simon et al., 2008), nanoclay has been widely used and studied in the industry or research, and its layer structure may be beneficial to the modification of asphalt binders. Therefore, two kinds of nanoclay have been selected to modify the control asphalt binder in this chapter.

9.3　Material properties and performance test plans

The materials used are nonmodified nanoclay (NMN) and polymer-modified nanoclay (PMN). The properties of raw nanoclay materials were examined by the Hitachi S-4700 field emission scanning electron microscope (FE-SEM) and Fourier transform infrared spectroscopy (FTIR). The microstructures and chemical compositions of

control NMN and PMN modified asphalt binders were also observed and tested by FE-SEM and FTIR. When the modified asphalt binders were prepared, the performance test plans were arranged to evaluate the properties of modified asphalt binders. (1) The rolling thin-film oven (RTFO) and pressure-aging vessel (PAV) test was conducted to simulate the short-term and long-term aging processes; (2) the rotational viscosity (RV) test of modified asphalt binders was conducted for the temperature range of mixing and testing; (3) the dynamic shear rheometer (DSR) test of modified asphalt binders was employed to obtain the complex shear modulus; (4) the bending beam rheometer (BBR) test was utilized to estimate the performance at low temperatures; and (5) the FTIR test was used to understand the molecular bonding in the modified asphalt binder, as well as the aging index and rate.

9.4   Preparation of nanoclay-modified asphalt binders

9.4.1   Materials

Nanoclay, layered mineral silicates, have several classes according to the chemical composition and morphology, such as montmorillonite, bentonite, kaolinite, etc. Montmorillonite is commonly used in industry and research. It can be modified by polymers to improve the heat resistance, biodegradability, mechanical properties (You et al., 2011). The raw nanoclay (NMN) used in this chapter is montmorillonite, and it is a 2:1 layered smectite with a plate structure. The layer of NMN (NMN is hydrophilic) is composed of sodium ions, and the high expansion pressure is shown in the microstructure. The structure of NMN leads to an exfoliation structure or crystal dispersion when it is modified by polymer (Jahromi and Khodaii, 2009; Drozd et al., 2011). The NMN microstructure images are observed by the Hitachi S-4700 FE-SEM (Figure 9.1). The composition of NMN or molecular bonding is examined by FTIR, and the images are shown in Figure 9.2.

   The PMN used in the chapter is normally produced from the hydrophilic nanoclay with the organic cation exchange. Montmorillonite can be dispersed in the polymer matrix to form PMN. The nanometer thickness in the nanocomposite can be transformed into the plate-like nanoparticles with the high (nm × μm) aspect ratio. Through the surface modification of the clay layers, the permeability is reduced, and tear and compression strengths improve. The microstructure images of PMN (the PMN is hydrophobic and organophilic via the modification by polysiloxane (Simon et al., 2008) are tested by FE-SEM and are shown in Figure 9.3. The composition of PMN or molecular bonding is examined by the FTIR, and the images are shown in Figure 9.4. The bulk densities of two nanoclay materials are 0.251 g/cm^3 (PMN) and 0.678 g/cm^3 (NMN), and both materials feature a maximum size of 200−400 nm in terms of aspect ratio (He and Shi, 2008).

   The asphalt graded PG 58-34 from a project site in Gladstone, Michigan, was used as the control asphalt binder. The control asphalt was premodified with acrylonitrile butadiene styrene (ABS) in order to improve the compatibility between the asphalt and polymers, and meet the low-temperature grade requirement. The microstructure of the control asphalt binder is tested by the FE-SEM, and the images are shown in

(a)

Layered structure and it is different from the PMN material

S4700 5.0kV 12.5mm ×20.0k SE(M)   2.00um

(b)

Agglomeration phenomena, layered and flat structure compared to the PMN

S4700 5.0kV 12.5mm ×3.00k SE(M)   10.0um
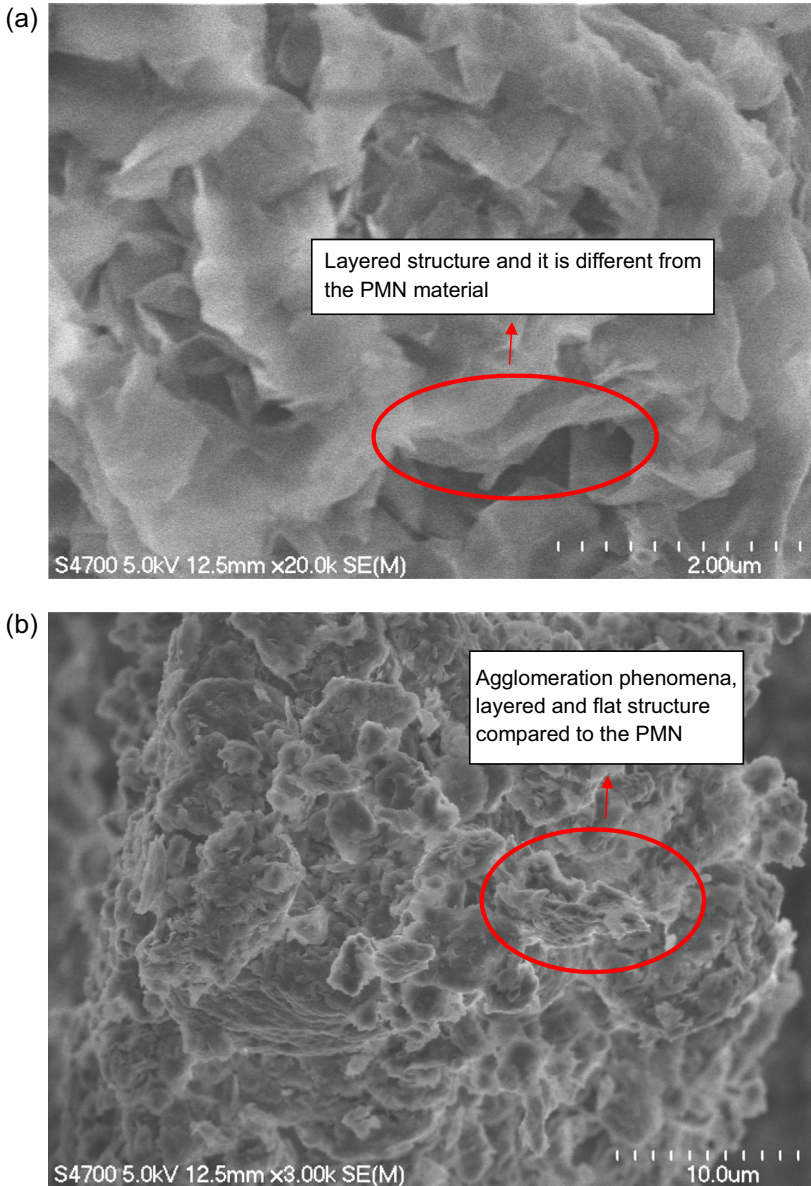
Figure 9.1 FE-SEM microstructure images of nonmodified nanoclay (NMN): (a) 20,000× magnification image of NMN, (b) 3000× magnification image of NMN, and (c) 1500× magnification image of NMN.
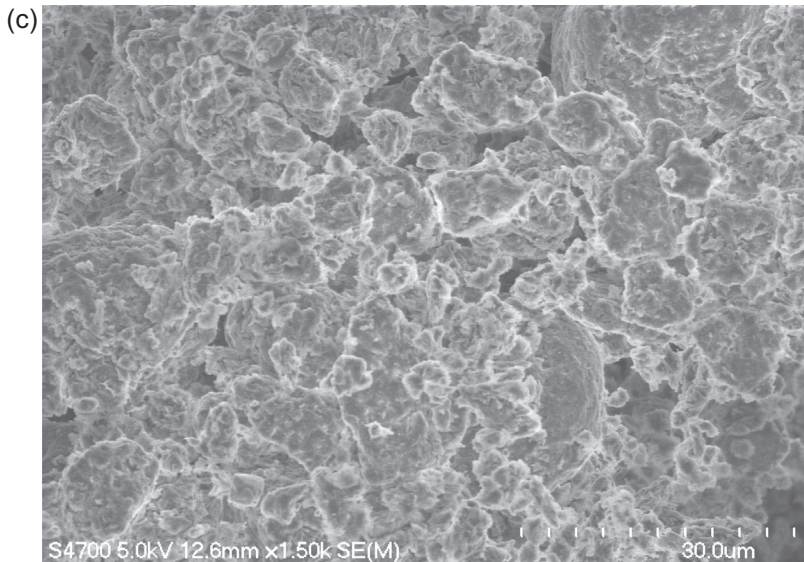
Figure 9.1 Continued.
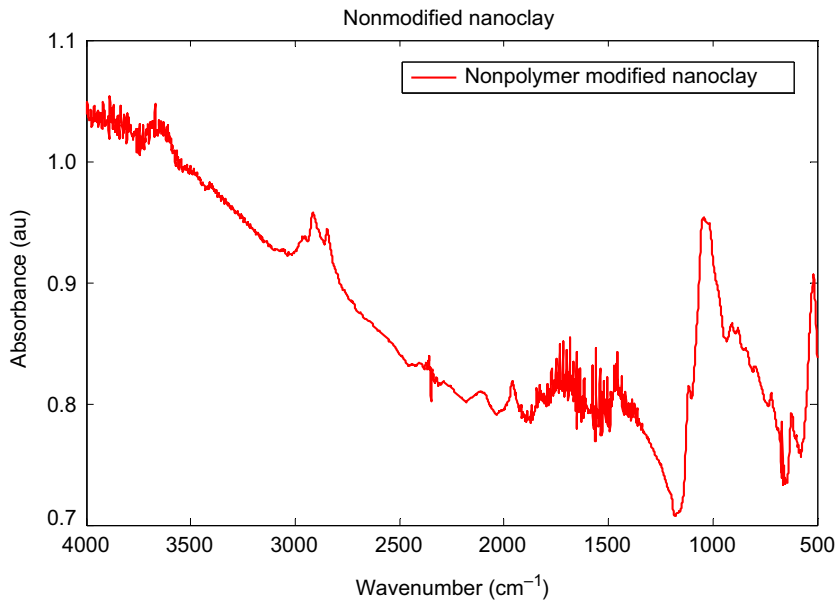
Figure 9.2 FTIR spectra of nonmodified nanoclay (NMN).

(a)

Layered structure and its surface is different from the NMN

S4700 5.0kV 12.7mm ×20.0k SE(M)   2.00um

(b)

Agglomeration phenomena, but the surface shows the "circle" shape and it aggregates together.

S4700 5.0kV 12.7mm ×3.00k SE(M)   10.0um
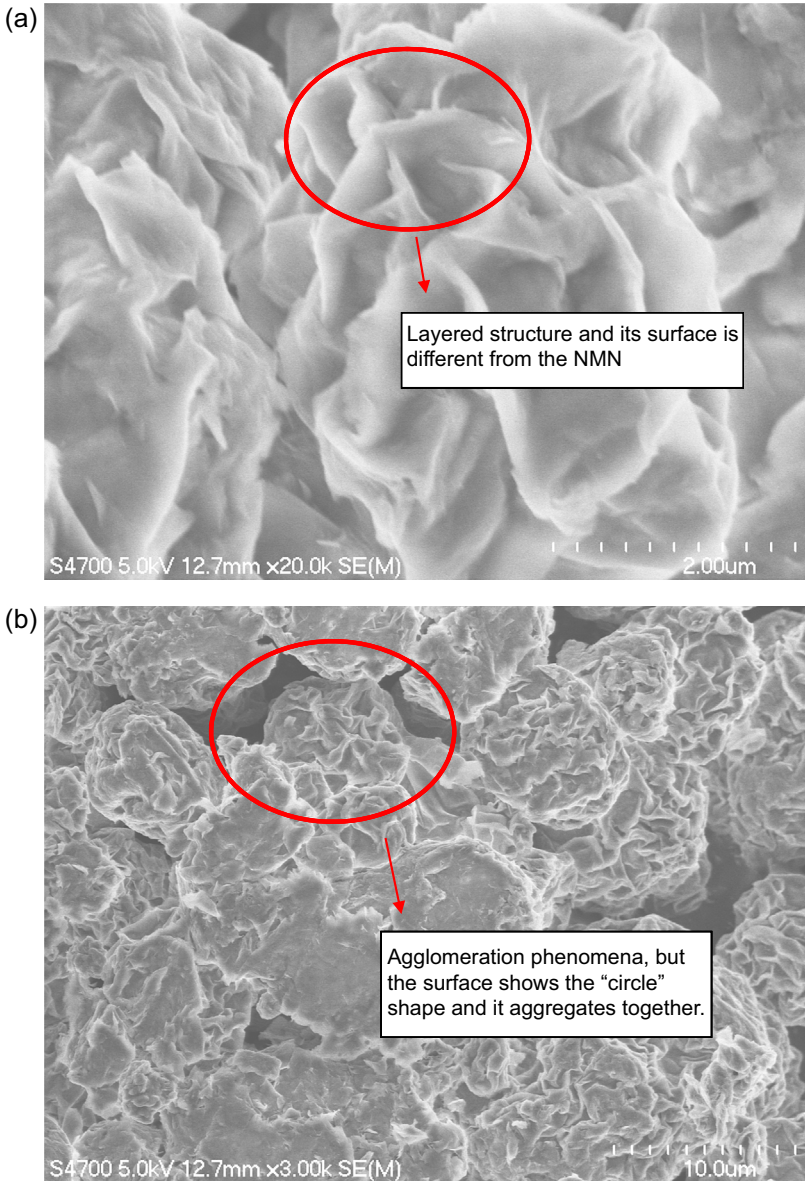
Figure 9.3 SEM microstructure images of polymer-modified nanoclay (PMN): (a) 20,000× magnification image of PMN, (b) 3000× magnification image of PMN, and (c) 1500× magnification image of PMN.
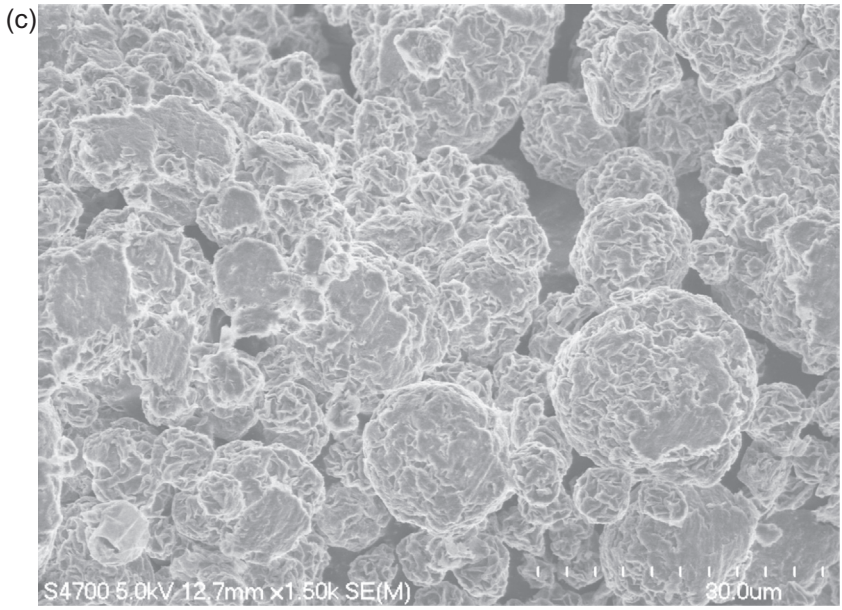
Figure 9.3 Continued.
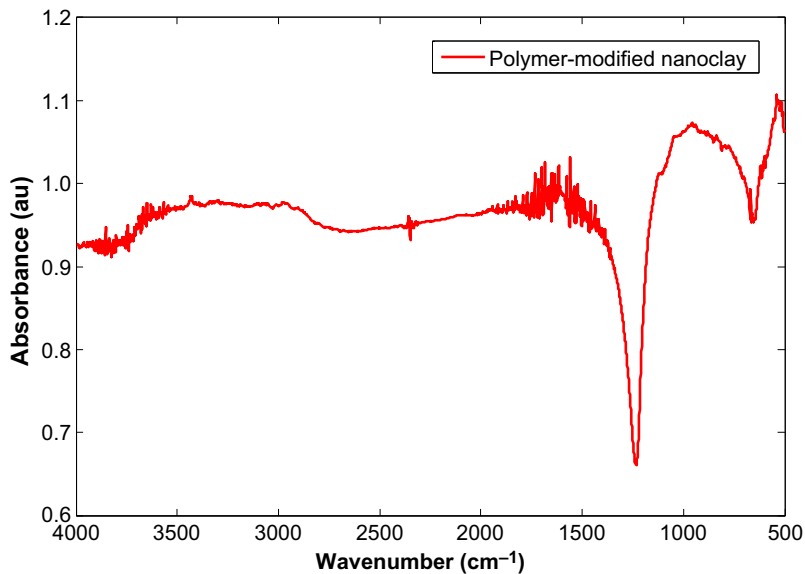
Figure 9.4 FTIR spectra of polymer-modified nanoclay (PMN).

Figure 9.5. The ABS presented in the control asphalt binder is tested by the FTIR spectra (FTIR section) (Figure 9.6).

Figure 9.1 shows the microstructure of the NMN material, and the agglomeration phenomena that occur in the particles of NMN due to the surface effects of nanomaterials when they are exposed to the air. The layer structure in the image is helpful for the asphalt binder to coat and react with. The shapes of NMN particles are irregular compared to the PMN particles, and the normal size ranges from 5 to 30 μm. Figure 9.3 shows the microstructure of the PMN material, and the shapes of PMN particles are like circles. This was caused by the size of the nanomaterials when they were exposed to the air under normal pressure. Due to the polysiloxane modification, the PMN particles keep their circular shape and exfoliated layer, so the structure is beneficial to melt with the base asphalt binder. The dispersion of PMN is slightly better, with an average conglomerate size of around 2 μm, when compared to NMN. From the micro-images of NMN and PMN materials, it is apparent that the agglomeration phenomena of materials occur, and some of the nanomaterials may stay at the nanometer-sized range. After the agglomeration of nanomaterials, the piece-shaped NMN and the circle-shaped PMN particles are observed by SEM. Note that although the SEM micrographs show particles of micron size, these nanoclay platelets (average spacing between platelets) still feature one of their dimensions at the nanometer level.

Figures 9.2 and 9.4 demonstrate the FTIR spectra of NMN and PMN materials. The FTIR spectra of NMN display the Si−O (Si) asymmetric stretching bonds (1085 cm^{-1}), the asymmetric vibration of Si−O (H) (near 975 cm^{-1}), and the O−H stretching bonds (3594 and 3735 cm^{-1}) in the NMN material. However, the peak areas (stretching C−C and C−O, and the bending C−H bonds located across 953−1180 cm^{-1}) of PMN material are more than those of the NMN material.

Figure 9.5 shows the plain structure of the control asphalt binder. The uneven surface of the control asphalt binder in the images is probably caused by making the sample. The white powders in the matrix could be the ABS, which is premodified in the base asphalt binder, and also is detected by the FTIR (FTIR section). The terrace structure is present in the edge of the control asphalt sample due to the process of making the sample. The control asphalt structure is observed at different magnifications to provide a comparison with the modified asphalt binders. Figure 9.6 shows the FTIR spectra of unaged, RTFO-aged, and PAV-aged control asphalt binders. The peak area of chemical bonding, at 1700 cm^{-1} (bending C═O conjugated), is increased intensively in the PAV-aged control asphalt binder relative to the unaged control asphalt binder. The violent oxidation reactions of the control asphalt binder accelerated significantly during the PAV aging process. It indirectly indicates that the carbonyl index ratio may be one of the aging indexes in the asphalt binder.

9.4.2 Modified asphalt binder sample

The NMN and PMN materials were weighted at concentrations of 2% and 4% by the weight of the control asphalt binder, and quickly added to the control asphalt binder. The NMN and PMN materials cannot be exposed to the air for too long to reduce the effect of agglomeration phenomena of nanomaterials. The modified asphalt binder was

(a)

It may be due to the pre-modification by the ABS

SU6600 20.0kV 11.3mm x1.00k BSE 30Pa   50.0um

(b)

Flat structure for the most part

SU6600 20.0kV 10.9mm x100 BSE 30Pa   500um
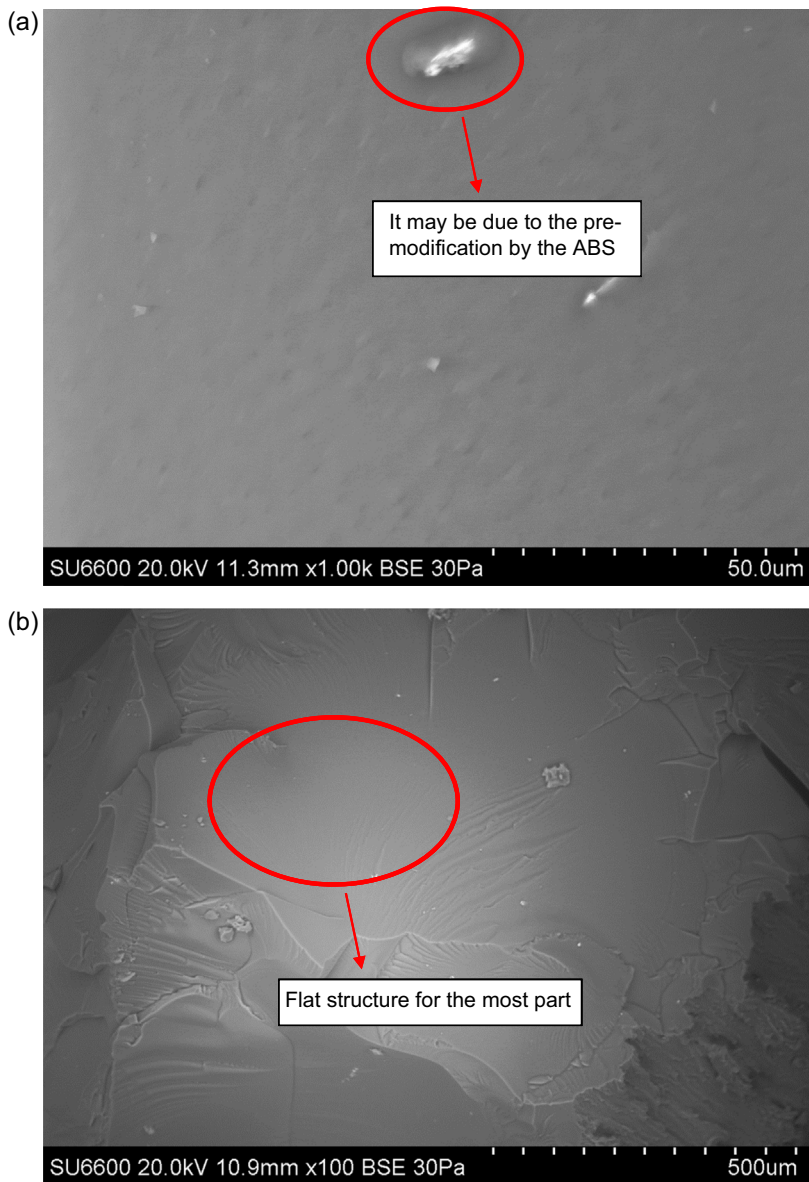
Figure 9.5 SEM microstructure images of control asphalt binder: (a) 1000× magnification image of control asphalt binder, and (b) 100× magnification image of control asphalt binder.
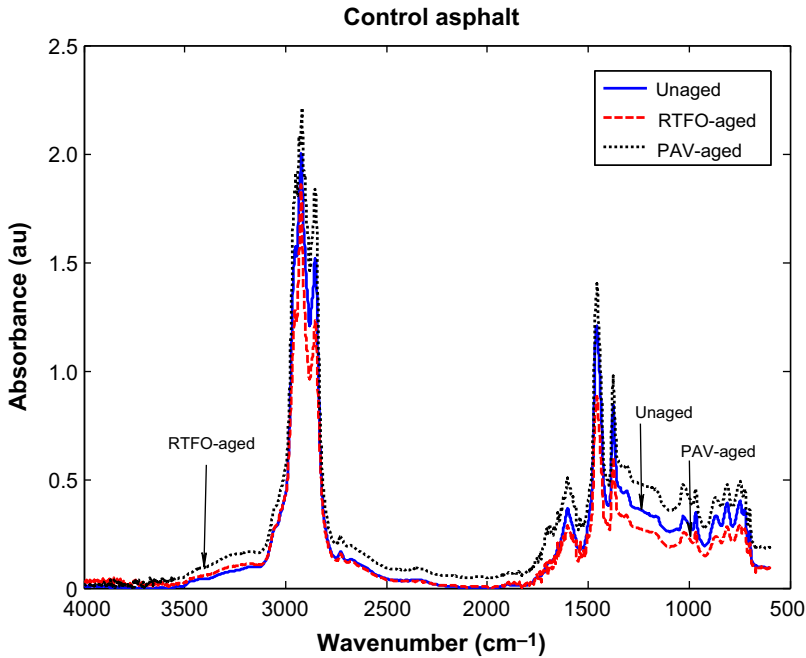
Control asphalt

Figure 9.6 FTIR spectra of control asphalt binder.

mixed using the high-shear mixing apparatus set at a 4000 rpm rotational speed and a temperature of around 135 °C. During the mixing of the modified asphalt binder, bubbles were floating to the surface of the asphalt binders, and the temperature of the modified asphalt binder increased. This might be due to chemical reactions between the nanomaterials and the control asphalt binder. All of the samples were mixed for around 2 h prior to the Superpave™ binder tests. In addition, the micro-images of NMN and PMN-modified asphalt binders were also obtained using a Hitachi SU6600 FE-SEM with a cryogenic stage, and the images are shown in Figures 9.7 and 9.8.

Figures 9.7 and 9.8 show the differences in the microstructures of NMN- and PMN-modified asphalt binders from the control asphalt binder. From these figures, it can be seen that agglomeration phenomena of nanomaterials has also happened in the asphalt binder and that the nanomaterials were melted uniformly in the control asphalt binder. Some large particles of NMN and PMN materials did not completely melt with the asphalt binder through the mixing process. Considering the mixing process and the condition, the effects of mixing and reactions are acceptable, because most of the particles melted and reacted with the asphalt binder. Based on the images of the control asphalt binder, the structures around the particles show the effect of a plate layer structure of NMN and PMN. The asphalt was intercalated into the plate layer of NMN material, and this could be due to the microstructure of NMN-modified asphalt binder. Compared to the structure of the NMN-modified asphalt binder, the

(a)

Physical dispersion of NMN in the asphalt matrix

SU6600 20.0kV 13.7mm x1.50k BSE 30Pa 12/9/2011   30.0um

(b)

Intercalation effects of NMN in the modified asphalt

Physical dispersion of NMN in the modified asphalt and chemical effects in the edge of NMN materials

SU6600 20.0kV 13.8mm x500 BSE 30Pa 12/9/2011   100um
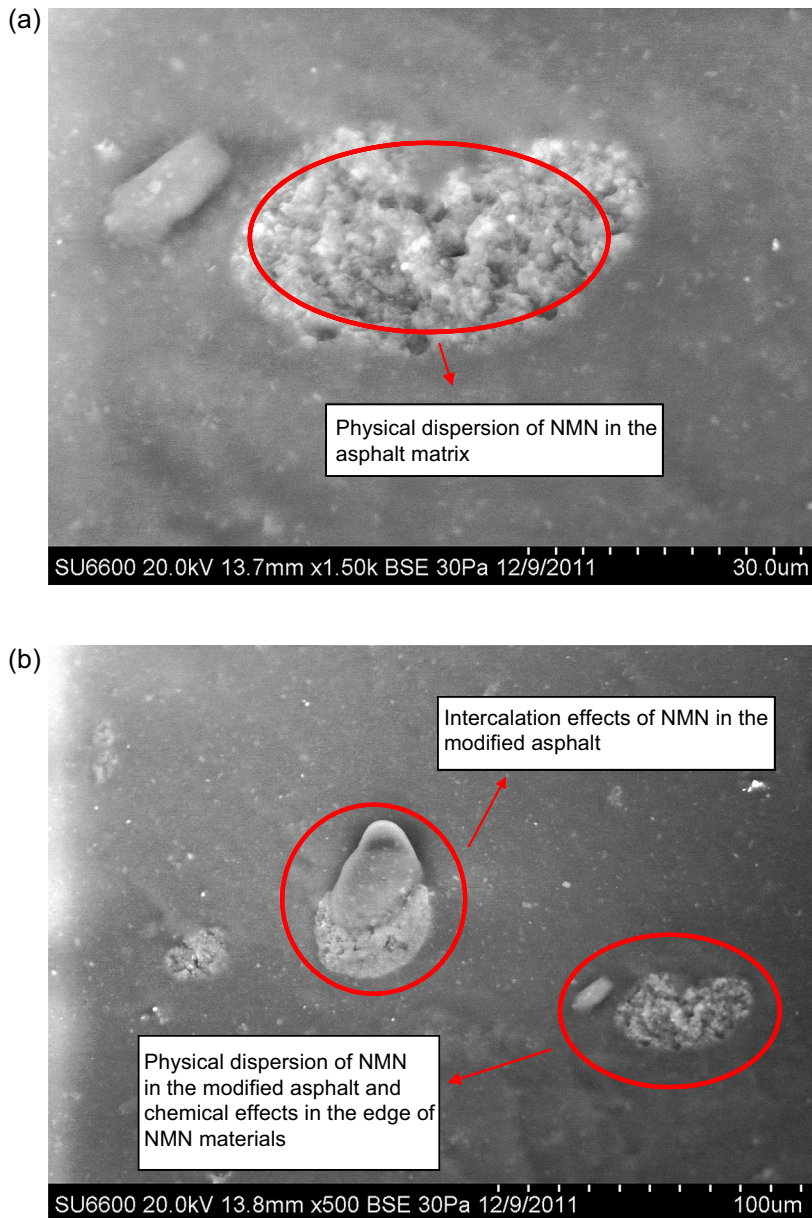
Figure 9.7 FE-SEM microstructure images of nonmodified nanoclay and NMN-modified asphalt binder: (a) 1500× magnification image of 4% NMN-modified asphalt binder, (b) 500× magnification image of 4% NMN-modified asphalt binder, and (c) 150× magnification image of 4% NMN-modified asphalt binder.

(c)

Physical dispersion and chemical reactions (intercalation and exfoliation) in the NMN-modified asphalt compared to the structure of the NMN material and the control asphalt. The surface of NMN-modified asphalt is different from that of the PMN-modified asphalt

SU6600 20.0kV 13.6mm x150 BSE 30Pa 12/9/2011   300um
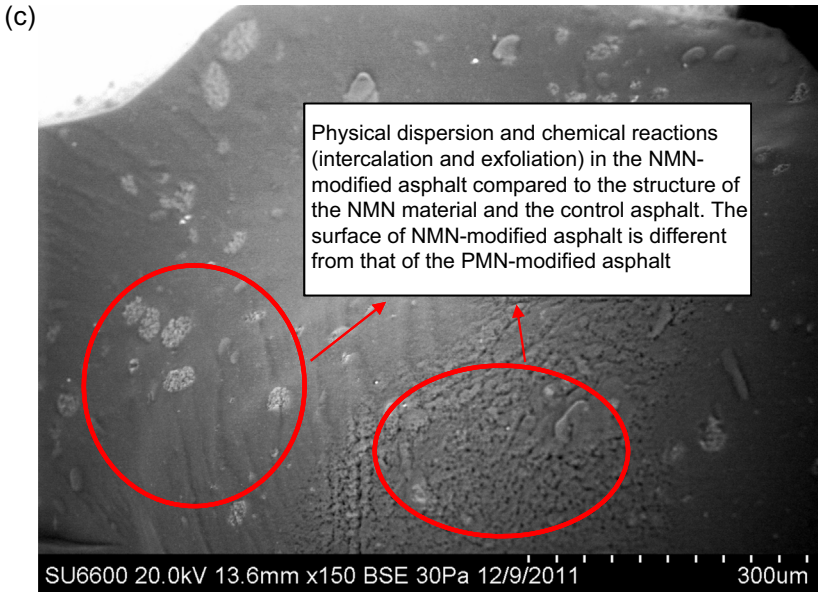
Figure 9.7 Continued.

asphalt was exfoliated into the plate layer of the PMN material. In other words, the NMN-modified asphalt binder has the most intercalated structure and the PMN-modified asphalt binder shows the most exfoliated structure through asphalt modification. Both structures hold the potential to improve the mechanical properties of modified asphalt binders.

9.5 Viscosity results of nanoclay-modified asphalt binders

The RV is the measurement of a fluid's resistance to flow. The asphalt samples were measured with the Brookfield viscometer at 100, 125, 135, 150, 175, and 190 °C. The 27# spindle was used in this test, and the test temperatures covered the range of mixing and compaction temperatures (AASHTO, 2006) in this chapter. The test results are shown in Figure 9.9.

Figure 9.9 shows the viscosity values of the control, NMN-modified, and PMN-modified asphalt binders. Compared to the control asphalt binder, the viscosity values of NMN-modified asphalt binders increase significantly, and the values of the 4% NMN-modified asphalt binder are higher than those of the 2% NMN-modified asphalt binder. However, the viscosity values of PMN-modified asphalt binders are almost on the same level with those of the control asphalt binder. The figure illustrates that all the viscosity data of asphalt binders under 135 °C pass the specification of the

(a)

The flat structure of PMN-modified asphalt is shown. It is likely that the effects of physical dispersion and chemical intercalation of PMN occur compared to the structure of PMN and control asphalt. The surface of PMN in the asphalt is different from the surface of PMN in the air.

SU6600 20.0kV 13.4mm x1.00k BSE 30Pa 12/9/2011   50.0um

(b)

Physical dispersion, and the effects of intercalation and exfoliation of PMN occur in the PMN-modified asphalt binder

SU6600 20.0kV 13.4mm x450 BSE 30Pa 12/9/2011   100um

Figure 9.8 FE-SEM microstructure images of polymer-modified nanoclay: (a) 1000× magnification image of 4% PMN-modified asphalt binder, (b) 450× magnification image of 4% PMN-modified asphalt binder, and (c) 100× magnification image of 4% PMN-modified asphalt binder.

Physical dispersion and chemical reactions (intercalation and exfoliation) are shown in the PMN-modified asphalt compared to the control asphalt; it is also different from the structure of NMN-modified asphalt

SU6600 20.0kV 13.2mm x100 BSE 30Pa 12/9/2011   500um
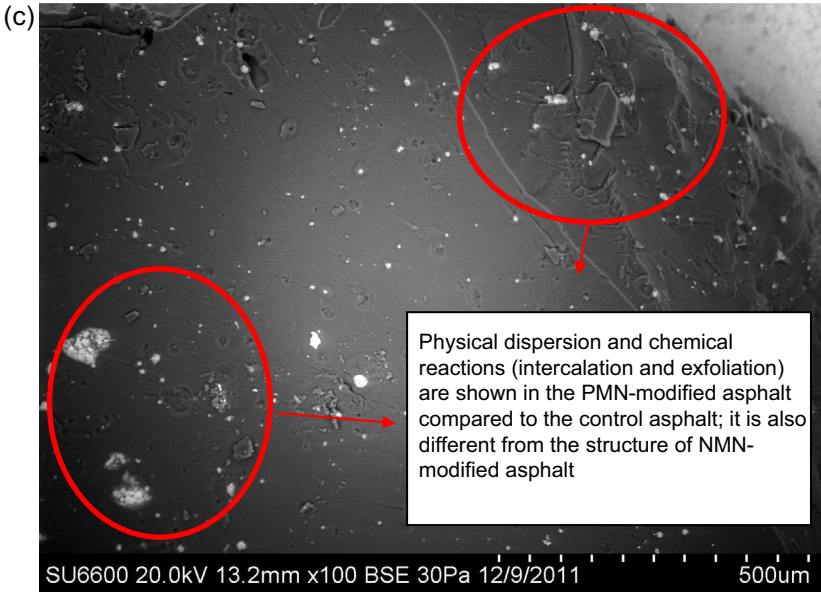
Figure 9.8 Continued.
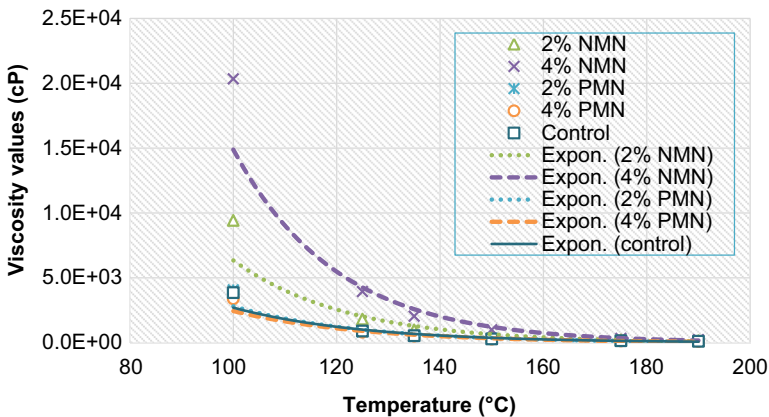
Figure 9.9 Viscosity values of the control and nanomaterial-modified asphalt binders.

Superpave™ Standard, and are lower than the limit of 3 Pa s. The viscosity of asphalt binders indicates the pumpability, mixability, and workability of binders. The high viscosity of asphalt binders leads to the high mixing and compaction temperatures, and may also contribute to the resistance to rutting. The NMN-modified asphalt binders hold the potential for improvement of rutting resistance, and the PMN-modified asphalt binder may lead to better fatigue cracking compared to the control asphalt binder.

9.6   DSR results of nanoclay-modified asphalt binders

The DSR is used to characterize the viscous and elastic behavior of the asphalt binder at medium and high temperatures. The complex shear modulus ($|G^*|$) and phase angle (δ) of asphalt binders are obtained from the tests. The modulus is used to evaluate the rutting potential of the asphalt binder at an unaged or short-term aging condition, and the phase angle represents the time lag between the applied shear stress and the resulting shear strain. When the phase angle is zero, the subject asphalt binder is a purely elastic material, and when the phase angle is 90°, it is a purely viscous material. A high modulus indicates that it is a stiffer asphalt binder at test temperatures, and that it has the potential to resist permanent deformation. The energy calculation equation is shown in Eqn (9.1) for the dissipated work per load cycle due to rutting.

$$\text{Rutting: Wc} \;=\; \pi\sigma_0^2\left[\frac{1}{G^*/\sin\delta}\right] \quad \text{(stress-controlled)} \tag{9.1}$$

And for dissipated work per load cycle due to fatigue cracking, the energy formula is shown in Eqn (9.2):

$$\text{Fatigue cracking: Wc} \;=\; \pi\varepsilon_0^2(G^*\sin\delta) \quad \text{(strain-controlled)} \tag{9.2}$$

where:

Wc = work dissipated per load cycle
σ = stress applied during load cycle
ε = strain during load cycle
G^* = complex shear modulus
δ = phase angle.

The test for the resistance to permanent deformation is conducted on the unaged and RTFO-aged asphalt binder, and the fatigue cracking test is tested on the PAV-aged asphalt binder. Furthermore, when the load is applied in each cycle, the work from each loading is transferred into the pavement. A portion of the work is absorbed by the pavement and reflected as the elastic response. The remaining energy is converted into damage in the form of rutting, fatigue cracking, and crack propagation. Therefore, the low dissipated energies per load cycle indicate that the asphalt binder and mixture have good resistance to rutting in the stress-controlled model. However, the high dissipated energies per load cycle lead to better rutting resistance in the asphalt binders and mixtures under the strain-controlled model. The stress-controlled model analyses are adopted in this chapter, and the results are shown below.

9.6.1   NMN-modified asphalt binder

Figure 9.10 demonstrates the complex shear modulus master curves of the NMN-modified asphalt binder and the control asphalt binder. From the figure, it can be
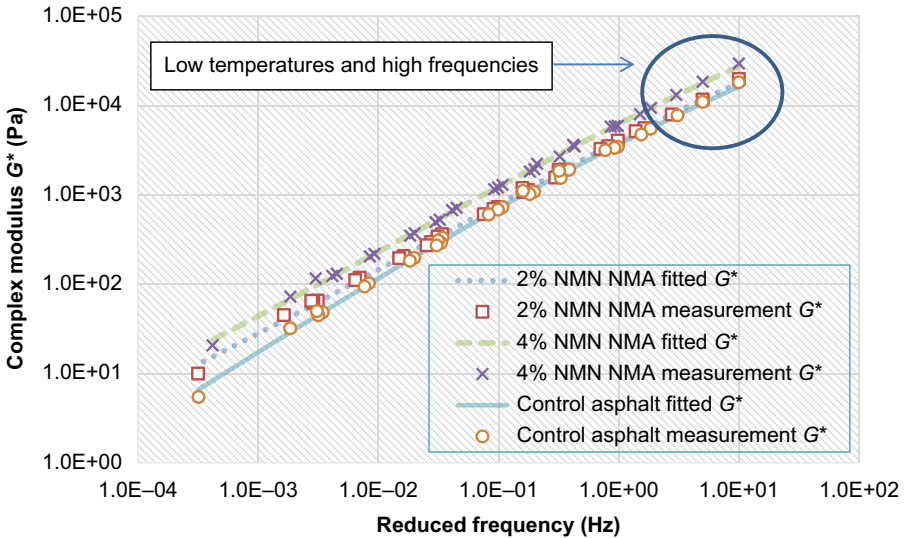
Figure 9.10 Complex shear modulus ($|G^*|$) master curves of control and NMN-modified asphalt binders.

deduced that the complex modulus values of the 2% and 4% NMN-modified asphalt binder are higher than those of the control asphalt binder, and the complex shear modulus values of the 2% NMN-modified asphalt binder are close to those of the control asphalt binder at low temperatures or at high frequencies. However, the values of the 2% NMN-modified asphalt binder are higher than those of control asphalt binder under high temperatures and low frequencies. With the addition of 4% NMN material into the control asphalt binder, the complex shear modulus increases by an average of 170% whereas the 2% NMN-modified asphalt just increases by an average of 45%. Based on the literature reviews (Jahromi and Khodaii, 2009; Simon et al., 2008), when the NMN material is added into the control asphalt binder, it is likely that the ions and the layer of NMN are intercalated and exfoliated partially in the asphalt binder due to the cation exchanges. Ca^{2+}, Mg^{2+} and ammonium in asphalt are the major exchangeable cations in the reaction process. The layer intercalations and separations in the NMN result in a high surface energy that makes intensive interactions with the asphalt binder (Figure 9.11). After the reactions, more dense and solid materials are melted, and a stable bonding framework is formed. Therefore, the asphalt binder microstructure causes improvement of the complex shear modulus, and the NMN-modified asphalt binder has a potential resistance to rutting. Furthermore, the work dissipated per load cycle is calculated for the influence of rutting, and the results are shown in Figure 9.12.

Figure 9.12 shows that the amounts of work dissipated per loading cycle of the control asphalt binder are higher than those of the 2% and 4% NMN-modified asphalt binder, and the work dissipated per loading cycle of 2% NMN-modified asphalt binder is higher than that of the 4% NMN-modified asphalt binder. Moreover, the work dissipated per load cycle decreases by an average of 40% with the addition of 4% NMN in
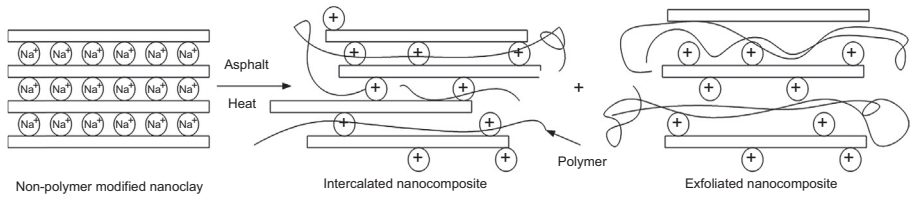
Figure 9.11 Schematic illustration of nonmodified nanoclay microstructure changing in the asphalt binder.
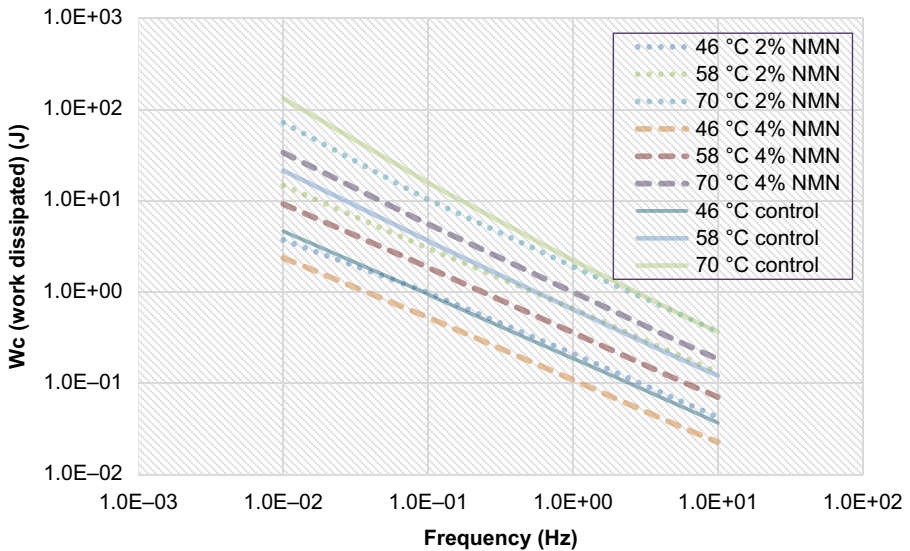
Figure 9.12 Work dissipated per load cycle of the control and NMN-modified asphalt binders under different temperatures (rutting influence).

the control asphalt binder, whereas the 2% NMN-modified asphalt binder decreases by an average of 10% relative to the control asphalt binder. However, the complex shear modulus of the NMN-modified asphalt binder is increased relative to the control asphalt in Figure 9.10. Furthermore, it indicates that the addition of NMN material into the control asphalt binder improves the resistance to rutting, and from the dissipated work perspective, the addition of NMN to the control asphalt binder enhances the resistance to permanent deformation of the modified asphalt binder. Therefore, the NMN-modified asphalt binder has a better resistance to rutting relative to the control asphalt binder.

9.6.2 PMN-modified asphalt binder

Figure 9.13 presents the complex shear modulus master curves of the control and PMN-modified asphalt binders. The complex modulus ($|G^*|$) values of the control
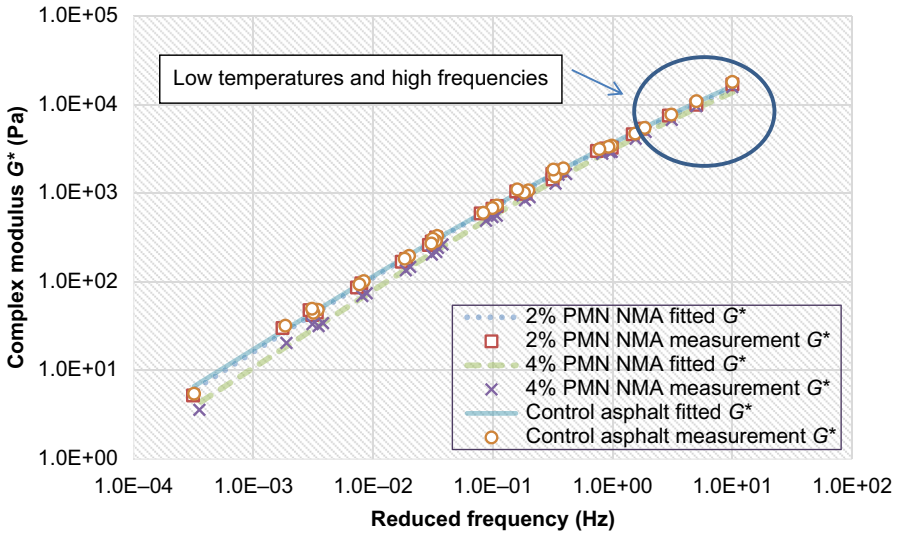
Figure 9.13 Complex shear modulus ($|G^*|$) master curves of control and PMN-modified asphalt binders.

asphalt binder are higher than those of the 4% PMN-modified asphalt binder, and the modulus of the control asphalt binder is almost the same as that of the 2% PMN-modified asphalt binder. With the addition of 4% PMN to the control asphalt binder, the complex shear modulus of the modified asphalt decreases by an average of 33%, and the average modulus values of the 2% PMN-modified asphalt binder decrease by an average of 6%. In addition, it is noted that the PMN can disperse readily in polymers, and has an excellent resistance to temperature and good resistance to certain acids and solvents. In comparison with the NMN material, PMN is changed from a hydrophilic to a hydrophobic one. Based on the literature review (Jahromi and Khodaii, 2009; Simon et al., 2008), due to the mechanical shear force and the thermodynamic driving force, the PMN layer structure can be easily exfoliated in the asphalt binder and the compatibility of the polymer improves. Considering the exfoliation of the layer, it is likely that the surface energy increases and the ion and cation exchanges in the asphalt binder become intensive (Figure 9.14). The PMN material changes the microstructure of the asphalt binder through chemical reactions, and causes a lower complex shear modulus and a reduction of water permeability. The amounts of work dissipated per loading cycle in the control and PMN-modified asphalt binders are displayed in Figure 9.15.

Figure 9.15 illustrates that the 4% PMN-modified asphalt binder has the highest work dissipated per loading cycle of rutting, whereas the control asphalt binder has the lowest dissipated work per loading cycle. In addition, the work of the 4% PMN-modified asphalt binder increases by an average of 25%, whereas that of the 2% PMN-modified asphalt binder increases by an average of 10% compared to the control asphalt binder. The PMN-modified asphalt binder has a higher work dissipated
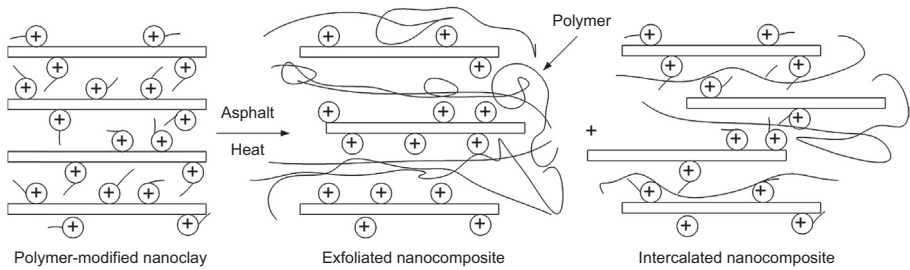
Figure 9.14 Schematic illustration of a polymer-modified nanoclay microstructure changing in the asphalt binder.
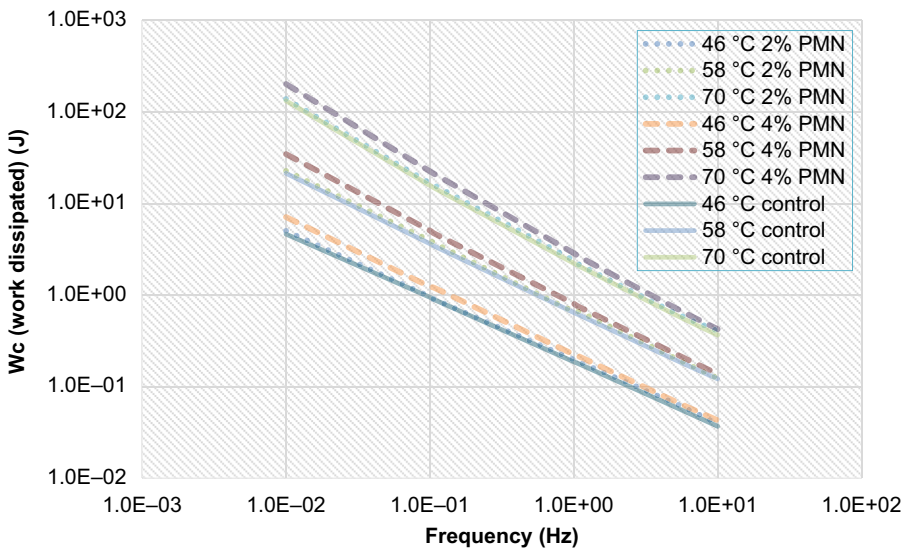
Figure 9.15 Work dissipated per load cycle of the control and PMN-modified asphalt binders under different temperatures (rutting influence).

per loading cycle relative to the NMN-modified asphalt binder. Because of the polymer modification in the nanoclay, PMN has more potential to form the new micro-structures of an asphalt binder through chemical reactions to enhance the ability to recover. From the dissipated work standpoints, the resistance to rutting in the PMN-modified asphalt binder may not improve. Therefore, it can be deduced that fatigue cracking of the PMN-modified asphalt binder might be better than that of the control asphalt binder at intermediate temperatures.

9.6.3 NMN-modified asphalt binder after the RTFO aging process

Figure 9.16 reveals the complex shear modulus master curves of the control and NMN-modified asphalt binders after RTFO aging. The figure shows that the complex
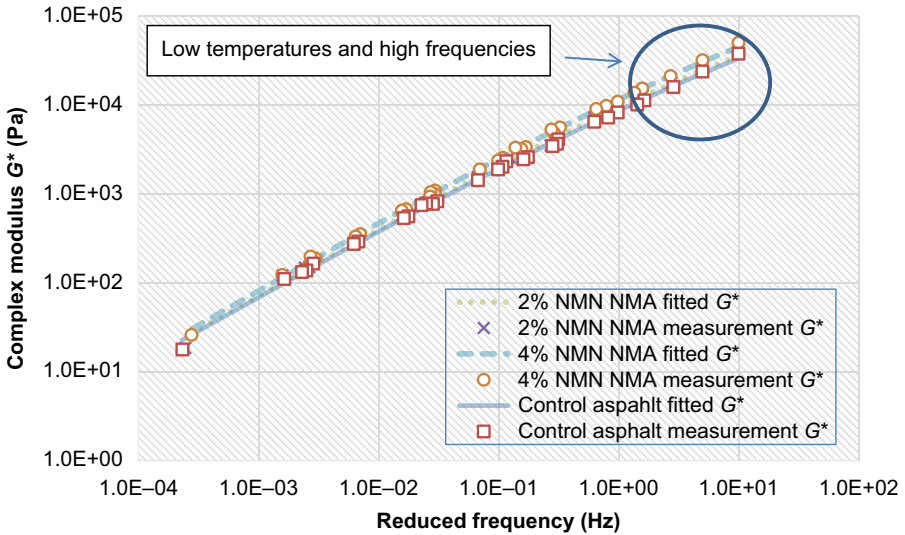
Figure 9.16 Complex shear modulus ($|G^*|$) master curves of control and NMN-modified asphalt binders after the RTFO aging process.

shear modulus of the 4% NMN-modified asphalt binder is higher than that of the 2% NMN-modified asphalt binder and the control asphalt binder under different temperatures. Moreover, the complex shear modulus ($|G^*|$) increases by an average of 15%, whereas the average values of the 2% PMN-modified asphalt binder increase by an average of 7% with the addition of 4% PMN to the control asphalt. The NMN was dispersed well in the control asphalt, and a stable network was formed after the RTFO aging. The strength of the modified asphalt increased. Through the RTFO aging, the NMN material had more time and conditions to react with the asphalt binder. The new stable structure is established during the process, and the performance of the NMN-modified asphalt binder is close to the condition when under construction. The resistance to rutting of the NMN-modified asphalt binder improves at medium and high temperatures compared to the control asphalt binder. Furthermore, the work dissipated per load cycle of rutting was performed. The results are shown in Figure 9.17.

Figure 9.17 shows the work dissipated per load cycle of the control and NMN-modified asphalt binder after RTFO aging. The work dissipated per load cycle of rutting influence on the control asphalt binder is higher than those of the 2% and 4% NMN-modified asphalt binder under different temperatures after RTFO aging. Additionally, with the addition of 4% NMN in the control asphalt binder, the dissipated work decreases by an average of 30%, whereas that of 2% NMN-modified asphalt binder increases by an average of 8% compared to the control asphalt binder. From the work-dissipated angle, with the addition of NMN into the control asphalt binder, the binder's resistance to rutting improves significantly after the RTFO aging process. Furthermore, the complex shear modulus of the NMN-modified asphalt
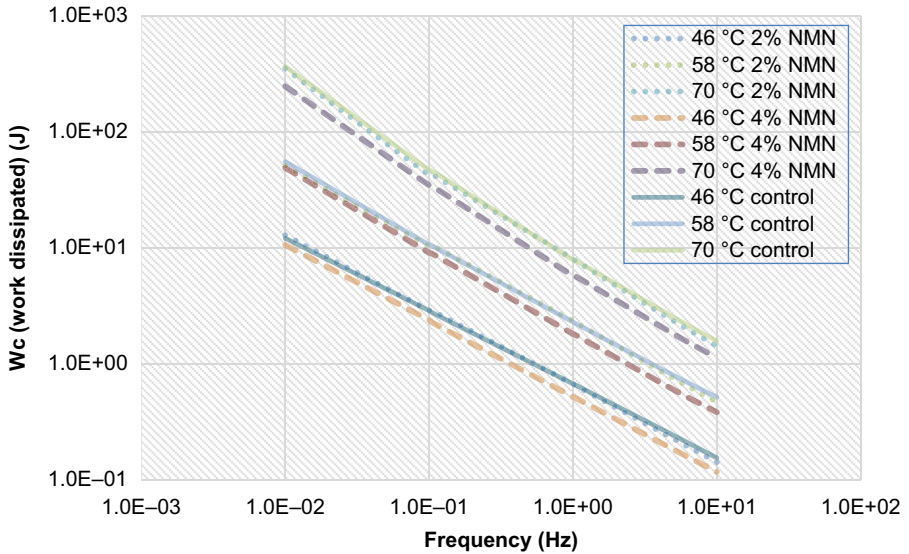
Figure 9.17 Work dissipated per load cycle of the control and NMN-modified asphalt binders after RTFO aging (rutting influence).

binder increases. The potential of rutting resistance increases. Therefore, the NMN-modified asphalt binder has a better rutting resistance at medium and high temperatures compared to the control one.

9.6.4 PMN-modified asphalt binder after the RTFO aging process

Figure 9.18 displays the complex shear modulus master curves of the control and PMN-modified asphalt binders after the RTFO aging. The figure shows that the complex shear modulus of the 4% PMN-modified asphalt binder is lower than that of the 2% PMN-modified asphalt binder and the control asphalt binder under various temperatures. The average values of the 2% PMN-modified asphalt binder are almost the same as those of the control asphalt binder. With the addition of the 4% PMN material to the base asphalt binder, the complex shear modulus decreases by an average of 13%, whereas the 2% PMN-modified asphalt binder decreases by an average of 8%. After the RTFO aging, due to its polymer modification and compatibility, the PMN was sufficiently melted into the asphalt binder. The properties (high heat resistance and lining application) of PMN are presented, and the new stable framework in the modified asphalt binder is formed. The complex shear modulus of the PMN-modified asphalt binder does not change much after the modification due to its microstructure, but the modified asphalt binder does hold the potential for the improvement of resistance to fatigue cracking. Furthermore, the work dissipated per load cycle due to rutting is calculated and shown in Figure 9.19.
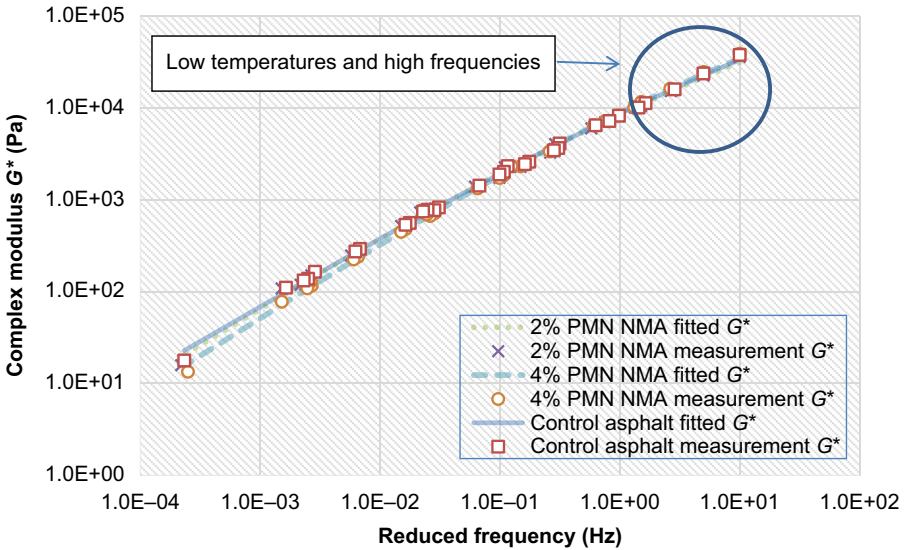
Figure 9.18 Complex shear modulus ($|G^*|$) master curves of the control and PMN-modified asphalt binders after the RTFO aging process.
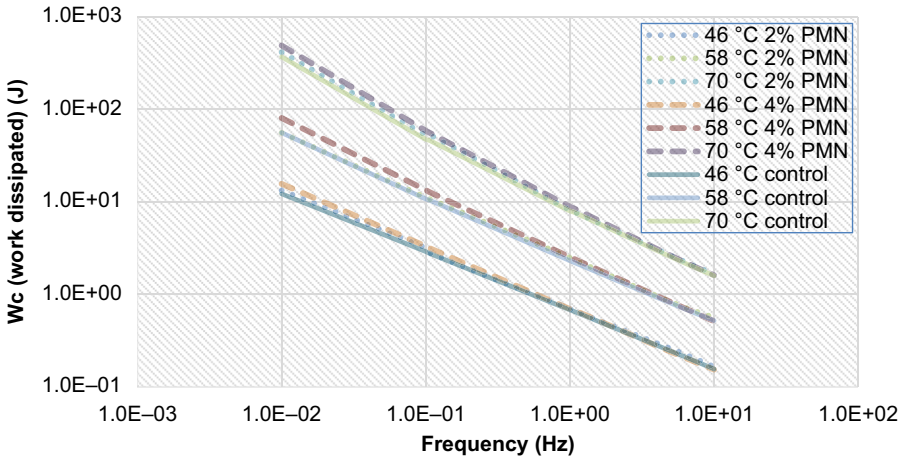
Figure 9.19 Work dissipated per load cycle of the control and PMN-modified asphalt binders after the RTFO aging (rutting influence).

Figure 9.19 shows that the control asphalt binder and 2% PMN-modified asphalt binder almost have the same amount of work dissipated per loading cycle after the RTFO aging, and the 4% PMN-modified asphalt binder has a higher work dissipated due to the influence of rutting. With the addition of 4% PMN to the control asphalt, the dissipated work increases by an average of 9%, whereas that of the 2% PMN-modified

asphalt binder increases by an average of 6%. Therefore, the addition of the 4% PMN material to the control asphalt binder may not enhance the rutting resistance of the modified asphalt binder. However, the fatigue cracking resistance of the PMN-modified asphalt binder may increase relative to the control asphalt binder.

9.7   BBR results of nanoclay-modified asphalt binders

According to the Superpave™ specification, the low-temperature performance of an asphalt binder is evaluated by the BBR test. The test evaluates the binder's possible abilities of stress relaxation and thermal cracking in the asphalt bending beam samples. From the standard test, the deflection curves can be drawn (Liu et al., 2009, 2010b; Lu and Redelius, 2007). Then, Eqn (9.3) is used to calculate the stiffness of the asphalt binder. In this research, the test temperature is $-24\,°C$, and the stiffnesses and m-values are shown in Figure 9.20 and in Table 9.1.

$$S(t) = \frac{PL^3}{4bh^3\delta(t)} \qquad (9.3)$$

where:

P = Applied constant load (100 g or 0.98 N)
L = Distance between beam supports (102 mm)
b = Beam width (12.5 mm)
h = Beam thickness (6.25 mm)
$S(t)$ = Asphalt binder stiffness at a specific time
$\delta(t)$ = Deflection at a specific time.
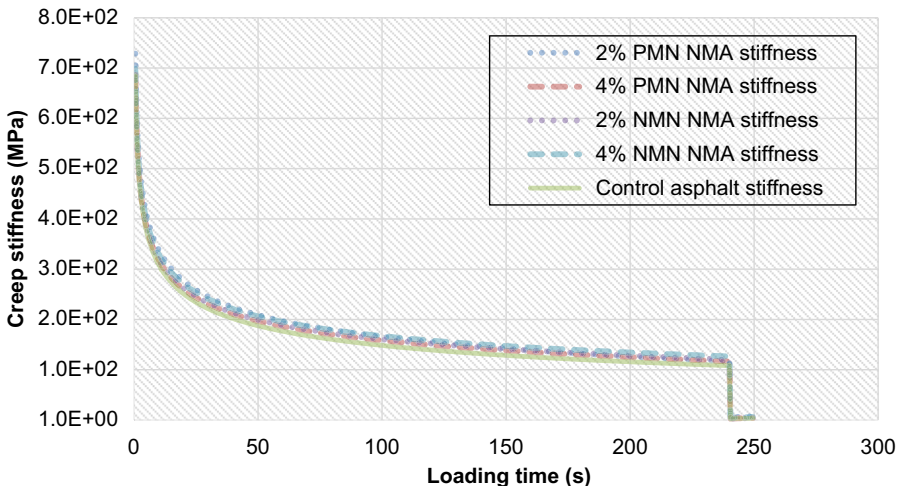
Figure 9.20 Creep stiffness of control and nanomodified asphalt binders.

Table 9.1 *m*-values of control and nanomodified asphalt binders at 60 s

Asphalt binder type	Time (s)	Deflection (mm)	Measured stiffness (MPa)	*m*-value	Remarks
Control asphalt binder	60.0	0.445	178	0.317	Passes the specification
2% NMN-modified asphalt binder	60.0	0.414	189	0.309	Passes the specification
4% NMN-modified asphalt binder	60.0	0.404	196	0.304	Passes the specification
2% PMN-modified asphalt binder	60.0	0.436	182	0.339	Passes the specification
4% PMN-modified asphalt binder	60.0	0.425	187	0.315	Passes the specification

Figure 9.20 shows that the control asphalt binder has higher deflections and lower stiffnesses than the other asphalt binders during the loading time, and that the PMN-modified asphalt binder has lower stiffnesses than the NMN-modified asphalt binder for the polymer modification in the nanoclay. This indicates that the control asphalt binder has a better stress relaxation ability and low-temperature performance, and that the low-temperature performance of the PMN-modified asphalt binder is also better than that of the NMN-modified asphalt binder. However, it is noticed that the deflection and stiffness of the NMN and PMN-modified asphalt binders are close to those of the control asphalt binder. In addition, according to the Superpave™ specification, all values at the 60 s loading time are lower than 300 MPa, and the *m*-values at 60 s loading time are higher than 0.300 from Table 9.1. The low-temperature grades of the NMN and PMN-modified asphalt binders are the same as that of the control asphalt binder. Therefore, the low-temperature performance and stress relaxation ability of the NMN and PMN-modified asphalt binders are the same as those of control asphalt from the specification.

9.8   FTIR results of nanoclay-modified asphalt binders

FTIR methodology can detect molecular vibrations that may be in the form of two atoms in a diatomic molecule experiencing a simple coupled motion to each individual atom in a large polyfunctional molecule undergoing motion. From the infrared spectra, the material information for the chemical bonds and the structure of the materials is obtained. The ethylene, sulfoxide, aliphatic branched, aliphatic, aromatic, and carbonyl bonds, all in the infrared spectra, related to the performance of asphalt binders are investigated. The wavenumbers of main bands are shown in Table 9.2. The silicon substrate with 350 μm thickness is used in this chapter, and the test results are shown in Figures 9.21 and 9.22.

Figures 9.21 and 9.22 show the FTIR trends of the control and nanoclay-modified asphalt. These trends are similar between the control and modified asphalt. There is no obvious new peak in the spectra of the modified asphalt compared to the control one due to the fact that the related peaks are overlapped during the FTIR detection. According to the bands of bonding in Table 9.2, the ratio changes of chemical bonding will be calculated for the sake of avoiding the effect of samples thickness (Ouyang et al., 2006b). Based on Eqns (9.4)−(9.9), the ratio changes in the modified asphalt binders before and after RTFO and PAV aging are shown in Figure 9.23.

$$I_{CH=CH} = \frac{\text{Area of the ethylene band centered around 966 cm}^{-1}}{\sum \text{Area of the spectral bands between 2000 and 600 cm}^{-1}} \quad (9.4)$$

$$I_{S=O} = \frac{\text{Area of the sulfoxide band centered around 1030 cm}^{-1}}{\sum \text{Area of the spectral bands between 2000 and 600 cm}^{-1}} \quad (9.5)$$

Table 9.2 Assignations of the main bands of the FTIR spectra (Larsen et al., 2009)

Wavenumber (cm^{-1})	Assignations[a]
3594, 3735	ν O−H
2924, 2853	ν C−H aliphatic
1735	ν C=O
1700	ν C=O conjugated
1600	ν C=C aromatic
1460	δ C−H of −(CH$_2$)$_n$− (aliphatic index)
1376	δ C−H of CH$_3$ (aliphatic branched)
1030	ν S=O sulfoxide
966	δ C−H transdisubstituted −CH=CH− (butadiene block)
748, 690	δ C−H aromatic monosubstitued (styrene block)

[a]ν = stretching, δ = bending.

$$I_{C-H \text{ of } CH_3} = \frac{\text{Area of the aliphatic branched band centered around 1376 cm}^{-1}}{\sum \text{Area of the spectral bands between 2000 and 600 cm}^{-1}} \quad (9.6)$$

$$I_{C-H \text{ of } -(CH_2)_n-} = \frac{\text{Area of the aliphatic index band centered around 1460 cm}^{-1}}{\sum \text{Area of the spectral bands between 2000 and 600 cm}^{-1}} \quad (9.7)$$

$$I_{C=C} = \frac{\text{Area of the aromatic band centered around 1600 cm}^{-1}}{\sum \text{Area of the spectral bands between 2000 and 600 cm}^{-1}} \quad (9.8)$$

$$I_{C=O} = \frac{\text{Area of the carbonyl band centered around 1690 cm}^{-1}}{\sum \text{Area of the spectral bands between 2000 and 600 cm}^{-1}} \quad (9.9)$$

Figure 9.23 shows the ratio changes of chemical bonds in the control and modified asphalt binders before and after the RTFO and PAV aging processes. Based on the literature review (Cortizo et al., 2004; Larsen et al., 2009; Wu et al., 2009; Ouyang et al., 2006b; Zhang et al., 2011; Xu and Huang, 2011b), the carbonyl index indicates the degree of oxidation in the asphalt binder. The carbonyl index (C=O) in the modified asphalt binders decreases slightly after the RTFO aging process and increases significantly after the PAV aging process when compared with the ratios of unaged
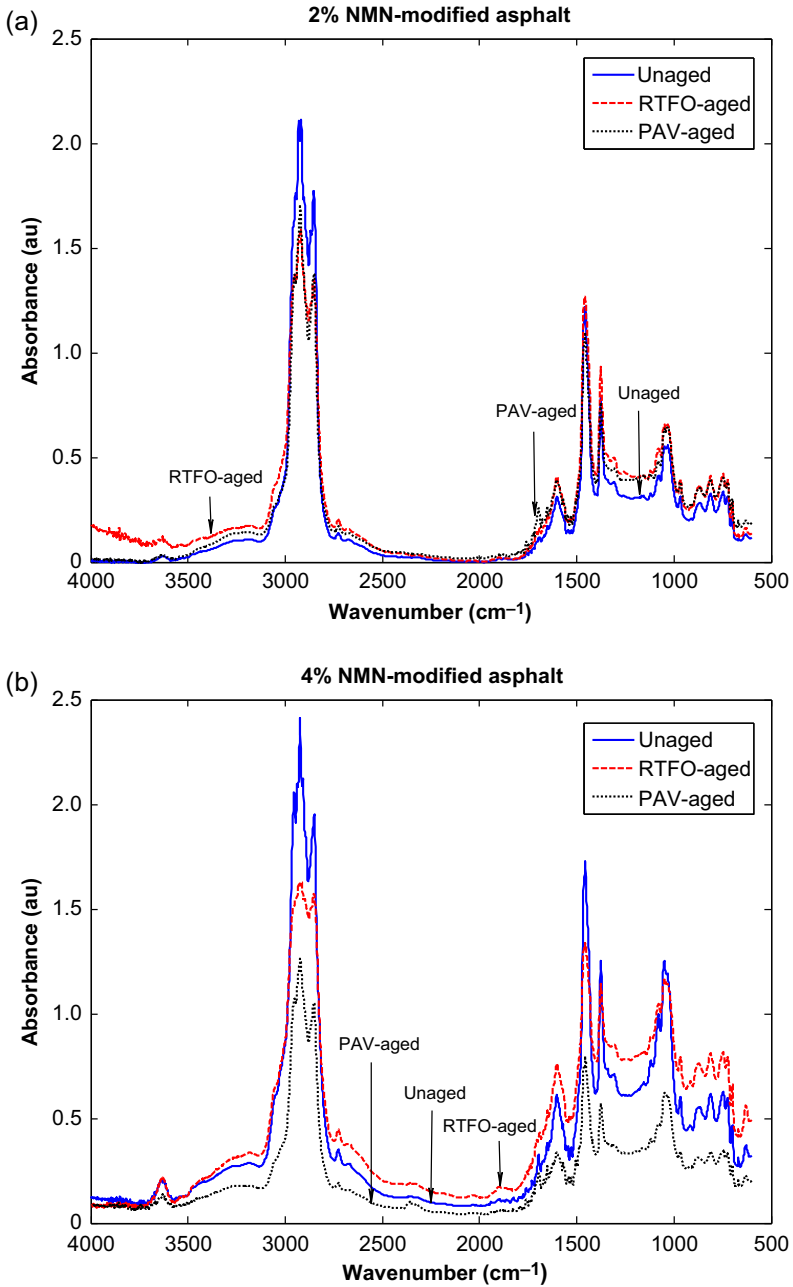
Figure 9.21 FTIR spectra of NMN-modified asphalt binder: (a) 2% NMN-modified asphalt binder, and (b) 4% NMN-modified asphalt binder.

(a)

(b)
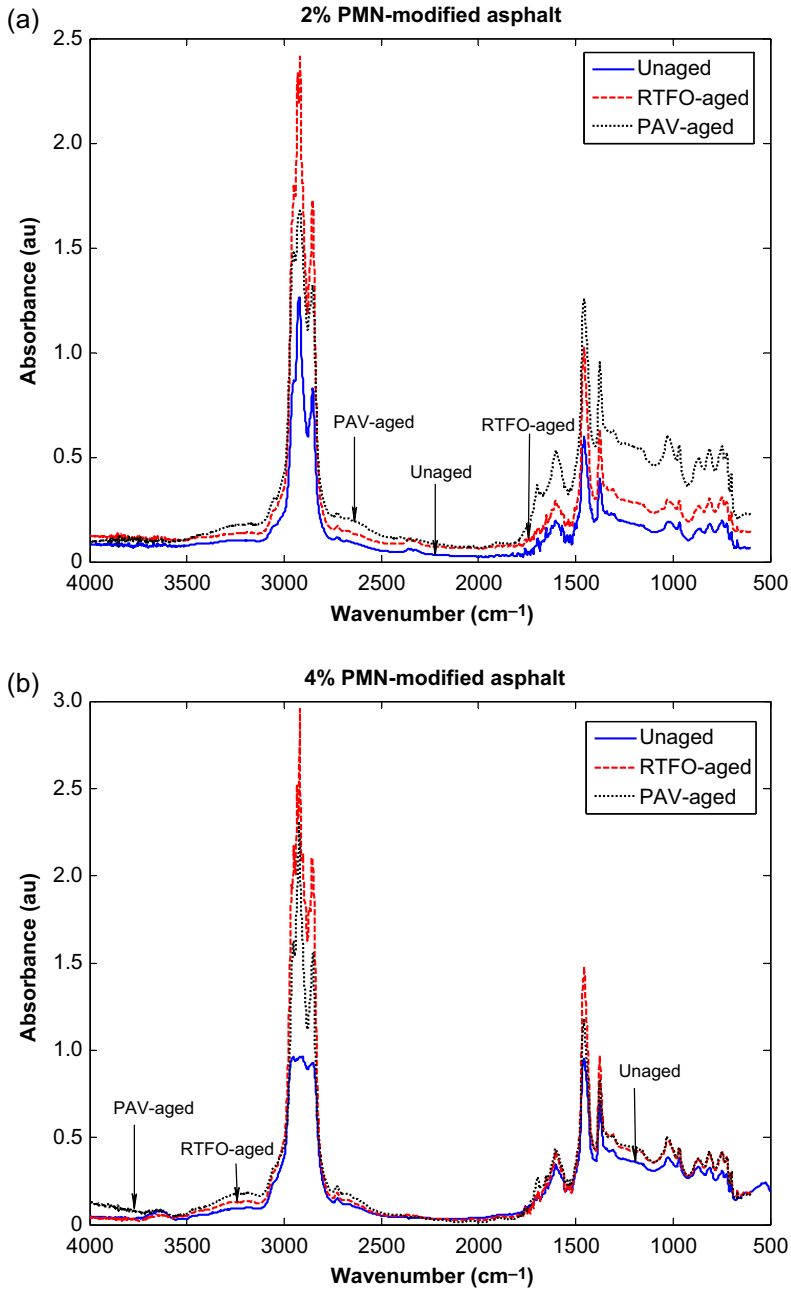
Figure 9.22 FTIR spectra of PMN-modified asphalt binder: (a) 2% PMN-modified asphalt binder, and (b) 4% PMN-modified asphalt binder.

(a)

(b)

(c)
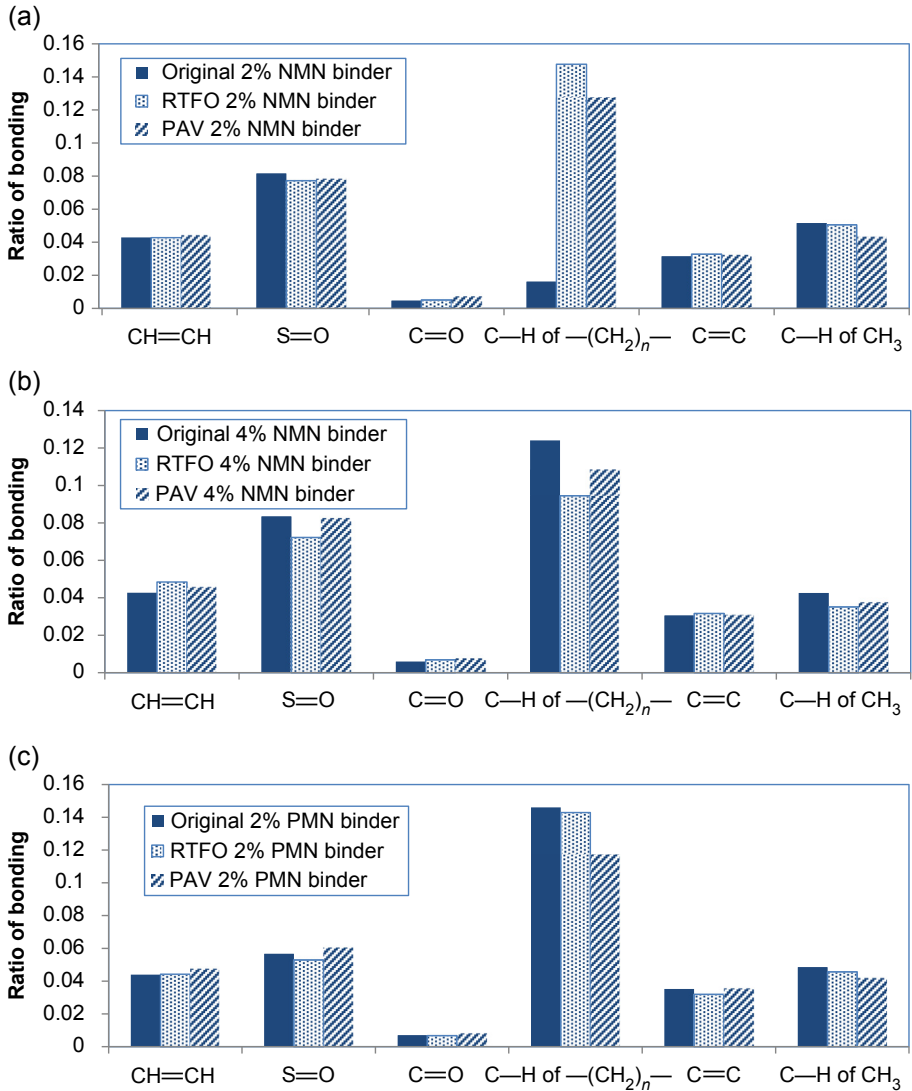
Figure 9.23 Ratio of bonds in the control and modified asphalt binders: (a) Ratio of bonds in the 2% NMN-modified asphalt binder, (b) ratio of bonds in the 4% NMN-modified asphalt binder, (c) ratio of bonds in the 2% PMN-modified asphalt binder, (d) ratio of bonds in the 4% PMN-modified asphalt binder, and (e) ratio of bonds in the control asphalt binder.

(d)

(e)
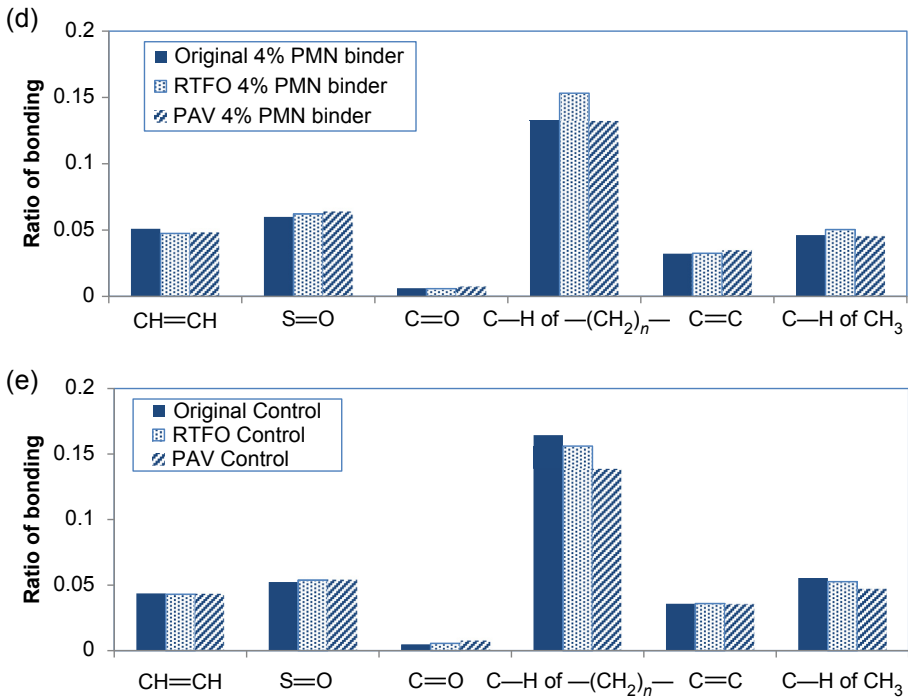
Figure 9.23 Continued.

asphalt binders. It is possible that the addition of the nanopowders to the asphalt binder can delay and weaken the oxidation reaction. Meanwhile, the sulfoxide index (S=O) in the control and modified asphalt binders after the RTFO and PAV aging shows a different trend with the carbonyl index. From previous research results (Ouyang et al., 2006b), the sulfoxide index (S=O) ratio may decrease in the asphalt binder after the RTFO and PAV aging process, and the results in this study coincide with it. Therefore, the sulfoxide index is not mainly considered as an aging index in the asphalt binder and can be a reference in the test.

The control asphalt was modified by ABS, and the butadiene index was observed from FTIR tests. Based on the research results of Cortizo et al. (Cortizo et al., 2004; Larsen et al., 2009), during the aging process of the asphalt binder, the terminal vinyl (bands 910 and 995 cm^{-1}) reacted preferentially to the *trans*-double bonding (bending C−H of *trans*-disubstituted −CH=CH−, band 996 cm^{-1}). Moreover, the addition of the ultrafine materials and reactions with the polymer (asphalt binder) may lead to the increase of bending C−H of *trans*-disubstituted −CH=CH− in the modified asphalt binder. However, when the aging reaction occurs in the modified asphalt binder, the ratio of band 996 cm^{-1} decreases in the asphalt binder. The trends of bending C−H of *trans*-disubstituted −CH=CH− in the control and modified asphalt binders are shown in Figure 9.23.

9.9 Discussions and conclusions

Based on the test results of the control and nanoclay-modified asphalt binders in this chapter, the following conclusions can be drawn:

1. With the addition of nanoclay to the control asphalt binder, the viscosity of the NMN-modified asphalt binder increases significantly; however, the viscosity of the PMN-modified asphalt binder maintains the same level as that of the control asphalt binder. The rutting resistance of the NMN-modified asphalt binder improves and the fatigue cracking resistance may enhance in comparison to those of the control asphalt binder. The viscosity data of asphalt at 135 °C pass the requirement set by the Superpave™ Standard, and these data indicate that the construction paving temperature is not affected.
2. The addition of NMN material into the control asphalt binder increases the complex shear modulus. However, the addition of the PMN material into the control asphalt binder decreases the complex shear modulus relative to the control asphalt binder before or after the RTFO and PAV aging processes. From the standpoint of the amount of work dissipated, with the addition of NMN to the control asphalt binder, the high-temperature properties of unaged and RTFO-aged modified asphalt binders improve. However, the high-temperature properties of the PMN-modified asphalt under unaged and RTFO-aged states are not significantly enhanced. Moreover, the addition of the PMN material into the control asphalt binder improves the recovery ability of the asphalt binder.
3. The BBR test results show that the stiffnesses of NMN and PMN-modified asphalt binders approach that of the control asphalt binder. From the Superpave™ grade angle, the stress relaxations and low-temperature performance of the NMN and PMN-modified asphalt binders are the same as those of the control asphalt.
4. The FTIR data show that the oxidation reaction may be weakened in the modified asphalt binder with the addition of nanoclay in the asphalt binder when they are exposed to the sunlight and heated.

In summary, the nanoclay in the asphalt binder enhances the resistance to rutting and fatigue cracking, and also improves the antioxidation effect of the modified asphalt binders. Therefore, the nanomaterial application in pavement engineering would create a new way for asphalt modification and material industry. In addition, the performance tests for the nanoclay-modified asphalt mixtures are planned and used to thoroughly evaluate the effect of nanoclay in asphalt binders and asphalt mixtures. The emission tests and cost management or life cycle assessment are potential studies for nanoclay applications in civil engineering, as well as the application of other nanomaterials.

Acknowledgment

building materials. The authors sincerely appreciate Elsevier's support. Any opinion, finding, and conclusion or recommendation expressed in this material are those of authors and do not necessarily reflect the review of any organization.

References

Abdelrahman, M.A., Carpenter, S.H., 1999. Mechanism of Interaction of Asphalt Cement with Crumb Rubber Modifier. Transportation Research Board.

Ahmedzade, P., Tigdemir, M., Kalyoncuoglu, S.F., 2007. Laboratory investigation of the properties of asphalt concrete mixtures modified with TOP-SBS. Construction and Building Materials 21 (3), 626−633.

Airey, G.D., 2002. Rheological evaluation of ethylene vinyl acetate polymer modified bitumens. Construction and Building Materials 16 (8), 473−487.

Al-Hadidy, A.I., Yi-qiu, T., 2010. Comparative performance of the SMAC made with the SBS and ST-modified binders. Journal of Materials in Civil Engineering, American Society of Civil Engineering (ASCE) 22 (6), 580−587.

Awanti, S.S., Amarnath, M.S., Veeraragavan, A., 2008. Laboratory evaluation of SBS modified bituminous paving mix, 20 (4), 327−330.

Bertollo, S.A.M., Fernandes, J.L., Bernucci, L.L.B., Moura, A.V., 2003. Feasibility of the Use of Crumb Rubber as Asphalt Pavement Material. Universidade do Minho, Portugal.

Cheng, J., Shen, J., Xiao, F., 2011. Moisture susceptibility of warm-mix asphalt mixtures containing nanosized hydrated lime. Journal of Materials in Civil Engineering 23 (11), 1552−1559.

Cortizo, M.S., Larsen, D.O., Bianchetto, H., Alessandrini, J.L., 2004. Effect of the thermal degradation of SBS copolymers during the ageing of modified asphalts. Polymer Degradation and Stability 86 (2), 275−282.

Drozd, D., Szczubialka, K., Nowakowska, M., 2011. Novel hybrid photosensitizers: photoactive polymer-nanoclay. Journal of Photochemistry and Photobiology A: Chemistry 215 (2−3), 223−228.

Fu, H., Xie, L., Dou, D., Li, L., Yu, M., Yao, S., 2007. Storage stability and compatibility of asphalt binder modified by SBS graft copolymer. Construction and Building Materials 21 (7), 1528−1533.

Ghile, D.B., 2006. Effects of Nanoclay Modification on Rheology of Bitumen and on Performance of Asphalt Mixtures. Delft University of Technology, Delft, The Netherlands (M.S. thesis).

Goh, S.W., Akin, M., You, Z., Shi, X., 2011. Effect of deicing solutions on the tensile strength of micro- or nano-modified asphalt mixture. Construction and Building Materials 25 (1), 195−200.

He, X., Shi, X., 2008. Chloride permeability and microstructure of Portland cement mortars incorporating nanomaterials. Transportation Research Record: Journal of the Transportation Research Board 2070 (1), 13−21.

Huang, B., Mohammad, L.N., 2002. Numerical Analysis of Crumb-rubber Modified Asphalt Pavements at the Louisiana Accelerated Loading Facilities. University of Mississippi 1 (2), 59−71.

Iskender, E., Aksoy, A., Ozen, H., 2012. Indirect performance comparison for styrene-butadiene-styrene polymer and fatty amine anti-strip modified asphalt mixtures. Construction and Building Materials 30, 117−124.

Jahromi, S.G., Khodaii, A., 2009. Effects of nanoclay on rheological properties of bitumen binder. Construction and Building Materials 23 (8), 2894−2904.

Jamal Khattak, M., Khattab, A., Rizvi, H.R., 2013. Characterization of carbon nano-fiber modified hot mix asphalt mixtures. Construction and Building Materials 40, 738−745.

Khattak, M.J., Khattab, A., Rizvi, H.R., 2011. Mechanistic Characteristics of Asphalt Binder and Asphalt Matrix Modified with Nano-fibers, 41165 ed. ASCE, Dallas, TX, p. 492.

Khattak, M.J., Khattab, A., Rizvi, H.R., Zhang, P., 2012. The impact of carbon nano-fiber modification on asphalt binder rheology. Construction and Building Materials 30, 257−264.

Khattak, M.J., Khattab, A., Zhang, P., Rizvi, H., Pesacreta, T., 2013. Microstructure and fracture morphology of carbon nano-fiber modified asphalt and hot mix asphalt mixtures. Materials and Structures 46 (12), 2045−2057.

Khodaii, A., Mehrara, A., 2009. Evaluation of permanent deformation of unmodified and SBS modified asphalt mixtures using dynamic creep test. Construction and Building Materials 23 (7), 2586−2592.

Kim, S., Loh, S.W., Zhai, H., Bahia, H.U., 2001. Advanced Characterization of Crumb Rubber-Modified Asphalts, Using Protocols Developed for Complex Binders. Transportation Research Record: Transportation Research Board, pp. 15−24.

Larsen, D.O., Alessandrini, J.L., Bosch, A., Cortizo, M.S., 2009. Micro-structural and rheological characteristics of SBS-asphalt blends during their manufacturing. Construction and Building Materials 23 (8), 2769−2774.

Li, D., Xia, H., Peng, J., Zhai, M., Wei, G., Li, J., et al., 2011. Radiation preparation of nano-powdered styrene-butadiene rubber (SBR) and its toughening effect for polystyrene and high-impact polystyrene. Radiation Physics and Chemistry 76 (11−12), 1732−1735.

Liu, D.-L., Bao, S.-Y., 2007. Research of improvement of SBS modified asphalt pavement performance by organic monotmorillonite. Journal of Building Materials, China 10 (4), 500−504.

Liu, D.-L., Yao, H.-B., Bao, S.-Y., 2007. Performance of nano-calcium carbonate and SBS compound modified asphalt. Zhongnan Daxue Xuebao (Ziran Kexue Ban)/Journal of Central South University (Science and Technology) 38 (3), 579−582.

Liu, S., Ma, C., Cao, W., Fang, J., 2009. Influence of aluminate coupling agent on low-temperature rheological performance of asphalt mastic. Construction and Building Materials 24 (5), 650−659.

Liu, G., Kai, Q., Ye, R., 2010a. Heat Reflectivity Properties of Asphalt Mixtures Modified with Nano A/SBS-II: Prediction of Temperature in Asphalt Pavement, 41127 ed. ASCE, Beijing, China, p. 413.

Liu, S., Cao, W., Shang, S., Qi, H., Fang, J., 2010b. Analysis and application of relationships between low-temperature rheological performance parameters of asphalt binders. Construction and Building Materials 24 (4), 471−478.

Lu, X., Redelius, P., 2007. Effect of bitumen wax on asphalt mixture performance. Construction and Building Materials 21 (11), 1961−1970.

Mojtaba Ghasemi, S.M.M., Tahmooresi, Majid, Jalal, RezaKamali, Reza, Taherzade, 2012. Modification of stone matrix asphalt with nano-SiO$_2$. Journal of Basic and Applied Scientific Research 2 (2), 1338−1344.

Ouyang, C., Wang, S., Zhang, Y., Zhang, Y., 2006a. Improving the aging resistance of styrene-butadiene-styrene tri-block copolymer modified asphalt by addition of antioxidants. Polymer Degradation and Stability 91 (4), 795−804.

Ouyang, C., Wang, S., Zhang, Y., Zhang, Y., 2006b. Improving the aging resistance of asphalt by addition of zinc dialkyldithiophosphate. Fuel 85 (7−8), 1060−1066.

Shang, L., Wang, S., Zhang, Y., Zhang, Y., 2011. Pyrolyzed wax from recycled cross-linked polyethylene as warm mix asphalt (WMA) additive for SBS modified asphalt. Construction and Building Materials 25 (2), 886−891.

Simon, M., Stafford, K., Ou, D., 2008. Nanoclay reinforcement of liquid silicone rubber. Journal of Inorganic and Organometallic Polymers and Materials 18 (3), 364−373.

Wang, H., Dang, Z., You, Z., Cao, D., 2012. Effect of warm mixture asphalt (WMA) additives on high failure temperature properties for crumb rubber modified (CRM) binders. Construction and Building Materials 35, 281−288.

Wang, H., Dang, Z., Li, L., You, Z., 2013. Analysis on fatigue crack growth laws for crumb rubber modified (CRM) asphalt mixture. Construction and Building Materials 47, 1342−1349.

Wu, S.-p., Pang, L., Mo, L.-t., Chen, Y.-c., Zhu, G.-j., 2009. Influence of aging on the evolution of structure, morphology and rheology of base and SBS modified bitumen. Construction and Building Materials 23 (2), 1005−1010.

Xiang, L., Cheng, J., Que, G., 2009. Microstructure and performance of crumb rubber modified asphalt. Construction and Building Materials 23 (12), 3586−3590.

Xiao, F., Amirkhanian, S.N., Shen, J., Putman, B., 2009. Influences of crumb rubber size and type on reclaimed asphalt pavement (RAP) mixtures. Construction and Building Materials 23 (2), 1028−1034.

Xiao, F., Amirkhanian, A.N., Amirkhanian, S.N., 2011. Influence of carbon nanoparticles on the rheological characteristics of short-term aged asphalt binders. Journal of Materials in Civil Engineering 23 (4), 423−431.

Xu, T., Huang, X., 2011a. Study on combustion mechanism of asphalt binder by using TG-FTIR technique. Fuel 89 (9), 2185−2190.

Xu, T., Huang, X., 2011b. A TG-FTIR investigation into smoke suppression mechanism of magnesium hydroxide in asphalt combustion process. Journal of Analytical and Applied Pyrolysis 87 (2), 217−223.

Yang, Z., Hollar, J., Shi, X., 2011. Surface-sulfonated polystyrene microspheres improve crack resistance of carbon microfiber-reinforced Portland cement mortar. Anglais 45 (13), 3497−3505.

Yao, H., You, Z., Li, L., Goh, S.W., Mills-Beale, J., Shi, X., et al., 2013. Evaluation of asphalt blended with low percentage of carbon micro-fiber and nanoclay. Journal of Testing and Evaluation 41 (2), 278−288.

Yildirim, Y., 2007. Polymer modified asphalt binders. Construction and Building Materials 21 (1), 66−72.

You, Z., Mills-Beale, J., Foley, J.M., Roy, S., Odegard, G.M., Dai, Q., et al., 2011. Nanoclay-modified asphalt materials: preparation and characterization. Construction and Building Materials 25 (2), 1072−1078.

Zhang, F., Yu, J., 2011. The research for high-performance SBR compound modified asphalt. Construction and Building Materials 24 (3), 410−418.

Zhang, H., Wang, Y., Wu, Y., Zhang, L., Yang, J., 2005. Study on flammability of montmorillonite/styrene-butadiene rubber (SBR) nanocomposites. Journal of Applied Polymer Science 97 (3), 844−849.

Zhang, J., Wang, J., Wu, Y., Wang, Y., Wang, Y., 2008. Preparation and properties of organic palygorskite SBR/organic palygorskite compound and asphalt modified with the compound. Construction and Building Materials 22 (8), 1820−1830.

Zhang, B., Xi, M., Zhang, D., Zhang, H., Zhang, B., 2009. The effect of styrene-butadiene-rubber/montmorillonite modification on the characteristics and properties of asphalt. Construction and Building Materials 23 (10), 3112−3117.

Zhang, F., Yu, J., Han, J., 2011. Effects of thermal oxidative ageing on dynamic viscosity, TG/DTG, DTA and FTIR of SBS- and SBS/sulfur-modified asphalts. Construction and Building Materials 25 (1), 129−137.

Mechanical and environmental resistance of nanoparticle-reinforced pavement materials

10

Ning Xie

School of Materials Science and Engineering and Shandong Provincial Key Laboratory of Preparation and Measurement of Building Materials, University of Jinan, Jinan, Shandong, China; School of Civil Engineering, Harbin Institute of Technology, Harbin, China

10.1   Introduction

Portland cement concrete is a commonly used building material in modern civilization. Portland cement, as the most important binder material of concrete, is the main component that determines the overall properties of the concrete infrastructures. With the development of global industrialization, the needs for cement concrete materials keep increasing every year, especially in many developing countries. As a result, the amount of Portland cement production increases annually with the market expansion. However, Portland cement production is an extremely energy-intensive process and accounts for considerable greenhouse gases emissions; therefore, with the urgent need to mitigate the negative environmental footprint of concrete production and maintenance activities, there has been a steady increase in interest and research activity regarding improving the sustainability and durability of concrete infrastructures.

The durability of concrete infrastructures in service environments is of great interest to both scientific studies and practical applications (Richardson, 2008; Bullard et al., 2011; Jennings, 2008; Rozière et al., 2009; Shi et al., 2010, 2012). Many approaches have been implemented to improve the durability of concrete with a focus on modifying the performances of the cementitious binders (Nehdi et al., 2004; Shi et al., 2012; Bagheri et al., 2012; Pacheco-Torgal et al., 2012). Polymer modification, fiber reinforcement, and air entrainment were widely used approaches to enhance the performances of the concrete infrastructures. Although these methods have their merits for enhancing the properties of the concrete, all of them still have limitations when they are applied in the field.

The overall performances of any material are determined by their microstructures; therefore, how to control the microstructures of a material is the most important issue to realize a high performance that can satisfy the critical requirements when the material is applied in the field. Currently, it is widely accepted that the hardened cementitious binder is composed of complex nanosized crystals and amorphous hydration products (shown as the high-resolution transmission electron microscope (HRTEM) image in Figure 10.1). Therefore, how to precisely control the microstructures of these phases from the nanoscale is the most effective way to realize
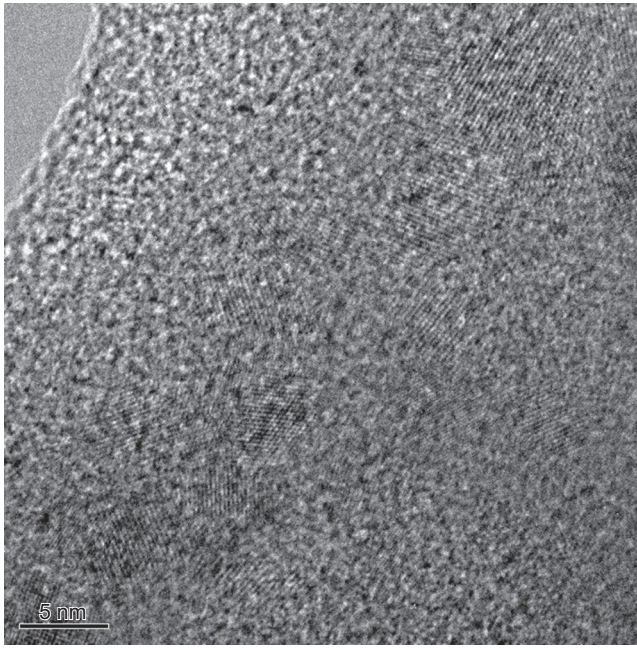
Figure 10.1 High-resolution transmission electron microscope of complex nanosized crystals and amorphous hydration products in hardened cement paste.

the performance enhancement of the concrete materials (Monteiro et al., 2009; Lim and Mondal, 2014). This is the most important reason why nanoparticles can play a key role in helping with microstructure control from nanoscale and thus enhancing the durability of the concrete materials.

The nanostructure of the cement binder phase has been extensively investigated in recent decades (Xu and Viehland, 1996; Allen et al., 2007a). It was found that the Ca:Si ratio of the C-S-H phase in hardened cement paste generally varies from 1.2 to 2.1, and has an average value of about 1.75 (Richardson, 1999). It was found that the nanoscale $Ca(OH)_2$ phase could be calculated, and the formula of the solid C-S-H, $(CaO)_x(SiO_2)(H_2O)_y$, could be determined by the number of x and y (Thomas et al., 1998). Bernal (1952) thought that, in the cement paste, the SiO_2 in the hydration products can be divided into two types, namely, CSH(I) and C_2SH(II). It was claimed that the monomeric silicate anion $[SiO_2(OH)_2]_2^-$ exists in both phases with a general formula expressed as $Ca[SiO_2(OH)_2]Ca(OH)_2]_xH_2O_y$, where x would be 1 for C_2SH(II) and between 0 and 0.5 for CSH(I). A few models have demonstrated that the C-S-H mainly fall into two types (Allen et al., 2007a). One is that the silicate anions are thoroughly monomeric, and another one is that the linear silicate chain is present in 1.4 nm tobermorite or some other minerals (Taylor, 1986).

Due to the nanostructures of the cement paste, it is not a surprise that the addition of the nanoparticles will largely change the hydration process of the concrete materials. So far, several types of nanomaterials have been widely used as additives to reinforce concrete infrastructures, including titanium dioxide, iron oxide, alumina and silica

nanoparticles, nanoclay, and nanostructured carbon materials (Hanus and Harris, 2013). Although the mechanisms of the concrete reinforced by nanoparticles are not yet crystal clear, there still are some hypotheses that are responsible for the benefits of the modification. First, it was assumed that the nanosized particles will act as the *nucleus* to help the formation and growth of the cementitious hydration products (Li et al., 2006a); second, they can act as fillers to block the nanosized pores in the amorphous cementitious hydration products (Kim et al., 2014a; Hou et al., 2014); and, third, it will change the morphologies of the parallel packing C-S-H structure and form new types of C-S-H structures with higher density (Feng et al., 2013).

Some studies claimed that, with the addition of nano-TiO_2 particles, the hydration rate of the cement-based materials can be accelerated and thus result in early-age mechanical properties enhancement. It was believed that the nano-TiO_2 particles will accelerate both the peak reaction rate and the early-age hydration degree, and the hydration products were formed on the surfaces of the TiO_2 nanoparticles and the C_3S (Chen et al., 2012; Jayapalan et al., 2009). Meanwhile, the evening-age mechanical properties were reduced sharply, with the content of the nano-TiO_2 particles increased from 5 wt% to 10 wt% (Meng et al., 2012).

The effect of the TiO_2 nanoparticle on the early-age hydration kinetics to the tricalcium silicate (C_3S) was quantitatively presented by Lee and Kurtis (2010) via the Avrami model (Avrami, 1939, 1940, 1941), shown as:

$$X = 1 - \exp[-(k_{avr}t)^n] \tag{10.1}$$

where X is the transformed volume fraction as a function of time; and k_{avr} is the effective rate constant as a function of constant linear growth rate. Provided Eqn (10.1) is differentiated with respect to time; thus, the hydration rate can be expressed as:

$$R = Ank_{avr}^n(t - t_0)^{n-1} \exp\{-[k_{avr}(t - t_0)^n]\} \tag{10.2}$$

where R is the hydration rate, A is a normalization constant to match the isothermal calorimetry data, and t_0 is the time delay between the time of mixing and the start of nucleation and growth kinetics. A boundary nucleation model (BN model) was modified by Thomas (2007) to describe the hydration kinetics of C_3S, shown as:

$$X = 1 - \exp\left[-2O_V^B \int_O^{G_r} (1 - \exp(-Y^e))dy\right] \tag{10.3}$$

where:

$$Y^e = \frac{\pi I_B}{3}G^2t^3\left[1 - \frac{3y^2}{G^2t^2} + \frac{2y^3}{G^3t^3}\right]\left(\text{if} \quad t > \frac{y}{G}\right)$$

$$Y^e = 0 \quad \left(\text{if} \quad t < \frac{y}{G}\right) \tag{10.4}$$

where y and Y^e are temporary variables, which will disappear after integration; and X depends on three well-defined physical parameters: G, the linear growth rate of transformed phase; I_B, the nucleation rate per unit area of untransformed boundary; and O_V^B, the boundary area per unit volume. These results demonstrate that the TiO_2 nanoparticles can act as nucleation sites and accelerate the early hydration process.

Unlike the nano-TiO_2 particles, which only act as catalysts or inert additives, the addition of the nano SiO_2 and nanomontmorillonites will lead to a pozzolanic reaction between Portland cement paste and the nano SiO_2 (He and Shi, 2008). The nanosheets of montmorillonites distributed in a mortar or concrete matrix may also result in microstructural regularity and act as a dense barrier and "fiber reinforcement."

Single-walled carbon nanotubes (SWCNTs) also can accelerate the hydration reaction of C_3S in cement and influence the morphology and location of both the initial C_3S and the tricalcium aluminate (C_3A) hydration products (Makar and Chan, 2009). Vera-Agullo et al. (2009) reported that, with proper dispersion, the carbon nanofilaments (either multiwalled nanotubes or nanofibers) can accelerate the cement hydration process, and so do the nanosilica and nanoclays. The mortar bars, with the addition of 0.125 wt% of carbon nanofiber, showed great performance derived from both physical and chemical mechanisms.

Currently, the research on nanotechnology-based concrete materials is still burgeoning (He and Shi, 2008; Birgisson et al., 2010, 2012). In the past decade, rapid progress, improved availability of advanced nanomaterials, and improved characterization techniques have led to numerous engineering and mechanistic studies of nanotechnology for concrete materials (Garcia-Luna and Bernal, 2006; Bittnar et al., 2009; Shi et al., 2010; Lee and Kurtis, 2010). Nanotechnology has demonstrated its clear benefits in empowering the development of concrete with enhanced mechanical properties and durability with exposure to aggressive environments (Birgisson et al., 2010, 2012; Chang et al., 2007; Keyvani, 2007; Mondal et al., 2010; Sanchez and Sobolev, 2010; Said et al., 2012; Metaxa et al., 2013; Zapata-Ordúz et al., 2014).

10.2 Nanoparticle-reinforced pavement materials

Pavement is one of the most important infrastructures in our daily lives. There are several types of pavements that are currently used: highway pavements, sidewalk pavements, airport pavements, parking lots, and bridge decks. The properties of these pavements differ according to their specific application requirements. Asphalt concrete pavements are largely used in highways, whereas concrete pavements are largely applied in sidewalks and bridge decks. A considerable amount of airport pavements are using cement concrete pavement, and many parking lots are also paved with cement concrete.

As a promising technology in many industrial fields, nanotechnology has also been applied in the production of concrete and proven to enhance its intrinsic properties and environmental resistance (Madani et al., 2012; Sanchez and Sobolev, 2010; Pacheco-Torgal et al., 2013; Pachego-Torgal, 2014). A wide variety of nontoxic

nanomaterials, such as nanoclays, nano iron oxide, nano silica, nano titanium dioxide, nano alumina, and nano carbon materials, have been used to improve the mechanical properties, enhance the chemical resistance, and reduce the shrinkage and permeability of concrete, all of which contribute to extending the service life of concrete infrastructures (Amirkhanian et al., 2011; Balaguru and Chong, 2006; Birgisson et al., 2010, 2012). In addition, with the development of nanotechnology in many industrial areas, the production capability of nanomaterials has greatly increased in recent decades, which leads to a dramatic cost reduction of nanomaterials; this trend is expected to continue. The future is bright to achieve the wide application of nanotechnologies in infrastructure construction and maintenance activities.

10.2.1 Asphalt materials modified by nanomaterials

The study of asphalt materials modified by nanomaterials has sparked great interest in recent years. It was found that the overall performance of the asphalt materials can be modified by the addition of various nanomaterials (You et al., 2011; Merusi et al., 2012; Yang and Tighe, 2013; Shafabakhsh et al., 2014). Parviz (2011) summarized the types of nanomaterials and the benefits of the asphalt pavements modified with them. Fang et al. (2013) demonstrated the mechanisms of the nanomodification from the compatibility, stability, and aging resistance perspectives. The mechanical properties of asphalt materials modified by nanoclay were investigated by El-Shafie et al. (2012). It was found that the addition of small amount of nanoclay particles has evidently positive effects on the mechanical performances of asphalt material. Carbon nanofibers, as another important additives, have been added into the neat asphalt to enhance the viscoelastic and fatigue performance (Khattak et al., 2012), and the microstructures were characterized by SEM analysis. Dry and wet processes were applied for investigation. It was found that, with the addition of some nanomaterials, both the viscoelastic and rutting resistance can be improved (Khattak et al., 2013).

In addition to the neat asphalt materials, the polymer-modified asphalt materials with the addition of nanoclay were investigated (Sureshkumar et al., 2010; Golestani et al., 2012; Yao et al., 2012). It was found that the nanoclay is helpful for compatibility between the poly ethylene-co-vinyl acetate (EVA) and the asphalt binder. The linear and branch styrene-butadiene-styrene (SBS)-modified asphalt materials with or without addition of nanoclay were prepared, and their physical, mechanical, rheological, and storage stability were compared. The results showed that the linear SBS−nanocomposite modified asphalt is willing to form an exfoliated structure, whereas the branch SBS−nanocomposite modified asphalt is willing to form an intercalated structure. The nanoclay has positive effects on enhancing the physical properties, rheological behaviors, and storage stability of the polymer-modified asphalt. The softening points and viscosity increased, whereas the penetration decreased. The ductility and elastic recovery were largely influenced by the addition of the nanoclay, and the best rutting resistance was obtained with the ratio of SBS to nanoclay of 100:25.

Apart from the basic pavement mechanical and durability properties evaluation, other merits of the nanomodified asphalt pavements were introduced. The addition of the nanoclay used as the flame retardants on fire reaction was investigated

(Bonati et al., 2013). In this study, the fire behavior and the smoke release properties of the nano organo-clay modified asphalt mixtures were evaluated. It was found that with the synergic use of aluminum hydroxide, magnesium hydroxide, and nanoclay, the fire-resistant behavior of the asphalt mixture can be considerably improved.

The durability of asphalt materials modified by nanomaterials exposed to various deicing solutions ($NaCl$, $MgCl_2$, and $CaCl_2$) and water environments was evaluated (Goh et al., 2011). In this study, the mixtures were prepared with various amounts of nanoclay and/or nanofibers. The moisture susceptibility and deicer impacts were assessed. The results indicated that after seven freeze−thaw cycles, the addition of nanoclay and nanofibers would enhance the moisture susceptibility performance, which is helpful to reduce the moisture damage potential of the pavements. Ameri et al. (2013) used zycosoil as a nano-organosilane antistripping additive to modify the moisture resistance of the hot mixed asphalt (HMA) under freeze−thaw environments. It was found that the resilient modulus ratio of the mixtures was enhanced, and the adhesion bond between the aggregates and the asphalt binders increased as well. Similar results were obtained by Nejad et al. (2012).

10.2.2   Cement concrete materials modified by nanomaterials

For cement concrete materials, nano SiO_2 particles are the most widely used material as the reinforcement additive (Madini et al., 2012; Tobón et al., 2012; Singh et al., 2013; Aleem et al., 2014; Hou et al., 2014). It has been proven that both the sustainability and mechanical properties can be evidently improved with a small amount of nano SiO_2 particles (Senff et al., 2009, 2010). In addition to SiO_2 nanoparticles, TiO_2 nanoparticles are another important additive to modify the performance of cement concrete pavements (Jalal et al., 2013; Feng et al., 2013; Li et al., 2014). Unlike SiO_2 nanoparticles, which acts only as the reinforcement additives of the concrete, TiO_2 nanoparticles can also play a self-cleaning role due to their photocatalytic capability (Ballari et al., 2011; Chen et al., 2011; Matějka et al., 2012; Guo et al., 2013; Sugrañez et al., 2013; Yousefi et al., 2013; Essawy and Aleem, 2014; Karapati et al., 2014; Senff et al., 2014). In addition, due to the specific high solar reflective capability of TiO_2 nanoparticles, they are also used to mitigate the heat island effect in urban areas (Santamouris, 2013). Another important nanomaterial used as the reinforcement is carbon nanotubes (Li et al., 2013, 2014), which were used to prepare self-deicing pavements, or self-sensing concrete to monitor the stress and strain on concrete infrastructures.

Most recently, the effects of the types, sizes, shapes, and pore distribution of nanoparticles on the reinforcement were investigated (Givi et al., 2010, 2013; Hou et al., 2013; Quercia et al., 2012, 2013, 2014). It has been proven that the specific surface area, the volume of the micropores, and the average size of the primary nanoparticles are key factors determining the final properties of the reinforced concrete materials. This is a good start to help optimizing the modification process, and more microstructure characterization methods should be applied to elucidate the real mechanisms of the reinforcement in future studies.

10.3   Mechanical and environmental resistance

The requirements of concrete pavements are much more critical than those of concrete buildings, because pavements have to face multiple effects, including the wear from the interaction between the vehicle tires and the pavements, the mechanical forces from the traffic loading, the deicing chemical attacks, and the wet−dry and freeze−thaw damage cycles. These influencing factors largely affect the durability of concrete pavements. Therefore, the mechanical and environmental resistance of concrete has to be enhanced to satisfy the critical requirements due to the aggressive application environments.

10.3.1   Mechanical performance

The mechanical performance of the pavement materials modified by nanoparticles has greatly interested in recent years (Rashad, 2013a). The most widely used nanomaterials are nano SiO_2, nano TiO_2, nanoclay, carbon nanotubes, and nanofibers (Morsy et al., 2011; Nazari and Riahi, 2011a,b; Kawashima et al., 2012; Santagata et al., 2012; Beigi et al., 2013; Shakhmenko et al., 2013; Kim et al., 2014b; Aleem et al., 2014). Some researchers also reported the mechanical-performance modification of cementitious materials with the addition of nano Fe_2O_3, Al_2O_3, ZrO_2, ZnO/ZnO_2, and other oxide nanoparticles (Nazari and Riahi, 2011a,c; Riahi and Nazari, 2011; Bhuvaneshwari et al., 2012; Oltulu and Sahin, 2011, 2013, 2014; Yuan et al., 2013; Rashad, 2013b; Safiuddin et al., 2014; Senff et al., 2014; Barbhuiya et al., 2014; Hosseini et al., 2014; Senff et al., 2014).

In 2004, Li and her coauthors studied the compressive and flexural strengths of the cement mortar modified by TiO_2, SiO_2, and Fe_2O_3 nanoparticles. It was found that the mechanical properties were evidently enhanced with addition of the nanoparticles (Li et al., 2004). In 2006, they reported the wear-resistance performance of the concrete pavement materials modified with TiO_2 and SiO_2 nanoparticles (Li et al., 2006a). The results showed that the abrasion resistance of the concrete containing nanoparticles is much larger than that containing polypropylene fibers or plain concrete. In addition, the performance of the concrete modified by nano TiO_2 is better than those modified by nano SiO_2.

Similar results were obtained recently (Ltifi et al., 2011; Stefanidou and Papayianni, 2012; Behfarnia and Salemi, 2013). The compressive strength of the cement concrete materials modified by nano SiO_2 or nano Al_2O_3 was studied by Behfarnia and Salemi (2013). It was found that the 28 and 120 d compressive strengths of the concrete mixed with 5 wt% of nano SiO_2 increased 30% and 45%, respectively. The positive modification effect of the compressive strength by adding nano Al_2O_3 particles was also proven by Li et al. (2006b). In this study, it was found that, with addition of 7 wt% Al_2O_3 nanoparticles, the 7 d compressive strength of the modified cement mortar increased by 30%, and with addition of 5 wt% Al_2O_3 nanoparticles, the 28 d elastic modulus increased by 143%.

Other than the chemical composition of the nanoparticles, the effects of the particle size on the mechanical properties of the concrete were analyzed as well (Haruehansapong et al., 2014). In this study, the chosen particle size of the nano

SiO_2 were about 12, 20, and 40 nm. The compressive strength-testing results demonstrated that the performance of the samples modified with the particle size of 40 nm is higher than that of the other two due to the agglomerations and ineffective dispersion of the smaller-sized nanoparticles.

Recently, the effects of the dispersion condition of the nanoparticles on the properties of cement concrete were investigated (Kong et al., 2012, 2013; Wang et al., 2013; Horszczaruk et al., 2014). In Horszczaruk's study, acetone and water were used as the dispersants to compare the effects of nanoparticles dispersion on the mechanical properties of the cement composites. It was found that the addition of the mesoporous nano SiO_2 spheres in the acetone has higher modification efficiency on mechanical properties than those dispersed in water.

Unlike the results presented above, Senff reported a different phenomenon of the compressive strength of the cement mortar modified by nano SiO_2 and nano TiO_2. It was claimed that the compressive strength was not sensitively increased, whereas the rheological behavior and plastic viscosity performances were enhanced significantly, with the addition of the nanoparticles (Senff et al., 2012).

Another interesting study reported that the compressive strength enhancement of the cement concrete modified by nano SiO_2 was not evident if using slump rather than weight content as reference, because the addition of nano silica will largely change the workability performance of the concrete materials (Berra et al., 2012).

It must be noted here that, so far, little study was focused on the low dosage of the nanoparticles, especially doses lower than 1 wt%. Many of the investigations gave the testing results with the weight fraction from 3 wt% to 10 wt%. Therefore, it is necessary to find out if the low dosage works as well as the high dosage in cement concrete. Our recent study (Feng et al., 2013) presented the mechanical performance of the cement paste with a low-dosage addition of TiO_2 nanoparticle (less than 1%). Figure 10.2 presents the 28-day three-point flexural strength as a function of the nano-TiO_2 content by the weight fraction of the cement paste, with the water/cement ratio fixed at 0.4. It reveals that mixing a small amount (0.1 wt%) of nano TiO_2 into the cement can increase its flexural strength by 4.5% (from 11.53 to 12.05 MPa). However, the benefits diminished with further increase of the nano-TiO_2 nanoparticles. The flexural strength of cement paste reached a peak value of 12.48 MPa, with mixing 1.0 wt% of nano-TiO_2 particles.

10.3.2 Environmental resistance

The durability of pavements exposed to various aggressive environments has substantial economic, social, and environmental implications. The issue is exacerbated in cold regions, where the pavement material is at risk of freeze−thaw cycling and physical and chemical attack by deicing chemicals (Pigeon and Pleau, 1995). Physical attack by deicing chemicals can lead to the damage of pavements in the common forms of scaling, map cracking, or paste disintegration (Sutter et al., 2008). Deicing chemicals may also pose fatal effects on concrete pavement materials through their reactions with cement binder and aggregates, and thus lead to the reduction of the integrity and strength of the concrete pavement materials (Sutter et al., 2008; Shi et al., 2009,
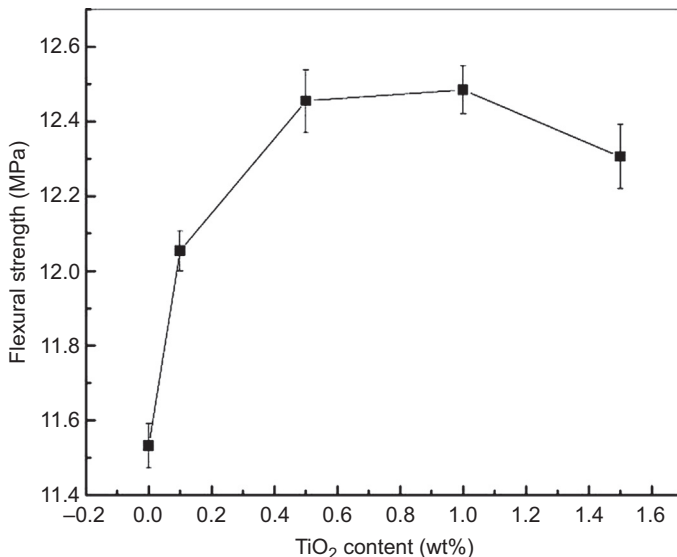
Figure 10.2 Three-point flexural strength as a function of nano TiO$_2$ dosage in cement paste. Feng et al. (2013). Reprinted with permission from Industrial & Engineering Chemistry Research. Copyright (2013) American Chemical Society.

2010, 2011). Finally, roadway deicers often use chlorides to decrease the freezing point, and the chloride anions' ingression into the pavement materials can introduce the rebar or dowel bar corrosion in concrete and results in premature deterioration of the reinforced concrete (Shi et al., 2012; Liu and Shi, 2012; Yu et al., 2010).

To the best of our knowledge, only limited studies have been conducted to evaluate the environmental resistance of pavement materials modified by nanoparticles to freeze−thaw damage or salt scaling. As a result, there is a need to focus on understanding the modification mechanisms from the nanoscale for preserving pavements in the presence of deicing chemicals and to reveal the main characteristics of the nanomodification that protects the pavement from aggressive environments. Although studies of the durability of the nanoparticle-modified pavement exposed to aggressive environments have not been very fruitful, some studies have demonstrated that the durability of both the asphalt pavements and cement concrete pavements is able to be improved by adding nanomaterials (Li et al., 2007; Zhang and Li, 2011; Givi et al., 2013).
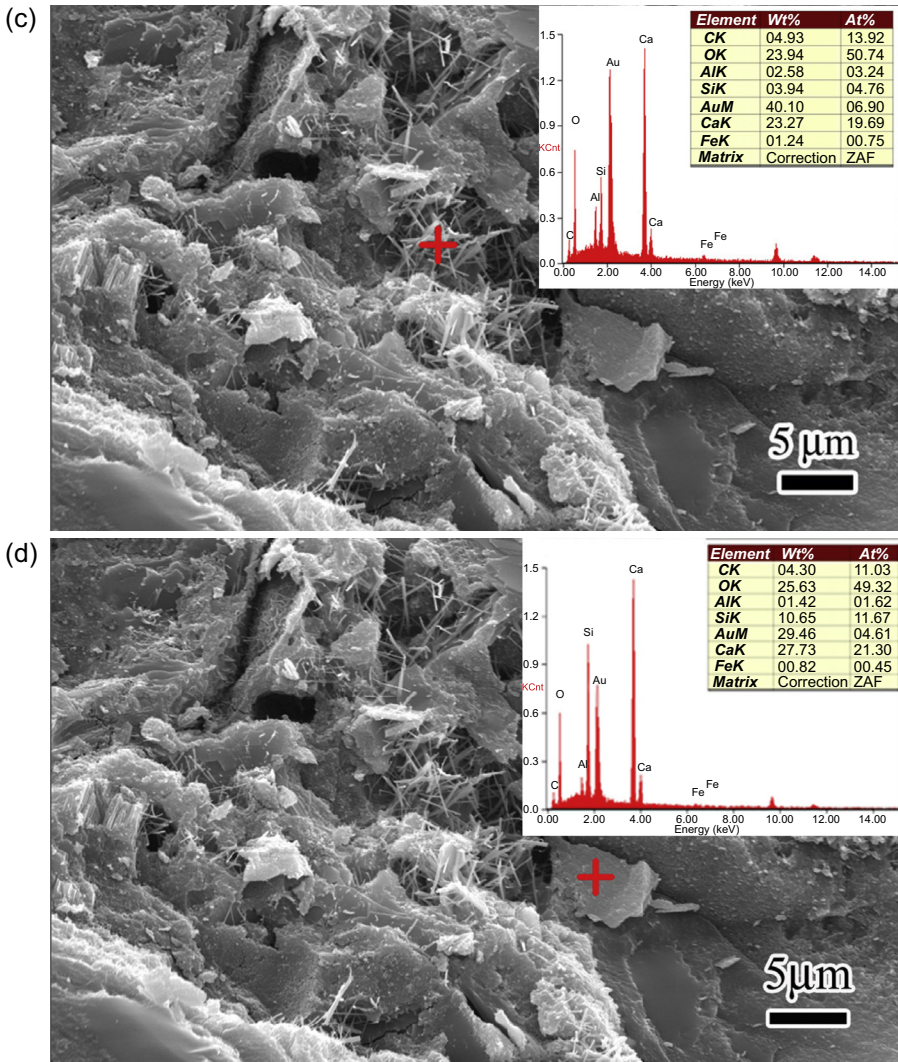
The freeze−thaw resistance of the cement concrete materials modified by nano silica and nano alumina was investigated by Behfarnia and Salemi (2013). In this study, the cement concrete modified with nano silica and nano alumina experienced up to 300 freeze−thaw cycles in water and was compared with normal cement concrete as control. Figure 10.3 shows the external dimensions of the tested samples. As can be seen in Figure 10.3, the freeze−thaw resistance of the concrete is considerably improved with the addition of nanoparticles. The strength loss of the concrete mixed with 5 wt% of nano silica was only 16%, whereas the controlled one showed 100% strength loss after 300 freeze−thaw cycles.
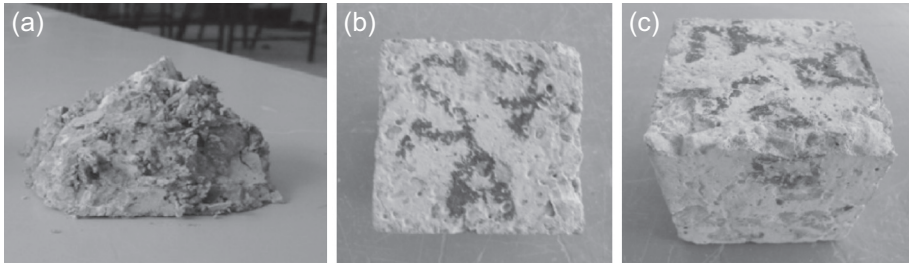
Figure 10.3 Concrete samples experienced 300 F/T cycles of (a) control sample, (b) with 5 wt% nano SiO$_2$, and (c) with 3 wt% nano Al$_2$O$_3$.
Behfarnia and Salemi (2013). Reprinted with permission from Construction and Building Materials. Copyright (2013) Elsevier.

Salemi also proved that the nano SiO$_2$ has a considerably positive effect on the freeze−thaw resistance of the concrete pavement (Salemi and Behfarnia, 2013). With the addition of 5 wt% nano SiO$_2$ or nano Al$_2$O$_3$, the mechanical properties of the concrete increased by 8%, whereas the freeze−thaw resistance increased by over 80% comparing with the plain concrete.

Most recently, a similar study has been investigated by Leòn et al. (2014). In this study, four types of cement mortars—control, 5% nano SiO$_2$, 5% nano Al$_2$O$_3$, and a mix of 2.5% n-SiO$_2$ and 2.5% n-Al$_2$O$_3$—were prepared, and their mechanical properties, abrasion resistance, and freeze−thaw resistance were tested. In addition, the porosity and pore distribution were investigated by mercury intrusion porosimetry (MIP), and the relationship between the C-S-H gel and Ca(OH)$_2$ was characterized by thermal gravimetric analysis (TGA).

However, unlike the results of the former studies (Behfarnia and Salemi, 2013; Salemi and Behfarnia, 2013), in which the freeze−thaw resistance of the cement concrete modified with nano Al$_2$O$_3$ is better than that modified with nano SiO$_2$, Leòn's study claimed that the addition of the nano Al$_2$O$_3$ has little or negative effects on the freeze−thaw resistance of the cement mortar. Two possible reasons might be the origins of the disagreement. First, the average size of the nano Al$_2$O$_3$ used in Behfarnia's study was about 8 nm, whereas in Leòn's study, it was about 260−550 nm. Second, the dosage of the nano Al$_2$O$_3$ particles was different. Behfarnia's dosage is up to 3 wt%, whereas Leòn's is 5 wt%. Although the effect of the nano Al$_2$O$_3$ modification was not the same, both these studies agreed that the nano SiO$_2$ has a positive effect on the anti-freeze−thaw performances of cement matrix composites.

10.4 Microstructures of nanoparticle-reinforced cement-based composites

As we mentioned in this chapter, the overall performances of all engineering materials are determined by their microstructures. Therefore, the appropriate microstructure characterization of the pavement materials modified by nanoparticles is the most

important approach that not only sheds lights on the potential mechanisms of the modification, but also helps optimize the designation process of the pavement materials with respect to the overall performance.

In the past decade, thanks to the rapid progress and improved availability of advanced characterization techniques, numerous engineering and mechanistic studies of nanotechnology for cementitious materials have been presented (Ye et al., 2007; Li et al., 2007; Han et al., 2013). Recently, to demonstrate the microstructure of the cement paste from nanoscale, many technologies such as nuclear magnetic resonance (NMR) (Kim et al., 2013; Edwards et al., 2007), small-angle X-ray (SAXS) (Haeussler et al., 2009), small-angle neutron scattering (SANS) (Allen and Thomas, 2007b), and pair distribution function (PDF) approaches have been utilized (Skinner et al., 2010). Scanning electron microscope with energy dispersive spectrometer (SEM/EDS) (Chen et al., 2010) and transmission electron microscope (TEM) (Xu and Viehland, 1996) have been used for observing the microstructure and analyzing the chemical composition of cement-based materials; atomic force microscope (AFM) has been used for observing the morphology and evaluating mechanical properties from nanoscale (Sáez de Ibarra et al., 2006); and differential scanning calorimetry (DSC) (Wei et al., 2012) and X-ray diffraction (XRD) (Scrivener et al., 2004; Kim et al., 2013) have also been used to analyze the composition of the hydration products and crystalline structures of Portland cement paste, respectively.

Currently, the most widely used tool for the microstructure analysis of the concrete modified by nanomaterials is SEM (Qing et al., 2007; Kong et al., 2012; Meng et al., 2012; Lv et al., 2014). The microstructures of Portland cement paste modified by SiO_2 and Fe_2O_3 nanoparticles and by carbon nanotubes have been reported (Li et al., 2004). Figure 10.4 shows the SEM images of the fracture surfaces of the cement modified with Fe_2O_3 and SiO_2 nanoparticles, respectively. As demonstrated in Figure 10.4, there are several typical phases shown with clear morphologies, including layer-shaped $Ca(OH)_2$, amorphous C-S-H phase, and pores, shown as areas 1, 2, and 3, respectively.

0%	3wt% Nano Fe_2O_3	3 wt% Nano SiO_2
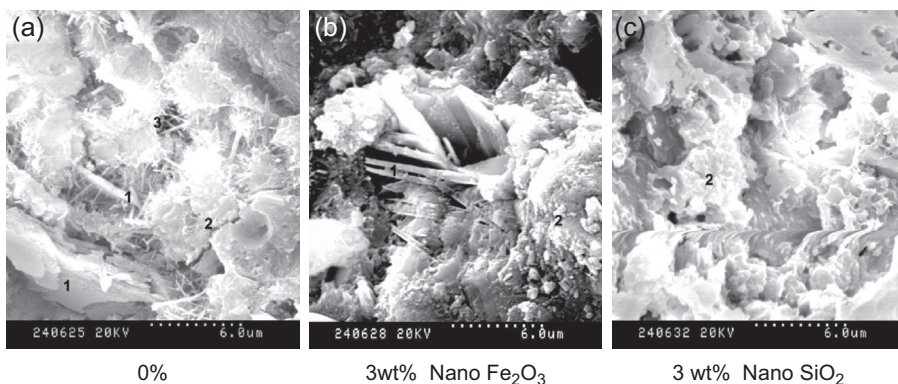
Figure 10.4 SEM images of the crack surfaces of the cement modified with Fe_2O_3 and SiO_2 nanoparticles.
Li et al. (2004).
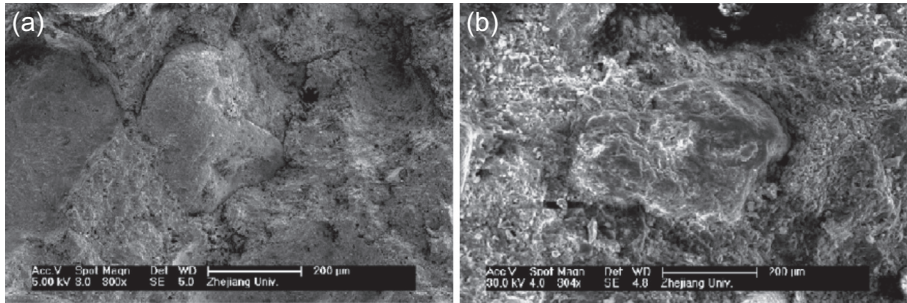
Figure 10.5 SEM images of the crack surfaces of the cement modified (a) without and (b) with Al_2O_3 nanoparticles.
Li et al. (2006). Reprinted with permission from Materials Letters. Copyright (2006) Elsevier.

The SEM images of the fracture surfaces of the nano Al_2O_3 modified cement mortar have been shown in Figure 10.5. The authors claimed that the interfaces between the aggregates and the cement binder will largely be affected by the nano Al_2O_3 particles that were absorbed on the surfaces of the aggregates.

Figure 10.6(a) and (b) shows the comparison of the SEM images of the fracture surfaces of the hardened Portland cement paste with and without the addition of TiO_2 nanoparticles (at 1.0 wt%). In the low-magnification mode (shown in Figure 10.6(a)), some microcracks perpendicular to the fracture surface of the sample can be observed (area A). The flat areas represent the microcrack surfaces that are parallel to the fracture surface of the sample (area B). Furthermore, some areas with clear internal defects and micropores (area C) can be observed as well. With the TiO_2 nanoparticles, the hydration products were distributed more homogeneously than the plain cement paste (shown as area D in Figure 10.6(b)), and the density and size of the microcracks and micropores were evidently reduced. Meanwhile, some nanosized needle-shaped new type of hydration products can be observed (area E).

In former studies, it has been proven that the nanoparticles can act as nuclei to grow nanotubes, nanobelts, or nanowires with proper external conditions. In cementitious materials, it is also believed that the nanosized particles can act as nuclei to form new types of needle-shaped (or wire-shaped) hydration products. Figure 10.6(c) and (d) demonstrates the high-magnification image with the EDS results of the needle-shaped hydration products in area E (Figure 10.6(b)). As illustrated from the EDS results, the chemical composition of the needle-shaped hydration products was different from that of the other phase adjacent to it. Despite the Ca contents, the needle-shaped products featured a Ca−Si ratio of 5:1 and Al−Si ratio of 3:5, whereas the other phase near the needle-shaped products featured a Ca−Si ratio of 2:1 and an Al−Si ratio of 1:6. Compared with the normal hydrate products, these in situ grown nanosized needle-shaped products can fill the submicron pores and cracks in the paste more efficiently, and reinforce the paste by bridging the cracks.

This needle-shaped hydration products were also observed by other studies (Meng et al., 2012). However, it is still a tough challenge to directly elucidate the fine microstructures and the chemical compositions of this new type of hydration products.
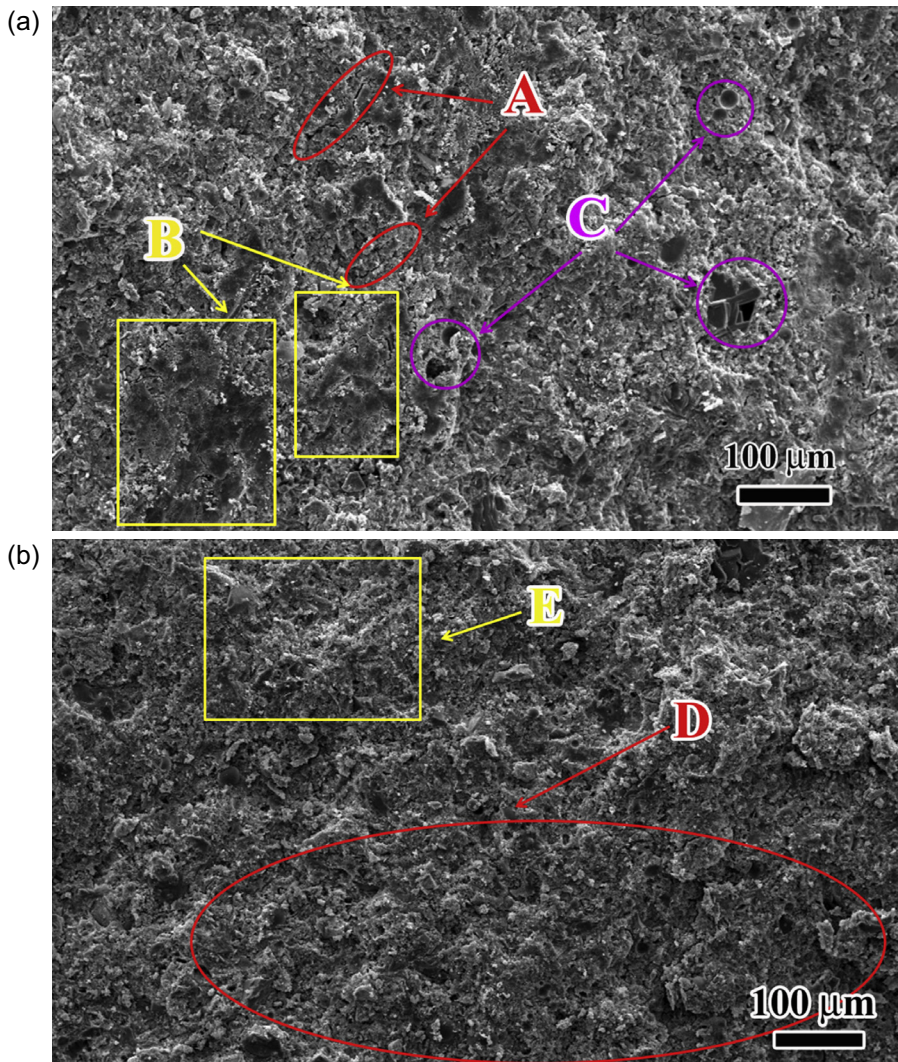
Figure 10.6 SEM morphology of the fracture surfaces: (a) low magnification of regular cement paste; (b) low magnification of cement paste modified by nano TiO_2; and (c, d) high magnification of cement paste modified by nano TiO_2 (insert: EDS data).
Feng et al. (2013). Reprinted with permission from Industrial & Engineering Chemistry Research. Copyright (2013) American Chemical Society.

(c)

Element	Wt%	At%
CK	04.93	13.92
OK	23.94	50.74
AlK	02.58	03.24
SiK	03.94	04.76
AuM	40.10	06.90
CaK	23.27	19.69
FeK	01.24	00.75
Matrix	Correction	ZAF

(d)

Element	Wt%	At%
CK	04.30	11.03
OK	25.63	49.32
AlK	01.42	01.62
SiK	10.65	11.67
AuM	29.46	04.61
CaK	27.73	21.30
FeK	00.82	00.45
Matrix	Correction	ZAF

Figure 10.6 Continued.

There is an argument that the needle-like hydration products are ettringite; see Figures 10.6 and 10.7 (Pourjavadi et al., 2012; Feng et al., 2013). Pourjavadi believes that the needle-shaped hydration products are ettringite, whereas Feng thinks that the needle-like hydration products are new types of C-S-H that were grown with the help of the nanoparticles as the nucleus. Figure 10.6(c) gives the EDS analysis of the needle-shaped phases. As can be seen in the EDS results, it was found that the needle-shaped phases were composed of Ca, Al, and O; large amounts of Si and
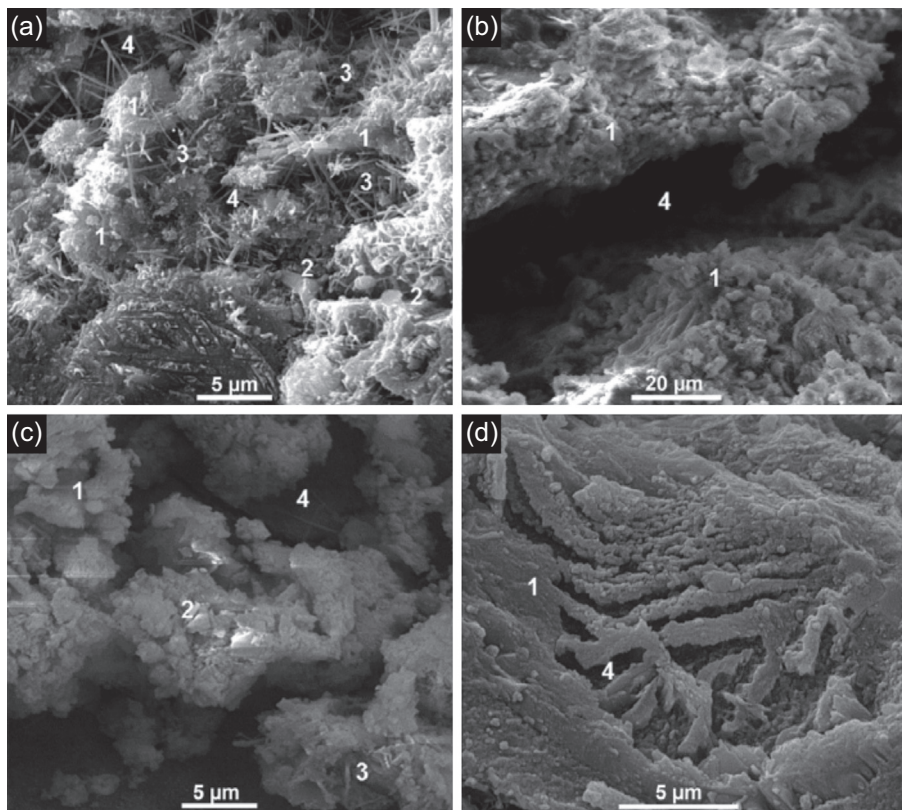
Figure 10.7 SEM images of pastes cured at room condition for 28 days: (a) mix Z-0 (control); (b) mix O-0 (1 wt% NS); (c) mix Z-3 (0.3 wt% SAP); and (d) mix O-3 (1 wt% NS + 0.3 wt% SAP). 1 = CASAH; 2 = Ca(OH)$_2$; 3 = ettringite; and 4 = pores. Pourjavadi et al. (2012). Reprinted with permission from Materials and Design. Copyright (2012) Elsevier.

little S were observed. As a result, it was claimed by the authors that the needle-shaped phase is not only the ettringite phase.

TEM is another effective tool to analyze the phase structure and their chemical compositions. Although a few studies demonstrated the microstructure of the hydration products via TEM (Xu and Viehland, 1996), very limited studies were quantitatively investigated from the chemical composition and crystallography perspective. Recently, the microstructures of the hydration products were investigated in our lab via TEM/EDS at the nanoscale (to avoid the damage of microstructures during the preparation process, the samples for TEM analysis were carefully cut from hardened cement paste and followed by sandpaper polishing and ionic sputtering, rather than using the ground powders of the hardened cement). Corresponding to the SEM results, the TEM image of the needle-shaped hydration product phase in cement after being modified with nano TiO$_2$ particles is shown in Figure 10.8(a). In addition, Figure 10.8(b) and (c)
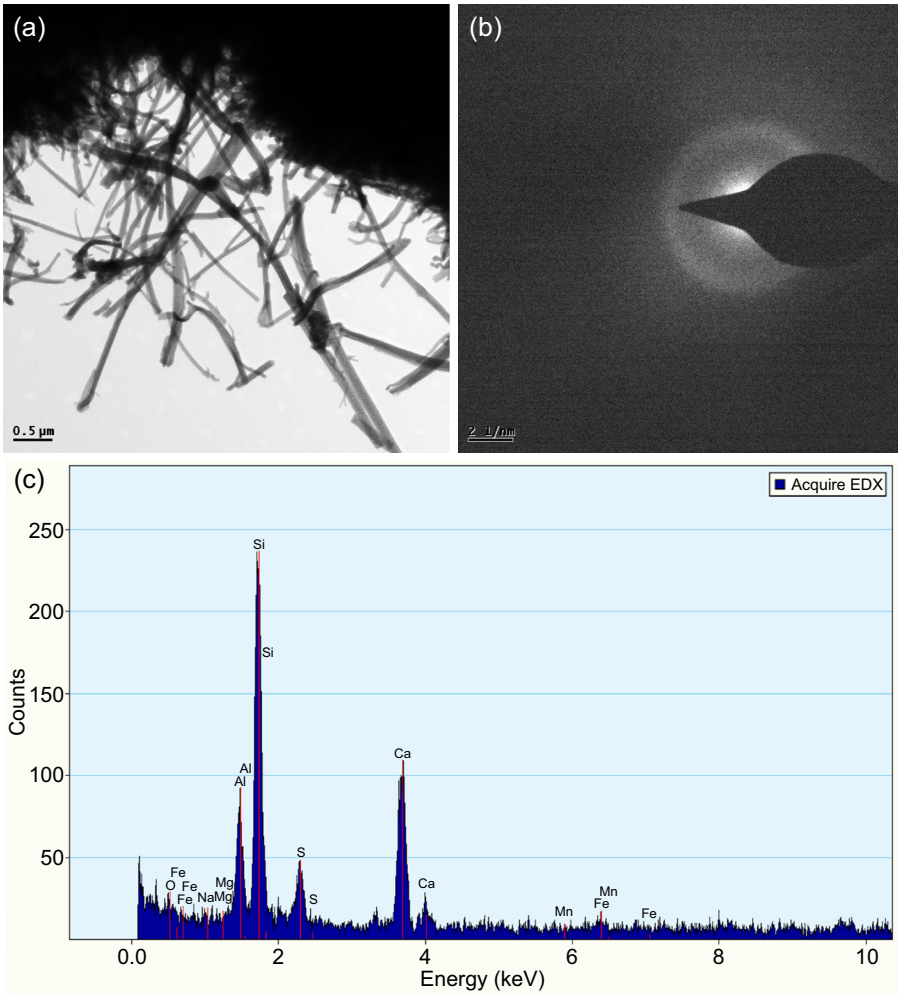
Figure 10.8 (a) TEM image of the needle-shaped hydration product phase in cement after modified with nano TiO_2 particles. (b, c) These demonstrate the selected area electron diffraction (SAED) pattern and the quantitative EDS analysis result corresponding to the area of (a).

demonstrates the selected area electron diffraction (SAED) pattern and the quantitative EDS analysis result corresponding to the area of Figure 10.8(a). As can be seen in Figure 10.8(a), the diameters of the needle-shaped hydration products range from 50 to 200 nm, and the SAED pattern shows little typical diffraction rings or spots. The EDS results show that the chemical compositions of the needle-shaped phase are Si, Ca, Al, and a small amount of S. As a result, it can be claimed that this needle-shaped hydration product should not be considered as ettringite due to the following two reasons. First, the ettringite is a crystal with a chemical composition of $3CaO \cdot Al_2O_3 \cdot 3CaSO_4 \cdot 32H_2O$, which means that little Si should be detected in

the EDS analysis results. Second, the diffraction spots of the ettringite could have been evidently observed in the SAED pattern corresponding to the TEM images. These two conditions were both not satisfied in our TEM analysis results. The details and the mechanisms of this product still need further investigation in our future studies.

Apart from SEM and TEM analysis, XRD has been widely used to characterize the crystal phases of the hardened cement (Qing et al., 2007; Feng et al., 2013; Aleem et al., 2014). Figure 10.9 shows an XRD pattern comparison of the ordinary Portland cement paste with and without modification of nanoparticles at various weight contents. By using Portlandite as the reference, it further proves that the hydration process of the cement pastes has been changed with the addition of TiO_2 or SiO_2 nanoparticles. As mentioned, the amount of $Ca(OH)_2$ is not a constant value during the hydration process, and it is inversely proportional to the quantity of the C-S-H gels. As can be seen in the XRD results, the main characteristic Portlandite peaks were reduced by about 20−30% with the addition of TiO_2 nanoparticles (Figure 10.9(a)), confirming the role of nano TiO_2 in consuming Portlandite crystals via the pozzolanic reaction. Such consumption of Portlandite leads to a denser microstructure and formation of desirable C-S-H gel, contributing to high mechanical properties of the cement materials. Similar results were observed in nano SiO_2 modification samples (Aleem et al., 2014), in which the crystal peaks of $Ca(OH)_2$ were considerably decreased with the addition of nano SiO_2 particles.

With the addition of the TiO_2 nanoparticles, during the hydration process, the O^{2-} in $-O-Ti-O-$ bonding will be changed with the appearance of OH^- and form an $H-O-Ti-O-H$ structure, and the H^+ in $O-H$ will be replaced by Ca^{2+} to form an
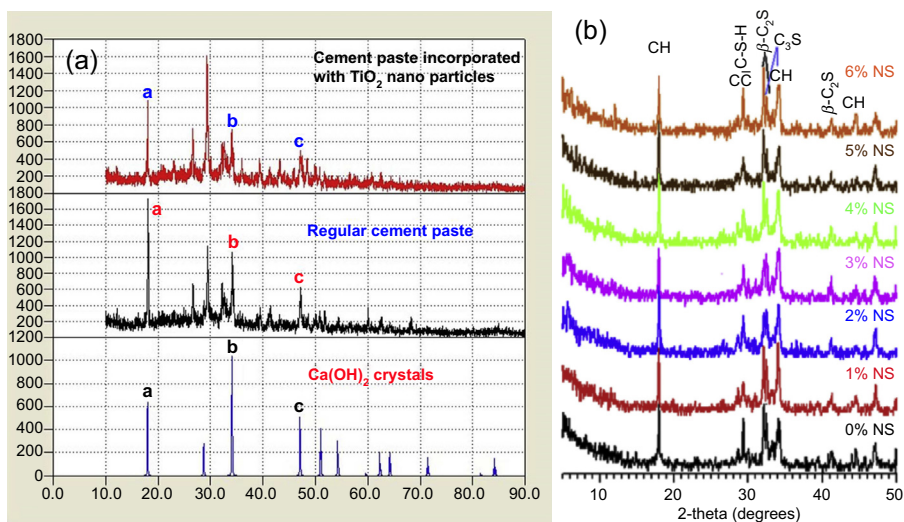
Figure 10.9 XRD patterns of the nano-TiO_2 modified Portland cement paste versus the regular Portland cement paste and Portlandite (a) nano TiO_2 modification *(Feng et al. (2013). Reprinted with permission from Industrial & Engineering Chemistry Research. (Copyright (2013) American Chemical Society)* and (b) nano SiO_2 modification *(Aleem (2014). Reprinted with permission from Construction and Building Materials. (Copyright (2014) Elsevier).*

$O-Ca-$ bond, which leads to the formation of a nanosized $-Ca-O-Ti-O-Ca-$ structure. However, because the quantity of the $-O-Ti-O-$ is relatively small, once the small amount of $-Ca-O-Ti-O-Ca-$ structure has been formed, the rest of the Ca^{2+} will react with Si^{4+} and OH^- and form the needle-shaped morphology by using the nanosized $-Ca-O-Ti-O-Ca-$ structure as the seed. In addition, the requirement of the reaction condition between the $Ca(OH)_2$ and TiO_2 to form $CaTiO_3$ is very critical, and normally needs the reaction temperature to be as high as 1000 K; therefore, the $CaTiO_3$ crystal is hard to form during the hydration process. It can be further seen from the XRD pattern of the cement paste with the addition of TiO_2 nanoparticles that no $CaTiO_3$ peaks can be detected. Based on the results of previous investigations, in the cement-based materials, the crystallized nano TiO_2 should be considered as an inert additive (Feng et al., 2013; Chen et al., 2012).

In the hardened cement paste modified by nanoparticles, during the crack propagation process, the needle-shaped hydration products can act as fibers that will bridge the cracks and thus effectively reinforce the cement paste by pulling out or deforming. Unlike the directly mixed fibers in the cement matrix, with the addition of the TiO_2 nanoparticles, the needle-shaped hydration products could be considered as in situ grown fibers that have relatively higher bonding strength in the matrix than the directly mixed fibers. This is both a physical and a chemical bonding on the cement matrix. Therefore, the increase of the crack propagation resistance provided by the in situ needle-shaped hydration products could be obtained. Unlike the mixed fibers in cement pastes, however, the quantity, length, and mechanical properties of the needle-shaped hydration products still cannot be obtained directly; therefore, it is still hard to precisely predict the final properties of the cement concrete modified by nanoparticles. As a result, the development of the micromechanical models for predicting the properties of this in situ growing fiber-reinforced cementitious materials is a new research topic for future studies.

Other than SEM, TEM, and XRD, AFM is another effective tool to characterize the nanostructure of the cement paste modified by nanoparticles (Feng et al., 2013). In Feng's study, AFM was applied to demonstrate the roughness and morphological information of the cement paste modified by TiO_2 nanoparticles. The as-fabricated bottom surface without further polishing was used for the AFM observation to avoid any potential changes of the surface condition by polishing process. The AFM height and deflection images were obtained in contact mode, and the phase images were obtained under the tapping mode. Figure 10.10 presents the AFM surface morphology of the normal cement paste and the cement paste modified with TiO_2 nanoparticles with 1.0 wt%, in a 1×1 μm^2 area. As can be seen in this figure, the regular normal cement paste and cement paste modified by TiO_2 nanoparticles feature a microstructure with distinct characteristics. Although the microstructure of the normal cement paste was very rough (Figure 10.10(a)), the nanomodified cement paste appeared much flatter (Figure 10.10(b)). It can be observed, from Figure 10.10(c) and (d), that the step heights of the normal cement paste and the nanomodified cement paste were 2.882 and 1.006 nm, respectively.

The roughness testing results demonstrate the microstructure uniformity of the cement pastes. In general, a lower roughness value, which means a more uniform
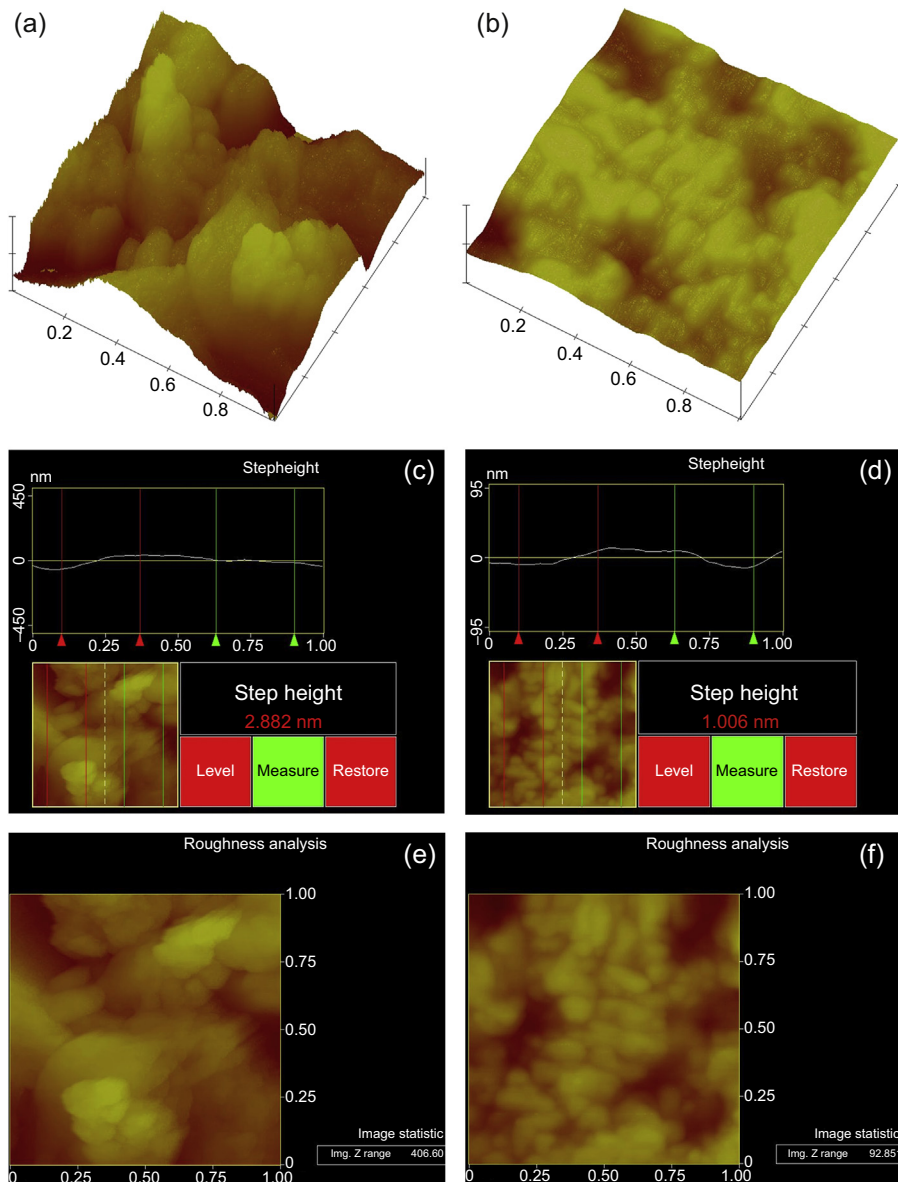
Figure 10.10 AFM observations of (a) height image of regular cement paste; (b) height image of cement paste modified by nano TiO$_2$ particles; (c) step height of; (d) step height of; (e) roughness of regular cement paste; and (f) roughness of cement paste modified by nano TiO$_2$; in $1 \times 1 \ \mu m^2$ area.

Feng et al. (2013). Reprinted with permission from Industrial & Engineering Chemistry Research. Copyright (2013) American Chemical Society.

and dense microstructure, represents higher mechanical properties and lower permeability of the cement paste. Figure 10.10(e) and (f) shows the roughness analysis results of the normal cement paste and the nano-TiO_2 modified cement paste. As can be seen in this figure, the cement paste modified by TiO_2 nanoparticles has a much lower roughness value (92.851 nm) than the normal cement paste (406.60 nm), suggesting the pore refinement by nanomodification. Similar results were obtained by analyzing the pore structure of the cement paste modified by various nanoparticles (Oltulu and Sahin, 2014).

Figure 10.11 presents the AFM data of the height and phase images of the normal cement paste and the cement paste modified with TiO_2 nanoparticles with 0.1 wt%, in a 10×10 μm^2 area. By comparing the height images of these two types of cement paste (Figure 10.11(a) and 10.11(b)), it can be concluded that the addition of TiO_2
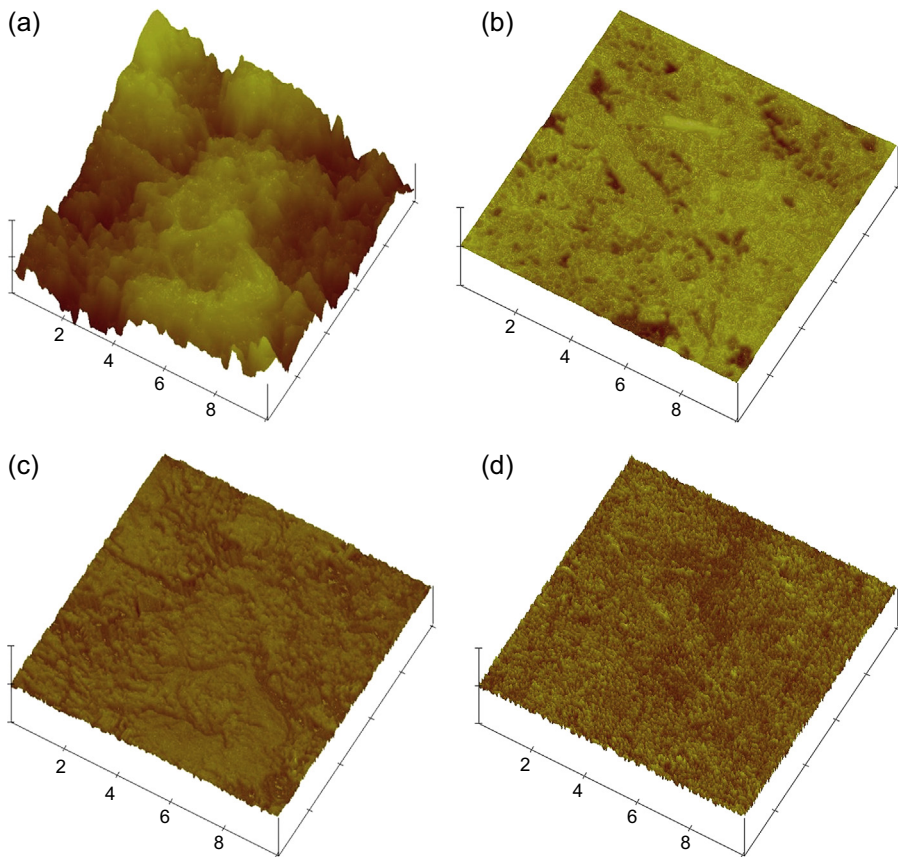
Figure 10.11 AFM observations of (a) height image of regular cement paste; (b) height image of cement paste modified by nano TiO_2; (c) phase image of regular cement paste; and (d) phase image of cement paste modified by nano TiO_2; in 10×10 μm^2 area.
Feng et al. (2013). Reprinted with permission from Industrial & Engineering Chemistry Research. Copyright (2013) American Chemical Society.

nanoparticles can lead to a flatter surface. Similarly, by comparing the phase images of the cement paste with and without adding TiO_2 nanoparticles (Figure 10.11(c) and (d)), it can be concluded that the phases of the paste modified by nano TiO_2 particles have much finer microstructures than the normal cement paste.

In a hydration process of normal Portland cement, the chemical reaction can be expressed as:

$$2Ca_3SiO_5 + 6H_2O \rightarrow 3(CaO)\cdot2(SiO_2)\cdot4(H_2O) + 3Ca(OH)_2 \tag{10.5}$$
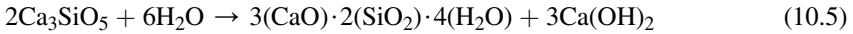
After the addition of the TiO_2 nanoparticles, the reaction environment has been changed because of the variation of the Ca^{2+} concentration; therefore, the chemical reaction will be changed as:

$$2Ca_3SiO_5 + 6H_2O \rightarrow x(CaO)\cdot2(SiO_2)\cdot y(H_2O) + (6\text{-}x)Ca(OH)_2 \tag{10.6}$$
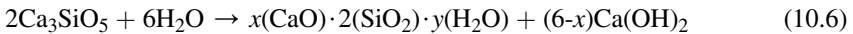
In this equation, the value of x varies with the Ca^{2+} concentration, which is a function of the content of the TiO_2 nanoparticles. This means the quantity of the $Ca(OH)_2$ is no longer a constant value. Due to the Ca content being a constant, based on Eqn (10.6), Ca can exist either as C-S-H gel or $Ca(OH)_2$ in a hardened cement paste. In other words, the lower amount of Portlandite, the higher amount of C-S-H gel. It is thus desirable to convert the noncementitious Portlandite into cementitious C-S-H gel. Any increase in the C-S-H amount or decrease in the Portlandite amount in cement paste will lead to higher performance of the hardened concrete.

10.5   Future trends

Future studies on the *mechanical and environmental resistance of nanoparticle-reinforced pavement materials* should focus on the following parts. First, investigation of the dispersion approaches of the nanoparticles in the cement or asphalt matrix is the most important factor that determines the final performance of pavements. Second, dosage optimization is still a challenge to obtain a stable and cost-effective pavement construction. Third, the mechanisms of nanoparticle reinforcement should be further studied from the microstructure characterization perspective. Fourth, how to choose appropriate nanoparticle types is another important issue that has to be considered. Fifth, the durability of the pavement materials modified by nanoparticles under synergistic aggressive environments, such as freeze−thaw cycles, deicing chemicals, and overweight loadings, should be systematically investigated. And, finally, micromechanical models for predicting the properties of the nanoparticle-reinforced pavement materials are new research topics for future studies.

The dispersion condition of the nanoparticles in the cement or asphalt matrix is the most important factor that determines the reinforcement effects. Although the dispersion approaches of the nanoparticles in various solutions have been investigated systematically in recent decades, it is still a very challenging topic if one considers the cost and the specific requirements of the cement or asphalt matrix. So far, it is still not very easy to obtain a stable and optimized dispersion condition of the nanoparticles in the cement or asphalt matrix.

Disagreement of the modification results according to the dosage is always the top challenge. Many studies have found that the mechanical properties of the pavement materials modified by nanoparticles were not linearly increased with increasing weight content of the nanoparticles. It reduces when the dosage reaches a critical value. Therefore, how to effectively optimize the dosage has to be systematically investigated from both the cost and performance perspectives. In addition, in the past decade, the dosage of the nanoparticles in the pavement materials, including asphalt and cement, ranged from 3 wt% to 10 wt% (and some were as high as 20 wt%). In those studies, the performance of the reinforcement effect was not very stable. The optimized dosage of various nanoparticles is still not well agreed. Furthermore, few studies focused on the modification effect of the low dosage (below 1 wt%) or ultralow dosage (below 0.1 wt%), which is an effective way to minimize the cost and benefit the dispersion of the nanoparticles.

The mechanisms of the pavement materials modified with various nanoparticles are still not very clear. Further studies from the microstructure characterization perspective should be applied systematically. Although SEM, XRD, DSC, and AFM were used to analyze the microstructure of the nanoparticle-modified pavement materials, the details or a quantitative characterization from nanoscale is still necessary to elucidate the modification mechanisms. In situ HRTEM, PDF, NMR, SAXS, and SANS approaches could be utilized to shed more light on the microstructure changes that occur with the addition of various nanoparticles.

Currently, although most of the studies agreed that the nanoparticles have positive effects on the performance of the pavement materials, the modification effects with various nanoparticles is not well agreed, especially with the addition of Al_2O_3 or Fe_2O_3 nanoparticles. In addition, even with the same chemical composition, the modification effects largely count on the shape, size distribution, pore structures, and different crystallization degrees of the nanoparticles. This is another important research direction for future studies.

Most importantly, study on the durability of nanoparticle-modified pavement materials under synergistic aggressive environments, including freeze−thaw cycle damage, deicing chemical attacks, and overweight loading, is still very limited. The mechanisms of durability enhancement of the nanomodification is the first priority to realize sustainability. However, to investigate this topic, the critical requirements for the testing devices have largely limited a deep understanding of this topic; therefore, it is necessary to design and develop some specific testing devices to investigate environmental resistance of nanomodified pavement materials under synergistic aggressive conditions.

Acknowledgments

References

Aleem Abd El, S., Heikal, M., Morsi, W.M., 2014. Hydration characteristic, thermal expansion and microstructure of cement containing nano-silica. Construction and Building Materials 59, 151−160.

Ameri, M., Kouchaki, S., Roshani, H., 2013. Laboratory evaluation of the effect of nano-organosilane anti-stripping additive on the moisture susceptibility of HMA mixtures under freeze−thaw cycles. Construction and Building Materials 48, 1009−1016.

Amirkhanian, A.N., Xiao, F., Amirkhanian, S.N., 2011. Characterization of unaged asphalt binder modified with carbon nano particles. International Journal of Pavement Research and Technology 4 (5), 281−286.

Allen, A.J., Thomas, J.J., Jennings, H.M., 2007. Composition and density of nanoscale calcium-silicate-hydrate in cement. Nature Materials 6, 311−316.

Allen, A.J., Thomas, J.J., 2007. Analysis of C-S-H gel and cement paste by small-angle neutron scattering. Cement and Concrete Research 37, 319−324.

Avrami, M., 1939. Kinetics of phase change I-general theory. Journal of Chemical Physics 7, 1103−1112.

Avrami, M., 1940. Kinetics of phase change II-Transformation-time relations for random distribution of nuclei. Journal of Chemical Physics 8, 212−224.

Avrami, M., 1941. Granulation, phase change, and microstructure-kinetics of phase change III. Journal of Chemical Physics 9, 177−184.

Balaguru, P., Chong, K., 2006. Nanotechnology and concrete: research opportunities. In: Proceedings of ACI Session on "Nanotechnology of Concrete: Recent Developments and Future Perspectives" Nov. 7, Denver, USA.

Bagheri, A.R., Zanganeh, H., Moalemi, M.M., 2012. Mechanical and durability properties of ternary concretes containing silica fume and low reactivity blast furnace slag. Cement and Concrete Composites 34 (5), 663−670.

Ballari, M.M., Yu, Q.L., Brouwers, H.J.H., 2011. Experimental study of the NO and NO_2 degradation by photocatalytically active concrete. Catalysis Today 161 (1), 175−180.

Barbhuiya, S., Mukherjee, S., Nikraz, H., 2014. Effects of nano-Al_2O_3 on early-age microstructural properties of cement paste. Construction and Building Materials 52, 189−193.

Behfarnia, K., Salemi, N., 2013. The effects of nano-silica and nano-alumina on frost resistance of normal concrete. Construction and Building Materials 48, 580−584.

Beigi, M.H., Berenjian, J., Lotfi Omran, O., Sadeghi Nik, A., Nikbin, I.M., 2013. An experimental survey on combined effects of fibers and nanosilica on the mechanical, rheological, and durability properties of self-compacting concrete. Materials and Design 50, 1019−1029.

Bernal, J.D., 1952. The structure of cement hydration compounds. In: Proceedings of the 3rd International Symposium on Chemistry of Cement. London, pp. 216−236.

Berra, M., Carassiti, F., Mangialardi, T., Paolini, A.E., Sebastiani, M., 2012. Effects of nanosilica addition on workability and compressive strength of Portland cement pastes. Construction and Building Materials 35, 666−675.

Bhuvaneshwari, B., Sasmal, S., Baskaran, T., Iyer, N.R., 2012. Role of nano oxides for improving cementitious building materials. Journal of Civil Engineering and Science 1 (2), 52−58.

Birgisson, B., Taylor, P., Armaghani, J., Shah, S., 2010. American road map for research for nanotechnology-based concrete materials. Transportation Research Record: Journal of the Transportation Research Board 2142, 130−137.

Birgisson, B., Mukhopadhyay, A.K., Geary, G., Khan, M., Sobolev, K., 2012. Nanotechnology in Concrete Materials: A Synopsis. Transportation Research E-Circular (E-C170).

Bittnar, Z., Bartos, P.J., Nemecek, J., Smilauer, V., Zeman, J. (Eds.), 2009. Nanotechnology in Construction: Proceedings of the NICOM3. Springer Science & Business Media.

Bonati, A., Merusi, F., Bochicchio, G., Tessadri, B., Polacco, G., Filippi, S., Giuliani, F., 2013. Effect of nanoclay and conventional flame retardants on asphalt mixtures fire reaction. Construction and Building Materials 47, 990−1000.

Bullard, J.W., et al., 2011. Mechanisms of cement hydration. Cement and Concrete Research 41, 1208−1223.

Chang, T.P., Shih, J.Y., Yang, K.M., Hsiao, T.C., 2007. Material properties of Portland cement paste with nano-montmorillonite. Journal of Materials Science 42 (17), 7478−7487.

Chen, J., Sorelli, L., Vandamme, M., 2010. A coupled Nanoindentation/SEM-EDS study on low water/cement ratio Portland cement paste: evidence for C-S-H/Ca(OH)$_2$ nanocomposites. Journal of the American Ceramic Society 93, 1484−1493.

Chen, J., Kou, S.C., Poon, C.S., 2011. Photocatalytic cement-based materials: comparison of nitrogen oxides and toluene removal potentials and evaluation of self-cleaning performance. Building and Environment 46 (9), 1827−1833.

Chen, J., Kou, S.C., Poon, C.S., 2012. Hydration and properties of nano-TiO$_2$ blended cement composites. Cement and Concrete Composites 34 (5), 642−649.

Edwards, C.L., Alemany, L.B., Barron, A.R., 2007. Solid-state Si-29 NMR analysis of cements: comparing different methods of relaxation analysis for determining spin-lattice relaxation times to enable determination of the C$_3$S/C$_2$S ratio. Industrial and Engineering Chemistry Research 46, 5122−5130.

El-Shafie, M., Ibrahim, I.M., Abd El Rahman, A.M.M., 2012. The addition effects of macro and nano clay on the performance of asphalt binder. Egyptian Journal of Petroleum 21 (2), 149−154.

Essawy, A.A., Aleem, S.A.E., 2014. Physico−mechanical properties, potent adsorptive and photocatalytic efficacies of sulfate resisting cement blends containing micro silica and nano-TiO$_2$. Construction and Building Materials 52, 1−8.

Fang, C., Yu, R., Liu, S., Li, Y., 2013. Nanomaterials applied in asphalt modification: a review. Journal of Materials Science and Technology 29 (7), 589−594.

Feng, D., Xie, N., Gong, C., Leng, Z., Xiao, H., Li, H., Shi, X., 2013. Portland cement paste modified by TiO$_2$ nanoparticles: a microstructure perspective. Industrial and Engineering Chemistry Research 52 (33), 11575−11582.

Garcia-Luna, A., Bernal, D.R., 2006. High strength micro/nano fine cement. In: de Miguel, Y., Porro, A., Bartos, P.J.M. (Eds.), NICOM 2: 2nd International Symposium on Nanotechnology in Construction. RILEM Publications SARL.

Givi, A.N., Rashid, S.A., Aziz, F.N.A., Salleh, M.A.M., 2010. Experimental investigation of the size effects of SiO$_2$ nano-particles on the mechanical properties of binary blended concrete. Composites Part B: Engineering 41 (8), 673−677.

Givi, A.N., Rashid, S.A., Aziz, F.N.A., Salleh, M.A.M., 2013. Influence of 15 and 80 nano-SiO$_2$ particles addition on mechanical and physical properties of ternary blended concrete incorporating rice husk ash. Journal of Experimental Nanoscience 8 (1), 1−18.

Goh, S.W., Akin, M., You, Z., Shi, X., 2011. Effect of deicing solutions on the tensile strength of micro-or nano-modified asphalt mixture. Construction and Building Materials 25 (1), 195−200.

Golestani, B., Moghadas Nejad, F., Sadeghpour Galooyak, S., 2012. Performance evaluation of linear and nonlinear nanocomposite modified asphalts. Construction and Building Materials 35, 197−203.

Guo, M.Z., Ling, T.C., Poon, C.S., 2013. Nano-TiO$_2$-based architectural mortar for NO removal and bacteria inactivation: influence of coating and weathering conditions. Cement and Concrete Composites 36, 101−108.

Haeussler, F., Tritthart, J., Amenitsch, H., 2009. Time-resolved combined SAXS and WAXS studies on hydrating tricalcium silicate and cement. Advances in Cement Research 21, 101−111.

Hanus, M.J., Harris, A.T., 2013. Nanotechnology innovations for the construction industry. Progress in Materials Science 58 (7), 1056−1102.

Han, B., Yang, Z., Shi, X., Yu, X., 2013. Transport properties of carbon-nanotube/cement composites. Journal of Materials Engineering and Performance 22, 184−189.

Haruehansapong, S., Pulngern, T., Chucheepsakul, S., 2014. Effect of the particle size of nanosilica on the compressive strength and the optimum replacement content of cement mortar containing nano-SiO$_2$. Construction and Building Materials 50, 471−477.

He, X., Shi, X., 2008. Chloride permeability and microstructure of Portland cement mortars incorporating nanomaterials. Transportation Research Record: Journal of the Transportation Research Board 2070, 13−21.

Horszczaruk, E., Mijowska, E., Cendrowski, K., Mijowska, S., Sikora, P., 2014. Effect of incorporation route on dispersion of mesoporous silica nanospheres in cement mortar. Construction and Building Materials 66, 418−421.

Hosseini, P., Hosseinpourpia, R., Pajum, A., Khodavirdi, M.M., Izadi, H., Vaezi, A., 2014. Effect of nano-particles and aminosilane interaction on the performances of cement-based composites: an experimental study. Construction and Building Materials 66, 113−124.

Hou, D., Ma, H., Li, Z., 2014. Morphology of calcium silicate hydrate (CSH) gel: a molecular dynamic study. Advances in Cement Research 27 (3), 135−146.

Hou, P., Kawashima, S., Kong, D., Corr, D.J., Qian, J., Shah, S.P., 2013. Modification effects of colloidal nanoSiO$_2$ on cement hydration and its gel property. Composites Part B: Engineering 45 (1), 440−448.

Jalal, M., Fathi, M., Farzad, M., 2013. Effects of fly ash and TiO$_2$ nanoparticles on rheological, mechanical, microstructural and thermal properties of high strength self compacting concrete. Mechanics of Materials 61, 11−27.

Jayapalan, A.R., Lee, B.Y., Kurtis, K.E., 2009. Effect of nano-sized titanium dioxide on early age hydration of Portland cement. Nanotechnology in Construction 3, 267−273.

Jennings, H.M., 2008. Refinements to colloid model of C-S-H in cement: CM-II. Cement and Concrete Research 38, 275−289.

Karapati, S., Giannakopoulou, T., Todorova, N., Boukos, N., Antiohos, S., Papageorgiou, D., Trapalis, C., 2014. Functionalization for efficient NO$_x$ removal in photoactive cement. Applied Surface Science 319, 29−36.

Kawashima, S., Kim, J.H., Corr, D.J., Shah, S.P., 2012. Study of the mechanisms underlying the fresh-state response of cementitious materials modified with nanoclays. Construction and Building Materials 36, 749−757.

Keyvani, A., 2007. Huge opportunities for industry of nanofibrous concrete technology. International Journal of Nanoscience and Nanotechnology 3 (1), 3−12.

Khattak, M.J., Khattab, A., Rizvi, H.R., Zhang, P., 2012. The impact of carbon nano-fiber modification on asphalt binder rheology. Construction and Building Materials 30, 257−264.

Khattak, M.J., Khattab, A., Rizvi, H.R., 2013. Characterization of carbon nano-fiber modified hot mix asphalt mixtures. Construction and Building Materials 40, 738−745.

Kim, K.M., Heo, Y.S., Kang, S.P., Lee, J., 2014a. Effect of sodium silicate-and ethyl silicate-based nano-silica on pore structure of cement composites. Cement and Concrete Composites 49, 84−91.

Kim, J.J., Rahman, M.K., Al-Majed, A.A., Al-Zahrani, M.M., Reda Taha, M.M., 2013. Nanosilica effects on composition and silicate polymerization in hardened cement paste cured under high temperature and pressure. Cement and Concrete Composites 43, 78−85.

Kim, H.S., Song, M., Seo, J.W., Shin, U.S., 2014b. Preparation of electrically conductive bucky-sponge using CNT-cement: conductivity control using room temperature ionic liquids. Synthetic Metals 196, 92−98.

Kong, D., Du, X., Wei, S., Zhang, H., Yang, Y., Shah, S.P., 2012. Influence of nano-silica agglomeration on microstructure and properties of the hardened cement-based materials. Construction and Building Materials 37, 707−715.

Kong, D., Su, Y., Du, X., Yang, Y., Wei, S., Shah, S.P., 2013. Influence of nano-silica agglomeration on fresh properties of cement pastes. Construction and Building Materials 43, 557−562.

Lee, B.Y., Kurtis, K.E., 2010. Influence of TiO_2 nanoparticles on early C_3S hydration. Journal of the American Ceramic Society 93, 3399−3405.

León, N., Massana, J., Alonso, F., Moragues, A., Sánchez-Espinosa, E., 2014. Effect of nano-SiO_2 and nano-Al_2O_3 on cement mortars for use in agriculture and livestock production. Biosystems Engineering 123, 1−11.

Li, H., Xiao, H.G., Yuan, J., Ou, J., 2004. Microstructure of cement mortar with nano-particles. Composites Part B: Engineering 35 (2), 185−189.

Li, H., Zhang, M.H., Ou, J.P., 2006a. Abrasion resistance of concrete containing nano-particles for pavement. Wear 260 (11), 1262−1266.

Li, Z., Wang, H., He, S., Lu, Y., Wang, M., 2006b. Investigations on the preparation and mechanical properties of the nano-alumina reinforced cement composite. Materials Letters 60 (3), 356−359.

Li, H., Zhang, M.H., Ou, J.P., 2007. Flexural fatigue performance of concrete containing nano-particles for pavement. International Journal of Fatigue 29 (7), 1292−1301.

Li, H., Zhang, Q., Xiao, H., 2013. Self-deicing road system with a CNFP high-efficiency thermal source and MWCNT/cement-based high-thermal conductive composites. Cold Regions Science and Technology 86, 22−35.

Li, H., Zhang, Q., Xiao, H., 2014. Analytic investigations of CNFP-based self-deicing road system on the deicing performance. Cold Regions Science and Technology 103, 123−132.

Lim, S., Mondal, P., 2014. Micro-and nano-scale characterization to study the thermal degradation of cement-based materials. Materials Characterization 92, 15−25.

Liu, Y., Shi, X., 2012. Stochastic modeling of service life of concrete structures in chloride-laden environments. Journal of Materials in Civil Engineering 24 (4), 381−390.

Ltifi, M., Guefrech, A., Mounanga, P., Khelidj, A., 2011. Experimental study of the effect of addition of nano-silica on the behaviour of cement mortars. Procedia Engineering 10, 900−905.

Lv, S., Liu, J., Sun, T., Ma, Y., Zhou, Q., 2014. Effect of GO nanosheets on shapes of cement hydration crystals and their formation process. Construction and Building Materials 64, 231−239.

Madani, H., Bagheri, A., Parhizkar, T., 2012. The pozzolanic reactivity of monodispersed nanosilica hydrosols and their influence on the hydration characteristics of Portland cement. Cement and Concrete Research 42 (12), 1563−1570.

Makar, J.M., Chan, G.W., 2009. Growth of cement hydration products on single-walled carbon nanotubes. Journal of the American Ceramic Society 92, 1303−1310.

Matějka, V., Matějková, P., Kovář, P., Vlček, J., Přikryl, J., Červenka, P., Kukutschová, J., 2012. Metakaolinite/TiO$_2$ composite: photoactive admixture for building materials based on Portland cement binder. Construction and Building Materials 35, 38−44.

Meng, T., Yu, Y., Qian, X., Zhan, S., Qian, K., 2012. Effect of nano-TiO$_2$ on the mechanical properties of cement mortar. Construction and Building Materials 29, 241−245.

Merusi, F., Giuliani, F., Polacco, G., 2012. Linear viscoelastic behaviour of asphalt binders modified with polymer/clay nanocomposites. Procedia-Social and Behavioral Sciences 53, 335−345.

Metaxa, Z.S., Konsta-Gdoutos, M.S., Shah, S.P., 2013. Carbon nanofiber cementitious composites: effect of debulking procedure on dispersion and reinforcing efficiency. Cement and Concrete Composites 36, 25−32.

Mondal, P., Shah, S., Marks, L., Gaitero, J., 2010. Comparative study of the effects of microsilica and nanosilica in concrete. Transportation Research Record: Journal of the Transportation Research Board 2141, 6−9.

Monteiro, P.J.M., Kirchheim, A.P., Chae, S., Fischer, P., MacDowell, A.A., Schaible, E., Wenk, H.R., 2009. Characterizing the nano and micro structure of concrete to improve its durability. Cement and Concrete Composites 31 (8), 577−584.

Morsy, M.S., Alsayed, S.H., Aqel, M., 2011. Hybrid effect of carbon nanotube and nano-clay on physico−mechanical properties of cement mortar. Construction and Building Materials 25 (1), 145−149.

Nazari, A., Riahi, S., 2011a. The effects of SiO$_2$ nanoparticles on physical and mechanical properties of high strength compacting concrete. Composites Part B: Engineering 42 (3), 570−578.

Nazari, A., Riahi, S., 2011b. TiO$_2$ nanoparticles effects on physical, thermal and mechanical properties of self compacting concrete with ground granulated blast furnace slag as binder. Energy and Buildings 43 (4), 995−1002.

Nazari, A., Riahi, S., 2011c. The effects of zinc dioxide nanoparticles on flexural strength of self-compacting concrete. Composites Part B: Engineering 42 (2), 167−175.

Nehdi, M., Pardhan, M., Koshowski, S., 2004. Durability of self-consolidating concrete incorporating high-volume replacement composite cements. Cement and Concrete Research 34 (11), 2103−2112.

Nejad, F.M., Azarhoosh, A.R., Hamedi, G.H., Azarhoosh, M.J., 2012. Influence of using nonmaterial to reduce the moisture susceptibility of hot mix asphalt. Construction and Building Materials 31, 384−388.

Oltulu, M., Şahin, R., 2011. Single and combined effects of nano-SiO$_2$, nano-Al$_2$O$_3$ and nano-Fe$_2$O$_3$ powders on compressive strength and capillary permeability of cement mortar containing silica fume. Materials Science and Engineering-A-Structural Materials 528 (22), 7012.

Oltulu, M., Sahin, R., 2013. Effect of nano-SiO$_2$, nano-Al$_2$O$_3$ and nano-Fe$_2$O$_3$ powders on compressive strengths and capillary water absorption of cement mortar containing fly ash: a comparative study. Energy and Buildings 58, 292−301.

Oltulu, M., Şahin, R., 2014. Pore structure analysis of hardened cement mortars containing silica fume and different nano-powders. Construction and Building Materials 53, 658−664.

Pacheco-Torgal, F., Ding, Y., Jalali, S., 2012. Properties and durability of concrete containing polymeric wastes (tyre rubber and polyethylene terephthalate bottles): an overview. Construction and Building Materials 30, 714−724.

Pacheco-Torgal, F., Miraldo, S., Ding, Y., Labrincha, J.A., 2013. Targeting HPC with the help of nanoparticles: an overview. Construction and Building Materials 38, 365−370.

Pacheco-Torgal, F., 2014. Eco-efficient construction and building materials research under the EU framework programme horizon 2020. Construction and Building Materials 51, 151−162.

Parviz, A., 2011. Nano materials in asphalt and tar. Australian Journal of Basic and Applied Sciences 5 (12), 3270−3273.

Pigeon, M., Pleau, R., 1995. Durability of Concrete in Cold Climates. E and FN Spon, New York, NY.

Pourjavadi, A., Fakoorpoor, S.M., Khaloo, A., Hosseini, P., 2012. Improving the performance of cement-based composites containing superabsorbent polymers by utilization of nano-SiO_2 particles. Materials and Design 42, 94−101.

Qing, Y., Zenan, Z., Deyu, K., Rongshen, C., 2007. Influence of nano-SiO_2 addition on properties of hardened cement paste as compared with silica fume. Construction and Building Materials 21 (3), 539−545.

Quercia, G., Hüsken, G., Brouwers, H.J.H., 2012. Water demand of amorphous nano silica and its impact on the workability of cement paste. Cement and Concrete Research 42 (2), 344−357.

Quercia, G., Lazaro, A., Geus, J.W., Brouwers, H.J.H., 2013. Characterization of morphology and texture of several amorphous nano-silica particles used in concrete. Cement and Concrete Composites 44, 77−92.

Quercia, G., Spiesz, P., Hüsken, G., Brouwers, H.J.H., 2014. SCC modification by use of amorphous nano-silica. Cement and Concrete Composites 45, 69−81.

Rashad, A.M., 2013a. A synopsis about the effect of nano-Al_2O_3, nano-Fe_2O_3, nano-Fe_3O_4 and nano-clay on some properties of cementitious materials−A short guide for civil engineer. Materials and Design 52, 143−157 (complete).

Rashad, A.M., 2013b. Effects of ZnO_2, ZrO_2, Cu_2O_3, CuO, $CaCO_3$, SF, FA, cement and geothermal silica waste nanoparticles on properties of cementitious materials−A short guide for civil engineer. Construction and Building Materials 48, 1120−1133 (complete).

Riahi, S., Nazari, A., 2011. Physical, mechanical and thermal properties of concrete in different curing media containing ZnO_2 nanoparticles. Energy and Buildings 43 (8), 1977−1984.

Richardson, I.G., 1999. The nature of C-S-H in hardened cements. Cement and Concrete Research 29, 1131−1147.

Richardson, I.G., 2008. The calcium silicate hydrates. Cement and Concrete Research 38, 137−158.

Rozière, E., Loukili, A.R., Hachem, E., Grondin, F., 2009. Durability of concrete exposed to leaching and external sulphate attacks. Cement and Concrete Research 39, 1188−1198.

Sáez de Ibarra, Y., Gaitero, J.J., Erkizia, E., Campillo, I., 2006. Atomic force microscopy and nanoindentation of cement pastes with nanotube dispersions. Physica Status Solidi A 203, 1076−1081.

Safiuddin, M., Gonzalez, M., Cao, J., Tighe, S.L., 2014. State-of-the-art report on use of nano-materials in concrete. International Journal of Pavement Engineering 1−10 (ahead-of-print).

Said, A.M., Zeidan, M.S., Bassuoni, M.T., Tian, Y., 2012. Properties of concrete incorporating nano-silica. Construction and Building Materials 36, 838−844.

Salemi, N., Behfarnia, K., 2013. Effect of nano-particles on durability of fiber-reinforced concrete pavement. Construction and Building Materials 48, 934−941.

Sanchez, F., Sobolev, K., 2010. Nanotechnology in concrete−a review. Construction and Building Materials 24 (11), 2060−2071.

Santagata, E., Baglieri, O., Tsantilis, L., Dalmazzo, D., 2012. Rheological characterization of bituminous binders modified with carbon nanotubes. Procedia-Social and Behavioral Sciences 53, 546−555.

Santamouris, M., 2013. Using cool pavements as a mitigation strategy to fight urban heat island—a review of the actual developments. Renewable and Sustainable Energy Reviews 26, 224−240.

Scrivener, K.L., Füllmann, T., Gallucci, E., Walenta, G., Bermejo, E., 2004. Quantitative study of Portland cement hydration by X-Ray diffraction/rietveld analysis and independent methods. Cement and Concrete Research 34, 1541−1547.

Senff, L., Labrincha, J.A., Ferreira, V.M., Hotza, D., Repette, W.L., 2009. Effect of nano-silica on rheology and fresh properties of cement pastes and mortars. Construction and Building Materials 23 (7), 2487−2491.

Senff, L., Hotza, D., Repette, W.L., Ferreira, V.M., Labrincha, J.A., 2010. Mortars with nano-SiO_2 and micro-SiO_2 investigated by experimental design. Construction and Building Materials 24 (8), 1432−1437.

Senff, L., Hotza, D., Lucas, S., Ferreira, V.M., Labrincha, J.A., 2012. Effect of nano-SiO_2 and nano-TiO_2 addition on the rheological behavior and the hardened properties of cement mortars. Materials Science and Engineering: A 532, 354−361.

Senff, L., Tobaldi, D.M., Lemes-Rachadel, P., Labrincha, J.A., Hotza, D., 2014. The influence of TiO_2 and ZnO powder mixtures on photocatalytic activity and rheological behavior of cement pastes. Construction and Building Materials 65, 191−200.

Shafabakhsh, G., Mirabdolazimi, S.M., Sadeghnejad, M., 2014. Evaluation the effect of nano-TiO_2 on the rutting and fatigue behavior of asphalt mixtures. Construction and Building Materials 54, 566−571.

Shakhmenko, G., Juhnevica, I., Korjakins, A., 2013. Influence of sol-gel nanosilica on hardening processes and physically-mechanical properties of cement paste. Procedia Engineering 57, 1013−1021.

Shi, X., Akin, M., Pan, T., Fay, L., Liu, Y., Yang, Z., 2009. Deicer impacts on pavement materials: introduction and recent developments. The Open Civil Engineering Journal 3, 16−27.

Shi, X., Fay, L., Peterson, M.M., Yang, Z., 2010. Freeze-thaw damage and chemical change of a Portland cement concrete in the presence of diluted deicers. Materials and Structures 43, 933−946.

Shi, X., Fay, L., Peterson, M.M., Berry, M., Mooney, M., 2011. A FESEM/EDX investigation into how continuous deicer exposure affects the chemistry of Portland cement concrete. Construction and Building Materials 25 (2), 957−966.

Shi, X., Xie, N., Fortune, K., Gong, J., 2012. Durability of steel reinforced concrete in chloride environments: an overview. Construction and Building Materials 30, 125−138.

Singh, L.P., Karade, S.R., Bhattacharyya, S.K., Yousuf, M.M., Ahalawat, S., 2013. Beneficial role of nanosilica in cement based materials—A review. Construction and Building Materials 47, 1069−1077.

Skinner, L.B., Chae, S.R., Benmore, C.J., Wenk, H.R., Monteiro, P.J.M., 2010. Nanostructure of calcium silicate hydrates in cements. Physical Review Letters 104, 195502.

Stefanidou, M., Papayianni, I., 2012. Influence of nano-SiO_2 on the Portland cement pastes. Composites Part B: Engineering 43 (6), 2706−2710.

Sugrañez, R., Álvarez, J.I., Cruz-Yusta, M., Mármol, I., Morales, J., Vila, J., Sánchez, L., 2013. Enhanced photocatalytic degradation of NO_x gases by regulating the microstructure of mortar cement modified with titanium dioxide. Building and Environment 69, 55−63.

Sureshkumar, M.S., Filippi, S., Polacco, G., Kazatchkov, I., Stastna, J., Zanzotto, L., 2010. Internal structure and linear viscoelastic properties of EVA/asphalt nanocomposites. European Polymer Journal 46 (4), 621−633.

Sutter, L., Peterson, K., Julio-Betancourt, G., Hooton, D., Van Dam, T., Smith, K., 2008. The Deleterious Chemical Effects of Concentrated Deicing Solutions on Portland Cement Concrete. South Dakota Department of Transportation (Final Report SD2002-01-F, April).

Taylor, H.F.W., 1986. Proposed structure for calcium silicate hydrate gel. Journal of the American Ceramic Society 69, 464−467.

Tobón, J.I., Payá, J.J., Borrachero, M.V., Restrepo, O.J., 2012. Mineralogical evolution of Portland cement blended with silica nanoparticles and its effect on mechanical strength. Construction and Building Materials 36, 736−742.

Thomas, J.J., Jennings, H.M., Allen, A.J., 1998. Determination of the neutron scattering contrast of hydrated Portland cement paste using H_2O/D_2O exchange. Advanced Cement Based Materials 7, 119−122.

Thomas, J.J., 2007. A new approach to modeling the nucleation and growth kinetics of tricalcium silicate hydration. Journal of the American Ceramic Society 90, 3282−3288.

Vera-Agullo, J., et al., 2009. Mortar and concrete reinforced with nanomaterials. Nanotechnology in Construction 3, 383−388.

Wang, B., Han, Y., Liu, S., 2013. Effect of highly dispersed carbon nanotubes on the flexural toughness of cement-based composites. Construction and Building Materials 46, 8−12.

Wei, Y.Q., Yao, W., Xing, X.M., Wu, M.J., 2012. Quantitative evaluation of hydrated cement modified by silica fume using QXRD, ^{27}Al MAS NMR, TG-DSC and selective dissolution techniques. Construction and Building Materials 36, 925−932.

Xu, Z., Viehland, D., 1996. Observation of a mesostructure in calcium silicate hydrate gels of Portland cement. Physical Review Letters 77, 952−955.

Yang, J., Tighe, S., 2013. A review of advances of nanotechnology in asphalt mixtures. Procedia-Social and Behavioral Sciences 96, 1269−1276.

Yao, H., You, Z., Li, L., Shi, X., Goh, S.W., Mills-Beale, J., Wingard, D., 2012. Performance of asphalt binder blended with non-modified and polymer-modified nanoclay. Construction and Building Materials 35, 159−170.

Ye, Q., Zhang, Z.N., Kong, D.Y., 2007. Influence of nano-SiO_2 addition on properties of hardened cement paste as compared with silica fume. Construction and Building Materials 21, 539−545.

You, Z., Mills-Beale, J., Foley, J.M., Roy, S., Odegard, G.M., Dai, Q., Goh, S.W., 2011. Nanoclay-modified asphalt materials: preparation and characterization. Construction and Building Materials 25 (2), 1072−1078.

Yousefi, A., Allahverdi, A., Hejazi, P., 2013. Effective dispersion of nano-TiO_2 powder for enhancement of photocatalytic properties in cement mixes. Construction and Building Materials 41, 224−230.

Yu, H., Shi, X., Hartt, W.H., Lu, B., 2010. Laboratory investigation of reinforcement corrosion initiation and chloride threshold content for self-compacting concrete. Cement and Concrete Research 40, 1507−1516.

Yuan, H., Shi, Y., Xu, Z., Lu, C., Ni, Y., Lan, X., 2013. Influence of nano-ZrO_2 on the mechanical and thermal properties of high temperature cementitious thermal energy storage materials. Construction and Building Materials 48, 6−10.

Zapata-Ordúz, L.E., Portela, G., Suárez, O.M., 2014. Weibull statistical analysis of splitting tensile strength of concretes containing class F fly ash, micro/nano-SiO_2. Ceramics International 40 (5), 7373−7388.

Zhang, M.H., Li, H., 2011. Pore structure and chloride permeability of concrete containing nano-particles for pavement. Construction and Building Materials 25 (2), 608−616.

The self-heating carbon nanofiber polymer composite and its applications in deicing and snow thawing of pavement

11

Hui Li [1,2], Qiangqiang Zhang [1,2], Huigang Xiao [1,2]
[1]Key Lab of Structures Dynamic Behavior and Control (Harbin Institute of Technology), Ministry of Education, Harbin, China; [2]School of Civil Engineering, Harbin Institute of Technology, Harbin, China

11.1   Preface

In this chapter, we discuss the self-heating performance of an electrically conductive carbon nanofiber polymer (CNFP) composite and its applications on pavement deicing and snow thawing based on remarkable electrothermal properties. There are four sections in this chapter: (1) introduction of CNFP composites: their necessity, objective, and purpose will be elaborated as comprehensively as possible. In addition, the research progress on conductive composites, carbon nanomaterials, and corresponding deicing/snow thawing in the past two decades will be overviewed concisely. (2) The one-dimensional (1D) CNFP-based paper-like conductive composite and its applications on pavement deicing/snow thawing. Thereinto, the corresponding investigation involves the fabrication process, the thermally and electrically conductive characteristics, the electrothermal properties, the temperature-dependent effect of resistivity, and the applications on pavement deicing/snow thawing (including the conceptual configuration and technological construction of self-heating pavement, the operation system, and the evaluation of working efficiency). Particularly, various parameter-associated studies during the deicing performance of the CNFP-based system were systematically conducted in this section; these involved parameters such as ambient temperature, input power (heat flux density), ice and snow thickness, and optimal index of time and energy efficiency. Next presented are (3) the conclusion, followed by (4) the acknowledgments and references.

11.2   Introduction

On many occasions in winter, the ice accretion and snow falling often lead to tremendous economic losses and safety hazards for many important infrastructures, such as aerodynamic stall of aircrafts and wind turbines, galloping of power lines, instability

of marine structures, possibly shutting down traffic for a long time (pavement, bridge decks, highways, airport grounds, etc.), or even the tragedy of human casualties. Accordingly, the official statistics have indicated that snow and ice are the cause of 10−15% of traffic accidents annually (Yehia et al., 2000; Feng and Li, 2009; Hou et al., 2002). Despite the fact that certain amounts of either deicing or anti-icing approaches have been developed, such as mechanical tools, chimerical salts (Wang et al., 2006; Shi et al., 2009), terrestrial heat or solar-energy-heating instruments (Ferrara and Haslett, 1975; Long and Baldwin, 1981; Tanaka, 1981; Lee, 1984; Fridman, 2009), conductive concretes, or other heating candidates (Yehia et al., 2000; Hou et al., 2002; Chung, 2001; 2004a,b; Tuan and Yehia, 2004; Zhao et al., 2010, 2011; Zhang et al., 2015), they are still far from optimal and extensively applicable due to such fatal or detrimental shortages as lower heating efficiency, environmental pollution and concrete/steel bar erosions (Litvan, 1976; Harnick et al., 1980; Lee et al., 2000; Wang et al., 2006; Novotny et al., 2008; Shi et al., 2009; Kim and Koretsky, 2013), high electric resistivity and degeneration of electrothermal performance (Yehia et al., 2000), and low thermal conductivity (Zhao et al., 2010, 2011).

Delightfully, the unprecedented prosperities of material markets stimulate the everlasting developments of advanced technologies or authorized science research. Herein, one amazing member of the carbon nanomaterial family—carbon nanofibers and carbon nanotubes (CNFs/CNTs)—has been miraculous in various technological revolutions and progress reports on research in multidisciplinary fields since Lijima reported his successful fabrication in 1991 (Lijima, 1991), including physics, material science, electronics, communication, and chemistry. This hollow and rodlike material is formed by curling graphene nanosheets with a certain chiral and sp^2-sp^3 hybrid bonds; due to this special structure, it presents several distinguishing characteristics in chemical, physical, and mechanical properties, such as an extraordinary Young's modulus, higher fracture strength, excellent thermal conductivity, outstanding mobility of charge carriers, and larger specific surface area. These remarkable properties make it promising to develop serials of novel functional materials or specific devices, such as CNT/CNF-based polymer composites, field effect devices, energy storage materials, and new generations of electrical conductors (Lin et al., 2014; Xu et al., 2015; Zhang et al., 2015). Especially, based on the excellent electrical conductivity of individual CNT/CNFs, one promising application is to develop paper-like bulk with expected electrothermal properties to implement deicing applications.

Therefore, CNFP composites made from CNFs exhibit low resistance, high thermal conductivity, and high temperature stability and can be incorporated into a self-deicing pavement system as a highly efficient heating element based on its remarkable electrothermal performance. Additionally, the unique thermally conductive properties of CNTs make them promising heat transfer candidates (Chang et al, 2009; Chung, 1994, 2001; Peebles, 1994; Hone et al., 1999; Moisala et al., 2006; Saito et al., 1998).

In this section, based on its good electrothermal properties, the CNFP-based self-heating system for pavements consisting of a thermally insulated epoxy substrate, a CNFP high-efficiency heating element, an AlN−ceramic wafer insulated capsulation layer, and a multiwalled carbon nanotube (MWCNT)/cement-based highly thermoconductive layer, is proposed in this study. The high efficiency, repeatability,

low cost, and feasibility of this CNFP-based pavement self-heating system for both deicing and snow-thawing applications are validated through this study. The electric and thermoelectric properties of CNFPs, which is composed of individual carbon nano-fibers (10−200 nm), are tested. The property of high thermoelectric efficiency is veri-fied, and the resistivity of the CNFP exhibited piecewise linear temperature-dependent characteristics within a certain temperature range (0−280 °C). To ensure the efficient operation of the CNFP, an AlN−ceramic wafer (0.5 mm) is employed as the electroin-sulated layer because of its favorable insulating and thermoconductive properties. The constructed system is applied in deicing and field snow-thawing studies, in which the effects of ambient temperature, heat flux density, and ice thickness on the deicing and snow-thawing performance of the self-heating system are investigated. The efficiency, repeatability, cost, and feasibility of the self-heating pavement system in both deicing and snow-thawing applications are analyzed. Indices for evaluating the deicing and snow-thawing efficiency of the self-heating pavement system are proposed, and the optimal values for each parameter are presented.

11.3 CNFP film

11.3.1 The fabrication process

As shown in Figure 11.1, the fabrication process of CNFPs is divided by five steps: Firstly, the CNFs with a diameter range of 10−100 nm are synthesized by the chemical vapor deposition method (CVD). Secondly, 1 g CNF powder is dispersed into 5 g Triton X-100 to form a paste-like mixture, and then the mixture is dissolved into
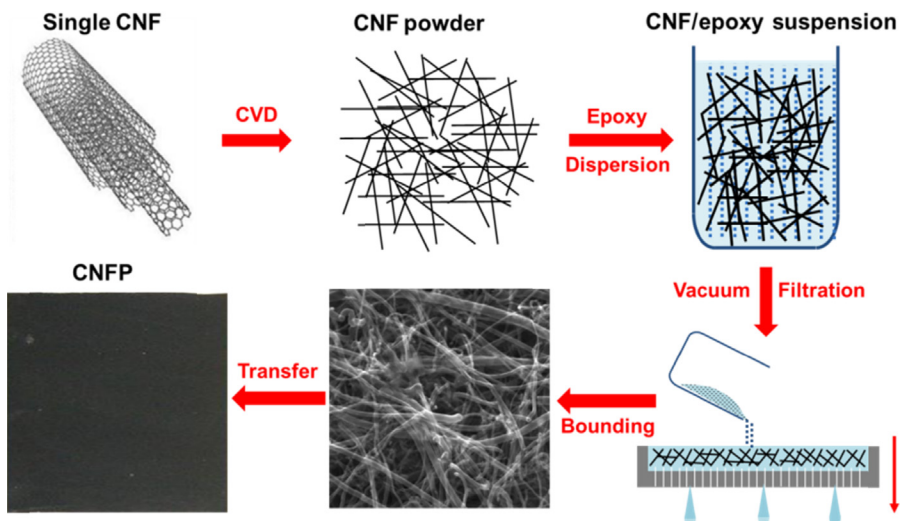
Figure 11.1 The fabrication process of carbon nanofiber polymer (CNFP) film.

5 L deionized water to obtain the uniform solution. Thirdly, the CNF solution is filtered through a filter membrane with a pore size of 1 μm under the vacuum conditions of 20 Pa for about 10 min. Fourthly, the filtered-formed CNF film with filter membrane is treated under 80 °C for 24 h to form the tight interface bonding among CNFs. Finally, the solidified CNF film is separated from filter membrane in the wetting condition of acetone; eventually, the 0.38-mm-thick paper-like CNFP film is obtained.

11.3.2 The property investigation of CNFPs

11.3.2.1 The characteristics of microstructures

It is well known that the microstructure at the nanoscale is the critical factor dominating the physical performance of the material, including its mechanical, thermal, and electrical properties. To investigate the effects of the microelement distribution in CNFPs on the electrothermal properties, it is necessary to survey the micro-morphologies of the CNFP. As shown in Figure 11.2(a–f), scanning electron microscope (SEM) images of a CNFP show its particular micro-morphologies and consistent distributions of CNFs. The larger diameter CNFs (200–50 nm) overlap and joint mutually to build the dominating skeleton of structure and form the conductive pathways for the rapid mobility of charger carriers, which is revealed by an SEM image in the form of chessboard-like bounded nodes. In addition, the small-diameter CNFs alternatively wrap around the large elements to form strong bounded
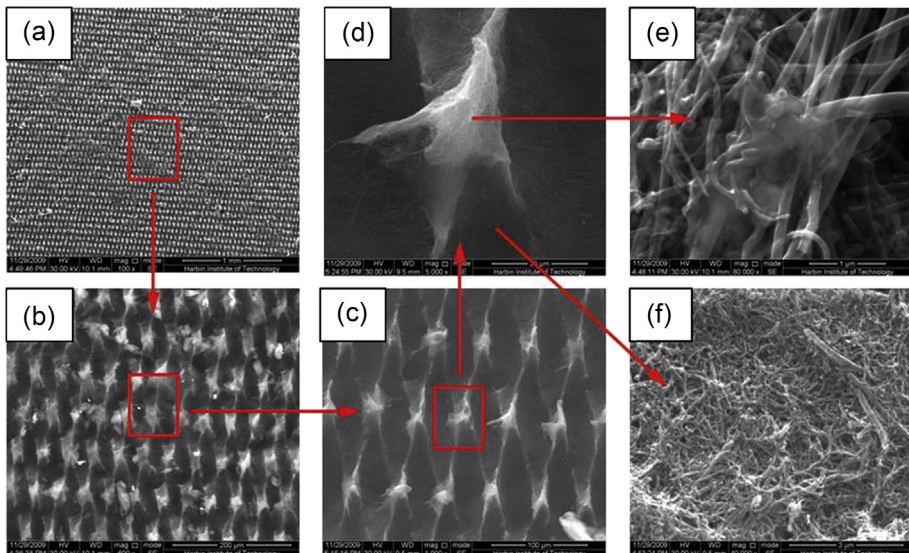
Figure 11.2 SEM images of CNFPs in varied magnifications: (a) 1 mm, (b) 100 μm, (c) 50 μm, (d) a node, (e) fiber in a node (1 μm), and (f) fiber connection in a node (3 μm). Reprinted with permission from Li et al. (2013) Copyright 2013: Elsevier.
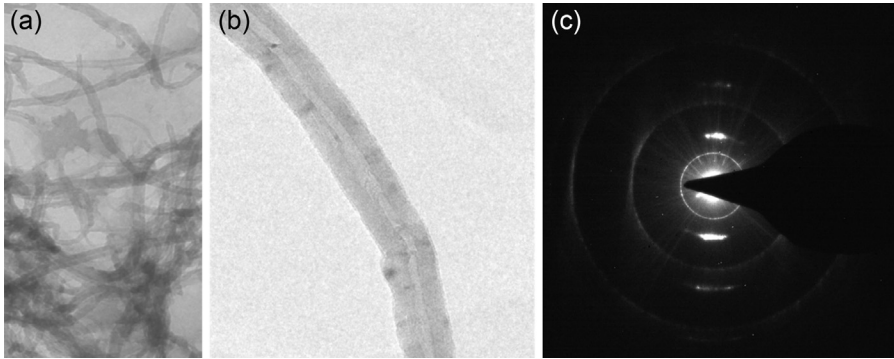
Figure 11.3 Transmission electron microscope (TEM) images of CNFs: (a) a TEM image of 20 nm, (b) a single CNF TEM image of 10 nm, and (c) a typical selected area electron diffraction (SAED) of CNF.

interactions, enrich the connection among the large elements, and even further perfect the conductive networks, with more possible channels for the mobility of charger carriers.

The corresponding versions of CNFs are investigated by transmission electron microscopy (TEM) to detect the layer information and typical characteristics of single CNFs, as shown in Figure 11.3(a); the connection feathers of large- and small-diameter CNFs in SEM images are further confirmed by TEM micrographs. Figure 11.3(b) and (c) illuminate the typical characteristics of CNFs (bamboo joint, center hollow, and bracket bright spots of selected area electron diffraction (SAED)).

11.3.2.2 The mechanical properties of CNFP

As shown in Figure 11.4, a CNFP with the dimensions $50 \times 25 \times 0.38$ mm is prepared for the test of mechanically uniaxial static tension, and the tensile test is
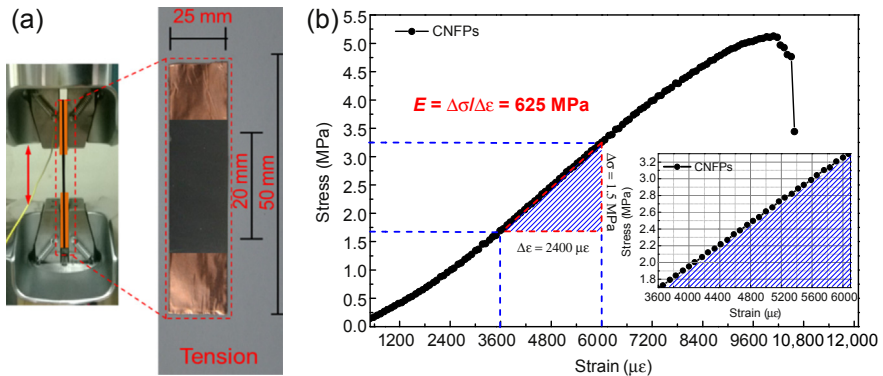
Figure 11.4 The investigation of mechanical properties of CNFPs by uniaxial static tensile test. (a) The test schematic and sample dimensions setup and (b) the strain−stress relationship curve.

conducted by an electrical universal material testing machine (Instron-5569, UK) with a loading rate of 0.5 mm/min. The result of strain versus stress reveals a desirable Young's modulus and a tensile strength of 0.625 GPa and 5.0 MPa, respectively. Obviously, CNFP as a paper-like material can resist possible mechanical formation during applications with those promising mechanical properties. Additionally, the ultimate tensile strain ($\sim 10,000 \ \mu\varepsilon$) is almost three times larger than that of the normal cement-based composite ($\sim 3500 \ \mu\varepsilon$), which implies that, as a heating element, CNFP would not be mechanically tensioned to break as long as the fracture of slab does not occur. The fundamental reason for this is due to the strong bounded $\pi-\pi$ interaction and alternatively wrapping among the CNFs, as seen in the SEM images shown in Figure 11.2, this kind of connection style would be not only beneficial to desirable mechanical properties but also greatly essential for CNFPs to inherit the excellent electrical and thermal properties from individual CNFs.

11.3.2.3   The electrically conductive properties of CNFPs

CNFP specimens with dimensions of $20 \times 40 \times 0.38$, $20 \times 60 \times 0.38$, and $20 \times 80 \times 0.38$ mm (considering the size effect) are used for measuring the resistivity. Firstly, all samples are sandwiched between two glass plates (100×100 mm) to remove the absorbed water at 150 °C for 2 h; DAD-87 is then printed transversely on the dried CNFP samples to form the electrodes with the width of 3 mm. Finally, DAD-40, which consists of two components, is mixed at a ratio of 1:1 and used to connect the copper wires to the formed electrodes. The fabricated CNFP samples are shown in Figure 11.5(b).

To incorporate a CNFP into a self-heating pavement system as a heating element, it is necessary to investigate its temperature-dependent electrical resistivity under various temperature conditions. As shown in Figure 11.5(a), the four-probe method is adopted to measure the longitudinal resistance of the CNFP samples under ambient temperature conditions ($-30 \sim 300$ °C) in a refrigerator or in a temperature-controllable oven. A DC current, I_{out}, is applied at the two outer contacts, and the two inner contacts are
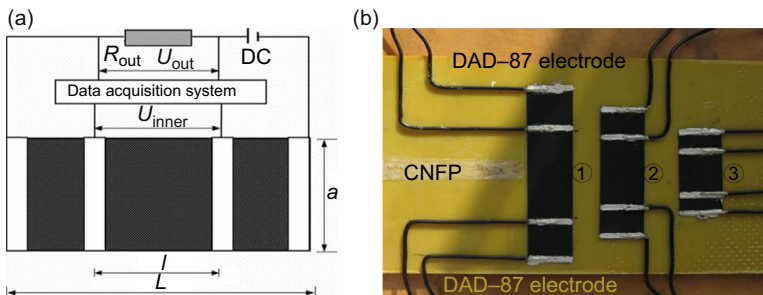
Figure 11.5 The four-probe method schematic of CNFP specimens used for investigating electrically conductivity: (a) the schematic of the DC circuit for the temperature-dependent resistivity, with n equal to 1:1, 1:2, and 1:3 and (b) measuring the resistivity with three different specimen sizes of ① $20 \times 40 \times 0.38$, ② $20 \times 60 \times 0.38$, and ③ $20 \times 80 \times 0.38$ mm. Reprinted with permission from Li et al. (2013) Copyright 2013: Elsevier.

used for measuring the voltage U_{inner}. A DC circuit, developed by Han et al. (Li et al., 2008), is used to measure the resistance of the CNFP sample as follows:

$$R = \frac{U_{inner} \times R_{ref}}{U_{out}} = \frac{U_{inner}}{I_{out}} \qquad (11.1)$$

where R_{ref} is the standard reference resistor, as shown in Figure 11.5(a); U_{out} is the voltage applied to R_{out}; R and U_{inner} are the resistance and voltage of the two inner contacts of the CNFP sample, respectively; and I_{out} is the current flowing through R_{ref}. I_{out} and U_{inner} are measured simultaneously to calculate R in series in the circuit.

Based on Ohm's law, the longitudinal resistivity of each CNFP specimen is calculated as follows:

$$\rho = \frac{R \cdot S}{l} = \frac{U_{inner} \times R_{ref}}{U_{out}} \frac{S}{l} = \frac{U_{inner}}{I_{out}} \frac{\Delta h'}{n} \qquad (11.2)$$

where S and l are, respectively, the cross-sectional area and the distance between the inner contacts of the CNFP sample, as shown in Figure 11.5(b); Δh and a are the thickness and width of the sample; and $n = l/a$ is the ratio of l to the width a, which is $n = 1{:}1$, $1{:}2$, and $1{:}3$ in this study.

The temperature-dependent resistivity of CNFP is shown in Figure 11.6. The resistivity of CNFP exhibits distinctly temperature-dependent characteristics. The curve of the resistivity to the surrounding temperature can be categorized into three regimes. In regime 1 (over the range of $-30 \sim 0\,°C$), the resistivity remains constant (0.72 Ω mm). In regime 2 (over the range of $0-280\,°C$), the resistivity of CNFP decreases linearly with an increase in temperature, exhibiting strongly temperature-dependent characteristics. It is well known that the resistivity of isolated CNFs is dependent on temperature because of the increased possibility of thermal excitation of hot electrons with an increase in temperature (Kane et al., 1998). Similarly, as a monolith of individual CNFs, the resistivity of CNFP decreases linearly as the temperature increases from 0 to 280 $°C$ due to the thermal excitation of hot electrons and even the thermal-expansion-enhanced interface bonding between CNFs, which corresponds
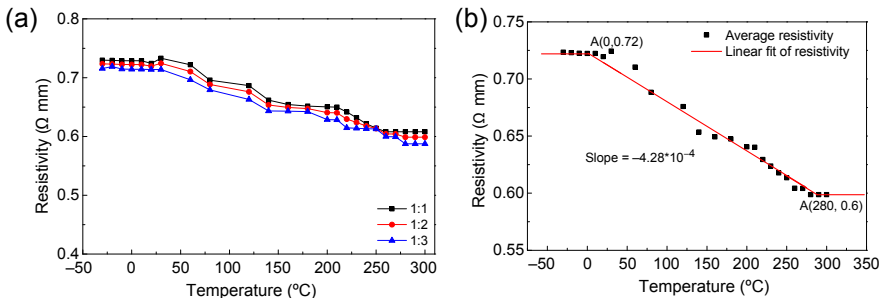
Figure 11.6 The temperature-dependent resistivity of CNFP: (a) resistivity with three n ratios equal to 1:1, 1:2, and 1:3 and (b) the average resistivity and linear curve fit. Reprinted with permission from Li et al. (2013) Copyright 2013: Elsevier.

to an improvement in the electrical properties of CNFP. In regime 3 (over 280 °C), the resistivity of CNFP remains constant (0.6 Ω mm) and is again independent of the surrounding temperature. Statistically, the resistivity of CNFP is independent of the specimen size.

Based on the temperature dependence of the resistivity as shown in Figure 11.6, a piecewise linear model of the resistivity of CNFP is proposed in the following form (units are Ω mm):

$$\rho_{CNFP} = \begin{cases} 0.72 & T < 0\,°C \\ 0.72 - 4.28 \times 10^{-4}\,T & 0\,°C \leq T \leq 280\,°C \\ 0.6 & T \geq 280\,°C \end{cases} \qquad (11.3)$$

11.3.2.4 The electrothermal properties of CNFP

A CNFP sample with the dimensions of $35 \times 70 \times 0.38$ mm is used for investigating the electrothermal properties, and the similar procedures as mentioned in this chapter for electrical resistivity study are also implemented to prepare the sample here (Figure 11.7). CNFP specimens are placed in a refrigerator or in a temperature-controllable oven to simulate changeable ambient temperatures, and then DC power is applied between the two electrodes to heat the specimens. The temperature is monitored using a Center 309 thermometer with a constant applied voltage under a certain ambient temperature. The applied voltages are 4, 6, 8, and 10 V, and the ambient temperature is varied in the range of -30 to 100 °C.

The increase in the temperature of the CNFP as a function of time and applied voltage under various ambient temperatures is shown in Figure 11.8 and Table 11.1. It can be seen that the electrothermal properties of CNFP greatly depend on ambient temperature. The temperature dramatically increases with time over the first 100 s and then approaches a stable temperature after 600 s. This equilibrium temperature depends on the surrounding temperature; for example, the equilibrium temperature is 22.8 °C for an ambient temperature of -30 °C, but it is approximately 55 °C for 0 °C. When the ambient temperature is higher than 0 °C, the equilibrium temperature becomes over 88 °C for a surrounding temperature of 20 and 40 °C, 100−120 °C for a surrounding temperature of 60 and 80 °C, and approximately 145.8 °C for a
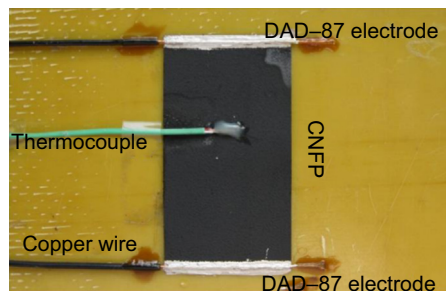
Figure 11.7 The schematic for investigation of electrothermal properties. Reprinted with permission from Li et al. (2013) Copyright 2013: Elsevier.
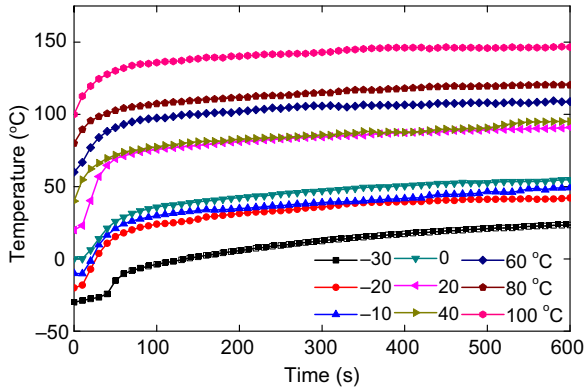
Figure 11.8 The electrothermal investigation of CNFPs at various ambient temperatures with an applied voltage of 4 V.
Reprinted with permission from Li et al. (2013) Copyright 2013: Elsevier.

Table 11.1 Equilibrium temperature of a CNFP under various ambient temperatures and applied voltages (°C)

Applied voltage (V)	Ambient temperatures (°C)								
	−30	−20	−10	0	20	40	60	80	100
4	22.8	42	49	55	88	92	108	120	145.8
6	81	105	109	118	147	157	162	147	196
8	140	155	170	177	210	215	220	225	246
10	191	210	221	230	235	240	245	263	270

surrounding temperature of 100 °C. The temperature dependence of the electrothermal properties of CNFPs can be attributed to the quantized transition of electronic energy, which determines electron transport activity in CNFs. Furthermore, CNFPs can reach the same stable temperature over 25 °C at an ambient temperature of −30 to 0 °C, which indicates that CNFPs are good candidates for the highly efficient heating element required for deicing in winter (below 0 °C). Due to the unique electron transport mechanism of a single CNF and the microtopography of CNFPs, as shown by the SEM picture in Figure 11.3, electron transport in the material can be highly efficient, which leads to the high efficiency of the electrothermal property of CNFPs.

11.4 Application of CNFP-based self-heating pavement system on deicing and snow thawing

11.4.1 Integration of CNFP-based self-heating pavement system

Based on their remarkable electrothermal properties, CNFPs can be employed as heating elements to develop a novel self-heating deicing and snow-thawing pavement

system. Conceptually, CNFP-based self-heating pavement consists of four functional elements: a heating element, a thermal transfer layer, an electro-insulated layer, and a thermally insulated substrate. The configuration of the CNFP-based self-heating pavement developed in this study is shown in Figure 11.9. CNFP is selected as a heating element. An epoxy sandwich layer is chosen as a thermal insulation substrate and placed between the soil and the CNFP layer to make sure the heat energy flows upward. In terms of the mechanical requirements of a pavement, the cement-based composite is designed to be the thermal conduction layer and is placed over the CNFP heating element. This is particularly to further enhance the thermal transferring capacity and enforce the mechanical properties of a cement-based thermal conduction layer. MWCNTs are adopted to improve thermal conductivity and mechanical properties of cement-based composites. According to the optimized experimental results in literature of Li et al. (2013), the optimal percentage of MWCNTs for improving the thermal conductivity of cement-based composites filled with MWCNTs is 3%; the thermal conductivity coefficient corresponding to this percentage is 2.83 W/(m K). Cement-based composites filled with MWCNTs would be qualified for incorporation into the CNFP-based self-deicing pavement system. Practically, when the MWCNT/ cement-based composite is covered by ice or snow, an AlN−ceramic wafer is used for encapsulating the CNFP heating element layer to guarantee electrical insulation and to simultaneously ensure efficient heat transfer upward. In summary, an epoxy thermal insulation substrate, a CNFP heating element, an AlN−ceramic wafer insulated encapsulation layer, and an MWCNT/cement-based thermal conductive layer are integrated into a self-heating pavement that can be used for deicing and snow thawing, as shown in Figure 11.9.

The operation of the CNFP-based self-heating pavement system is illuminated as follows: An external DC power source is firstly applied at the CNFP layer; in this study, the power source is supplied by solar energy or normal power grid and could be automatically selected. Then, an anemoscope, temperature sensors, and K-type thermocouples are used to measure the wind, the ambient temperature, and the temperature in the deicing system. These analog signals eventually are collected by sensors and are transformed to a digital signal by digital-to-analog/analog-to-digital (DA/AD) boards, and then transported to a PC to determine the optimal heat flux density input (Li et al., 2014).
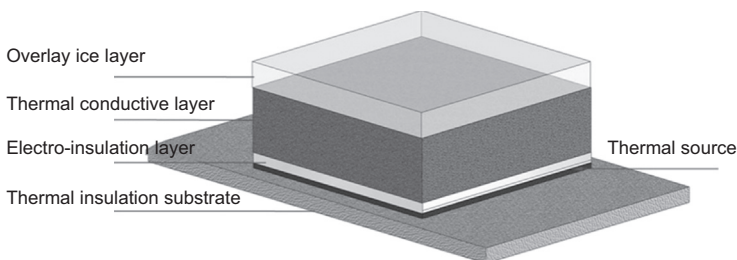
Figure 11.9 The configuration of the CNFP-based self-heating pavement system. Reprinted with permission from Li et al. (2013) Copyright 2013: Elsevier.

11.4.2 The applications of deicing and snow thawing

The setup for the deicing and snow-thawing experiment is shown in Figure 11.10. The heat flux density, ice and snow thickness, and ambient temperature are selected as the three critical factors to be investigated in this experiment. The heat flux densities used in this experiment are 600, 1000, 1400, and 1800 W/m^2. The ice is formed in a refrigerator with sizes of $100 \times 100 \times 10$, $100 \times 100 \times 15$, and $100 \times 100 \times 20$ mm. The ambient temperatures are -30, -20, and -10 °C. The temperature distribution in the system is monitored by the embedded K-type thermocouples (Center 309 thermometer); in total, four K-type thermocouples are used in the system. Two of them are embedded at the interface between the thermal conduction layer and the ice layer; at the upper surface of the ice layer, a third one is embedded at 12.5 mm above the bottom of the thermal conduction layer, and the last one is placed on the side wall of the system to monitor the surrounding temperature. The anemoscope and caliper are fixed at the experiment site for measuring the wind and the ice thickness. The corresponding comprehensive deicing efficiency is evaluated using the proposed indices, which are described later in this chapter. For the snow-thawing application, the applied heat flux densities are 600, 800, and 1000 W/m^2 with snow thicknesses of 20, 30, 40, and 50 mm. However, the snow-thawing process is affected by multiple factors, such as wind speed, ambient temperature, heat flux density, and snow thickness, so it is difficult to quantify the effect of the individual factors on the performance of the system for melting snow.

11.4.2.1 Deicing application

From a practical point of view, the most important impacts for this system are the deicing time and the energy consumption. Therefore, the time cost and energy consumption are proposed as the relevant performance indices and are used to evaluate the deicing efficiency.

Firstly, the temperature distribution is obtained from the embedded thermocouples. The temperature is recorded at the interface of the cement-based thermal conduction layer, and the ice is shown in Figure 11.11 for an ambient temperature of -10 °C; ice thicknesses of 10, 15, and 20 mm; and four heat flux densities. Figure 11.11 shows
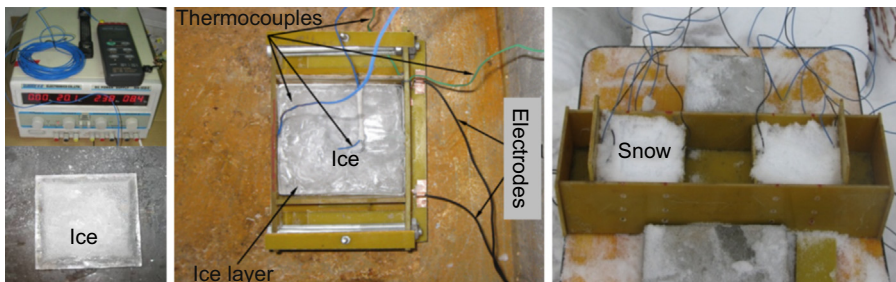
Figure 11.10 The experiment setup schematic of deicing and snow-thawing experiments. Reprinted with permission from Li et al. (2013) Copyright 2013: Elsevier.
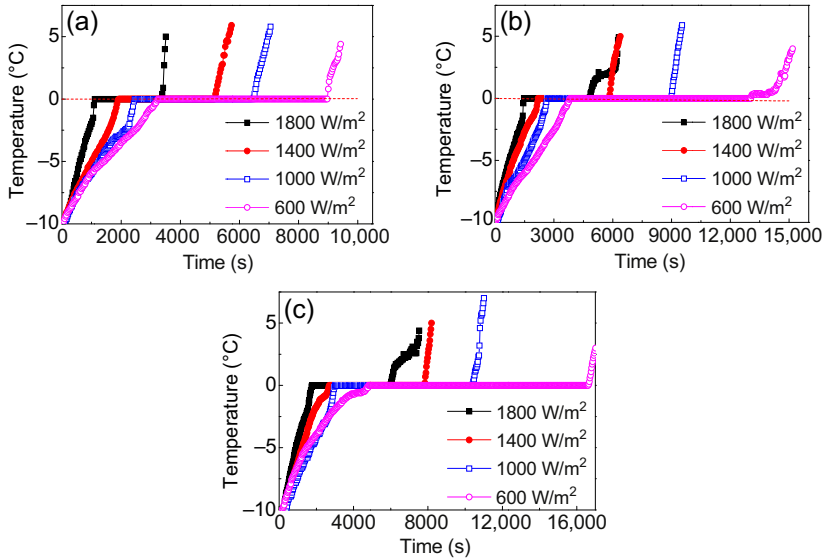
Figure 11.11 The temperature distribution at the interface between the ice layer and the cement-based thermal conduction layer at an ambient temperature of −10 °C and for an ice thickness of (a) 10 mm, (b) 15 mm, and (c) 20 mm.
Reprinted with permission from Li et al. (2013) Copyright 2013: Elsevier.

that the temperature-versus-time curves can be divided into three stages: an ice-specific heat stage (<0 °C), an ice-phase change stage (≈ 0 °C), and a water-specific heat stage (>0 °C). During the ice-specific heat stage, the temperature rapidly increases up to 0 °C, the phase change begins, the ice begins to melt, and the temperature is fixed until the completion of ice melting. The total duration of these two stages is referred to as the time cost for ice deicing. After the ice phase change is completed, the temperature at the upper surface of the ice layer has reached the freezing point, as the third region in Figure 11.11 shows.

The results show that a higher heat flux density corresponds to a steeper heating gradient and a lower time cost for deicing. However, for the same heat flux density and ambient temperature, thicker ice requires more time for deicing. The first stage of the curve represents many of the characteristics associated with the heat flux density, such as the start of deicing and the speed of the temperature rise. The time consumption and energy expenditure related to the latent heat of the ice (335 kJ/kg) for deicing can be obtained from the second stage.

For the other ambient temperatures of −20 and −30 °C, the times of the initiation and completion of deicing in the temperature curves are listed in Table 11.2. The energy consumption is calculated by multiplying the heat flux density q_w (W/m^2) by the time required to finish the deicing process ($E = q_w t$); the results are listed in Table 11.3. The effect of the heat flux density and ice thickness on the deicing time is the same as for an ambient temperature of −10 °C. Additionally, a lower ambient temperature

Table 11.2 Times of initiation and completion of deicing

Temperature (°C)	Thickness (mm)	Time (s)							
		600 (W/m^2)		1000 (W/m^2)		1400 (W/m^2)		1800 (W/m^2)	
		Start	Finish	Start	Finish	Start	Finish	Start	Finish
−10	10	3240	8970	2460	6450	1920	5130	1230	3360
	15	3810	13,020	2670	8970	2190	5820	1530	4830
	20	4800	16,500	2880	10,230	2700	7650	1650	5820
−20	10	4830	14,460	2730	7500	2580	6750	1830	5430
	15	5160	15,750	3330	9930	2760	7590	2550	6750
	20	5490	17,130	3660	11,130	2970	8130	3000	7500
−30	10	6180	16,880	4410	8670	2880	7230	2670	6120
	15	6630	20,100	4920	11,250	3540	9120	3180	8190
	20	7200	22,920	5580	14,010	3990	10,080	4110	9300

Reprinted with permission from Li et al. (2013) Copyright 2013: Elsevier.

Table 11.3 **Energy consumption for deicing**

Temperature (°C)	Ice thickness (mm)	Energy (kJ)			
		600 (W/m²)	1000 (W/m²)	1400 (W/m²)	1800 (W/m²)
−10	10	53.82	64.5	71.82	60.48
	15	78.12	89.7	81.48	86.94
	20	99	102.3	107.1	104.76
−20	10	86.76	75	94.5	97.74
	15	94.5	99.3	106.26	121.5
	20	102.78	111.3	113.82	135
−30	10	101.28	86.7	101.22	110.16
	15	120.6	112.5	127.68	147.42
	20	137.52	140.1	141.12	167.4

Reprinted with permission from Li et al. (2013) Copyright 2013: Elsevier.

corresponds to a longer deicing time. Of most interest is that, for most of the cases listed in Table 11.2, the energy consumption for deicing is lower with a smaller heat flux density, whereas the time for deicing is longer.

The effect of ice thickness

The data in Tables 11.2 and 11.3 are depicted in Figure 11.12. At a specific ambient temperature, both the energy and time required to deice a certain amount of ice increase approximately linearly with the ice thickness for heat flux densities of 600, 1000, 1400, and 1800 W/m². This trend occurs because the energy consumed by ice heating and phase change are linear functions of ice thickness and account for more than 90% of the effective energy. Other energy expenditures, such as dissipation and system heating, are independent of the thickness of the ice at the same ambient temperature. Therefore, the approximate linear relationship between both deicing time and energy consumption and ice thickness is acceptable and reasonable.

The effect of ambient temperature

For a certain amount of ice, the latent heat expenditure is fixed, and the specific heat energy consumption is a linear function of the ambient temperature. Moreover, a lower ambient temperature results in a higher temperature gradient and increased energy transfer between the system and the surroundings. Therefore, the energy and time required to deice a certain amount of ice for heat flux densities of 600, 1000, 1400, and 1800 W/m² reduce with the increase in ambient temperature, as shown in Figure 11.13. Based on the effective insulation measurements for the surrounding system and the bottom layer (PVC insulated plates, >0.14 W/m K, purchased in Harbin, China), the energy that dissipates to the environment is only a small portion of the
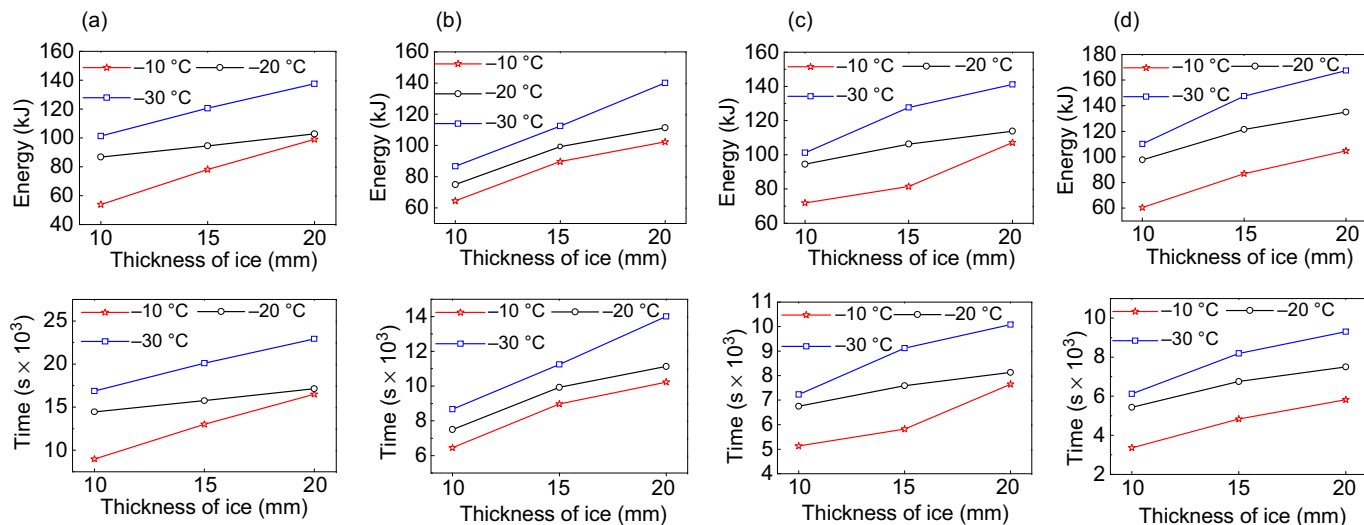
Figure 11.12 The effect of ice thickness on the energy and time required to deice a certain amount of ice under specified conditions (heat flux density and ambient temperature): (a) 600 W/m^2, (b) 1000 W/m^2, (c) 1400 W/m^2, and (d) 1800 W/m^2.
Reprinted with permission from Li et al. (2013) Copyright 2013: Elsevier.
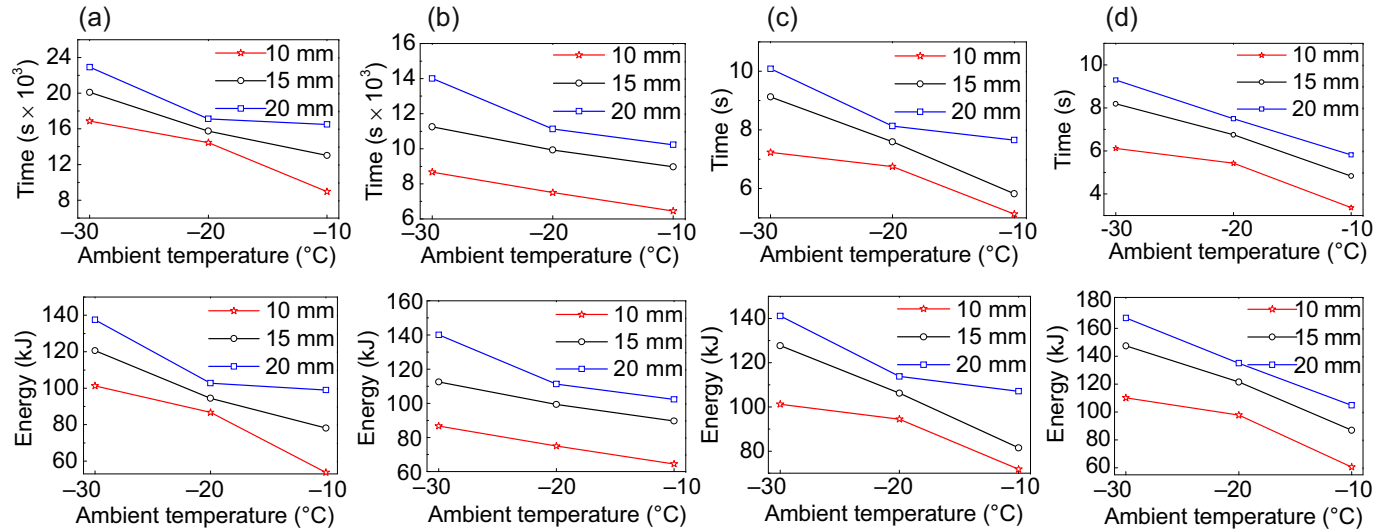
Figure 11.13 The effect of ambient temperature on the energy and time required to deice a certain amount of ice with applied heat flux densities of (a) 600 W/m², (b) 1000 W/m², (c) 1400 W/m², and (d) 1800 W/m².

Reprinted with permission from Li et al. (2013) Copyright 2013: Elsevier.

entire energy. Consequently, it is reasonable to conclude that the consumptions of time and energy for deicing are approximately linear functions of the ambient temperature.

The effect of heat flux density

For fixed conditions (ice thickness and ambient temperature), the energy and time requirements for the deicing process are constant. The heat flux density refers to the energy input to a unit area per unit time and essentially dictates the heating rate and temperature gradient, as shown in Figure 11.11. A higher heat flux density results in a faster heating rate and a smaller time expenditure for deicing. As shown in Figure 11.14, the deicing time decreases with the increase in heat flux density, with a very fast decay at the beginning followed by a relatively slower decay. The results indicate that increasing the heat flux density is effective for deicing in the range of $600-1000$ W/m^2 but that the effectiveness increases little when the heat flux density exceeds 1000 W/m^2. The energy is the product of the heat flux density and the time used for deicing; the higher the heat flux density, the less the expenditure of time, so a minimum energy consumption value (optimal value) should exist, as shown in Figure 11.14. For example, 1000 W/m^2 is the optimal heat flux density for ice with a thickness of 10 mm at an ambient temperature of $-20\,°C$.

11.4.2.2 Snow-thawing application

The performance of the CNFP-based self-heating pavement system for thawing snow in a natural environment is also investigated as the same experimental setup described in Figure 11.10. As shown in Figure 11.15, at the beginning the temperature increased rapidly from the initial state to the freezing point ($0\,°C$). The snow then absorbed enough energy to achieve its latent heat, began to melt, and formed a moving interface between the melted water and the rest of the snow; the temperature at the melting interface is stable at $0\,°C$ until the snow vanished. As shown in Figure 11.15(a), for the same initial temperature of $-12\,°C$, the gray line for a snow thickness of 30 mm has a steeper gradient, and snow melting began earlier. This result is the same as that of the black line and the black dashed line for the 40- and 50-mm-thick snow at an initial temperature of $-22\,°C$. Although melting the thicker snow requires more energy, because of the lower thermal conductivity of snow (~ 0.1 W/(m K) for new snow), the thicker snow layer actually played a more active role in heat preservation as a porous medium and prevented heat loss into the surrounding air. A similar phenomenon is also present in other cases, as shown in Figure 11.15, except for the cases with 40- and 50-mm-thick snow at an initial temperature of $-23\,°C$, as shown in Figure 11.15(b). The results for these cases are different because of the relatively lower heat flux density input and the extremely low surrounding temperature exceeding the heat preservation capability of the specimen. Therefore, the time cost for melting the snow is determined by a combination of the energy requirement and the heat preservation effect.

As shown in Figure 11.16, with a heat flux density of 600 W/m^2, it took approximately 6000, 6500, 7500, and 6800 s to melt snow with thicknesses of 20, 30, 40, and 50 mm with a surrounding temperature of -9.1, -9.2, -9.7, and $-10\,°C$,
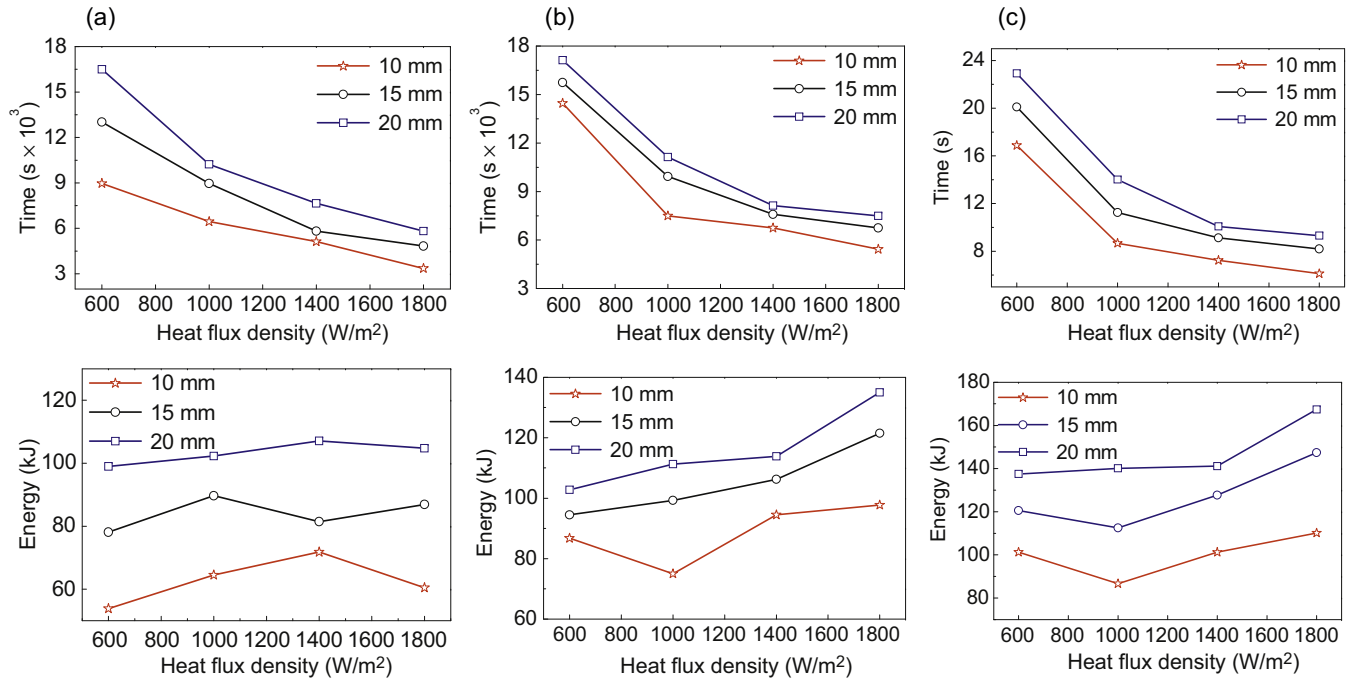
Figure 11.14 The effect of heat flux density on the energy and time required to deice a certain amount of ice at ambient temperatures of (a) −10 °C, (b) −20 °C, and (c) −30 °C.

Reprinted with permission from Li et al. (2013) Copyright 2013: Elsevier.
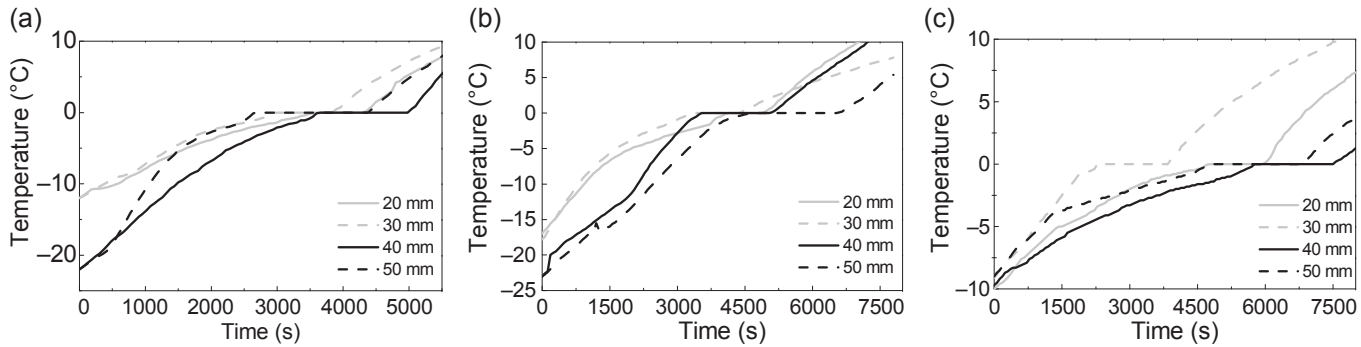
Figure 11.15 The change in temperature with time at the interface between the thermal conductive layer and the snow layer for four different snow thicknesses and heat flux densities of (a) 1000 W/m², (b) 800 W/m², and (c) 600 W/m².

Reprinted with permission from Li et al. (2013) Copyright 2013: Elsevier.
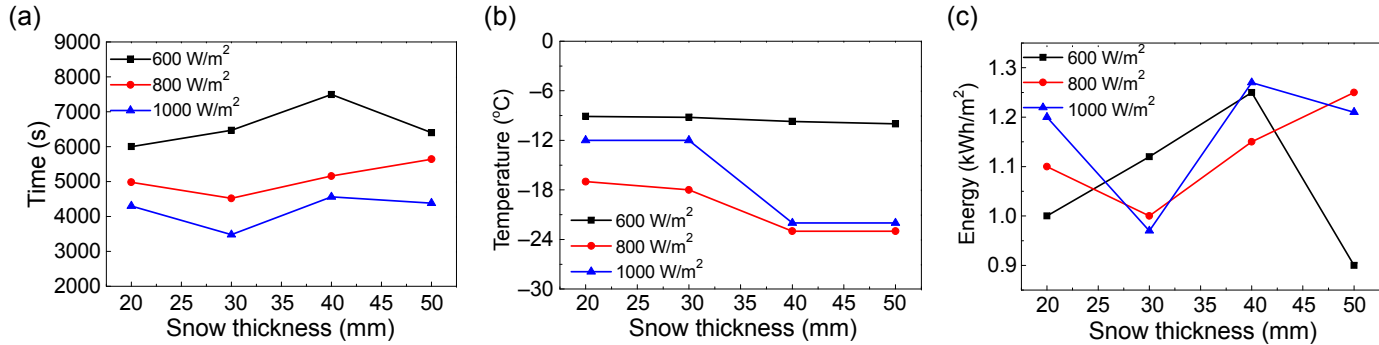
Figure 11.16 Effect of multiple factors on the snow-thawing process: (a) time cost, (b) the corresponding surrounding temperature, and (c) energy expenditure per unit area (kWh/m^2).

Reprinted with permission from Li et al. (2013) Copyright 2013: Elsevier.

respectively; the corresponding energy consumption for these cases is 1.0, 1.12, 1.28, and 1.10 kWh/m^2. In contrast with the other results, a heat flux density of 600 W/m^2 is most efficient and profitable for 30-mm-thick snow at a normal low temperature ($-10\,°$C), with a minimum consumption of time and energy that results from the joint effect of heat preservation and dissipation under similar surrounding conditions.

Similarly, because of the previously mentioned heat preservation effect, 800 W/m^2 is more efficient and preferable for thicker snow (30 mm) at extreme ambient temperature conditions ($-17\,°$C). Overall, it makes sense that the time and energy costs increase as the snow thickness increases for similar ambient conditions.

In contrast to the lower heat flux densities, 1000 W/m^2 is more efficient and preferable for thicker snow (40 mm) at the extreme ambient temperature conditions ($-23\,°$C) because of the relatively longer melting time but higher efficiency, which is also a result of the heat preservation effect associated with thicker snow.

11.4.3 The evaluation of efficiency based on the priority of time and energy options

Considering the time and energy consumption efficiency associated with deicing, the optimal heat flux density option may not coincide with the other parameters being specified, which require that the least energy and the shortest time expenditure be used to deice a certain amount of ice. However, it is impossible to optimize both time and energy because the shortest time cost does not usually accompany the most economic energy requirement. Therefore, three evaluation indices could be used to determine the expected options for the heat flux density for a certain amount of ice. The first choice is defined as a comprehensive index, β, which accounts for the optimal time and energy efficiency as follows (a balance between time and energy consumption):

$$\beta = (T/T_{\max}) + (E_c/E_{c,\max}) \tag{11.4}$$

where T and E_c are the time and energy used for deicing; and $T_{\max}$ and $E_{c,\max}$ are the longest time and maximum energy required for deicing a certain amount of ice with varying heat flux density under the same ambient conditions. To minimize the confusion regarding the equation working conditions, the heat flux cannot be zero and should be in a reasonable range to ensure that the deicing process is finished in a finite time period. The second index considers only the energy concerned (i.e., the requirement of minimum power consumption). The last index considers only the shortest time expenditure for an emergency case.

As shown in Table 11.4 and Figure 11.17, at an ambient temperature of $-10\,°$C, the optimal heat flux densities are 1800, 1400 or 1800, and 1800 W/m^2 for ice with thicknesses of 10, 15, and 20 mm, where the minimum time−energy indices are 1.217, 1.34, and 1.331, respectively. These optimal values are reasonable because for the heat flux density of 1800 W/m^2, the time efficiency is much higher than the increase in energy consumption. At an ambient temperature of $-20\,°$C, the most appropriate heat flux densities are 1000, 1000, and 1400 W/m^2 for ice with thicknesses of 10, 15, and 20 mm, where the minimum time-energy indices of 1.286, 1.356, and 1.318, respectively,

Table 11.4 Comprehensive index of time−energy for the evaluation of deicing efficiency

Temperature (°C)	Ice thickness (mm)	600 W/m²	1000 W/m²	1400 W/m²	1800 W/m²
−10	10	1.749	1.617	1.572	1.217
	15	1.871	1.689	1.355	1.340
	20	1.924	1.575	1.464	1.331
−20	10	1.888	1.286	1.434	1.376
	15	1.778	1.448	1.356	1.429
	20	1.761	1.474	1.318	1.438
−30	10	1.919	1.301	1.347	1.363
	15	1.818	1.323	1.320	1.407
	20	1.822	1.448	1.283	1.406

Reprinted with permission from Li et al. (2013) Copyright 2013: Elsevier.

represent the optimal balance between the time efficiency and the energy consumption. Furthermore, 1000 and 1400 W/m² could be the best choices for ice thicknesses of 10 and 20 mm. There are two acceptable heat flux densities, 1000 and 1400 W/m², for deicing 15-mm-thick ice because of their similar indices of 1.323 and 1.320, but when the efficiency of time is also considered, 1400 W/m² should be the first choice.

When a single index is considered (i.e., the least energy consumption or the shortest time expenditure at an ambient temperature of −10 °C, as shown in Figure 11.18 and Tables 11.2 and 11.3), a heat flux density of 600 W/m² is the optimal choice for the 10-mm-thick ice by virtue of having the lowest energy consumption (53.82 kJ). However, in an emergency situation, 1800 W/m² could be selected because it requires the least time. For ice of thicknesses of either 15 or 20 mm, a heat flux density of 600 W/m² is a reasonable choice if time is not a limitation because it has the lowest energy requirement. In an emergency situation, 1800 W/m² must be applied to meet the minimum time requirement, although more energy is consumed.

Figure 11.19 presents the time and energy consumption for deicing a certain amount of ice at an ambient temperature of −20 °C. The trends in the curves shown in Figure 11.18 imply the existence of the critical phenomenon, which is that the second optimal solution is more practical than the absolute optimal solution. For ice with thicknesses of 10, 15, and 20 mm, although the time is slightly longer when the heat flux density is 1000, 1400, and 1400 W/m² than when it is 1800 W/m², the energy consumption is much smaller at these heat flux densities than at 1800 W/m². These values are consistent with the time−energy index shown in Figure 11.15. Therefore, the optimal solution is that the regular heat flux density (1000−1400 W/m²) would be offered for ambient temperatures of −20 ∼ −10 °C with the anticipated associated good energy and time efficiency.
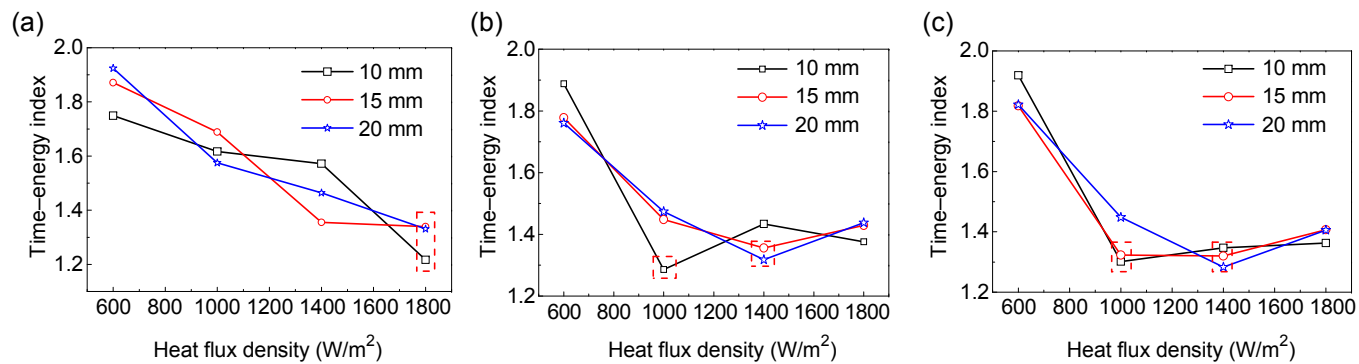
Figure 11.17 Index of time−energy in deicing for ambient temperatures of (a) −10 °C, (b) −20 °C, and (c) −30 °C.
Reprinted with permission from Li et al. (2013) Copyright 2013: Elsevier.
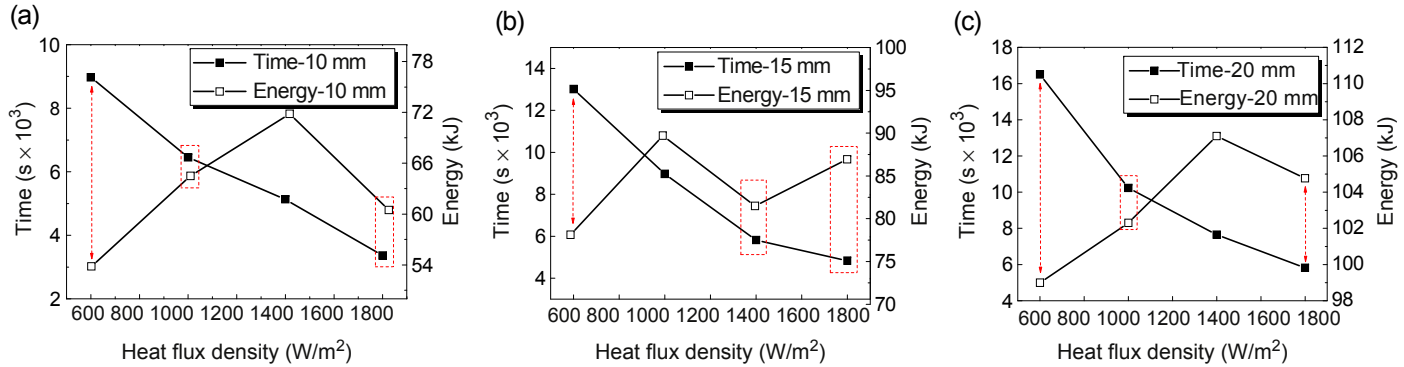
Figure 11.18 The evaluation of the prior options for time and energy consumption on deicing efficiency at an ambient temperature of $-10\,^{\circ}\mathrm{C}$ for ice thicknesses of (a) 10 mm, (b) 15 mm, and (c) 20 mm.

Reprinted with permission from Li et al. (2013) Copyright 2013: Elsevier.
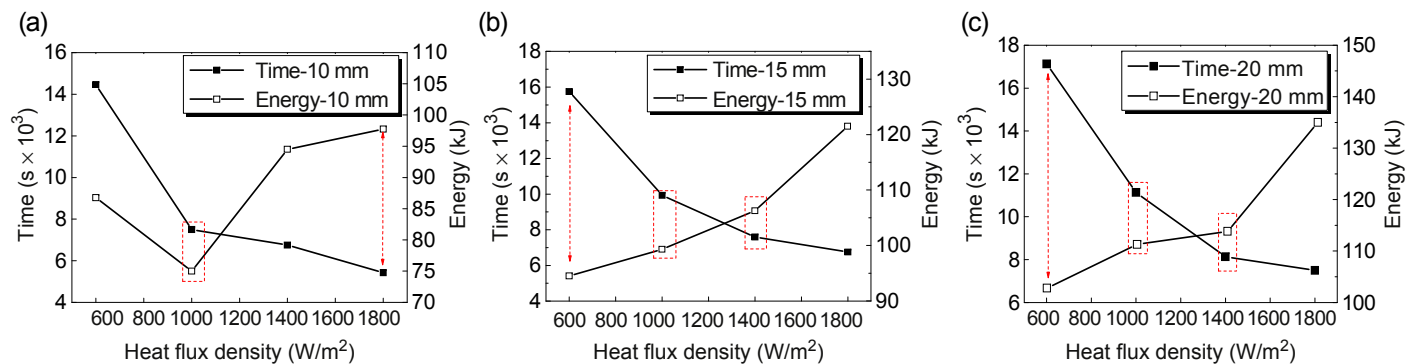
Figure 11.19 The evaluation of the prior options for time and energy consumption on deicing efficiency at an ambient temperature of $-20\,^{\circ}$C for ice thicknesses of (a) 10 mm, (b) 15 mm, and (c) 20 mm.
Reprinted with permission from Li et al. (2013) Copyright 2013: Elsevier.

Similar to the results shown in Figure 11.19, the second optimal point is more practical for the ambient temperature of $-30\,°C$, as shown in Figure 11.20. The optimal heat flux density for an ice thickness of 10 mm is 1000 W/m^2 (smallest energy requirement with a relatively short time requirement); the optimal heat flux densities for ice thicknesses of 15 and 20 mm are, respectively, 1000 and 1400 W/m^2.

Moreover, for 20-mm-thick ice at $-30\,°C$, the energy requirement increased slightly with the increase of heat flux density from 600 to 1400 W/m^2, but the time is significantly reduced. If there is no limitation for time cost, the 600, 1000, and 1400 W/m^2 heat flux densities could be used, but the optimal density is 1400 W/m^2 because of the combined efficiency of time and energy, with a minimum time−energy index of 1.283 as presented in Table 11.4. Generally, 1400 W/m^2 is an appropriate option that could be widely applied in severely harsh weather for deicing.

11.4.4   The evaluation of economic expense

The price for electric power in China is currently 0.083 \$/(kW h). The cost of deicing per unit area using the proposed technology is calculated and is listed in Table 11.5. For the low-temperature case (-10 to $0\,°C$), 0.11−0.22 \$/m^2 is sufficient for deicing ice in the thickness range of 10−20 mm. For lower temperature conditions (-20 to $-10\,°C$), the cost is 0.15−0.28 \$/m^2, which is much lower than the other current techniques listed in Table 11.6 (Lee et al., 2000; Litvan, 1976; Harnick et al., 1980; George and Charles, 2011). The cost is calculated based on the present economic costs and the operating efficiency of various deicing methods. The estimated expense of each mechanical method includes the labor costs (>11.00 ¥/h in China, http://finace.sina.com.cn/g/20100809/07058444689.shtml) and the work efficiency. For the chemical methods, the cost depends on the market price (NaCl, 0.31 \$/kg; CMA, 3.1 \$/kg) and the amount consumed (NaCl, 0.3−0.6 kg/m^2; CMA, 0.56−1.13 kg/m^2).

As shown in Table 11.6, for similar situations, the cost of using conductive concrete to deice the same amount of ice (Yehia et al., 2000) is almost four times the cost of the approach proposed in this chapter. Common salt (sodium chloride) is not recommended due to the severe environmental pollution and corrosion of reinforced concrete associated with its use, even though it is only half the cost of the approach proposed in this study (Lee et al., 2000; Litvan, 1976; Harnick et al., 1980; George and Charles, 2011). Moreover, the application of some nonpolluting chemical salts (e.g., calcium chloride and acetic acid calcium magnesium) is also limited because of their much higher cost (0.26−0.7 \$/m^2, 1.75−3.51 \$/m^2). The proposed deicing technique is an excellent option, especially for the extremely low-temperature case ($\sim -30\,°C$), because at a maximum cost of no more than 0.29 \$/m^2 the deicing cost is much lower. The solar energy used as the power source in this study is an abundant source of energy, increasing the feasibility of this proposed deicing system for practical applications.

Furthermore, the cost of the self-heating technique (0.05−0.11 \$/m^2) proposed in this study is approximately half that of the snow-thawing method developed by Hou et al. (2002) based on conductive concrete filled with CF (1.85%). The technique
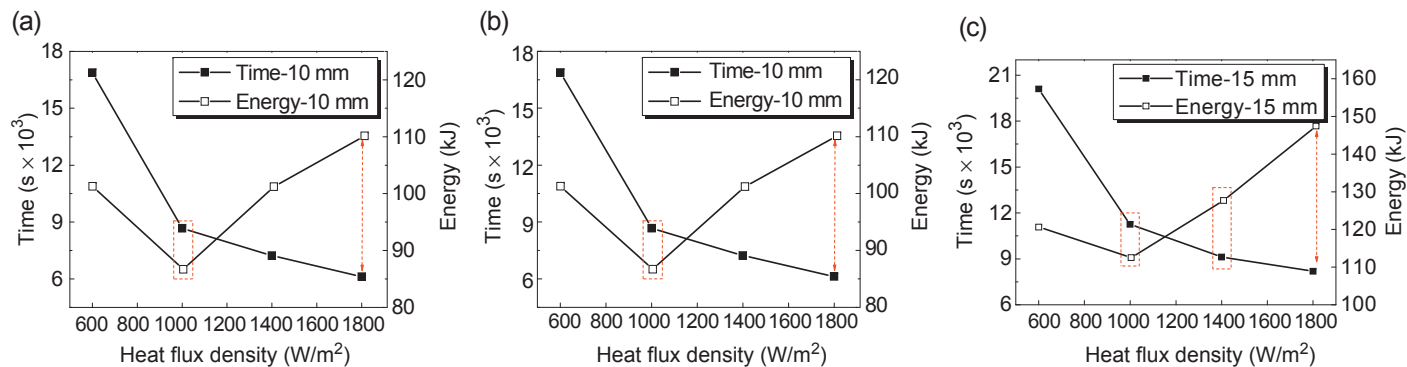
Figure 11.20 The evaluation of the prior options for time and energy consumption on deicing efficiency at an ambient temperature of $-30\,°\text{C}$ with ice thicknesses of (a) 10 mm, (b) 15 mm, and (c) 20 mm.
Reprinted with permission from Li et al. (2013) Copyright 2013: Elsevier.

Table 11.5 Economic expenditure per unit area for deicing a certain thickness of ice

Ambient temperature (°C)	Ice thickness (mm)	Economic expenditure ($/m²)			
		600 W/m²	1000 W/m²	1400 W/m²	1800 W/m²
−10	10	0.11	0.14	0.15	0.12
	15	0.15	0.18	0.17	0.18
−20	20	0.21	0.22	0.22	0.22
	10	0.18	0.15	0.20	0.20
	15	0.20	0.20	0.22	0.25
	20	0.22	0.23	0.23	0.28
−30	10	0.22	0.18	0.22	0.23
	15	0.25	0.23	0.26	0.31
	20	0.29	0.29	0.29	0.35

Reprinted with permission from Li et al. (2013) Copyright 2013: Elsevier.

Table 11.6 Cost of deicing using different approaches at an ambient temperature of −20 °C

Ice thickness (mm)	Economic expenditure ($/m²)					
	NaCl	CaCl	CMA	Conductive concrete	Mechanical	CNFP
10	0.09	0.26−0.35	1.75	>0.56	>0.1	0.15−0.2
15	0.13	0.40−0.53	2.65	>0.56	>0.1	0.2−0.25
20	0.18	0.53−0.70	3.51	>0.73	>0.1	0.22−0.28

Reprinted with permission from Li et al. (2013) Copyright 2013: Elsevier.

proposed in this study is also verified as being only 1/10−1/6 of the cost calculated by Yehia et al. (2000) in the bridge snow-thawing study based on conductive concrete filled with steel fiber. In summary, the investigations of deicing and snow melting verified that the self-heating/snow-thawing technique proposed in this study offers the advantages of less time, lower energy consumption, feasible operation, intelligent control, and environmental protection. This system can be widely used in pavements, pavement, highways, and bridges. In addition, the integration of a self-energy harvesting system with this self-heating/snow-thawing system will be competitive in the future.

11.5 Conclusion

A self-heating pavement system based on a CNFP electroheating element is proposed. The feasibility and efficiency of the self-heating pavement system are validated through experiments. This study resulted in the following conclusions.

CNFP provides good electrothermal properties at ambient temperatures below 0 °C, with a rapid heating reaction and stable resistivity (0.72 Ω mm). These properties indicate that CNFP can be employed as a highly efficient heating element to generate a stable heat flux density for a self-heating pavement system. For example, a stable heat flux density of 1000 W/m^2 can be generated by CNFP with an applied current of 2.3 A.

The high deicing efficiency and low energy consumption of the proposed self-heating pavement system with electrothermal materials have been validated. The deicing performance is affected by the thickness of the ice layer, the surrounding temperature, the heat flux density, and the wind speed. The experimental results indicate that the deicing time and energy consumption increase with an increase in ice thickness but decrease with an increase in the surrounding temperature. As another essential factor affecting the deicing performance, a larger heat flux density results in a decreased time cost as a hyperbolic function but has an uncertain influence on energy consumption. Therefore, the optimal option for the heat flux density is determined by an evaluation of the time−energy index, β, as the most rational power affordance. For example, with an ambient temperature of −10 °C, the optimal heat flux density is 1800, 1400 or 1800, and 1800 W/m^2 for ice with thicknesses of 10, 15, and 20 mm, which corresponds to minimum indices of 1.217, 1.34, and 1.331, respectively. The high performance of the CNFP-based self-heating pavement system for snow melting is also validated through an experimental study.

In terms of the evaluation criteria of efficiency, time, energy supply, cost, and environmental impacts, the deicing and snow-melting investigation verified that the proposed self-heating pavement system is a competitive and promising deicing and snow-thawing technique. It may have the potential to be widely used in bridges, highways, pavement, and airport infrastructures.

Acknowledgments

References

Chang, C., Michelle, H., Song, G., Yi-Lungand, M., Li, H., 2009. A feasibility study of self-heating concrete utilizing carbon nanofiber heating elements. Smart Materials Structures 18, 127001−127005.

Chung, D.D.L., 1994. Carbon Fiber Composites. Butterworth-Heinemann, Boston, US.

Chung, D.D.L., 2001. Comparison of submicron-diameter carbon filaments and conventional carbon fibers as fillers in composites materials. Carbon 39, 1119−1125.

Chung, D.D.D., 2004a. Electrically conductive cement-based composites. Advances in Cement Research 16, 176.

Chung, D.D.D., 2004b. Self-heating structural materials. Smart Materials and Structures 13, 562−565.

Feng, J.H., Li, H., 2009. Development of self-heating concrete using carbon nano-fiber paper. In: Tomizuka, M. (Ed.), Proc. of SPIE. (San Diego California, US 9−12 March 2009) (The International Society for Optical Engineering, Sensors and Smart Structures Technologies for Civil, Mechanical, and Aerospace Systems) Vol. 7292. (CA: San Diego).

Ferrara, A.A., Haslett, R., 1975. Prevention of Preferential Bridge Icing Using Heat Pipes. Federal Highway Administration, Washington, D.C. FHWA-RA-75−111.

Fridman, P.L., 2009. Assessing the impact of pavement deicing products on aircraft and airfield infrastructure. Airport Management 3, 223−237.

George, G.K., Charles, C.R., 2011. An investigation of infrared deicing through experimentation. Cold Regions Science and Technology 65, 79−87.

Harnick, A.B., Meier, V., Rosli, A., 1980. Combined influence of freezing and deicing salt on concrete: physical aspects durability of building materials and components. ASTMSTP 691, 474−484.

Hone, J., Whitney, M., Piskoti, C., Zettl, A., 1999. Thermal conductivity of single-walled carbon nanotubes. Physical Review B 59, 2514−2516.

Hou, Z.F., Li, Z.Q., Tang, Z.Q., 2002. Research on making and application of carbon fiber electrically concrete for deicing and snow-thawing. Journal of Wuhan Institute of Technology (Natural Journal Edition) 24, 32−34.

Kane, C.L., Mele, E.J., Lee, R.S., Fischer, J.E., Petit, P., Dai, H., Thess, A., Smalley, R.E., Verschueren, A.R.M., Tans, S.J., Dekker, C., 1998. Temperature-dependent resistivity of single-wall carbon nanotubes. EPL 41, 683−688.

Kim, S.Y., Koretsky, C., 2013. Effects of pavement salt deicers on sediment biogeochemistry. Biogeochemistry 112 (1−3), 343−358.

Litvan, G.G., 1976. Frost action in cement in the presence of deicers. Cement and Concrete Research 6, 351−356.

Lee, R.C., 1984. Bridge heating using ground source heat pipes. Transportation Research 962, 51−57.

Lee, H., Cody, R.D., Cody, A.M., Spry, P.G., 2000. Effects of various deicing chemicals on pavement concrete deterioration. In: Proc. Mid-continent Transportation Symp. Iowa, Ames, pp. 151−155.

Li, H., Xiao, H., Ou, J., 2008. Electrical property of cement-based composites filled with carbon black under long-term wet and loading condition. Composites Science and Technology 68, 2114−2119.

Li, H., Zhang, Q., Xiao, H., 2013. Self-deicing pavement system with a CNFP high-efficiency thermal source and MWCNT/cement-based high-thermal conductive composites. Cold Regions Sciences and Technology 86, 22−35.

Li, H., Zhang, Q., Xiao, H., 2014. Analytic investigations of CNFP-based self-deicing pavement system on the deicing performance. Cold Regions Science and Technology 103, 123−132.

Lijima, 1991. Helical microtubes of graphitic carbon. Nature 354, 56−58.

Lin, D., et al., 2014. Three-dimensional printing of complex structures: man made or toward nature? ACS Nano 8, 9710−9715.

Long, D.C., Baldwin, J.S., 1981. Snow and Ice Removal from Pavement Using Stored Earth Energy. Federal Highway Administration. FHWA-TS-80−227, 78.

Moisala, A., Li, Q., Kinloch, I.A., Windle, A.H., 2006. Thermal electrical conductivity of single and multi-walled carbon nanotube-epoxy composites. Composites Science and Technology 66, 1285−1288.

Novotny, E.V., Murphy, D., Stefan, H.G., 2008. Increase of urban lake salinity by pavement deicing salt. Science of the Total Environment 406 (1−2), 131−144.

Peebles, L.H., 1994. Carbon Fibers: Formation, Structure, and Properties. CRC Press, Boca Raton, FL, US.

Saito, R., Dresselhaus, G., Dresselhaus, M.S., 1998. Physical Properties of Carbon Nanotubes. Imperial College Press, London, UK.

Shi, X., et al., 2009. Deicer impacts on pavement materials: introduction and recent developments. The Open Civil Engineering Journal 3, 16−27.

Tanaka, O., 1981. Snow melting using heat pipes. Advances in Heat Pile Technology 25, 2272−2284.

Tuan, C.Y., Yehia, S., 2004. Evaluation of electrically conductive concrete containing carbon products for deicing. ACI Materials Journal 101, 287−293. M32.

Wang, K., Nelsen, D.E., Nixon, W.A., 2006. Damaging effects of deicing chemicals on concrete materials. Cement and Concrete Composites 28, 173−188.

Xu, X., et al., 2015. Self-sensing, ultralight, and conductive 3D graphene/iron oxide aerogel elastomer deformable in a magnetic field. ACS Nano 9, 3969−3977.

Yehia, S., Tuan, C.Y., Ferdon, D., Bing, C., 2000. Conductive concrete overlay for bridge deck deicing: mixture proportioning, optimization and properties. ACI Materials Journal 97, 172−181.

Zhang, Q., et al., 2015. Mechanically robust honeycomb graphene aerogel multifunctional polymer composites. Carbon. http://dx.doi.org/10.1016/j.carbon.2015.05.102.

Zhao, H., Wang, S., Wu, Z., Che, G., 2010. Concrete slab installed with carbon fiber heating wire for bridge deck deicing. Journal of Transportation Engineering 136, 500−509.

Zhao, H., Wu, Z., Wang, S., Zheng, J., Che, G., 2011. Concrete pavement deicing with carbon fiber heating wires. Cold Regions Science and Technology 65, 413−420.

Sensing sheets based on large-area electronics and integrated circuits

12

Branko Glisic, Naveen Verma
Princeton University, Princeton, NJ, USA

12.1   Introduction

Traditional strain-monitoring approaches are mostly based on discrete point sensors, which provide one with sparse detection of strain field anomalies. However, reliable and robust identification of damage calls for dense sensor arrays that cover large areas of structure. The main challenge for implementation of such a sensor network is scalability to the size of civil structures in terms of cost, ease of installation, spatial resolution, and data management and analysis. Emerging electronic technologies can address this challenge by providing flexible-form-factor, low-cost, ultra-low-energy computation and precise instrumentation necessary for smart sensing. Patterned large-area electronics (LAE) is an emerging technology that allows the dense integration of sensors and energy harvesters on an inexpensive (plastic) substrate (e.g., kapton) that can cover large areas of structures (Parashkov et al., 2005). In addition to sensors, this technology can enable large-area interconnect and semiconductor devices, which are useful for specific circuit functionality. However, the latter have significantly lower performance and energy efficiency compared to commonly available silicon devices. This challenge can be overcome by hybrid systems that combine and exploit the energy-efficient instrumentation and processing provided by silicon integrated circuits (ICs) and the large-area connectivity and distributed sensing capabilities of LAE. As a result, a strain sensing sheet based on LAE and ICs is being created at Princeton University, enabling robust and reliable detection of minute strain field anomalies, determination of their position and extent with centimeter resolution, and quantification of anomalies using probabilistic approaches. The concept of the hybrid sensing sheet and its current state of advancement are presented in this chapter.

12.2   Concept of direct sensing

The initialization of damage in structures frequently has a local character and occurs in the form of strain-field anomalies. Typical examples include local buckling (bowing) in steel as a consequence of loss of local stability microcracks in steel, which are early indicators of fatigue; and cracks in concrete, which are early indicators of damage

caused by frost, alkali reaction, or corrosion in reinforcing bars. Early damage identi-
fication (i.e., detection, localization, and quantification) can greatly aid preservation
and maintenance activities, and significantly improve structural safety.

The primary challenge in traditional strain-monitoring approaches, based on discrete
sensors, is that their spatial resolution is limited (i.e., the sensors are sparsely placed at
mutually distant locations over the structure). Consequently, damage detection at
points distant from sensors is unreliable. To support this statement, early-age strain
measurements collected from the Streicker Bridge at the Princeton University campus
using embedded long-gauge fiber-optic sensors are given in Figure 12.1 (Yao and
Glisic, 2012). The sensors with a gauge length of 60 cm (labeled P10h11U,
P10h11D, and P10h11L; see Figure 12.1) were embedded in a cross section of the
bridge during pouring of concrete. Early-age cracking occurred in the cross section
and involved the locations P10h11U and P10h11D, and thus the corresponding sensors
were directly activated. The crack created a strain field anomaly that was reliably iden-
tified as a large change in the strain, which was at least one order of magnitude higher
than the noise (uncertainty) of the monitoring system combined with noise from usual
strain sources, such as temperature variations and live load. The sensor P10h11L,
which was installed less than a meter away from the two other sensors (see Figure 12.1),
did not cross the crack, and thus it was indirectly affected by the crack. It measured only
a small change in the strain magnitude (as shown in the figure), which is comparable
and thus extremely difficult to distinguish from usual strain sources. Other sensors in
the bridge that were at distances of 2 m or more did not register any relevant change
in the strain (Hubbell and Glisic, 2013).

The error limits of the monitoring system were 4 $\mu\varepsilon$ (Hubbell and Glisic, 2013), but
the tiny crack of ~ 0.1 mm (Abdel-Jaber and Glisic, 2015) would be detected by the
directly affected sensors even if the precision of the monitoring system was an order of
magnitude lower. This demonstrates that direct contact of sensors with the damage
(i.e., the concept of direct sensing) not only provides high reliability and sensitivity,
but also enables very high robustness to conditions found in real-life settings.

Hence, full reliability in damage detection can be achieved only if the strain sensor
is in direct contact with the damage. If that is not the case, the damage detection is
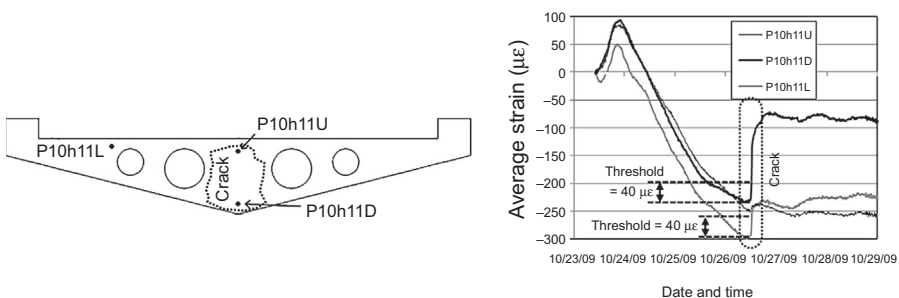
Figure 12.1 Left: Position of discrete fiber-optic sensors within a cross section of the
Streicker bridge; right: direct crack detection versus indirect crack detection in the Streicker
bridge (Yao and Glisic, 2012).

either simply impossible or must be performed indirectly, requiring complex data analysis algorithms whose reliability is in general challenged by strain-field perturbations caused by the usual variability of influences found in real-life settings (live load fluctuations, temperature and humidity variations, etc.).

Discrete strain sensors can have short or long gauge length. Typical examples of the former are resistive strain gauges, vibrating-wire sensors, and fiber Bragg-grating sensors (FBGs); typical examples of the latter are interferometric fiber-optic sensors (SOFOs) and specially packaged FBGs (Glisic and Inaudi, 2007). Although long-gauge sensors have better spatial coverage and thus are more suitable for direct sensing, general key shortcomings of both types of discrete sensors are (1) their insensitivity to the anomalies that do not occur in the close proximity of the sensors (Wipf et al., 2007), and, importantly, (2) the number of sensors required to cover large areas of structures, thereby imposing tedious installation, complex cabling, and challenging data management and analysis (Heise, 1965).

Distributed fiber-optic sensing technologies (Glisic and Inaudi, 2007) offer significant improvements with respect to discrete sensing technologies. A distributed sensor (sensing cable) is continuous and sensitive at each point along its length. Thus, it practically enables one-dimensional (1D) strain-field monitoring. Nevertheless, the damage occurring in areas far from sensors is not directly detected. The reliability in damage detection for various types of sensors is schematically presented and compared in Figure 12.2 (modified from Glisic and Adriaenssens, 2010).

Figure 12.2 shows that if the exact location of the damage occurrence is not known at the time of installation of sensors (which is frequently the case in real-life settings),

	Damage "A"	Damage "B"	Damage "C"	Damage "E"
Short-gauge	Direct, reliable detection	Indirect or impossible	Indirect or impossible	Indirect or impossible
Long-gauge	Direct, reliable detection	Direct, reliable detection	Indirect or impossible	Indirect or impossible
Distributed	Direct, reliable detection	Direct, reliable detection	Direct, reliable detection	Indirect or impossible
2D sensor	Direct, reliable detection	Direct, reliable detection	Direct, reliable detection	Direct, reliable detection

Figure 12.2 Schematic comparison between damage detection capabilities of short-gauge, long-gauge, and 1D distributed sensors, and 2D distributed sheet sensor.
Modified from Glisic and Adriaenssens (2010).

only a 2D distributed sensor or a 2D array of densely spaced sensors can provide reliable damage detection based on direct sensing. The main challenge of the technology that may potentially enable 2D direct sensing is scalability to the size of civil structures, as it has to address conformability to irregular surfaces, physical robustness to environmental influences, big data management and analysis, and practical power supply. A hybrid solution combining the best performances of LAE and ICs into strain sensing sheets is one way to successfully address the challenge of large-scale 2D direct sensing.

12.3   LAE and ICs

LAE and silicon complementary metal−oxide semiconductor (CMOS) ICs provide highly disparate characteristics in terms of electrical operation, form factor, and cost. The motivation behind a hybrid system that combines the two technologies is to exploit their respective strengths to enable systems for very large-scale sensing and monitoring. The two technologies derive their characteristics, and thus their strengths and weaknesses, from the associated methods of fabrication. Here, an overview is provided. Following this, the complementary strengths of the technologies are identified for realizing the various system functions required for embedded structural-health-monitoring applications.

Silicon ICs represent the dominant technology used for electronic devices today. The basic device on which these are based is the metal−oxide semiconducting field effect transistor (MOSFET). The MOSFET forms the basis for implementing the vast majority of functions within state-of-the-art ICs in use today. The functions that have been of primary focus include computation, instrumentation, communication, and so on. To drive the advancement of these functions (in terms of performance, scale/complexity, and accessibility), the IC semiconductor industry has focused on improving the performance and cost of the MOSFET. Over the last 50 years, the well-known trend referred to as Moore's law has been the primary means for achieving this improvement. An important characteristic of silicon MOSFETs is that they require high-temperature processing ($\sim 1000\ ^\circ$C) to achieve the desired electrical characteristics. This restricts the materials that can be employed during fabrication, in turn limiting the types of devices and types of substrates that are possible for fabricating devices. From an application perspective, this translates into limitations in terms of diversity of functions and form factor.

LAE is a technology whose fabrication differs from that of silicon CMOS in that LAE is based on processing thin films of materials at low temperatures ($\sim 200\ ^\circ$C). This has the important characteristic of being compatible with a wide range of different materials and substrates. From an application perspective, this translates into the ability to form diverse types of devices, especially for sensing and energy harvesting, and the ability to integrate these onto substrates such as glass or plastics, which can be physically large and conformal. As a result, over the last 10 years, research in LAE has led to demonstrations of an extremely rich set of transducers for sensing, actuation, and

energy harvesting (Someya et al., 2008). Examples have included sensors for strain (Zhou et al., 2006), pressure (Someya et al., 2004), and vibrations; actuators for visual display, mechanical force (Jafferis and Sturm, 2013), and audio; and energy harvesters for solar, thermal, and mechanical (Qi et al., 2010).

However, the use of such devices within systems inevitably requires supporting functionality for instrumentation, power management, embedded computation, and communication. Generally speaking, the implementation of such functionality is based on transistors. Indeed, thin-film transistors (TFTs) are possible in LAE. In fact, these are in widespread use today in flat-panel display applications, where transistors on glass are required to distribute signals to drive pixels. Thanks to this application, which has given rise to a \$100 billion/year industry, TFT manufacturing on glass has benefitted from its own scaling trends, resulting in larger substrates and lower cost per area. Today, manufacturing is done on glass substrates of nearly 10 m^2 at a cost of roughly \$200/m^2.

Despite such scaling and such success in display applications, LAE TFTs pose substantial challenges for realizing generalized sensing systems. The reason is that their performance and energy efficiency are orders of magnitude below those of the benchmark transistors used in electronic devices today, namely, silicon MOSFETs. The reason for discrepancy is low-temperature processing, which yields the benefits in terms of sensing and energy harvesting for LAE (as mentioned in this chapter) but also leads to low electrical performance. For quantitative comparison, Table 12.1 (Hu et al., 2014a) compares key electrical parameters for silicon MOSFETs (at the 130 nm technology generation) with those for LAE TFTs (based on amorphous silicon (a-Si), the dominant technology used today in flat-panel displays).

The mobility for electrical current (μ_e) indicates how fast electrical charge can move through a material across which an electric field exists (i.e., due to application of a voltage); the capacitances ($C_{GD}/_{GS}$) indicate how much charge is required to generate a voltage change; the gate-dielectric thickness ($t_{dielectric}$) indicates how

Table 12.1 Comparison of the electrical parameters of LAE thin-film transistors (based on low-temperature processed amorphous silicon (a-Si) and silicon MOSFETs (at the 130 nm technology generation) (Hu et al., 2014a)

	LAE TFT (a-Si)	Silicon IC (130 nm)
Mobility (μ_e)	μ_e: 2 cm^2/Vs	μ_e: 1000 cm^2/Vs
$t_{dielectric}$	280 nm	2.2 nm
V_{DD}	6 V	1.2 V
$C_{GD}/_{GS}$	3.3 fF/μm	0.34 fF/μm
f_T	1 MHz	150 GHz

many current-causing carriers are generated as a result of a voltage applied to the transistor's input electrode (gate); and the unity−current−gain frequency (f_T) indicates the signal frequency beyond which a transistor's output current falls below its input current, thus negating the ability to amplify input signals. Their orders-of-magnitude inferior parameter values suggest that TFTs alone cannot viably enable the supporting functionality necessary for the large-scale sensing made possible by LAE. Thus, there is a need to explore hybrid systems that combine LAE with silicon ICs.

To motivate hybrid systems on a high level, Table 12.2 (Hu et al., 2014a) considers the core system functions required: sensing, power management, communication, and computation. The complementary strengths of the two technologies toward realizing these functions in the context of large-scale sensing are summarized. For sensing, LAE enables the formation of diverse and expansive sensor arrays, whereas silicon ICs enable precision instrumentation and signal acquisition. For power management, LAE enables physically large energy harvesters capable of harvesting substantial power from ambient sources, and silicon ICs enable efficient (low-loss) control and power conversion circuitry. For communication, LAE enables large-area interconnects for low-energy wired communication among distributed sensing subsystems as well as the possibility of large-dimensioned antennas for improving the efficiency of wireless communication, whereas silicon ICs enable high-speed, energy-efficient data transceiver circuitry. Computation is a function that has particularly benefitted from Moore's law scaling, enabling silicon ICs to provide high-performance, energy-efficient operations on a very large scale. LAE, on the other hand, does not provide comparable performance for computation.

From this discussion, it follows that hybrid systems represent an appropriate choice, whereby the highly complementary strengths of LAE and silicon ICs can be jointly exploited. Practically, the challenge with hybrid systems arises due to the interfacing that is required between the two technologies. In particular, the interfaces pose the

Table 12.2 Summary of the respective strengths of LAE and silicon ICs for realizing core system functions (Hu et al., 2014a)

	Silicon ICs	LAE
Sensing	+ Precision instrumentation	+ Diverse transducers, large substrates
Power management	+ (Dynamic) control, DC/DC conversion, regulation	+ Large-dimensioned energy harvesters
Communication	+ Physical-layer transceivers (wired/wireless)	+ Low-loss interconnect for 1 cm−10 m telemetry + Large-dimensioned antennas
Computation	+ >1B high-performance logic gates	− Low-power performance/ density/efficiency devices

primary limitation to system scalability and efficiency. Thus, the primary focus for engineering practical hybrid systems is developing architectures for the various system functions that are built around scalable and low-cost strategies for interfacing the two technologies. Although LAE TFTs are not preferred for implementing the core system functions, they can play an important role in enhancing the use and operation of the interfaces. A prototype system taking this approach is described in further detail in Section 12.4.2.

12.4 LAE/IC sensing sheets

12.4.1 General

LAE/IC sensing sheets consist of the following main components (Glisic and Verma, 2011), as shown in Figure 12.3:

1. 2D distributed array of strain sensors patterned on inner layer of kapton (polyimide) substrate combined with the patterned interconnect and functional LAE;
2. ICs, which serve as intelligence units, interfaced to the sheet via scalable noncontact interfaces for sensor readout, data management and analysis, power management, and communication; and
3. Protective outer layer with integrated flexible solar-energy harvester (photovoltaic); the latter is combined with power converters and batteries patterned in the LAE sheet to power the full system.

The individual sensor patterned on the sensing sheet is actually a full-bridge resistive strain gauge. It consists of four resistors, two oriented in the measuring direction and two perpendicular to that direction, as shown in Figure 12.4 (Tung et al., 2014),
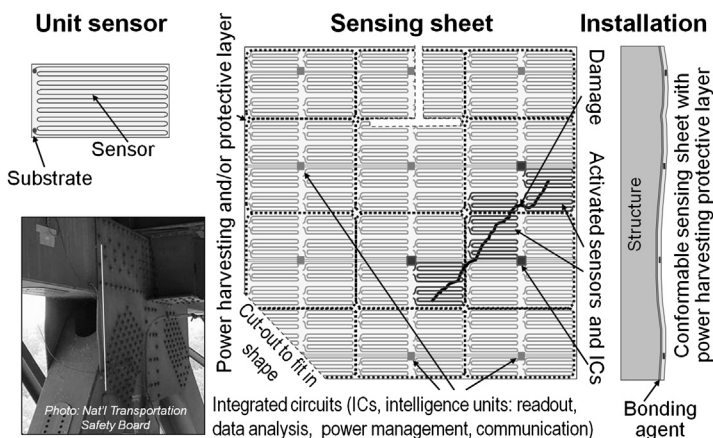
Figure 12.3 Schematic concept of the sensing sheet: its components and its application (Tung et al., 2014).
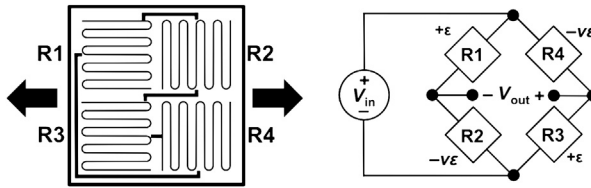
Figure 12.4 Left: Configuration of the full-bridge sensor with strain measurement direction indicated by arrows; right: corresponding Wheatstone bridge scheme for sensor readout (Tung et al., 2014).

and mutually connected to form an (electrical) Wheatstone bridge (Perry and Lissner, 1955). The full-bridge configuration is chosen for sensors because of its capability for differential sensing. This significantly improves robustness against nondesired external and internal interferences (e.g., makes sensors virtually insensitive to temperature and humidity variations, and to inherent shrinkage of concrete) and enables the alternating-current readout scheme to be applied to the sensors by avoiding large sinusoidal baseline signals (Glisic and Verma, 2011).

The flexible kapton (polyimide) substrate allows conformability to the surface of the monitored structure. Each IC is responsible for a group of sensors, as indicated by dashed lines in Figure 12.3. It reads the attributed sensors sequentially, processes the collected data, and analyzes the data. IC communicates with the sensors via noncontact links and with neighboring ICs wirelessly. This flexible scheme allows for independent reading of individual sensors, and thus damage or malfunction of one or several sensors does not affect the functioning of the reminder of the sensing sheet. This also allows tailor-cutting the sensing sheet in order to fit it to the shape of a monitored area (see Figure 12.3). In addition, an appropriate pattern of the interconnect makes sensors accessible to multiple neighboring ICs, so in the event of damage or malfunctioning of one IC, the neighboring ICs can access the group of sensors originally attributed to that IC and keep the sensing sheet operational.

All ICs communicate with the master node, which in turns communicates with a monitoring center using wired or wireless communication. The network of ICs enables distributed data management and analysis, and transmits the data to the monitoring center, in general, only on demand or when damage is detected. In this manner, efficient data management and flow are established, and only a relatively modest amount of critical data is transmitted to the monitoring center, as opposed to traditional approaches where large amounts of raw data would be transmitted to the monitoring center and then analyzed.

Assuming that the damage is detected, the location and spatial extent of the damage can then simply be determined by identifying the locations (coordinates) of sensors activated by the damage. An example in Figure 12.3 illustrates this concept: the damage is represented by a solid line, and activated sensors by shaded color. Figure 12.3 also shows that accuracy in damage localization and extent depends on the size and spatial arrangement of sensors. Thus, the design of the sensing sheet, which includes the size and spatial arrangement of sensors, depends on the level of reliability in

damage detection and accuracy in damage localization that is to be achieved, and on the strain distribution in the monitored structure. For example, for uniform probability of damage occurrence in terms of damage position, extent, and orientation, it can be shown that the use of a large number of smaller sensors uniformly distributed within the sheet provides better performance than using a smaller amount of larger sensors that are not uniformly distributed (Yao and Glisic, 2014).

The sensing sheet is currently available only in the form of a prototype (i.e., it is not commercially available at the time of writing of this book); nevertheless, its components and the concept are proven at the experimental level, as shown in the following subsections.

12.4.2 Hardware components

As mentioned in Section 12.3, the primary challenge when it comes to realizing hybrid LAE/IC systems is the interfacing required between the two technologies. With silicon ICs having a physically small and rigid form factor and LAE having a large and conformal form factor, a challenge arises because no high-volume process exists today for robust electrical bonding of small, rigid devices to large, flexible sheets. To overcome this challenge, the sensing-sheet architecture (Hu et al., 2014a,b) employs noncontact electrical interfacing through inductors and capacitors. Inductors generate a magnetic field and capacitors generate an electric field, both of which enable electrical signal coupling at a distance. Generally, the strength of the coupling depends on the physical sizes of the inductors and the capacitors as well as the distance over which the signal is being coupled. Thus, the interfaces necessitate careful engineering and new innovations for enabling the subsystem architectures.

Figure 12.5 shows a system-level block diagram of a prototype described in Hu et al. (2014a). To realize the interfaces, the small silicon ICs are bonded to a credit-card-sized flexible carrier, on which planar inductors and capacitors are patterned. This process is similar to that used for high-volume radiofrequency ID tag assembly today. Coupling inductors and capacitors are then also patterned on the LAE sheet, and system assembly of multiple such IC patches with multiple LAE-sheet sites is achieved through low-cost sheet lamination. The resulting inductor and capacitors have dimensions of 2−3 cm, and the lamination requires roughly 100-μm-thick adhesive, enabling efficient proximity coupling.

With such interfaces, the system can distribute functionality as preferred between the LAE and silicon IC technologies. For the power management subsystem, LAE performs photovoltaic energy harvesting and DC-to-AC power inversion using TFT circuits, whereas the silicon ICs perform power rectification and voltage conversion, to enable full-system self-powering. For the sensing subsystem, LAE performs strain sensing and individual sensor accessing via TFT circuits, whereas the silicon ICs perform signal acquisition and readout for sensing over the large-scale array. For communication, LAE provides long wired interconnects, and the silicon ICs provide self-calibrating data transceivers.

Figure 12.6 illustrates details of the hybrid sensing subsystem (Hu et al., 2014b). Switches in the LAE domain select the strain gauges one at a time. To enable use
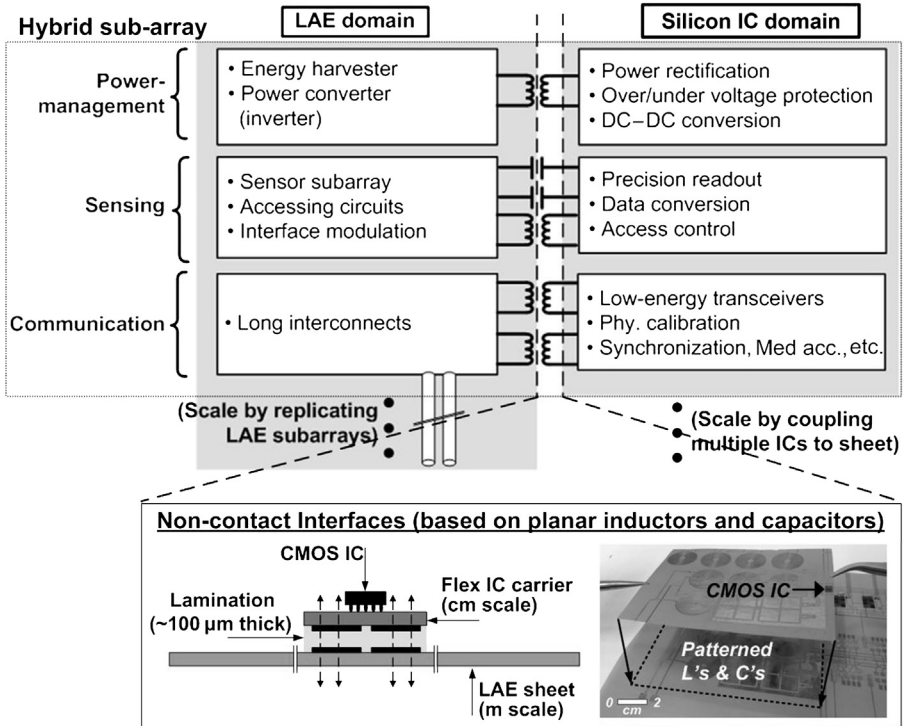
Figure 12.5 Block diagram of prototyped self-power strain-sensing hybrid system
(Hu et al., 2014a).
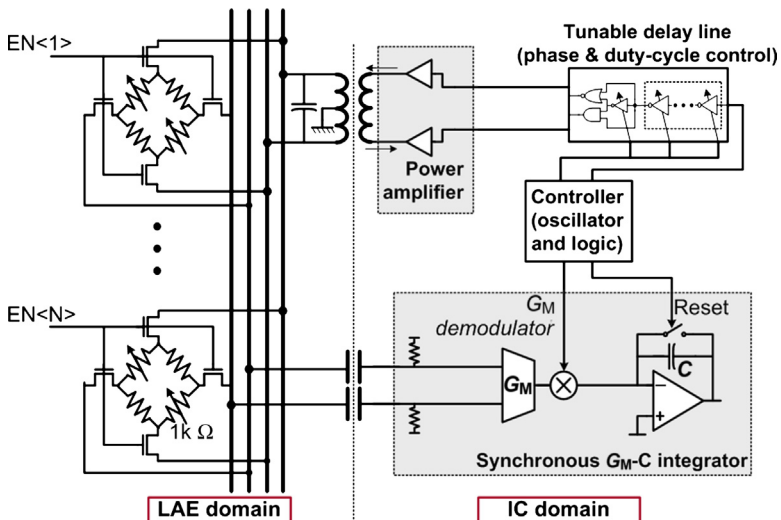
Figure 12.6 Hybrid sensing subsystem (Hu et al., 2014b).

of noncontact interfaces, the selected strain gauge is biased using an AC signal provided by the CMOS IC through an inductive interface. The differential voltage output that results from the strain gauge is thus AC modulated, enabling it to then be coupled back to the CMOS IC through a capacitive interface. To readout the strain signal, the CMOS IC demodulates the differential voltage using a synchronous integrator, which demodulates the strain signal back to DC, filtering stray noise through integration.

Figure 12.7 illustrates details of the hybrid power management subsystem (Hu et al., 2014a). DC power harvested from solar modules must be converted to AC power for transmission to the CMOS IC via noncontact interfaces. To accomplish this, the subsystem employs a TFT oscillator, wherein oscillations are achieved by meeting a resonance condition between inductors patterned on the LAE sheet and the capacitors inherent to the TFTs. Such an oscillator presents advantages for LAE, as its performance depends largely on the quality of inductors, which can be comparatively high, as compared to the performance of the transistors, which is comparatively low. Once transmitted to the CMOS IC, the AC power is rectified, monitored, and regulated to three different voltage levels (0.6, 1.2, and 2.4 V) in order to power the entire system.

Figure 12.8 illustrates details of the hybrid communication subsystem for transmitting data between ICs distributed on the LAE sheet (Hu et al., 2014b). In the transmitter, digital data are modulated to the resonant frequency of the LAE interconnect network; this makes the drive-point impedance appear large, reducing the power consumption of the transmitter. Generally, the precise resonant frequency is hard to know a priori. For this reason, the transmitter employs a calibration phase, wherein the modulation frequency is swept using a digitally controlled oscillator (DCO). The local receiver monitors the transmitted signal level such that the frequency peak,
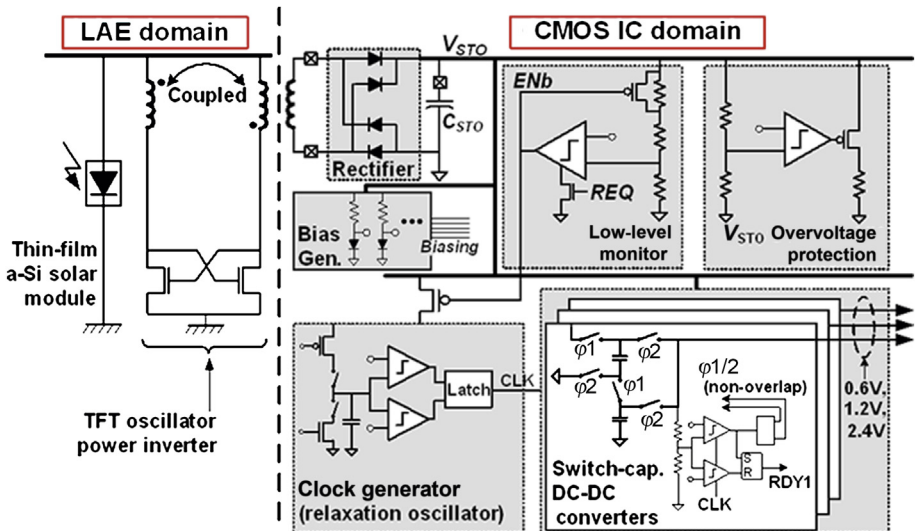
Figure 12.7 Hybrid power management subsystem (Hu et al., 2014a).
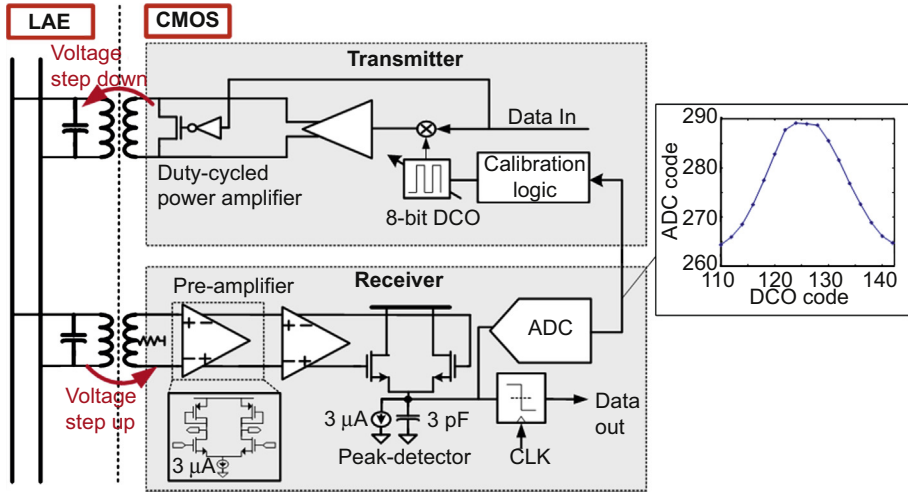
Figure 12.8 Hybrid communication subsystem (Hu et al., 2014b).

corresponding to the resonant point, can be identified. During normal operation, the receiver then senses the transmitted signal and demodulates it to baseband digital pulses using a peak detector followed by a comparator.

A photograph of the prototyped system is shown in Figure 12.9. The LAE components are fabricated in-house at Princeton University on 50-μm-thick polyimide, and the silicon IC is designed at Princeton University and fabricated using standard foundry services provided by IBM in 130 nm technology generation. Detailed characterization of all subsystems has been performed, and operation of the system applied to a cantilever beam in the lab has been demonstrated. All results are described in Hu et al. (2014a). Future plans for deployment on an in-use structure are being developed.
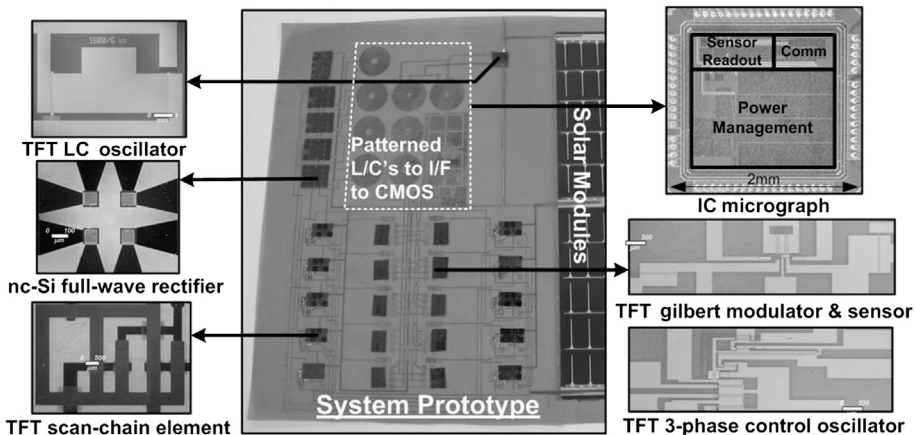
Figure 12.9 Photographs of integrated prototype system (Hu et al., 2014a).

12.4.3 Interpretation of a measurement of an individual sensor

The strain-field anomaly manifests as either a perturbation in a continuous strain field (e.g., yielding or bowing of steel) or a discontinuity in a strain field (e.g., cracking in steel or concrete). The former will be accurately measured by individual sensors making part of the LAE/IC sensing sheet as a high strain change, yet within the ultimate limit of strain of the monitored material. However, the latter will generate a very high strain in the individual sensors, and consequently either the sensors will fail or their individual readings will not represent exact strain in monitored material (i.e., around the location of crack), but rather the strain within the sensor body generated by the crack opening. Moreover, in sensors that did not fail, quantitatively equal crack openings will generate different strain outputs due to stress concentration in the sensors and adhesive (used to attach the sensing sheet to the structure), irregular crack shape, and degradation of the material at location of the crack (degradation of crack mouths is typical for concrete). Figure 12.10 shows results of 10 tests performed on a specimen of cracked concrete (Tung et al., 2014). In order to keep the cost of tests low, the sensor used in the test was a commercially available full-bridge strain gauge.

The test results show dispersion in relation (regression lines) between crack opening and sensor reading. This implies that the crack width cannot be evaluated deterministically, but rather probabilistically. The experiments indicate that the regression lines have log-normal distribution, and consequently for a given reading of the sensor the evaluation of the crack opening should be interpreted in terms of expected value and confidence intervals. For example, if a sudden strain change of 3000 με (1 με $= 10^{-6}$ m/m) is registered by an individual sensor, one can conclude that a crack occurred (typical tensional ultimate strain in concrete is 60−200 με, that is, much smaller than 3000 με). Based on log-normal distribution shown in Figure 12.10, the
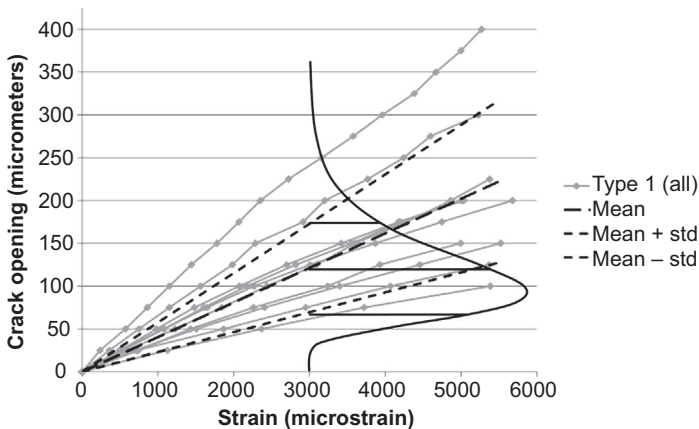
Figure 12.10 Crack opening versus strain for full-bridge strain sensor. Mean ± one standard deviation and log-normal distribution for the calibration coefficient shown (Tung et al., 2014).

expected crack opening is 121 µm, but the most likely value of the crack opening is 95 µm. In addition, there is 73% confidence that the crack opening ranges between 70 and 173 µm ($\pm$ one standard deviation from the mean) and 96% confidence it ranges between 18 and 224 µm ($\pm$ two standard deviations from the mean). Although this nondeterministic approach may seem inconclusive at first instance, it should be observed at a larger (i.e., sensing-sheet) scale: a crack occurrence will certainly activate several neighboring individual sensors in the sensing sheet (see Figure 12.3), and the probabilistic information about crack opening obtained from multiple individual sensors is combined to narrow down the confidence intervals and determine the size of the crack opening.

12.4.4 Laboratory testing

A series of reduced-scale tests were performed in the laboratory to assess and validate the concept of the sensing sheet. The tests involved cyclic loading of four steel plates instrumented with sensing-sheet prototypes. Each plate had a deep notch on the boundary, which induced stress concentration that generated fatigue crack. The crack's occurrence, propagation, and extent were monitored using the sensing sheets. Although in total four plates were tested using two different designs of sensing sheet, only one representative test is presented in this section, to keep it concise and informative. More detail about the other tests can be found in Yao and Glisic (2015).

The arrangement of sensors within the sensing sheet was determined based on the known point of the crack occurrence (at the notch) and its approximate propagation direction (perpendicular to the applied force). The arrangement consisted of a primary "grid" of equidistantly spaced sensors (see Figure 12.11(a)) whose aim was to be in direct contact with the crack, and a secondary "grid" whose aim was to assess the influence of the crack on the sensors that are in close proximity to the damage, but not directly intersecting it. The size of the sensing sheet was 150 × 150 mm, and the total number of sensors within the sheet was 31 (11 × 14 mm each). To decrease the cost of the tests while keeping the focus on the test aims, the sensing sheets consisted of interconnect and sensors only. The acquisition of sensor measurements was performed using a commercially available strain-gauge reading unit. This resulted in a setup that enabled key experiments and provided good representation of the sensing sheet conceptual performance. A steel plate instrumented with the sensing sheet and placed in the testing machine is shown in Figure 12.11(a).
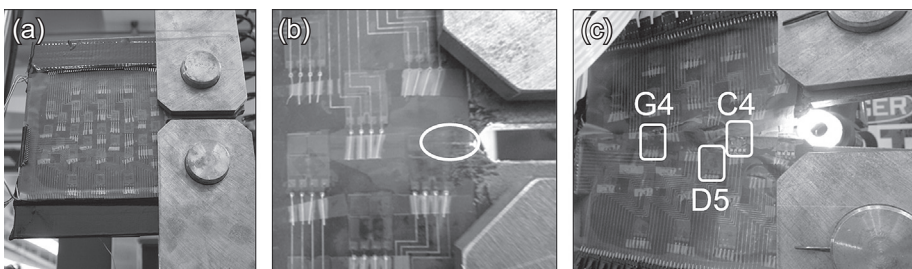
Figure 12.11 (a) Testing setup; (b) initiation of crack (encircled); and (c) failed plate. Modified from Yao and Glisic (2015).

The machine enabled cycling loading with a typical range between 53 and 125 kN applied until the plate failed (i.e., until the displacement between the arms of the machine reached 25.4 mm). The initiation of the crack in each plate occurred before 40,000 cycles were achieved. Further cycling did not cause immediately a significant propagation of the crack; however, the crack propagation abruptly accelerated when the plate was close to failure. Figure 12.11(b) and (c) shows crack initiation and a failed plate, respectively.

To present the general response of the sensing sheets to crack initiation and propagation, three typical time series of strain registered by individual sensor are shown in Figure 12.12. The selected sensors are denoted with C4, D5, and G4 in Figure 12.11(c). The crack propagated from right toward left (see Figure 12.11), and consequently it first met the sensor C4, then propagated toward the sensors D5 and G4. It is important to highlight that in the case of tests on concrete (see Section 12.4.3), the sensor could function properly even if exposed to a crack opening of few millimeters, mostly due to concrete degradation around crack mouths, which allowed stress relaxation in the sensor. However, that was not the case for cracks in steel, which would immediately damage an intersecting sensor due to lack of degradation of crack mouths and the consequent lack of stress relaxation in the sensor.

The following patterns were identified in diagrams in Figure 12.12: (1) if there is no crack in proximity of the sensor, then there is no significant change in the strain output; (2) if the crack approaches the sensor, then strain significantly increases and this indicates that the damage is in the neighborhood of the sensor; (3) steel yields at approximately 2000 $\mu\varepsilon$, and strain increases with a higher rate; (4a) if the crack tip intersects the sensor at any stage in phases (2) or (3), the sensor fails and this fact (failure of sensor) is used to detect and localize the damage (see sensor C4 in Figure 12.12(a) and sensor G4 in Figure 12.12(c)); and (4b) if the crack "passes" nearby the sensor, the strain output decreases significantly and damage is detected and localized based on this decrease (see sensor D5 in Figure 12.12(b)). Note that although the patterns in phases (4a) and (4b) are important for damage detection and localization, those in phases (2) and (3) are also important as they can be used to predict the propagation of the crack, and thus they can be used to alert the responsible engineers on a potentially escalating structural safety issue.

Sensor C4 was the first to be intersected by the propagating crack at approximately 7850 s from the beginning of the test, and it failed as soon as it was "touched" by the crack tip (see Figure 12.12(a)). Consequently, the crack was detected at that location through the damaging of the sensor. Sensor D5 was the next sensor affected by the propagating crack at approximately 9770 s from the beginning of the test (see Figure 12.12(b)); however, this sensor was not directly intersected by the crack and thus was not damaged. Crack was detected at that location indirectly as a decrease in the strain output. Finally, sensor G4 was affected by the crack at approximately 9860 s from the beginning of the test, and because its location was on the crack propagation line, it failed when the crack tip reached it (see Figure 12.12(c)); in other words, the crack was detected at that location through the damage of the sensor (similar to sensor C4).

Due to manufacturing defects, some sensors lost electrical contact during tests and could not provide strain measurements. Based on the strain time-series collected from all functioning sensors (shown as black dots in Figure 12.13), real-time 2D strain-field
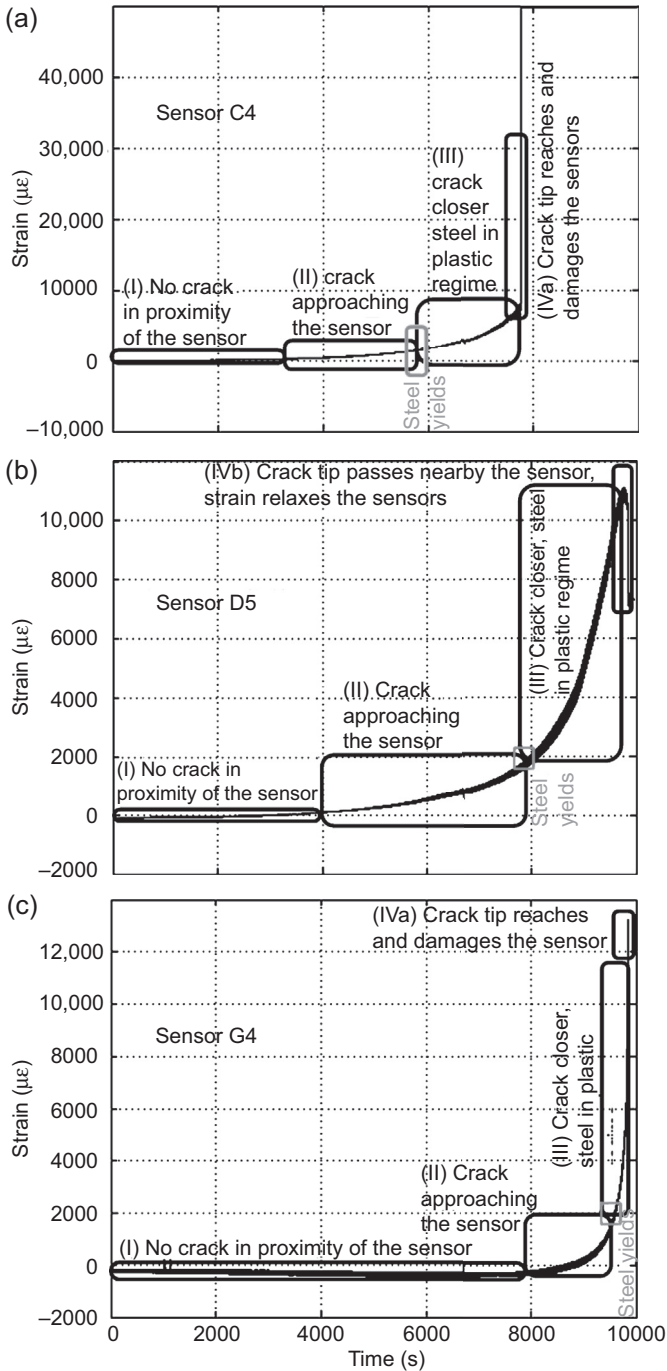
Figure 12.12 Typical sensor readings: (a) Sensor C4; (b) Sensor D5; and (c) Sensor G4.
Note: Scale for strain is not the same for the three graphs.
Modified from Yao and Glisic (2015).
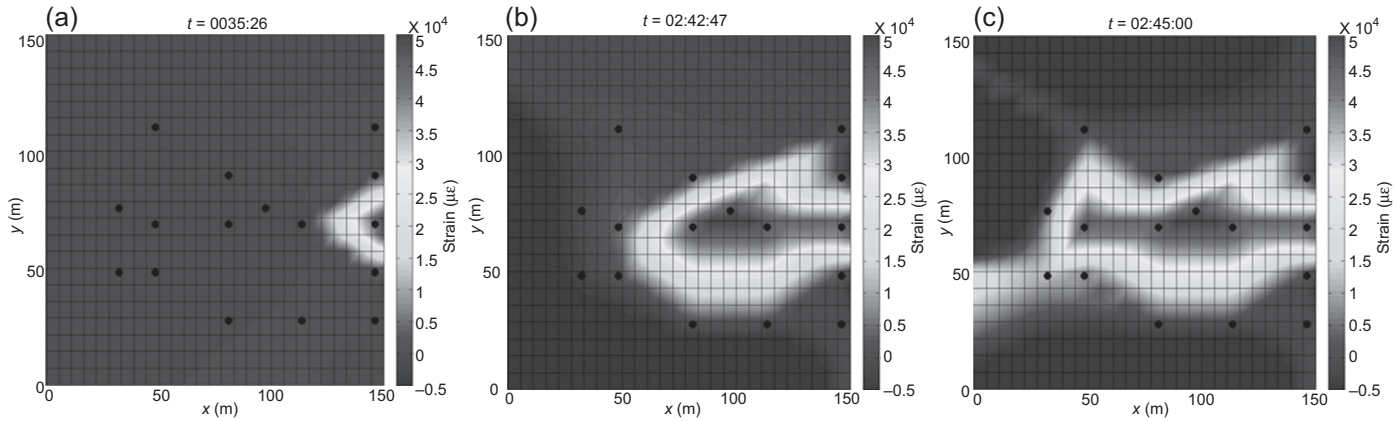
Figure 12.13 Strain field in plate evaluated by the sensing sheet at various stages of the test: (a) crack initiation; (b) crack propagation; and (c) final extent of crack.

Modified from Yao and Glisic (2015).

history graphs have been created (Yao and Glisic, 2015). Three illustrative examples are shown in Figure 12.13. The strain values at points not directly equipped with sensors were derived using linear interpolation. The diagram in Figure 12.13(a) shows the strain field at the crack initiation, the diagram in Figure 12.13(b) shows the strain field during crack propagation, and the diagram in Figure 12.13(c) shows the strain field at final crack extension (i.e., at the conclusion of the test). Two important conclusions are derived from Figure 12.13: (1) the sensing sheet was able to detect the crack initiation, follow its propagation, and evaluate its extension; and (2) even though some sensors malfunctioned, the remainder of the sensors was sufficient to capture the critical characteristics of the damage. This demonstrates inherent redundancy and robustness of the sensing sheet.

In conclusion, the tests validated the sensing sheet as a reliable 2D distributed sensor for damage detection, localization, and evaluation of its extent. Moreover, the tests confirmed that direct sensing is an effective and viable approach for damage identification.

12.5 Future trends

The future trends in LAE/IC sensing sheets are already emerging. They can be roughly classified in three areas, presented as follows.

A logical suite for LAE/IC sensing sheets is enabling multifunctional and multi-sensing capabilities for more comprehensive structural health monitoring. Several individual sensor types were proven to be enabled by LAE such as pressure sensors (Someya et al., 2004), temperature sensors (Graz et al., 2009), and sensors based on piezoelectric principles (Seminara et al., 2013). All these sensors can be combined with strain sensors either within the same layer of the substrate or within different layers, with the aim of creating multisensing capabilities for the sensing sheet. In particular, piezoelectric transducers could be used for acoustic emission sensing and active wave propagation monitoring, and provide detection of subsurface damage, extending the sensing sheet's distributed sensing capabilities from 2D to 3D. Moreover, piezoelectric transducers can provide for additional power harvesting in structures exposed to extensive vibrations (e.g., bridges, wind turbines, and aircrafts), which will add to the multifunctional nature of the sensing sheet.

Another direction is development of strain-sensing sheets containing individual sensors manufactured of different materials (e.g., conductive polymers) and based on different physical sensing principles (e.g., capacitance). One example is a soft elastomeric capacitor consisting of (1) a thermoplastic elastomer matrix of polystyrene−co-ethylene−co-butylene−co-styrene (SEBS), which is (2) doped with titanium dioxide (TiO_2) and placed between two electrodes made of SEBS mixed with carbon black particles (Laflamme et al., 2013). This type of individual sensor features identical sensitivity to strain in both directions. Thus, it has great promise for damage detection in surface structures (plates and shells) loaded in both directions, where the strain field anomalies have similar probability of occurrence in both directions. In addition, its measurement range can reach 200,000 με (20%), which makes it

particularly suitable for detection of large strain-field anomalies. Another example is strain sensors based on water-dispersible, polymer acid−doped polyaniline, PANI-PAAMPSA (Yoo et al., 2007), which after certain treatments can exhibit negative resistance when exposed to tension, and vice versa (i.e., positive resistance when subjected to compression). This makes them particularly suitable for the identification of various strain components combined within regular strain measurement, such as shrinkage and thermal strain (Sezen et al., 2015).

Stretchable LAE is a recent revolutionary extension of flexible LAE. While flexible LAE, used in LAE/IC sensing sheets, permits for limited conformity and small reversible deformation, stretchable LAE is printed on elastomeric substrates that allows for large yet reversible (elastic) deformation of the patterned electronics (Wagner and Bauer, 2012). The Young's modulus of individual components of stretchable LAE can span 12 orders of magnitude (Wagner and Bauer, 2012); however, they are made compatible by appropriate architecture and patterning of electronics. The principal applications of stretchable LAE are currently found in the biomedical industry. Nevertheless, large deformation allowed by stretchable LAE can be beneficial in creating a new generation of sensing sheets, which can actually be renamed "sensing skins" due to their high elasticity. In particular, large allowable strain in sensing skin can prevent malfunction of sensors and circuits due to local structural damage (e.g., crack opening), which can generate large local strains in the substrate. Furthermore, it can allow for tailor-made deployment without sacrificing or cutting out the sensors or ICs. Finally, it can allow for full conformity of sensing skin to geometrically complex parts of structures. The principal functional components of stretchable electronics such as ICs (Sekitani and Someya, 2012), conformable sensors (Kim et al., 2012) and power harvesters (Kornbluh et al., 2012) are already proven. Transition to SHM applications has not yet happened, but the pioneering works in that direction are very promising (Salowitz et al., 2014).

12.6   Sources of further information and advice

More information concerning LAEs and ICs can be found in the journals and conferences listed here.

Journals
- *Applied Physics Letters*
- *IEEE Electron Device Letters*
- *IEEE Journal of Solid-State Circuits*
- *IEEE Transactions on Electron Devices*
- *Proceedings of the IEEE*

Conferences
- *Materials Research Society Meeting*
- *International Solid-State Circuits Conference*
- *VLSI Symposia on Circuits and Technology*
- *International Thin-film Transistor Conference*

General information concerning structural health monitoring can be found in the following books:

- Wenzel, H., 2009. Health Monitoring of Bridges, John Wiley & Sons, Inc, Chichester, UK.
- Karbhari, V.M., Ansari, F. (Eds.), 2009. Structural Health Monitoring of Civil Infrastructure Systems, Woodhead Publishing in Materials, Sawston, Cambridge, UK.
- Glisic, B., Inaudi, D., 2007. Fiber Optic Methods for Structural Health Monitoring, John Wiley & Sons, Inc, Chichester, UK.
- Balageas, D., Fritzen, C.P., Güemes, A. (Eds.), 2006. Structural Health Monitoring, John Wiley & Sons, Inc, Chichester, UK.
- Andersen, J.E., Fustinoni, M., 2006. Structural Health Monitoring Systems, COWI-Futurec, L&S S.r.l.Servizi Grafici, Milano, Italy.
- Ansari, F. (Ed.), 2005. Sensing Issues in Civil Structural Health Monitoring, Springer, Dordrecht, Netherlands.
- Wenzel, H., Pichler, D., 2005. Ambient Vibration Monitoring, John Wiley & Sons, Inc, Chichester, UK.

More information on specific sensing technology development and applications in structural health monitoring can be found in papers published in specialized journals and conferences. A nonexhaustive list is given below.

Journals

- *IEEE Sensors Journal*
- *Measurement Science and Technology*
- *Sensors and Actuators A: Physical*
- *Smart Materials and Structures*
- *Structural Health Monitoring: An International Journal*
- *Journal of Civil Structural Health Monitoring*
- *Structural Control and Health Monitoring*
- *Structural Monitoring & Maintenance*

Conferences

- International Conference on Structural Health Monitoring of Intelligent Infrastructure (SHMII)
- International Workshop of Structural Health Monitoring (IWSHM)
- European Workshop of Structural Health Monitoring (EWSHM)
- Damage Assessment of Structures (DAMAS)
- SPIE Smart Structures/NDE

Acknowledgments

References

Abdel-Jaber, H., Glisic, B., 2015. Analysis of the status of pre-release cracks in prestressed concrete structures using long-gauge sensors. Smart Materials and Structures 24, art. no. 025038, 12 pp.

Glisic, B., Adriaenssens, S., 2010. Streicker Bridge: Initial evaluation of life-cycle cost benefits of various structural health monitoring approaches. In: Bridge Maintenance, Safety, Management and Life-cycle Optimization − Proceedings of the 5th International Conference on Bridge Maintenance, Safety and Management, pp. 2112−2118.

Glisic, B., Inaudi, D., 2007. Fibre Optic Methods for Structural Health Monitoring. John Wiley & Sons, Inc, Chichester, UK.

Glisic, B., Verma, N., 2011. Very dense arrays of sensors for SHM based on large area electronics. In: Structural Health Monitoring 2011: Condition-Based Maintenance and Intelligent Structures − Proceedings of the 8th International Workshop on Structural Health Monitoring, 2, pp. 1409−1416.

Graz, I., Krause, M., Bauer-Gogonea, S., Bauer, S., Lacour, S.P., Ploss, B., Zirkl, M., Stadlober, B., Wagner, S., 2009. Flexible active-matrix cells with selectively poled bifunctional polymerceramic nanocomposite for pressure and temperature sensing skin. Journal of Applied Physics 106, 034503−034511.

Heise Jr., R.E., 1965. Low-cycle fatigue-crack indications by strain gages operating in elastic strain fields. Journal of Experimental Mechanics 5, 19A−24A.

Hu, Y., Huang, L., Rieutort-Louis, W., Sanz Robinson, J., Sturm, J.C., Wagner, S., Verma, N., 2014a. Self-powered system for large-scale strain sensing by combining CMOS ICs with large-area electronics. IEEE Journal of Solid-State Circuits (JSSC) 49 (4), 838−850.

Hu, Y., Rieutort-Louis, W., Sanz Robinson, J., Huang, L., Glisic, B., Sturm, J.C., Wagner, S., Verma, N., 2014b. Large-scale sensing system combining large-area electronics and CMOS ICs for structural health monitoring. IEEE Journal of Solid-State Circuits (JSSC) 49 (2), 513−523.

Hubbell, D., Glisic, B., 2013. Detection and characterization of early-age thermal cracks in high-performance concrete. ACI Materials Journal 110, 323−330.

Jafferis, N.T., Sturm, J.C., 2013. Fundamental and experimental conditions for the realization of traveling-wave-induced aerodynamic propulsive forces by piezoelectrically deformed plastic substrates. Journal of Microelectromechanical Systems 22 (2), 495−505.

Kim, D.-H., Lu, N., Huang, Y., Rogers, J.A., 2012. Materials for stretchable electronics in bioinspired and biointegrated devices. MRS Bulletin 37 (3), 226−235.

Kornbluh, R.D., Pelrine, R., Prahlad, H., Wong-Foy, A., McCoy, B., Kim, S., Eckerle, J., Low, T., 2012. Dielectric elastomers: stretching the capabilities of energy harvesting. MRS Bulletin 37 (3), 246−253.

Laflamme, S., Saleem, H.S., Vasan, B.K., Geiger, R.L., Chen, D., Kessler, M.R., Rajan, K., 2013. Soft elastomeric capacitor network for strain sensing over large surfaces. IEEE/ASME Transactions on Mechatorincs 18, 1647−1654.

Parashkov, R., Becker, E., Riedl, T., Johannes, H.-H., Kowalsky, W., 2005. Large area electronics using printing methods. Proceedings of the IEEE 93, 1321−1329.

Perry, C.C., Lissner, H.R., 1955. The Strain Gage Primer. McGraw-Hill Book Company, Inc., New York, NY, USA.

Qi, Y., Jafferis, N.T., Lyons Jr., K., Lee, C.M., Ahmad, H., McAlpine, M.C., 2010. Piezoelectric ribbons printed onto rubber for flexible energy conversion. Nano Letters 10, 524−528.

Salowitz, N., Guo, Z., Roy, S., Nardari, R., Li, Y.-H., Kim, S.-J., Kopsaftopoulos, F., Chang, F.-K., 2014. Recent advancements and vision toward stretchable bio-inspired networks for intelligent structures. Structural Health Monitoring 13 (6), 609−620.

Sekitani, T., Someya, T., 2012. Stretchable organic integrated circuits for large-area electronic skin surface. MRS Bulletin 37 (3), 236−245.

Seminara, L., Pinna, L., Valle, M., Basiricò, L., Loi, A., Cosseddu, P., Bonfiglio, A., Ascia, A., Biso, M., Ansaldo, A., Ricci, D., Metta, G., 2013. Piezoelectric polymer transducer arrays for flexible tactile sensors. IEEE Sensors Journal 13, 4022−4029.

Sezen, M., Register, J.T., Yao, Y., Glisic, B., Loo, Y.L., 2015. Exploiting the Different Polarity in Piezoresistive Characteristics of Conducting Polymers for Strain Gauge Applications. American Physical Society March Meeting 2015 (abstract).

Someya, T., Sekitani, T., Iba, S., Kato, Y., Kawaguchi, H., Sakurai, T., 2004. A large-area, flexible pressure sensor matrix with organic field-effect transistors for artificial skin applications. Proceedings of the National Academy of Science 101, 9966−9970.

Someya, T., Pal, B., Huang, J., Katz, H.E., 2008. Organic semiconductor devices with enhanced field and environmental responses for novel applications. MRS Bulletin 33, 690−696.

Tung, S.-T., Yao, Y., Glisic, B., 2014. Sensing sheet: the sensitivity of thin-film full-bridge strain sensors for crack detection and characterization. Measurement Science and Technology 25, 075602, 14pp.

Wagner, S., Bauer, S., 2012. Materials for stretchable electronics. MRS Bulletin 37 (3), 207−213.

Wipf, T.J., Phares, B.M., Doornink, J.D., Griemann, L.F., Wood, D.L., 2007. Evaluation of Steel Bridges (Volume I): Monitoring the Structural Condition of Fracture-critical Bridges Using Fiber Optic Technology. Final Report. Bridge Engineering Center, Center for Transportation Research and Education (CTRE), Iowa State University, Ames, Iowa, USA.

Yao, Y., Glisic, B., 2012. Reliable damage detection and localization using direct strain sensing. In: Bridge Maintenance, Safety, Management, Resilience and Sustainability − Proceedings of the Sixth International Conference on Bridge Maintenance, Safety and Management, pp. 714−721.

Yao, Y., Glisic, B., 2014. Probabilistic damage detection based on large area electronics sensing sheets. In: Proceedings of the 7th European Workshop on Structural Health Monitoring − EWSHM 2014, on USB Memory Stick.

Yao, Y., Glisic, B., 2015. Detection of steel fatigue cracks with strain sensing sheets based on large area electronics. Sensors 15, 8088−8108.

Yoo, J.E., Cross, J.L., Bucholz, T.L., Lee, K.S., Espe, M.P., Loo, Y.-L., 2007. Improving the electrical conductivity of polymer acid-doped polyaniline by controlling the template molecular weight. Journal of Materials Chemistry 17, 1268−1275.

Zhou, L., Jung, S., Brandon, E., Jackson, T., 2006. Flexible substrate micro-crystalline silicon and gated amorphous silicon strain sensors. IEEE Transactions on Electron Devices 53 (2), 380−385.

Strain sensing and structural health monitoring using nanofilms and nanocomposites

13

Bo Mi Lee [1], Sumit Gupta [2], Kenneth J. Loh [1,2], Satish Nagarajaiah [3]
[1]University of California-Davis, Davis, CA, USA; [2]University of California-San Diego, La Jolla, CA, USA; [3]Rice University, Houston, TX, USA

13.1 Introduction

Civil infrastructure systems, including building, bridges, pipelines, dams, and power plants, among others, can experience damage during their operational service lifetimes. Damage can occur due to structures being subjected to excessive loading, fatigue, environmental deterioration, blast, and extreme events. In general, damage is defined as undesired abnormalities occurring in the material or geometry of the structural system, namely fatigue cracks and corrosion, which have the potential to adversely affect its behavior, performance, and safety (Farrar and Worden, 2007). When initial damage takes place, it often does not immediately reduce or affect structural functionality. However, if defects or flaws go undetected for long periods of time and are allowed to grow, they can jeopardize system performance and safety. In the worst case, catastrophic structural failure can occur.

In order to enhance the ability to detect and quantify damage, one approach is to mount sensors (e.g., strain gages or accelerometers) onto structural surfaces and to measure their response to ambient or forced excitations (Wang et al., 2007). Because these sensors can only measure response at their instrumented position, densely distributed sensors need to be installed so as to capture their complete behavior (Loh et al., 2009). However, their high costs, the difficulty in installing and maintaining the long lengths of coaxial cables that connect sensors to a centralized data repository, and power requirements often prohibit such an approach (Cho et al., 2008). Consequently, most real-world structural health monitoring (SHM) applications utilize a limited number of sensors installed per structure. The result of this is that only global structural behavior could be captured, and the measured response might not reveal component-level structural damage that has the potential to rapidly propagate to cause failure.

More recently, a new SHM paradigm using continuous thin films coated onto structural surfaces has been proposed (Kanoun et al., 2014a; Obitayo and Liu, 2012). These films, engineered using specific nanomaterials to give them sensitivity to a particular external stimulus, are unique in that every location of the material's electrical properties is sensitive to some damage feature. In that regard, they are inherently densely

distributed sensors, provided that one could map the distribution of electrical properties in an efficient and reliable fashion. To date, various types of nanomaterials (e.g., carbon nanotubes (CNTs) (Baughman et al., 2002), carbon black (CB) (Knite et al., 2004), graphene (Bae et al., 2013; Tian et al., 2014), and nanoparticles (Loh and Chang, 2011; Suri et al., 2002)), have been employed for fabricating nanofilm sensors.

In particular, CNT-based nanocomposites and nanofilms have garnered significant attention since the discovery of CNTs by Iijima (1991). The unique electrical, mechanical, thermal, and optoelectronic properties of CNTs have motivated many researchers to develop novel pressure (Stampfer et al., 2006), thermal (Fung et al., 2004), chemical (Wei et al., 2006), electrochemical (Wang, 2005), and mechanical sensors (Alamusi et al., 2011). This chapter will focus on CNT-based strain sensors, because strain measurements provide valuable information regarding the deformation and stress state of the structure being monitored. To assemble these CNT-based nanofilm strain sensors, various fabrication methods have been employed, including buckypaper (vacuum filtration), in situ polymerization, evaporation, spin coating, layer-by-layer (LbL) (Stampfer et al., 2006), and spraying, among many others (Loh and Azhari, 2012). Although each of these fabrication techniques offers pros and cons suitable for different applications, it's even more important to realize that the electrical, mechanical, and coupled electromechanical properties of CNT-based nanocomposites can be influenced by how they are assembled (Alamusi et al., 2011).

The objective of this chapter is not to provide an exhaustive review of CNT-based nanofilm strain sensors but, rather, to highlight current research progress regarding CNT-based strain sensors fabricated using different techniques. Section 13.2 presents buckypaper nanofilms, followed by LbL nanofilm fabrication in Section 13.3. The chapter continues with a discussion of electrical impedance tomography (EIT) in Section 13.4, which enables one to map the spatial conductivity distribution of nanofilms so that they can be used for sensing distributed strain or damage in structures. Section 13.5 describes another different nanofilm fabrication approach using spray-coating, and the integration of these sprayed films with cementitious composites is discussed in Section 13.6. Section 13.7 presents an overview of other fabrication methodologies suitable for manufacturing CNT-based strain sensors. Finally, this chapter concludes with a brief summary and discussion of future research directions.

13.2 Buckypaper

Early efforts to develop CNT-based nanofilms employed a vacuum filtration−based fabrication method (Dharap et al., 2004a). Since the composite is made of aggregates of buckytubes (i.e., CNTs) composed of 60 carbon fullerene, it is referred to as buckypaper (Wikipedia contributors, 2014). The general process to fabricate buckypaper is as follows: dispersion of CNTs in solution, vacuum filtration of the suspension through the porous membrane, drying filtered contents, and peeling off the freestanding nanotube-based film. Initial work performed by Baughman et al. (1999) introduced single-walled carbon nanotube (SWCNT)-based buckypaper as an actuator, where it

was shown that large strains ($\sim 1\%$) could be achieved by using small excitation voltages (within 1 V), especially in contrast to ferroelectric material-based actuators that could only generate $\sim 0.1\%$.

In addition to using buckypaper for actuation, researchers have investigated their use as strain sensors (Dharap et al., 2004a; Kang et al., 2006). Dharap et al. (2004a) pioneered early research for producing SWCNT-based buckypaper strain sensors by first mixing unpurified SWCNTs in N,N-dimethylformamide (DMF) at a concentration of 0.25 mg/mL. The SWCNT−DMF solution was then filtered using 0.2 mm Teflon membrane, followed by peeling off the buckypaper from the filter membrane after drying. Additional heating in a vacuum oven was performed for 24 h. It was observed by scanning electron microscopy that nanotubes were randomly oriented in the buckypaper (Figure 13.1(a)), and the film thickness was uniform and ~ 10 μm (Figure 13.1(b)). Its percolated morphology was important for achieving an electrically conductive buckypaper thin film.

The thin film was affixed onto a $30.48 \times 3.81 \times 0.17$ mm^3 brass specimen with a poly(vinyl chloride) (PVC) film in between the two. Bonding of the film was achieved by using high-strength epoxy and a vacuum bonding method, which would ensure perfect strain transfer and electrical insulation (Figure 13.2(a)). Uniaxial tensile and compressive strains to ± 400 με were applied to the specimen, and voltage was measured using a four-point probe method (i.e., by interrogating the film using a constant amplitude direct current (DC) input). The two outer electrodes were used for injecting DC, whereas the voltage response was measured using the two inner electrodes.

Upon conducting these tests, a linear change in voltage was detected, which resulted from two possible different effects (i.e., a change in dimension and change in resistivity of the buckypaper). When applied tensile strain was increased from 0 to 400 με, the change in voltage was about 170 μV. It was found that the main contribution to cause the change in voltage was the buckypaper's resistivity response (149 μV, $\sim 88\%$), as opposed to changes in the film dimensions (21 μV, $\sim 12\%$) (Dharap et al., 2004a). Continued work (Dharap et al., 2004b) evaluated the flexural strain-sensing properties of these buckypapers by applying four-point bending
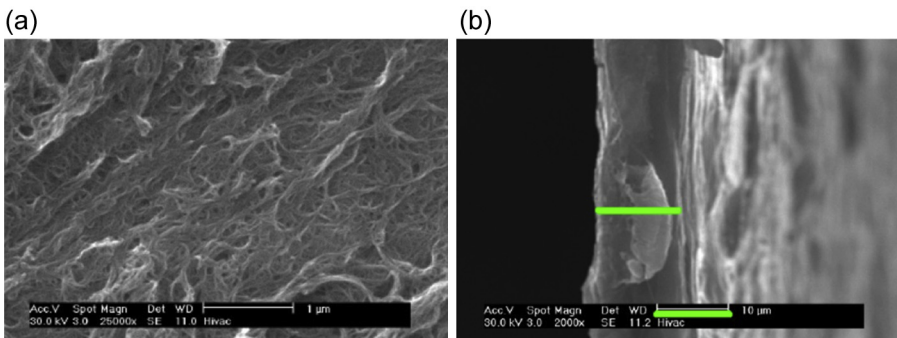
Figure 13.1 Scanning electron microscope (SEM) image of an SWCNT-based buckypaper showing (a) a random orientation of nanotube bundles and (b) the film is 10 μm thick (Dharap et al., 2004a).

(a)

(b)
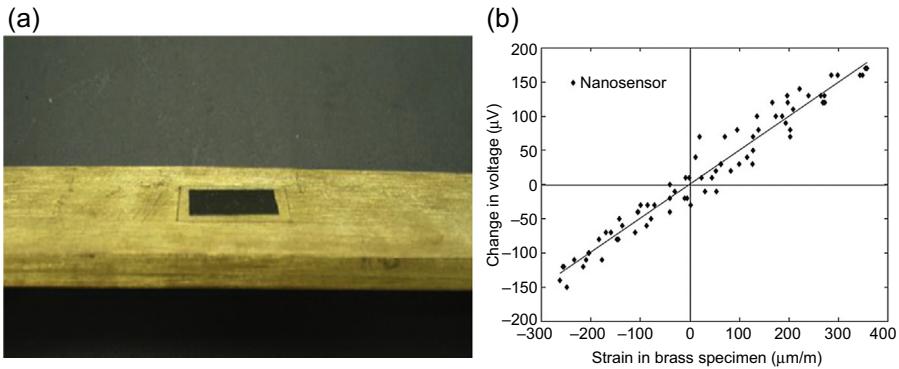
Figure 13.2 (a) An SWCNT-buckypaper was attached to a brass specimen for electromechanical testing. (b) The change in voltage of an SWCNT-buckypaper responded linearly when subjected to tensile and compressive strains (Dharap et al., 2004a).

(i.e., pure bending; and see Figure 13.3(a)). Similar to the previous tests, it was found that the voltage increased linearly from 0 to 200 µV when flexural strain increased from 0% to 0.06% (Figure 13.3(b)). In order to explain the nanoscale mechanisms responsible for enabling strain sensitivity in buckypapers, and to explore non-contact strain sensing at the macro-scale, Raman spectroscopy was employed to measure the vibrational properties of individual CNTs as the buckypaper was strained (Li et al., 2004). It was found that the Raman peaks of the G-band (which was indicative of carbon−carbon bonds stretching in tangential modes) shifted downward by 2 cm^{-1} when the tensile strain was increased from 0.03% to 0.094% (Figure 13.4(a)) (Li et al., 2004). Also, Raman wavenumber data of various tensile strain conditions were collected, and it was observed that the Raman wavenumber shifted downward when tensile strain increased (Figure 13.4(b)). Although Raman spectroscopy is not a practical tool for SHM applications (since it requires a bulky and elaborate setup), the data obtained helped explain that individual CNTs were being stretched when tension was applied to the nanofilm; also, the investigations showed the feasibility of non-contact strain sensing using nanofilms and laser-based Raman spectroscopy at the macro-scale for the first time.

It should be mentioned that other groups have also investigated the use of SWCNT-based buckypaper nanofilms for strain sensing. For example, Kang et al. (2006) also constructed 100% SWCNT-buckypaper and SWCNT/poly(methyl methacrylate) (PMMA)−casted thin films and conducted quasistatic and dynamic cantilevered beam tests. During fabrication, additional high-temperature annealing (320 °C) was performed to remove residual solvents and contaminants. Although SWCNT-buckypaper showed higher strain sensitivity (S), namely ∼7 versus ∼5.5 for SWCNT/PMMA−casted nanofilms, it exhibited nonlinear behavior after applied strains exceeded 500 µε.

Besides SWCNT-based buckypaper nanofilms, multiwalled carbon nanotubes (MWCNTs) were also employed for their metallic electrical properties and lower costs (Vemuru et al., 2009). Vemuru et al. (2009) applied static loads to an MWCNT-buckypaper specimen, and the nanofilm was characterized by linear
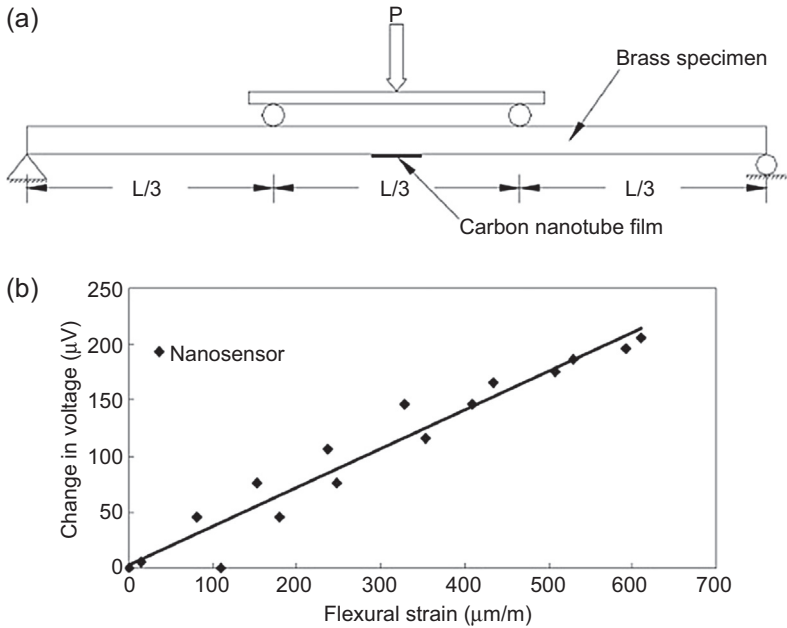
Figure 13.3 (a) An SWCNT-buckypaper was attached to a brass specimen, and four-point bending tests were conducted. (b) The voltage response of the SWCNT-buckypaper confirms its linear piezoresistive performance with respect to applied flexural strains (Dharap et al., 2004b).
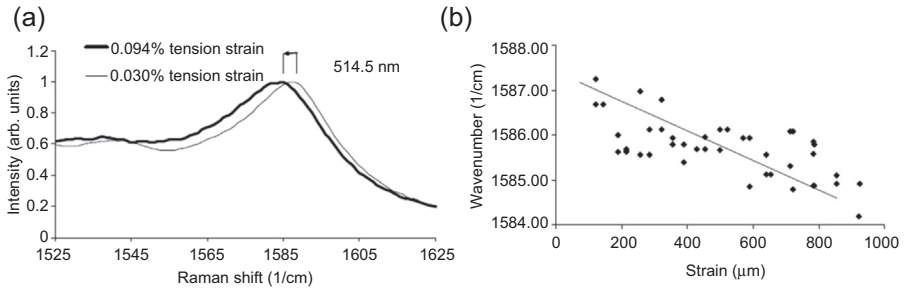
Figure 13.4 (a) The Raman shift in G-band modes of the SWCNT-based buckypaper was plotted when subjected to 0.094% and 0.030% tensile strains. (b) The G-band position of SWCNTs in the nanofilms decreased with increasing tensile strains (Li et al., 2004).

piezoresistive response until tensile strain reached 1000 $\mu\varepsilon$ with a gage factor of 0.35. In addition, quasistatic tensile cyclic-load tests revealed that the MWCNT-buckypapers exhibited fully reversible electromechanical properties (Vemuru et al., 2009). In addition to varying the type of CNTs used (i.e., SWCNTs or MWCNTs), other parameters such as the polymer and loading profile can also affect the strain-sensing properties of the bulk film (Rein et al., 2011). For example, different CNTs were embedded in three different types of epoxy matrices, and it was found

that SWCNTs in the brittle epoxy matrix had the highest strain sensitivity ($S \sim 2.2$). In contrast, for large strains ($\sim 30\%$), MWCNT-based strain sensors showed the most consistent sensitivity as compared to the nonlinear response of SWCNT-based strain sensors. Recent experimental work found that the film aspect ratio can also affect the electromechanical behavior of SWCNT−epoxy buckypapers (Zhang et al., 2015). At low strains ($\varepsilon < 2000\ \mu\varepsilon$), the strain sensitivity of low-aspect-ratio thin films (3:1) exhibited lower strain sensitivity ($S = 1.93$) than other cases ($S = 2.33, 2.14, 3.88$, and 3.61 for film aspect ratios of 6:1, 9:1, 12:1, and 15:1, respectively); the strain-sensing response was also nonlinear. For higher strains, the strain sensitivity was about the same (~ 6), and it was linear for all specimens with different aspect ratios. Furthermore, the damage detection capability of the SWCNT−epoxy thin film was validated by introducing a V-notch to the composite, and a dramatic increase in resistance was observed when tensile strain was $\sim 1000\ \mu\varepsilon$.

In general, many researchers have investigated the use of CNT-based buckypaper nanofilms for strain sensing. Since vacuum filtration allows one to precisely control the concentration of various components in the buckypaper (e.g., CNTs and surfactants), the technique was employed to study how component densities influence the physical properties of the film; examples include percolation phenomena and temperature- and frequency-dependent properties (Hu et al., 2010). In addition, this nanofilm assembly methodology can produce highly uniform and reproducible thin films. Despite these advantages, buckypaper is fabricated directly on top of the filter membrane, and an additional transfer step after filtration is usually necessary. The transfer process can be cumbersome and difficult, especially since the film may be damaged when it is peeled off (Hu et al., 2010).

13.3   LbL nanofilm fabrication

The LbL nanofilm fabrication method was initially proposed to assemble polymeric multilayered thin films, one monolayer at a time, by leveraging the van der Waals attraction and electrostatic force interactions between polyanion and polycation species dissolved in aqueous solutions (Decher, 1997). Because this technique is amenable to integrating monolayers of many different materials within one thin-film structure, complicated film architectures can be designed by simply varying the type and deposition sequence of different materials (Decher, 1997). For instance, Mamedov et al. (2002) fabricated LbL CNT-based nanocomposites that exhibited remarkable mechanical properties. To be specific, the tensile strength of the LbL SWCNT−polyelectrolyte (PE) films was as high as 325 MPa, which was considerably higher than that of carbon fiber composites (~ 53 MPa) and several times higher than that of SWCNT−poly(vinyl alcohol) (PVA) ribbons (~ 150 MPa). In addition, this technique ensured homogeneous nanocomposites with minimal structural defects due to phase segregation (Mamedov et al., 2002; Loh et al., 2007, 2008; Hou et al., 2007; Loyola et al., 2013a).

In addition to achieving outstanding mechanical reinforcement, LbL was also employed for designing CNT-based thin films with electromechanical properties suitable for strain sensing. For example, Loh et al. (2007) assembled CNT−PE nanofilms by sequentially dipping a charged glass substrate in positively charged polycationic PE solution (i.e., PVA or polyaniline (PANI)), followed by a negatively charged polyanionic solution with CNTs dispersed in poly(sodium 4-styrenesulfonate) (PSS) solution (dipping time was 5 min in each solution). Here, uniform dispersion of CNT solutions was achieved by 180 min of bath ultrasonication, followed by 90 min of high-powered probe sonication. The substrate and its adsorbed film were rinsed in 18 MΩ deionized water for 3 min and dried in air for 15 min after the assembly of each monolayer. This LbL cycle created a film with one bilayer and was then repeated (n times) until the desired number of bilayers was obtained. Films can be denoted as (CNT-PSS/PVA)$_n$ or (CNT-PSS/PANI)$_n$, which indicates its constituents and the number of bilayers (Loh et al., 2007).

Using the aforementioned procedure, homogeneous LbL nanofilms with uniform thicknesses were obtained (Figure 13.5) (Loh et al., 2007). Similar to the aforementioned works on buckypaper, a main goal was to evaluate the strain-sensing performance of these LbL nanofilms. To do so, 20×10 mm^2 LbL films were affixed onto PVC coupons. Second, a variety of different types of films were investigated, namely the type of CNTs (i.e., unpurified SWCNTs (u-SWCNTs) and purified SWCNTs (p-SWCNTs), as well as purified double-walled carbon nanotubes (p-DWCNTs)), and these films were fabricated using different concentrations of solutions. The film and PVC coupon specimens were subjected to tensile-compressive cyclic tests using an MTS-810 load frame. The applied load, the cross-head displacement, and the film's electrical resistance were recorded simultaneously.
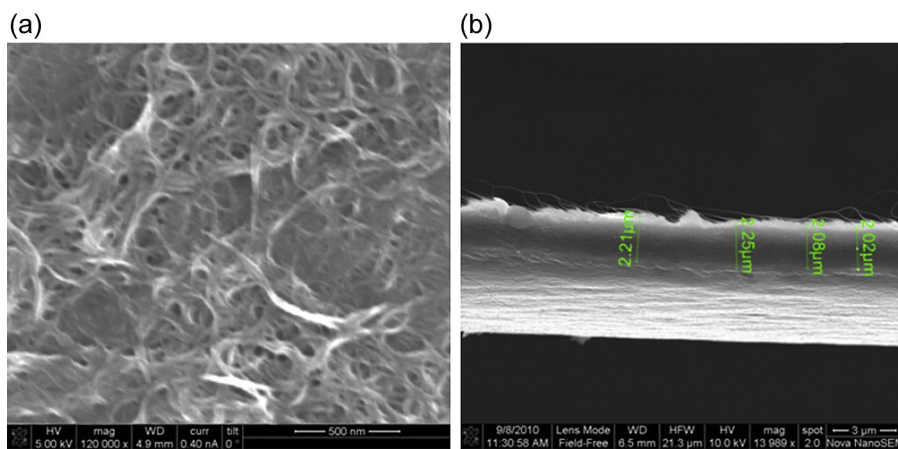
Figure 13.5 (a) An SEM image of an (SWCNT-PSS/PVA)$_{200}$ LbL nanofilm showed the deposition of dispersed nanotubes and exceeded the percolation threshold. (b) The SEM image of the film cross section demonstrated the nanofilm's uniformity (Zhao et al., 2011).

First, among the three different types of film tested, *p*-SWCNT-PSS/PVA and *p*-DWCNT-PSS/PVA thin films exhibited clear piezoresistive responses (Figure 13.6) (Loh et al., 2007). The lower performance of *u*-SWCNT-PSS/PVA may be due to impurities inherent to the *u*-SWCNTs, as well as poor dispersion of the *u*-SWCNT-PSS solution. Despite this, the results presented in Figure 13.6 clearly demonstrated that the films could be used as strain sensors. Their strain sensitivity was also sensitive to initial fabrication parameters, where higher CNT concentrations and better dispersion (enabled by higher concentrations of PSS) improved bulk film strain sensitivity. However, it should be mentioned that these films exhibited nominal resistance drifts that could be fitted using an exponential decay model. The results shown in Figure 13.6 reflect the films' strain-sensing response after drift has been numerically removed during postprocessing of the collected data (Loh et al., 2007). From Figure 13.6, one can also observe that the films' electrical response was characterized by rounded peaks at the maximum and minimum applied strains, despite the fact that the films were subjected to sawtooth tensile-compressive cyclic-load patterns. Continued electrical impedance spectroscopy (EIS) studies demonstrated that the phenomena observed in Figure 13.6 were due to the films' electrical impedance sensitivity to applied strains (Loh et al., 2008). In fact, the electrical properties of these LbL nanofilms not only were resistive but also were better characterized by a parallel resistor–capacitor equivalent circuit.

The ability to impose nanoscale control during film fabrication and the ease of translating nanomaterial properties to the macroscale are important and attractive features of LbL assembly. As was demonstrated by Mamedov et al. (2002), SWCNT-PE LbL nanofilms exhibited impressive mechanical properties. Similarly, Loh et al. (2007) showed that LbL thin films were characterized by linear piezoresistivity up to 10,000 µε, as compared to buckypaper whose linear response was demonstrated up to ~500 µε (Dharap et al., 2004a; Kang et al., 2006). In addition, LbL enables one to design nanofilms with specific material properties or engineering functionalities, simply by changing film constituents during deposition or by modifying the order in which different nanomaterial or PE species are deposited. This flexibility during fabrication allowed the incorporation of other PE species, such as polyaniline, for designing nanofilm pH sensors for biosensing or for monitoring corrosion in structural components (Loh et al., 2007). Despite these advantages, LbL is not compatible with roll-to-roll fabrication, which means that its production is time-consuming and limited to relatively small films.
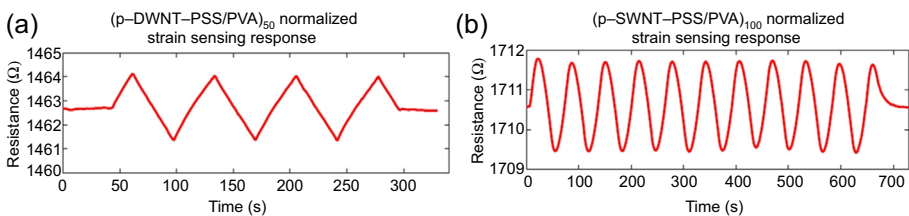
Figure 13.6 The electromechanical response of (a) *p*-DWCNT-PSS/PVA and (b) *p*-SWCNT-PSS/PVA thin films confirmed that their electrical properties were highly sensitive to tensile-compressive cyclic loads (Loh et al., 2007).

13.4   Spatial structural sensing enabled by EIT

Unlike conventional mechanical and electrical-based sensors, CNT-based nanofilms are unique in that the entire material is sensitive to strain (or other damage stimuli). Therefore, one could manually probe and measure resistance at discrete locations on the nanofilm to determine structural strains at every location in the film, so as to generate a two-dimensional (2D) strain map. However, this approach of manual probing is neither practical nor scalable for large-scale SHM applications.

An alternative technique is to employ an EIT algorithm, which allows one to reconstruct the spatial conductivity (or resistivity) distribution of a conductive body, such as the aforementioned strain-sensitive nanofilms (Loh et al., 2009; Hou et al., 2007). In short, EIT is a well-known soft-field tomography technique that originated from and found extensive applications in the biomechanics and biomedical domains (Saulnier et al., 2001). Instead of directly measuring the electrical properties at every location in the conductive body, a set of electrodes is established along the periphery of and to enclose the conductive body, thereby defining the sensing area. Electrical current is injected through a pair of boundary electrodes and allowed to flow through the conductive body, while boundary voltages are measured at the remaining pairs. The conductivity distribution of the sensing area of the body can be estimated by solving the inverse problem and by using current–voltage data. For conductive bodies such as nanofilms, they are assumed to be 2D.

Before one could solve the EIT inverse problem, the forward problem must be defined. The 2D Laplace's equation relates the conductivity distribution of the body (σ) and voltage distribution (u), and it is expressed in Cartesian (x, y) coordinates here:

$$\nabla \cdot [\sigma(x, y)\nabla u(x, y)] = 0 \tag{13.1}$$

Equation (13.1) assumes that electrical current is only supplied and grounded at the boundaries, and that current is neither generated nor grounded within the sensing area. This second-order differential equation represents the strong form of an EIT problem. For practical purposes, the finite element method is adopted (Holder, 2004; Polydorides, 2002; Vauhkonen, 1997). The weak form can then be derived using the weighted residual method to obtain:

$$\iint_{\Omega} \sigma \nabla \phi \nabla u \, dx dy = 0 \tag{13.2}$$

where ϕ is the finite-element shape function. The voltage distribution, u, can be approximated (u^h) as a linear combination of shape functions (ϕ_i):

$$u^h = \sum_{i=1}^{n} u_i \phi_i \tag{13.3}$$

where u_i is the values of voltage at the ith node in the finite element domain. A complete electrode model also can be adopted to implement the boundary conditions,

especially considering that the voltage drops at the electrodes due to contact imped-
ance (Holder, 2004; Vauhkonen, 1997). In doing so, given a known conductivity
distribution and applied electrical current, the forward problem can be solved to reveal
the theoretical boundary voltages at the electrodes.

From an experimental standpoint, the EIT inverse problem needs to be solved,
where the conductivity distribution needs to be estimated using applied current injec-
tions and the corresponding experimental boundary voltage measurements ($u_{measured}$).
Although different optimization schemes can be employed, Loh et al. (2009) used the
Gauss−Newton algorithm. During each iteration, the conductivity distribution is
updated, and the forward problem is solved to obtain the corresponding voltage distri-
bution ($u_{computed}$). The error (e) between $u_{measured}$ and $u_{computed}$ is calculated at every
iteration, and the inverse problem is iterated and solved until e, as defined in Eqn
(13.4), is less than or equal to the specified threshold value:

$$e = \|u_{measured} - u_{computed}\|^2 \Big/ \|u_{measured}\| \leq 0.05\% \qquad (13.4)$$

In that case, the converged solution or the estimated conductivity distribution is
assumed to closely represent that of the actual conductive body. An overview of the
computational steps as part of the EIT spatial conductivity reconstruction process is
depicted in Figure 13.7.
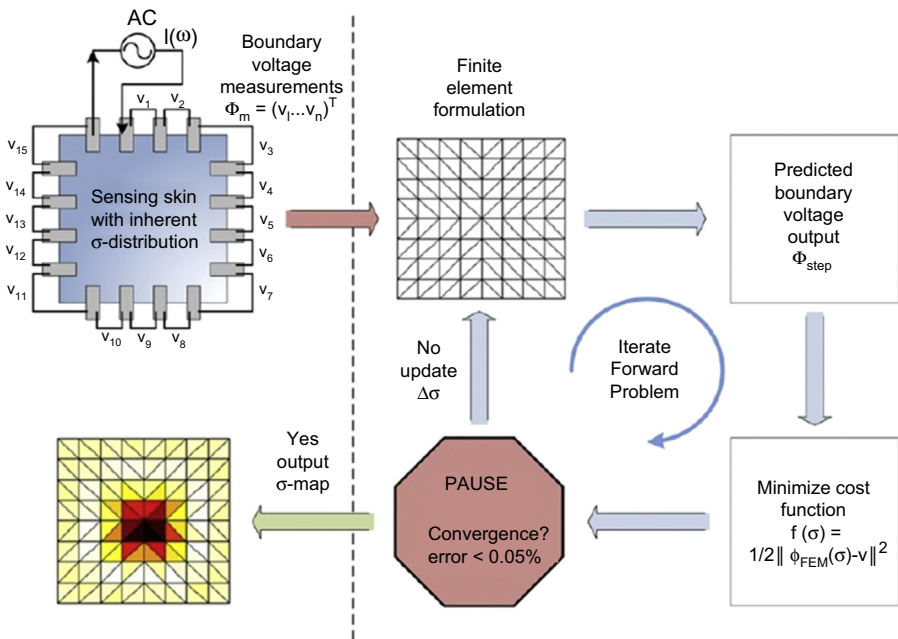
Figure 13.7 The electrical impedance tomography spatial conductivity reconstruction process is
illustrated (Loh et al., 2009).
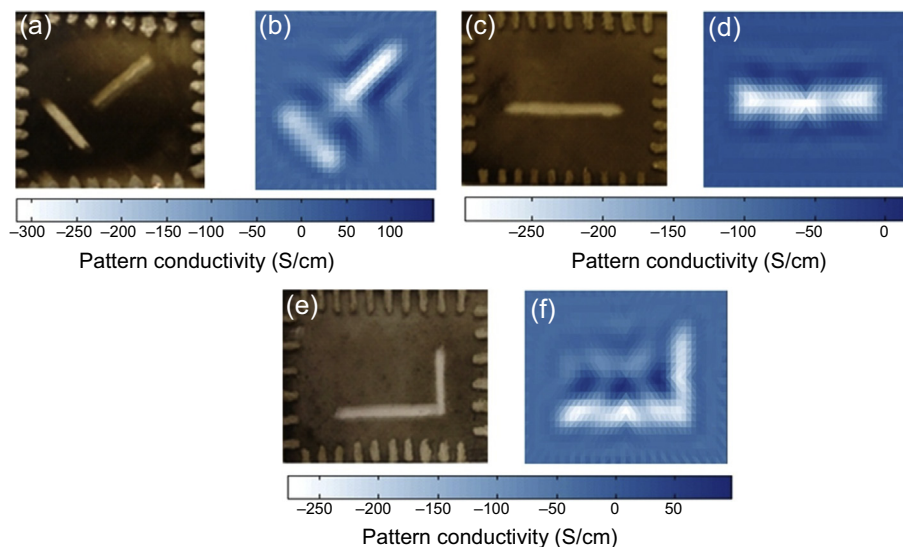
Figure 13.8 LbL (SWCNT-PSS/PVA)$_{50}$ thin films were subjected to mechanical etching to form different patterns and regions of zero electrical conductivity. Pictures of the etched film with (a) a double slash, (c) a straight line, and (e) an L-shaped pattern are shown, along with the corresponding EIT spatial conductivity maps for the (b) double slash, (d) line, and (f) L-shape (Hou et al., 2007).

Numerous experiments were conducted to validate the EIT spatial conductivity mapping algorithm applied to LbL CNT-based thin films for SHM applications. In particular, the objective was to use the nanofilms as distributed sensors for identifying the severity and location of damage due to strain, impact, pH, and corrosion, among others. Early work by Hou et al. (2007) demonstrated that EIT was able to identify defects in SWCNT−PE LbL thin films. Using the LbL fabrication method described in Section 13.3 and by Loh et al. (2007), 25 × 25 mm^2 SWCNT-PSS/PVA thin films were made and then instrumented with eight boundary electrodes along each edge of the nanofilm. EIT was performed to reconstruct the conductivity map of the pristine or undamaged nanofilms. Then, select regions of films were etched away to form defects in the shape of two slits (Figure 13.8(a)), a straight line (Figure 13.8(c)), and an L-shape (Figure 13.8(e)). EIT was performed again to obtain the spatial conductivity distributions of the damaged cases. The differences between the damaged and undamaged EIT conductivity maps are shown in Figure 13.8(b), (d), and (f). It is clear from the results shown in Figure 13.8 that there is good correlation between the pictures of the damaged films and the spatial conductivity distributions, thereby successfully validating EIT for locating defects due to conductivity changes occurring in the nanofilms.

Likewise, Loh et al. (2009) deposited (SWCNT-PSS/PVA)$_{50}$ LbL nanofilms onto glass substrates, instrumented them with 32 boundary electrodes, and attached the films to PVC coupons for tensile-compressive load tests to ±2000 με. During loading and unloading, the load frame was commanded to pause at 1000 με intervals to allow
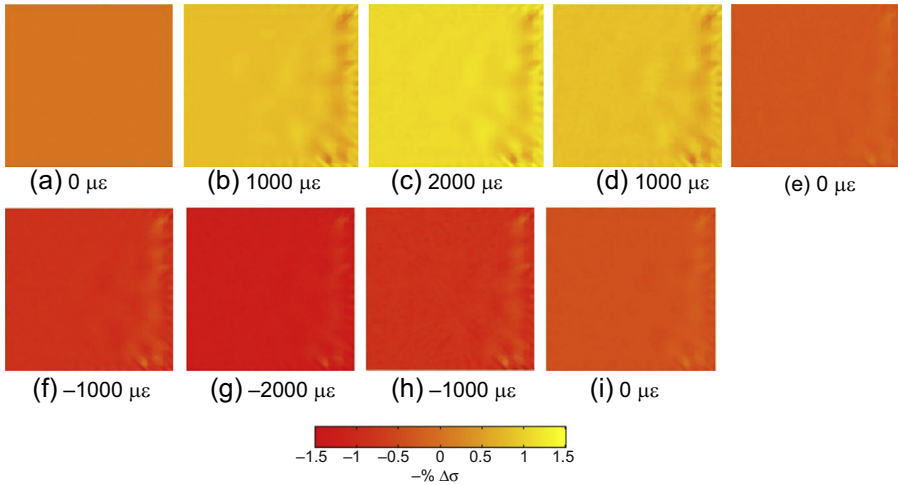
Figure 13.9 A one-cycle tensile-compressive load pattern (to ±2000 $\mu\varepsilon$, pausing every 1000 $\mu\varepsilon$) was applied to an (SWCNT-PSS/PVA)$_{50}$ thin film deposited on a glass substrate and epoxy-mounted to a PVC coupon. The EIT spatial conductivity maps show that the films could measure uniform strain distributions and the magnitude of strain applied to the specimen (Loh et al., 2009).

time for EIT data acquisition. A representative result is summarized in Figure 13.9, and it can be observed that the specimen's conductivity decreased uniformly as applied strain was increased. These results were consistent with those reported in Section 13.3, where the resistance of LbL CNT-based thin films increased in tandem with increasingly applied strains. In addition, to better quantify sensing performance, the average conductivity of each EIT map was computed, and the results are plotted in Figure 13.10. It's clear that the negative percentage change in average spatial conductivity (i.e., similar to the percentage change in resistivity) was well correlated with the applied load pattern.

In addition to strain sensing, LbL nanofilms were engineered with pH-sensing properties by incorporating polyaniline (PANI) in lieu of PVA (Loh et al., 2007). Loh et al. (2007) showed that SWCNT-PSS/PANI films would exhibit an increase in electrical resistance as the nanofilm was subjected to more alkaline pH buffer solutions. Therefore, in order to demonstrate that EIT can be coupled with SWCNT-PSS/PANI films to realize an electrochemical spatial sensor, nanofilms were fabricated and instrumented with boundary electrodes (Hou et al., 2007). Five circular plastic wells were mounted on the surface of an (SWCNT-PSS/PANI)$_{100}$ thin film (using vacuum grease), and the wells were used for pipetting in and out different pH buffer solutions. The first test involved pipetting in pH 7, 7.5, 8, 8.5, and 9 solutions, one in each well. After EIT data acquisition was finished, the buffer solutions were removed and replaced with mildly acidic solutions (i.e., pH 7, 6.5, 6, 5.5, and 5). The spatial conductivity maps (i.e., by calculating the conductivity difference between the pH buffer−exposed film and the pristine film to reveal the change in conductivity) are shown in Figure 13.11.
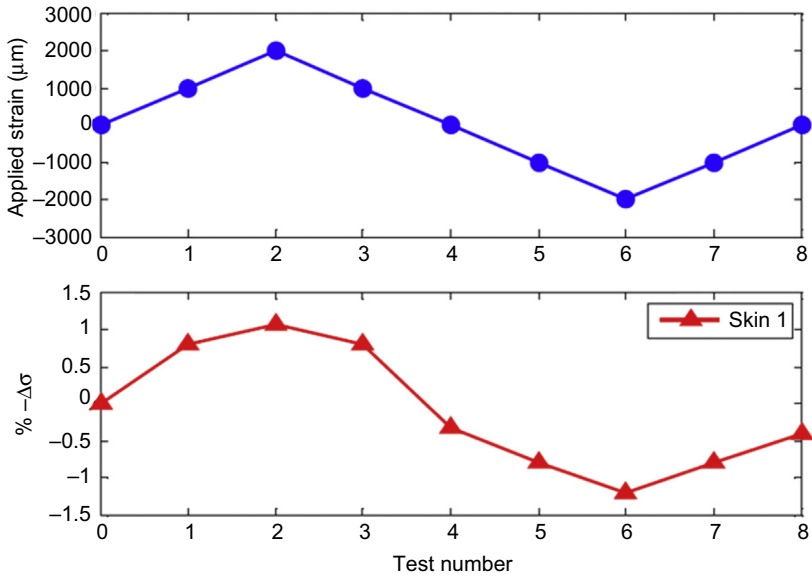
Figure 13.10 A one-cycle tensile-compressive loading pattern (± 2000 $\mu\varepsilon$, pausing every 1000 $\mu\varepsilon$) was applied to an (SWCNT-PSS/PVA)$_{100}$ thin film. The film's average conductivity was computed using each EIT result, and the negative percentage change in conductivity varied in tandem with the magnitude of applied strain (Loh et al., 2009).
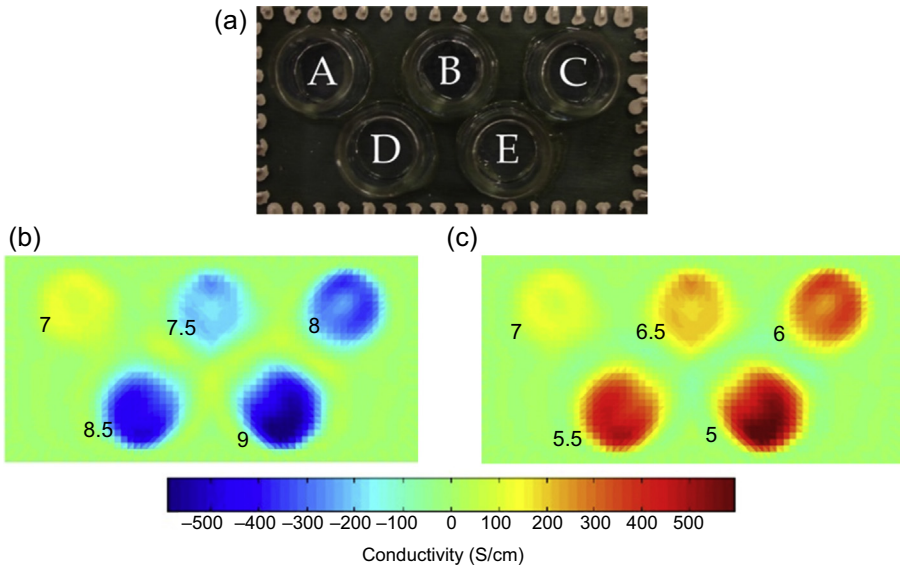
Figure 13.11 (a) Five plastic wells were mounted to the surface of an (SWCNT-PSS/PANI)$_{100}$ nanofilm pH sensor and were exposed to nine different pH buffer solutions. The EIT spatial conductivity maps show that the film was able to detect changes in localized conductivity due to the film being simultaneously exposed to buffer solutions of (b) pH 7, 7.5, 8, 8.5, and 9 and (c) pH 7, 6.5, 6, 5.5, and 5 (Loh, 2008).

As expected, regions exposed to more alkaline solutions decreased in conductivity, and the opposite was true when acidity increased (Figure 13.11). All in all, although EIT is a technique with longstanding roots in the biomedical field, this work is the first time when EIT has been integrated with the unique sensing attributes of nanofilms to realize a true densely distributed sensor capable of sensing the severity and location of structural damage.

13.5   Spray coating

Although the LbL technique enables the multiscale design of nanofilms (e.g., nano-engineered films with unique sensing or mechanical attributes), it is time-consuming and difficult to create films with large dimensions, as mentioned in Section 13.3. Instead, spray coating is a powerful tool that can deposit materials over large spatial areas in a short time. For example, early work by Kaempgen et al. (2005) employed an airbrush to deposit CNT−sodium dodecyl sulfate (SDS) solutions to form transparent CNT coatings. During spray fabrication, the temperature of the substrate was maintained at 100 °C to accelerate coating drying. It should be noted that the density of CNTs was controlled by the number of sprayed layers, rather than by the material used. Depending on the solvent, the drying temperature can be adjusted accordingly too (Hu et al., 2010).

Likewise, CNT-based strain sensors can be cost-effective and extended to large-scale applications if they can be sprayed easily onto structural surfaces. Kang et al. (Kang et al., 2006) deposited MWCNT-based thin films onto a rotorcraft blade to form a long, continuous neuron sensor. EIS was employed to derive an equivalent circuit model that characterized the electrical properties of the nanofilm sensor. Dynamic tests showed that the amplitude of voltage of the damaged cantilever beam decreased ∼25% as compared to the intact case. The MWCNT−neuron was also sensitive to corrosion, such that the equivalent circuit's capacitance changed by orders of magnitude due to electrochemical oxidation.

More recently, Loyola et al. (2013b) developed an MWCNT−polyvinylidene fluoride (PVDF) latex-based ink formulation, and high-quality thin films could be sprayed (using an airbrush) onto virtually any substrate, including glass fiber−reinforced polymer composite structures. The MWCNT-based ink formulation consisted of two parts: an MWCNT−PSS suspension and a PVDF latex solution. The first part was obtained by dispersing MWCNTs in a 2 wt.% PSS solution with small quantities of N-methyl-2-pyroolidone added. Dispersion was achieved by bath ultrasonication and high-energy tip sonication. The second solution consisted of a Kynar Aquatec latex solution, which was based on a dispersion of 150 nm PVDF particles. The two-part solution was mixed together immediately prior to film fabrication, and spraying was performed using a Paasche airbrush. The specimens were air dried or thermally annealed in a vacuum oven.

Continued work by Mortensen et al. (2013) used the aforementioned airbrushing technique for creating MWCNT−latex strain sensors, which were then cut to form 1.7×75 mm^2 specimens. Freestanding films were mounted in a Test Resources
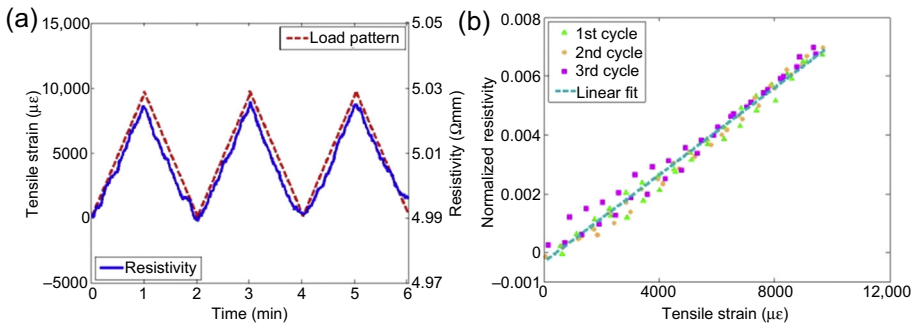
Figure 13.12 (a) The resistivity time history of a freestanding MWCNT−latex nanofilm (fabricated by airbrushing) was overlaid with the applied tensile cyclic pattern. (b) The normalized change in resistivity of the specimen increased in tandem with applied tensile strain, thereby confirming its linear piezoresistive properties (Mortensen et al., 2013).

150R load frame, and the films were subjected to numerous cycles of tensile loading up to 10,000 με. The electrical resistance of the film was measured simultaneously, and a representative overlay of the resistance and applied-strain time histories is presented in Figure 13.12(a). In addition, the normalized change in resistance of the nanofilm was plotted with respect to its applied strain to reveal its linear piezoresistive performance. Strain sensitivity of the bulk films was estimated by fitting a linear least-squares line, as shown in Figure 13.12(b). Strain sensitivity was equivalent to the slope of the linear best-fit line and was ∼0.77. It was also shown that postfabrication thermal annealing could be used to improve nanofilm electrical, mechanical, and electromechanical properties (Mortensen et al., 2013). Despite these advances, great care was needed during manual spraying to ensure that nanofilms were uniformly deposited. Future work in automated or robotic spray fabrication tools would address this issue and facilitate scaling up of this technology.

13.6 Nanofilm-enhanced cementitious composites

Although CNT-based nanofilms (particularly those that are sprayed) can be applied onto structural surfaces for SHM and damage detection applications, damage can originate from within the structural material. In that regard, nanofilms would not be able to directly detect damage until that damage propagated to reach the surface. In particular, concrete and cement composites are susceptible to internal damage that often is not detectable by measuring structural response parameters on their surface. As mentioned in previous chapters of this book, this is one of the main reasons why many researchers modified cement composites with different types of nanofillers and conductive additives, so as to enable them to become self-sensing and multifunctional materials. For example, Chen and Chung (1996) demonstrated that, when carbon fibers were embedded in the cement matrix, the electrical resistance of concrete varied in response to applied cyclic loads. Although its change in resistance was reversible in response to

cyclic loading, cracks or hole-like damage caused irreversible changes in resistance. Similarly, others utilized CNTs as conductive fillers for enhancing the self-sensing characteristics of cement composites (Han et al., 2009; Sui and Liu, 2005; Wille and Loh, 2010; Kang et al., 2009). Despite these advancements, directly incorporating nanomaterials (such as CNTs) within cement matrices leads to numerous limitations that prevent their adoption in real-world applications. These challenges include poor dispersion, poor workability of the concrete mix, changes in casting procedures, and extremely high costs.

A new nanotechnology-enabled cement composite design approach was proposed and demonstrated by Loh and Gonzalez (2015). Instead of dispersing large quantities of CNTs within the cementitious matrix to form a percolated morphology, the new approach aimed at modifying the cementitious matrix−aggregate interface with CNT-based nanofilms. The procedure began by airbrushing MWCNT-based inks directly on top of fine and/or coarse aggregates, where the nanofilm preparation and fabrication procedures followed those presented by Loyola et al. (2013b) and Mortensen et al. (2013). Upon coating the aggregates, the film-coated aggregates were initially air dried, followed by additional drying in a vacuum oven. The coated aggregates were then used to cast nanofilm-enhanced mortar and concrete plates with a size of $45 \times 45 \times 10$ mm^3. It should be mentioned that copper mesh electrodes were embedded to form leads for two-point probe resistance measurements, or multiple boundary electrodes were included for EIT spatial sensing. Most EIT spatial-sensing tests employed 16 boundary electrodes arranged in a 4×4 pattern (Figure 13.13).

Similar to Section 13.4, spatial damage detection tests were conducted using cementitious composite specimens instrumented with an array of boundary electrodes. First, specimens were interrogated by commanding a Keithley 6221 current source to inject 1 mA of DC across a pair of boundary electrodes. Second, an Agilent 34980A multifunction switch with an embedded digital multimeter (DMM) was used for measuring the voltages among the remaining non-current-carrying electrode pairs. A sample current injection and voltage measurement pattern is depicted in Figure 13.13. Then, the Agilent 34980A would switch the current injection electrode while taking the appropriate boundary voltage measurements. The hardware system is fully automated and controlled using a MATLAB program. In another example, the same EIT algorithm described in Section 13.4 was employed, but for this case, the algorithm and finite element formulation were modified to include bilinear quadrilateral elements.

Damage detection validation tests were then conducted for evaluating the sensing capabilities of these nanofilm-enhanced cementitious composites. As an example, a nanofilm-enhanced mortar plate was subjected to artificial damage by sequentially drilling holes (using a 6.5 mm masonry drill bit) near the four corners of the plate. Before damage was imposed on the specimen, an EIT spatial resistivity map of the undamaged plate was obtained, which served as the baseline. EIT measurements were then obtained after each additional drilled hole. Figure 13.14 shows pictures taken after each hole was drilled through the plate, as well as the corresponding resistivity distributions determined by solving the EIT inverse problem. For instance, Figure 13.14(a) shows the nanofilm-enhanced plate with a hole drilled near the bottom-left corner. The corresponding EIT results shown in Figure 13.14(b) clearly indicate localized
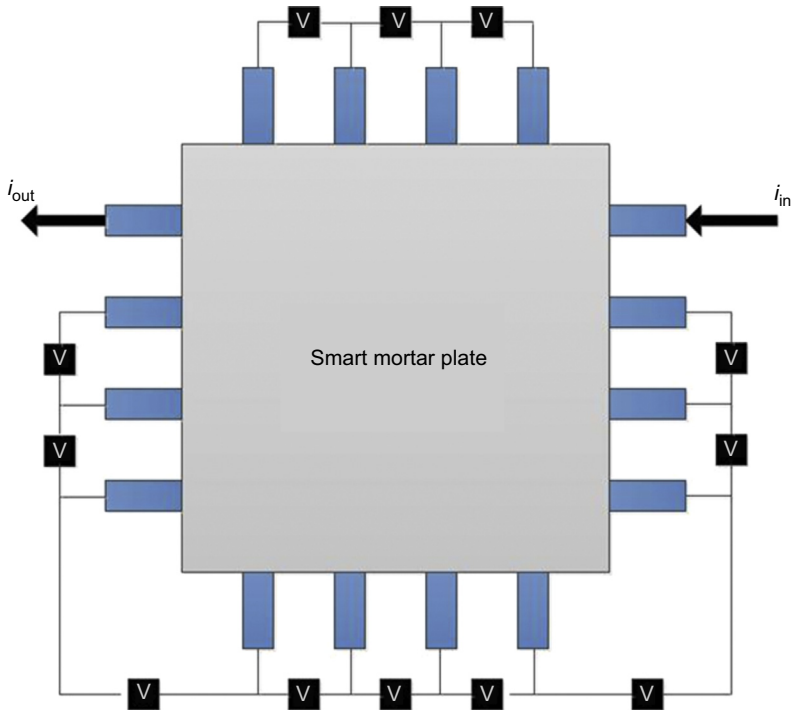
Figure 13.13 Smart mortar plate specimens (45×45 mm^2) were casted with 16 embedded copper mesh boundary electrodes. The schematic shows a sample EIT current injection pattern, in which two electrodes were used for current injection, and the voltage was measured at the remaining boundary electrodes.

increases in resistance (or resistivity) near the location of the damage. The remaining parts of Figure 13.14 confirm that damage location can be accurately identified using EIT and the nanofilm-enhanced mortar plates.

Aside from drilling holes, a crack-like damage was simulated on the backside of a nanofilm-enhanced mortar plate (Figure 13.15). The artificial crack had an average depth of ∼2.5 mm. Similarly, EIT was conducted before and after the crack was introduced, and Figure 13.15(a) shows the picture of the damaged specimen along with the corresponding EIT spatial resistivity distribution. It is clear from Figure 13.15(b) that the length, geometry, and severity of the crack-like damage were successfully resolved. Overall, these results validated the fact that nanofilm-enhanced cementitious composites, when coupled with EIT, can be used for spatial damage detection. Even more impressive was that the amount of CNTs used and its costs were orders of magnitude lower than the current state of the art, which relied on dispersing CNTs directly in the cementitious matrix. The nanofilm-coated aggregates could still enhance electrical conductivity and damage sensitivity. In addition, workability, casting procedures, and costs were not impacted due to the use of these nanofilm-coated aggregates. Thus, there is great potential for scaling this technology for constructing and monitoring large-scale civil infrastructure systems.
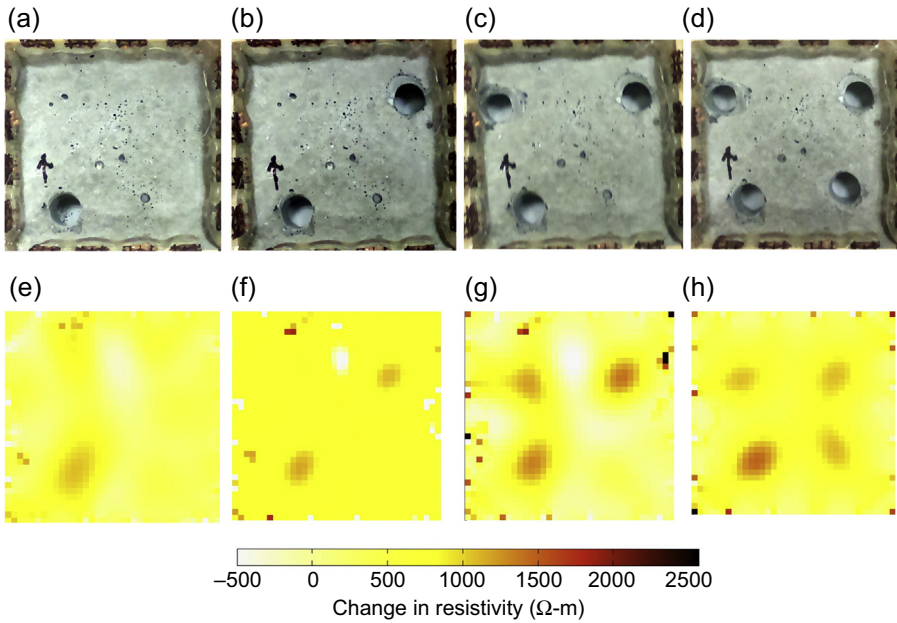
Figure 13.14 Four holes were drilled near the four corners using a 6.5 mm masonry drill bit at the (a) bottom left, (b) top right, (c) top left, and (d) bottom right corners. Subsequent changes in resistivity distribution are shown in (e−h), respectively.
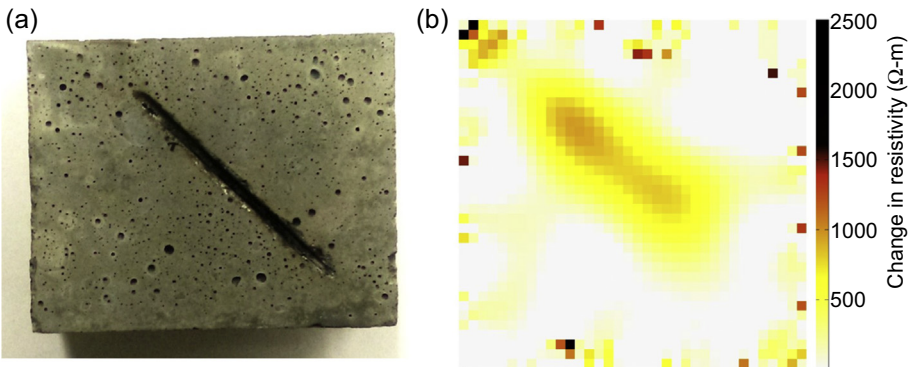
Figure 13.15 (a) A crack-like damage was introduced to a nanofilm-enhanced mortar plate by cutting a slit on the backside of the specimen. (b) The corresponding EIT result and the localized change in resistivity confirm that damage location and severity can be detected using this technique.

13.7 Other nanofilm fabrication methodologies

CNT-based nanofilms can also be dispersed using in situ polymerization (Kang et al., 2009; Park et al., 2002; Hu et al., 2008), spin coating (Kanoun et al., 2014a; Jo et al., 2010; Hellstrom et al., 2009), dip coating (Hu et al., 2010), and inkjet printing

(Kordás et al., 2006), among many others. In situ polymerization (Kang et al., 2009; Park et al., 2002) relies on dispersing CNTs in a liquid monomer or precursor polymers of low molecular weight prior to full polymerization. Because of this, higher interfacial strength between CNTs and the polymer matrix can be realized. For instance, Kang et al. (2009) assembled SWCNT−polyimide nanocomposites using in situ polymerization. Electromechanical tests were performed, and the results yielded strain sensitivities of 4.21 and 0.89 for 0.05 and 10 wt.% SWCNT−polyimide nanofilms, respectively. Hu et al. (2008) deposited MWCNTs in an epoxy matrix, and the nanofilm exhibited nonlinear piezoresistive responses when low CNT concentrations (1 and 2 wt.%) were used, whereas linear responses were obtained with higher CNT concentrations (3, 4, and 5 wt.%). Pham et al. (2008) used two different fabrication methods (i.e., dry blending and solution casting) for embedding MWCNTs in a PMMA matrix. Uniaxial tensile strain tests ($\varepsilon < 10{,}000 \ \mu\varepsilon$) revealed that MWCNT−PMMA nanofilms assembled by dry blending were more sensitive to applied strains than those made with solution casting Kanoun et al. (2014a) and Dinh-Trong et al. (2009) drop-casted three different types of MWCNT-based nanofilms with different polymer matrices: SDS, deoxycholic acid, and polyethylene oxide. Among the three polymers, SDS offered stable mechanical behavior under low-tensile-strain conditions up to ∼3500 $\mu\varepsilon$. Spin coating was also employed for building CNT-based nanocomposites, especially for extremely thin films (ranging from a few nanometers to hundreds of nanometers) (Kanoun et al., 2014a; Jo et al., 2010; Hellstrom et al., 2009). Spin coating was performed by pipetting a few drops of CNT-based solution onto the center of substrate, and the substrate was spun at selected speeds and times to control film thickness. Jo et al. (2010) assembled SWCNT-based thin film using an amphiphilic surfactant and concluded that transparent electrodes could be created using spin coating; the films were characterized by high optical transmittance (71%) and low surface resistivity (59 Ω/sq). Kordás et al. (2006) inkjet-printed functionalized MWCNT−$(CO_2H)_n$ on two different substrates (i.e., paper and plastic). Regardless of the type of substrate, sheet resistivity decreased as the number of printed layers increased, similar to what Ryu et al. (2014) had found. In general, inkjet printing is beneficial due to its cost-effectiveness, ease of use, low cost, direct patterning, and versatility (Kanoun et al., 2014a; Kordás et al., 2006). Nanocomposite and Zinc oxide based strain sensing has also been investigated successfully (Srivastava et al., 2011; Hemtej et al., 2010).

Most recently promising noncontact strain sensing using SWCNT and urethane coating and portable laser based near infrared spectroscopy has been developed (Withey et al., 2012, Sun et al., 2015). More details of this new approach can be found in Chapter 15 of this book.

13.8 Summary

This chapter presented a general overview of the historical developments and recent research on CNT-based nanofilm strain sensors. The aim of the chapter was not to present an exhaustive review on this subject matter but, rather, to showcase the breadth of

work. The chapter began with a discussion of CNT-based buckypapers that were fabricated by vacuum filtration of dispersed CNT solutions. This was one of the earliest works in creating CNT-based nanofilm strain sensors that sought to leverage the impressive electrical properties of individual nanotubes and yet be able to translate their nanoscale properties to the macro scale. The second part of this chapter transitioned into the broad area of LbL nanofilms, in which CNT-based films were shown to exhibit improved electromechanical properties suitable for sensing and SHM. These films were mechanically strong yet flexible and exhibited linear piezoresistive properties up to 10,000 με. Even more important was that LbL enabled the seamless integration of different nanomaterial and polyelectrolyte species in a highly controlled fashion with nanoscale resolution, simply by controlling fabrication solution constituents, concentrations, and the deposition sequence. An example was presented in which polyaniline could be incorporated in LbL CNT-based nanofilms for the design of pH sensors suitable for environmental or corrosion monitoring.

Despite these advances, fabrication techniques such as buckypaper and LbL suffer from a major limitation, namely, their difficulty in transitioning this technology from the laboratory to large-scale manufacturing and implementation. These films were typically very small in size and were time-consuming to fabricate. An alternative solution was presented in which airbrushing was employed for depositing MWCNT-based thin films. It was shown that MWCNT−latex strain sensors could be deposited in a short time, at low cost, and onto virtually any structural surface. Furthermore, to scale this technology for large-scale civil infrastructure SHM applications, a novel solution was proposed that entailed spraying MWCNT−latex thin films onto aggregates and then using film-coated aggregates for casting cementitious composites. It was found that these nanofilm-enhanced cementitious composites exhibited significantly improved damage sensitivity and can be produced at very reasonable costs.

Beyond the development of the various types of multifunctional nanofilms presented in this chapter, EIT permitted mapping of the 2D spatial conductivity (or resistivity) distribution of nanofilms and nanofilm-enhanced cementitious composites. Since these nanofilms were sensitive to damage at every location and were already precalibrated to strain (or other stimuli), EIT spatial conductivity mapping allowed one to use the nanofilms as true densely distributed sensors. The results, whether they were for LbL nanofilms, airbrushed MWCNT−latex films, or nanofilm-enhanced cementitious composites, successfully demonstrated that EIT was able to assess damage severity and location.

Despite these advances, there still remain numerous research challenges that lie ahead in order to realize CNT-based sensing systems for SHM of real-world civil infrastructure systems. The ability to exercise precise nanoscale control and to scale nanomaterial properties up to the bulk scale continues to be one of the toughest research questions that need to be solved. In addition, there is a dire need to innovate in techniques for manufacturing nanofilms, particularly deriving roll-to-roll and scalable nanomanufacturing techniques, so that their large-scale production can be realized at low costs. Finally, techniques for encoding different engineering functionalities within a material architecture to realize multifunctional and nanostructured systems are direly needed.

References

Alamusi, Hu, N., Fukunaga, H., Atobe, S., Liu, Y., Li, J., 2011. Piezoresistive strain sensors made from carbon nanotubes based polymer nanocomposites. Sensors 11 (11), 10691.

Baughman, R.H., Zakhidov, A.A., de Heer, W.A., 2002. Carbon nanotubes-the route toward applications. Science 297 (5582), 787−792.

Bae, S.-H., Lee, Y., Sharma, B.K., Lee, H.-J., Kim, J.-H., Ahn, J.-H., 2013. Graphene-based transparent strain sensor. Carbon 51 (0), 236−242.

Baughman, R.H., Cui, C., Zakhidov, A.A., Iqbal, Z., Barisci, J.N., Spinks, G.M., Wallace, G.G., Mazzoldi, A., De Rossi, D., Rinzler, A.G., Jaschinski, O., Roth, S., Kertesz, M., 1999. Carbon nanotube actuators. Science 284 (5418), 1340−1344.

Chen, P.-W., Chung, D., 1996. Carbon fiber reinforced concrete as an intrinsically smart concrete for damage assessment during static and dynamic loading. Materials Journal 93 (4), 341−350.

Cho, S., Yun, C.-B., Lynch, J.P., Zimmerman, A.T., Spencer Jr., B.F., Nagayama, T., 2008. Smart wireless sensor technology for structural health monitoring of civil structures. Steel Structures 8 (4), 267−275.

Dharap, P., Li, Z., Nagarajaiah, S., Barrera, E.V., 2004a. Nanotube film based on single-wall carbon nanotubes for strain sensing. Nanotechnology 15 (3), 379.

Dharap, P., Li, Z., Nagarajaiah, S., Barrera, E.V., 2004b. Flexural strain sensing using carbon nanotube film. Sensor Review 24 (3), 271−273.

Decher, G., 1997. Fuzzy nanoassemblies: toward layered polymeric multicomposites. Science 277 (5330), 1232−1237.

Dinh-Trong, N., Steitz, J., Lei, B., Kanoun, O., 2009. Influence of the composition of MWCNTs layers on the properties of strain gauges. Nanotechnology 477−480. IEEE-NANO 2009. 9th IEEE Conference on.

Farrar, C.R., Worden, K., 2007. An introduction to structural health monitoring. Philosophical Transactions of the Royal Society of London A 365 (1851), 303−315.

Fung, C.K.M., Wong, V.T.S., Chan, R.H.M., Li, W.J., 2004. Dielectrophoretic batch fabrication of bundled carbon nanotube thermal sensors. Nanotechnology, IEEE Transactions on 3 (3), 395−403.

Hu, L., Hecht, D.S., Grüner, G., 2010. Carbon nanotube thin films: fabrication, properties, and applications. Chemical Reviews 110 (10), 5790−5844.

Hou, T.-C., Loh, K.J., Lynch, J.P., 2007. Spatial conductivity mapping of carbon nanotube composite thin films by electrical impedance tomography for sensing applications. Nanotechnology 18 (31), 315501.

Holder, D.S., 2004. Electrical Impedance Tomography: Methods, History and Applications. CRC Press, London.

Han, B., Yu, X., Kwon, E., 2009. A self-sensing carbon nanotube/cement composite for traffic monitoring. Nanotechnology 20 (44), 445501.

Hu, N., Karube, Y., Yan, C., Masuda, Z., Fukunaga, H., 2008. Tunneling effect in a polymer/ carbon nanotube nanocomposite strain sensor. Acta Materialia 56 (13), 2929−2936.

Hellstrom, S.L., Lee, H.W., Bao, Z., 2009. Polymer-assisted direct deposition of uniform carbon nanotube bundle networks for high performance transparent electrodes. ACS Nano 3 (6), 1423−1430.

Hemtej, G., Vemuru, V.S.M., Kumar, A., Botello-Mendez, A., Vajtai, R., Terrones, M., Nagarajaiah, S., Ajayan, P.M., 2010. Flexible piezoelectric ZnO-paper nanocomposite strain sensor. Small 6 (15), 1641−1646. http://dx.doi.org/10.1002/smll.201000254.

Iijima, S., 1991. Helical microtubules of graphitic carbon. Nature 354 (6348), 56−58.

Jo, J.W., Jung, J.W., Lee, J.U., Jo, W.H., 2010. Fabrication of highly conductive and transparent thin films from single-walled carbon nanotubes using a new non-ionic surfactant via spin coating. ACS Nano 4 (9), 5382−5388.

Kanoun, O., Müller, C., Benchirouf, A., Sanli, A., Dinh, T.N., Al-Hamry, A., Bu, L., Gerlach, C., Bouhamed, A., 2014. Flexible carbon nanotube films for high performance strain sensors. Sensors 14 (6), 10042−10071.

Knite, M., Teteris, V., Kiploka, A., Kaupuzs, J., 2004. Polyisoprene-carbon black nanocomposites as tensile strain and pressure sensor materials. Sensors and Actuators a: Physical 110 (1−3), 142−149.

Kang, I., Schulz, M.J., Kim, J.H., Shanov, V., Shi, D., 2006. A carbon nanotube strain sensor for structural health monitoring. Smart Materials and Structures 15 (3), 737.

Kaempgen, M., Duesberg, G.S., Roth, S., 2005. Transparent carbon nanotube coatings. Applied Surface Science 252 (2), 425−429.

Kang, I.P., Lee, J.W., Choi, G.R., Jung, J.Y., Hwang, S.H., Choi, Y.S., Yoon, K.J., Schulz, M.J., 2006. Structural health monitoring based on electrical impedance of a carbon nanotube neuron. Key Engineering Materials 321, 140−145.

Kang, J.H., Park, C., Scholl, J.A., Brazin, A.H., Holloway, N.M., High, J.W., Lowther, S.E., Harrison, J.S., 2009. Piezoresistive characteristics of single wall carbon nanotube/polyimide nanocomposites. Journal of Polymer Science Part B: Polymer Physics 47 (10), 994−1003.

Kordás, K., Mustonen, T., Tóth, G., Jantunen, H., Lajunen, M., Soldano, C., Talapatra, S., Kar, S., Vajtai, R., Ajayan, P.M., 2006. Inkjet printing of electrically conductive patterns of carbon nanotubes. Small 2 (8−9), 1021−1025.

Li, Z., Dharap, P., Nagarajaiah, S., Barrera, E., Kim, J.D., 2004. Carbon nanofilm sensor. Advanced Materials Journal 16 (7), 640−643. http://dx.doi.org/10.1002/adma.200306310.

Loh, K., Hou, T.-C., Lynch, J., Kotov, N., 2009. Carbon nanotube sensing skins for spatial strain and impact damage identification. Journal of Nondestructive Evaluation 28 (1), 9−25.

Loh, K., Chang, D., 2011. Zinc oxide nanoparticle-polymeric thin films for dynamic strain sensing. Journal of Materials Science 46 (1), 228−237.

Loh, K.J., Azhari, F., 2012. Recent advances in skin-inspired sensors enabled by nanotechnology. JOM 64 (7), 793−801.

Loh, K.J., Lynch, J.P., Shim, B.S., Kotov, N.A., 2008. Tailoring piezoresistive sensitivity of multilayer carbon nanotube composite strain sensors. Journal of Intelligent Material Systems and Structures 19 (7), 747−764.

Loh, K.J., Kim, J., Lynch, J.P., Kam, N.W.S., Kotov, N.A., 2007. Multifunctional layer-by-layer carbon nanotube−polyelectrolyte thin films for strain and corrosion sensing. Smart Materials and Structures 16 (2), 429.

Loyola, B.R., Zhao, Y., Loh, K.J., Saponara, V.L., 2013a. The electrical response of carbon nanotube-based thin film sensors subjected to mechanical and environmental effects. Smart Materials and Structures 22 (2), 025010.

Loyola, B.R., Saponara, V.L., Loh, K.J., Briggs, T.M., O'Bryan, G., Skinner, J.L., 2013b. Spatial sensing using electrical impedance tomography. Sensors Journal, IEEE 13 (6), 2357−2367.

Loh, K.J., Gonzalez, J., 2015. Cementitious composites engineered with embedded carbon nanotube thin films for enhanced sensing performance. Journal of Physics: Conference Series 628, 012042.

Loh, K.J.-H., 2008. Development of Multifunctional Carbon Nanotube Nanocomposite Sensors for Structural Health Monitoring. University of Michigan.

Mamedov, A.A., Kotov, N.A., Prato, M., Guldi, D.M., Wicksted, J.P., Hirsch, A., 2002. Molecular design of strong single-wall carbon nanotube/polyelectrolyte multilayer composites. Nature Materials 1 (3), 190−194.

Mortensen, L.P., Ryu, D.H., Zhao, Y.J., Loh, K.J., 2013. Rapid assembly of multifunctional thin film sensors for wind turbine blade monitoring. Key Engineering Materials 569, 515−522.

Obitayo, W., Liu, T., 2012. A Review: carbon nanotube-based piezoresistive strain sensors. Journal of Sensors 2012, 1−15.

Polydorides, N., 2002. Image Reconstruction Algorithms for Soft-field Tomography. University of Manchester, UMIST.

Park, C., Ounaies, Z., Watson, K.A., Crooks, R.E., Smith Jr., J., Lowther, S.E., Connell, J.W., Siochi, E.J., Harrison, J.S., Clair, T.L.S., 2002. Dispersion of single wall carbon nanotubes by in situ polymerization under sonication. Chemical Physics Letters 364 (3−4), 303−308.

Pham, G.T., Park, Y.-B., Liang, Z., Zhang, C., Wang, B., 2008. Processing and modeling of conductive thermoplastic/carbon nanotube films for strain sensing. Composites Part B: Engineering 39 (1), 209−216.

Rein, M.D., Breuer, O., Wagner, H.D., 2011. Sensors and sensitivity: carbon nanotube buckypaper films as strain sensing devices. Composites Science and Technology 71 (3), 373−381.

Ryu, D., Meyers, F.N., Loh, K.J., 2014. Inkjet-printed, flexible, and photoactive thin film strain sensors. Journal of Intelligent Material Systems and Structures 1−12. http://dx.doi.org/10.1177/1045389X14546653.

Suri, K., Annapoorni, S., Sarkar, A.K., Tandon, R.P., 2002. Gas and humidity sensors based on iron oxide−polypyrrole nanocomposites. Sensors and Actuators B: Chemical 81 (2−3), 277−282.

Stampfer, C., Helbling, T., Obergfell, D., Schöberle, B., Tripp, M.K., Jungen, A., Roth, S., Bright, V.M., Hierold, C., 2006. Fabrication of single-walled carbon-nanotube-based pressure sensors. Nano Letters 6 (2), 233−237.

Saulnier, G.J., Blue, R.S., Newell, J.C., Isaacson, D., Edic, P.M., 2001. Electrical impedance tomography. IEEE Signal Processing Magazine 18 (6), 31−43.

Sui, L.L., Liu, T.-J., 2005. State-of-the-art of multifunctional and smart concrete. Key Engineering Materials 302, 424−431.

Sun, P., Bachilo, S.M., Weisman, R.B., Nagarajaiah, S. (web-published 8/10/2015). Carbon nanotubes as non-contact optical strain sensors in smart skins. Journal of Strain Analysis for Engineering Design. http://dx.doi.org/10.1177/0309324715597414.

Srivastava, R.K., Vemuru, V.S.M., Zeng, Y., Vajtai, R., Nagarajaiah, S., Ajayan, P.M., Srivastava, A., 2011. The strain sensing and thermal−mechanical behavior of flexible multi-walled carbon nanotube polystyrene composite films. Carbon 49 (12), 3928−3936. http://dx.doi.org/10.1016/j.carbon.2011.05.031.

Tian, H., Shu, Y., Cui, Y.-L., Mi, W.-T., Yang, Y., Xie, D., Ren, T.-L., 2014. Scalable fabrication of high-performance and flexible graphene strain sensors. Nanoscale 6 (2), 699−705.

Vemuru, S., Wahi, R., Nagarajaiah, S., Ajayan, P., 2009. Strain sensing using a multiwalled carbon nanotube film. Journal of Strain Analysis for Engineering Design 44 (7), 555−562.

Vauhkonen, M., 1997. Electrical Impedance Tomography and Prior Information. University of Kuopio.

Wang, Y., Lynch, J.P., Law, K.H., 2007. A wireless structural health monitoring system with multithreaded sensing devices: design and validation. Structure and Infrastructure Engineering 3 (2), 103−120.

Wei, C., Dai, L., Roy, A., Tolle, T.B., 2006. Multifunctional chemical vapor sensors of aligned carbon nanotube and polymer composites. Journal of the American Chemical Society 128 (5), 1412−1413.

Wang, J., 2005. Carbon-nanotube based electrochemical biosensors: a review. Electroanalysis 17 (1), 7−14.

Wikipedia contributors, 2014. Buckypaper. The Free Encyclopedia. https://en.wikipedia.org/w/index.php?title=Buckypaper&oldid=637009327.

Wille, K., Loh, K., 2010. Nanoengineering ultra-high-performance concrete with multiwalled carbon nanotubes. Transportation Research Record: Journal of the Transportation Research Board 2142, 119−126.

Withey, P.A., Vemuru, V.S.M., Bachilo, S.M., Nagarajaiah, S., Weisman, R.B., 2012. Strain paint: noncontact strain measurement using single-walled carbon nanotube composite coatings. Nano Letters 12 (2), 3497−3500. http://dx.doi.org/10.1021/nl301008m.

Zhang, Z., Wei, H., Liu, Y., Leng, J., 2015. Self-sensing properties of smart composite based on embedded buckypaper layer. Structural Health Monitoring 1−10. http://dx.doi.org/10.1177/1475921714568405.

Zhao, Y., Loyola, B.R., Loh, K.J., 2011. Characterizing the viscoelastic properties of layer-by-layer carbon nanotube−polyelectrolyte thin films. Smart Materials and Structures 20 (7), 075020.

In situ sensing in glass fiber-reinforced polymer composites via embedded carbon nanotube thin films

14

Bryan R. Loyola
Sandia National Laboratories, Livermore, CA, USA

14.1 Introduction

The use of fiber-reinforced composite materials has drastically increased in the past several decades. Due to this, an increased interest in long-term structural performance and monitoring of these materials has led to several methods to perform in-service assessments. This chapter covers the recent research in the area of embedding carbon nanotube (CNT)-based thin films into glass fiber-reinforced polymer (GFRP) composites. Significant detail is given on the manufacturing process and measurement strategies of the research that has been conducted in this field. Finally, typical results are described for the methods discussed pertaining to sensing strain and detecting damage in GFRP composites.

14.1.1 Chapter outline

To best divulge the details in performing structural health monitoring (SHM) using embedded CNT-based thin films in GFRP composites, this chapter is distributed into four sections: background, fabrication of embedded CNT-based thin films, methods for sensing strain and damage with embedded CNT-based thin films, and typical results developed from these methods. Extensive background on embedded sensing methods for fiber-reinforced polymer (FRP) composites is presented to give the reader perspective on the current state of the field. Next, the fabrication methods are described; those appearing in this chapter are, to the author's knowledge, the only methods previously reported in the reviewed literature. The methods for using the CNT-based thin films for sensing purposes consist of direct current (DC) resistance measurements, which are more commonly known, and electrical impedance spectroscopy and electrical impedance tomography, which are more recently employed methods. Finally, typical results from these aforementioned methods are presented from embedded CNT thin films in GFRP structures. Future thrust areas resulting from the current state of the art are presented as a guide to readers desiring to enter this field of SHM.

14.2   Background

Structural engineers are continually finding ways to incorporate higher performing materials into structures to increase safety, efficiency, and manufacturability in aircraft, automobiles, civil structures, pressure tanks, and spacecraft. One of these newer materials is fiber-reinforced polymer composites, using primarily glass (GFRP) or carbon (CFRP) fiber reinforcement. Specifically, these materials have high strength-to-weight ratios, resistance to fatigue, and high conformability in the manufacturing process. However, there materials are still susceptible to damage from a multitude of avenues, such as impact, high levels of mechanical strain, chemical penetration, and multiaxial fatigue. These events can lead to damage modes such as delamination, matrix cracking, fiber breakage, and matrix blistering, to name a few. These tend to occur internal to the laminate structure, rendering the damage nearly undetectable to visual inspection. As visual inspection is the prominent means for damage detection in numerous industries, this poses a tremendous problem. In fact, unexpected structural failure in composite structures has already occurred in some Airbus A310 series aircraft involving the GFRP sandwich structure of the rudders. Hydraulic fluid was found to leak into the rudder, causing delamination or disbonding of the GFRP in the rudder, which grew over time from continued loading and hydraulic fluid exposure. Specifically, Air Transat Flight 961 from Varadero, Cuba, to Quebec, Canada, experienced full rudder detachment near Miami, Florida, causing it to make a return to Varadero. A joint investigation between the Canadian and American transportation safety organizations made the determination that this could have been prevented had the delaminations been detected at an earlier stage (Rosenker, 2006).

For this reason, numerous operator-based methods have been applied to this problem, such as using ultrasonics, X-ray, thermography, and dye penetrant methods. These have all been demonstrated to detect some if not all of the damage modes specified previously with high resolution. However, these all require a skilled technician to perform these measurements by hand, or to use very expensive automated equipment to scan large structures like aircraft wings. The field of SHM has shifted focus to apply distributed sensors across or throughout structures. A handful of sensors have been the predominant focus for detecting damage in FRP composites: strain gages, optical fibers, and wave-based methods, which are used to detect strain fields, cracking, or discontinuities in the FRP composites. Distributed strain gages (Haksoo et al., 2008; Kesavan et al., 2006, 2008; Rumsey and Paquette, 2008) and optical fiber Bragg gratings (Amano et al., 2007; Antunes et al., 2011; Betz et al., 2002; Kersey et al., 1997; Sohn et al., 2001) are distributed across a surface to sense for changes in a structure's strain field due to the presence of damage with reference to a known baseline to a type of mechanical loading. Small-diameter optical fibers without incorporated sensors have been embedded within FRP composites that allow for the use of optical methods to detect the length of the fiber. When the detection method measures a drastic decrease in the fiber length, it can indicate that the fiber has been broken, potentially indicating a crack (Bastianini et al., 2005; Kuang and Cantwell, 2003). Finally, wave-based methods including acoustic emission and ultrasonic sensing have also been used that were distributed across a structure. In the case of acoustic emission, the system

detects acoustic waves generated from damage events, such as delamination or fiber breakage (Beattie, 1997; Ciampa and Meo, 2012; Ian et al., 2002; Wenger et al., 1996; Yun, 2011). Using the emission characteristics (i.e., frequency, duration, and amplitude), several papers have demonstrated the ability to distinguish between these types of damage. Ultrasonic-based methods use piezoelectric transducers to emit an ultrasonic pulse, which propagates across the structure (Chambers et al.; Choi and Chang, 1994; Kessler and Raghavan; Lin and Chang, 2002; Tang et al., 2011). If the wave encounters any discontinuities in the structure, then the wave is scattered, which is then detected by the same piezoelectric sensor or another one. To protect the sensors, allow for better coupling to the structure, and increase sensitivity, it is desired to embed these sensors. However, it has been found that embedding optical fibers with diameters larger than 100 μm (Tsutsui et al., 2004) and embedding piezoelectric sensor/actuator disks (Winkelmann et al., 2008) lead to decreased fatigue life of the composite structures. In addition, most of these methods require expensive and heavy equipment to perform these types of sensing, which will require some miniaturizing on their part to be usable in weight- and/or size-restrictive environments such as aircraft.

An orthogonal approach to damage detection from the previously described methods is to monitor the electrical properties of the FRP composites. With a fiber that is already conductive (i.e., carbon fibers), this is readily done by measuring the electrical conductivity or impedance of the composite as it is loaded or before and after damage. This is done by injecting a DC or alternating current (AC) and making some sort of voltage measurements. Like strain gages, the resistance of a material will change due to strain, which has been shown in the literature (Wang and Chung, 2000, 2007; Wang et al., 1999). In addition, if the conductive materials are damaged, the resistance of the region will increase due to a disruption in the conductive pathways (Irving and Thiagarajan, 1998; Todoroki, 2008; Todoroki et al., 2002; Wang and Chung, 2006; Wang et al., 2005). However, GFRP is highly nonconductive, requiring a conductive material be introduced to the system to enable electrical conductivity-based damage detection methods. This has been accomplished in two distinct ways: by incorporating conductive particles directly into the epoxy matrix of the GFRP composites, or embedding a thin film of nanoparticles directly on or between the layers of fibers. The former method is discussed in another section of this book. The latter approach typically utilizes CNTs, which were first reported by Iijima (1991). CNTs are one or more concentrically structured wrapped tubes of graphene, which exhibit high mechanical, thermal, and electrical properties (Baughman et al., 2002). In fact, CNTs were determined to be a very effective filler material for nonconductive materials to impart higher levels of conductivity into what has come to be called a nanocomposite (Thostenson et al., 2001). As for thin films based on CNTs, numerous researchers have investigated these structures either as pure CNT thin films (i.e., buckypapers) (Dharap et al., 2004; Rein et al., 2011) or as incorporated with a polymer matrix and called CNT nanocomposites (De et al., 2009; Hu et al., 2010; Kang et al., 2006; Loh et al., 2007; Shindo et al., 2011; Vemuru et al., 2009; Zhao et al., 2011). The reported characterization of these materials has demonstrated the strain sensitivity of the resistance of these thin films. To this point, only three examples of CNT thin films have been reported to have been embedded in the structure

of a GFRP composite. First, multiwalled carbon nanotube (MWCNT)−polyelectrolyte thin films were directly deposited onto glass fiber weaves that were infused with an epoxy resin to complete the GFRP composite (Loyola et al., 2010a). Second, an MWCNT−polyvinylidene fluoride (PVDF) thin film was spray deposited into unidirectional glass fiber weaves, which were then infused with epoxy, creating embedded sensing layers in the GFRP composite (Loyola et al., 2013a,b). Finally, Sureeyatanapas and Young (2009) incorporated single-walled carbon nanotubes (SWCNTs) into an amine silane coupling agent and directly applied it to a glass fiber surface for use as a strain sensor. As will be shown in this chapter, embedding CNT thin films into a GFRP composite for strain- and damage-sensing applications demonstrates a lot of promise for this sensing avenue.

14.3　Embedded CNT thin films

Over the next section, three distinct methods for embedding CNT thin films into the structure of GFRP composites are discussed.

14.3.1　Layer-by-layer deposited MWCNT−PSS/PVA thin films

The first method for CNT thin film deposition is based on a layer-by-layer (LbL) polyelectrolyte deposition methodology. The basis for this depositional process is the electrostatic attraction between deposited layers of polycationic poly(vinyl alcohol) (PVA) and polyanionic poly(4-sodium styrene sulfonate) (PSS), which combine to create a robust film that is controllable on the nanoscale (Decher and Schlenoff, 2003). The MWCNTs are incorporated into the film via polymer wrapping by the PSS chains, which also enable a stable solution of MWCNT−PSS. Despite being of a discrete iterative nature, this process yields highly isotropic thin films of carbon nanotubes of high mechanical performance mainly due to the strong hydrogen bonding between the two polyelectrolytes (Kozlov et al., 2003).

The embedded thin films start off with a unidirectional glass fiber weave (type 7715, Applied Vehicle Technology) as the depositional substrate. These substrates are then immersed in a solution of 0.5 wt% of PVA that has been dissolved into deionized (DI) water at 100 °C and cooled to room temperatures. The substrates are immersed for 5 min, ideally being spun in the liquid to enhance the polyanionic deposition across the surface (Decher and Schlenoff, 2003). The substrate is then rinsed for 1 min in DI water for a total of three times to remove any unbound PVA solution and dried for 5 min with dry nitrogen. The substrate is then immersed in the MWCNT−PSS solution for 5 min. This solution is created by a 1 wt% solution of PSS with 1 mg/mL MWCNTs stably dispersed in it using 30 min of ultrasonic power using a 1/8-in tip sonicator at 135 W and 5 s on/off pulses. PSS has been shown to wrap itself around CNTs, thus disallowing rebonding to other CNTs causing agglomeration (Yang et al., 2010). This is the mechanism that ensures a stable dispersion of the MWCNTs is obtained. Once the substrate has been submerged and spun in the

solution, the substrates are again rinsed three times at 1 min apiece. This is followed by drying for 5 min under dry nitrogen. The deposition of both PVA and MWCNT−PSS equates to one bilayer of the film. The deposition process is continued until the desired number of bilayers have been deposited, resulting in a film that is indicated by [MWCNT−PSS/PVA]$_n$, where n is the number of bilayers in the film. A pictorial of this process is available in Figure 14.1.

The resulting films from the LbL process are highly uniform, as illustrated by the scanning electron microscopy (SEM) image in Figure 14.2(a). The dense network of MWCNTs is held together by a web of the polyelectrolytes. In addition, the films are shown to conformally coat the glass fibers of the weave in the SEM image in Figure 14.2(b), which will hopefully lead to good strain transfer between the fiber and the film. With the thin films deposited on the woven fabric, the fabric was cut into rectangles with dimensions of 3 mm by 70 mm with the long dimension in the direction of the fibers. To electrically connect to the thin films during testing, two electrodes were placed 15 mm apart with the bottom electrode placed 10 mm from the bottom of the specimen. To electrically connect the specimen to external electrical measurement equipment, 30 AWG wires were stripped slightly longer than the width of the specimens and then positioned at the location of each electrode and adhered with silver paint for electrical connection to the MWCNT−PSS/PVA thin film. The weaves were then infused with a two-part epoxy system (Pro-Set 125/237) using a wet layup process, then fully cured for 15 h at room temp and 8 h at 80 °C. At this point, the MWCNT−PSS/PVA film is fully embedded within the GFRP structure of the specimen.
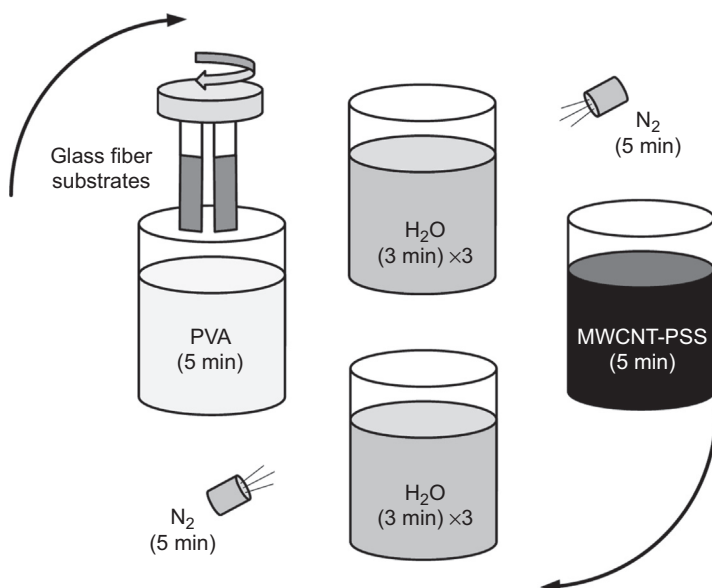
Figure 14.1 Schematic of the layer-by-layer thin film deposition process.

(a)   (b)
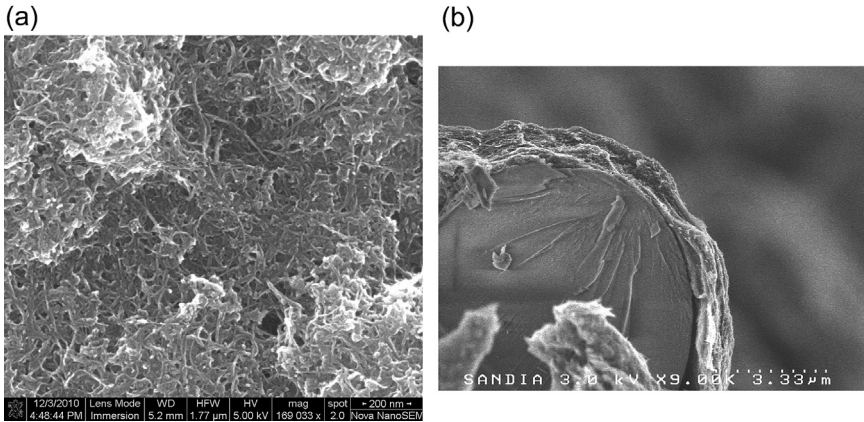
Figure 14.2 Scanning electron microscope image of a representative MWCNT−PSS/PVA LbL film on a glass slide (a) and covering a glass fiber (b).

The LbL deposition process allows for nanoscale control of the thickness of the films, which leads to control of the resistance of the films. The full characterization of the response to strain and other environmental stimuli has been reported (Loyola et al., 2013c). The main drawback of the LbL process is the requirement for the substrate to be immersed in the polyelectrolyte solutions. This drastically reduces the area over which the films can be deposited.

14.3.2 Spray-deposited MWCNT−PVDF thin films

A spray-deposited MWCNT−polyvinylidene fluoride (PVDF) film has been developed to allow for deposition of a conductive MWCNT thin film across large regions, like an aircraft wing or sections of a bridge. The paint is based on a latex paint system, which is an emulsion of PVDF nanoparticles that when coalesced together create a robust film. By using a latex formulation, a segregated network of MWCNTs is created as the MWCNTs cannot penetrate the PVDF spheres, which allows the PVDF nanoparticles to act as a guide for creating the MWCNT network. A schematic of this is shown in Figure 14.3(a). It is believed that this configuration allows for a lower percolation threshold in these MWCNT−PVDF nanocomposites.

To incorporate the MWCNTs into the latex paint system, a two-part formulation was developed. The first part contained the stably dispersed MWCNTs, using PSS as a polymer wrapping dispersal agent. An appropriate amount of MWCNTs were added to a 2 wt% solution of PSS to result in a 5 wt% loading of MWCNTs in the final film. The polar solvent N-methyl-2-pyrrolidone (NMP) is added as a coalescing agent for the PVDF latex particles. NMP has a twofold role as it also aids in the dispersal of the MWCNTs during the deagglomeration step. Next, this solution was tip sonicated (Branson S-450D) with a $\frac{1}{4}$-in tip at 30% amplitude for 30 min with 5 s on/off pulsing to deagglomerate the MWCNTs into a stable solution with the PSS and NMP called the MWCNT ink. After the first part of the formulation is complete, the second part
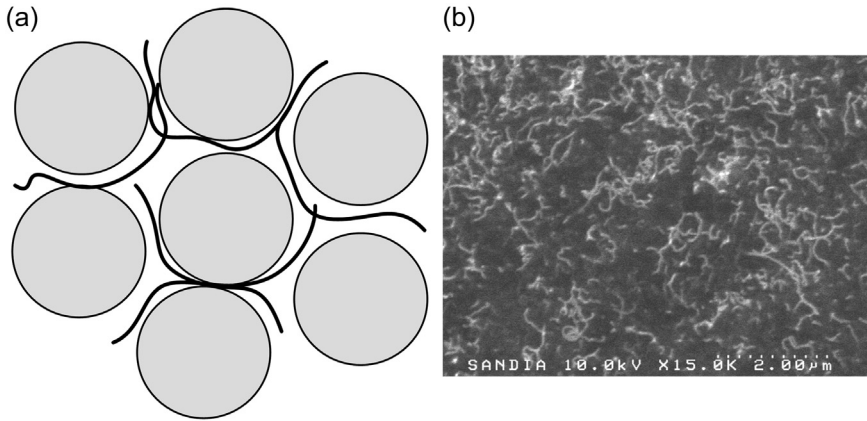
Figure 14.3 Schematic (a) and scanning electron microscope image (b) of the MWCNT−PVDF latex-based paint.

of the formulation contains the PVDF latex formulation (Arkema Kynar Aquatec) and enough water to ensure that the total solid content in the combined paint formulation is at 13 wt%. This will ensure a formulation that is sprayable. The Kynar and water are combined in a large container, and the ink was added to the Kynar solution and thoroughly mixed. Within 20 min, the paint solution is spray deposited onto glass fiber weaves (Vectorply E-LR 0908) that have been cleaned using ethanol and dried using nitrogen. The film is spray deposited using an airbrush attached to a dry nitrogen line. The wet spray-deposited film is then placed in a 60 °C convection oven for 15 min or until completely dry. After the film is fully dry, the fiber weave with deposited thin film can be infused with epoxy to create a GFRP structure. An image of the MWCNT−PVDF thin film spray deposited on an aluminum substrate is presented in Figure 14.3(b). In this image, the MWCNTs are clearly visible as the light worm-like structures, which are clearly evenly distributed across the thin film. As presented later in this chapter, this will allow for a fully percolated network of MWCNTs enabling a conductive nanocomposite.

Once the thin film is deposited on the glass fiber weave, it is ready to be infused with epoxy to make into a GFRP composite with an embedded sensor. To measure the resistance response to strain, the same 3 × 70 mm specimens are fabricated with the applied electrodes and wiring prior to the wet layup manufacturing of the composite. To fabricate the specimens for the distributed sensing methodology discussed in Section 14.4.3, a different approach is taken. The GFRP composite in the distributed sensing case will be several glass fiber weave plies thick. The glass fiber weaves with the deposited thin films will only be on the outer facing layers. To allow for direct electrical connection to these embedded films, single-sided copper tape with a protective paper backing is used to prevent the epoxy from coating the electrode and maintaining electrical contact with the film. A copper tape (3M) was cut into 3 × 3 mm squares to act as the electrodes. The MWCNT−PVDF film was coated with conductive silver paint at the point where the electrode was to be positioned. The tape is placed copper

side down, or sticky side with protective paper facing upward. The rest of the glass fiber weaves were stacked in the desired stack sequence and infused with a two-part epoxy (Pro-Set 117LV/237) using a vacuum-assisted resin transfer molding (VARTM) process. The composite is cured for 15 h at room temperature and at 80 °C for 8 h. Once the composite has been cured, a razor blade is used to cut around the electrodes, and the protecting backing of the tape is removed, exposing the electrode. The specific number and positions of the electrodes will be discussed in Section 14.4.4. For further details on the fabrication process of these embedded MWCNT−PVDF GFRP composites, please refer to these works from Loyola et al. (2013a,b).

14.3.3 Sizing-based SWCNT glass fiber coatings

The final example of an embedded thin film sensor was created by Sureeyatanapas and Young (2009). Their method focused on incorporating SWCNTs into the amino-silane coupling agent, which is then deposited onto the surface of individual fibers. A solution of SWCNTs 0.1 wt% in ethanol was produced using 120 min of sonication. To this mixture, enough amino-silane (3-aminopropyl-triethoxysilane) coupling agent was added to raise the silane concentration of the SWCNT solution to 1.5 vol%. The amino-silane was then mixed and hydrolyzed over a period of 15 min. Finally, the deposition of the SWCNT−amino-silane solution onto the fiber surface was performed by immersing the fibers in the solution and heating it in an oven to 120 °C for 120 min. The fibers could then be infused with epoxy, which will adhere to the amino-silane coupling agent that is bonded to the fiber surface and the SWCNTs. The cross-section of a single fiber with deposited SWCNT−amino-silane coating and infused epoxy is shown in Figure 14.4. As commented on by Suryeeatanna and
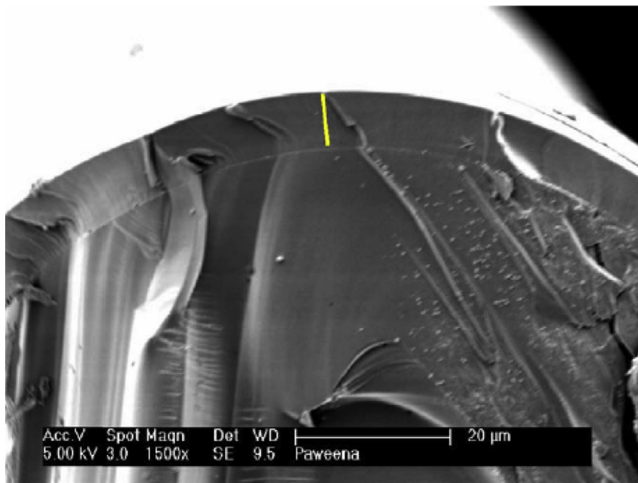
Figure 14.4 Glass fiber with deposited SWCNT−amino-silane coating and epoxy encapsulation layer.
Reprinted from Sureeyatanapas and Young (2009) with permission from Elsevier.

Young, the SWCNT−amino-silane layer is too thin to identify in this SEM image, but it is indeed present. This approach could easily be implemented for depositing the thin films onto larger glass fiber weaves. Afterward, either the strain sensitivity specimen approach or distributed electrode approach discussed over the past two subsections could be applied. Once prepared, GFRP composites can be fabricated with a wet layup or VARTM approach.

14.4 Electrical sensing measurements of embedded CNT thin films

Once the CNT-based sensors have been embedded within a GFRP composite, the change in the electrical properties as a function of applied strain and induced damage must be characterized. Three main methods for performing this electrical characterization have been performed in the literature. The methods include direct current (DC) electrical resistance, electrical impedance spectroscopy (EIS), and electrical impedance tomography (EIT). The first two methods are discrete electrical measurements in the time and frequency domains, respectively. On the other hand, EIT enables spatially distributed electrical measurements within a predefined sensing area. These three methods will be described in detail throughout this section.

14.4.1 DC resistance

The most frequently reported values for CNT thin-film-based strain sensing are DC resistance measurements. This time-domain electrical measurement method involves injecting an electrical current and measuring the corresponding voltage across the specimen. In general, there are two different configurations of DC resistance measurements: two-point and four-point DC resistance measurements. As indicated in the name, two-point resistance measurements are made by connecting to the conductive material using only two electrodes. Typically, these electrodes are fabricated such that they are across the width of a rectangular sample to enable a uniform current distribution. In one electrode, a specified current is injected and the other is set to ground. The voltage between these two electrodes is then measured. A schematic of this measurement is presented in Figure 14.5(a). The resistance is then calculated using Eqn (14.1):

$$R = \frac{V}{I} \tag{14.1}$$

The drawback to two-point resistance measurements is that the measurement includes the contact resistance between the electrodes and the specimen, which can lead to misconceptions regarding the material's electrical properties if the contact resistance is high. In order to remove the contact resistance from the resistance measurement, the four-point method is used. This method involves four electrodes,
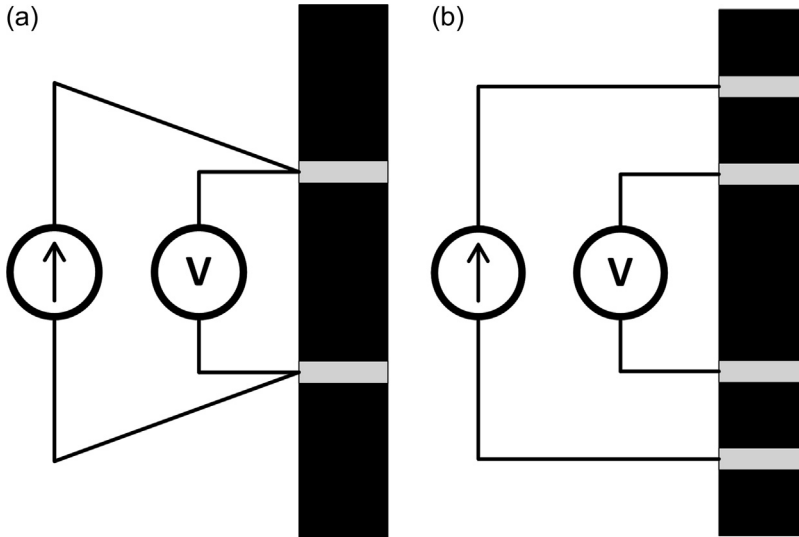
Figure 14.5 Schematics of the setup for a two-point (a) and four-point (b) resistance measurement.

which either are placed across the width of a rectangular sample in four places or are four points that are aligned. The latter configuration is commonly used for sheet resistance measurements on wafers in the semiconductor industry and called four-point probe resistance measurements. The current is injected between the outer electrodes, and the voltage is measured between the inner electrodes. The same calculation is used for these four-point resistance measurements as for the two-point resistance measurements. In this case, the calculated resistance value is for the region between the two inner electrodes. In order to perform these measurements, a current source and voltage meter are necessary, or a digital multimeter (DMM) is used with a two-point or four-point resistance setting. Some examples of commercially available DMMs that can take these measurements are a Keithley 2100 or an Agilent 34,411A.

14.4.2 Electrical impedance spectroscopy

EIS is an electrical measurement of the electrical impedance of a material over the frequency domain. These measurements are performed much like the DC resistance measurements, except that an alternating current (AC) is injected across the materials between two electrodes, and the complex AC voltage is measured at those two electrodes or at two electrodes located between the current electrodes. The AC current is injected with a frequency that is increased from the minimum specified frequency to the maximum specified frequency in a number of specified increments. How the complex AC voltage is measured is covered in several EIS texts in great detail (Barsoukov and Macdonald, 2005; Lvovich, 2012), and this complete measurement

(a)

(b)
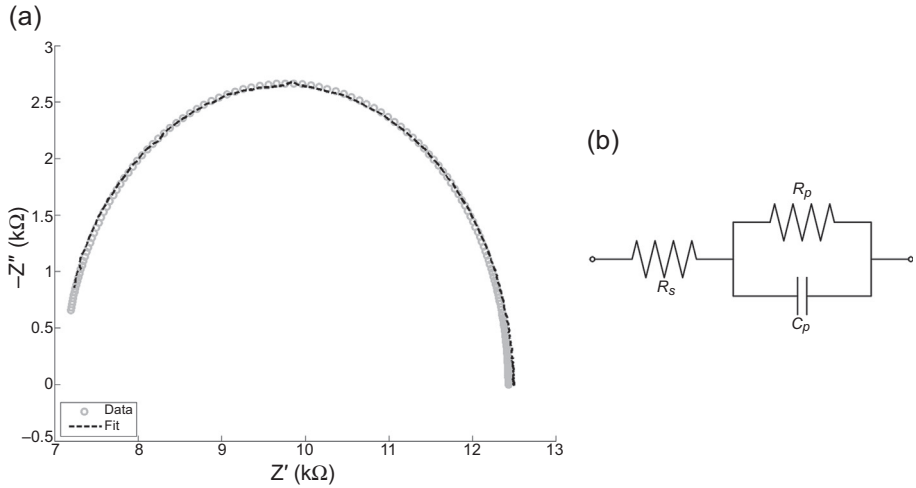
Figure 14.6 Example of an EIS measurement of an MWCNT−PSS/PVA thin film and the fit equivalent circuit typically used to fit EIS responses to applied strain in MWCNT−PSS/PVA thin films (a) and a diagram of the equivalent circuit used to model the film impedance (b).

is usually conducted by an impedance analyzer like Agilent's 4294A. Using an analogous equation to that of Ohm's law, one can calculate the complex electrical impedance for each frequency measured by an impedance analyzer (Eqn (14.2)).

$$\tilde{Z}(\omega) = \frac{\tilde{V}(\omega)}{\tilde{I}(\omega)} = Z' + iZ'' = |Z|e^{i\phi} = |Z| \angle \phi \tag{14.2}$$

The complex impedance is typically written in complex notation, Euler notation, or polar notation, shown respectively in Eqn (14.2). A typical EIS measurement for an MWCNT−PSS/PVA thin film is plotted in a Cole−Cole plot in Figure 14.7(a), which plots the real component of the complex impedance on the x-axis and the negative complex component of the impedance on the y-axis. Typically, the EIS measurements are fit to an equivalent circuit, like the one illustrated in Figure 14.7(b). The calculated complex impedance for this circuit is presented in Eqn (14.3).

$$\tilde{Z}(\omega) = Z'(\omega) + iZ''(\omega) = \left(R_s + \frac{R_p^{-1}}{R_p^{-2} + \omega^2 C_p^2} \right) - i \left(\frac{\omega C_p}{R_p^{-2} + \omega^2 C_p^2} \right) \tag{14.3}$$

This equivalent circuit yields an impedance response that is a half circle that is positively offset from the y-axis when plotted in a Cole−Cole plot, just like that from the EIS measurements of the MWCNT−PSS/PVA thin films. It should be noted that this equivalent circuit is nonunique and there are other equivalent circuits that will render the same impedance spectra (Barsoukov and Macdonald, 2005). This particular
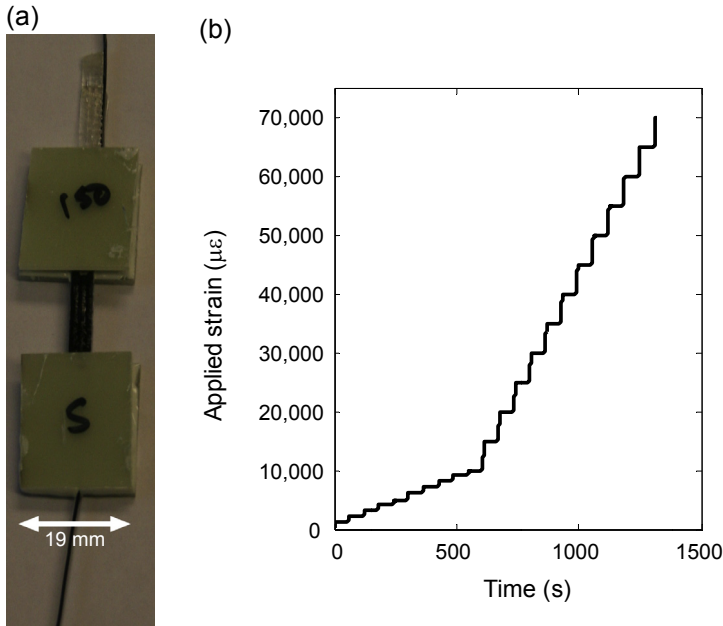
Figure 14.7 Example of a GFRP composite with embedded LbL thin film tensile coupon (a) and an example of a stepped strain test profile to which the specimens are subjected (b). Reprinted from Loyola et al. (2010a) with permission from Springer.

equivalent circuit was chosen due to the fact that it was originally used to model the EIS response from zirconia−yttria electrolyte thin films (Bauerle, 1969). Furthermore, these thin films were intended to detect transverse cracking in a GFRP composite under high levels of tensile loads, so the capacitive term was thought to be sensitive to these cracks by demonstrating an increase in capacitance (Loyola et al., 2010a). To fit the EIS measurements to this equivalent circuit, a nonlinear least squares methods can be implemented, like the function "lsqnonlin" in MATLAB (The Mathworks Inc, 2010). The nonlinear least squares fit to the data in Figure 14.7(a) (gray dots) is presented in the same figure as the black dashed line. The resulting equivalent circuit elements are presented in Table 14.1. It is these equivalent circuit values that are normally measured as a function of strain, damage, or environmental factor when using EIS measurements for electrical characterization.

Table 14.1 Equivalent circuit element values for the EIS measurement illustrated in Figure 14.6(a)

R_s	R_p	C_p
7105.6 Ohms	5327.6 Ohms	80.95 pF

14.4.3 Characterization of electrical property response to applied tensile strain

In order to couple these time-domain resistance and frequency-domain EIS measurements with mechanical testing, a few accommodations need to be made in the test setup to allow for both simultaneously. Assuming the specimens are configured in the same fashion as described in Section 14.3.1, the electrodes will be located in the same location where the load frame grips will engage the specimen in a tensile configured test. To protect the electrodes and ensure the load frame grips have solid contact with the specimen, tabs are attached to the specimen in the grip region. One example of these tabs is GFRP squares that are adhesively bonded to the GFRP composite with an embedded CNT thin film. Specifically, in the case of the specimens discussed in Section 14.3.1, the specimens were tabbed with four 1-in squares of G10/FR4 that are adhesively bonded to the GFRP specimen using Hysol 907, which was cured at 60 °C for 2 h. The finished specimen looks like the one shown in Figure 14.6(a).

Once the specimens are prepared, the tensile test must be configured to allow for the resistance measurements and any other measurements that are to be taken. Typically, the DMM is configured to take the resistance measurements continuously while the mechanical test is occurring. As DMMs can typically measure at rates into the kilohertz range, it is prudent to sample at a frequency at least that of the sample rate at which load frame is sampling the displacement, load, and/or strain. To obtain accurate strain measurements, strain gages or laser extensometers are typically employed and sampled at the same rate as the load frame. By sampling the resistance at the same rate or higher than the load frame, the linear interpolation can be employed to time-sync the load frame (load, displacement, and strain) to the resistance measurements for easy data analysis. However if several electrical measurements need to be taken, as in the case of taking concurrent electrical impedance spectroscopy (EIS) and DC resistance measurements, then a stepped strain profile is needed. The resistance and EIS measurements discussed in Section 14.5.1 and Section 14.5.2 were taken with this strategy. In general, the electrical measurements are taking with monotonically increasing strain. As there is interest in the electrical response to strain in the elastic and the postelastic regimes, two sampling frequencies were adopted. First, in the lower strain regime of $0-10,000$ $\mu\varepsilon$, the load frame was paused in steps of 1000 $\mu\varepsilon$ to have a higher resolution understanding of the response in the elastic regime as well as the transition point to the postelastic regime. From 10,000 $\mu\varepsilon$ to failure, the load frame is commanded to pause in increments of 10,000 $\mu\varepsilon$. The size of these steps was to nominally ensure that the tensile tests lasted less than 10 min, as mandated by the ASTM D3039 standard (ASTM International, 2008). Each pause was held for 60 s to allow for a DC resistance and an EIS measurement.

14.4.4 Electrical impedance tomography

Electrical impedance tomography (EIT) is an electrical soft-tomographic method that is capable of reconstructing the impedance or conductivity across a surface or volume. EIT measurements are based on a sensing region that is defined by a set of boundary
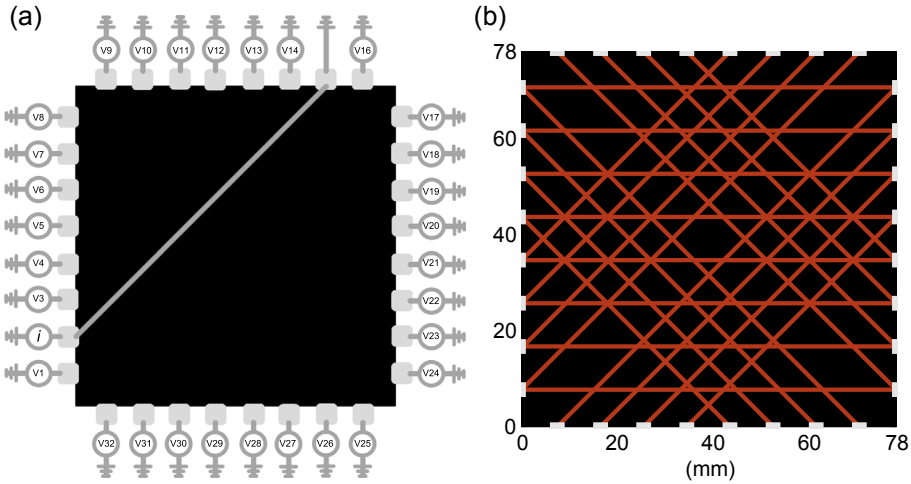
Figure 14.8 Illustration of an EIT measurement scheme (a) and a proposed current injection pattern for sensing with embedded MWCNT−PVDF thin films on unidirectional glass fiber weaves (b).
Figure 14.8(b) reprinted from Loyola et al. (2013a) with permission from SAGE.

electrodes. A current is propagated between two of these electrodes, and the resulting voltage distribution is measured at the remaining boundary electrodes. In the work presented here, the sensing area is defined to be a square that is bordered by eight equally spaced electrodes on each side, totaling 32 electrodes. An illustration of this scheme is presented in Figure 14.8(a), where current is injected at electrode 2 and electrode 15 is grounded. This measurement is performed several times for different current injection pairs to build a large set of voltage measurements. One such current injection pattern is illustrated in Figure 14.8(b) for a thin film deposited on a unidirectional glass fiber mat aligned in the vertical direction. Electrical conductivity and voltage are linked through Laplace's equation:

$$\nabla \cdot \sigma \nabla u = 0 \tag{14.4}$$

Typically, one knows the conductivity distribution across a surface or volume; and, using the boundary conditions, the voltage can be calculated. As EIT involves mapping boundary measurements to area or volume conductivity values, which leads to solving an ill-posed inverse problem. This problem is somewhat easy to understand if one looks at the finite element method approach to these reconstructions. Typically, analytical solutions to Laplace's equation (Eqn (14.4)) are not known or possible for most geometries, so a numerical solution is required in the form of the finite element method.

The finite element method is implemented using the weak form of Laplace's equation, which is an integral form of Eqn (14.4). This new formulation is presented in Eqn (14.5):

$$\iint_{\Omega} \nabla \phi \cdot \sigma_{\Omega} \cdot \nabla u \, dx dy = 0 \tag{14.5}$$

In Eqn (14.5), ϕ is the linear shape function for a given node, σ_Ω is the conductivity in element Ω, and u is the voltage value at a node around element Ω. Equation (14.5) governs the physics of all nonelectrode node relations. As most of the glass fiber mats that the thin films will be deposited upon have a directionality of the weave, the conductivity can be highly anisotropic. To accommodate this, the scalar electrical conductivity is replaced with a matrix value, as shown in Eqn (14.6).

$$\tilde{\sigma} = \begin{bmatrix} \sigma_x & 0 \\ 0 & \sigma_y \end{bmatrix} = \begin{bmatrix} 1 & 0 \\ 0 & \dfrac{\sigma_y}{\sigma_x} \end{bmatrix} \sigma_x \tag{14.6}$$

To implement the boundary conditions associated with the electrodes, Eqns (14.7) and (14.8) are used to account for the current injection, ground condition, and voltage measurements.

$$\int_{E_l} \sigma \frac{\partial u}{\partial v} \, \mathrm{d}s = I_l \tag{14.7}$$

$$u + z_l \sigma \frac{\partial u}{\partial v} = V_l \tag{14.8}$$

Equation (14.7) is used to account for the current that is injected into electrode l. To account for the grounded electrode and to calculate the voltage at the remaining electrodes, Eqn (14.8) is used where V_l is the voltage at electrode l.

As stated previously, this application of the finite element method to the Laplace equation is just performing the forward problem, or measuring the voltage distribution across a known conductive material. However, if the boundary voltage measurements are known for a set current pattern, then the inverse problem must be solved to determine the conductivity distribution. Due to the awkwardness of the inverse problem, it took until 1980 for a solution to be found by Calderon (2006). After 1980, several new solution strategies have been developed, including a linear method developed by Adler and Guardo called maximum a posteriori (MAP) (Adler and Guardo, 1996). MAP linearizes the EIT inverse problem by reconstructing changes in electrical conductivity as a function of changes in the voltage measurements for an identical current injection pattern. The approach taken is given in Eqn (14.9).

$$\frac{\Delta\sigma}{\sigma_0} = \left(H^T W H + \lambda R\right)^{-1} H^T W \left(\frac{\Delta V}{V_0}\right) \tag{14.9}$$

The MAP approach solves for the normalized change in conductivity using the normalized change in voltage, primarily using the sensitivity matrix (H). The sensitivity matrix calculates how an infinitesimally small change in conductivity in a single element changes the boundary voltage measurements, otherwise known as

the Jacobian. One of the benefits to performing normalized differential imaging is that the calculation is insensitive to the specified current amplitudes and specified conductivity distribution during the sensitivity matrix calculation. During the EIT measurement, replicate voltage measurements are taken to gain a distribution for each of the voltage measurements. Typically, these distributions are Gaussian and these related statistics are taken into account using the variance matrix W, calculated as shown in Eqn (14.10).

$$W_{i,i} = \frac{1}{\alpha_i}, \; W_{i,j} = 0 \quad \text{for} \quad i \neq j \tag{14.10}$$

The variance matrix is constructed using the variance of voltage measurement i, which is specified as α_i.

As the inverse calculation is ill-posed, a way to stabilize the solution is necessary, and this is typically done through regularization. The regularization implemented with the MAP algorithm is based on a smoothing approach, implemented via a high-pass filter. This exact approach is defined via the regularization matrix R and is a Gaussian high-pass filter (Adler and Guardo, 1996). The regularization hyperparameter governs the amount of smoothness in the reconstruction solution. Adler and Guardo have developed a metric called the noise figure (NF), which is the ratio of the signal-to-noise ratio (SNR) of the voltage measurements and the signal-to-noise ratio of the reconstruction using those voltage measurements as the specified hyperparameter value (Adler and Guardo, 1996; Graham and Adler, 2006). The exact equation is given in Eqn (14.11):

$$\text{NF} = \frac{\text{SNR}_V}{\text{SNR}_\sigma(\lambda)} \tag{14.11}$$

The hyperparameter that leads to the SNR for the voltage measurements equaling that of the reconstructed conductivity distribution is chosen, which corresponds to an NF of 1. Once the hyperparameter is determined, the reconstruction of any differential EIT measurements can be made assuming the same geometry, current injection pattern, and current magnitude between the two measurements and the FEM model used to determine the sensitivity matrix and hyperparameter values.

14.5 Typical results from in situ electrical measurements of CNT thin films exposed to mechanical strain or damage

This section presents several examples of strain sensing and damage detection that have been performed with embedded thin films in GFRP composites. These show the promise of this emerging field that will allow for the implementation of smart GFRP structures.

14.5.1 DC resistance

Numerous researchers have focused on using CNT-based thin films applied to a structure to perform strain measurements using DC resistance (Dharap et al., 2004; Vemuru et al., 2009; Loh et al., 2008; Loyola et al., 2010b, 2011; Rein et al., 2011). These thin films have been generally found to be strain sensitive, much in the manner that foil-based strain gages are. Due to their direct deposition and distributed nature, these films also tend to be sensitive to damage on the substrate as well (Loyola et al., 2013c). This is also the case for embedded films. As an example, Figure 14.9 contains the plot of the DC resistance strain response of an MWCNT−PVDF thin film embedded on a quasi-unidirectional glass fiber weave, as described in Section 14.3.1. The specimen was subjected to a monotonically increasing stepped displacement profile, as described in Section 14.4.3. As shown in Figure 14.9, the response of the DC resistance is nonlinear, and is indicative of a quadratic-type response. It is believed that these nonlinear responses are due to traverse cracking of the GFRP, which causes tearing in the CNT thin films. This has been seen in surface-mounted CNT-based thin films (Loyola et al., 2013c; Thostenson and Chou, 2006), and it is assumed that this occurs in embedded films as well. However, there has yet to be a journal article to prove this.

Typically, the nonlinear region is preceded by a linear region that is due to elastic deformation of the thin film and responds much like a strain gage. Such an example can be found among the EIS equivalent circuit element responses in Figure 14.10(b) for an MWCNT−PSS/PVA thin film embedded on an identical quasi-unidirectional glass fiber fabric. In this case, there is a linear region that extends to 10,000 µε before
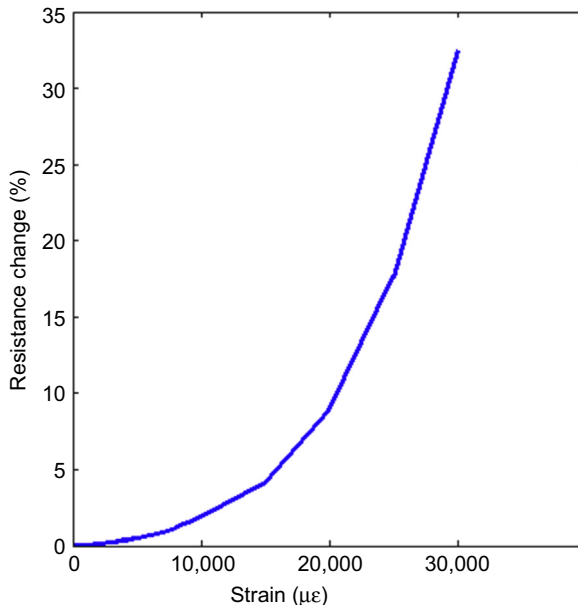
Figure 14.9 Resistance response to applied strain of a 5 wt% MWCNT−PVDF thin film.

(a)

(b)
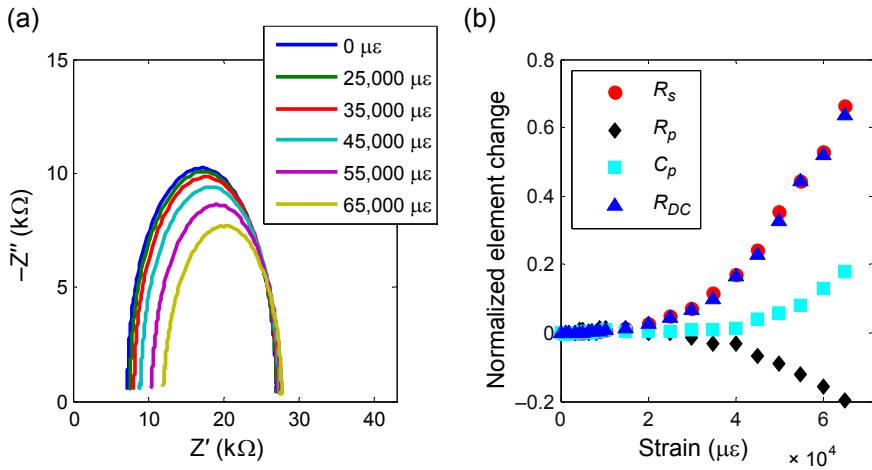
Figure 14.10 EIS response to applied strain of an embedded MWCNT−PSS/PVA thin film. Reprinted from Loyola et al. (2010a) with permission from Springer.

transitioning to a nonlinear response to strain. Within this linear strain response regime, the normalized change in resistance and hence the strain sensitivity (S) are given in Eqns (14.12) and (14.13).

$$\frac{\Delta R}{R_0} = S\varepsilon = (1 + 2v)\varepsilon \tag{14.12}$$

$$S = 1 + 2v \tag{14.13}$$

Most solid materials have a poison ratio (v) from 0.3 to 0.5, which corresponds to strain sensitivities from 1.6 to 2 for purely geometric strain sensitivities. From the work performed by Loyola et al., it was shown that the strain sensitivity for MWCNT−PSS/PVA films embedded in GFRP composites on average ranges from 0.55 to 1.37. It is thought that these lower than expected strain sensitivities are due to changes in the resistivity of the MWCNT−PSS/PVA thin films from reorganization of the MWCNTs. This phenomenon is not well understood, but it could also be a contributing factor in the nonlinear response seen in high-strain regimes. This is an area of research that would be valuable to progress the use of this sensing method.

14.5.2 Electrical impedance spectroscopy

In addition to focusing on DC resistance strain sensitivity, EIS strain sensitivity can yield additional information obtained from the frequency domain. MWCNT−PSS/PVA specimens were fabricated in the fashion specified in Section 14.4.3. These specimens were subjected to monotonically increasing strain with pauses as specified in the same section. An example of the effect of the applied strain on the EIS measurements

is apparent in the Cole−Cole plot in Figure 14.10 of the EIS spectra taken at several applied strain levels. As the applied strain increases, the high-frequency region of the impedance spectrum increases in real impedance while the negative value of the complex impedance decreases. In order to understand how these spectra changes affect the equivalent circuit elements, each EIS spectrum was fit to the equivalent circuit model, given in Eqn (14.3). Once these values were determined for each level of strain, they can be plotted as a function of applied strain as done in Figure 14.10(b). From these data, it is determined that the DC resistance value matches that of the R_s element of the EIS equivalent circuit model.

The parallel components of the equivalent circuit strain response are more complex to interpret. A significant response from R_p and C_p does not occur until the high-strain regime in which the DC resistance and R_s are nonlinear. As the response in this strain regime is suspected to be due to cracking within the film transmitted from the substrate, it is assumed that these responses in the parallel circuit elements are in fact due to these effects, but hypotheses of effects of the Poisson effect compressing the MWCNTs together have also been made (Loyola et al., 2010a, 2013c; Thostenson and Chou, 2006). It would stand to reason that it is the inter-CNT interactions that are governing this response, as this would be analogous to the work that Bauerle performed with zirconia−yttria electrolyte thin films (Bauerle, 1969). In the case of those thin films, the parallel components captured the grain boundary effects to the electrical impedance spectra.

14.5.3 Electrical impedance tomography

Using DC resistance or EIS measurements for strain or damage sensing yields discrete or averaged results between the two or four electrodes of the measurement. However, it is extremely valuable to obtain spatial information as well. This would allow for a location, size, and severity determination, which would allow technicians to quickly find and repair damage to a structure. Specimens that were fabricated using the approach specified in Section 14.3.2 were subjected to two kinds of damage, and EIT measurements were taken before and after each damage event for differential EIT reconstructions. To demonstrate the ability of the embedded MWCNT−PVDF sensor in a GFRP composite used in conjunction with differential EIT measurements to detect defined amounts of damage, the EIT specimens were drilled with 6.35 mm holes at nine places distributed across the sensing area. The example given in Figure 14.11(a) is a specimen that has been drilled three times in a diagonal pattern. The corresponding EIT reconstruction is presented in Figure 14.11(b). The conductivity change due to the two holes drilled near the electrodes is easily discernible. This is because the resolution and sensitivity of the EIT method are highest near the electrodes and decrease as the damage gets farther from the electrodes. Typically, the total conductivity change across the sensing area from any point of damage has the same total integrated effect, but it may be spread out over a larger area, making it harder to see in contrast to more isolated areas of conductivity change.

As these damage detection methods need to be able to detect damage from real-world events, EIT sensing specimens of the same configuration were subjected

(a)

(b)
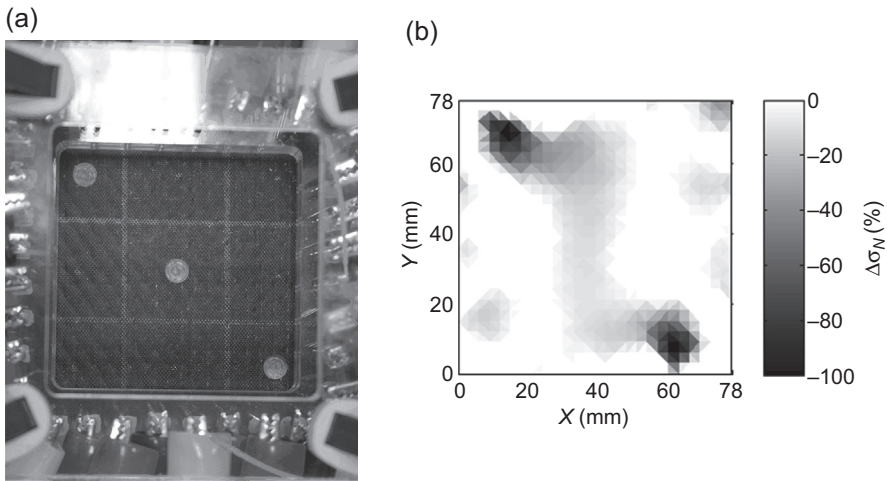
Figure 14.11 Photographic image of a drilled EIT specimen (a) and the corresponding EIT reconstruction (b).
Reprinted from Loyola et al. (2013a) with permission from SAGE.

(a)

(b)
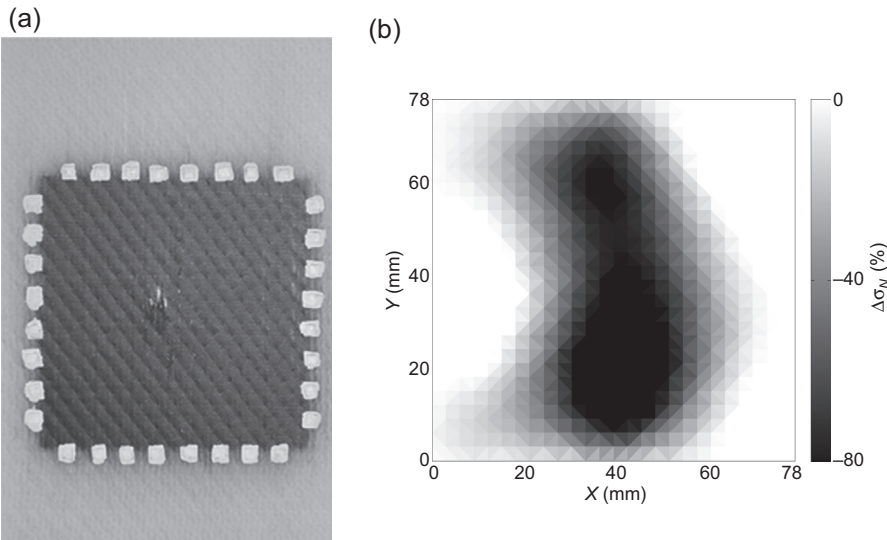
Figure 14.12 Photographic image of an impacted GFRP specimen with embedded MWCNT−PVDF thin film and EIT sensing region (a) and corresponding EIT reconstruction (b).

to drop-weight impact events of 20, 60, 100, and 140 J using a 38.1 mm hemispherical tup. Figure 14.12(a) shows the back side of one of these specimens that was subjected to 100 J of energy. In the center of the sensing area, the GFRP has blown out, which is a typical damage mode above the perforation threshold. The corresponding change in

conductivity as captured by the EIT method is presented in Figure 14.12(b). The conductivity change is distributed vertically across the reconstruction area, which is most likely due to not capturing the anisotropy of the conductivity of the MWCNT−PVDF thin film from the underlying unidirectional glass fiber mat, which is aligned vertically. As the electrical network is completely broken in the perforated area, the response expected would be a 100 percent decrease in that area. However, due to the spreading of the conductivity change by the EIT reconstruction, it is reconstructed at only a magnitude of 80 percent. These aspects should be considered whenever analyzing EIT reconstructed data.

14.6 Present challenges and future directions

Embedding CNT-based thin films is still in its infancy, and it has several important hurdles that must be surmounted to make this a viable option for structural health monitoring in most GFRP structures. For use as a strain sensor, the biggest challenge will be identifying the phenomenological reason for the nonlinear response at higher strain values. As the thin films are embedded, determining which phenomenon is the cause of this response will be embedded as well. To fully understand these responses will most likely require a research group employing micro-X-Ray computed tomography concurrent with DC resistance or EIS measurements while a specimen is under uniaxial tension. Furthermore, a more systematic approach to implementing EIS as an analytical tool is necessary. Hypothetically, the equivalent circuit used to fit the EIS responses is a very reasonable approach. However, that equivalent circuit response is not unique, as other equivalent circuits can reproduce the same impedance spectra. It may be that a modeling approach will need to be taken to evaluate these responses. If a research group can understand the resistance and inductance of each CNT, the resistance and capacitance of each CNT junction, and the effect of the electrodes, then a full understanding of these may be possible.

Electrical impedance tomography has been a field in medical imaging since Calderon developed the solution to the EIT inverse problem. Although a number of algorithms to solve a variety of the EIT problems exist, the method for taking these measurements is still in its infancy for structures. How does one conduct multilayer sensing in an FRP composite? The electrodes or wiring can easily contribute to a degradation of the performance of a structure. Second, the sensitivity and resolution of EIT are much lower at the center of a sensing area, which is another hurdle that will have to be tackled. Finally, the speed with which EIT measurements are taken will need to be improved. The EIT measurements included in this chapter all took about 90 s apiece. This is prohibitively long for an in situ strain-sensing or damage detection device if monitoring is required at a rate to catch the damage mode development in progress, such as cracking, delamination, and fiber breakage during a low-velocity impact event.

There are plenty of new topics that are left to understand within the disciplines encompassed by the methods used for embedded damage detection using CNT-based thin films in GFRP composites.

14.7   Key sources of information

As of July 26, 2014, Google Scholar reports that there are about 702,000 references focused on CNTs. Although most of these do not focus on CNT thin films, there are still a significant number of journal articles focused on this research. There are a few very good review articles that outline how CNTs are being used for SHM as well as other purposes (Baughman et al., 2002; Li et al., 2008; Thostenson et al., 2001). In addition, it would be extremely difficult to include here the number of books dedicated to this subject as well. However, a book dedicated to using CNT nanocomposites for SHM has been edited by Paipetus and Kostopoulos entitled "Carbon Nanotube Enhanced Aerospace Composite Materials," which focuses on various approaches that have been taken that utilize CNTs in aerospace-related composite structures (Paipetis and Kostopoulos, 2013). Prior to embarking on any research associated with CNTs, it is wise to perform a thorough literature search, as undoubtedly a group has performed research similar to any new ideas. However, with the number of CNT sensors that are available, novel applications are still possible.

As for EIT, the best resource is in the form of an EIT script library called EIDORS: Electrical Impedance Tomography and Diffuse Optical Tomography Reconstruction Software (EIDORS Collaboration, 2012). This is a collaborative software package that runs on MATLAB (The Mathworks Inc, 2010) or Octave (Octave Collaboration, 2014), and can perform all of the reconstruction steps required to perform EIT measurements and reconstructions. Secondly, a textbook edited by David Holder entitled "Electrical Impedance Tomography: Methods, History, and Applications" gives many examples of data collection methods, reconstruction strategies, and medical applications that have been performed using EIT (Holder, 2010). Finally, only a handful of papers have been released on using EIT for SHM purposes. These papers have focused on strain sensing (Loyola et al., 2013b; Loh et al., 2009), crack detection (Lazarovitch et al., 2002), corrosion detection (Pyo et al., 2011; Hou et al., 2007), pH sensing (Loh et al., 2007), impact detection (Loyola et al., 2013a; Loh et al., 2009), and tactile sensing (Alirezaei et al., 2007, 2009).

Acknowledgments

References

Amano, M., Okabe, Y., Takeda, N., Ozaki, T., December 1, 2007. Structural health monitoring of an advanced grid structure with embedded fiber bragg grating sensors. Structural Health Monitoring 6 (4), 309−324.

Antunes, P., Lima, H., Alberto, N., Bilro, L., Pinto, P., Costa, A., Rodrigues, H., Pinto, J.L., Nogueira, R., Varum, H., André, P.S., 2011. Optical sensors based on fiber bragg gratings for structural health monitoring new developments in sensing technology for structural health monitoring. In: Mukhopadhyay, S.C. (Ed.), Lecture Notes in Electrical Engineering. Springer, Berlin Heidelberg, pp. 253−295.

ASTM International, 2008. ASTM D3039/D3039M - 08 Standard Test Method for Tensile Properties of Polymer Matrix Composite Materials. ASTM Standard D3039.

Adler, A., Guardo, R., 1996. Electrical impedance tomography: regularized imaging and contrast detection. IEEE Transactions on Medical Imaging 15 (2), 170−179.

Alirezaei, H., Nagakubo, A., Kuniyoshi, Y., 2007. A highly stretchable tactile distribution sensor for smooth surfaced humanoids. In: 7th IEEE-RAS International Conference on Humanoid Robots, Pittsburgh, Pennsylvania, USA, pp. 167−173.

Alirezaei, H., Nagakubo, A., Kuniyoshi, Y., 2009. A tactile distribution sensor which enables stable measurement under high and dynamic stretch. In: IEEE Symposium on 3D User Interfaces, Lafayette, Louisiana, USA, pp. 87−93.

Betz, D., Staudigel, L., Trutzel, M.N., 2002. Test of a fiber Bragg grating sensor network for commercial aircraft structures. In: Optical Fiber Sensors Conference Technical Digest, Portland, Oregon, USA vol. 1, pp. 55−58.

Bastianini, F., Corradi, M., Borri, A., Tommaso, A., 2005. Retrofit and monitoring of an historical building using "Smart" CFRP with embedded fibre optic Brillouin sensors. Construction and Building Materials 19 (7), 525−535.

Beattie, A., 1997. Acoustic emission monitoring of a wind turbine blade during a fatigue test. In: American Society of Mechanical Engineers Wind Energy Symposium, Reno, NV, USA, pp. 239−248.

Baughman, R., Zakhidov, A., De Heer, W., 2002. Carbon nanotubes−the route toward applications. Science 297 (5582), 787.

Barsoukov, E., Macdonald, J., 2005. Impedance Spectroscopy: Theory, Experiment, and Applications. Wiley-Interscience, Hoboken, NJ, USA.

Bauerle, J., 1969. Study of solid electrolyte polarization by a complex admittance method. Journal of Physics and Chemistry of Solids 30 (12), 2657−2670.

Ciampa, F., Meo, M., January 1, 2012. Impact detection in anisotropic materials using a time reversal approach. Structural Health Monitoring 11 (1), 43−49.

Chambers, J., Wardle, B., and Kessler, S., Durability Assessment of Lamb Wave-Based Structural Health Monitoring Nodes. In: 47th AIAA/ASME/ASCE/AHS/ASC Structures, Structural Dynamics, and Materials Conference, Newport, Rhode Island, USA.

Choi, K., Chang, F., 1994. Identification of foreign object impact in structures using distributed sensors. Journal of Intelligent Material Systems and Structures 5 (6), 864.

Calderon, A.P., 2006. On an inverse boundary value problem. Computational and Applied Mathematics 25 (2−3), 133−138.

Dharap, P., Li, Z., Nagarajaiah, S., Barrera, E., 2004. Nanotube film based on single-wall carbon nanotubes for strain sensing. Nanotechnology 15, 379−382.

Decher, G., Schlenoff, J.B., 2003. Multilayer Thin Films. Wiley-VCH, Weinheim, Germany.

De, S., Lyons, P.E., Sorel, S., Doherty, E.M., King, P.J., Blau, W.J., Nirmalraj, P.N., Boland, J.J., Scardaci, V., Joimel, J., 2009. Transparent, flexible, and highly conductive thin films based on polymer−nanotube composites. ACS Nano 3 (3), 714−720.

EIDORS Collaboration, 2012. Electrical Impedance Tomography and Diffuse Optical Tomography Reconstruction Software.

Graham, B., Adler, A., 2006. Objective selection of hyperparameter for EIT. Physiological Measurement 27 (S65).

Haksoo, C., Sukwon, C., Hojung, C., 2008. Structural health monitoring system based on strain gauge enabled wireless sensor nodes. In: 5th International Conference on Networked Sensing Systems. Kanazawa, Japan, pp. 211−214.

Hu, N., Karube, Y., Arai, M., Watanabe, T., Yan, C., Li, Y., Liu, Y., Fukunaga, H., 2010. Investigation on sensitivity of a polymer/carbon nanotube composite strain sensor. Carbon 48 (3), 680−687.

Holder, D.S., 2010. Electrical Impedance Tomography: Methods, History and Applications. Institute of Physics Publishing, London, United Kingdom.

Hou, T., Loh, K., Lynch, J., 2007. Spatial conductivity mapping of carbon nanotube composite thin films by electrical impedance tomography for sensing applications. Nanotechnology 18 (31), 315501.

Ian, R., Peter, F., Stuart, M., 2002. Optical fibre acoustic emission sensor for damage detection in carbon fibre composite structures. Measurement Science and Technology 13 (1), N5.

Irving, P., Thiagarajan, C., 1998. Fatigue damage characterization in carbon fibre composite materials using an electrical potential technique. Smart Materials and Structures 7 (4), 456−466.

Iijima, S., 1991. Helical microtubules of graphitic carbon. Nature 354 (6348), 56−58.

Kesavan, A., Deivasigamani, M., John, S., Herszberg, I., 2006. Damage detection in T-joint composite structures. Composite Structures 75 (1−4), 313−320.

Kesavan, A., John, S., Herszberg, I., September 1, 2008. Strain-based structural health monitoring of complex composite structures. Structural Health Monitoring 7 (3), 203−213.

Kersey, A., Davis, M., Berkoff, T., Dandridge, A., Jones, R., Tsai, T., Cogdell, G., Wang, G., Havsgaard, G., Pran, K., 1997. Transient load monitoring on a composite hull ship using distributed fiber optic Bragg grating sensors. In: Smart Structures and Materials 1997: Smart Sensing, Processing, and Instrumentation. San Diego, CA, USA, pp. 421−430.

Kuang, K., Cantwell, W., 2003. Use of conventional optical fibers and fiber Bragg gratings for damage detection in advanced composite structures: a review. Applied Mechanics Reviews 56, 493.

Kessler, S., Raghavan, A., 2009. Vector-based damage localization for anisotropic composite laminates. In: Proceedings of the International Workshop on Structural Health Monitoring. Stanford, CA, USA.

Kang, I., Schulz, M.J., Kim, J.H., Shanov, V., Shi, D., 2006. A carbon nanotube strain sensor for structural health monitoring. Smart Materials and Structures 15, 737.

Kozlov, M., Quarmyne, M., Chen, W., McCarthy, T., 2003. Adsorption of poly (vinyl alcohol) onto hydrophobic substrates. A general approach for hydrophilizing and chemically activating surfaces. Macromolecules 36 (16), 6054−6059.

Li, C., Thostenson, E.T., Chou, T.-W., 2008. Sensors and actuators based on carbon nanotubes and their composites: a review. Composites Science and Technology 68 (6), 1227−1249.

Lin, M., Chang, F., 2002. The manufacture of composite structures with a built-in network of piezoceramics. Composites Science and Technology 62 (7−8), 919−939.

Loh, K.J., Kim, J., Lynch, J.P., Kam, N.W.S., Kotov, N.A., 2007. Multifunctional layer-by-layer carbon nanotube polyelectrolyte thin films for strain and corrosion sensing. Smart Materials and Structures 16 (2), 429−438.

Loyola, B.R., La Saponara, V., Loh, K.J., 2010a. In situ strain monitoring of fiber-reinforced polymers using embedded piezoresistive nanocomposites. Journal of Material Science 45 (24), 6786−6798.

Loyola, B.R., Briggs, T.M., Arronche, L., Loh, K.J., Saponara, V.L., O'Bryan, G., Skinner, J.L., 2013a. Detection of spatially distributed damage in fiber-reinforced polymer composites. Structural Health Monitoring 12 (3), 225−239.

Loyola, B.R., Saponara, V.L., Loh, K.J., Briggs, T.M., O'Bryan, G., Skinner, J.L., 2013b. Spatial sensing using electrical impedance tomography. IEEE Sensors Journal 13 (6), 2357−2367.

Loyola, B.R., Zhao, Y., Loh, K.J., Saponara, V.L., 2013c. The electrical response of carbon nanotube-based thin film sensors subjected to mechanical and environmental effects. Smart Materials and Structures 22 (2).

Lvovich, V.F., 2012. Impedance Spectroscopy: Applications to Electrochemical and Dielectric Phenomena. John Wiley & Sons, Hoboken, New Jersey, USA.

Loh, K.J., Lynch, J.P., Shim, B.S., Kotov, N.A., 2008. Tailoring piezoresistive sensitivity of multilayer carbon nanotube composite strain sensors. Journal of Intelligent Material Systems and Structures 19 (7), 747−764.

Loyola, B.R., La Saponara, V., Loh, K.J., 2010b. Characterizing the self-sensing performance of carbon nanotube-enhanced fiber-reinforced polymers. In: Nondestructive Characterization for Composite Materials, Aerospace Engineering, Civil Infrastructure, and Homeland Security 2010, San Diego, CA, USA, pp. 76490F−76512F.

Loyola, B.R., La Saponara, V., Loh, K.J., 2011. Investigating the electromechanical performance of carbon nanotube strain sensors embedded in GFRP composites. In: Nondestructive Characterization for Composite Materials, Aerospace Engineering, Civil Infrastructure, and Homeland Security 2011, San Diego, CA, USA.

Loh, K.J., Hou, T.C., Lynch, J.P., Kotov, N.A., 2009. Carbon nanotube sensing skins for spatial strain and impact damage identification. Journal of Nondestructive Evaluation 28 (1), 9−25.

Lazarovitch, R., Rittel, D., Bucher, I., 2002. Experimental crack identification using electrical impedance tomography. NDT and E International 35 (5), 301−316.

Octave Collaboration, 2014. GNU Octave.

Paipetis, A., Kostopoulos, V., 2013. Carbon Nanotube Enhanced Aerospace Composite Materials. Springer, Dordrecht, Netherlands.

Pyo, S., Loh, K.J., Hou, T.C., Jarva, E., Lynch, J.P., 2011. A wireless impedance analyzer for automated tomographic mapping of a nanoengineered sensing skin. Smart Structures and Systems 8 (1), 139−155.

Rosenker, M.V., 2006. Safety recommendation A-06-27 and -28. In: National Transportation Safety Board.

Rumsey, M.A., Paquette, J.A., 2008. Structural health monitoring of wind turbine blades. In: SPIE Smart Structures/NDE, San Diego, CA, USA.

Rein, M.D., Breuer, O., Wagner, H.D., February 7, 2011. Sensors and sensitivity: carbon nanotube buckypaper films as strain sensing devices. Composites Science and Technology 71 (3), 373−381.

Sohn, H., Farrar, C., Hunter, N., Worden, K., 2001. Applying the LANL Statistical Pattern Recognition Paradigm for Structural Health Monitoring to Data from a Surface-Effect Fast Patrol Boat. Los Alamos National Laboratory vol. LA-13761-MS.

Shindo, Y., Kuronuma, Y., Takeda, T., Narita, F., Fu, S.Y., 2011. Electrical resistance change and crack behavior in carbon nanotube/polymer composites under tensile loading. Composites Part B: Engineering 39−43.

Sureeyatanapas, P., Young, R.J., 2009. SWNT composite coatings as a strain sensor on glass fibres in model epoxy composites. Composites Science and Technology 69 (10), 1547−1552.

Tang, H.-Y., Winkelmann, C., Lestari, W., La Saponara, V., 2011. Composite structural health monitoring through use of embedded PZT sensors. Journal of Intelligent Material Systems and Structures 22 (8), 739−755.

Tsutsui, H., Kawamata, A., Sanda, T., Takeda, N., December 2004. Detection of impact damage of stiffened composite panels using embedded small-diameter optical fibers. Smart Materials and Structures 13 (6), 1284−1290.

Todoroki, A., 2008. Delamination monitoring analysis of CFRP structures using multi-probe electrical method. Journal of Intelligent Material Systems and Structures 19 (3), 291−298.

Todoroki, A., Tanaka, Y., Shimamura, Y., 2002. Delamination monitoring of graphite/epoxy laminated composite plate of electric resistance change method. Composites Science and Technology 62 (9), 1151−1160.

Thostenson, E., Ren, Z., Chou, T.-W., 2001. Advances in the science and technology of carbon nanotubes and their composites: a review. Composites Science and Technology 61 (13), 1899−1912.

The Mathworks Inc, 2010. MATLAB 2014a.

Thostenson, E.T., Chou, T.-W., 2006. Carbon nanotube networks: sensing of distributed strain and damage for life prediction and self healing. Advanced Materials 18 (21), 2837−2841.

Vemuru, S., Wahi, R., Nagarajaiah, S., Ajayan, P., 2009. Strain sensing using a multiwalled carbon nanotube film. The Journal of Strain Analysis for Engineering Design 44 (7), 555−562.

Wenger, M.P., Blanas, P., Shuford, R.J., Das-Gupta, D.K., 1996. Acoustic emission signal detection by ceramic/polymer composite piezoelectrets embedded in glass-epoxy laminates. Polymer Engineering and Science 36 (24), 2945−2954.

Winkelmann, C., Tang, H.-Y., La Saponara, V., 2008. Influence of embedded structural health monitoring sensors on the mechanical performance of glass/epoxy composites. In: SAMPE 2008, Long Beach, CA, USA.

Wang, S., Chung, D., 2000. Piezoresistivity in continuous carbon fiber polymer-matrix composite. Polymer Composites 21 (1), 13−19.

Wang, S., Chung, D., 2007. Negative piezoresistivity in continuous carbon fiber epoxy-matrix composite. Journal of Materials Science 42 (13), 4987−4995.

Wang, X., Fu, X., Chung, D., 1999. Strain sensing using carbon fiber. Journal of Materials Research 14 (3), 790−802.

Wang, S., Chung, D.D.L., 2006. Self-sensing of flexural strain and damage in carbon fiber polymer-matrix composite by electrical resistance measurement. Carbon 44 (13), 2739−2751.

Wang, S., Chung, D.D.L., Chung, J.H., 2005. Impact damage of carbon fiber polymer−matrix composites, studied by electrical resistance measurement. Composites Part A: Applied Science and Manufacturing 36 (12), 1707−1715, 12.

Yun, J., 2011. Development of Structural Health Monitoring Systems Incorporating Acoustic Emission Detection for Spacecraft and Wind Turbine Blades. Electrical and Computer Engineering, Virginia Tech.

Yang, W., Wang, Y., Li, J., Yang, X., 2010. Polymer wrapping technique: an effective route to prepare Pt nanoflower/carbon nanotube hybrids and application in oxygen reduction. Energy & Environmental Science 3 (1), 144−149.

Zhao, Y., Loyola, B.R., Loh, K.J., 2011. Mechanical and viscoelastic characterization of layer-by-layer carbon nanotube-polyelectrolyte thin films. Smart Materials and Structures 20 (7), 075020.

Strain-sensing smart skin: a noncontact optical strain sensor using single-walled carbon nanotubes

15

Satish Nagarajaiah, R. Bruce Weisman, Peng Sun,
Sergei M. Bachilo, Yongchao Yang
Rice University, Houston, TX, USA

15.1   Introduction

In structural engineering, routine inspection and maintenance are vital to ensure safe operation and optimized service life of critical structures. Strain measured on the surface of any structure provides direct firsthand information about its condition. Traditional technologies used for measuring strain, such as resistance strain gages and fiber Bragg grating (FBG) sensors (Hill and Meltz, 1997), can monitor only at discrete locations and along specific directions, and have limited ability to measure strains on small length scales (Obitayo and Liu, 2012).

By exploiting the dependence of the electronic properties of carbon nanotubes (CNTs) on their atomic structure, Peng and Cho (2000) discovered that surface strain can modulate the conductance of CNTs quantitatively and predictably. Dharap et al. (2004) reported a nanotube-based film sensor based on strain-induced changes in electrical transport properties. For many years, piezoelectric strain sensors have been successfully used as vibration sensors in smart structures, providing the benefits of simple interface circuitry and high sensitivity (Yong, 2013). Recently, microelectromechanical system (MEMS) double-ended tuning fork (DETF) strain gauges (Myers, 2010) have been investigated as sensors, based on the dependence of their resonant frequency on strain. Although these newer strain-sensing approaches can achieve high spatial resolution and strain sensitivity, they still require electrical connections to the sensor elements in order to obtain strain readings.

Aside from the aforementioned pointwise strain gauge techniques, various full-field noncontact optical methods have also been developed. The existing noncontact optical methods can be classified into two types (Pan et al., 2009): (1) interferometric techniques, such as holography interferometry, speckle interferometry, Moire interferometry, and photoelasticity; and (2) noninterferometric techniques, such as the grid method (Goldrein et al., 1995), digital image correlation (DIC) (Pan, 2007; Hamada et al., 2014), and digital volume correlation (DVC) with X-ray microcomputed tomography (Germaneau et al., 2008). The interferometric techniques have been proposed and developed over the past few decades. They identify material changes based on variations

in transmission intensities, phase changes, diffraction properties, or interference fringe patterns (Ajovalasit et al., 2010). Although they can provide full-field strain measurements without physical contact, they usually require a model of actual structure, tedious calculations to separate the values of principal stresses, and expensive equipment. The noninterferometric techniques have been extensively investigated and improved for reducing computation complexity, achieving high accuracy measurements of deformations. However, the DIC or DVC methods suffer some disadvantages, such as the requirements for a random gray intensity distribution or speckle pattern distribution, heavy dependence on the quality of the imaging system, relatively low strain measurement accuracy in small deformation measurements, and inability to measure strains induced when the object is in service and not under direct observation by the imaging system (Pan et al., 2009).

Over the past two decades, Raman spectroscopy has been used as a standard characterization tool for carbon nanostructures. Tensile or compressive stress applied to single-walled carbon nanotubes (SWCNTs) induces strains and measurably perturbs the nanotube Raman spectrum. Probing such shifts in phonon frequencies is an effective way to assess the degree of load transfer to the nanoparticle when the surrounding material is under an applied stress. In this way, Raman spectroscopy has been explored by several researchers as a method to monitor nanotube films in strain-sensing applications (Zhao et al., 2002; Li et al., 2004b; Mu et al., 2009; De la Vega et al., 2011). Raman spectroscopy has also been used to detect the strain on graphene flakes embedded in graphene−polymer composite coatings (Raju et al., 2014). However, the main drawback of Raman-based strain measurement approaches is the weakness of the Raman scattering signals. As a result, the acquisition times needed to achieve adequate signal-to-noise ratios are impractically long for real field applications.

We describe here a novel noncontact method for strain monitoring based on the spectral properties of SWCNTs. In our method, SWCNTs are unobtrusively embedded in a thin polymeric coating applied to the substrate of interest. Strain in the substrate is transmitted through the coating, deforming the embedded nanotubes and causing predictable changes in their electronic structure. These changes are detected optically, without physical contact, as strain-induced spectral shifts of the characteristic SWCNT fluorescence peaks in the near-IR spectral region. Substrate strains can be quantitatively deduced at any location on the surface and along any direction simply by positioning the excitation beam and orienting its polarization plane. The use of such coatings containing nanoscale sensors promises improved simplicity and versatility for an important tool in structural health monitoring.

15.1.1 Background

SWCNTs are a family of highly elongated tubular structures composed of carbon atoms covalently bonded into specific ordered forms. Each form has a well-defined diameter and roll-up angle, and is uniquely labeled by a pair of integers, (n,m) (Reich et al., 2004). Among the remarkable properties of SWCNTs are their well-defined spectral transitions that vary systematically with physical structure (O'Connell et al., 2002), reflecting the quantum confinement of π-electrons perpendicular to the tube axis. As shown in Figure 15.1, most SWCNT structural species are semiconducting and show
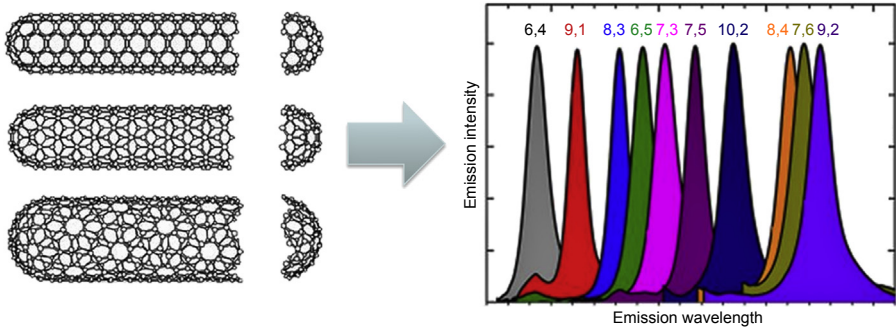
Figure 15.1 Different nanotube species correspond to different characteristic emission peaks.

robust photoluminescence (fluorescence emission) at distinct near-infrared (IR) wavelengths corresponding to their semiconducting band gaps (O'Connell et al., 2002; Weisman and Bachilo, 2003; Yang and Han, 2000).

It is known from theory and experiment that axial stretching or compression of SWCNTs causes predictable changes in electronic structure that systematically shift their spectral transitions (Yang and Han, 2000; Minot et al., 2003; Li et al., 2004a; Maki et al., 2007; Leeuw et al., 2008; Huang et al., 2008; Valavala et al., 2008). Previous studies on individual nanotubes have confirmed that these shifts occur in opposite directions for *mod 1* and *mod 2* nanotubes (for which mod($n - m$,3) = 1 or 2), as shown in Figure 15.2, and that the magnitudes of the spectral shifts are proportional to cos(3θ) (where θ is the
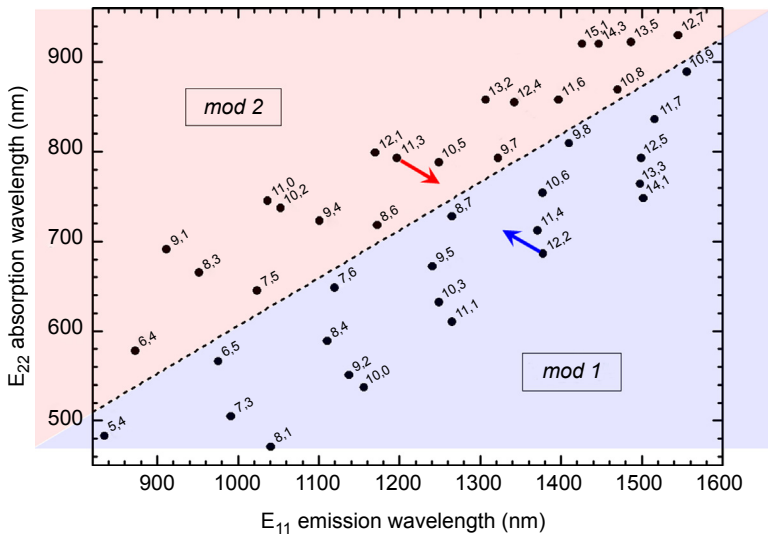
Figure 15.2 Absorption and emission peak wavelengths for various (*n,m*) SWCNT structural species. Nanotubes with *mod 1* character are in the blue (lower) shaded region; those with *mod 2* character are in the pink (upper) shaded region. The red and blue arrows show the directions of mod-dependent shifts in spectral peak positions caused by axial stretching.
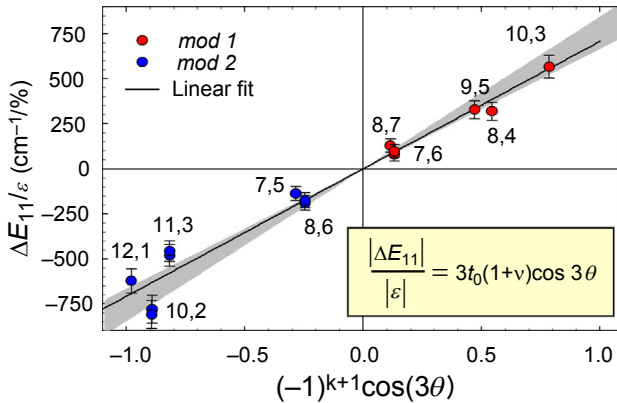
Figure 15.3 Strain-induced spectral shifts of near-IR fluorescence peaks of different (n,m) species of SWCNTs (Leeuw et al., 2008).

nanotube roll-up angle), as shown in Figure 15.3. These shifts in SWCNT fluorescence spectra are large enough to reveal axial strains below 0.1%, suggesting the possibility of a practical noncontact optical method to measure strains in large-scale objects using embedded SWCNTs as the sensors. This approach represents an attractive alternative to CNT-based sensors based on strain-induced changes in electrical transport properties or Raman spectra (Li et al., 2004b; Dharap et al., 2004; Vemuru et al., 2009; Srivastava et al., 2011) because fluorescence spectroscopy requires no electrical connections and provides stronger signals and faster data acquisition than Raman.

In the scheme that is described in this chapter, the structural surface of interest is coated with a thin polymer-based film embedded with dilute, individualized SWCNTs. If the coating adheres strongly both to the substrate and to the embedded nanotubes, then load transfer will be efficient, strain in the coating will match that of the substrate, and the embedded nanotubes will be axially deformed proportionally to the spatial projection of the coating strain along the nanotube axis. One can then quantitatively monitor the nanotube strain at any position of interest by irradiating that spot with a visible laser of suitable wavelength and capturing the resulting near-IR fluorescence for spectral interpretation.

15.2 First-generation S⁴ films (Withey et al., 2012; Sun et al., 2014)

15.2.1 Formulation, application, and mechanical testing

Raw SWCNTs from the Rice University high-pressure carbon monoxide (HiPco) reactor were added to a consumer-grade exterior varnish at a weight percent of approximately 0.02% and dispersed by ultrasonic agitation. The mixture was spin-coated several times onto a roughened poly(methyl methacrylate) (PMMA) test substrate and allowed to cure. The final coating thickness was approximately 25 μm. The

specimen was tested using a custom-built four-point bending jig, while strain was monitored by resistive foil strain gages on the S^4 film and the PMMA substrate bar. Strain values on the bar surface and in the polymer film were found to be nearly equal. We adjusted the strain in steps of 0.05% (500 με) during loading and unloading.

15.2.2 Optical strain measurement

Fluorescence of the embedded SWCNTs was excited with polarized 660 nm light from a 70 mW diode laser. As shown in Figure 15.4, the laser beam was filtered to remove near-IR components. A rotatable half-wave plate allowed adjustment of the beam's polarization plane before focusing onto the specimen. Sample fluorescence was collected by the focusing lens, reflected by a dichroic mirror, passed through a long-pass filter to block stray excitation light, and focused into a multimode optical fiber that led to a near-IR spectrometer. The multichannel InGaAs detector in the spectrometer captured the sample's full emission spectrum by integrating for a few seconds without scanning. To deduce strain, we analyzed the spectrum to find peak emission wavelengths of (7,5) and (7,6) SWCNTs in the film by fitting local Gaussian functions to their known emission bands.

15.2.3 Results and discussion

We made a series of measurements to test the feasibility of noncontact strain measurement using films with randomly oriented, structurally unsorted SWCNTs. Figure 15.5 shows typical SWCNT emission spectra measured from the specimen when unstrained and when strained in tension to 5500 με along a direction parallel to the excitation laser's polarization axis. The insets show that the peaks attributed mainly to (7,5) and (7,6) SWCNTs shift in opposite directions with strain, as expected (see Figures 15.2 and 15.3), because of their different *mod* categories. We exploited this effect by monitoring the difference between (7,6) and (7,5) peak wavelengths as the test plate was loaded and unloaded. The results (Figure 15.6) show linear dependences during loading and unloading, with an average hysteresis
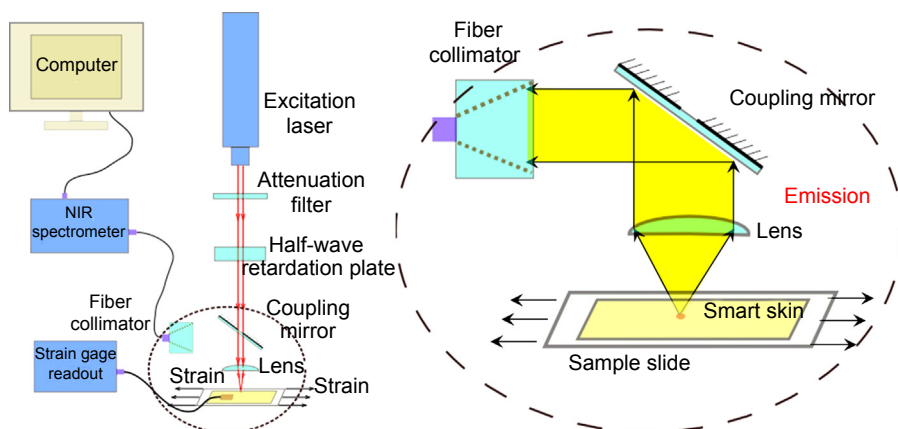
Figure 15.4 Schematic diagram of the first-generation test apparatus (Sun et al., 2014).
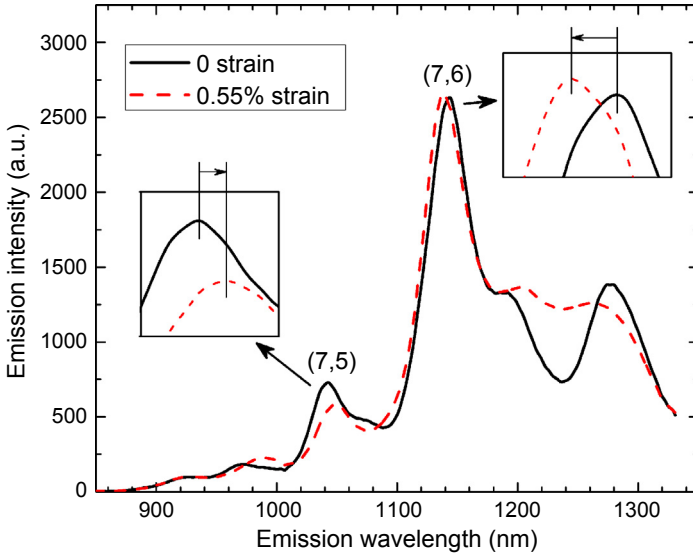
Figure 15.5 Emission spectra from an S^4 film with substrate strains of 0 (black solid line) and 5550 με (red dashed line). Insets illustrate the opposite shifts in peak positions for features dominated by (7,5) and (7,6) SWCNTs (Withey et al., 2012).
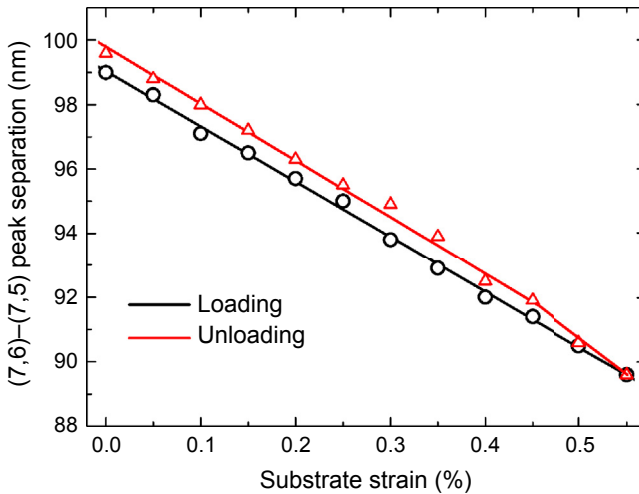
Figure 15.6 Strain variation of differential spectral shift. The difference in peak emission wavelengths of (7,6) and (7,5) nanotubes in a polymeric coating is plotted versus strain readings from a resistive strain gage on the substrate. Black circles show loading data; red triangles are subsequent unloading data. Straight lines show linear fits to the data (Withey et al., 2012).

corresponding to 400 µε on the strain axis. At high strain values, we would expect nonlinearities and large irreversible behaviors similar to those observed in single-nanotube studies, as SWCNTs may slip within the polymer film (Leeuw et al., 2008). However, we instead attribute the small uniform hysteresis seen in Figure 15.6 to mechanical relaxation of the strained polymer film.

When the S^4 film is exposed with linearly polarized light, those nanotubes aligned along the polarization axis will be selectively excited and will therefore dominate the emission spectrum, because the strongest spectral transitions of nanotubes are highly anisotropic (Miyauchi et al., 2006; Lefebvre et al., 2004; Casey et al., 2008). This should allow one to determine the strain axis by optical means. To test, we measured the dependence of the (7,6)−(7,5) peak separation on the polarization angle of the excitation laser relative to the applied strain axis, under fixed specimen strain. The resulting data (see Figure 15.7) can be fit well by the function:

$$\Delta\lambda = A\cos^2(\alpha - \alpha_0) + C \tag{15.1}$$

where α and α_0 are the laboratory angles of the laser polarization and the fixed strain axis, respectively; C is the peak separation with no strain; and A is an amplitude equal to the peak-to-valley difference in Figure 15.8. The large measured modulation amplitude confirms that our method can selectively resolve and measure strains along different directions of a substrate by polarization control.
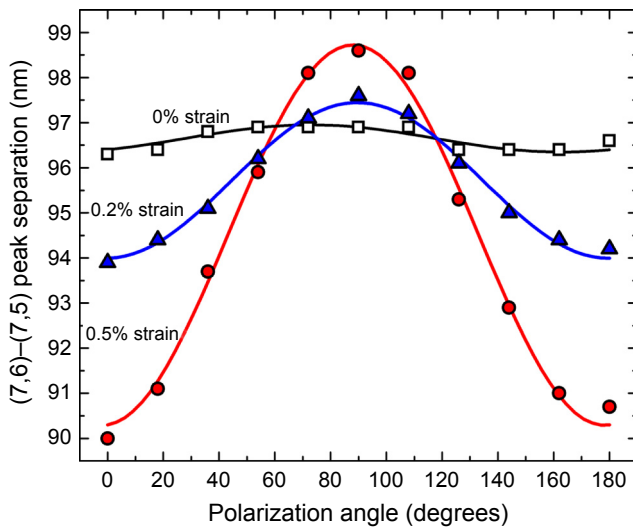
Figure 15.7 Polarization selectivity of differential spectral shift. The difference in peak emission wavelengths of (7,6) and (7,5) nanotubes in an S^4 film is plotted against the angle between the applied strain axis and the excitation laser polarization axis. Applied strain magnitudes were 0 (open squares), 2000 µε (triangles), and 5000 µε (circles). The solid curves show $\cos^2$ fits (Withey et al., 2012).
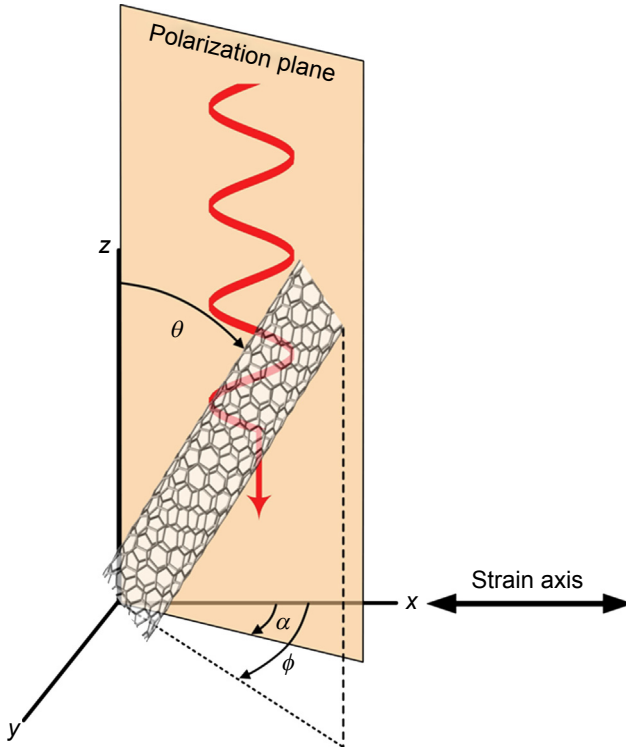
Figure 15.8 Diagram showing relevant axes and angles (Withey et al., 2012).

Properties of the polymeric film material will be important in practical implementations of this noncontact strain-sensing method. The material must be reasonably transparent for the red and near-IR wavelengths of nanotube excitation and emission, and it should not significantly quench the intrinsic fluorescence of embedded SWCNTs. It also needs to support dispersions of individualized SWCNTs, have good interfacial adhesion, and display mechanical and environmental durability. Our initial studies found that a consumer-grade polyurethane-based varnish seems to be a promising host material for S^4 films. Properties of the SWCNTs used in the film are also important. The nanotubes should be nearly pristine and unbundled to give bright near-IR fluorescence, and should have a good abundance of those specific (n,m) species used in the spectral analysis. Ideally, customized SWCNT formulations could be prepared by enriching the desired (n,m) species through advanced sorting methods such as density-gradient ultracentrifugation (Arnold et al., 2006; Ghosh et al., 2010).

Unlike our prior microscopic study of individual SWCNTs in a strained polymer (Leeuw et al., 2008), each spectral measurement on the coated test plate probes an ensemble of embedded SWCNTs that have random in-plane angles ϕ (Figure 15.8). The distribution in polar angle θ is not known a priori. In principle, it might vary from a uniform (random) distribution to a delta function at $\theta = 90°$, depending on

forces exerted on nanotubes during film curing. We can write the orientational distribution function as $f(\theta, \phi) = (1/2\pi)f(\theta)$. The relative probability that an individual SWCNT in the film (see Figure 15.8) will absorb light from a plane-polarized excitation beam propagating along the z-axis with the polarization plane intersecting the x−y plane at an angle α to the x-axis is $\sin^2(\theta)\cos^2(\phi - \alpha)$. For strain applied parallel to the x-axis, the angular dependence of Δ, the resulting spectral shift in nanotube fluorescence, will be $\Delta(\theta, \phi, \alpha) = \Delta_{max}(\cos^2\beta - \eta\sin^2\beta)$, where Δ_{max} is the shift for that (n,m) species when the strain is applied parallel to the tube axis, $\beta = \arccos(\sin\theta\cos\phi\cos\alpha + \sin\theta\sin\phi\sin\alpha)$ equals the angle between the nanotube axis and the strain axis, and η is Poisson's ratio for the host polymer. The two terms in $\Delta(\theta, \phi, \alpha)$ express nanotube axial strains caused by the host's x-axis and transverse (Poisson effect) deformations, respectively. The measured emission spectrum from each (n,m) species will actually be a superposition of peaks from nanotubes having various orientations, with corresponding variations in intensities and strain-induced spectral shifts. We can express $S(\Delta)$, the intensity-weighted distribution of spectral shifts, as

$$S(\Delta) = \int_0^{2\pi} \int_0^{\pi} f(\theta, \phi)\, \Delta(\theta, \phi, \alpha)\, \sin^2(\theta)\cos^2(\phi - \alpha)\, \sin(\theta)\mathrm{d}\theta\, \mathrm{d}\phi, \quad (15.2)$$

or

$$S(\Delta) = \frac{1}{2\pi} \int_0^{2\pi} \int_0^{\pi} f(\theta)\, \Delta(\theta, \phi, \alpha)\, \sin^3(\theta)\cos^2(\phi - \alpha)\, \mathrm{d}\theta\, \mathrm{d}\phi. \quad (15.3)$$

This describes how an ensemble of orientationally distributed SWCNTs in a strained environment gives an overall emission spectrum that is broadened and less shifted in peak position than would be observed from the same nanotubes if they were aligned parallel to the strain axis and parallel to the surface. By evaluating Eqn (15.3) using the Δ_{max} values found from theory and prior experiments and comparing the result with some other experimental data, we deduce that SWCNTs are preferentially aligned parallel to the surface, presumably through application and curing of the polymer film.

The results obtained from first-generation S[4] tests demonstrate proof-of-principle for the method. It should be feasible to measure a strain field over a wide area simply by moving the optical system to each point of interest and capturing emission spectra for several polarization settings of the excitation beam. The measurement grid can be as coarse or fine as desired, because the SWCNT sensors are present throughout the coating. To obtain absolute strain values, one can apply empirical calibrations determined for the specific strain paint formulations and application methods that were used. Of course, for real field applications, it is also necessary to have a strain reader system that is small and lightweight enough to be readily portable.

15.3   Second-generation S⁴ films (Sun et al., 2015)

In this section, we will describe more recent progress toward our noncontact optical strain measurement technology that is based on spectral shifting of SWCNT fluorescence peaks under axial strain. As was described in this chapter in our proof-of-principle demonstrations (Withey et al., 2012; Sun et al., 2014), SWCNTs are embedded in a thin polymer film that is applied to the surface of interest to give a thin "strain-sensing smart skin" or "S⁴." Surfaces might include aircraft wings and fuselages, helicopter body and rotors, building beams and columns, bridge beams and piers, pressure vessels, and pipelines. Each SWCNT in the film acts as an independent sensor, and strain can be measured anywhere on the surface by irradiating that point with an interrogating laser beam and collecting and analyzing the resulting nanotube fluorescence spectrum. The strain axis can also be found by rotating the polarization plane of the laser beam to selectively interrogate SWCNTs oriented in different directions. Furthermore, we envision the S⁴ films as multifunctional, because they may provide mechanical and chemical protection to the surface in addition to serving as strain sensors.

There are several challenges to practical implementation of the S⁴ method. One is tailoring the SWCNT composition and dispersion in the composite film to optimize the precision with which fluorescence peak positions can be found (Sun et al., 2014). Another is developing instrumentation that can efficiently generate, capture, and interpret fluorescence spectra from the S⁴ film, yet remain small and light enough for handheld field use. Progress toward both of these goals is described further in this section.

15.3.1   Second-generation smart skin formulation and application

We begin with raw Rice University HiPco SWCNT product that, in addition to the desired individualized nanotubes, contains carbonaceous and metallic impurities as well as bundled SWCNTs. For improved strain-sensing performance, this material should be processed to disaggregate the bundled SWCNTs (O'Connell et al., 2002), remove impurities, and select a subset of (n,m) structures to simplify the S⁴ fluorescence spectrum and allow more precise determination of peak wavelengths. We address these goals with a combination of selective dispersion and centrifugation.

Dispersion is achieved using the organic polymer poly(9,9-dioctylfluorenyl-2,7-diyl), or PFO, which is known to selectively coat and solubilize a small subset of SWCNT structures. We dissolve the PFO in toluene, add raw SWCNTs, apply ultrasonic agitation to disperse the nanotubes, and centrifuge to remove impurities. The supernatant then contains disaggregated, selected SWCNTs coated with PFO. Selective extraction by PFO significantly simplifies the sample's emission spectrum, as illustrated in Figure 15.9. This extract is ultrasonically mixed with a consumer-grade commercial exterior varnish under controlled conditions to obtain the composite that is applied to surfaces to form S⁴ films.

Proper application of a smooth polymeric film containing well-dispersed SWCNTs is essential for accurate strain measurements. For testing, we spin coat the composite
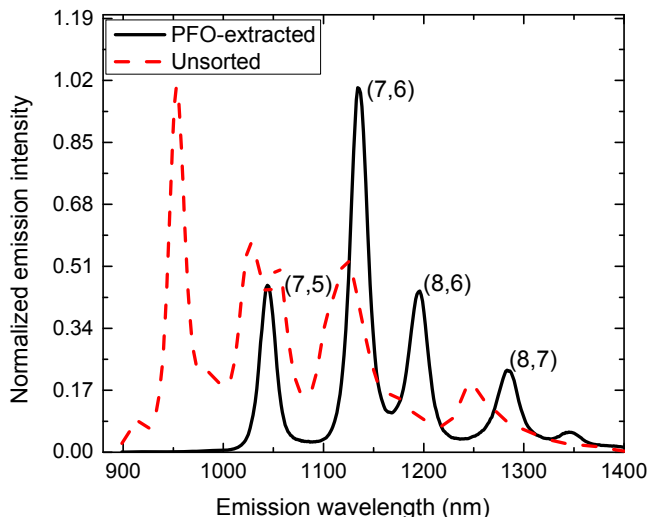
Figure 15.9 Fluorescence spectra from an unsorted dispersion of HiPco SWCNTs (red dashed line) and a HiPco sample extracted into a toluene solution of PFO (black solid line). Peaks from the PFO-extracted sample are labeled with the corresponding (*n,m*) indices (Sun et al., 2015).

containing SWCNTs, PFO, toluene, and urethane varnish onto a test bar that has been cleaned to remove organic surface contaminants. The applied film is then allowed to cure under ambient conditions. In order to increase the measured fluorescence intensities, we sometimes apply additional layers by repeating the spin-coating process, allowing several hours of room temperature curing between coats. The resulting films, shown in Figure 15.10, are typically c. 15—20 μm thick. Figure 15.11 shows short-wave IR (SWIR) fluorescence microscope images of such S^4 films. The right-panel image illustrates the excellent dispersion and individualization that can be achieved using
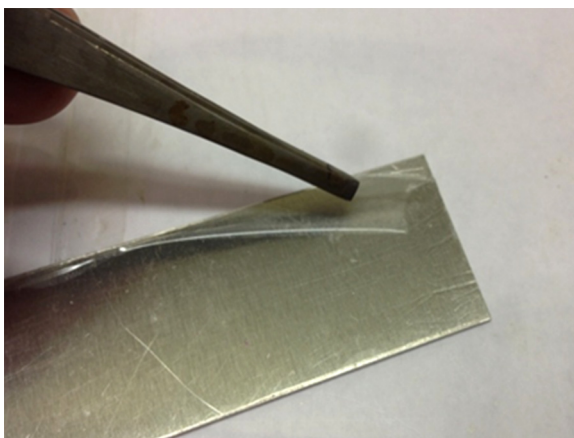
Figure 15.10 S^4 film on a steel test plate (Sun et al., 2015).
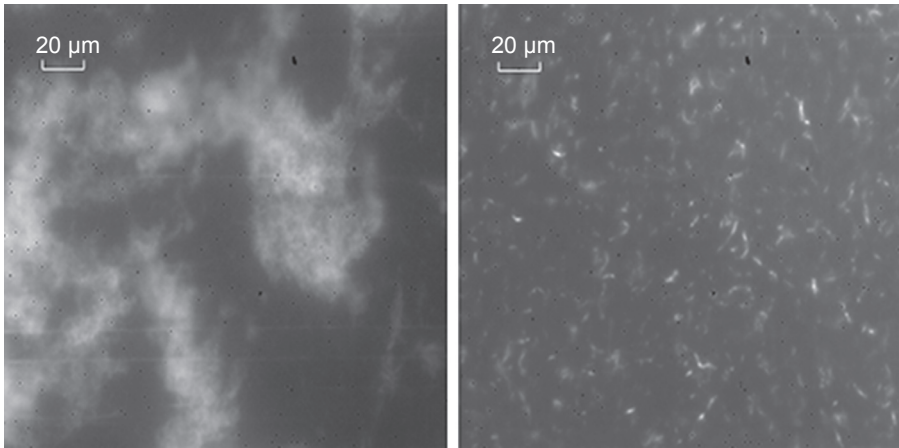
Figure 15.11 Short-wave IR fluorescence microscopy images of smart skin films. The left frame shows unevenly dispersed SWCNTs (unsorted) in PMMA; the right frame shows well-dispersed, randomly oriented SWCNTs (PFO-extracted) in urethane (Sun et al., 2015).

the PFO-based protocol described here. Industrial scale use of the S^4 method will, of course, need to rely on application methods such as brush or spray coating.

15.3.2   Second-generation S^4 measurements

Figure 15.12 shows the schematic diagram of our second-generation optical strain reader. A compact diode laser emitting at 660 nm provides light that efficiently excites
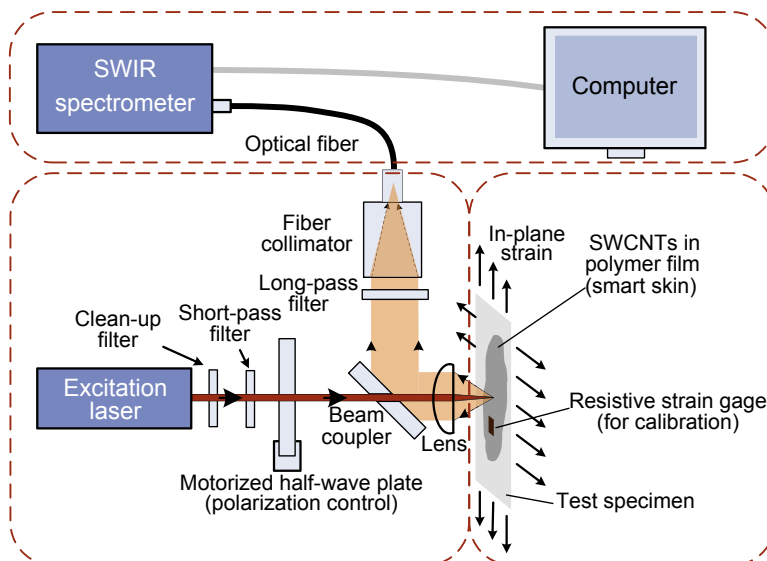
Figure 15.12 Schematic diagram of prototype S^4 strain probe (Sun et al., 2015).

(7,5) and (7,6) SWCNT structures, which are among those extracted by PFO. The laser beam passes through a short-pass filter and a half-wave retardation plate on a computer-controlled polar rotation mount that allows automated adjustment of its polarization plane. Then the excitation beam passes through a small hole in a coupling mirror before being focused onto the sample by an aspheric lens. Fluorescence emitted from the S^4 film is captured and collimated by the same aspheric lens. It is then reflected by the coupling mirror into a fiber collimator that focuses into an optical fiber leading to a spectrometer designed for sensitive multichannel detection of near-IR spectra. The footprint of our second-generation optical reader is only $4 \times 6''$ (102×152 mm), not including the relatively small spectrometer module. It therefore seems clear that optical strain readers can be made compact and light enough for hand-held field use (as shown in Fig 15.13).

To make calibrated S^4 performance tests on PMMA test specimens, we use reference readings from two conventional resistive foil strain gages: one bonded on top of the S^4 film close to the optical measurement point, and the other mounted at the corresponding location on the opposite surface of the specimen bar. Readings from those two strain gages are compared in real time to check the efficiency of load transfer from substrate to polymer. We find that for S^4 films thinner than c. 20 μm, the applied strains measured on the opposite surface of the bar nearly match the strains measured at the surface of the film.

We determined the fluorescence peak positions from (7,5), (7,6), and (8,6) SWCNTs in S^4 films by fitting separate local Gaussian functions to the emission peaks near 1050, 1140, and 1200 nm, as illustrated in Figures 15.14 and 15.15. This fitting is more reliable and precise than with first-generation S^4 films because SWCNT samples selectively extracted with PFO give far simpler emission spectra.

Resolution is one key factor defining the performance of a sensor system. Strain resolution is the smallest measurable change in strain, and in our S^4 method it is

(a) (b)
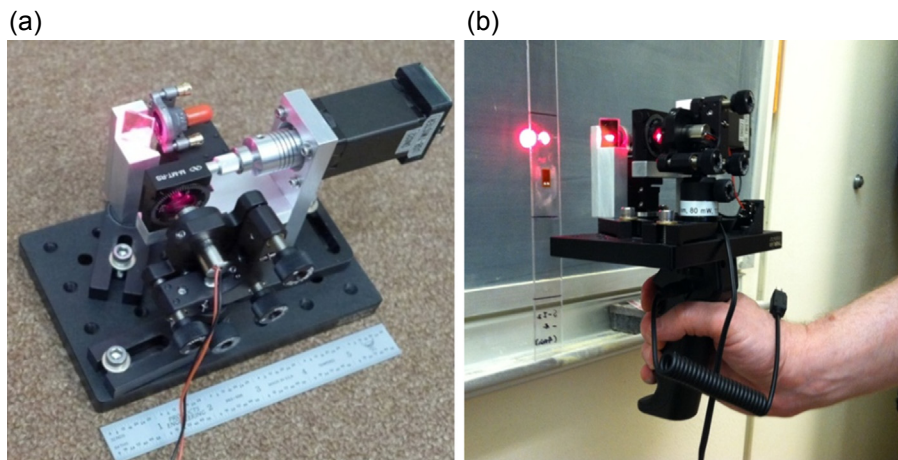
Figure 15.13 Photographs of the prototype second-generation S^4 strain probe head: (a) Probe head on its $4 \times 6''$ base; and (b) probe head with handle (Sun et al., 2015).
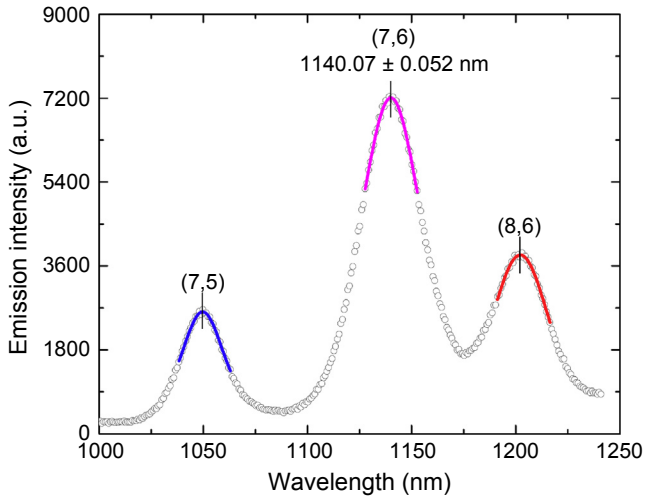
Figure 15.14 Fluorescence spectrum from a second-generation S^4 film made with sorted SWCNTs. Note the high precision with which peak positions can be found by curve fitting (Sun et al., 2015).
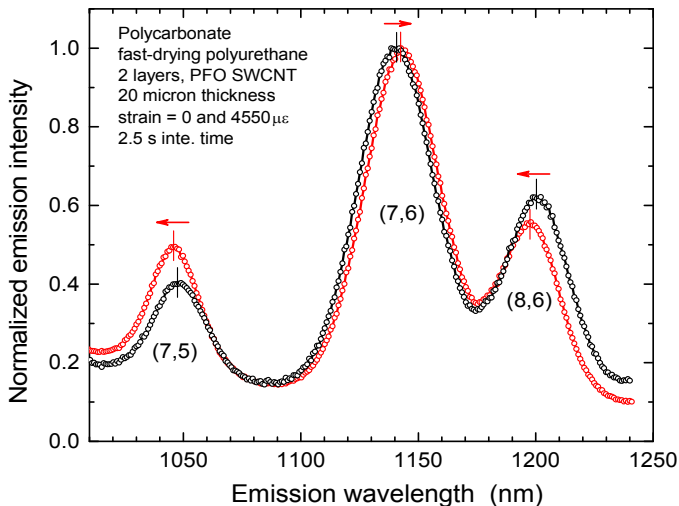
Figure 15.15 Strain-induced spectral shifts in SWCNT fluorescence spectra from a second-generation S^4 film (Sun et al., 2015).

determined with precision by measuring fluorescence peak wavelengths. This is in turn controlled by the spectral resolution of the spectrometer, the spectral width of the fluorescence peak, and the signal-to-noise ratio of the measured spectrum. Because our spectrometer's resolution of 2 nm is significantly sharper than the width of SWCNT fluorescence features, spectral resolution is not a limiting factor for resolution. The signal-to-noise ratio depends on excitation laser intensity, SWCNT

concentration in the film, SWCNT fluorescence quantum yield, optical collection efficiency, detector sensitivity and noise, data acquisition time, and data averaging. For the dominant (7,6) peak, we find that approximately 20 s of data acquisition from a typical S^4 film allows us to determine the peak wavelength with a standard deviation near 0.052 nm. The theoretically predicted (7,6) strain coefficient (slope of peak position with strain $\frac{d\lambda_{(7,6)}}{d\varepsilon}$), is approximately 1.2 nm/mε, predicting a standard deviation in strain measurement of c. 45 με. Actual strain uncertainties can exceed this value because the effective strain coefficient of an ensemble of randomly oriented SWCNTs is smaller than that of a single aligned nanotube, and slippage of nanotubes within the polymer film can also reduce the coefficient. However, one can improve strain resolution by combining peak position measurements from different SWCNT (n,m) structures, because the strain coefficients have signs and magnitudes that depend on (n,m). For example, we generally monitor the difference between the (7,5) and (7,6) peak positions, which has a predicted net coefficient of 3.5 nm/mε, or nearly three times that of (7,6) alone. The spatial resolution, or gage length, of the S^4 method is intrinsically small because it equals the diameter of the excitation beam at the film surface. This dimension is normally approximately 0.1 mm, but with tighter focusing it can readily be reduced to a few micrometers, if necessary. On the other hand, the gage length can be increased as needed by scanning the laser probe over the desired range during the period of spectral acquisition to obtain a spatially averaged strain value.

For testing, we subjected PMMA specimens coated with the second-generation SWCNT smart skin to tensile deformation over the strain range from 0 to 1500 με using a custom-built four-point bending jig. Figure 15.16 shows the sequence of applied
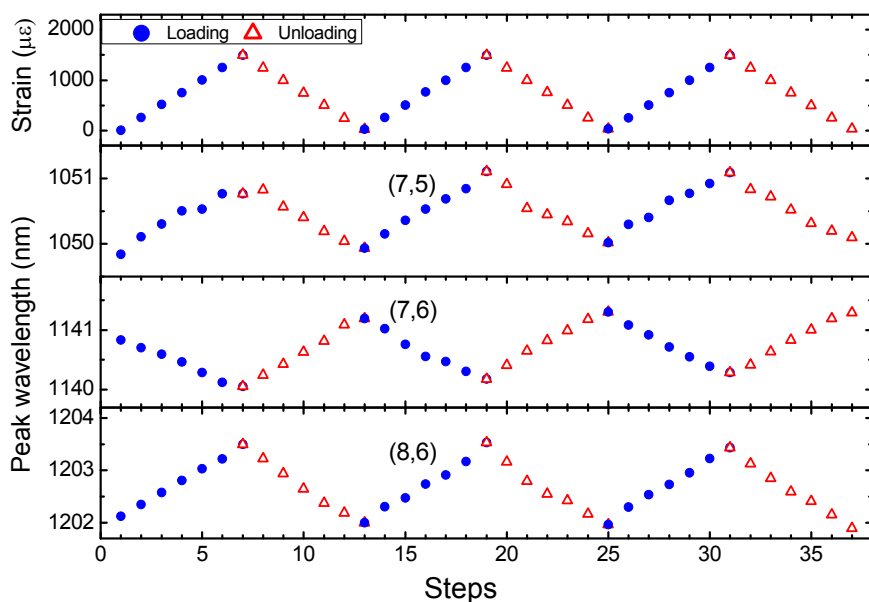
Figure 15.16 Response of SWCNT peak positions to cyclic tensile strain in specimen (Sun et al., 2015).

deformations and the resulting changes in three spectral peak positions. We observe that the (7,5), (7,6), and (8,6) peaks shifted systematically with the applied strain, thus confirming efficient and reversible load transfer from the PMMA bar to the polymeric coating to the embedded SWCNTs.

The spectral peak positions are plotted as a function of tensile strain in Figure 15.17. This figure omits data from the first cycle, in which there is apparently some relaxation of initial nanotube strains induced by shrinkage forces during curing of the S^4 film. The observed strain coefficient for the (7,5)−(7,6) peak separation for loading and unloading curves is less than the theoretical prediction for nanotubes aligned with the strain axis. We attribute this to the random distribution of SWCNT orientations in the film and some slippage of nanotubes in the polymer host because of imperfect adhesion.
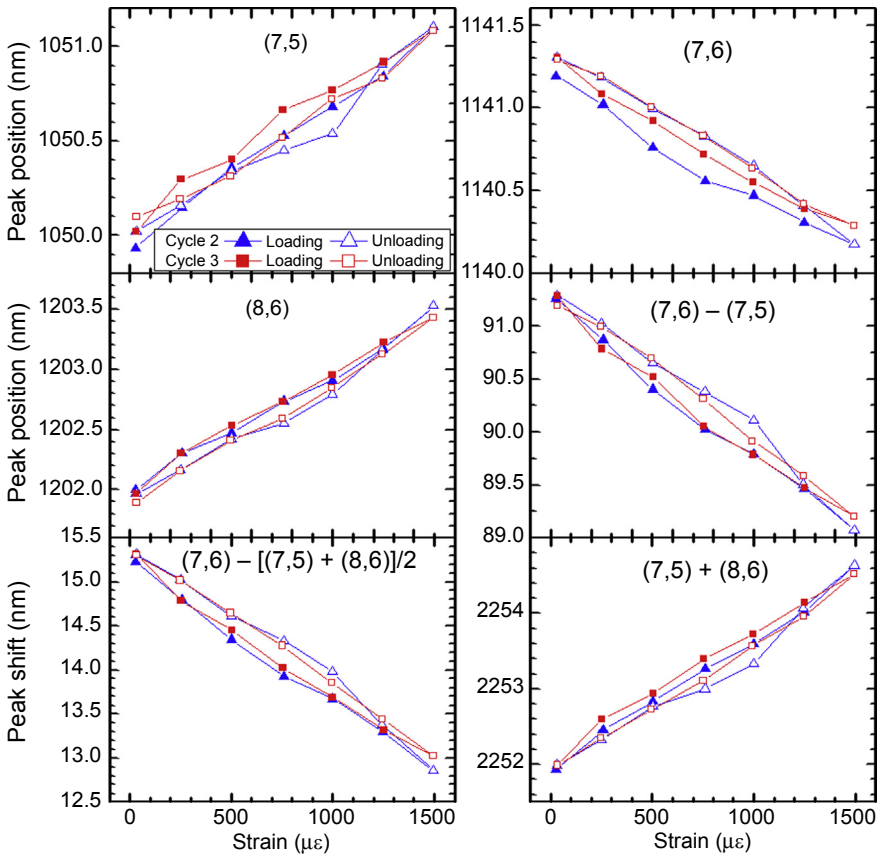
Figure 15.17 SWCNT peak positions and shifts versus tensile strain on specimen (Sun et al., 2015).
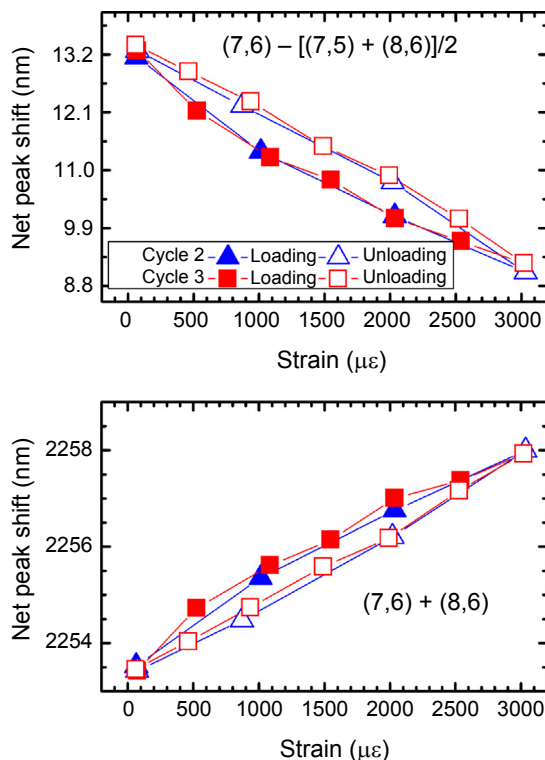
Figure 15.18 Combinations of SWCNT peak positions versus tensile strain on specimen. The spectral peaks used for each frame are listed. Data for the first cycle have been omitted for the same reason as described in the text for Figure 15.17 (Sun et al., 2015).

As the test specimen underwent deformation cycles with strains up to 3000 µε, the loading and unloading curves diverged, leading to a visible hysteresis loop (see Figure 15.18). We hypothesize that this reflects molecular-level damage at the nanotube−polymer interface in the smart skin. Further investigations on this subject are needed.

Figure 15.19 shows the spectral response of the three major SWCNT peaks during cyclic tensile deformation. Apart from relaxation processes in the first cycle, our data suggest that the coating shows nearly elastic deformation behavior. The zero-strain peak positions for the remaining eight cycles agree closely, suggesting no further relaxation of residual strain. The downward drift of the (8,6) peak position at 5000 µε during the first five loading−unloading cycles is likely due to further relaxation of initial strains and friction at the interface between the polymer and nanotube. However, the drift appears to stabilize after the fifth cycle. Further optimization of the S^4 film formulation and application may reduce the observed drift effects.
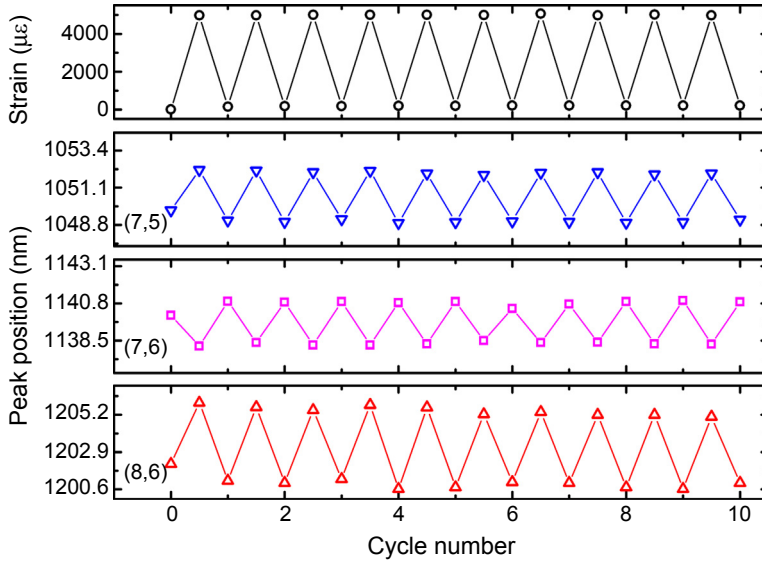
Figure 15.19 Response of SWCNT peak positions to cyclic tensile strain from 0 to 5000 με in an S^4-coated PMMA specimen (Sun et al., 2015).
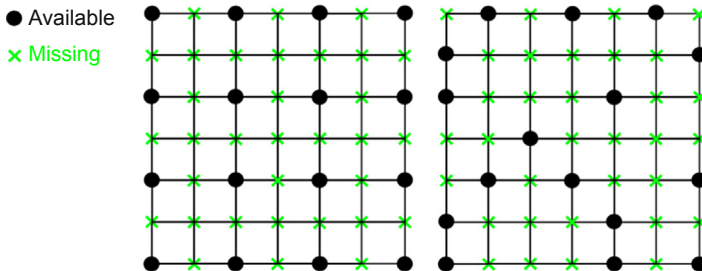
Figure 15.20 The uniform undersampling method (left); and the random undersampling method (right).

15.4 Damage detection strategy

A major application of the S^4 method in structural health monitoring will be to find localized damage in surfaces of interest. This involves constructing a surface strain map based on many sequential strain measurements made individually at different positions on the surface. To minimize the time and effort of inspections, it is therefore important to be able to find localized damage with as few strain measurements as possible. In this section, we describe a multiscale computational scheme for rapid detection of damage from a full two-dimensional (2D) strain map that has been deduced from a sparse (highly undersampled) set of randomly positioned strain measurements. Figure 15.20 illustrates the difference between uniform and random undersampling. This process involves an ill-posed (not well-defined) inverse mathematical

problem without an analytical solution; it is necessary for us to infer the whole matrix and detect irregularity from only relatively few randomly distributed measurements.

Starting with implicit knowledge of the data structure of the strain matrix, we make a general mathematical assumption that the matrix is low rank. Then, we can use optimization methods to recover a matrix that is as low rank as possible, while being consistent with the available measurements, to approach the original (true) strain matrix. The strategy developed exploits the intrinsic data structure of the true strain field: typically, it is highly correlated without many edges and hence has a low-rank structure, unless damage (manifested as sparse innovation in the 2D measurement) occurs and destroys the low-rank structure. Therefore, taking advantage of the implicit low-rank structure, the new theory of matrix completion enables global recovery of the full measurement from few randomly sampled (strain) measurements. The recovered strain field measurement is further decomposed, by principal component pursuit, into a superposition of a low-rank background component and a sparse innovation component. This isolates the region of local damage, which can then be probed with finer spatial resolution in subsequent measurements.

When acquiring strain data in order to detect damage, one strategy (global random sampling) is to use as few measurement points as possible to speed the inspection process. If no damage is detected with high undersampling, one would then make additional measurements at positions selected randomly (nonbiased sampling) from the remaining region of the whole structure, until the density of measured points is sufficient to detect any damage region that may be present. This type of iterative procedure can be implemented automatically.

A preferred alternative strategy involves local or biased sampling. Because damage is a local, sparse phenomenon, if the first iteration with a high undersampling factor or very few measurements identifies a suspect damage region, then further measurements are made only within the suspect region until the damage is well localized. In practice, such an alternative procedure requires an expert to pick the suspect damage region at the first iteration, while the rest of the steps can be automatically implemented. Figure 15.21 schematically illustrates these two different iterative schemes, and
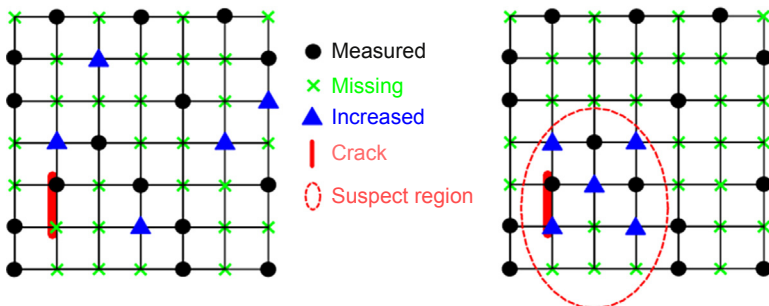
Figure 15.21 The iterative procedure by increasing the random measurements to improve the damage detection accuracy: (left) Global random sampling to additionally increase measurements; and (right) local random sampling to additionally increase measurement only within the suspect damage region, which is picked at the first iteration.
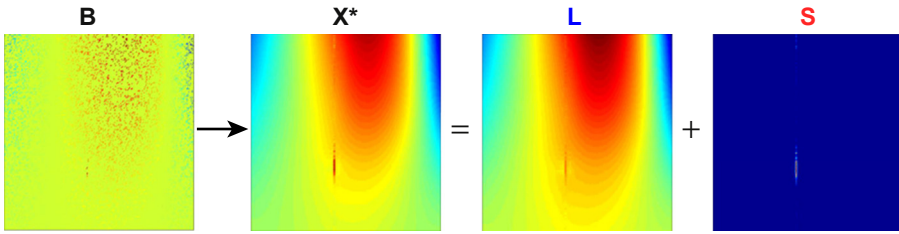
Figure 15.22 The computational framework of the proposed two-step damage detection method using a set of partial random strain measurements (the strains at nonsampled positions are shown as light green). The first step, matrix completion, recovers the full matrix; and the second step, low-rank plus sparse decomposition, separates into a superposition of a low-rank background component plus a sparse innovation component that indicates damage.
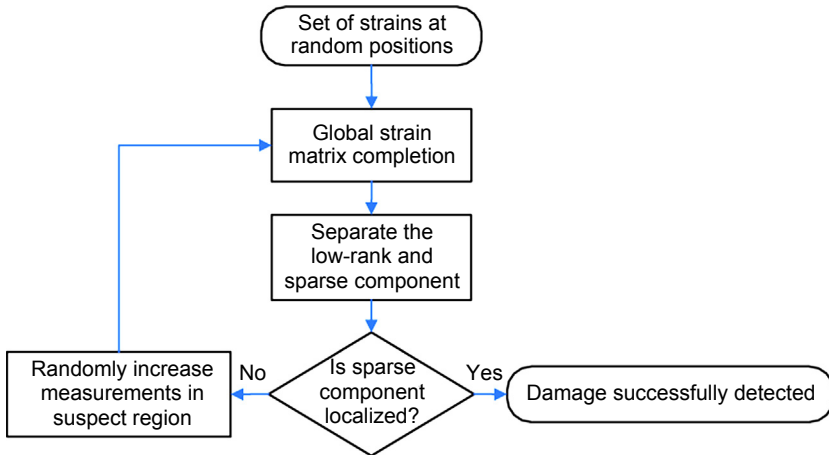
Figure 15.23 The flowchart implementing the iterative procedure of the proposed damage detection method using partial random strain measurements and a two-step computational framework.

Figure 15.22 and Figure 15.23 illustrate the computational framework and the flowchart of the proposed damage detection method, respectively.

Our new scheme is based on the implicit sparse and low-rank data structure of the strain field (2D) measurement. The advantages of the method are that it is purely data-driven without using any model or prior knowledge with regard to the structure; it is implemented blindly, without relying on operator expertise; and it executes efficiently (usually within a very few seconds).

15.5 Conclusions and outlook

In this chapter, we have described our progress toward the practical implementation of a novel noncontact optical strain measurement method that uses CNTs in polymeric

films as nanoscale sensors. Strain can be measured anywhere on the surface by irradiating that point with an interrogating laser beam and collecting and analyzing the resulting nanotube fluorescence spectrum. The strain axis can also be found by rotating the polarization plane of the laser beam to selectively interrogate SWCNTs oriented in different directions. Our first-generation smart skin composite ("S^4") was prepared by dispersing raw SWCNTs into commercial polyurethane varnish. Promising results obtained with this material led to the development of a second-generation composite in which the SWCNTs were preprocessed by structural selection and purification. Second-generation S^4 films display strong, well-structured fluorescence spectra that allow improved optical strain determinations. Test results show promising repeatability for the S^4 method, although distortions from imperfect interfacial adhesion between polymer film and SWCNTs can be seen, especially at higher strain levels. We expect that the fidelity of these optical strain measurements will improve as further refinements are made in the formulation and application of the composite films. We also described a multiscale computational scheme intended to improve the efficiency of detecting damaged regions on surfaces. The scheme exploits the implicit data structure of the 2D strain map and can be implemented for automated damage detection using a small number of local strain measurements. We expect that noncontact optical strain measurement using SWCNT smart skins will evolve into a robust technology with widespread practical applications.

References

Ajovalasit, A., Petrucci, G., Scafidi, M., 2010. RGB photoelasticity: review and improvements. Strain 46 (2), 137−147. Available at: http://onlinelibrary.wiley.com/doi/10.1111/j.1475-1305.2008.00571.x/abstract (accessed 18.02.15.).

Arnold, M.S., et al., October 2006. Sorting carbon nanotubes by electronic structure using density differentiation. Nature Nanotechnology 1, 60−65.

Casey, J.P., et al., 2008. Chirality-resolved length analysis of single-walled carbon nanotube samples through shear-aligned photoluminescence anisotropy. ACS Nano 2 (8), 1738−1746.

De la Vega, A., et al., 2011. Simultaneous global and local strain sensing in SWCNT−epoxy composites by Raman and impedance spectroscopy. Composites Science and Technology 71 (2), 160−166. Available at: http://linkinghub.elsevier.com/retrieve/pii/S0266353810004239 (accessed 18.02.15.).

Dharap, P., et al., 2004. Nanotube film based on single-wall carbon nanotubes for strain sensing. Nanotechnology 15 (3), 379−382. Available at: http://stacks.iop.org/0957-4484/15/i=3/a=026?key=crossref.9ff9fe25ca793555c85d976f863a8924 (accessed 18.02.15.).

Germaneau, A., Doumalin, P., Dupré, J.-C., 2008. Comparison between X-ray micro-computed tomography and optical scanning tomography for full 3D strain measurement by digital volume correlation. NDT and E International 41 (6), 407−415. Available at: http://linkinghub.elsevier.com/retrieve/pii/S0963869508000339 (accessed 18.02.15.).

Ghosh, S., Bachilo, S.M., Weisman, R.B., 2010. Advanced sorting of single-walled carbon nanotubes by nonlinear density-gradient ultracentrifugation. Nature Nanotechnology 5 (6), 443−450. Available at: http://dx.doi.org/10.1038/nnano.2010.68.

Goldrein, H., Palmer, S., Huntley, J., 1995. Automated fine grid technique for measurement of large-strain deformation maps. Optics and Lasers in Engineering 23 (195), 305−318. Available at: http://www.sciencedirect.com/science/article/pii/014381669500036N (accessed 18.02.15.).

Hamada, S., et al., 2014. Strain mapping with high spatial resolution across a wide observation range by digital image correlation on plastic replicas. Materials Characterization 98, 140−146. Available at: http://linkinghub.elsevier.com/retrieve/pii/S1044580314003027 (accessed 21.01.15.).

Hill, K., Meltz, G., 1997. Fiber Bragg grating technology fundamentals and overview. Journal of Lightwave Technology 15 (8), 1263−1276. Available at: http://132.248.12.175/jhcordero/ Cursos/Facultad_Ingenieria/Articulos/fiber_gratings_fundamentals.pdf (accessed 18.02.15.).

Huang, M., et al., April 2008. Direct measurement of strain-induced changes in the band structure of carbon nanotubes. Physical Review Letters 100, 1−4.

Leeuw, T.K., et al., 2008. Strain measurements on individual single-walled carbon nanotubes in a polymer host: structure-dependent spectral shifts and load transfer. Nano Letters 8 (3), 826−831. Available at: http://www.ncbi.nlm.nih.gov/pubmed/18298093.

Lefebvre, J., et al., 2004. Photoluminescence from an individual single-walled carbon nanotube. Physical Review B 69, 1−5.

Li, L.-J., et al., October 2004a. Chirality assignment of single-walled carbon nanotubes with strain. Physical Review Letters 93, 6−9. Available at: http://link.aps.org/doi/10.1103/ PhysRevLett.93.156104.

Li, Z., et al., 2004b. Carbon nanotube film sensors. Advanced Materials 16 (7), 640−643. Available at: http://doi.wiley.com/10.1002/adma.200306310 (accessed 18.02.15.).

Maki, H., Sato, T., Ishibashi, K., 2007. Direct observation of the deformation and the band gap change from an individual single-walled carbon nanotube under uniaxial strain. Nano Letters 7, 890−895.

Minot, E.D., et al., April 2003. Tuning carbon nanotube band gaps with strain. Physical Review Letters 90, 156401.

Miyauchi, Y., Oba, M., Maruyama, S., 2006. Cross-polarized optical absorption of single-walled nanotubes by polarized photoluminescence excitation spectroscopy. Physical Review B − Condensed Matter and Materials Physics 74, 1−6.

Mu, M., et al., 2009. An in situ Raman spectroscopy study of stress transfer between carbon nanotubes and polymer. Nanotechnology 20 (33), 335703. Available at: http://www.ncbi. nlm.nih.gov/pubmed/19636105 (accessed 18.02.15.).

Myers, D., 2010. MEMS Resonant Strain Sensor Integration. University of California, Berkeley. Available at: https://escholarship.org/uc/item/11v8j97m.pdf (accessed 18.02.15.).

O'Connell, M.J., et al., 2002. Band gap fluorescence from individual single-walled carbon nanotubes. Science 297 (5581), 593−596.

Obitayo, W., Liu, T., 2012. A review: carbon nanotube-based piezoresistive strain sensors. Journal of Sensors 2012, 1−15. Available at: http://www.hindawi.com/journals/js/2012/ 652438/ (accessed 02.02.14.).

Pan, B., et al., 2009. Two-dimensional digital image correlation for in-plane displacement and strain measurement: a review. Measurement Science and Technology 20 (6), 062001. Available at: http://stacks.iop.org/0957-0233/20/i=6/a=062001?key=crossref.37cf26a6947e54eb5498e6 7742a4e2ad (accessed 23.01.14.).

Pan, B., 2007. Full-field strain measurement using a two-dimensional Savitzky-Golay digital differentiator in digital image correlation. Optical Engineering 46 (3), 033601. Available at: http://opticalengineering.spiedigitallibrary.org/article.aspx?doi=10.1117/1.2714926 (accessed 13.02.14.).

Peng, S., Cho, K., 2000. Chemical control of nanotube electronics. Nanotechnology 11 (2), 57. Available at: http://iopscience.iop.org/0957-4484/11/2/303 (accessed 18.02.15.).

Raju, A.P.A., et al., 2014. Wide-area strain sensors based upon graphene-polymer composite coatings probed by Raman spectroscopy. Advanced Functional Materials 24 (19), 2865−2874. Available at: http://doi.wiley.com/10.1002/adfm.201302869 (accessed 11.02.15.).

Reich, S., Thomsen, C., Maultzsch, J., 2004. Carbon Nanotubes: Basic Concepts and Physical Properties. Wiley-VCH, Weinheim.

Srivastava, R.K., et al., 2011. The strain sensing and thermal-mechanical behavior of flexible multi-walled carbon nanotube/polystyrene composite films. Carbon 49 (12), 3928−3936. Available at: http://dx.doi.org/10.1016/j.carbon.2011.05.031.

Sun, P., et al., 2014. "Smart Skin" optical strain sensor using single wall carbon nanotubes. In: Lynch, J.P., Wang, K.-W., Sohn, H. (Eds.), SPIE 9061, Sensors and Smart Structures Technologies for Civil, Mechanical, and Aerospace Systems. San Diego, USA, pp. 906113−906120. Available at: http://dx.doi.org/10.1117/12.2046539.

Sun, P., et al., 2015. Carbon nanotubes as non-contact optical strain sensors in smart skins. The Journal of Strain Analysis for Engineering Design 1−8. Available at: http://sdj.sagepub.com/lookup/doi/10.1177/0309324715597414.

Valavala, P.K., et al., 2008. Self-consistent calculations of strain-induced band gap changes in semiconducting (n,0) carbon nanotubes. Physical Review B − Condensed Matter and Materials Physics 78, 1−6.

Vemuru, S.M., et al., 2009. Strain sensing using a multiwalled carbon nanotube film. The Journal of Strain Analysis for Engineering Design 44, 555−562.

Weisman, R., Bachilo, S., 2003. Dependence of optical transition energies on structure for single-walled carbon nanotubes in aqueous suspension: an empirical Kataura plot. Nano Letters 3 (9), 1235−1238. Available at: http://pubs.acs.org/doi/abs/10.1021/nl034428i (accessed 30.01.14.).

Withey, P.A., et al., 2012. Strain paint: noncontact strain measurement using single-walled carbon nanotube composite coatings. Nano Letters 12 (7), 3497−3500. Available at: http://www.ncbi.nlm.nih.gov/pubmed/22694748.

Yang, L., Han, J., 2000. Electronic structure of deformed carbon nanotubes. Physical Review Letters 85 (1), 154−157.

Yong, Y., 2013. A novel piezoelectric strain sensor for simultaneous damping and tracking control of a high-speed nanopositioner. IEEE/ASME Transactions 18 (3), 1113−1121. Available at: http://ieeexplore.ieee.org/xpls/abs_all.jsp?arnumber=6202343 (accessed 18.02.15.).

Zhao, Q., Frogley, M.D., Wagner, H.D., 2002. Direction-sensitive strain-mapping with carbon nanotube sensors. Composites Science and Technology 62 (1), 147−150. Available at: http://linkinghub.elsevier.com/retrieve/pii/S0266353801001877.

Future trends and directions

16

Kenneth J. Loh [1,2], Satish Nagarajaiah [3]
[1]University of California-Davis, Davis, CA, USA; [2]University of California-San Diego, La Jolla, CA, USA; [3]Rice University, Houston, TX, USA

16.1   Summary

This book summarizes some of the latest mainstream research efforts toward the applications of nanotechnology for the development of advanced materials for civil, construction, and structural engineering. The goal is to transition conventional civil engineering materials (whose main purpose is to bear and resist loads) to create next-generation multifunctional nanocomposites that incorporate properties such as sensing, damage tolerance, and deicing, among many others. Of particular interest is how nanotechnology, specifically nanomaterials, can be incorporated and effectively used for elucidating multiple engineering functionalities in civil engineering materials such as cementitious composites and pavements.

The book is not meant to be an exhaustive literature review of the subject matter, but instead focuses on showcasing the diversity and breadth of this multidisciplinary field that intersects civil engineering, materials science, chemistry, electrical engineering, and construction practices. A large body of work presented in this book is aimed at incorporating nanomaterials such as nanotubes, nanofibers, and nanoparticles during the construction of infrastructure materials. For example, carbon nanotubes have been used extensively as conductive additives for cementitious composites. An objective of mixing these conductive additives is to enhance the electrical properties of the pristine cement paste, mortar, and/or concrete and to enable self-sensing. In doing so, one could measure changes in the material's electrical properties and correlate them to structural damage, thereby enabling in situ structural health monitoring.

Besides modifying the design of construction materials, another emerging approach is to design nanocomposite coatings or nanofilms that can be applied onto or embedded underneath structural surfaces. Part III of this book starts with some of the earliest developments in this area with the discussion of surface-mounted strain sensors based on carbon nanotube—based buckypapers. Since then, others have advanced manufacturing techniques to allow for large-scale deposition of these nanofilms onto a variety of different structural surfaces. Damage detection and localization using these films are also possible.

16.2   Future trends

Despite these aforementioned recent advances in multifunctional nanocomposites for civil and structural engineering, several grand challenges still need to be resolved before these innovative materials can be adopted for practice. The first grand challenge is scalability—how can nanomaterials be effectively incorporated at reasonable amounts and costs so that the desired material attribute is achieved without sacrificing the original properties of the pristine host material? For example, much research conducted on smart cementitious composites requires the use of 0.1−0.5% carbon nanotubes by weight of cement. Assuming that 1 m^3 of concrete requires at least 250 kg of cement and that multiwalled carbon nanotubes (MWNTs) cost $1000/kg, this amounts to $1250 additional costs for a 1 m^3 batch of 0.5% (MWNT-based) smart concrete. Thus, more effective techniques (e.g., by modifying the composite's cement− aggregate interface with nanomaterials or nanofilms) are direly needed.

The second grand challenge is multifunctionality—how can one encode specific engineering functionalities or material properties? The majority of research today has shown that cementitious composites, asphalt, and even fiber-reinforced polymer composites can be engineered to possess self-sensing capabilities and/or improved mechanical properties. However, research is needed for investigating how other functionalities can be incorporated, such as for sensing chloride ingress (for corrosion monitoring), self-healing, energy dissipation, and/or power harvesting, among others. Similar to the previous grand challenge, achieving these functionalities should not come at the cost of the other desirable attributes of civil engineering materials.

Lastly, when these advanced nanoengineered materials are ready for large-scale validation or real-world implementation, their construction procedures need to be addressed. Unlike small-scale specimens that are fabricated in highly controlled laboratory environments and with very specialized equipment, these conditions are not available (or practical) when multifunctional nanocomposites are casted in the field. As such, these innovative materials need to be designed within the framework of acceptable construction practices. Either current construction practices can continue to be used or only slight (and low-cost) modifications are necessary.

Index